

# **BOND BEHAVIOUR OF FRP BARS IN CONCRETE**

A thesis submitted for the degree of Doctor of Philosophy  
in the Faculty of Engineering of the University of Sheffield

**by**

**Zenon Achillides**

**Dipl. Eng (NTU Athens)**

**Centre for Cement and Concrete**

**Department of Civil and Structural Engineering**

**The University of Sheffield**

**July 1998**

*To my wife for her support and patience  
and to my parents for their encouragement*

# ABSTRACT

This thesis investigates the bond behaviour of Fibre Reinforced Polymer (FRP) reinforcing bars in concrete elements both analytically and experimentally.

Two series of experiments were conducted. In the first series, more than 100 cube specimens were tested in direct pullout. The mode of bond failure of FRP bars in the pullout tests was found in most cases to differ substantially from that of deformed steel bars. Within this series the parameters that influence bond development were examined. The bond strengths developed by CFRP and GFRP bars appear to be very similar, and just below what is expected from deformed steel bars.

In the second series of experiments, nine beams were tested in four-point bending to examine the bond splitting behaviour of FRP single anchorages and splices. CFRP bars develop higher bond splitting strength than respective GFRP bars, which contradicts the findings of pullout tests. The lower elastic modulus of GFRP bars is thought to play an important role to their lower bond splitting strength. For this reason, the suitability of the cube tests for measuring the bond strength of FRP bars for practical purposes is questioned. Spliced bars appear to develop similar bond splitting strength to single bar anchorages. The distribution of bond stresses along the anchorage length and the effect of flexural cracks on the bond development were also examined. The thesis also discuss other parameters that influence bond splitting such as transverse reinforcement, concrete cover, and support action.

An analytical study was conducted to enhance further the understanding of the bond behaviour of FRP bars. Both the pullout and beam tests were modelled by using FE packages. Non-linear springs describing the bond behaviour of short embedment lengths were chosen and used for predicting the behaviour of longer embedments. The influence of flexural cracking was also considered in the case of beams. The analytical results showed a good correlation with the respective experimental.

Finally, some important issues regarding the design of anchorage lengths for FRP reinforcing bars were addressed and a method of working towards the formulation of design recommendations is suggested.

# ACKNOWLEDGEMENTS

I would like to express my deepest gratitude to my supervisor and friend, Dr. Kypros Pilakoutas for his continuous support and inspiration during this project. His lateral thinking and guidance had help me overcome successfully any obstacles found in this project.

I would like also to thank Professor Peter Waldron for his overall supervision of my work and his valuable guidance towards the completion of this project.

Having worked in the laboratories I have made many friends to whom I am indebted for their expert technical support. I thank particular:

- My special friend and EUROCRETE technician Jose Garcia whose help and patience during my long hours in the laboratories was invaluable.
- The supervisors of the laboratory Shawn Waters and Shane Smith for their expert technical support and co-operation.
- The technicians Roger Grace, Jonathan Wood and Andy Marshall who provided me with their technical support when I mostly needed it.

Finally, I would like to acknowledge the technical and financial assistance offered by the Centre for Cement and Concrete of the University of Sheffield, the EUROCRETE project and the CONFIBRECRETE network.

# TABLE OF CONTENTS

|   |            |
|---|------------|
| <b>ABSTRACT</b>   | <b>I</b>   |
| <b>ACKNOWLEDGEMENTS</b>   | <b>II</b>  |
| <b>TABLE OF CONTENTS</b>  | <b>III</b> |
| <b>ABBREVIATIONS</b>  | <b>IX</b>  |
| <b>NOTATION</b>   | <b>X</b>   |
| <br>  |            |
| <b>1 INTRODUCTION</b>   | <b>1</b>   |
| 1.1 INTRODUCTORY REMARKS  | 1          |
| 1.2 RESEARCH OBJECTIVES   | 4          |
| 1.3 LAYOUT OF THE THESIS  | 4          |
| <br>  |            |
| <b>2 LITERATURE REVIEW ON THE BOND BEHAVIOUR OF DEFORMED STEEL AND FRP BARS</b> | <b>7</b>   |
| 2.1 BOND OF STEEL BARS  | 7          |
| 2.1.1 General   | 7          |
| 2.1.2 Steel bar-concrete interaction  | 8          |
| 2.1.3 Factors that influence bond behaviour                                     | 10         |
| 2.1.3.1 Concrete strength   | 11         |
| 2.1.3.2 Bar diameter  | 11         |
| 2.1.3.3 Transverse pressure   | 11         |
| 2.1.3.4 Transverse reinforcement  | 12         |
| 2.1.3.5 Bar spacing and concrete cover  | 13         |
| 2.1.4 Pullout tests   | 14         |
| 2.1.5 Analytical approach to bond splitting failure                             | 16         |
| 2.1.6 Splices   | 22         |
| 2.1.6.1 Crack patterns  | 22         |
| 2.1.6.2 Forces induced by splices in the surrounding concrete                   | 23         |
| 2.1.6.3 Equations for calculating the bond strength of splices                  | 26         |
| 2.1.7 Codes of practice   | 30         |
| 2.1.7.1 British Standard 8110 (1985)  | 30         |

|         |   |    |
|---------|---|----|
| 2.1.7.2 | Eurocode 2 (1989)   | 32 |
| 2.1.7.3 | ACI Building Code 318 (1995)                                      | 33 |
| 2.1.7.4 | Commentary on codes of practice                                   | 35 |
| 2.2     | <b>FRP REINFORCEMENT FOR CONCRETE STRUCTURES</b>                  | 38 |
| 2.2.1   | General   | 38 |
| 2.2.2   | Basic mechanical properties                                       | 41 |
| 2.2.2.1 | Tensile strength and elongation at failure                        | 41 |
| 2.2.2.2 | Modulus of elasticity   | 42 |
| 2.2.2.3 | Shear strength  | 42 |
| 2.3     | <b>BOND OF FRP REINFORCING BARS TO CONCRETE</b>                   | 43 |
| 2.3.1   | General   | 43 |
| 2.3.2   | Experimental investigations on pullout bond behaviour of FRP bars | 44 |
| 2.3.2.1 | USA - Canada  | 44 |
| 2.3.2.2 | Europe  | 49 |
| 2.3.2.2 | Japan   | 50 |
| 2.3.3   | Splitting mode of bond failure of FRP bars                        | 51 |
| 2.3.4   | Analytical approach to the bond behaviour of FRP bars             | 54 |
| 2.3.5   | Codes of practice and design recommendations                      | 56 |
| 2.4     | <b>NECESSITY FOR FURTHER RESEARCH</b>                             | 62 |
| <br>    |   |    |
| 3       | <b>EXPERIMENTAL METHODOLOGY</b>                                   | 64 |
| 3.1     | <b>PULLOUT TESTS</b>  | 64 |
| 3.1.1   | Background  | 64 |
| 3.1.2   | Study parameters  | 65 |
| 3.1.3   | Specimen preparation  | 66 |
| 3.1.3.1 | Bar preparation   | 66 |
| 3.1.3.2 | Mould preparation   | 67 |
| 3.1.3.3 | Casting and curing procedure                                      | 67 |
| 3.1.3.4 | Material properties   | 68 |
| 3.1.4   | Experimental set up   | 71 |
| 3.1.5   | Testing procedure   | 74 |
| 3.1.6   | Analysis of measurements  | 75 |

|         |  |     |
|---------|--|-----|
| 3.2     | BEAM TESTS   | 77  |
| 3.2.1   | Background   | 77  |
| 3.2.2   | Study parameters of the experimental series                  | 79  |
| 3.2.3   | Specimen preparation   | 80  |
| 3.2.3.1 | Preparation of reinforcement cages                           | 80  |
| 3.2.3.2 | Mould preparation  | 81  |
| 3.2.3.3 | Casting and curing   | 82  |
| 3.2.3.4 | Material properties  | 82  |
| 3.2.3.5 | Beam preparation before testing                              | 84  |
| 3.2.4   | Instrumentation  | 84  |
| 3.2.4.1 | Strain gauge arrangement on reinforcing bars and shear links | 84  |
| 3.2.4.2 | Arrangement of LVDTs on the beam                             | 86  |
| 3.2.5   | Experimental set up  | 88  |
| 3.2.6   | Testing procedure  | 89  |
| 3.2.7   | Analysis of measurements                                     | 90  |
| 4       | EXPERIMENTAL RESULTS   | 92  |
| 4.1     | PULLOUT TESTS  | 92  |
| 4.1.1   | Bond stress versus Slip curve                                | 93  |
| 4.1.2   | Mode of bond failure of FRP bars                             | 96  |
| 4.1.2.1 | Residual bond strength of FRP bars                           | 99  |
| 4.1.3   | Factors that influence the bond behaviour of FRP bars        | 101 |
| 4.1.3.1 | Type of bar fibres   | 101 |
| 4.1.3.2 | Embedment length   | 104 |
| 4.1.3.3 | Concrete strength  | 106 |
| 4.1.3.4 | Bar diameter   | 107 |
| 4.1.3.5 | Cross sectional shape of the bar                             | 109 |
| 4.1.3.6 | Surface deformations   | 110 |
| 4.2     | BEAM TESTS   | 112 |
| 4.2.1   | Phases 1 to 3  | 112 |
| 4.2.1.1 | General  | 112 |
| 4.2.1.2 | Bond stress profile on main reinforcing bars                 | 113 |

|          |  |            |
|----------|--|------------|
| 4.2.1.3  | Bond failures in phases 1 to 3   | 115        |
| 4.2.2    | Phase 4  | 117        |
| 4.2.2.1  | Beams GB29 and GB30  | 117        |
| 4.2.2.2  | Beam GB31  | 122        |
| 4.2.2.3  | Beam CB32  | 127        |
| 4.2.2.4  | Beams CB33 and GB36  | 130        |
| 4.2.2.5  | Beam GB35  | 135        |
| 4.2.2.6  | Beam GB34  | 138        |
| 4.2.2.7  | Beam CB37  | 143        |
| <b>5</b> | <b>ANALYTICAL STUDY</b>  | <b>147</b> |
| 5.1      | PULLOUT CUBE TEST MODEL  | 147        |
| 5.1.1    | Description of the model   | 148        |
| 5.1.1.1  | Geometry - elements  | 148        |
| 5.1.1.2  | Spring characteristics   | 150        |
| 5.1.2    | Results  | 153        |
| 5.1.2.1  | Load-Slip curve  | 153        |
| 5.1.2.2  | Distribution of normal and bond stresses over the<br>embedment length          | 154        |
| 5.1.2.3  | Prediction of the bond behaviour of larger embedment<br>lengths                | 155        |
| 5.2      | BEAM TEST MODEL  | 159        |
| 5.2.1    | Model of beam CB19   | 160        |
| 5.2.1.1  | Description of the model   | 160        |
| 5.2.1.2  | Results - comparisons  | 162        |
| 5.2.2    | Model of beam CB20   | 164        |
| 5.2.2.1  | Description of the model   | 164        |
| 5.2.2.2  | Results  | 169        |
| 5.2.2.3  | Parametric study on the load-slip values of the<br>characteristic spring curve | 170        |
| 5.2.3    | Model of beams CB32 and CB37   | 177        |
| 5.2.3.1  | Description of the models  | 177        |
| 5.2.3.2  | Results  | 181        |

## REFERENCES

235

### APPENDIX A: REINFORCEMENT ARRANGEMENT AND

#### INSTRUMENTATION OF BEAMS IN PHASES 1-3

242

- |     |   |     |
|-----|---|-----|
| A.1 | Reinforcement arrangement in beams GB5 to GB8       | 242 |
| A.2 | Reinforcement arrangement in beams GB9 to GB16      | 243 |
| A.3 | Reinforcement arrangement in beams CB17 to CGB22    | 244 |
| A.4 | Reinforcement arrangement in beams AB23 to AB28     | 245 |
| A.5 | Arrangement of strain gauges in beams of phases 1-3 | 246 |

### APPENDIX B: REINFORCEMENT ARRANGEMENT AND

#### INSTRUMENTATION IN PHASE 4 BEAMS

247

- |     |   |     |
|-----|---|-----|
| B.1 | Reinforcement and strain gauge arrangement in beams GB29 and GB30 | 247 |
| B.2 | Reinforcement and strain gauge arrangement in beams GB31 and CB32 | 248 |
| B.3 | Reinforcement and strain gauge arrangement in beams CB33 and GB34 | 249 |
| B.4 | Reinforcement and strain gauge arrangement in beams GB35 and GB36 | 250 |
| B.5 | Reinforcement and strain gauge arrangement in beam CB37           | 251 |
| B.6 | Arrangement of LVDTs used in beam testing                         | 252 |

### APPENDIX C: PULLOUT TEST RESULTS

253

- |     |  |     |
|-----|--|-----|
| C.1 | Summary of pullout test results, Tables C.1.1-C.1.6                | 253 |
| C.2 | Bond-slip curves for pullout tests presented in Tables C.1.2-C.1.6 | 259 |

### APPENDIX D: MICROSCOPE IMAGES OF FRP BOND FAILURES

275

### APPENDIX E: BEAM TEST RESULTS

278

- |     |  |     |
|-----|--|-----|
| E.1 | Summary of beam test results, Tables E.1.1 - E.1.3 | 278 |
| E.2 | Test results of phase 1-3 beams                    | 281 |
| E.3 | Strain gauge readings of phase 4 beams             | 329 |

|          |  |            |
|----------|--|------------|
| 5.2.3.3  | Modelling of beam CB37 by using different mesh size  | 184        |
| 5.2.4    | Discussion   | 186        |
| <b>6</b> | <b>GENERAL DISCUSSION</b>  | <b>189</b> |
| 6.1      | FRP BAR-CONCRETE INTERACTION   | 189        |
| 6.2      | PULL-THROUGH BOND FAILURE OF FRP BARS  | 192        |
| 6.1.2    | Suitability of cube tests for measuring the bond strength<br>of FRP bars                                       | 192        |
| 6.1.3    | Influence of the experimental conditions on bond strength  | 194        |
| 6.3      | SPLITTING BOND FAILURE OF FRP BARS   | 196        |
| 6.3.1    | Experimental evidence  | 196        |
| 6.3.2    | Analytical approach to the bond splitting failure  | 197        |
| 6.3.3    | Estimation of angle $\alpha$ for GFRP and CFRP bars  | 203        |
| 6.3.4    | Radial stresses induced by splices in the surrounding concrete   | 208        |
| 6.3.5    | Additional factors that influence the bond splitting behaviour<br>of FRP bars                                  | 211        |
| 6.3.6    | Influence of flexural cracking on the distribution of bond<br>stresses over the anchorage bar in beam elements | 214        |
| 6.3.6.1  | Distribution of normal and bond stresses between<br>successive cracks  | 214        |
| 6.3.6.2  | Influence of flexural cracking on bond development<br>over the anchorage length                                | 217        |
| 6.3.7    | Discussion towards design recommendations and future work  | 220        |
| 6.3.7.1  | Parameters to be considered in the formulation of an<br>anchorage length formula for FRP bars                  | 220        |
| 6.3.7.2  | Suggested method of working towards the formulation<br>of design recommendations                               | 223        |
| 6.3.7.3  | Splices  | 228        |
| <b>7</b> | <b>CLOSURE</b>   | <b>229</b> |
| 7.1      | GENERAL CONCLUSIONS  | 229        |
| 7.2      | SUGGESTIONS FOR FUTURE WORK  | 233        |

# ABBREVIATIONS

|      |   |   |
|------|---|---|
| ACI  | = | American Concrete Institute                       |
| AFRP | = | Aramid Fibre Reinforced Polymers                  |
| BS   | = | British Standards                                 |
| CCC  | = | Centre for Cement and Concrete                    |
| CEB  | = | Comite Euro-international du Beton                |
| CFRP | = | Carbon Fibre Reinforced Polymers                  |
| EC   | = | Eurocode  |
| FE   | = | Finite Elements                                   |
| FIB  | = | Federation Internationale du Beton                |
| FRP  | = | Fibre Reinforced Polymers                         |
| GFRP | = | Glass Fibre Reinforced Polymers                   |
| HFRP | = | Hybrid (Glass + Carbon) Fibre Reinforced Polymers |
| JSCE | = | Japanese Society of Civil Engineers               |
| RC   | = | Reinforced Concrete                               |

# NOTATION

|               |   |   |
|---------------|---|---|
| $A$           | = | Area of the bar cross section   |
| $A_t, A_{tr}$ | = | Area of transverse reinforcement passing through the splitting plane        |
| $c$           | = | Smallest concrete cover to reinforcing bar                                  |
| $c_x, c_y$    | = | Concrete covers to reinforcing bar parallel to x, y-axis                    |
| $d, d_b$      | = | Diameter of bar   |
| $E$           | = | Young's modulus of reinforcing bar  |
| $E_C$         | = | Young's modulus of CFRP bar   |
| $E_G$         | = | Young's modulus of GFRP bar   |
| $f_{ct}$      | = | Concrete tensile strength   |
| $f_{cu}$      | = | Concrete cube compressive strength  |
| $f_{cy}$      | = | Concrete cylinder compressive strength                                      |
| $f_{sp}$      | = | Splitting stress induced in the surrounding concrete by the reinforcing bar |
| $f_y$         | = | Tensile strength of steel bars  |
| $f_{y,d}$     | = | Design tensile strength of steel bars                                       |
| $L, l_s$      | = | Anchorage length  |
| $s$           | = | Spacing of transverse reinforcement   |

## *Greek Symbols*

|               |   |  |
|---------------|---|--|
| $\alpha$      | = | Inclination angle of the resulting force induced in the surrounding concrete by the bar and the bar axis |
| $\varepsilon$ | = | Normal bar strain  |
| $\delta_{ue}$ | = | Unloaded end slip of reinforcing bar   |
| $\delta_{le}$ | = | Loaded end slip of reinforcing bar   |
| $\tau$        | = | Local bond stress  |
| $\tau_{av}$   | = | Average bond stress over a certain length  |
| $\tau^*$      | = | Maximum average bond stress over a certain length  |
| $\tau_{sl}$   | = | Average bond stress when the free end of the bar started slipping  |
| $\tau_{sp}$   | = | Average bond stress when bond splitting initiates  |

$\tau_r$  = Residual bond stress (due to frictional resistance)

$\sigma_f$  = Tensile strength of FRP bars

# CHAPTER 1

## INTRODUCTION

### 1.1 INTRODUCTORY REMARKS

In construction, steel reinforced concrete is the most widely used structural material in the world. However, it is well known that, under certain environments, the corrosion of steel reinforcement can lead to the deterioration or even collapse of structural elements and, hence, imposes a major maintenance and strengthening financial penalty. In an attempt to increase structural durability, thick concrete covers and highly alkaline concretes have been widely adopted by the world's construction industry at considerable expense. Other more modern solutions to the durability problem include epoxy coated steel reinforcement, stainless steel reinforcement and cathodic protection, all of which add further costs or complicate construction. Billions of dollars are spent every year world-wide in repairing and strengthening concrete structures, whose reinforcement has deteriorated due to corrosion and this has contributed for research to focus on alternative solutions (Pilakoutas, Achillides and Waldron, 1997a).

In the past five to ten years, a considerable amount of research has been taking place, in an attempt to investigate an alternative solution for using continuous Fibre Reinforced Polymers (FRP) in concrete construction and repair. There is a great enthusiasm and expectation amongst many engineers that the use of advanced composites will mark the first major change in structural materials for nearly a century (Pilakoutas et al, 1997b).

FRP materials offer a promising solution since many types of them have been successfully used for many years in other industries (such as the automobile and sports manufacturing industries) and more recently in construction (figure 1.1). There are many examples of structural applications that have demonstrated that the speed and convenience of strengthening and repairing concrete structures using advanced composites produce cost effective solutions (Head, 1996). In addition, structures reinforced with FRP bars have been in service under aggressive environments in various parts of the world, for more than 15 years, without any structural problems (ACI Committee 440 (1996), Seible and Karbhari (1996), Rostasy (1996)).

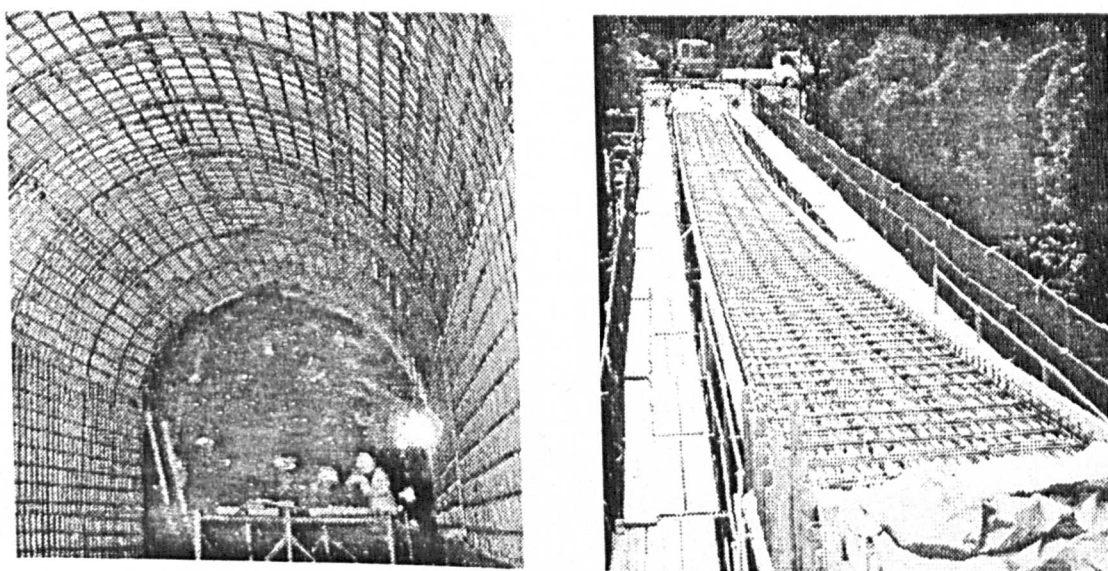


Figure 1.1: Examples of application of FRP reinforcement in tunnels and bridges in Japan

Nevertheless, before FRP materials are widely accepted in construction industry, research has to be done on all aspects of their structural behaviour. One of the fundamental aspects of structural behaviour is bond development, since bond is the key for the “co-operation” of reinforcing bars and concrete. An adequate level of bond is required between reinforcement and concrete to transmit forces from one to another (Achillides and Pilakoutas, 1996).

Bond of steel reinforcement to concrete has been studied extensively in the last 40 years and a huge amount of experimental and analytical work has been published on this subject (CEB Bulletin 151, 1982). However, the design formulae of the various design codes of practise, do not incorporate any provisions for the use of alternative

reinforcing materials other than steel. In the most extreme cases some provisions for epoxy coated bars are considered. The introduction of FRP reinforcing bars had created the necessity for the development of design specifications that will allow engineers to use these materials as reinforcement in concrete structures.

In order to overcome this problem, engineers and researchers round the world are currently intensifying their efforts to understand how these new materials actually interact with concrete, in order to be able to contribute towards the formulation of design codes of practice. A part of this research effort was the EUROCRETE project (Clarke and Waldron, 1996) and currently the CONFIBRECRETE network.

EUROCRETE was a 4-year research project, which investigated the use of non-ferrous (FRP) reinforcement in concrete structures. It involved both academia and industrial partners across Europe. The Centre for Cement and Concrete of the University of Sheffield was the main academic research centre in the project and significant amount of experimental and analytical work was undertaken here. The EUROCRETE project was successfully completed in May 1997 and an exploitation company aiming to supply FRP reinforcement is currently being established (Pilakoutas et al, 1997b).

Recently, the FIB (Federation International du Beton, formerly CEB) established a Task Group aiming to develop guidelines for design of concrete structures reinforced with FRP materials. The European Union is funding a Network of researchers (CONFIBRECRETE), co-ordinated by Dr. Pilakoutas at the University of Sheffield, to assist in that task.

This study forms a part of the research effort undertaken by the EUROCRETE project and the CONFIBRECRETE network, hoping that its contribution will help to the faster introduction of the FRP materials in the codes of practice. During the progress of this work the author also made contributions and benefited from the work of Party 8 of *fib* Task Group 4.2 on Bond of Non-metallic Reinforcement.

## **1.2 RESEARCH OBJECTIVES**

The main aim of this study is to investigate and understand the various aspects of the bond behaviour of FRP reinforcing bars in concrete elements and arrive at some conclusions that will help the development of design guidelines for use of FRP reinforcement. In order to achieve this aim, various objectives were identified as presented below:

- Review the literature on the bond behaviour of deformed steel bars to concrete in order to understand the various parameters that influence bond characteristics and identify current practices dealing with the various problems associated with bond of steel bars.
- Understand the difference in bond characteristics between FRP and steel reinforcement.
- Investigate experimentally the parameters that affect bond development on FRP bars.
- Examine the influence of the various experimental conditions on bond development and mode of bond failure.
- Assess the importance of bond splitting in FRP anchorages and splices.
- Develop a modelling procedure to simulate the bond behaviour of FRP bars.
- Examine the various analytical approaches to bond splitting failure developed for steel bars, and try to modify them to incorporate the effect of FRP bars.

The above objectives are addressed in the subsequent chapters, following the layout given below.

## **1.3 LAYOUT OF THE THESIS**

In chapter 2, a literature survey on the bond behaviour of steel and FRP bars in concrete is presented. The chapter begins with an overview of the most relevant

literature examining the bond behaviour of steel bars. Emphasis is given on the factors that influence bond, the splitting mode of bond failure, as it is observed in spliced reinforcement, and the approach of various codes of practice on bond. An overview is then presented on the current studies investigating the bond behaviour of FRP bars. Finally, the author identifies aspects of the subject that have not been adequately covered and where this study is likely to contribute.

The description of two experimental series that were conducted to investigate the bond of FRP bars is given in chapter 3. In the first series, more than 100 cube specimens were tested in direct pullout, whereas in the second, nine beams reinforced with single anchorage bars and splices were tested in four-point bending. This chapter mainly presents the parameters under investigation, the preparation of the specimens and the experimental procedure followed.

In chapter 4, the experimental results are reported and analysed. The mode of bond failure of FRP bars in the case of pullout tests is examined and compared with the respective failure of steel bars. The influence of various parameters on the bond development is also evaluated. In the case of beam tests, the splitting mode of bond failure in single bars and splices is investigated. The strain and bond stress distribution over the anchorage length is reported, as well as the contribution of the shear links on the bond splitting strength of reinforcing bars. The bond splitting strength developed in single anchorages and splices are calculated and discussed.

Chapter 5 reports mainly on the analytical part of this study. Two FE packages are used in modelling the bond between FRP bars and concrete in both cube and beam tests. For the pullout cube test modelling an elastic approach is used, where only the bond interaction is simulated with non-linear springs. The spring characteristics are taken from experimental results. In the beam models, different modes of bond failure are studied. The flexural cracking behaviour of concrete is considered in this case and the bond interaction is simulated by using non-linear springs. The results of all models are compared with the experimental ones and relevant conclusions are drawn.

In chapter 6, the experimental and analytical results are further compared and discussed. The discussion is focused on both the pull-through and splitting modes of bond failure. A theoretical model describing the FRP bar-concrete interaction is introduced. The suitability of the pullout cube tests for measuring the bond strength of

FRP bars is then assessed, by considering the influence of the experimental conditions on bond development. The discussion then focuses on the splitting mode of bond failure, which is considered to be more critical for structural purposes. The bond splitting strengths developed by different types of FRP bars are compared and the importance of the modulus of elasticity on the bond splitting behaviour is highlighted. Various analytical approaches to calculate the bond splitting failure of single anchorage and spliced bars are applied in the case of FRP bars and relevant conclusions are drawn. The importance of flexural cracking on bond development is, also, further discussed. Finally, some thoughts are presented regarding the design of anchorage lengths for FRP reinforcing bars in concrete structures. Other important issues are addressed and a method of working towards the formulation of a design guidelines is suggested, based on the experience gained from this work.

In the final chapter, the general conclusions from the present study are drawn, together with recommendations for further research in the subject.

# **CHAPTER 2**

## **LITERATURE REVIEW ON THE BOND BEHAVIOUR OF DEFORMED STEEL AND FRP BARS**

This chapter presents some of the most relevant literature available on the bond behaviour of steel and FRP bars in concrete. In the first section, the bond behaviour of steel bars is examined, with the main emphasis being placed on the factors that influence the bond development and the splitting mode of bond failure as it is observed in spliced reinforcement. In the second section, a general presentation of FRP materials used as reinforcement in concrete members is given. In the third section, a brief description of a number of various studies investigating the pullout and splitting mode of failure of FRP bars in concrete is presented, together with the first design guidelines for the evaluation of anchorage lengths for FRP reinforcing bars. Finally in the last part, the author identifies areas on the bond behaviour of FRP bars that need further investigation.

### **2.1 BOND OF STEEL BARS**

#### **2.1.1 General**

Composite structures such as RC elements are able to resist externally imposed loads only if their constituent components interact adequately. The interaction between reinforcing bars and concrete in RC members takes place through bond stresses. When the bond strength and stiffness is adequate, the compatibility of deformations between the two materials is secured without substantial slip between them.

A vast amount of experimental and analytical work has been published in the last forty years investigating the bond behaviour of steel reinforcing bars in concrete. The whole effort was pioneered by names like Rehm (1961), Ferguson (1965), Goto (1971), Tepfers (1973), Tassios (1979), Eligehausen (1983) and others, whose work established the foundations for understanding the interaction between steel reinforcement and concrete.

In the following, a brief survey of the up to date literature on bond behaviour of steel reinforcing bars will be presented, without of course, being able to cover all the aspects and all the authors who contributed in the investigation of the subject (for an extensive literature survey on bond see for instance the literature review by the CEB Bulletin No. 151 (1982) and the Proceedings of the International Conference on Bond in Concrete, in Riga (1992)). Special consideration will be given to the splitting mode of bond failure of steel deformed bars as single anchorages and in splices. Finally, an overview of the main codes of practice in the area of bond will be presented.

### 2.1.2 Steel bar - Concrete interaction

CEB Bulletin 151 (1982) describes the interaction mechanism between a steel bar subjected to a pullout force and the surrounding concrete which is based on the theoretical model of bond stress - slip behaviour introduced by Tassios (1979), shown in figure 2.1.

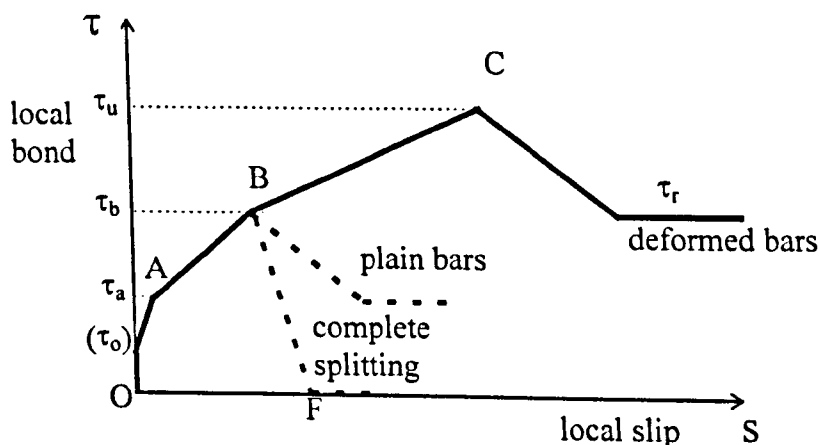


Figure 2.1: Theoretical model of local bond-slip relationship, Tassios (1979)

According to the Bulletin, for small values of bond stress (up to point  $\tau_0$  in figure 2.1) there is no slip between bar and concrete and the resistance mechanism depends mainly on the chemical adhesion between the steel bar and concrete.

As the pullout force increases, the chemical bond breaks down and a very different mechanism builds up depending on the type and characteristics of the irregularities of the surface of the reinforcing bar. This type of bond can be called mechanical bond. The ribs of the bar induce bearing stresses in the surrounding concrete (figure 2.2) and when the principal tensile stress exceeds the tensile strength of the concrete, transverse microcracks originate at the tips of the ribs (point A in figure 2.1) allowing the bar to start slipping.

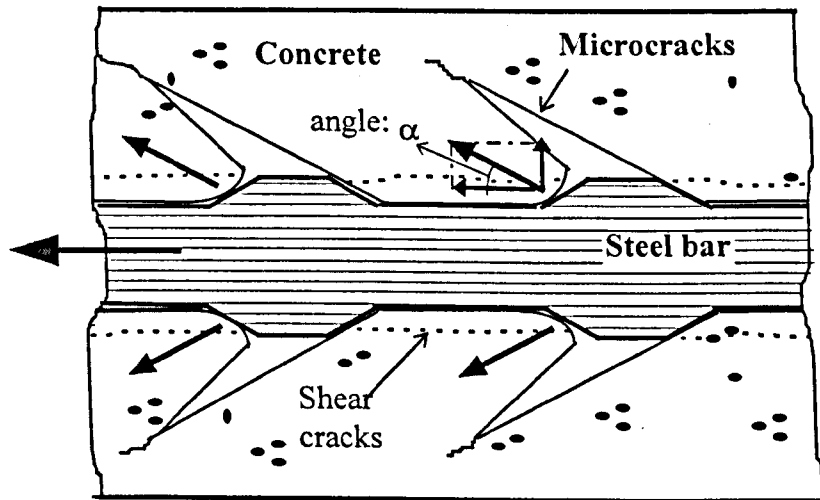


Figure 2.2: Forces between deformed bar and concrete, CEB Bulletin 151 (1982)

The formation of microcracks modifies the response of concrete to loading. The concrete stiffness diminishes and, therefore, larger slip increments are needed for further bond stress increments than before cracking (AB segment in figure 2.1). The radial forces induced by the ribs of the bar on to the concrete are balanced against rings of tensile stresses developed in the surrounding concrete (figure 2.3 by Tepfers, 1979). When the value of the tensile hoop stress exceeds the tensile strength of concrete, splitting cracks are initiated along the length of the reinforcing bar. These cracks start as internal longitudinal cracks which can not be seen on the surface of the concrete until

the load capacity of the concrete ring surrounding the bar is achieved (point B in figure 2.1).

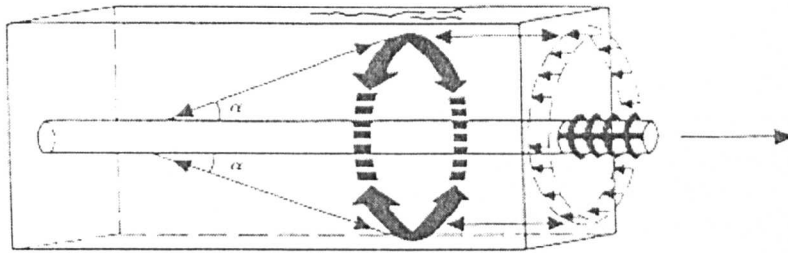


Figure 2.3: Schematic representation of how the radial components of the bond forces are balanced against tensile stress rings in the concrete in an anchorage zone (Tepfers, 1979)

When longitudinal cracks (splitting cracks) break through the whole cover of the pullout bar, the bond fails in a sudden mode without warning of ductile deformation (point F in figure 2.1). This type of bond failure is quite common in concrete structures reinforced with deformed steel bars.

However, if the splitting resistance of the surrounding concrete is high enough (thick concrete cover or sufficient amount of transverse reinforcement), the pullout load can be increased further. When approaching the maximum bond resistance (point C in figure 2.1) shear cracks initiate along a part or the total length of the concrete corbels between the ribs (figure 2.2). The eventual shear failure depends on the relation between the rib height and the clear distance between ribs.

After this stage, the only mechanism left is the frictional resistance ( $\tau_r$ ) between the bar and the rough concrete at the cylindrical surface where the shear failure occurred.

### 2.1.3 Factors that influence bond behaviour

The bond behaviour between concrete and steel reinforcement depends on many factors which influence the bond strength of anchored bars in concrete. It is important to understand the effect of these factors first, on steel bars so that comparisons can be

made when dealing with the bond behaviour of FRP bars to concrete. In the following, the main factors are presented and discussed:

### **2.1.3.1 Concrete strength**

According to CEB Bulletin 151 (1982), the strength of concrete in tension is of major importance when bond failure is caused by splitting. Splitting failure will only take place when the tensile hoop stresses (figure 2.3) reach or exceed the tensile strength of the surrounding concrete. This, generally, happens at a much lower load than the pullout mode of failure (see figure 2.1,  $\tau_u > \tau_b$ ) and the bond stress in the bar is lost abruptly. In addition, the residual bond strength, after splitting, is practically zero which, also, underlines the importance of avoiding this kind of failure.

For the above reasons, the tensile strength of concrete is the main factor which determines the ultimate load of anchorages. The tensile strength is indirectly included in the anchorage length equations of most codes of practice including the ACI Building Code (1995), Eurocode 2 (1989) and British Standards 8110 (1985).

### **2.1.3.2 Bar diameter**

Studies conducted by various authors (Soretz (1972), Kimura and Jirsa (1992), De Larrard (1993)) showed that the size of bar diameter influences the bond strength with bars with bigger diameters developing less bond strength than smaller bars. The ACI Building Code (1989) acknowledges this influence by including the cross section area of the bar in the calculations of the development length. The more recent ACI Building Code (1995) also acknowledges the influence of the bar diameter but in a more general and simplified form, by suggesting a reinforcement size factor in its development length formula (see section 2.1.7.3). Eurocode 2 (1989) takes the influence of bar diameter into consideration, only for bars with diameter greater than 32 mm whereas BS 8110 (1985) does not have any special provisions for this parameter.

### **2.1.3.3 Transverse pressure**

Transverse compression influences the bond behaviour of a reinforcing bar in two ways according to CEB Bulletin 151 (1982). It delays the onset of splitting failure

in a plane perpendicular to the direction of compressive stress and it increases the frictional force on the steel/concrete or concrete/concrete failure surface. The presence of transverse pressure results in higher ultimate bond stresses and in reduced values of slip at a particular load.

Experimental work by Gambarova et al (1992), confirmed that concrete splitting makes bond behaviour very sensitive to confinement. A special experimental arrangement for pullout testing was introduced in which the bond behaviour on steel bars was studied under controlled crack opening or confinement. The test results showed that at variable crack opening and roughly constant confinement, the bond peak-strength is adversely affected by crack opening, and that bond stiffness decreases rapidly at increasing crack opening. On the other hand, the test results at constant crack opening and variable confinement confirmed that bond peak-strength is definitely a linear function of the confinement stress.

In USA, Malvar (1992) conducted a series of pullout test of steel bars embedded in pre-cracked cylindrical concrete specimens. Various levels of confinement radial pressure were applied to the specimens during testing. The results indicate that bond stresses increase significantly with confining stress and that the maximum bond stress could be increased almost threefold by increasing the confinement stress from 500 to 4500 psi (3.5 to 31 MPa) at the bar level. In addition, he obtained consistent local bond stress versus slip relationships for various degrees of confining pressure that can be used for the development of "configuration-independent" models.

From the codes of practice, only EC2 (1989) considers the case of transverse pressure to the possible plane of splitting. In this case, the suggested design bond values are increased by a factor directly dependent on the value of transverse pressure.

#### **2.1.3.4 Transverse reinforcement**

The importance of transverse reinforcement in controlling the splitting mode of failure of deformed steel bars in concrete members has been studied extensively by various researches. Eligehausen et al (1983) investigated the influence of transverse reinforcement on bond behaviour. He concluded that the bond strength could be significantly improved by the presence of reinforcement transverse to the splitting crack. Their experimental results also showed that an upper limit might exist beyond which the

bond behaviour cannot be further improved by additional transverse reinforcement. Giuriani et al (1991) verified the above results with their experimental work and introduced a theoretical model for predicting the effect of transverse reinforcement on the bond behaviour of reinforcing bars. In a step further, the work of Plizzari et al (1996) introduced a maximum value of transverse reinforcement (stirrup index of confinement- $\Omega$ ) beyond which no significant increase of bond strength occurred.

CEB Bulletin 151 (1982) suggests that transverse reinforcement crossing the splitting crack is effective in improving the bond behaviour when the bond failure is associated with splitting of the concrete cover. The transverse reinforcement, in this case, restrains the opening of the crack although it does not influence the initiation of splitting cracks due to the low strain at which tension cracks form in concrete.

The importance of transverse reinforcement is also underlined in the codes of practice EC2 (1989) and BS8110 (1985). Both codes indicate a minimum amount of transverse reinforcement essential in the region of anchorage length of the main reinforcing bars. It may be assumed that the bond stresses suggested for design purposes in these codes incorporate the positive influence of this transverse reinforcement in their values.

### 2.1.3.5 Bar spacing and concrete cover

The bond behaviour of deformed steel bars is affected by the detailing of reinforcement in concrete members. The formation of splitting cracks and the respective bond strength are directly relevant to the arrangement of reinforcement in the cross section as shown in figure 2.4 adopted from Nagamoto and Kaku (1992).

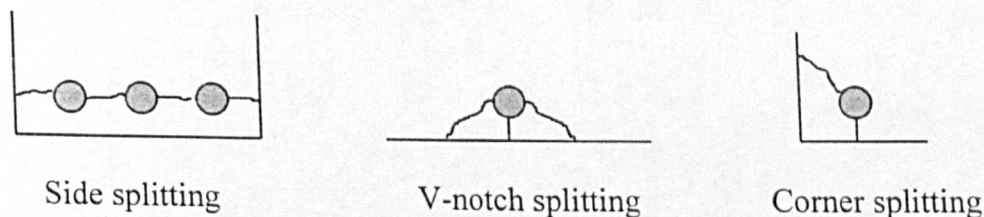


Figure 2.4: Formation of splitting cracks for single bars

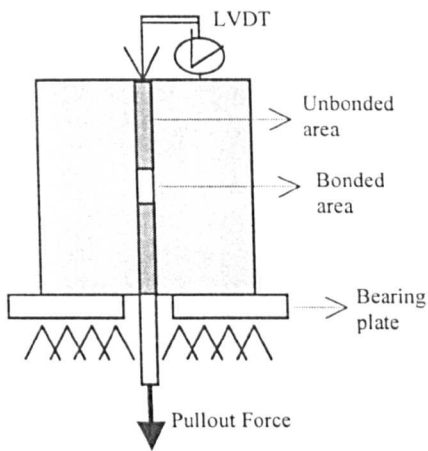
The three codes of practice (ACI, EC2 and BS8110) have special provisions for the proper arrangement of reinforcement in a concrete member. Special consideration is given to the detailing of spliced reinforcement where the formation of splitting cracks is crucial to the integrity of structural members.

All the above parameters and others that are less relevant to this research, influence the bond resistance of steel reinforcing bars in concrete members, in case of either a splitting or a pullout mode of failure. The need for understanding and quantifying the influence of those parameters on bond, led engineers to adopt various test procedures for investigating the bond behaviour of steel embeddings in concrete. The most commonly used and easily adopted test arrangement is the Pullout test, of which variations are presented in the following section.

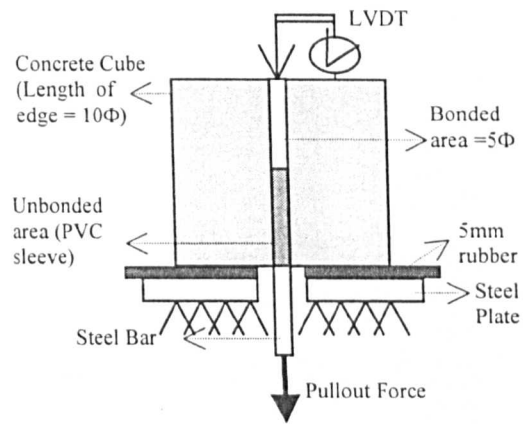
#### **2.1.4 Pullout tests**

Pullout test specimens are used for the evaluation of the bond performance of steel reinforcing bars. During the last 40 years, a vast number of different pullout test specimens has been produced by various researches to investigate the factors that influence bond behaviour of steel reinforcing bars embedded in concrete.

One of the first set-ups, proposed by Rehm (1961), is shown in figure 2.5. This test arrangement has been adopted by many researches in the years to follow with minor changes in order to eliminate its weak points. These relate to the friction developed between the concrete specimen and the bearing plate that provides additional confinement to the bonded area and can also assist the development of the arch-effect in the centre of the specimen during the test.



Rehm (1961)



RILEM/CEB/FIP (1970)

Figure 2.5: Pullout tests

For the above reasons, the RILEM/CEB/FIP standard pullout test arrangement (figure 2.5) moved the bonded length of the bar away from the centre of the specimen and introduced a rubber plate between the concrete block and the bearing plate to minimise the friction effects.

A different approach of test pullout test arrangement is adopted by the British Standard (Cairns, 1995). The test method uses a bar cast into a square prism (figure 2.6). Cover to the bar is 2.6 or more times the bar diameter and a confining helix of 6mm diameter mild steel at a pitch of 25 mm is provided to resist splitting. The length of the embedment length is specified as  $f_y \cdot d / 28$ . The test bar is required to sustain a load equal to the characteristic strength of the bar for a period of 2 min and with free end slip not exceeding 0.2 mm, in order to be classified as type 2 deformed bar. This load is equivalent to an average bond stress of 7 MPa.

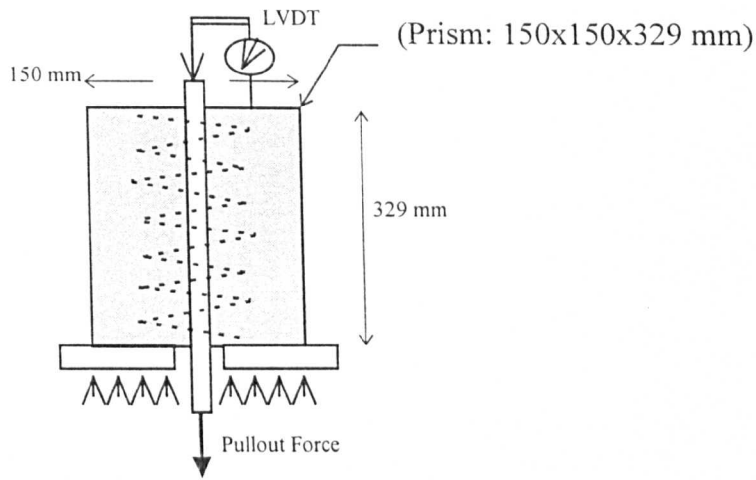


Figure 2.6: Standard bond pullout test specimen specified in BS4449 (1988) for 20 mm diameter steel bar

Cairns (1995) compared RILEM and BS tests and concluded that maximum bond strength values measured in both tests are considerably in excess of those used in design. However, when the bond strength was measured for specific free end slips, the tests provided a reasonable indication of bond strength where a splitting failure mode occurred.

### 2.1.5 Analytical approach to bond splitting failure

A reinforcing bar subjected to pullout load may either fail in a pull-through or a splitting mode of failure. In practice, the splitting mode is the most common type of bond failure in a structural member (e.g. beams, columns and slabs). In addition, splitting failure is more critical than pull-through failure, since it happens at a much lower stress level and the residual bond stress is practically zero. For the above reasons, engineers have concentrated their efforts in understanding the mechanisms that lead to the splitting mode of failure in concrete members.

Tepfers (1973) in his studies on the bond behaviour of steel deformed bars investigated the formation of splitting cracks in the concrete cover along anchored bars. According to Tepfers, the compressive stress induced by the ribs of the reinforcing bar to the concrete corbels (figure 2.2) subtends an angle  $\alpha$  with the bar axis. The horizontal component ( $\tau$ ) of this stress represent the bond stress developed on the bar whereas the radial component ( $f_{sp}$ ) represents the splitting stress induced in the concrete (figure 2.7).

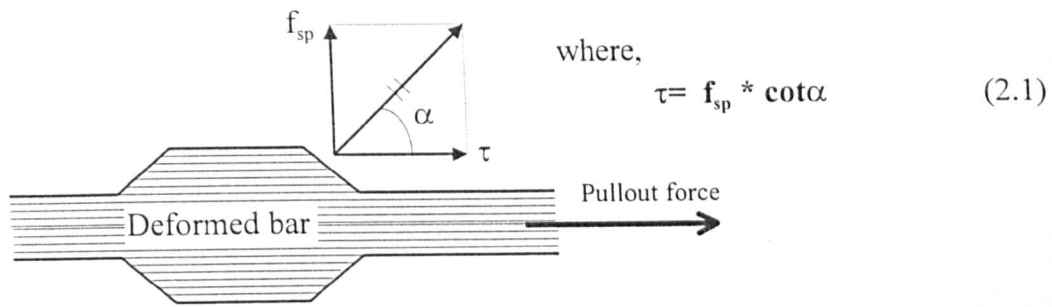


Figure 2.7: Stresses induced to the concrete

The radial stresses are balanced against rings of tensile stress in the concrete (figure 2.3). When the ring is stressed to levels beyond its tensile capacity, longitudinal cracks appear. To model this behaviour, Tepfers introduced the idea of a thick-wall concrete ring subjected to internal radial pressure, as shown in figure 2.8.

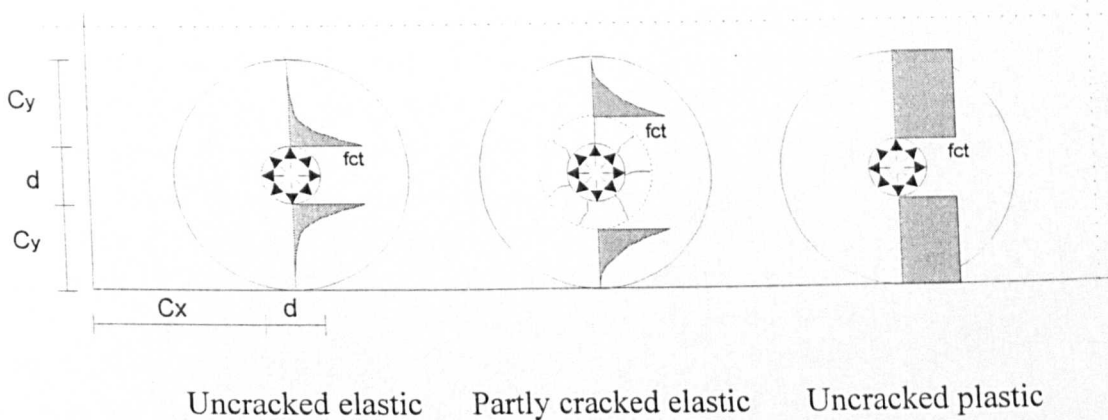


Figure 2.8: The distribution of tensile stresses for the three theories

The thickness of the ring is determined by the smallest possible dimension of the concrete covers ( $c_x, c_y$ ) of the reinforcing bar. Tepfers used three theories to determine the cracking resistance of the ring with regard to the distribution of stresses; the uncracked elastic, uncracked plastic and partly cracked elastic theories (figure 2.8).

The analysis resulted in three equations, one for each theory, for the calculation of the splitting bond strength, as shown below:

Uncracked elastic:

$$\tau = \frac{f_{ct}}{\tan \alpha} * \frac{(c_y + d/2)^2 - (d/2)^2}{(c_y + d/2)^2 + (d/2)^2} \quad (2.2)$$

Partly cracked elastic: 
$$\tau = \frac{f_{ci}}{\tan \alpha} * \frac{c_y + d/2}{1.664 * d} \quad (2.3)$$

Uncracked plastic: 
$$\tau = f_{ci} * 2 * c_y / (d * \tan \alpha) \quad (2.4)$$

where,

$\alpha$  : angle of bearing stresses induced by the ribs of the bar to the concrete as shown in figure 2.7.

Experimental results verified the suggested model since the bond values occurred between the partly cracked elastic and plastic stages, just as they were expected. According to Tepfers (1979), the partly cracked elastic stage gives values of the developed bond stresses just on the safe side of experimental results. In the above approach, Tepfers assumed that the value of angle  $\alpha$  should be taken equal to  $45^\circ$  since the properties of concrete are equal in tension and compression before the initiation of the first cracks in concrete. The results of various finite element analysis elastic bond models confirmed his assumption. However, after the formation of the first cracks, Tepfers noted that the value of angle  $\alpha$  is likely to change and will be dependent mainly on the geometrical configuration of the ribs of the steel bar.

A different kind of relationship between bond stresses ( $\tau$ ) and splitting stresses ( $f_{sp}$ ) was proposed by Cairns and Jones (1995,1996). They suggested that  $\tau$  is not directly proportional to  $f_{sp}$  as equation 2.1 implies, and that Tepfers' "hydraulic pressure assumption" (angle  $\alpha = 45^\circ$ ) is not valid. In order to support their view, they conducted a series of experiments with spliced steel bars embedded in concrete cubes as shown in figure 2.9.

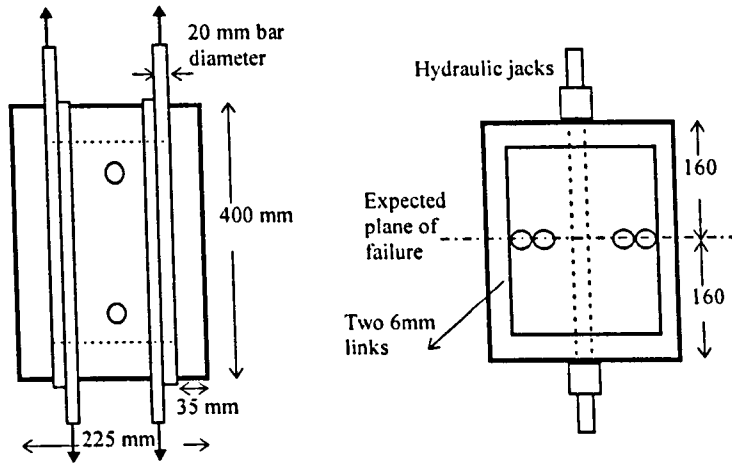


Figure 2.9: Details of test specimens (Cairns and Jones, 1996)

Their main idea was to impose lateral confining force vertical to the expected failure plane and investigate the change in the developed bond strength at different confinement levels. In addition, they pre-cracked some of the cube specimens along the expected failure plane before testing them, in order to examine the contribution of the tensile strength of concrete to the splitting resistance. Based on their experimental results and the experimental work of other researchers, Cairns and Jones (1996) suggested a new form of relationship in which the bond strength ( $f_b$ ) is regarded as a sum of non-splitting ( $f_{nsp}$ ) and splitting ( $f_{sp}$ ) components (eq. 2.5).

$$f_b = f_{sp} \cot\alpha + f_{nsp} \quad (2.5)$$

The non-splitting component was amounted to be around 67-70% of bond strength ( $f_b$ ) and was assumed to depend on the cohesive strength of concrete whereas the angle  $\alpha$  was estimated around  $72^\circ$ . The importance of the above approach lies in the fact that bond strength appears to be less dependent on the splitting resistance of concrete cover and confining reinforcement than is currently assumed. Cairns and Jones (1995) also suggested a new form of force equilibrium between reinforcing bar and surrounding concrete to identify the mechanism through which the non-splitting component arises (figure 2.10).

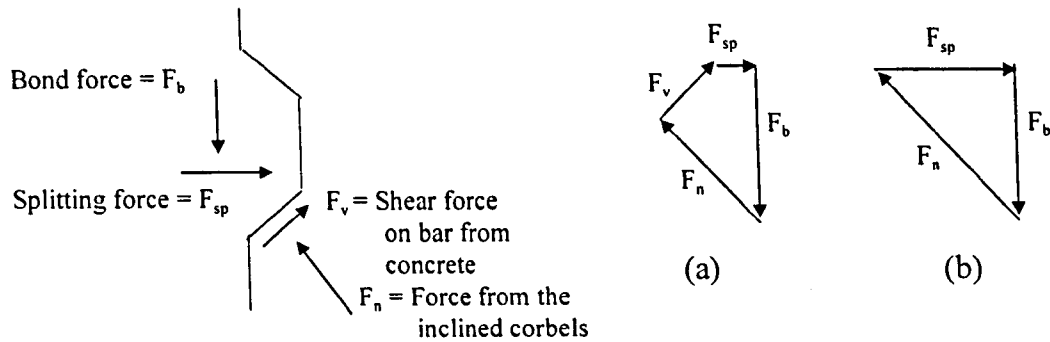
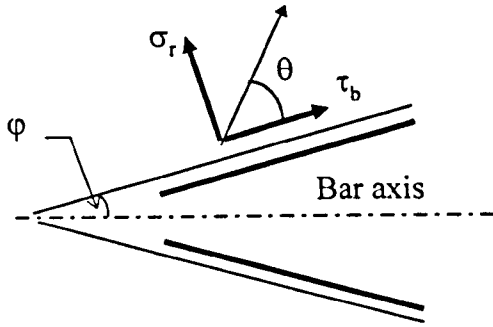


Figure 2.10: Forces associated with splitting bond behaviour (Cairns and Jones, 1995)

They introduced a fourth component  $F_v$ , in the equilibrium of forces (b) suggested by Tepfers (1973), representing the shear stress in the concrete on the inclined bearing surface of the rib. This shear stress is believed to entail the effect of concrete cohesion and the friction between bar and concrete. The suggested equilibrium (a) reduces the value of splitting force  $F_{sp}$  whereas a possible increase in the bond force  $F_b$  is not necessarily accompanied with an increase in  $F_{sp}$ . The author believes that Cairns and Jones forces approach might be useful to the understanding of the bond behaviour of FRP bars, and it will be discussed at a later stage of this study. The different material properties of FRP reinforcement comparing to the traditional steel reinforcing bars (such as the lower shear strength and elastic modulus of FRP bars in the transverse and axial direction) might play a significant role in their bond splitting behaviour to concrete.

Recently, some more models have been developed in order to predict the bond capacity of short anchorages and evaluate the pattern of splitting cracks during pullout tests. These models (such as Rosati and Schumm (1992), Van der Veen (1990), Den Uijl and Bigaj (1996)) are based on the splitting models of Tepfers. However, they take into account the crack cohesion along the radial splitting cracks, which is related to the softening behaviour of concrete in tension.

In the model of Den Uijl and Bigaj (1996) the ribbed bar is conceived as a conical bar (figure 2.11). The bond mechanism is assumed to be based on dry friction which makes the bond stress ( $\tau_b$ ) directly proportional to the radial compressive strength ( $\sigma_r$ ), (equation 2.6 in figure 2.11).



$$\tau_b = \sigma_r \cot\theta \quad (2.6)$$

$\cot\theta$  : coefficient of friction

$\varphi$  : angle between cone surface and bar axis

Figure 2.11: Bond model by Den Uijl and Bigaj (1996)

The most important aspect of this model is that it connects the slip of the bar ( $\delta$ ) with the radial displacement of the interface (equations 2.7 and 2.8).

$$\varepsilon_{r,rs} r_s = \delta \tan\varphi \quad (2.7)$$

$$\varepsilon_{r,rs} r_s = F_1(\delta, \varepsilon_s) \quad (2.8)$$

where,

$\varepsilon_{r,rs}$  : radial concrete strain at concrete-bar interface

$r_s$  : bar radius

$F_1(\delta, \varepsilon_s)$  : function of bar slip and bar normal strain

The first equation is valid for the case of splitting mode of failure where the most important influence is the wedging effect connected with the rib bearing mechanism. The Poisson effect is assumed to be small in this case and is therefore neglected. On the contrary in the second equation, suggested for a pullout failure, a number of factors are taken into account such as the Poisson effect of the bar, the compaction and the progressive smoothing of the sliding plane during pullout.

The relationship for  $\varepsilon_r$  in either case is taken from a concrete confinement model suggested by Den Uijl and Bigaj (1996) in the same study. This model calculates the radial strains in the concrete surrounding the reinforcing bar. Although the model is primarily based on Tepfers partly cracked splitting model, it includes the effect of concrete softening behaviour after the formation of cracks in its calculations. In contrast to Tepfers model, Den Uijl and Bigaj model considers the contribution of the cracked part of the concrete cylinder to the overall splitting resistance of the concrete (figure 2.12)

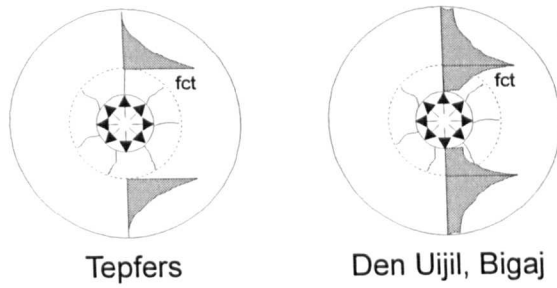


Figure 2.12: Partly cracked thick walled-cylinder

The splitting resistance found with this model falls between Tepfers lower and upper bounds for bond strengths and, generally, shows good agreement with the experimental results.

## 2.1.6 Splices

### 2.1.6.1 Crack patterns

The theories on the splitting mode of failure presented above are also used to describe the behaviour of splices. It is known from experiments that with normal concrete covers reinforcement fails mostly by splitting. Such failure is sudden and brittle for splices without transverse reinforcement whereas in the presence of stirrups splices usually fail in a less brittle manner. The most common splitting crack patterns that are developed during the failure of lapped splices are presented in figure 2.13.

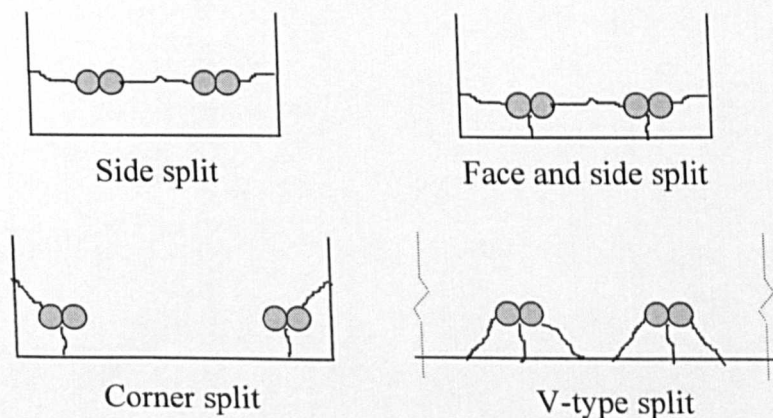


Figure 2.13: Ultimate splitting failure crack patterns (adopted from CEB Bulletin 151)

The failure patterns are valid both for splices with and without transverse reinforcement and depend mainly on the arrangement of reinforcement in the cross section. For example, splices at large spacing away from the corners fail, most commonly, in a V-type failure whereas closely spaced splices show a side split crack pattern. The corner pattern is usually observed for splices positioned close to the corners of structural elements.

### 2.1.6.2 Forces induced by splices in the surrounding concrete

When the splices are axially loaded, they impose radial pressure to the surrounding concrete that can lead to splitting. This radial pressure is proportional to the bond stress developed on the reinforcing bars, similar to single bar anchorages (see section 2.1.5). In order to understand the splitting action it would be useful to examine the distribution of the radial stresses around the spliced bars. The most known distributions were proposed by Tepfers (1973) and are shown in figure 2.14.

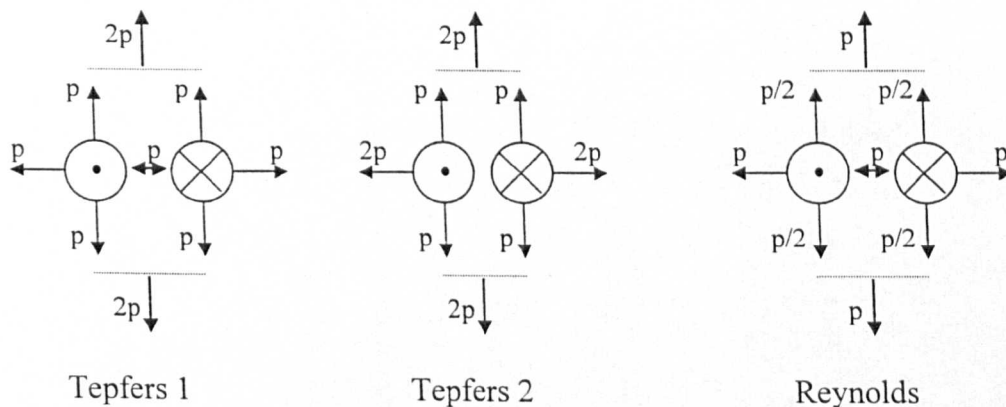


Figure 2.14: Possible distribution of radial stresses in splices

In the first one, the radial bond stress components for the spliced bars are of the same magnitude ( $p$ ) in all directions, similar to independent single anchorages, which results to a  $2p$  total splitting stress at the plane passing through the centre of the two bars. In order to form the second distribution, Tepfers assumed that the slip between the bars is double than that between an individual bar and the surrounding concrete. For this reason, he suggested that the bond at the interface between the two bars would

practically be destroyed. This assumption leads to a uniform splitting stress distribution around the group of spliced bars having twice the value of the radial stresses produced by single anchorages, as shown in figure 2.14 (Tepfers 2 distribution). In both Tepfers assumptions, the bond stresses generated by the spliced bars have the half value of the bond stresses generated by the same bars in single anchorages.

However, the creditability of the Tepfers assumptions appears to be questioned by the experimental work of various researchers around the world. Reynolds and Beeby (1982) examined the above models and commended that for both models the forces developed in a lap are considerably higher than those developed in a single anchorage and that bond strength should therefore be lower. They added that the orientation of the lapped bars in the first model would have a major effect on bond strength. In order to examine the validity of these models Reynolds (1982) conducted a large experimental series of spliced reinforcing bars embedded in beam elements. The results of this work showed that steel bars in splices or in single anchorage develop similar bond strengths and that the orientation of the lap has no effect on the formation of splitting cracks. The first conclusion was in agreement with the work of Orangun, Jirsa and Breen (1977) who were unable to detect differences in bond strength between laps and single bars.

Based on his experimental results, Reynolds (1982) suggested a third distribution of radial bond stresses around the lapped splices, shown in figure 2.14, which gives splitting stresses equal in all directions similar to the distribution of stresses around a single bar. In order to derive this distribution, Reynolds idealised the action of the concrete corbels around the spliced bars in the two transverse planes AA and BB, as shown in figure 2.15.

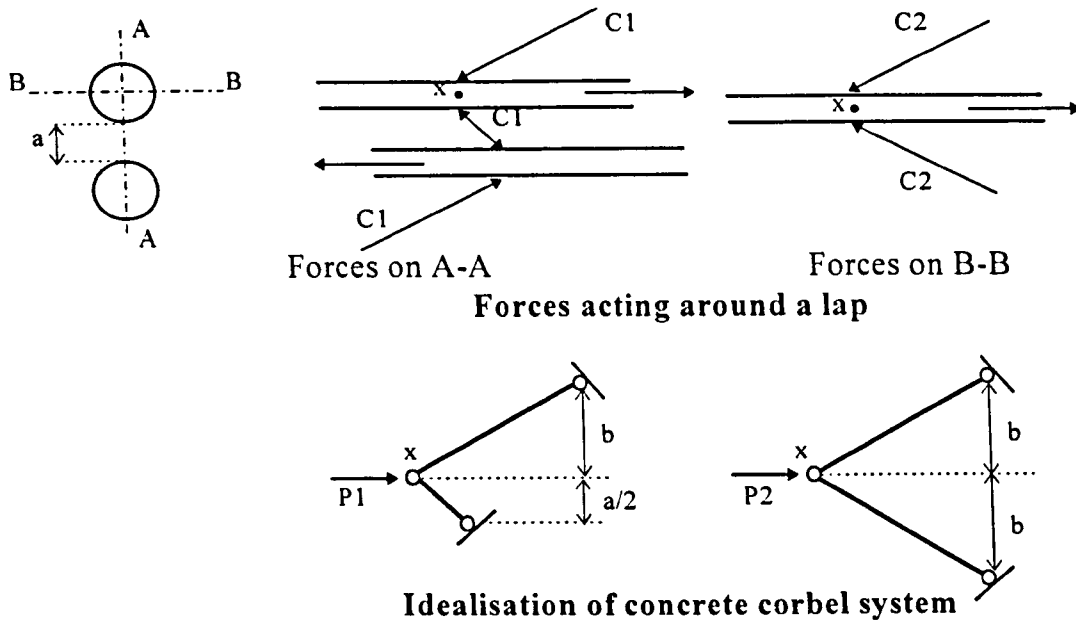


Figure 2.15: Reynolds (1982) model of concrete-bar interaction system

He assumed that a point X on the spliced bar subjected to a pullout load, would undergo the same axial deflection either been examined in AA or BB plane direction. He idealised the action of the concrete corbel force system on the bar, as shown in figure 2.15, and he assumed that both systems would undergo the same deflection. By solving the two systems, he found a relationship between forces P1 and P2. In this relationship, when the distance between the spliced bars,  $a$ , tends to be zero, P1 has double the value of P2. So, he resulted that the distribution of stresses around the spliced bars should be similar to the one shown in figure 2.14. However, the author believes that a significant drawback of Reynolds approach is that he ignored the influence of any side deflection of point X in the calculation of P1 force. The contribution of this side deflection of the force system to the bond behaviour of spliced bars might be significant and it has to be examined in more detail.

A more recent model of stress distribution around spliced bars was proposed by Cairns and Jones (1996). The model was based on an experimental series of testing lapped splices conducted by the authors and is shown in figure 2.16. The model suggests that a pair of lapped bars generate splitting force, vertical to the plane passing through the centres of spliced bars, only 30% greater than that generated by a single bar.

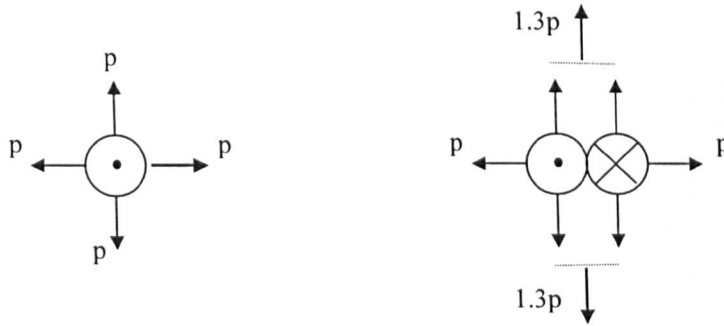


Figure 2.16: Proposed model of splitting stresses around single bar and lapped spliced.

### 2.1.6.3 Equations for calculating the bond strength of splices

All the above models are used in the formulation of equations for calculating the bond strength of lapped splices in concrete members. A number of equations to estimate the strength of splices are proposed by various researchers, as reported in CEB Bulletin 151.

Tepfers (1973) derived analytical expressions for the strength of splices failing by splitting, by equating the splitting forces to the tensile resistance of concrete. He assumed that the radial bond stress components causing splitting in the failure plane are constant along the lap length and of equal magnitude to the tangential bond stress,  $\tau$  (see figure 2.7). He also assumed a uniformly distributed tensile stress along the concrete failure surface, because of plastification of concrete (figure 2.17). It is proposed that the failure pattern with the lowest splitting resistance will determine the anchorage capacity of the lapped splice, depending on the geometry of the cross section (cover and spacing) and on the development of splitting cracks. Tepfers' analytical predictions were compared with 193 experimental beam test results (according to CEB Bulletin 151) and an acceptable agreement between them was observed.

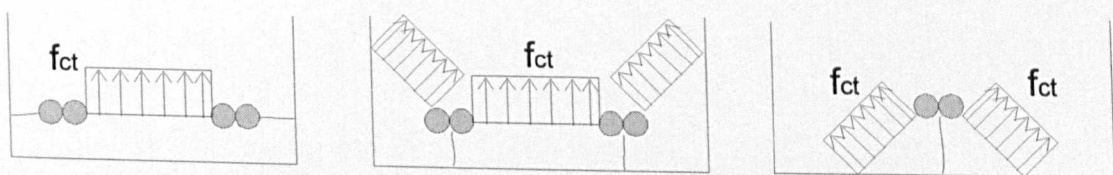


Figure 2.17: Typical splitting failure patterns with splitting stress models

Orangum, Jirsa and Breen (1977) employed an empirical approach to derive a predictive equation for the bond splitting strength of lapped bars. They suggested that the difficulties reported by various researchers in estimating the value of angle  $\alpha$ , between bond and radial stress (figure 2.7, see also sections 2.1.5 and 2.1.6.2), made an empirical approach to look more promising than a theoretical one. The constants of this equation were obtained from a non-linear regression analysis of a vast amount of experimental results of beam tests performed by various researchers. For splices without transverse reinforcement, the equation has the following form:

$$u_{cal} = (1.2 + 3c / d_b + 50d_b / l_s) \sqrt{f_{cy}} \quad (\text{in psi, in.}) \quad (2.9)$$

whereas, for splices with stirrups the value of  $u_{tr}$  given below is added to equation 2.9:

$$u_{tr} = \frac{1}{500} * \frac{A_{tr} f_{yt}}{s d_b} * \sqrt{f_{cy}} \leq 3 \quad (\text{in psi, in., in}^2) \quad (2.10)$$

where,

- $u_{cal}$  = bond splitting strength of splices without stirrups, psi
- $u_{tr}$  = contribution of stirrups in the bond splitting strength of splices, psi
- $f_{yt}$  = the yielding stress of stirrups, psi

and the other symbols according to the general notation.

The above researchers suggested the same equation for single bar anchorages failing in splitting since similar behaviour with splices has been observed. It has to be noted that the ACI Building Code (1995) formula for calculating development lengths for single anchorages and splices is based on equation 2.9 (see section 2.1.7.3).

A more theoretical approach was used by Eligehausen (1979), according to CEB Bulletin 151. He calculated the distribution of bond stresses and splitting forces along the splice length by solving the differential equation of bond for splices for realistic bond stress-slip laws by stepwise iteration. A relationship shown in figure 2.18, between the inner radial pressure and the bond stress, was assumed.

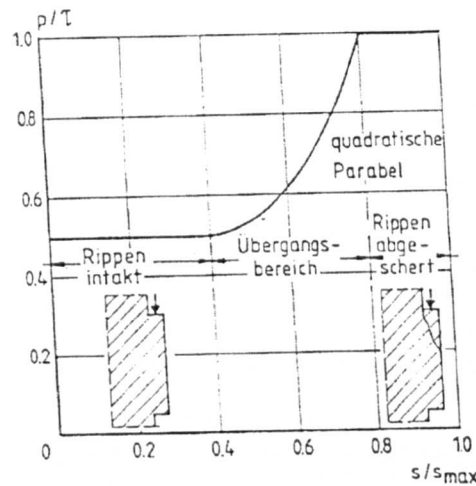


Figure 2.18: Ratio inner pressure,  $p$  to bond stress,  $\tau$  as a function of slip,  $s$  to slip  $s_{max}$  at failure for actual specimen. Internal bond cracks are assumed but not shown. (Eligehausen, 1979. Adopted from CEB Bulletin 151)

It is obvious from this relationship that the value of angle  $\alpha$  is around  $26^\circ$  at the beginning of cracking and increases with increasing slip up to  $45^\circ$ . According to CEB Bulletin 151, “Eligehausen calculated the splitting forces induced in the concrete with finite element analysis assuming elastic material behaviour. Failure was assumed when the mean tensile stress in the concrete averaged over a length of half a diameter, reached the tensile stress of concrete. By varying the model parameter (e.g. cover, spacing, bar diameter, area of transverse reinforcement) and comparing the corresponding relevant tensile stress with each other, the influence of the investigated parameter on the splice length was found and expressed analytically by fitting curves to the calculated values. In this way the study yielded equations for the calculation of the strength of splices”. Although the equations had a quite complicated form, they appeared to be reliable when compared with experimental results. The validity of equations was checked against 390 tests of spliced failures from 15 different resources, according to CEB Bulletin. An example of these equations is shown in the following figure:

$$\sigma_{su} = \sigma_{su}^c + \sigma_{su}^{ir} \leq \sigma_{su}^p$$

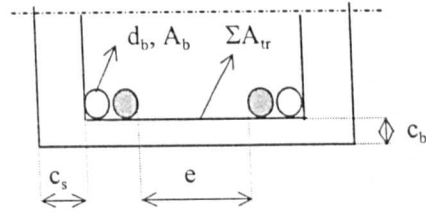
$$\bullet \sigma_{su}^c = 6.4 * \sqrt[4]{\frac{e}{d_b}} * \sqrt[4]{\frac{c_b}{d_b}} * \sqrt{f_c} * \sqrt[3]{\frac{l_d}{d_b}} * k_d$$

where:  $e = 2c_s \geq 1.7c_b, \leq 8.0c_b$

$$1.20 \geq k_d = \sqrt{\frac{10}{d_b}} \geq 0.75$$

$$\bullet \sigma_{su}^{ir} = 6.0 \sqrt{\frac{\Sigma A_{tr} f_{yt}}{A_b}} \text{ with } f_{yt} \leq 300 \text{ MPa}$$

$$\bullet \sigma_{su}^p = 3.2 f_c^{2/3} l_d / d_b$$



Notations:

$\sigma_{su}$  = steel stress at splice failure

$\sigma_{su}^c$  = steel stress anchored by splitting resistance of concrete (concrete contribution)

$\sigma_{su}^{ir}$  = steel stress anchored by transverse reinforcement (contribution of transverse reinforcement)

$\sigma_{su}^p$  = steel stress at pullout of bar

$f_c$  = cylinder compressive strength

$l_d, d_b$  = lap length, diameter of bar

Dimensions: MPa, mm, mm<sup>2</sup>

Figure 2.18: Equation for calculating the average strength of lapped splices.

Eligehausen (1979)

Finally, the equation for calculating the bond strength of splices and single bar anchorages according to BS8110 (1985), is based on the experimental work of Reynolds (1982). Reynolds tested thirty-nine beams in order to measure the bond strength ( $f_{bs}$ ) of steel reinforcing bars in splices and in single bar anchorages. He proposed equation 2.11 for anchorages and splices without transverse reinforcement:

$$f_{bs} = 0.25 \sqrt{f_{cu}} (0.5 + c/d) \quad (\text{in N/mm}^2, \text{ mm}) \quad (2.11)$$

This equation was initially derived from Tepfers partly-cracked bond stress equation 2.3. Reynolds assumed that the tensile strength of concrete is proportional to the square root of the compressive strength and rewrote equation 2.3 in a more general form (eq. 2.12).

$$f_{bs} = K \sqrt{f_{cu}} (0.5 + c/d) \quad (\text{in N/mm}^2, \text{ mm}) \quad (2.12)$$

Based on his experimental results and by considering the existing work of various researchers, Reynolds suggested the value of 0.25 as the most conservative value for the constant K, which results to equation 2.11.

The effect of transverse reinforcement was taken into account by adding the value of expression 2.13, in equation 2.11. In this expression, the stress in the transverse bars was taken well below the yield stress of steel. Since the lowest value of transverse steel stress observed in Reynolds experiments was 70 N/mm<sup>2</sup>, it was assumed to be a conservative stress value for stirrups for design purposes.

$$22 A_t / (sd) \quad (\text{in mm, mm}^2) \quad (2.13)$$

The above mentioned experimental and analytical investigations for evaluating the bond splitting strength of steel deformed bars in concrete members, formed the basis for the various formulas for calculating the anchorage length in most commonly used codes of practice, which are briefly presented in the following section.

## 2.1.7 Codes of practice

### 2.1.7.1 British Standard 8110 (1985)

BS 8110 introduces equation (2.14) from where the values for design ultimate anchorage bond stress,  $f_{bu}$  may be obtained.

$$f_{bu} = \beta \sqrt{f_{cu}} \quad (\text{in N/mm}^2) \quad (2.14)$$

In this equation  $f_{cu}$ , is the compressive strength of a 100 mm concrete cube and  $\beta$ , is a coefficient dependent on the bar type. For tension reinforcement in slabs or beams, where minimum links have been provided, the code gives a table of values for the bond coefficient  $\beta$ . For the most commonly used steel deformed bars,  $\beta$  is equal to 0.5 whereas for plain steel bars  $\beta$  takes the value of 0.28. The values of bond strength obtained from equation (2.14) incorporate a partial safety factor equal to 1.4. The code also underlines that in beams where minimum links have not been provided, the design bond stresses should be those appropriate to plain bars irrespective of the type of bar used.

The design bond stress values are introduced to the fundamental anchorage length formula (2.15), in order to calculate the basic design anchorage length,  $l_b$ .

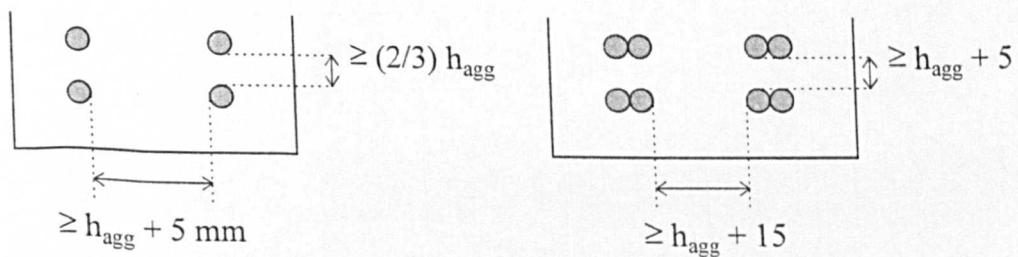
$$l_b = \frac{d f_{yd}}{4 f_{bu}} \quad (\text{in mm, N/mm}^2) \quad (2.15)$$

In the case of tension splices, the code introduces multiplication factors on the value of design anchorage length formula (2.15). These factors are shown in the table 2.1 depending on the arrangement of splices in the cross section of a structural member. The lap values introduced by table 2.1 must always be greater than 15 times the bar size or 300 mm, which ever is greater.

|                             |                  | Tension lap lengths                         |   |                    |
|-----------------------------|------------------|---|---|--------------------|
|                             |                  | Bars in top section as cast with cover < 2d | Corner bars not in top of section with cover < 2d | Otherwise          |
| Clear distance between laps | ≥ 75 mm and ≥ 6d | 1.4 l <sub>b</sub>                          | 1.4 l <sub>b</sub>                                | 1.0 l <sub>b</sub> |
|                             | Otherwise        | 2.0 l <sub>b</sub>                          | 1.4 l <sub>b</sub>                                | 1.4 l <sub>b</sub> |

Table 2.1: Multiplying factors for lap length

In addition, the code recommends minimum values for cover and spacing of reinforcement for single anchorages and splices; the cover to main reinforcing bars must not be less than the bar diameter whereas the minimum spacing of reinforcement for single anchorages and splices is shown in figure 2.19.



where,  $h_{agg}$  is the maximum size of aggregate

Figure 2.19: Minimum spacing of tension reinforcement

### 2.1.7.2 Eurocode 2 (1989)

In Eurocode 2, the design values for the ultimate bond stress,  $f_{bd}$  of tension reinforcement are given in a tabular form (table 2.2), for “good” bond conditions which apply to most common conditions in practice. “Bad” bond conditions take into account mainly the top bar effect and reduce the design bond strength by 30%.

| Concrete compressive strength, $f_{ck}$ (N/mm <sup>2</sup> ) | 12  | 16  | 20  | 25  | 30  | 35  | 40  | 45  | 50  |
|--|-----|-----|-----|-----|-----|-----|-----|-----|-----|
| Plain bars   | 0.9 | 1.0 | 1.1 | 1.2 | 1.3 | 1.4 | 1.5 | 1.6 | 1.7 |
| High bond bars with diameter $\Phi \leq 32$ mm               | 1.6 | 2.0 | 2.3 | 2.7 | 3.0 | 3.4 | 3.7 | 4.0 | 4.3 |

Table 2.2: Design values  $f_{bd}$  (N/mm<sup>2</sup>) for good bond conditions

The above design bond values derived from formulas depending on the concrete strength of the structural member and incorporate a safety factor equal to 1.5. The code also takes into account the possible presence of transverse pressure,  $p$  in N/mm<sup>2</sup>, to the expected plane of splitting. In this case, since the bond strength is favourably influenced (see section 2.1.3.3), EC2 code suggests an increase of the bond strength values by multiplying them by the factor  $1/(1-0.04p)$ .

According to EC 2, the required anchorage length,  $l_{b,net}$  may be calculated from the relationship:

$$l_{b,net} = \alpha_{\alpha} l_b (A_{s,req}/A_{s,prov}) > l_{b,min} \quad (\text{in mm, mm}^2) \quad (2.16)$$

where,

$l_b$  = basic anchorage length  $= (d/4) (f_{yd}/f_{bd})$

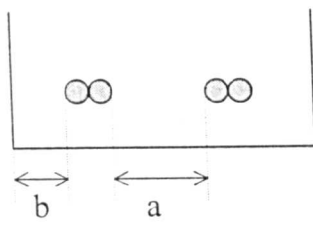
$l_{b,min}$  = Minimum anchorage length  $= 0.3 l_b (>10d)$

$\alpha_{\alpha}$  = 1, for straight bars

$A_{s,req}, A_{s,prov}$  = the area of reinforcement required by design - and actually provided

EC2 also recommends the use of a minimum amount of transverse reinforcement in the region of the anchorage length. The minimum total area of transverse reinforcement must be 25% of the area of one anchored bar and should be evenly distributed along the anchorage length.

For the case of splices, the required lap length,  $l_s$  (eq. 2.17) is the product of  $l_{b,net}$  with a factor  $\alpha_1$  according to figure 2.20.



(I)  $\alpha_1 = 1.0$ : For laps in tension where less than 30% of the bars in section are lapped and where  $a > 10d$  and  $b > 5d$

(II)  $\alpha_1 = 1.4$ : For laps in tension where either  
 (i) 30% or more of the bars at a section are lapped  
 or  
 (ii)  $a < 10d$  and  $b < 5d$

(III)  $\alpha_1 = 2.0$ : When (i) and (ii) are both satisfied

$$l_s = l_{b,net} \alpha_1 \geq l_{s,min} \quad (2.17)$$

Figure 2.20: Values for  $\alpha_1$  coefficient in lap splices

In all cases the required lap length must be greater than the minimum lap length,  $l_{s,min}$  calculated according to the relationship:

$$l_{s,min} = 0.3 \alpha_1 \alpha_{\alpha} l_b > 15d > 200 \text{ mm} \quad (2.18)$$

The code also recommends a minimum amount of transverse reinforcement for the spliced region. When the diameter of the lapped bars is less than 16 mm, or if the percentage of lapped bars in any section is less than 20%, then the minimum transverse reinforcement provided for other reasons (e.g. shear reinforcement, distribution bars) is considered as sufficient. Otherwise, the code recommends additional transverse reinforcement to be used.

### 2.1.7.3 ACI Building Code 318 (1995)

In the ACI Code, the concept of “Development Length” for anchorage of reinforcement is mainly used. This concept is based on the attainable average bond stress over the embedment length of the reinforcement. The main idea of the code results from an attempt to avoid the possibility of highly stressed bars to split thin sections of restrained concrete (ACI 318 Building Code Commentary, 1995). There are no provisions in the code for single bars embedded in a mass of concrete. No strength reduction factor is used in the relationship of calculating the development length since the relationship itself includes an allowance for understrength. It is also useful to note

that the endorsed development length values are still based on the general equation for development length suggested in the study of Orangun, Jirsa and Breen (1977).

According to the code, the development length,  $l_d$  of a deformed steel bar in tension is calculated in terms of the bar diameter,  $d_b$  from the relationship (2.19):

$$\frac{l_d}{d_b} = \frac{3}{40} \frac{f_v}{\sqrt{f_{cy}}} \frac{a\beta\gamma\lambda}{\left(\frac{c + K_{tr}}{d_b}\right)} \quad (2.19)$$

where,

$\alpha$  = reinforcement location factor

For reinforcing bars placed horizontally and more than 12 in. (30.5 mm) of concrete is cast in the member below the reinforcement the factor is equal to 1.3, otherwise 1.0

$\beta$  = coating factor

For epoxy coated bars with cover less than  $3d_b$ , or clear spacing less than  $6d_b$  the factor is 1.5. For all the other epoxy-coated bars the factor is 1.3 and for uncoated reinforcement is 1.0

However, the product of  $(\alpha\beta)$  need not be taken greater than 1.7.

$\gamma$  = reinforcement size factor

For No. 6 ( $d_b=19$  mm) and smaller bars the factor is 0.8, whereas for larger bars it is 1.0

$\lambda$  = lightweight aggregate concrete factor

For normal concrete the factor is 1.0.

$c$  = spacing or cover dimension, in.

It is defined as the smaller of either the distance from the centre of the bar to the nearest concrete surface or one-half the centre-to-centre spacing of the bars.

$K_{tr}$  = transverse reinforcement index =  $A_{tr} f_{yt} / (1500 s n) \leq 2.5$

where,

$A_{tr}$  = total cross sectional area of all transverse reinforcement which is within the spacing  $s$  and which crosses the potential plane of splitting through the reinforcement being developed, in.<sup>2</sup>

- $f_{yt}$  = specified yield strength of transverse reinforcement, psi
- $s$  = maximum spacing of transverse reinforcement within  $l_b$ , in.
- $n$  = number of bars being developed along the plane of splitting

However, the code permits  $K_{tr}$  to be taken equal to zero as a design simplification even if transverse reinforcement is present. A limit on the term  $(c + K_{tr}) / d_b$  of 2.5 is also included to safeguard against pullout failures, according to the Code Commentary. In addition, the code underlines that the development length shall not be taken less than 12 in. for safety reasons.

Finally, in the case of tension lap splices the, ACI Code suggests a minimum length of lap according to the Class of the splice (A or B Class) as follows:

Class A splice.....Splice length =  $1.0 l_d$

Class B splice.....Splice length =  $1.3 l_d$

but not less than 12 in. for each case. The classes of splices are shown in table 2.3:

| As provided /<br>As required * | Maximum percent of $A_s$ (area of<br>tension reinforcement) spliced within<br>required lap length: |         |
|--------------------------------|--|---------|
|                                | 50   | 100     |
| Equal to or greater than 2     | Class A  | Class B |
| Less than 2                    | Class B  | Class B |

Table 2.3: Tension Lap Splices

- \* Ratio of area of reinforcement provided to the area of reinforcement required by analysis at splice locations

#### 2.1.7.4 Commentary on codes of practice

Although an overall comparison of the above codes of practice would be a quite interesting task, the author intends in this section to highlight only some general aspects of the codes which will be discussed or analysed at a later stage in this study.

Firstly, it is important to realise that the above codes are basically made for steel reinforcement. In some cases, epoxy coated steel bars are considered, which still have the same Young's modulus as normal steel bars. There are no provisions for

incorporating in their anchorage or development length formula materials with different modulus of elasticity, such as Fiber Reinforced Polymers. Therefore, it is possible that the bond formulas recommended by the codes may not be safe to be used in their existing form, for evaluating the anchorage length of FRP reinforcing bars. The same thing also applies in the case of the transverse reinforcement necessary to resist the splitting bond failure of the main reinforcing bars, since there are no provisions that will allow the engineer to use alternative types of materials.

Secondly in all the codes, design bond values, either defined explicitly (EC2 and BS8110) or implicitly (ACI code), are given without the use of a proper pullout or beam test that will generate these values. The recommended by the codes standardised tests develop bond values significantly different from the suggested design values. Until now, this did not create serious problems since all the codes based their design bond values on a large number of beam tests conducted by various researches who tested the same type of reinforcing material (steel) having similar cross-section shape and similar types a surface deformations. By considering all these experimental results and applying a conservative safety factor, the codes of practise produced reliable bond strength values for practical applications.

Unfortunately, this is difficult to be done in the case of the new reinforcing materials. The new FRP reinforcing bars can have variable material properties, cross-sectional shapes and surface deformations (see next section for more details). It would be impossible to conduct sufficient number of tests (similar to the number of tests conducted for steel bars) for all the kinds of the existing FRP bars in the market in a relatively short period of time. So, either the manufacturers of FRP bars will have to be constrained to produce only certain types of bars - which is unacceptable since it will kill any innovative new ideas - or the engineers will have to introduce in their codes a standardised test which will measure reliably the bond behaviour of any reinforcing bar. This test must be able to define which of those materials have the necessary bond properties to be used as reinforcement, otherwise the introduction of FRP reinforcement in the construction market will be significantly delayed.

A third point that is quite interesting to note in the above codes of practice is their different approach regarding the anchorage length of spliced reinforcement. EC2 and BS8110 appear to be much more conservative than the ACI Code. The Europeans believe that spliced bars develop significantly lower bond strength than the single bar

anchorage whereas the Americans, influenced by the work of Orangum, Jirsa and Breen (1977), believe that spliced bars and single anchorages develop similar bond strengths.

The importance of bar diameter on the development of bond strength is also differently expressed in the above codes of practice. Whereas the ACI Code suggests that bars with diameter greater than 19 mm develop less bond than smaller diameter bars, EC2 believes that this is applied only in bars with very large diameters (>32 mm). On the other hand, BS8110 does not have any provisions for various diameter bars. In the case of FRP reinforcing bars, the diameter is believed to play an important role in the bond behaviour of FRP bars to concrete because of the lower shear stiffness of FRP bars in the longitudinal direction (see section 4.1.3.4).

In the following section, a brief introduction to FRP bars will be presented as well as the experimental effort of various researchers around the world to understand and measure the bond behaviour of FRP reinforcing bars in concrete. Towards the end of the section, some the first published design codes of practice and recommendations relating to the bond performance of FRP bars will also be presented.

## 2.2 FRP REINFORCEMENT FOR CONCRETE STRUCTURES

### 2.2.1 General

In the last ten years, a considerable amount of research is taking place investigating the alternative solution of using of non-ferrous materials, known as Fibre Reinforced Polymers (FRP), as concrete reinforcement in concrete structures. These materials appear to be a promising solution to the problem of corrosion of steel reinforcement since many types of them have been successfully used in demonstrating structures world-wide, until now (see Introduction).

The first thing someone will notice about these materials is that they are completely different than steel. Different texture, weight, flexibility, colour and many more other parameters which introduce a new image for reinforcement in concrete structures. A closer look in their properties will highlight their strengths and weaknesses comparable to conventional steel reinforcement. Pilakoutas et al (1997b) presented their main advantages and disadvantages against steel as shown in the following table:

| ADVANTAGES   | DISADVANTAGES   |
|--|---|
| <ul style="list-style-type: none"> <li>• higher ratio of strength to self weight (10 to 15 times greater than steel )</li> <li>• carbon and aramid fibre reinforcement have excellent fatigue characteristics</li> <li>• excellent corrosion resistance and electromagnetic neutrality</li> <li>• low axial coefficient of thermal expansion.</li> </ul> | <ul style="list-style-type: none"> <li>• higher raw material cost</li> <li>• lower elastic modules (except some Carbon FRPs)</li> <li>• Glass FRP reinforcement suffers from stress corrosion</li> <li>• lack of ductility</li> </ul> |

Table 2.4: Main advantages/disadvantages of FRP materials

There are currently a number of manufacturers who are developing non-ferrous reinforcement as an alternative to the conventional steel in traditional structures, so, a

variation in the nature of end products is expected (Clarke, 1993). Usually, most of the FRP products consist of continuous glass, carbon or aramid fibres impregnated in a resin matrix (e.g. epoxy, polyester, vinyl ester). The fibre volume ratio of the most commonly used reinforcing bars is around 70%.

FRP materials are manufactured using several techniques (Bakis, 1993) including manual lay-up, FRP molding, tube rolling, filament winding, braiding, pultrusion and many others. Pultrusion is the most common method used for manufacturing of FRP rods in Europe and America. The pultrusion process is similar to that shown in figure 2.21, adopted from Ehsani (1993):

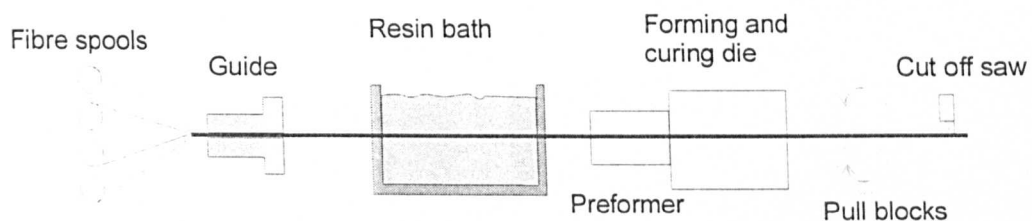


Figure 2.21: Pultrusion process

The process starts with several spools of fibres in the form of strands. The fibres are pulled through a series of guides where they are formed into the desired shape. Next, they pass through a resin path for impregnation. During the last stage, the resin/fibre matrix is passed through a heated die where the excess resin is squeezed out of the bar and the curing process initiates. A peel-ply may be added to the surface of the bar to form deformations that will improve its bond characteristics. The completed bar is pulled out of the die in a continuous process and is cut to the desired length.

FRP materials are available in a variety of shapes and sizes. Rods, plates, grids, spirals, links are some common examples used in the construction industry. FRP can easily be manufactured in any shape while the resin has not cured. After that stage, if thermosetting resins are used their shape can not be changed and this creates a potential problem in their use. Unlike steel, FRP materials with thermosetting resins can not be bent in site. Attempts to bend a straight bar will result to a concentration of stresses at the bending area leading to the fracture of the bar. In order to overcome this problem, a different design approach must be adopted by the engineers taking into account the

different material properties of FRP bars. FRP reinforcing bars made of thermoplastic resins are currently being developed.

An additional characteristic of the commercially available FRP bars is that they are produced having different kind surface deformations. The form of bar deformations differs from manufacturer to manufacturer depending on the process used. These deformations usually consist of resin or a combination of resin and fibre or even additional sand particles attached to the surface of the bar during the curing treatment. It is beyond the scope of this study to present in detail the different kinds of bar deformations available in the market. Useful information on this subject can be found in the recently published "Recommendation for design and construction of concrete structures using continuous fiber reinforcing materials" by the Japanese society of Civil Engineers (1997) and to the Proceedings of the 3<sup>rd</sup> International Symposium on Non-Metallic (FRP) reinforcement for concrete structures (1997). However, it is significant to understand that the different kinds of bar surfaces have a direct influence on the bond behaviour of these bars. Bond of FRP bars in concrete appears to depend mainly on the mechanical interlock of bar deformations and the surrounding concrete (see sections 2.1.2 and 4.1.3.6). The load level where this interlock breaks (maximum bond strength of the bar) is an important parameter that has to be assessed before using each bar in structural applications.

FRP bars can also be produced in a variety of cross-sectional shapes, unlike conventional reinforcing steel. The shape of the forming die used in the manufacturing process (see figure 2.21) determines the cross-sectional shape of an FRP bar. The cross-sectional shape is expected to influence to bond behaviour of the bar to concrete because of the different distribution of normal strains and stresses over different shaped bar cross-sections. This factor will be examined experimentally in another section of this study (see section 4.1.3.5).

In the following, FRP mechanical properties will be presented with emphasis being placed on the properties of FRP reinforcing bars.

## 2.2.2 Basic mechanical properties

FRP bars, unlike steel rebar, are strongly anisotropic. Their mechanical properties are different in the two transverse directions, having the longitudinal axis as the stronger one. In addition, their mechanical properties vary significantly from one product to another depending, mainly, on the nature and volume of fibres in the cross-section, the mechanical properties of resin and the fibre orientation (Ehsani, 1993). For these reasons, it is very difficult to specify universal values for the mechanical properties of all FRP materials so, only indicative values can be given.

### 2.2.2.1 Tensile strength and elongation at failure

Generally, FRP bars develop much greater tensile strength than conventional high strength steel depending on the nature of fibres. Glass FRP bars can develop more than two times the tensile strength of steel whereas Carbon and Aramid bars more than three times. A comparison of the tensile properties of FRP and steel bars is shown in figure 2.22.

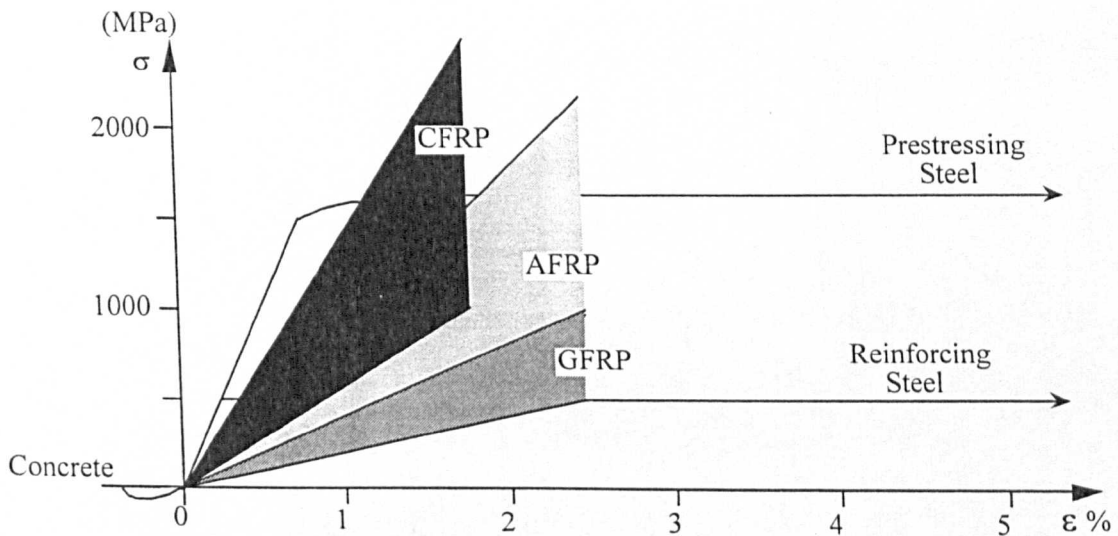


Figure 2.22: Stress versus strain relationship for FRP and steel bars  
(Pilakoutas et al, 1997b).

Ehsani (1995) suggests that the ultimate tensile strength of FRP bars, and specially Glass FRP bars, is sensitive to the reinforcing bar diameter and decreases rapidly with an increase in diameter. According to GangaRao and Faza (1993), the

fibres located near the centre of the bar cross-section are not subjected to as much stress as those fibres near the outer surface of the bar due to the resin dependent shear lag phenomenon. The above observations were also confirmed by the author's experimental work as will be presented in a following chapter.

The elongation of FRP bars (strain) also depends on the nature of fibres used. Carbon FRP bars exhibit less maximum elongation than Glass and Aramid FRP bars, as shown in the figure above. However, the ultimate strain values developed for all FRP bars appear also to depend significantly on the diameter of the bar used as reinforcement.

#### **2.2.2.2 Modulus of elasticity**

The Young Modulus of FRP bars is generally lower than that of steel. Glass FRP, usually, have the lowest elastic modulus, around 20 - 30 % of that of steel, and Carbon FRP the highest, between 50 - 70 % of that of steel, as shown in figure 2.22. It is noted that the modulus remains, practically, constant up to the failure point (elastic behaviour), unlike steel bars (ductile behaviour). This lower value of modulus of elasticity is expected to play an important role to the deformability of concrete members reinforced with FRP materials.

#### **2.2.2.3 Shear strength**

The shear strength of FRP materials is, generally, very low comparable to their tensile strength. FRP bars, for example, can be cut easily with a simple saw in a direction transverse to the longitudinal axis. This lower shear strength of FRP bars is quite probable to influence their bond behaviour to concrete especially in the case of the splitting mode of failure.

## 2.3 BOND OF FRP REINFORCING BARS TO CONCRETE

### 2.3.1 General

Bond between concrete and FRP reinforcing bars is one of the fundamental aspects of structural behaviour, which has to be examined before the wider acceptance of FRP materials in the construction industry. An adequate level of bond is required between reinforcement and concrete to transmit forces from one to another. Particular areas of concern are the anchorages at the end of bars since bending of FRP bars is not always possible, and the laps where high loads have to be transferred from one bar to an adjacent one.

The bond behaviour of FRP bars to concrete is expected to vary from that of conventional steel bars since various key parameters that influence bond performance are different. Such parameters include:

- The lower FRP modulus of elasticity
- The much lower shear strength and stiffness in the longitudinal and transverse direction
- The shear capacity of the resin matrix which is expected to control the strength of any deformations on the surface (Nanni, 1995)
- The high normal strains expected at failure

The bond behaviour of FRP reinforcing bars is also expected to be influenced by various other parameters such as creep, fatigue, temperature and environmental conditions. Due to their different composition, bond performance of FRP bars is expected to be more sensitive to the above parameters than bond of steel bars. Whilst the author recognises the importance of investigating the effect of these factors on bond, they do not form part of the scope of this study. Other researchers within the EUROCRETE project have examined the above subjects in more detail although the amount of work published is very limited until now. More information on the effect of

these parameters can be obtained from: Hattori A. et al (1995, 1997), Faza S. et al (1997) on bond creep, Takagi N. et al (1997), Shield C. et al (1997), Del Uijl (1995) on bond thermal and mechanical fatigue, Gentry and Hudak (1996) on the influence on bond of the thermal incompatibility of FRP bars and concrete, Al-Dulaijan et al, Al-Zahrani et al (1996), Uppuluri et al (1996), Sheard P. et al (1997) on the influence of environmental conditions on bond. However, this study will concentrate only on the static short-term bond behaviour of FRP bars to concrete under various experimental conditions.

Although many studies have been carried on this subject, the results obtained were specific to the particular kind of bar tested (Clarke, 1996). In the following, a brief description of a number of these studies from various parts of the world will be presented, investigating mainly the pull-through mode of bond failure of different kinds of FRP bars. In addition, some studies examining the splitting mode of bond failure of FRP bars and studies on bond modelling will be reported. The literature review will be concluded with a brief presentation of the existing codes of practice and design recommendations on bond of FRP bars.

## **2.3.2 Experimental investigations on pullout bond behaviour of FRP bars**

### **2.3.2.1 USA - Canada**

A systematic investigation of the bond behaviour of FRP reinforcing bars to concrete was conducted in the USA only in the last seven years. One of the first experimental works was published by Faza and GangaRao (1990) at West Virginia University. In this work, a series of beam type pullout tests were conducted (figure 2.23) in order to investigate the bond behaviour of Glass FRP bars ( $\sigma_t = 900$  MPa,  $E_G = 48$  GPa) in “high” strength concrete ( $f_{cy} = 45-52$  MPa).

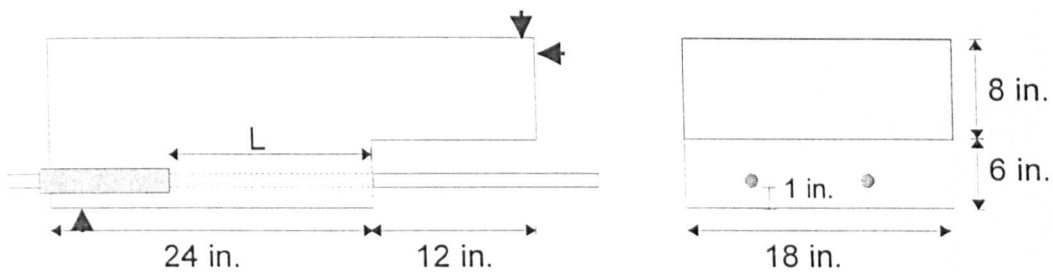


Figure 2.23: Beam type bond test arrangement by Faza and GangaRao (1990)

GFRP rough surface bars with diameters 9.5 mm (#3) and 25.4 mm (#8) were tested. Longitudinal and transverse reinforcement was provided in the beam specimen. The results showed that the #8 bars, having embedment lengths 406 mm (16d) and 610 mm (24d), developed maximum average bond strength values of 3.2 and 2.8 MPa respectively. The #3 bars failed in tension, so their ultimate bond capacity was not possible to be measured. Nevertheless, the authors suggested that the #3 bars could develop more than 2.7 MPa bond strength in the worst case of 610 mm (64d) embedment length. The authors did not mention in their report the mode of failure of #8 bars, but this is expected to be due to bond splitting.

The bond characteristics of four different types of GFRP reinforcing bars with different surface deformations were analysed experimentally by Malvar (1994, 1995) in University of California. The types of bars are shown in the figure below:

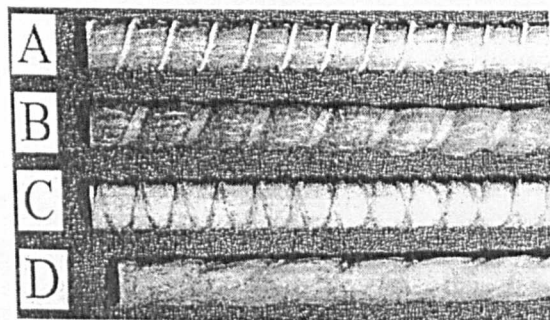


Figure 2.24: Bar types used by Malvar (1995)

Type A bars had an external helicoidal tow which both provided a protruding deformation and small indentation in the bar surface. The indentations on Type B bars were obtained by a stressed surface tow during fabrication. Type D bars were manufactured similar to type B but an outer resin layer was also added to the surface to

protect the fibres. Finally, type D bars have a helicoidal tow glued to the surface to provide only surface deformations.

A different experimental arrangement was adopted in this experimental series, where a #6 GFRP bar ( $d=19$  mm) was embedded in a 3in. diameter - 4 in. long, pre-cracked concrete cylinder subjected to a controlled amount of confining axisymmetric radial pressure. Only 67 mm of contact was allowed between the bar and concrete (figure 2.25).

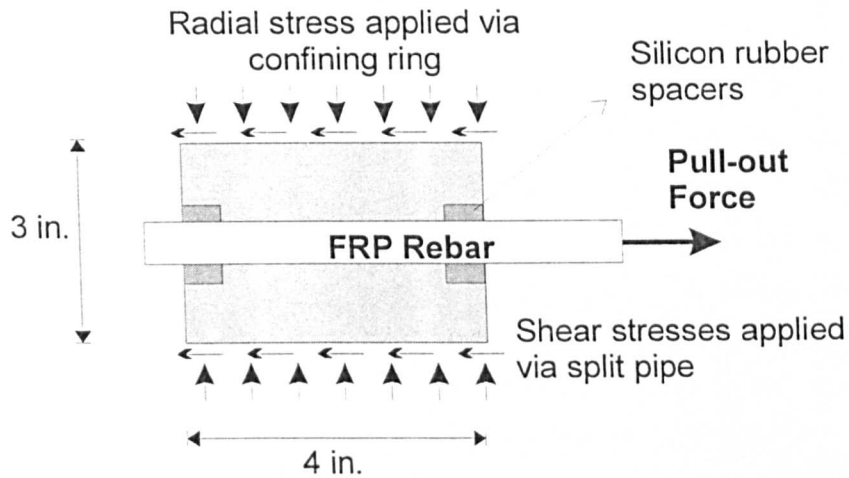


Figure 2.25: Test specimen (1in. = 25.4 mm)

For each type of reinforcing bars, bond stress-slip and bond stress-radial deformation relationships were obtained for five levels of confining pressure. The bars had tensile strength between 450 and 710 MPa, and modulus of elasticity 28 to 48 GPa. Malvar concluded that the bond strength of types A, B and D GFRP bars can be increased by increasing the confining pressure, but only when splitting of the concrete cylinder occurred. Small surface deformations, about 5.4 % of the bar diameter, were thought to be sufficient to provide adequate bond behaviour similar to that obtained from steel bars. The bond strength of steel bars was between 1.2 and 1.5 times the bond strength of these types of GFRP bars for an identical amount of confinement. Type C bars did not develop sufficient bond strength since the helicoidal tow was unglued at low load levels.

Similar bond strength ratios were obtained in the experiments of Larralde and Silva-Rodriguez (1993), at Drexel University at Philadelphia, although they used a different test arrangement and a different type of bar.

Another important series of investigations on the bond behaviour of FRP reinforcing bars was conducted by the research team of Nanni at Minnesota University. In the first series (Nanni et al, 1995), they have performed measurements on bond strength using conventional direct pullout tests with embedment lengths of 5 and 10 bar diameters. They tested both smooth and rough surface bars but special consideration was given to the latter. Three types of rough bars with different fibre/resin configuration were examined: glass-vinyl ester (GV), carbon-vinyl ester (CV) and carbon-epoxy (CE). The results showed that the bond strength of smooth bars (especially those with resin rich surface layer) was very low. On the other hand, the rough FRP bars developed bond strengths comparable to that of steel deformed bars. More specifically, GV and CV bars developed average bond stresses of 13 and 14 MPa, respectively, whereas CE bars developed bond strengths of 23 MPa. Steel deformed bars bond strength was around 15-20 MPa. All machined (rough) rods exhibited the same failure mechanism: shear off of lugs followed by sliding. Since the failure was controlled by resin, the concrete strength appeared to have insignificant influence on bond strength, provided the failure mode did not change (similar observations as Chaallal and Benmokrane, 1993). The height of bar deformations (height examined: 1.3 mm and 0.75 mm) had no significant effect on the bond strength and failure mode.

In the second series (Al-Zahrani et al, 1996), the same kind of test arrangement and materials were used. The only difference was the placement of a strain probe inside the FRP rod to monitor internal strain distribution (axial and hoop directions), at the region of embedment length, without affecting the FRP/concrete interface. Some interesting bond stress and strain distributions were obtained along the embedment length, similar to the distributions obtained in the analytical part of this study (see section 5.1.2.2).

Jerret and Ahmad (1995) used a different arrangement to measure the bond strength of 8mm CFRP bars ("Leadline", manufactured by Mitsubishi Kasei Corporation, with  $\sigma_t = 2000$  MPa,  $E_c = 147$  GPa) with long embedment lengths (19d, 38d, 57d). The specimens were cast vertically and were pulled-out from concrete slabs ( $f_{cy} = 45$  MPa) as shown in figure 2.26.

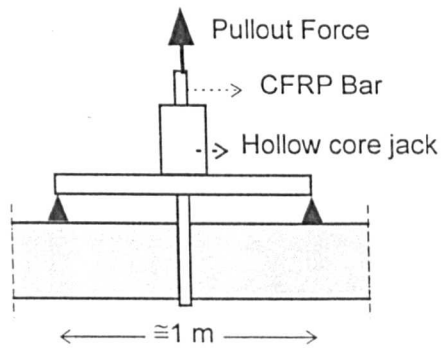


Figure 2.26: Indicative test arrangement

By using this test arrangement, the authors assumed that there would be no effect of reaction stresses arising from the loading frame, on the bond behaviour of the bar. The experimental results showed that the rough surface bars developed bond stresses between 7.3 to 7.8 MPa. A visual examination on the under side and upper side of the concrete slab was conducted after the pullout tests and no distress of the surrounding concrete was found.

In Canada, Benmokrane and Chaallal at Sherbrooke University, conducted two experimental series investigating the bond behaviour of GFRP bars, firstly in direct pullout and then in beam tests. The GFRP bars, supplied by a Canadian manufacturer (Pultrall Inc.), had a smooth surface on which deformations were added by helical winding the same kind of fibers and by sand coating particles. Their tensile strength was around 700 MPa and the elastic modulus around 45 GPa. Normal and high strength concretes ( $f_{cy} = 30$  and 80 MPa) were used in both series.

In the first series (Chaallal and Benmokrane 1993), the GFRP bars were embedded vertically in 150 x 300 mm concrete cylinders having anchorage lengths 5 or 10 times the bar diameter. Three bar diameters were tested (12.7 mm, 15.9 mm, 19.1 mm) in a large number of tests. The main conclusions from the tests were:

- The bond strength of glass-fibre rods in normal strength concrete varied from 11.1 to 15.1 MPa with average 12.9 MPa, which is 62% to 84% of that of steel deformed bars.
- The bond strength of FRP bars did not depend on the concrete strength in the same way as steel (for concrete strengths 30, 80 MPa).
- For reaching the ultimate tensile capacity of GFRP bars an anchorage length of 20d is necessary.

In the second series (Benmokrane, Chaallal and Tighiouart (1994,1996)), 20 beam tests were prepared according to RILEM/CEB (1978) specifications. Four different reinforcing bars diameters (12.7, 15.9, 19.1 and 25.4 mm) were examined and the embedment length in all the specimens was kept equal to 10d. All GFRP specimens failed by pullout and, in some of them, there was some evidence of the deformations of the reinforcing bars being sheared and damaged. The main conclusions from this series were:

- The maximum bond strength of GFRP reinforcing bars, varied between 6.4 to 10.6 MPa, which is lower than that of steel bars, approximately 60 to 90%, depending on the bar diameter.
- The bond strength observed from pullout tests was 5 to 80% higher than that obtained from beam tests, depending on the bar diameter.
- The distribution of bond stresses along the anchorage length of GFRP bars was found to be non-linear and similar to that of steel. The maximum bond stress moved progressively towards the free end of the reinforcing bar with increasing load.

#### 2.3.2.2 Europe

In Italy, Rosetti, Galeota and Giammateo (1995) investigated the bond relationship between GFRP bars with polyester matrix ( $\sigma_t = 450-490$  MPa,  $E_G = 31-40$  GPa) and concrete ( $f_{cu} = 50-70$  MPa). They used the conventional pullout test arrangement with embedment length 5 times the bar diameter. The experimental results showed that rough surface bars developed bond stresses less than 4.2 MPa with a great scatter of values. This does not seem to agree with results of other researchers and may be due to inadequate surface shear strength of the bars. Nevertheless, the results obtained were used to develop a model of the stress-slip relationship and to estimate the anchorage lengths needed to embed these bars in concrete.

In Sweden, Tepfers and Karlsson (1997) conducted two series of pullout tests in order to examine the bond behaviour of GFRP C-BARs to concrete ( $\sigma_t \cong 750$  MPa,  $E_G = 42$  GPa). In the first one, the bar was placed centrally in a 200 mm cube whereas in the second series, the bars were positioned eccentrically in a rectangular prism, as shown in figure 2.27. The bars used had diameter of 12 mm and 15 mm.

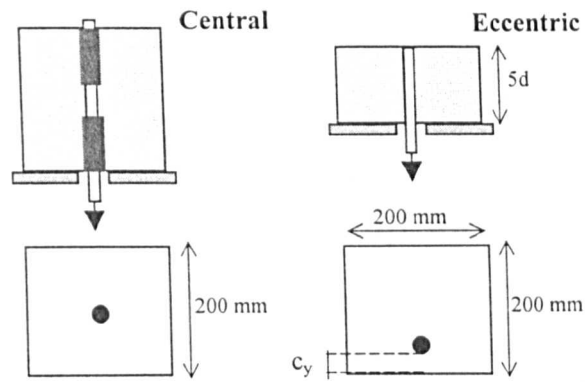


Figure 2.27: Pullout test specimens with central and eccentric placement of bar

In the first series, the embedment lengths examined were 3, 5, 7 times the bar diameter and the concrete compressive strength was between 25 and 55 MPa. The bars developed average bond strength of 20 MPa and 15 MPa, respectively. The authors concluded that the above bond values were similar to the ones developed by steel deformed bars and that the shear off strength of the bar ribs governs the bond strength of C-BARs at pullout.

In the second series of tests (eccentrically placed bars), the embedment length was constant equal to 5 times the bar diameter. The concrete cover to the bar ( $c_y$ ) varied between 1 and 2 times the bar diameter and the concrete strength varied between 25 and 55 MPa. All the specimens failed by splitting and the authors reported that the pressure from the C-BAR cracks the concrete cover at a higher load than what is the case for steel bars. This was attributed to the smoother and softer C-BAR surface, which causes less stress concentration to the surrounding concrete.

### 2.3.2.3 Japan

In Japan, the research and development of FRP concrete structures started in the 1980's. Atshico (1993) summarised a vast amount of known experimental results from pullout tests with FRP rods in concrete, published at the time. The tests were performed in accordance with the JSCE (Japan Society of Civil Engineers) standards. Since there were 13 makers of continuous fibre reinforcement using the three main kinds of fibres for their bars until that time, according to Sonobe (1993), Atshico's state-of-the-art report appears to give a very generalised summary of the existing results. It is not useful to present this extensive summary of results here, since the recently published Japanese

code for FRP reinforced concrete structures will be presented in detail later on in chapter.

### 2.3.3 Splitting mode of bond failure of FRP bars

In practical applications, the splitting mode is the most likely bond failure in a structural member, as it was mentioned in a previous paragraph. Splitting failure should be avoided because it happens at a much lower bond stress level than pullout slip failure and the residual bond stress of the reinforcing bar decreases rapidly to zero.

Having the above in mind, Fukuyama et al (1994) investigated the bond splitting strength of FRP-RC members and proposed a method for its evaluation. The importance of their study was highlighted by the Japanese Ministry of Construction, which included it in the draft Guidelines for Structural Design of FRP Reinforced Concrete Building Structures (1995). Fukuyama et al (1994) conducted two series of tests shown in figure 2.28. The first series of tests was conducted with a simple type of bond test and the second with a cantilever type of test which is very popular in Japan as a method to evaluate the bond splitting strength of RC members, although much more difficult in preparation. The test variables included the types of bar (carbon, glass, aramid bars braided or spiral) and the lateral reinforcement ratio ( $p_w$ ). The concrete strength of the specimens was around 34 MPa.

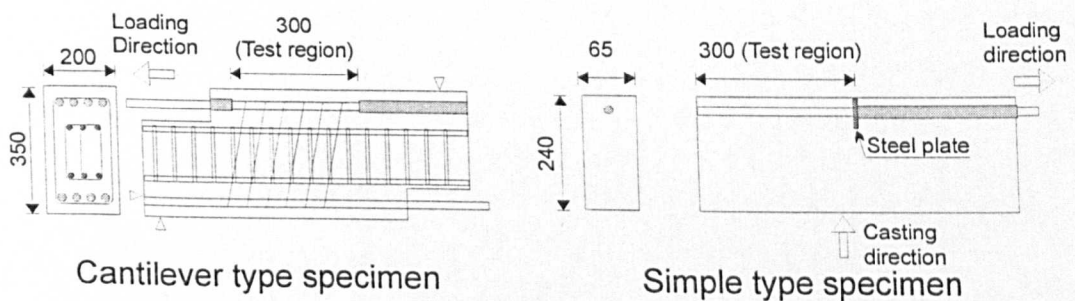


Figure 2.28: Test arrangement

The bond splitting strength was examined both for the case without lateral reinforcement ( $\tau_{co}$ ) and for the case with lateral reinforcement which results in higher strength by an amount  $\tau_{st}$ . The authors concluded that both bond splitting strengths are influenced by the elastic modulus of the longitudinal bar. As the elastic modulus is

lower,  $\tau_{co}$  is lower but  $\tau_{st}$  is higher. The  $\tau_{st}$  was not found to be influenced by the elastic modulus of lateral reinforcement in this series of tests. The authors also suggested that the bond splitting strength,  $\tau_{co}$ , from the simple bond test arrangement showed good agreement with the one from the cantilever type test. They proposed a formula to calculate the bond strength due splitting ( $\tau_{sp}$ ) of FRP reinforcing bars from the values of  $\tau_{co}$  and  $\tau_{st}$ , based on their experimental results:

$$\tau_{sp} = \tau_{co} + \tau_{st} \quad (2.20)$$

where,

$$\tau_{co} = 0.313 (0.5 + 0.4 b_i) K_{co} \sqrt{f_{cy}} \quad (\tau_{co} \text{ and } f_{cy} \text{ in MPa}) \quad (2.21)$$

$$K_{co} = \text{reduction factor} = 0.26 E^{0.29} \leq 1 \quad (E \text{ in GPa})$$

$$b_i = \text{normalised length of failure line with respect to a single longitudinal bar} = (b - N_l d) / N_l \quad (b \text{ and } d \text{ in cm})$$

$$b = \text{Width of beam cross-section}$$

$$N_l = \text{the number of longitudinal bars}$$

$$\tau_{st} = K_{st} (b / d) p_w \sqrt{f_c} \quad (t_{st} \text{ and } f_c \text{ in MPa}) \quad (2.22)$$

$$K_{st} = \text{coefficient} = 15.8 E^{-0.52} \quad (E \text{ in GPa})$$

$$p_w = \text{lateral reinforcement ratio} = a_w / (b s)$$

$$a_w = \text{sectional area of a pair of lateral reinforcement}$$

$$s = \text{spacing of lateral reinforcement}$$

However, the authors suggested that more research is necessary in order to generalise these formulas for other FRP bars.

In Germany, Faoro (1996) has underlined the importance of the elastic modulus of the reinforcing FRP bars in the bond splitting mechanism. He conducted a series of experiments in which coated and sanded GFRP bars and reinforcing steels of 8mm diameter were tested in pullout. The specimens had identical dimensions and short embedment lengths. According to Faoro, none of the GFRP bars failed due to splitting, whereas the pullout samples from the reinforcing steels remained completely intact. He presumed that the relatively low coefficient of elasticity and the higher deformability of the FRP bars in the transverse direction played an important role in the splitting

mechanism. He, also, suggested that it is not only the bond strength itself, but also the displaceability of bond that is of significance.

An experimental series investigating the bond splitting behaviour of spliced GFRP bars was conducted in Norway by SINTEF (1996), under the pan-european EUROCRETE Project (Clarke and Waldron, 1996). Three medium scale concrete beams (figure 2.29) were reinforced with 13.5 mm diameter GFRP spliced bars ( $\sigma_t = 1000$  MPa,  $E_G = 45$  GPa) and Plytron links ( $\sigma_t = 520$  MPa,  $E_G = 23.4$  GPa) were provided as shear reinforcement. All the specimens were cast using normal density concrete C35 of high workability and the bottom and side concrete cover to the spliced bars was 22.5 mm. The only variable in the test program was the splicing length.

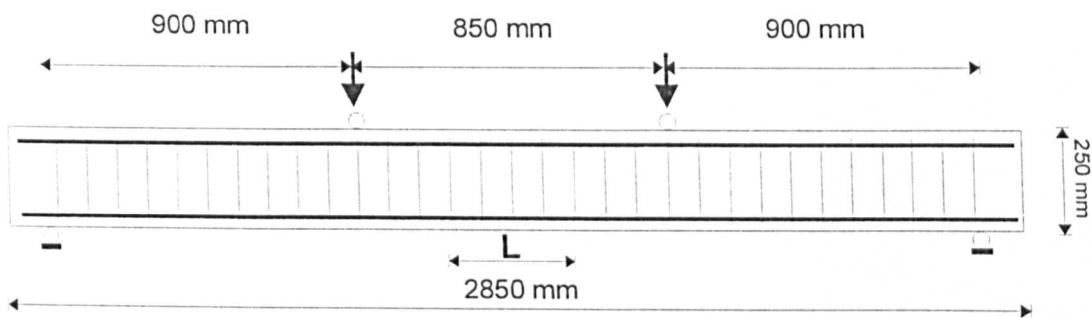


Figure 2.29: Specimens used in the experimental series

The results showed that the average bond strength developed in splices decreased as the splice length increased. For splice lengths ( $L$ ) 18.5d, 26d and 37d, the bond stresses developed were 4.0, 3.3 and 2.9 MPa, respectively. The authors suggested that if a full utilisation of the tensile strength of FRP bars was requested, the development length should be around 80 bar diameters.

In Sweden, Tepfers and Karlsson (1997) conducted a series of splice tests examining the splitting bond behaviour of GFRP C-BARs. Four beams were prepared and tested. Four C-BARs were spliced in the constant moment region of the beam and the bottom and side concrete covers were 30 mm and 45 mm, respectively. The splice lengths examined were 0.4, 0.6 and 0.8 m which corresponded to 27d, 40d and 50d, respectively ( $d = 15$  mm). The concrete compressive strength was around 25 MPa in all the beams. The results showed that C-BARs developed around 70% of the bond

splitting strength of Swedish steel deformed bars. The absolute bond splitting values developed were around 2.0, 1.7 and 1.3 MPa for the above splice lengths respectively.

In the University of Sherbrooke in Canada, Benmokrane et al (1997) tested 16 concrete beams reinforced with spliced GFRP bars. The bars were provided by Pultrall Inc. and had 12.7 and 15.9 mm diameters ( $\sigma_t = 700$  MPa,  $E_G = 45$  GPa). The test arrangement used was the four-point flexural bending test similar to the one shown in figure 2.29, but with different dimensions. They used conventional 11.3 mm steel stirrups placed 80 mm c/c through the whole length of the beam and the side and bottom concrete covers to the main bars were constant in all tests and equal to 30 mm. The concrete compressive strength varied from 37 to 55 MPa. The authors concluded that a splice length of around 100 times the bar diameter permits the development of the complete GFRP bars tensile strength. This value of splice length corresponds to a value of 1.75 MPa ultimate bond splitting strength for the certain kind of bars.

#### **2.3.4 Analytical approach of the bond behaviour of FRP bars**

From a bibliographic search, it emerges that even though many experimental programs have been conducted worldwide examining the bond characteristics of FRP bars, very little work has been published on analytical modelling.

In investigations by Cosenza, Manfredi and Realfonzo (1995,1996), three theoretical bond-slip relationships, by Malvar (1995), the Bertero-Popov-Eligehausen (BPE) model and the CMR model by the authors, were examined. The CMR was based on a modification of the BPE model, already used for steel, in order to model FRP-concrete bond. The three models were evaluated against experimental results gathered from various research projects. The analysis of the experimental data showed that :

- the bond performance of FRP bars depends on the characteristics of the outer surface and, for the same type of surface, depends on the manufacturing process.
- it is generally possible to obtain bond strengths in FRP bars of similar or greater magnitude than from steel.
- indented and grain covered bars seem to provide the best results in terms of bond strength.

The authors suggested that the Malvar model was able to reproduce the entire constitutive bond-slip curve by means of a single equation but it seemed to be less reliable than the modified version of the BPE model. The latter model represented the ascending branch of the bond-slip relationship ( $s \leq s_m$ ) by the following equation:

$$\tau / \tau_m = (s / s_m)^\alpha \quad (2.23)$$

and the softening branch ( $s > s_m$ ) by:

$$\tau / \tau_m = 1 - p (s / s_m - 1) \quad (2.24)$$

where,  $\tau_m$  is the peak bond stress and  $s_m$  the respective slip, as shown in figure 2.30, and  $\alpha$  and  $p$  are parameters based on the available experimental data.

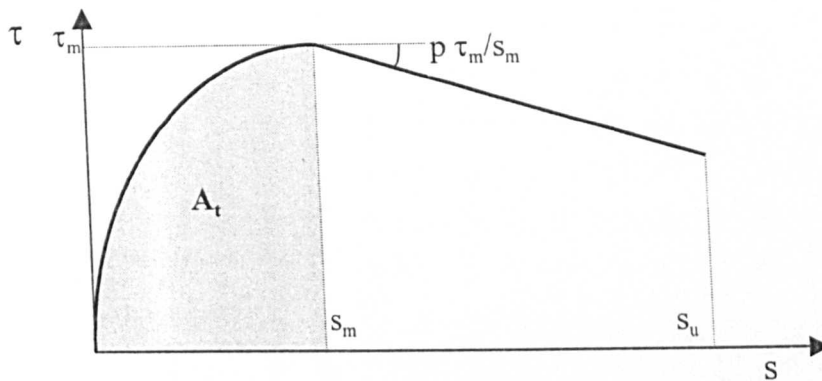


Figure 2.30: Modified BEP constitutive law

The value of parameter  $\alpha$  is derived by equating the area,  $A_t$ , under the ascending branch of the analytical curve to the area corresponding to the experimental curve as shown below:

$$A_t = \tau_m s_m / (1 + \alpha) \quad (2.25)$$

The value  $p$  is evaluated by a similar philosophy for the area underneath the experimental and analytical ( $A_s$ ) curves within the softening range. The authors also introduced the following analytical expression for calculating the anchorage length,  $L_m$ , based on the above model:

$$L_m = \sqrt{\frac{E * d * s_m^2}{A_r * (1 - \alpha)^2}} \quad (2.26)$$

A different approach for modelling the bond behaviour of FRP bars to concrete was adopted by Uppuluri et al (1996). The overall aim of that work was to develop test and analysis methods to predict the bond of FRP bars (Corrosion Proof bars and FRP bars with machined indentations).

For the case of CP bars, they developed two axisymmetric finite element models. The first model, which simulated the mechanical interlock between bar deformations and surrounding concrete, was used to predict the load-slip behaviour and the radial pressures induced during pullout. The second model simulated a smooth FRP rod/concrete specimen that used the average radial pressure from the first model to predict the load-strain behaviour of the bar.

For the machined bar, the FE model developed consists of a smooth rod in concrete with five non-linear spring elements connecting the concrete to FRP to simulate the five lugs on the machined rod. The characteristics of the springs were taken from shear tests of a single lug bar.

According to the authors, both models worked satisfactory and predicted the pullout behaviour of experimental specimens. However, no indication was given as to the accuracy of their predictions nor as to whether the models predicted both the branches (ascending and descending) of the experimental bond-slip curve.

### **2.3.5 Codes of practice and design recommendations**

The first design guidelines for the use of FRP reinforcing bars in concrete structures were produced in Japan. In 1995, the Building Research Institute of the Japanese Ministry of Construction published draft Guidelines for Structural Design of FRP Reinforced Concrete Building Structures in which there is a chapter dedicated to investigations on bond. In this chapter, the experimental and analytical work of Fukuyama et al (1994) on the bond splitting strength of FRP reinforcement is reported. The draft code suggests the use of the experimental arrangement introduced by Fukuyama et al (see section 2.3.3), for the calculation of the unconfined bond stress,  $\tau_{co}$

and of the increase in bond strength due to confinement,  $\tau_{st}$ . In case when data on  $\tau_{st}$  are insufficient, the calculations for the design bond value should be made on the safe side by simply ignoring  $\tau_{st}$ . The code also utilises relationships (2.21) and (2.22) for the evaluation of  $\tau_{co}$  and  $\tau_{st}$ , although it warns that the general applicability of these equations has not yet been confirmed.

The Japanese Society of Civil Engineers has, also, published the “Recommendation for Design and Construction of Concrete Structures using Continuous Fiber Reinforcing Materials” (1997). The JSCE code suggests that the basic development length of continuous fiber tension reinforcement should be obtained by appropriate experiments. In the code commentary, appropriate experiments are considered such test methods that reflect the actual bond characteristics within a concrete member, such as methods using test beams or lap jointed test specimens. The basic development length ( $l_d$ ) of FRP reinforcement may be calculated by using the following equation when expecting bond splitting failure.

$$l_d = \alpha_1 \{f_d / (4 f_{bod})\} d \geq 20 d \quad (2.27)$$

where,

$l_d$  = basic development length

$f_d$  = design tensile strength of reinforcement

$f_{bod}$  = design bond strength of concrete according to equation (2.28)

$$f_{bod} = \alpha_2 (0.28 f_{ck}^{2/3} / \gamma_c) \leq 3.2 \text{ MPa} \quad (2.28)$$

$\gamma_c = 1.3$

$\alpha_2$  = modification factor for bond strength of continuous fiber reinforcement;  $\alpha_2 = 1$  where bond strength due to splitting is equal to or greater than that of deformed steel bars; otherwise  $\alpha_2$  shall be less than 1 according to bond splitting test results

$f_{ck}$  = characteristic compressive strength of concrete

$\alpha_1 = \begin{cases} 1.0 & \text{for } k_c \leq 1.0 \\ 0.9 & \text{for } 1.0 < k_c \leq 1.5 \\ 0.8 & \text{for } 1.5 < k_c \leq 2.0 \\ 0.7 & \text{for } 2.0 < k_c \leq 2.5 \\ 0.6 & \text{for } 2.5 < k_c \end{cases}$

$$k_c = \frac{c}{d} + \frac{15A_t}{sd} \frac{E_t}{E_o} \quad (2.29)$$

$E_o$  = standard Young' s modulus (= 200 GPa)  
and the other symbols according to general notations

According to the commentary of JSCE code, the above adopted approach for calculating the basic development length is similar to the one used for steel deformed bars. The difference in this case, is the ratio  $E_t/E_o$  that is introduced when FRP bars are used as transverse reinforcement. Another important difference is the modification factor  $\alpha_2$  ( $\leq 1.0$ ) in the equation (2.28), that calculates the design bond strength, which applies when the bond splitting strength of FRP reinforcing bars is less than that of steel deformed bars.

In the USA, although a code of practice has not been published yet, some studies recommending design guidelines for the evaluation of the development length of FRP reinforcing bars have been reported. A summary of these studies is reported in the state-of-the-art report on Fiber Reinforced Plastic Reinforcement for Concrete Structures (1996), published by the ACI Committee 440.

GangaRao and Fasa (1993) were among the first to propose design guidelines for Glass FRP bars in concrete. They conducted a series of bond tests (see section 2.3.2) in beam and pullout specimens and used the experimental results for the evaluation of a development length ( $l_{db}$ ) formula. In this formula a reduction factor equal to 0.75 is used for safety reasons.

$$l_{db} = K A f_d / \sqrt{f_{cy}} \quad (\text{in psi, in, in}^2) \quad (2.30)$$

where,

$$\begin{aligned} K &= 0.06 \text{ (including the reduction factor 0.75)} \\ f_d &= \text{the design tensile strength of an FRP bar (psi)} \end{aligned}$$

If the maximum experimental bond stress value was used without the reduction factor the equation constant K would become 0.0426 for #3 bars ( $d = 9.5$  mm) and 0.0465 for #4 bars ( $d = 12.7$  mm).

Pleiman (1991), after a series of more than 70 pullout tests for examining the bond strength of Glass and Aramid FRP bars, concluded that the value of  $K$  in equation (2.30) should be 0.05 and 0.055 for GFRP and AFRP bars, respectively.

A more extensive series of investigations which resulted in design recommendations on the bond behaviour of GFRP reinforcing bars was conducted by Ehsani, Saadatmanesh and Tao (1995, 1996a, 1996b). The authors conducted an experimental series of 48 beam specimens, 18 pullout tests and 36 hooked bar specimens, as shown in figure 2.31.

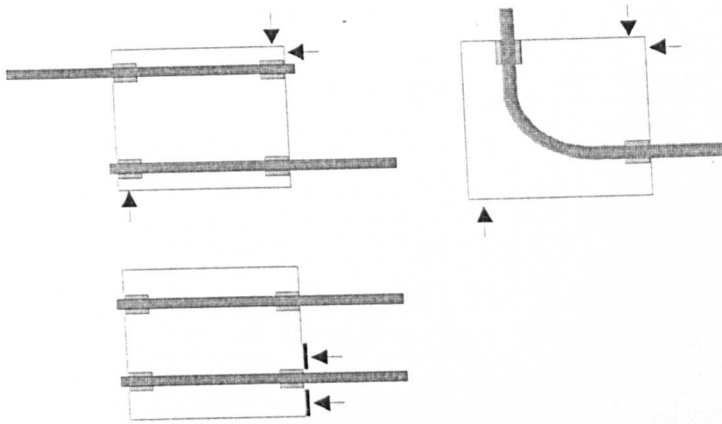


Figure 2.31: Test specimens

The GFRP bars used were supplied by a US manufacturer (International Grating Inc. Houston) and had standard diameters 9.5 mm (#3), 19 mm (#6) and 28.5 mm (#9). Their tensile strength was 931, 641, 531 MPa and the modulus of elasticity 46, 48, 50 GPa respectively. The tensile load was applied to the rebars in a gradual increment of load level until splitting of concrete, rebar pullout failure or rebar fracture occurred. The authors followed a similar procedure for the calculation of the development length as proposed by the ACI Code and concluded the following for straight GFRP bars:

- The embedment length has little effect on the stresses attained by GFRP bars until the loaded-end slip reaches 0.38 mm (0.015 in.) or the free-end slip reaches 0.064 mm (0.0025 in.). Therefore, it is recommended that the allowable slips at the loaded end and free-end of GFRP bars be limited to the above values.
- The development length of GFRP bars ( $l_{db}$ ) should be computed by equation (2.31) multiplied by a modification factor of 1.25 for top bars (as defined in the ACI Code, 1989) and 1.5 for cases when concrete cover is less than or equal to one bar diameter. This length shall not be less than that obtained from equation (2.32), which indicates

an upper limit in bond stress of 4.9 MPa. Finally, a minimum development length of 381 mm (15 in.) must be provided.

$$l_{db} = 0.047 A f_d / \sqrt{f_{cy}} \quad (\text{in psi, in}^2, \text{in}) \quad (2.31)$$

$$l_{db} = 0.00035 d f_d \quad (\text{in psi, in}) \quad (2.32)$$

where,

$f_d$  = the design tensile strength of an FRP bar (psi)

Finally in Canada, the Canadian Highway Bridge Design Code (1996) suggests that the development length,  $l_d$ , of FRP bars in tension shall be given by the following expression:

$$l_d = 0.45 \frac{k_1 * k_2}{d_{cs} + K_{tr} \frac{E_{frp}}{E_s}} \frac{F * f_{pu}}{f_{cr}} A \quad (2.33)$$

where,

$k_1$  = Bar location factor

$k_2$  = Bar surface factor, which is the ratio of the bond strength of FRP bar to that of the equivalent ordinary deformed steel bar  $\leq 1$

$f_{bu}$  = Tensile stress of a FRP bar (including a reduction factor = 0.9)

$d_{cs}$  = The smallest of the distance from the closest concrete surface to the centre of the bar or two-thirds the centre-to-centre spacing of the bars, mm

$K_{tr}$  = Transverse reinforcement index (specified in clause 8.15.2.2 of the Canadian code of practice), mm

$E_s, E_{frp}$  = Young's moduli of steel and FRP bars

$f_{cr}$  = Cracking strength of concrete, MPa

$F$  = A factor depended on the ratio  $R$  of the stresses due to factored dead loads to the stresses due to factored live loads in FRP reinforcing bars, according to the following table:

|        |      | R   |     |             |
|--------|------|-----|-----|-------------|
|        |      | 0.5 | 1.0 | 2.0 or more |
| F for: | GFRP | 1.0 | 0.8 | 0.7         |
|        | CFRP | 1.0 | 0.9 | 0.9         |
|        | AFRP | 1.0 | 0.6 | 0.5         |

The code also suggests that the minimum acceptable cover for FRP bars should be 25 mm.

## 2.4 NECESSITY FOR FURTHER RESEARCH

It is obvious from the above study that a considerable amount of experimental research has been conducted in the last ten years on the bond behaviour of FRP bars in concrete members. However, many important aspects of the subject have not yet been adequately covered and some not even investigated. A possible reason for these shortcomings may be the vast amount of different kinds of FRP bars available in the construction market which made the co-ordination of research work more difficult. The various kinds of available FRP bars are made of different kinds of fibres and resin, under different manufacturing procedures producing different surface characteristics. All these result in quite different bond characteristics of FRP bars as observed from the literature survey.

In this research study, the author intends to investigate in a more systematic way various aspects of bond behaviour of FRP bars in order to eliminate some of the identified shortcomings. By considering the current knowledge on the bond of FRP bars and compare it with that of steel bars, various areas that need further investigation can be identified:

- **Splitting behaviour of FRP bars**

In this area of investigation little research has been done, even though splitting is the most critical mode of bond failure for steel bars. The few authors that investigated this subject have identified that this mode of failure is similarly critical for FRP bars. A more systematic consideration will be given in this study on this topic both at the experimental and analytical level.

In addition, the splitting behaviour of spliced FRP bars has not yet been investigated adequately by researchers although it has important practical implications. This study intends to contribute to this topic by providing experimental and analytical data.

- **Analytical studies on the bond development of FRP bars**

It has been concluded in the previous section that very little work has been published on the analytical part of work. The reported design recommendations are empirically

derived from limited experimental data without much theoretical background. Furthermore, it is obvious that there is a lack in the literature of bond models that predict the bond behaviour of FRP bars over the complete range and in the case of bars in beams. Hence, a contribution needs to be made in this area.

- **Influence of specific factors on the bond behaviour of FRP bars in concrete**

In the case of steel bars, various factors have been reported that influence their bond behaviour in concrete. Most of these appear to influence the bond of FRP bars, in a similar way. In particular, the concrete strength seems to play a different role in the bond behaviour of FRP bars, whilst the bar diameter appears to be more important now than for steel bars. Other factors such as the concrete cover and the significance of transverse reinforcement are reported to be important in FRP bars too. However, some factors which are not considered for steel bars, such as the Young modulus and the deformability of FRP bars in the transverse direction, have been reported to influence significantly bond behaviour. Existing literature gives some indication as to how all the above factors influence the behaviour of FRP bars. However, more investigations are needed in this area of research in order to contribute to the understanding of the EUROCRETE bars and to clarify some ambiguous aspects of bond behaviour.

- **Bond behaviour of CFRP bars**

Current research, especially from North America, is concentrated on the behaviour of Glass FRP bars and does not give much attention to the bond behaviour of Carbon FRP bars. However, CFRP bars appear to develop better bond characteristics than the respective GFRP bars. This study will pay equal attention to the bond behaviour of both kinds of bars.

Finally, this study will suggest a method of working towards the formulation of design guidelines for calculating the bond strength of FRP bars, based on the experimental and analytical investigations conducted during this research project.

# **CHAPTER 3**

## **EXPERIMENTAL METHODOLOGY**

Two experimental series of tests were conducted to investigate the bond behaviour of non-ferrous reinforcement (FRP) in concrete structures. In the first series, more than 100 specimens were tested in direct pullout whereas in the second, the bond development of FRP reinforcing bars was examined in nine concrete beams tested in four point bending. Results are also used from other experiments undertaken for the EUROCRETE project and for which a specific attempt was made to obtain data relative to bond. In this chapter the choice of the experimental parameters, the preparation of specimens, the experimental set up and testing procedure and the mechanical properties of the materials used, are presented.

### **3.1 PULLOUT TESTS**

#### **3.1.1 Background**

Pullout tests are used commonly in the assessment of bond performance of steel reinforcing bars in concrete. Although the stress conditions developed in the concrete specimen during pullout tests are rarely encountered in practice and the bond values developed under those tests differ substantially from those developed in reinforced concrete elements in most practical conditions, pullout tests are widely adopted. This is because they offer an economical and simple solution for the evaluation of bond performance of reinforcing bars and represent in a simple manner the concept of anchoring a bar (Cairns, 1995). For the above reasons, pullout tests were adopted for the evaluation of bond behaviour of FRP bars in concrete.

The main aim of the bond tests was to obtain the bond-slip relationship at the loaded and free ends of FRP bars subjected to a pullout load. The pullout test arrangement had to facilitate this aim so, a careful evaluation of the pullout arrangement used for steel bars by previous researchers, was conducted in order to find the most appropriate set-up for the experimental purposes. The investigation resulted in two options of pullout tests; the Rehm and RILEM/CEB/FIP arrangements (see figure 2.5) both of which are used commonly for the evaluation of bond of steel bars.

However, the author was concerned about the accuracy of the measurements of slip at the end of the bar obtained by the RILEM/CEB/FIP test, since the embedment length of the bar is at the very end of the cube. In this case, any deformation at the end of the concrete due to the pullout load would be recorded as bar slipping although it is not actually slip. For this reason a modified version of Rehm's test was adopted. However, it has to be mentioned that at a later stage of this testing series some specimens were prepared having the bar-concrete contact area at the end of the bar, similar to the RILEM/CEB/FIP arrangement, in order to investigate differences in the bond development by the two arrangements.

### 3.1.2 Study parameters

The selection of primary variables for this study was based on existing experience of bond behaviour of steel bars in concrete. Their bond behaviour depends on many parameters that influence the strength and ductility of anchorages in concrete. Understanding the influence of these parameters on the bond development of FRP bars was a main objective of this study. The most important factors examined are given below:

- Concrete strength
- Embedment length
- Diameter of bar
- Shape of bar
- Type of bar fibres (Carbon, Glass, Aramid, Hybrid (Glass + Carbon))
- Type of bar surface (smooth/rough)
- Height of bar deformations
- Effect of embedment length location in the concrete cube

As it was mentioned in the previous chapter, these factors are expected to have a different influence on the bond behaviour of FRP bars since FRP materials are strongly anisotropic and have different mechanical properties than steel bars. A proper evaluation of the influence of these factors on bond development is crucial to the understanding of how actually these materials “co-operate” with concrete in structural members and for the estimation of adequate anchorage lengths.

### 3.1.3 Specimen preparation

#### 3.1.3.1 Bar preparation

The FRP bars were cut in 450 mm lengths to fit in the specially designed test rig. Prior to casting, they were properly marked so that the embedment length would lie in the middle of the concrete cube (figure 3.1). The embedment lengths were designed as multiples of the bar diameter to facilitate comparisons among different diameter bars.

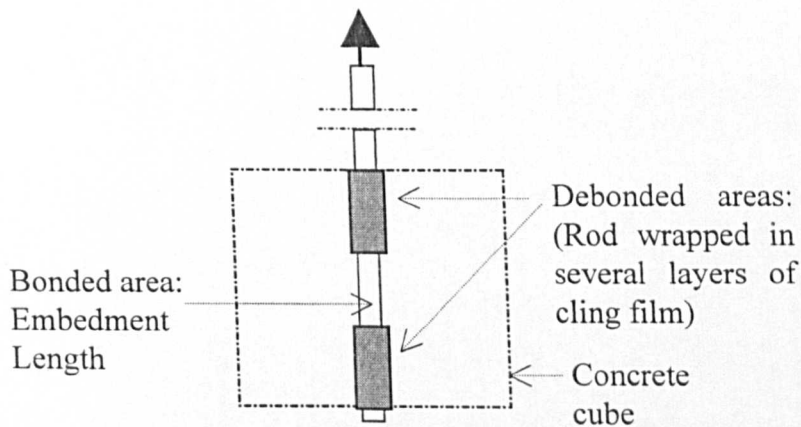


Figure 3.1: Bar preparation

The two ends of the bar in the concrete cube were wrapped with several layers of cling film in order to form non-contact (debonded) areas between bar and concrete. The debonded area at the loaded end was intended to minimise the effect of concrete surface cracking on the development of bond stresses during pullout testing. The debonded area at the free end was intended to minimise the influence of concrete surface deformation on the free-end slip measurements, as it was mentioned in section 3.1.1.

### 3.1.3.2 Mould preparation

The moulds used for casting the 150 mm concrete cubes were made of 8 mm thick metal. The bars were positioned vertical in the moulds as shown in figure 3.2.

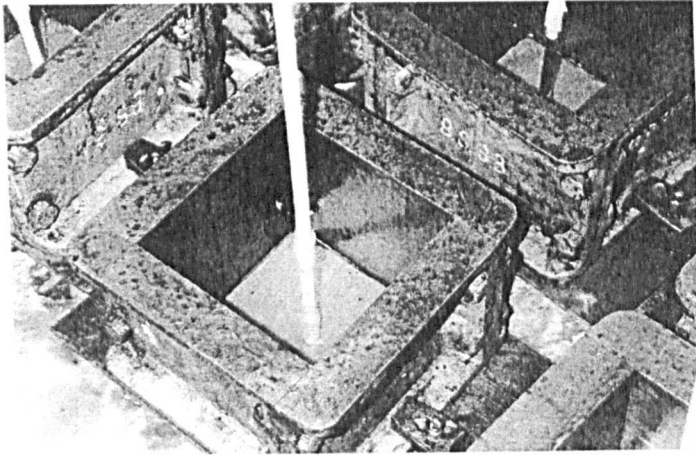


Figure 3.2: FRP bar in the mould before casting

At the bottom of the mould, a square piece of plywood, 8 mm thick, with a hole in the centre was positioned for keeping the FRP bar rigidly in a vertical position. The inside edges of the mould were sealed with waterproof silicon to accomplish watertightness. Before each casting, the inside of the mould was coated with a thin film of oil to make easier the de-moulding of concrete cubes.

### 3.1.3.3 Casting and curing procedure

The concrete was cast in the moulds in two layers of approximately equal thickness and each layer was vibrated either on the vibrating table or by the means of hammer vibrators. Special consideration was given during casting and vibrating in order not to disturb the verticality of the bar. Strict compacting and levelling was imposed on the specimen surface to eliminate voids and minimise geometric irregularities. Control specimens were taken from the same batch of concrete in order to be tested in compression and in indirect tension.

All the specimens were trowel finished one hour after the completion of casting and covered with nylon after about three hours (figure 3.3).

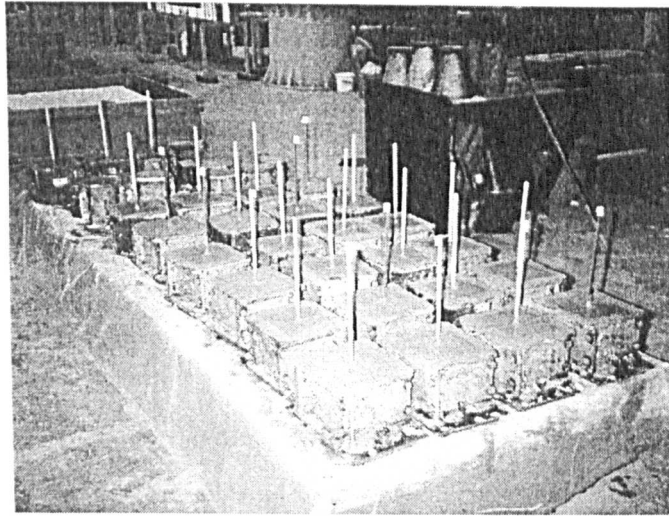


Figure 3.3: Specimens after casting

The specimens were left overnight in the moulds and the next day the moulds were opened. The concrete cubes were de-moulded, marked and transferred in the Curing Room of the laboratory where they were positioned on specially arranged shelves. The room temperature in the Curing Room was about 20°C and the humidity about 80%. During the first week, the specimens were watered every day and were left in the Curing Room for 28 days in total. The control specimens were cured under identical conditions.

#### 3.1.3.4 Material Properties

- **Concrete**

The concrete used for the pullout specimens was either prepared in the laboratory or supplied by outside agents of ready mix concrete, depending mainly on the number of concrete cubes included in each casting batch. More than ten castings were made during the three years of the research study. The required concrete strength varied each time to examine the influence of concrete strength on the bond development of FRP bars. Ordinary Portland cement was used in all of these mixes and the maximum aggregate size was 20 mm.

Three to six control samples (100 mm cubes and 200 x 100 mm cylinders) were taken from each batch of pullout specimens depending on the number of specimens prepared. At least, one cube and one cylinder were tested in direct compression and

indirect tension respectively, before the testing of each batch of specimens. The rest of them were tested after the completion of the test series. The concrete mixes had average compressive strengths in the range of 15.5 to 49.5 MPa. The concrete strength values for each batch of pullout tests are presented in Tables C.1.1 to C.1.6 in appendix C.1 together with the experimental results for each test.

- **FRP materials**

The FRP bars were supplied by the EUROCRETE Project. Three kinds of fibres were used for the manufacture of four types of reinforcing bars: Carbon, Glass, Aramid and Hybrid (Carbon + Glass together). However, the main emphasis was given in the two first types of bars, which seemed more promising for the purposes of the EUROCRETE project (figure 3.4).

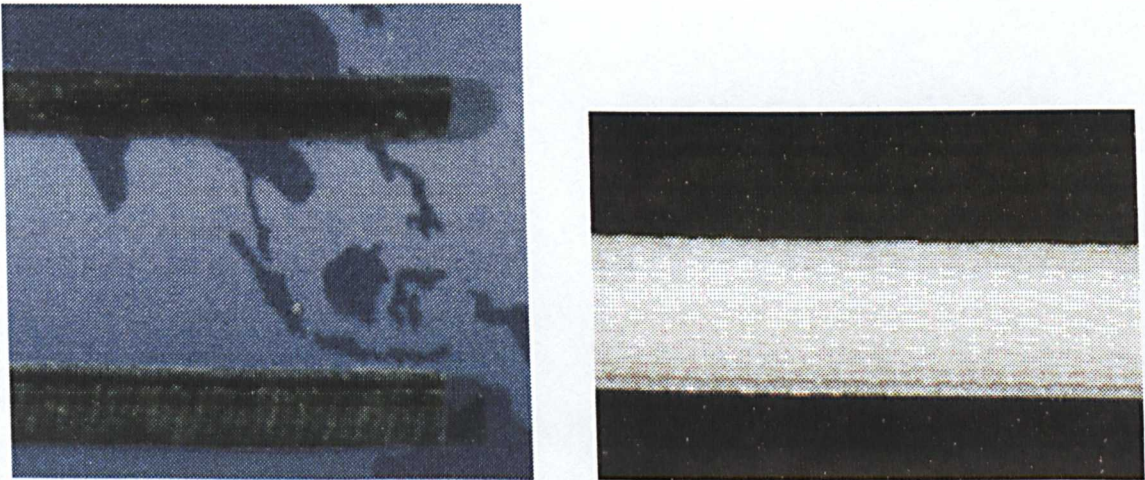


Figure 3.4: Samples of the EUROCRETE CFRP and GFRP bars

The bars had different types of cross-sectional areas, sizes and surface deformation textures. In table 3.1, the average geometric properties of all types of bars used in the pullout testing series are presented. The dimensions were measured by using an electronic Vernier micrometer.

| Type of Bar   | Surface texture                             | Dimensions of cross-section (mm)            | Cross-sectional area (mm <sup>2</sup> ) |
|---------------|---|---|---|
| GFRP round    | Rough                                       | 13.5  | 143.13                                  |
| GFRP round    | Rough                                       | 8.5   | 56.27                                   |
| GFRP round    | Medium rough                                | 10.5  | 86.59                                   |
| GFRP square   | Rough                                       | 8.5 x 8.5                                   | 72.25                                   |
| GFRP round    | Smooth                                      | 16  | 201.06                                  |
| Carbon round  | Rough                                       | 13.5  | 143.13                                  |
| Carbon round  | Rough                                       | 8   | 50.26                                   |
| Carbon ring   | Rough <sub>out</sub> , Smooth <sub>in</sub> | d <sub>out</sub> = 21, d <sub>in</sub> = 10 | 267.82                                  |
| Carbon square | Rough                                       | 8.5 x 8.5                                   | 72.25                                   |
| Aramid round  | Rough                                       | 13.5  | 143.13                                  |
| Aramid round  | Rough                                       | 8.5   | 56.27                                   |
| Aramid square | Rough                                       | 8.5 x 8.5                                   | 72.25                                   |
| Hybrid round  | Rough                                       | 13.5  | 143.13                                  |

Table 3.1: Types of bars used in pullout tests

The Young Modulus of EUROCRETE FRP bars were evaluated by direct tension tests according to ASTM regulations (Duranovic, 1995) and the average values obtained are presented in the table 3.2. The tensile strength of the various bars were difficult to be evaluated under conventional experimental conditions (the grips of the testing machine were damaging the bar at high tensile loads and premature failure occurred), so suppliers characteristic values are given in the table below.

|                        | GFRP  | CFRP   | AFRP  | HFRP  |
|------------------------|-------|--------|-------|-------|
| Young Modulus (MPa)    | 45000 | 115000 | 67000 | 51000 |
| Tensile strength (MPa) | >1000 | >1500  | >1500 | >1000 |

Table 3.2: Mechanical properties of FRP bars

### 3.1.4 Experimental set up

The pullout test arrangement adopted is shown in figure 3.5. The concrete cube with the embedded FRP bar was placed in a specially made steel frame that was positioned in the testing machine.

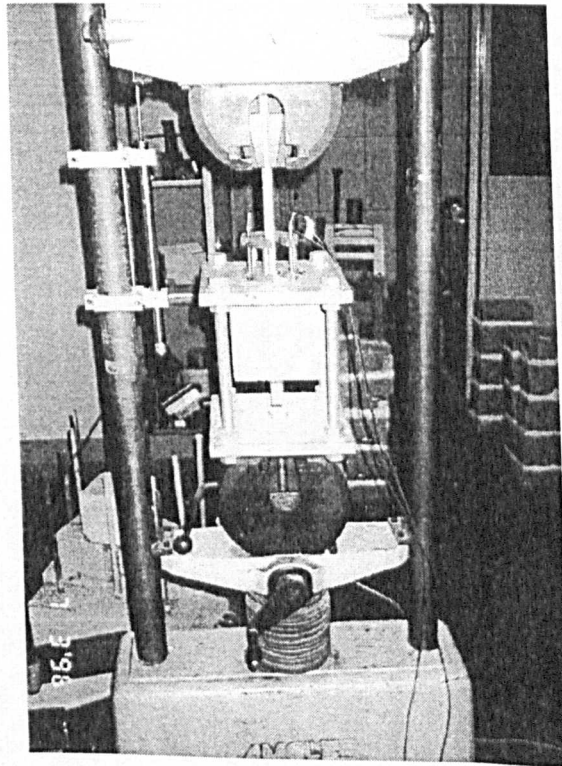
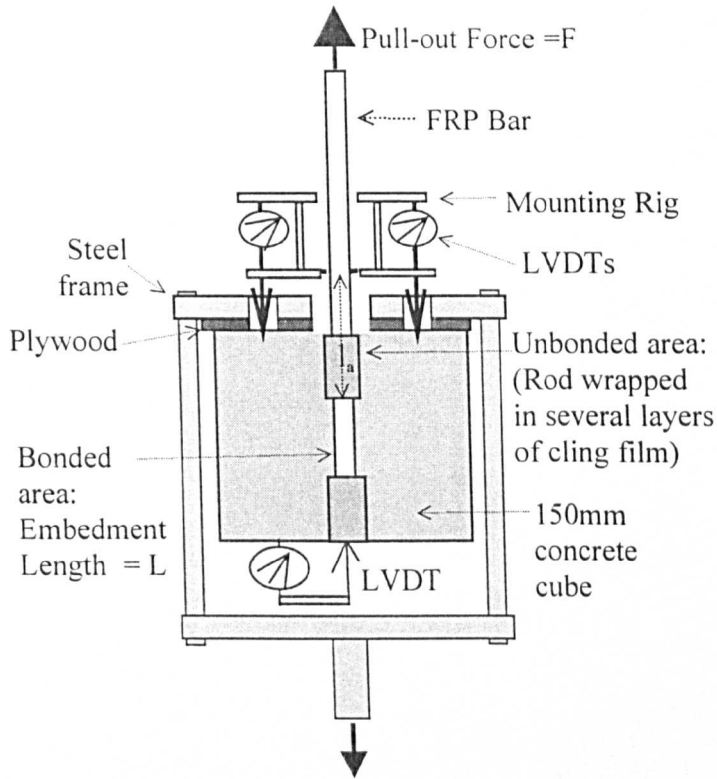


Figure 3.5: The pullout test arrangement

The rig consisted of two steel plates 25 mm thick which were connected at the four edges with four 20 mm diameter rods. The top plate had a 30 mm diameter hole in its centre allowing the FRP bar to run through. On this plate there were also another three additional holes in a triangular arrangement round the main hole which allowed three LVDTs, located at the loaded end of the specimen, to touch the top surface of the concrete cube. The bottom end of the rig was secured in the jaws of the testing machine, which provided the reaction to the pullout load imposed to the specimen.

Between the concrete block and the bearing steel plate, a 5mm thick wooden plate was introduced to secure the contact between the top surface of the concrete block and the steel bearing plate. This was necessary since small irregularities at the top surface of the cube might introduce some accidental bending on the bar during loading.

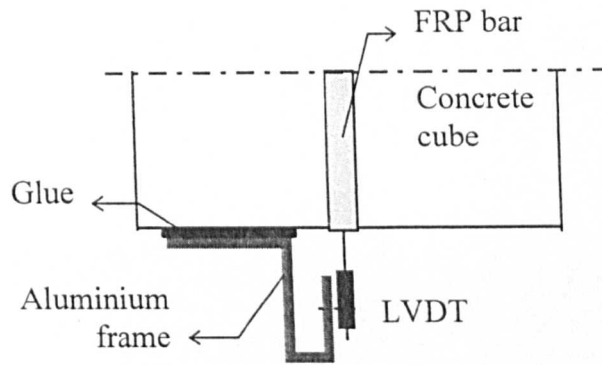
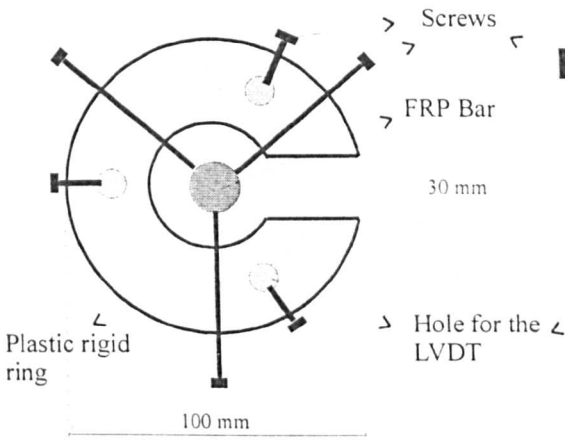


Figure 3.6: LVDT at the bottom face of the cube

Three LVDTs were used for measuring the slip of the bar at the loaded end and another one the slip at the free (unloaded) end of the bar. The latter one was attached on a small aluminium frame that was glued to the bottom surface of the concrete cube as shown in figure 3.6

The top three LVDTs were positioned on a specially manufactured mounting rig for measuring the loaded-end slip of the bar. Three measurements are necessary to estimate and eliminate the effects of accidental bending during loading. The mounting rig held the LVDTs in position attached to the FRP bar by means of three bottom screws as shown in figure 3.7.

Plan view of the Mounting Rig



Front view of the Mounting Rig

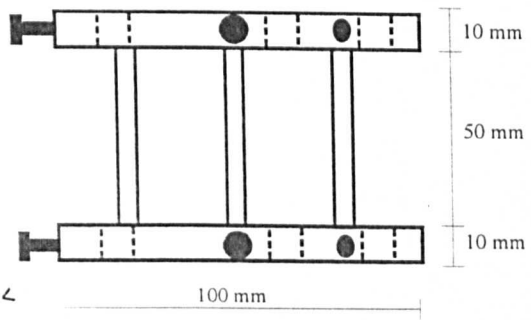


Figure 3.7: Mounting Rig

The mounting rig with the test specimen were positioned in a universal testing machine as shown in figure 3.5. The testing machine, controlled by an Electronic Control Unit (ECU) as shown in figure 3.8, can apply direct tension in load or deflection-control modes. Its load capacity was beyond 500 kN which was more than adequate for the test purposes.

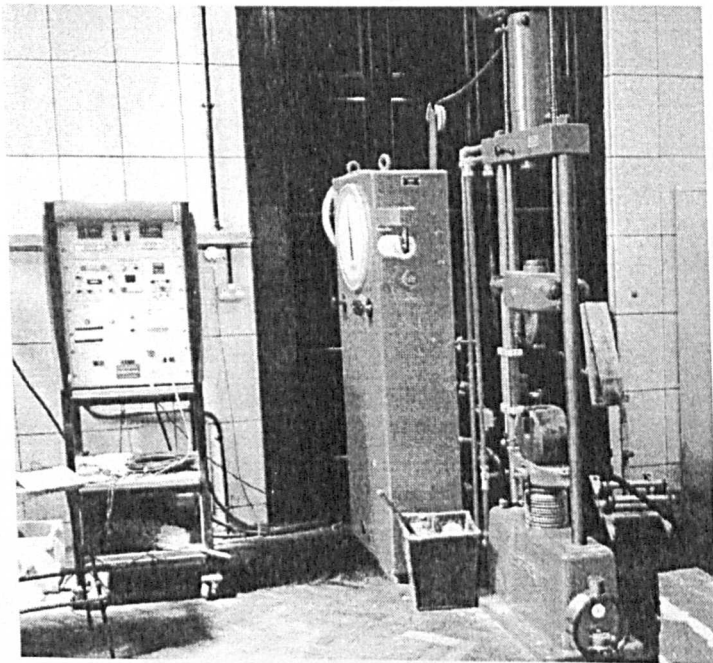


Figure 3.8: Testing machine and ECU

The ECU was connected to the ORION data acquisition system (figure 3.9) monitoring the load data from the ECU and the slip measurements from the LVDTs. The ORION system was linked to a PC that gathered the experimental data, which were made immediately accessible from the computer screen. This is very important during testing since the progress of the test can be monitored and action taken when something goes wrong.

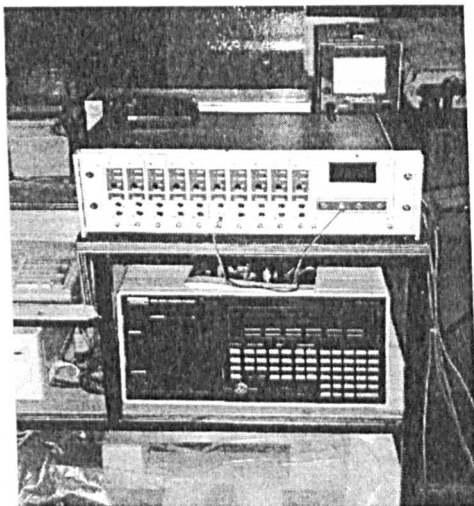


Figure 3.9: Data acquisition system (ORION)

### 3.1.5 Testing procedure

The LVDT was mounted to the small aluminium frame at the bottom of the cube just before the test. The specimen was then mounted in the testing frame and the wooden plate was inserted between the surface of the cube and the bearing steel plate. The projecting bar was gripped in the jaws of the testing machine and a 0.5 kN load was applied to the specimen in order to minimise the gap between the concrete surface and the steel plate. The LVDT mounting rig was then positioned at the top of the specimen so that the LVDTs touched the top surface of the cube. The rig was secured firmly on the bar at both levels of screws (see figure 3.7) and the LVDTs were adjusted in order to monitor up to 8 mm slip on the loaded end of the bar. The distance between the bottom level screws and the concrete surface was then measured with a small ruler. This distance was used in the calculation of the elongation of the bar due to pullout load,

which had to be subtracted from the slip measurements as will be explained in the following paragraph. The mounting rig was unscrewed at the top level so that only the bottom level screws were in contact with the bar and the test was ready to start.

After initialising the LVDTs measurements, the pullout load was applied to the specimen at a rate of about 0.1 kN/sec. During testing, the experimental data from the four LVDTs and the load cell were downloaded every 2 seconds to the monitoring PC. The load was applied in deflection control since the investigation of the bond behaviour after the peak bond stress was among the objectives of the study. Observations during testing were recorded, with special consideration being paid to the mode of bond failure. The test was only stopped when slip at the loaded end of the bar was greater than 8 mm.

After the end of the test, all the experimental data were saved in the computer system and the specimens were removed for further examination of the mode of bond failure of the FRP bar. Special consideration was given to specimens whose experimental results deviated significantly from the rest.

### 3.1.6 Analysis of measurements

The measurements obtained from the experimental results were used to produce the bond-slip curves of each specimen.

As mentioned earlier, the average slip measurement ( $\delta_{av}$ ) of the three LVDTs does not represent the actual slip because of the rebar extension above the embedment length. Hence, the measurements at loaded end contained two components: the actual slip of the bar relative to the concrete ( $\delta_{le}$ ) and the elongation of the portion of the bar from the transducer support point to the level of the bonded bar ( $\Delta l$ ). The bar elongation is calculated by using the elastic characteristics of the unbonded length ( $l_a$ , see figure 3.4). This value was subtracted from the measurement of the loaded end slip as shown in the following:

$$\begin{aligned}
 \delta_{av} &= (\delta_1 + \delta_2 + \delta_3) / 3 \quad \} \\
 \delta_{av} &= \delta_{le} + \Delta l \quad \} \Rightarrow \delta_{le} = (\delta_1 + \delta_2 + \delta_3) / 3 - F l_a / (E A) \quad (3.1) \\
 \Delta l &= F l_a / (E A) \quad \}
 \end{aligned}$$

where,

$\delta_1, \delta_2, \delta_3$  = Slip measurements of the three LVDTs

The bond-slip curve at the unloaded end of the bar is obtained directly from the slip measurement of the bottom LVDT ( $\delta_{ue}$ ) and the applied pullout load.

It has to be recognised that in both cases the deformation of the concrete surrounding the bar was not taken into account in the calculations of slip. However, it is reported in the literature that this deformation is very small when the embedment length lies in the middle of the concrete cube, comparing to the values of slip at the loaded and unloaded end. This was, also, verified by the results of the analytical study conducted by the author, which is presented in a following chapter.

The average bond stress at any stage in the test is the recorded pullout load on the bar divided by the nominal surface area of the embedment length of the bar. This is given by the relationship:

$$\tau_{av} = F / (\pi d L) \quad (3.2)$$

The maximum average bond value is obtained by (3.2) when the pullout load reaches its maximum value ( $F_{max}$ ) during the test.

## 3.2 BEAM TESTS

### 3.2.1 Background

The strain conditions encountered in a pullout specimen during conventional pullout testing are rarely encountered in practice, since concrete elements are mostly exposed to combined flexure and shear loads. Under flexural conditions, splitting of concrete in the tension zone is the most common mode of bond failure, which is substantially different and more dangerous than the pullout mode since it happens at a much lower bond stress level and the residual bond stress of the reinforcing bar decreases rapidly to zero.

In order to investigate and understand the bond behaviour of FRP reinforcing bars under flexural conditions, an experimental series of beam tests has been conducted under the EUROCRETE project. This series included four phases of testing over a period of three years and thirty-seven beams were tested during these phases.

- *Phases 1-3*

In the first three phases, 24 beams reinforced with FRP and steel bars were prepared and tested (Duranovic et al, 1995 and 1996). The beams were not designed to fail in bond since the investigation of the bond behaviour of FRP bars was not the main experimental objective. However, a large number of strain gauges were attached to the main reinforcement of the beams to record the strain values on the bars during the tests. These values were used by the author to calculate the developed bond stresses on the bars. Many useful results have emerged from the study of these beams that contributed to the understanding of bond behaviour of FRP bars. These results will be reported and analysed in the next chapter of this study.

Details of the reinforcement arrangement, the instrumentation used and the analytical results of the beams tested in the above experimental program are presented in reports by Duranovic et al (1995, 1996). However, since some of the results will be analysed and discussed in this study, some necessary details about the arrangement of

reinforcement in the beams and the instrumentation of the main reinforcing bars are presented in appendix A.

Appendices A.1 to A.4 show the reinforcement arrangement used in each beam in the above series of testing. The external confinement reinforcement used in some of the beams was generally for enhancing the concrete compressive strength and introducing additional ductility to the beams (Pilakoutas et al, 1997) when it was required by the experimental needs.

Appendix A.5 shows the arrangement of the strain gauges on the main reinforcing bars of the tested beams. The recorded longitudinal strain values are used in this study for monitoring the bond stress profile on the reinforcing bars during loading. Since the maximum bond demand was expected to be at the end of the bar, strain gauges were placed at a close spacing near the support region.

- ***Phase 4***

In this chapter, the experimental methodology followed in the fourth phase of beam testing program will be reported, which is very similar to the methodology of the previous phases. The primary objective of this phase was to examine the mode of bond failure of FRP reinforcing bars under beam conditions and the various parameters that influence their bond behaviour. For this purpose, nine medium scale beams (2500 x 250 x 150 mm) were prepared in order to fail in bond. Despite the fact that a detailed description of the arrangement of reinforcement in these beams is presented in appendix B, a brief summary of the experimental program is given in table 3.3.

| Beam | Anchorage length-L (mm) | Bottom Cover to Diameter Ratio | Main (bottom) - Shear reinforcement                           | Arrangement of main (bottom) reinforcement |
|------|-------------------------|--------------------------------|---|--|
|      |                         |                                |   |  |
| GB29 | L=250                   | 1.85                           | 3 GFRP bars (13.5mm) - GFRP links 75 mm c/c in the shear span |  |
| GB30 | L=300                   | 1.85                           | 3 GFRP bars (13.5mm) - GFRP links 75 mm c/c in the shear span |  |
| GB31 | L=300                   | 1.85                           | 4 GFRP bars (13.5mm) - GFRP links 75 mm c/c all the way       |  |
| CB32 | L=300                   | 3.13                           | 3 CFRP bars (8 mm) - GFRP links 75 mm c/c in the shear span   |  |
| CB33 | L=300                   | 3.13                           | 4 CFRP bars (8 mm) - GFRP links 75 mm c/c all the way         |  |
| GB34 | L=370                   | 2.94                           | 3 GFRP bars (8.5mm) - GFRP links 75 mm c/c in the shear span  |  |
| GB35 | L=300                   | 2.94                           | 3 GFRP bars (8.5mm) - GFRP links 75 mm c/c in the shear span  |  |
| GB36 | L=300                   | 2.94                           | 4 GFRP bars (8.5mm) - GFRP links 75 mm c/c all the way        |  |
| CB37 | L=580                   | 3.13                           | 3 CFRP bars (8 mm) - GFRP links 75 mm c/c in the shear span   |  |

Table 3.3: Summary of the experimental program

### 3.2.2 Study parameters of the experimental series

The selection of the study parameters was based on existing experience from steel reinforced beams as it is reported in the bibliography. Various researchers highlighted in their work numerous parameters that influence the splitting bond behaviour of reinforcing bars in beam elements (see chapter 2). However, in this

experimental study only some of these parameters were examined because of the limited available resources and time. The influence of these parameters on the bond behaviour of FRP reinforcing bars was expected to be different than in the case of steel bars since FRP materials have much different mechanical properties than steel. As Faoro (1996) suggested in his recent studies, the relatively low coefficient of elasticity and the higher deformability of the FRP bars in transverse direction could play an important role in the splitting mechanism.

In this experimental series, the influence of the following parameters on the bond behaviour of FRP bars were examined:

- The type of the bar (Carbon or Glass)
- The concrete cover to diameter ratio
- The anchorage length of the bar
- The arrangement of the reinforcing bar in the cross section
- The difference in bond development between single anchorages and spliced bars

### **3.2.3 Specimen preparation**

#### **3.2.3.1 Preparation of reinforcement cages**

After the FRP bars were cut in the appropriate size for each beam, the locations of the strain gauges were appropriately marked on the bar. The logic behind the arrangement of strain gauges in each beam is explained in detail in section 3.2.4.1. The strain gauges were attached to the bars by means of cement glue and after they were glued and connected to wires, they were covered with wax in order to be protected from the aggregate impact during casting. Strain gauges were attached on selected shear links of the beam in order to monitor their elongation during testing. For the construction of the reinforcement cages, plastic ties were used to hold bars and links in their positions. A completed cage is presented in figure 3.10:

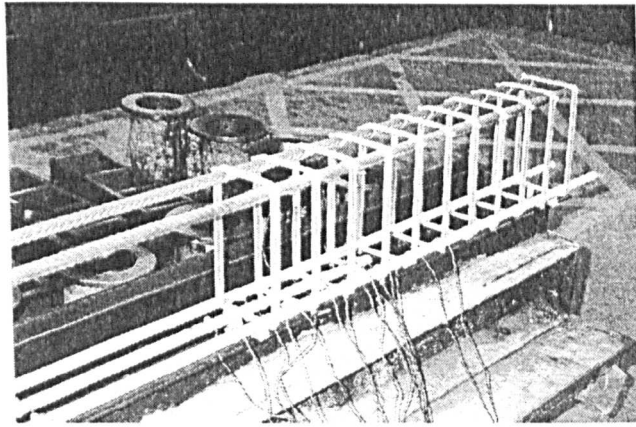


Figure 3.10: Reinforcement cage

### 3.2.3.2 Mould preparation

The moulds for the beams were made of steel channel-sections. Before the placement of the reinforcement cage, each mould was cleaned and its inside edges were sealed with waterproof silicon. A thin layer of oil was applied at the inner sides of the mould to make easier the de-moulding of the concrete beams. Then, the reinforcement cage was positioned in the mould with special consideration in establishing appropriate side and bottom distances from the sides of the mould. This was very important in this series of tests, since the concrete cover of the reinforcing bars was one of the main parameters of this study. For this reason, appropriate size spacers were used for this job. Figure 3.11 shows the reinforcement cage positioned in the mould just before casting:

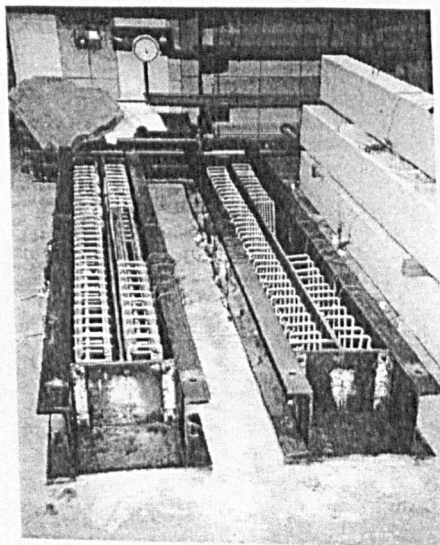


Figure 3.11: Beams ready for casting

### 3.2.3.3 Casting and curing

Four to five beams were cast each time from the same batch of concrete. The wet concrete was cast in three layers of approximately equal thickness. Each layer was vibrated with a pocker vibrator since it was not possible to use the vibrating table because of the size of the beams. For each beam, three cubes (100 mm size) and cylinders (200x100 mm) were taken as concrete control specimens. After casting was finished, strict compacting and levelling was imposed to the top side of the concrete beams to minimise geometric irregularities. The specimens were trowel finished two hours after casting and covered with wet hessian and nylon.

This type of curing was maintained for a week until a control cube was crushed. Control specimens were de-moulded the day after casting and placed next to the beams for identical curing conditions. The curing of the beams was stopped after the first week and the specimens were de-moulded and stored under standard laboratory conditions for another three weeks.

### 3.2.3.4 Material properties

- **Concrete**

Because of the large volume of concrete needed for each batch, the concrete was obtained from ready mix suppliers. It was ordered to have at least 35 N/mm<sup>2</sup> compressive strength, made from ordinary Portland cement with maximum aggregate size 20 mm and slump 50-60 mm. Three cubes and three cylinders were tested at the day of testing for each beam in direct compression and indirect tension, respectively. The average concrete strength values measured, are presented in table 3.4:

| Specimens | Day of testing | Cube compressive strength (N/mm <sup>2</sup> ) | Cylinder indirect tension strength (N/mm <sup>2</sup> ) |
|-----------|----------------|--|---|
| GB29-CB33 | 28-36          | 35.0   | 2.7   |
| GB34-CB37 | 28-33          | 45.0   | 3.6   |

Table 3.4: Concrete compressive and tensile strength

- **Reinforcement**

Details of the main reinforcement for each beam in this experimental series are presented in table 3.3. Carbon and Glass FRP round bars with rough surface and diameters 8, 8.5 and 13.5 mm were used as in the pullout tests previously reported, therefore, their mechanical properties in direct tension can be taken from table 3.2. However, their tensile strength in concrete under combined flexure and shear loads (beam conditions) was measured directly from bars that failed during the four phases of beam testing. These values are presented in the following table together with the respective elongation at failure, for the three different types of bars used in this series:

|  | GFRP bar<br>d = 13.5 mm | GFRP bar<br>d = 8.5 mm | CFRP bar<br>d = 8 mm |
|--|-------------------------|------------------------|----------------------|
| Tensile strength<br>under beam loading<br>conditions (MPa) | 700-750                 | 900-950                | 1300-1380            |
| Elongation at<br>failure (%)                               | 1.55-1.65               | 2.00-2.10              | 1.13-1.20            |

Table 3.5: Properties of reinforcing bars

The links used as shear reinforcement in the beams of this experimental series were specially manufactured filament wound rectangular (200 x 100 mm) GFRP links with 10 x 5 mm cross section. They were fixed at a standard spacing of 75 mm centre-to-centre either only in the shear span or along the whole beam, depending on the arrangement of the main reinforcement. This spacing was used in the previous phases of testing for similar beams and prevented shear failures so, the same spacing was adopted in this phase too. This amount of shear reinforcement, however, falls well below the minimum requirements proposed by Clarke et al (1997).

The tensile strength of the used links is different from that of the GFRP bars. The critical aspect that determines their tensile strength is the shape of the links. When the links were tested in tension (Duranovic, 1995), they all failed in the corner edges. The main reason for this is obviously the concentration of stresses at these points, due to the change of direction of the fibres in the link. Their tensile stress was measured to be around 425 MPa and their Young Modulus around 47 GPa.

Finally in most of the beams of this phase, compression reinforcement was used for three main reasons:

- to enhance the concrete compressive strength at the top of the beam
- to prevent any sudden, brittle failure of the beam which might damage the instrumentation at the back of the beam
- to keep the shear links in place during casting

Two 16 mm high yield deformed steel bars were used for this purpose in each beam. Their mechanical properties were not tested because of their insignificance in the analytical work of this study, but results from tests on similar bars exist in the literature.

### **3.2.3.5 Beam preparation before testing**

The day before testing, the front side of the beam was white washed and a grid (100 mm x 100 mm measured from the centre) was drawn on the front surface. The reason for this preparation was to make clearer and easier the location and marking of cracks during testing. In addition, the various clamps for the transducers, which are mounted at the back side of the testing frame, are glued at the proper positions on the back side of the beam. The beam was now ready to be positioned in the testing frame.

## **3.2.4 Instrumentation**

### **3.2.4.1 Strain gauge arrangement on reinforcing bars and shear links**

The most important operation during the preparation of the beam cages was the placement of strain gauges on the surface of the reinforcing bars and shear links. The strain gauges used, were foil type electronic gauges of two specific sizes; 10 x 3 mm and 6 x 2 mm. The bigger size was used on the 13.5 diameter bars and on the shear links whereas the smaller ones were used on the smaller diameter bars (8, 8.5 mm). Special consideration was given during the placement of the gauges on the bars in order to disturb the surface of the bar as little as possible.

The strain gauges on the bars were essential in this experimental program in order to monitor the normal strain values developed during the test which was necessary for the calculation of bond stresses, as will be explained in section 3.2.7. The location of

the strain gauges on each bar was based on the author's judgement depending on the specific purpose of each beam. Three to six strain gauges were, also, glued on specific shear links of the beam in order to monitor the stress developed in the links. The location of the strain gauges on the links depended on the general arrangement of the main reinforcement and it was different in each beam.

In appendix B, a detailed description of the arrangement of the strain gauges is given for each beam. However, the logic behind the location of the gauges on each beam is explained in the following:

- **Beams GB29, GB30, CB32**

The arrangement of strain gauges in these three beams was quite similar. The main objective was to monitor the strain distribution along the middle bar, which was designed to fail in bond, and compare it with the respective strain distribution of the two other fully anchored bars. The strain gauged shear links were located at the end of the anchorage length of the middle bar where the splitting crack was expected to form initially, in order to measure the contribution of transverse reinforcement on the bond splitting strength of the bar.

- **Beams GB31, CB33, GB36**

In these beams the main reinforcement was spliced in the region between the point loads. A different arrangement of strain gauges was applied to monitor the distribution of strains in the spliced region of the bars. The strain gauged shear links were also located in the spliced region where a side split (horizontal) type of failure was expected (see section 2.1.6). These gauges were expected to measure the contribution of links on the bond behaviour of bars before and after the formation of splitting cracks.

- **Beam GB35**

In this beam, the bar expected to fail in bond was positioned at the corner of the cross section. The crack pattern expected was a kind of corner split failure (see section 2.1.6) so, both the horizontal and vertical legs of the shear link were expected to resist this type of cracking. For this reason, the instrumentation of both legs was decided in order to measure this resistance force.

- **Beams GB34, CB37**

A special arrangement of strain gauges was adopted on the main reinforcing bars in these beams to examine the distribution of bond stresses between consecutive cracks. Three crack inducers (thin pieces of metal) were placed at the bottom side of three consecutive shear links in the anchorage length region of the middle bar. They were expected to induce the formation of flexural cracks at those specific points so that the evenly distributed strain gauges at that region could monitor the developed bond stresses between the cracks. The author was aware of the fact that these nine strain gauges over a short length of the bar (160 mm), would also reduce the bonded area of the bar. For this reason, the area covered by those strain gauges was deducted from the calculations of bond strength, as it will be explained in section 3.2.7.

In addition in beam CB37, strain gauges were attached at the horizontal, bottom leg of the shear links. Since the splitting crack was expected to develop below the middle bar the horizontal leg was more likely to contribute to the bond splitting strength of the bar than the vertical leg.

#### **3.2.4.2 Arrangement of LVDTs on the beam**

Twenty-seven LVDTs were used in each beam test to measure the deflections at specific points on the beam. The whole arrangement was adopted from the previous phases of beam testing (Duranovic et al, Feb.1995) and is presented in appendix B.6. Although, the purpose of most of these transducers was not directly related to the objectives of this study, their results were gathered for future investigation by other researchers.

All the LVDTs, except from Nos. 9, 26-30 and 32, were positioned on a specially made frame which was mounted to the back of the testing frame as shown in figure 3.12. These LVDTs were measuring horizontal and vertical deflections at specific points on the concrete beam during testing.

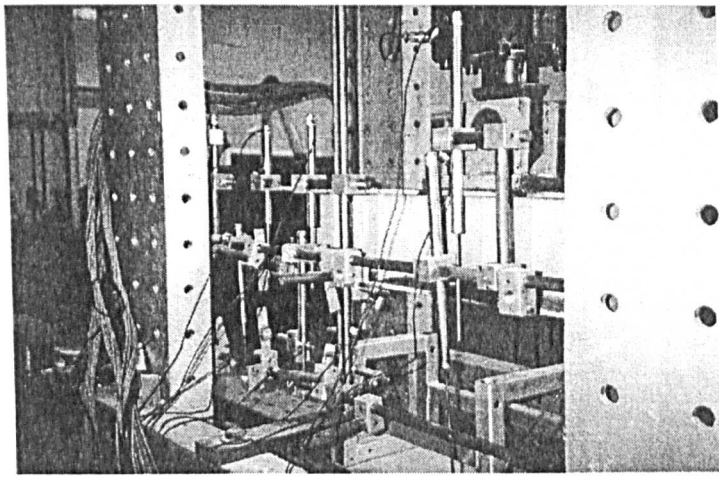


Figure 3.12: Arrangement of LVDTs at the back of the beam

LVDTs No.9 and 26 were positioned at the two end edges of the beam, touching the ends of the reinforcing bars in order to measure their slip during testing. In addition, LVDT No.32 and LVDTs 27 to 30 were placed at the top and at the side of the beam to monitor the top concrete strain and the concrete strain along the midspan cross-section. They all measured the concrete deformation over a 200 mm length.

However, in two of the tested beams the arrangement of LVDTs 27 to 30 was quite different. In beam GB30, these LVDTs were positioned at the bottom side of the beam to measure the splitting crack opening under the middle bar, as shown in figure 3.13. For the same reason, the LVDTs were arranged at the bottom side of beam GB31 to measure a possible crack opening under the spliced FRP bars.

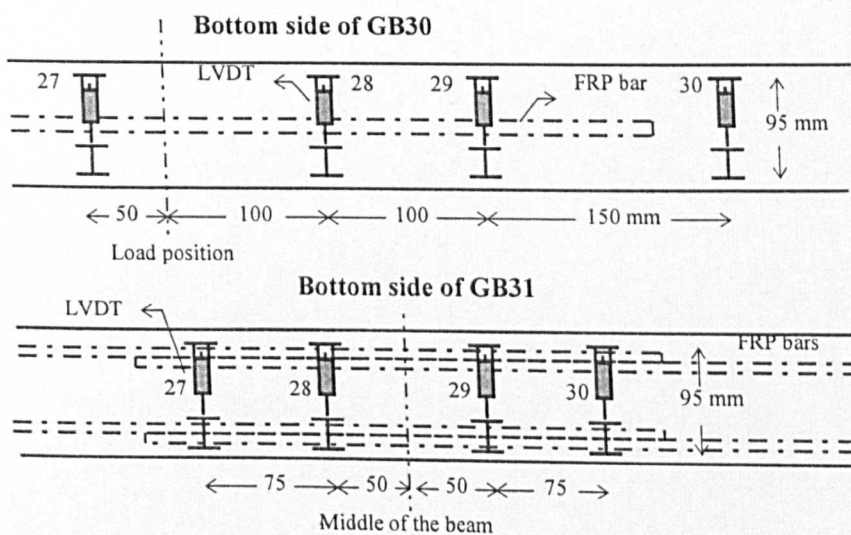


Figure 3.13: Arrangement of LVDTs No. 27-30 in beams GB30, GB31

### 3.2.5 Experimental set up

The experimental arrangement is shown in figures 3.14 and 3.15. The beam was supported over a span of 2.3 m through rollers over 100mm wide steel plates. The left support allowed the beam only to rotate while the right one allowed both rotation and horizontal movement.

The load was applied by a servo-controlled hydraulic actuator at two points, symmetrical to the centre through the same kind of rollers as used at the supports. Since the actuator was able to operate in either load or deflection control modes, the latter mode was preferred for this testing series. The actuator could impose up to 150 mm vertical deflection which was more than adequate for the deflections expected in this kind of beams.

The hydraulic actuator was controlled by an Electronic Control Unit which communicates information to the data acquisition system (ORION), connected to a PC, in a similar arrangement reported for the pullout tests (see section 3.1.4).

Before each test, all the wires from the LVDTs and strain gauges were connected to the ORION. The needles of the LVDTs, mounted on an instrumentation rig, were positioned over the respective clamps previously glued on the beam. LVDTs measuring relative displacements were also adjusted to monitor the expected displacements. All the instrumentation was initialised automatically from the ORION before each test.

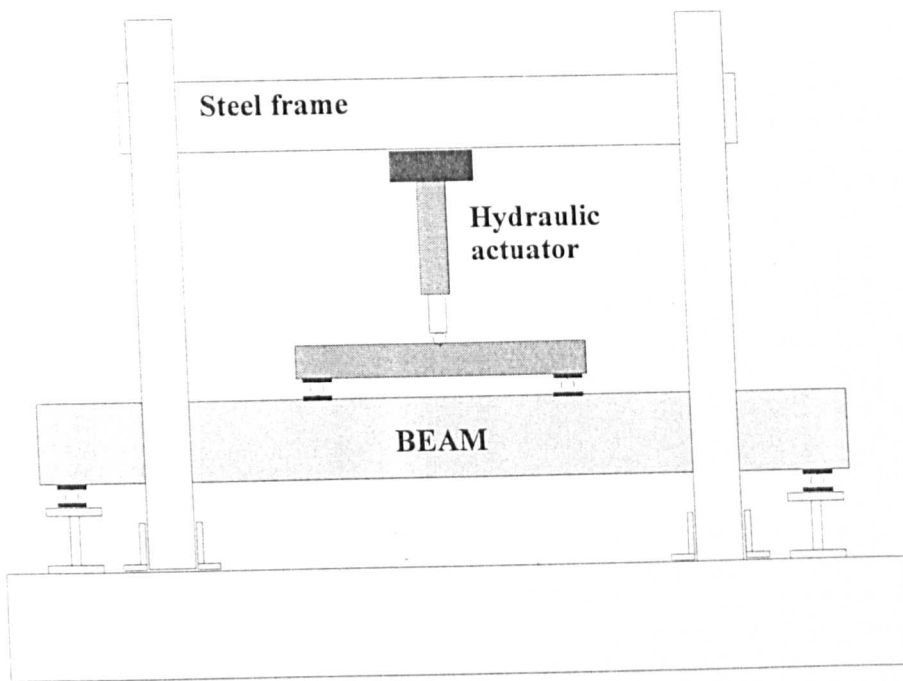


Figure 3.14: Test arrangement (simplified)

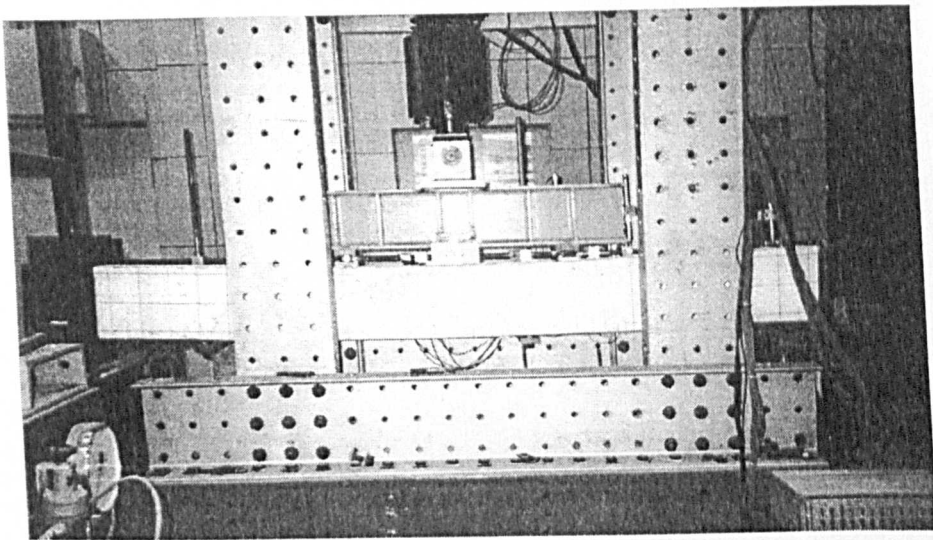


Figure 3.15: Photograph of the test arrangement

### 3.2.6 Testing procedure

The load was applied manually in the displacement control mode at about 5kN increments. Two loading cycles were performed. In the first, the load was increased up to 20 kN and the specimen was then unloaded whereas in the second, the specimen was

loaded up to failure. All the experimental data were downloaded to the PC system via the ORION system every 5 seconds.

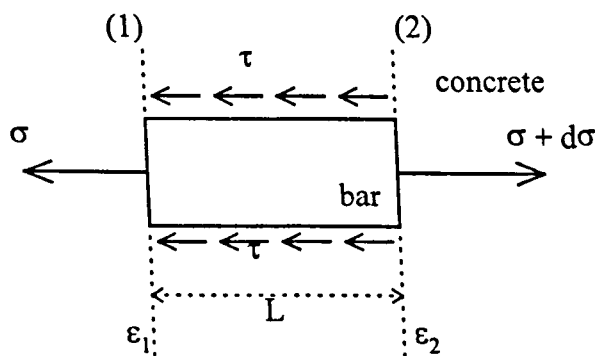
During the test, the developed cracks on the beam were marked and the biggest crack openings were measured with an optical instrument, every 5 or 10 kN depending on the expected load capacity of the beam. Photographs were, also, taken after each marking stage.

After the completion of each test, the beams were removed from the testing frame and a closer examination of the mode of failure was conducted. The failure cracking pattern was marked and further photos were taken of specific areas of interest on the beam.

### 3.2.7 Analysis of measurements

The values from the strain gauges attached on the reinforcing bars were used for the calculation of the developed bond stresses on the bars during testing.

It is known from the literature that the average bond stress between two points, for example (1) and (2), is proportional to the rate of change of strain along that length. From the force equilibrium over a certain length of a round bar in concrete, it can be deduced that:



$$(\sigma + d\sigma) A_{\text{bar}} = \sigma A_{\text{bar}} + \tau \pi d L \Rightarrow d\sigma A_{\text{bar}} = \tau \pi d L \Rightarrow$$

$$d\sigma \pi d^2 / 4 = \tau \pi d L \Rightarrow \tau = (d / 4) (d\sigma / L) = (d E / 4) (d\varepsilon / L) \Rightarrow$$

$$\tau = \frac{d * E}{4} * \frac{\varepsilon_2 - \varepsilon_1}{L} \tag{3.3}$$

So, by using the experimental strains, the average bond stress values between successive strain gauges or even, for the whole anchorage length, can be easily deducted.

However, special consideration has to be given to the calculation of the bond strength developed in beams GB34 and CB37 where the contact area between bar and concrete has been significantly disturbed because of the great number of strain gauges attached on the reinforcing bar. In the case of GB34, the reduction is estimated around 8% whereas for CB37 is around 5.5% of the total anchorage length area. This was calculated by dividing an area of 5mm x 160 mm (area disturbed by the adjacent strain gauges) by the anchorage length surface area in each case. Therefore, the developed average bond strength for the whole anchorage length must be multiplied by a factor 1.08 and 1.055 for the case of GB34 and CB37 beams, respectively.

# CHAPTER 4

## EXPERIMENTAL RESULTS

This chapter presents the experimental results from the pullout and beam tests described in the previous chapter. The mode of bond failure of reinforcing bars in each type of tests is examined and the various parameters that influence bond development are discussed.

### 4.1 PULLOUT TESTS

The results of 131 cube tests are used to evaluate the bond behaviour of FRP reinforcing bars to concrete. A summary of the experimental results is presented in tables C.1.1 to C.1.6 of appendix C.1. Since a large variety of FRP bars were tested, a single coding notation for presenting the parameters of each specimen is difficult to be applied. For this reason, a general coding notation is introduced describing the specimen features of the most commonly used bars, whereas for the rest of the cases individual notations are applied and explained in the result tables.

The general coding notation is applied for rough surface bars embedded in concrete cubes as follows: The first number of the code indicates the concrete cube compressive strength in MPa; the first letter denotes the kind of reinforcing bar used in the test (G for GFRP bar, C for CFRP, A for AFRP and H for Hybrid); the next letter denotes the type of the bar cross section (r for round and s for square); the second number indicates the ratio of embedment length to the bar diameter (applied only in round bars), the last letter denotes the size of the bar diameter (D for 13.5 mm, d for 8 or 8.5 mm and *d* for 10.5 mm). For example, 45Gr8D designates a 13.5 mm GFRP round

bar, cast in concrete with compressive strength 45 MPa, having embedment length equal to 8 times the bar diameter.

Bond-slip curves were produced for each test at the loaded and unloaded end of the bar in order to study the bond development of FRP bars and facilitate comparisons among the tests. These graphs are presented for most of the tests in appendix C.2. Since the preliminary tests conducted at the beginning of this study (table C.1.1 in appendix C.1) were performed without the presence of any transducer arrangement, no graphs are available for these tests. In addition, in few of the tests it was not possible to measure the unloaded end slip of the bar since the aluminium frame on which the transducer was mounted (see section 3.1.4), was accidentally unglued during the test. In these cases, the author decided to proceed with the testing procedure without the bottom transducer, instead of stopping the test and start again, since it was assumed that the bond capacity of the bar might be influenced if a second load cycle was imposed to the bar.

In the following, the most important observations of the experimental series are presented and the influence of the various parameters on the bond development of FRP bars to concrete is examined.

#### 4.1.1 Bond stress versus Slip curve

Figure 4.1 shows typical plots of bond stress versus slip of GFRP and CFRP reinforcing bars.

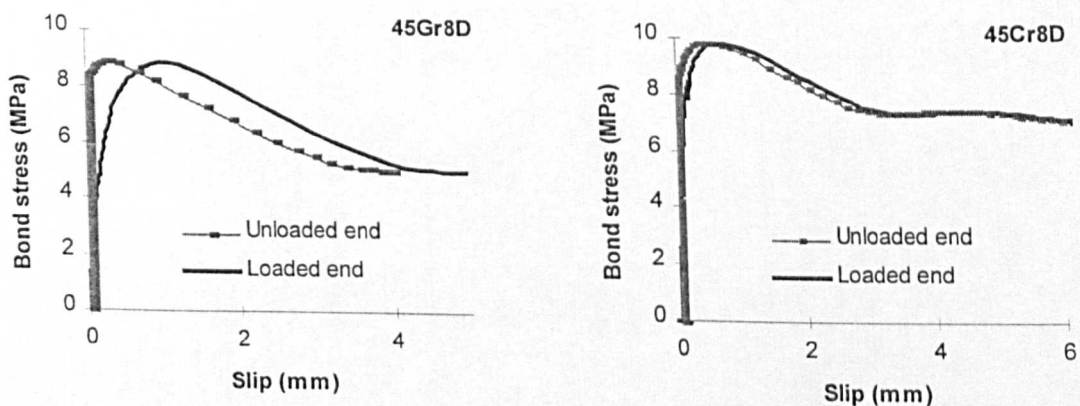


Figure 4.1: Typical bond - slip envelopes for GFRP and CFRP embeddings

As seen from the curves, the loaded end slips almost at the beginning of loading as soon as the chemical adhesion between bar and concrete breaks. According to CEB Bulletin 151 (1982), in the case of steel bars the bond resistance offered by adhesion is assumed to be rather small,  $\tau_o \cong 0.5-1.5$  MPa (see figure 2.1). However, the Bulletin does not say whether this value is taken from experimental data or it is a theoretical estimation of the contributing researchers.

In this experimental series, the author found difficulties in measuring accurately the adhesion between FRP bars and concrete since the required accuracy of slip measurements for this purpose was not determined anywhere in the literature. In addition, high accuracy in slip measurements could hardly be achieved at the beginning of the tests since many factors influenced the accuracy of the loaded end slip measurements at that stage. The most important of these factors were:

- the initial imposed load on the specimen (see section 3.1.5)
- the probable tilting of the mounting rig (see section 3.1.4) at the beginning of the test
- the non-verticality of the tested bar and
- the irregularities at the concrete cube surface.

Considering the above, the author decided to estimate graphically the bond level where the chemical adhesion of an FRP bar and the concrete breaks. The bond value where the slope of the bond - loaded end slip curve significantly decreases (point  $\tau_o$ , in figure 2.1), is assumed to be the required bond value due to chemical adhesion. The experimental results show that the adhesive bond strength seems to depend only on the bar diameter, whereas it appears to be independent of the type of bar and the concrete used in the specimens. The figure below shows the average value of adhesion measured in the experiments where smaller diameter bars develop greater adhesion with the surrounding concrete than larger bars.

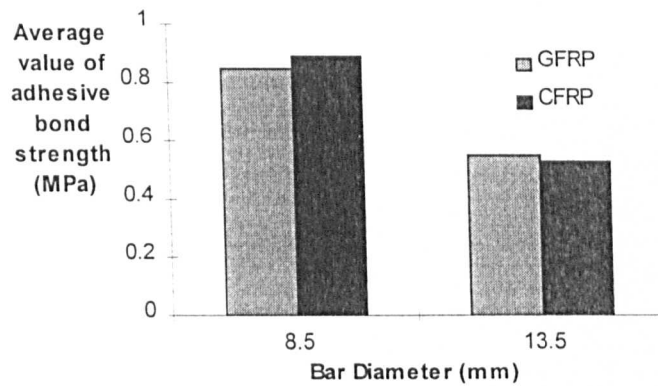


Figure 4.2: Average values of adhesive bond strength with respect to the bar type and diameter

Another important observation from the tests is that the unloaded end slip remains practically zero until the bond stress reaches quite high values compared with the ultimate bond strength value. The experimental results show that the ratio of the recorded bond values when the unloaded end started to slip ( $\tau_{sl}$ ) to the maximum bond strength is around 80% for both G and CFRP bars (figure 4.3). Although the ratio was initially assumed to depend on the elastic modulus of the bar, the results suggested no clear relationship between the two quantities.

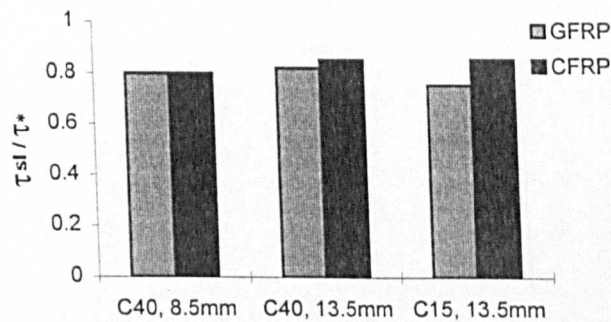


Figure 4.3: Ratio of bond stress when unloaded end starts to slip to maximum bond strength for C and GFRP bars

Furthermore, the initial slope of the loaded end bond-slip curve for CFRP bars appears to be stiffer than that of GFRP bars and this is assumed to be related to the difference in the elastic moduli of the two bars. However, the initial slope appears also

to be related to other parameters influencing the bond behaviour of the bar as will be examined in detail in section 4.1.3.

The post-maximum (residual) bond strength value appears to be more than 60% of the peak bond value in most of the specimens. This seemed to be an important attribute of FRP bars since the residual stress of deformed steel bars under similar tests was only 20 to 40% of the maximum value. However, by considering the failure mode of FRP bars, the above value appears to be rather “plasmatic” than real. The following section will explain in further detail the mode of failure of FRP bars as it was observed in the pullout tests and its relevance to the residual bond strength of the bar.

#### **4.1.2 Mode of bond failure of FRP bars**

In the current experimental series all the FRP bars failed in the designed pull-through mode of bond failure. The concrete cubes provided adequate confinement to the bars to enable them to reach their maximum bond strength. As expected, no signs of splitting cracks appeared on the cube specimens since the size of bar diameters used were comparatively small to the dimensions of the cube specimens.

However, by comparing the mode of failure of FRP bars to that of steel deformed bars under similar experimental conditions, the author observed an important difference. In section 2.1.2, the steel bar - concrete interaction was described based on the existing knowledge presented in CEB Bulletin 151. According to the Bulletin, when sufficient confinement is provided to a deformed steel bar during pullout, shear cracks develop between the bar ribs in the surrounding concrete and the bar fails in a pull-through mode. When this kind of failure happens, the bond strength of the bar depends mainly on the strength of the surrounding concrete.

In the case of FRP bars and for concrete strengths greater than 30 MPa, the bond failure occurs on the surface of the bar, and not in the concrete, by peeling part of the surface layer of the bar. Consequently, the bond strength of FRP bars is not controlled by the concrete strength but appears to be governed mainly by the shear strength of the resin of the bar. Figure 4.4 shows a characteristic GFRP specimen sample after the test.

The specimen was split after the test, for a closer investigation of the actual mode of bond failure.

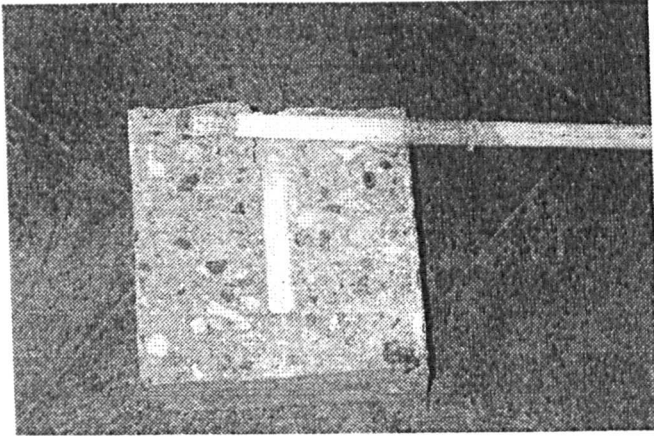
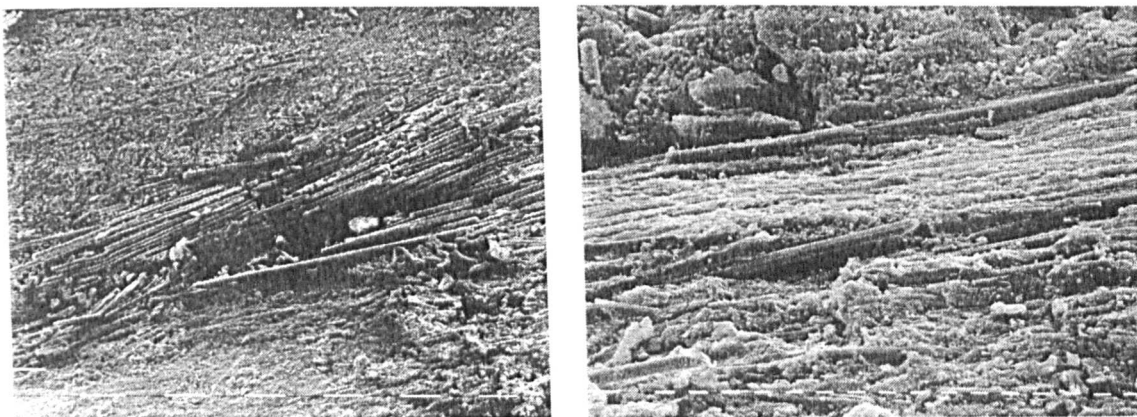


Figure 4.4: GFRP specimen after the test

It is obvious from the picture that white powder consisting of crushed resin and chopped glass fibres, is attached on the concrete cube at the place where the embedment length of the bar lies. On the other side, part of the bar's surface peeled-off and tiny fibres become visible on the surface of the bar.

In the cases of CFRP and AFRP bars the mode of bond failure was not so clearly visible. For example, in the case of CFRP specimens, only few small black lines were visible on the concrete side of the embedment length. No clear traces of crashed resin or extensive damage on the CFRP bar surface was observed. In order to investigate in more detail the mode of failure of all FRP bars, the author conducted a microscopic investigation on the bond failure interface of selected specimens (Achillides and Pilakoutas, 1997). Scanning Electron Microscope images from this investigation are presented in appendix D for three types of FRP bars (Glass, Carbon and Aramid). The investigation confirmed that the failure took place in the bar surface and not in the concrete, for all kinds of FRP bars used. Two characteristic images of the concrete side failure interface are presented here (figures 4.5, 4.6).



Figures 4.5, 4.6: Concrete side bond failure interface for GFRP and CFRP embedment respectively

Figure 4.5 shows, the failure interface on the concrete side of a GFRP specimen. It is obvious that there are pieces of glass fibres below the crashed resin layer. The same observation can be made in figure 4.6 where a concrete piece from a CFRP specimen is shown. The failure in both cases appears to develop at a critical interface between successive layers of fibres as shown schematically in figure 4.7. The shear strength between fibres and resin seems to control the bond capacity of FRP bars in both cases. The height of the failure interface from the bar axis is assumed to depend on the relative value of the shear strength between the fibres and resin and the concrete shear strength. In the current experiments, the height of the failure interface of GFRP bars ( $h_G$ ) is assumed to be lower than that of CFRP bars ( $h_C$ ), since the GFRP bars surface was found to be more extensively damaged.

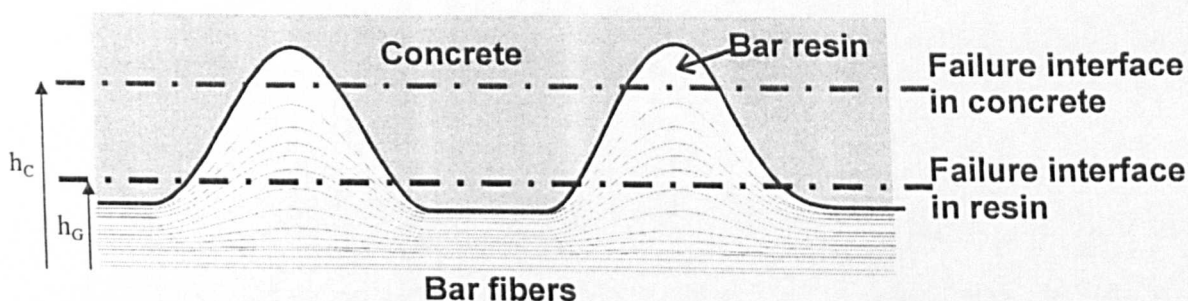


Figure 4.7: Shear failure at the surface layer of FRP bars

For lower strength concretes (around 15 MPa) FRP bars failed in a different mode, more similar to deformed steel bars. The concrete was crushed in front of the deformations of the bar and the bond strength seemed to be controlled mainly by the shear strength of the concrete. The bond strength values developed in this case were significantly lower than the ones developed in higher strength concretes, as will be shown in section 4.1.3.3.

#### 4.1.2.1 Residual bond strength of FRP bars

As a result of the mode of bond failure of FRP bars in higher strength concrete ( $f_{cu} > 30$  MPa), the recorded residual bond stress does not represent the real value of frictional stress developed at the failure interface. This is due to the fact that when the damaged part of the bar is slipping out of the cube during pullout, the undamaged part that follows enters the embedment length zone and adds additional resistance to the pullout load. This action enhances the recorded bond strength value that represents, apart from the frictional stress, the additional resistance produced by the wedging action of the undamaged bar.

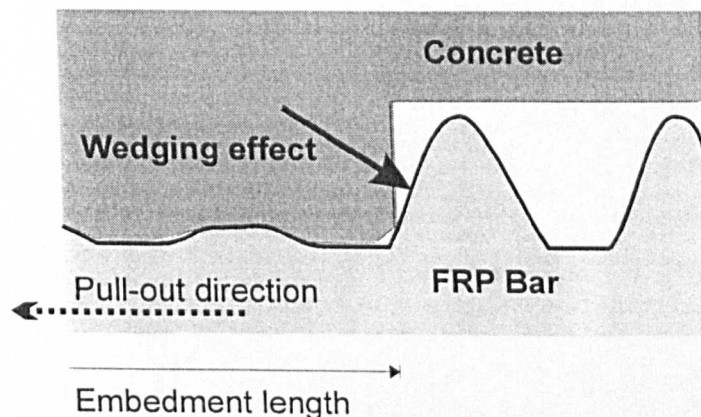


Figure 4.8: The wedging action by the undamaged part of the bar

The above phenomenon is unimportant for steel bars since the bond failure happens in the surrounding concrete as it is explained in section 2.1.2. In this case, the unbonded part of the bar which enters the embedment length zone does not contribute significantly to the bond resistance of the bar since the bond failure interface is approximately at the height of the tips of bar deformations.

In order to quantify the value of the residual bond stress related only to the frictional action, an additional series of experiments was conducted where some of the specimens had the embedment length at the very end of the cube as shown in figure 4.9 (similar to the RILEM/CEB pullout test, see section 2.1.4). The test arrangement and instrumentation used were similar to the one used during the experimental series presented in chapter 3.

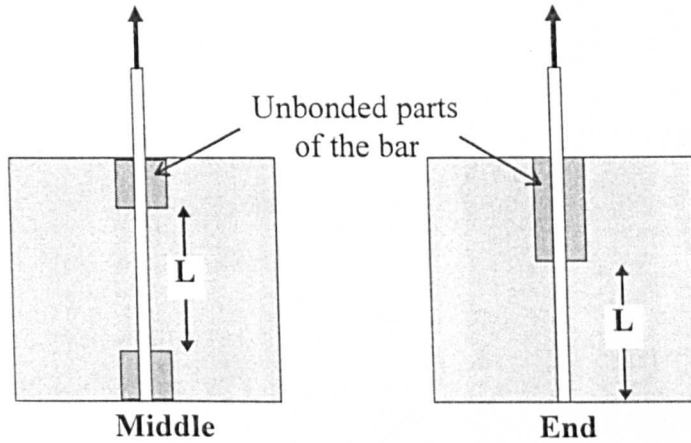


Figure 4.9: Embedment length ( $L$ ) at the middle and at the end of the cube specimen

The results of the additional series of tests are presented in table C.1.6 of appendix C.1 and the characteristic bond-slip curves in appendix C.2. The analysis of the results showed that the residual bond stress was much lower when the embedment length was at the end of the specimen. The difference in values was more important in GFRP than in CFRP bars (see figure 4.10 for round bars) and this appears to be due to the fact that the height of the bond failure interface  $h_G$  (see figure 4.7) was much lower than  $h_C$ .

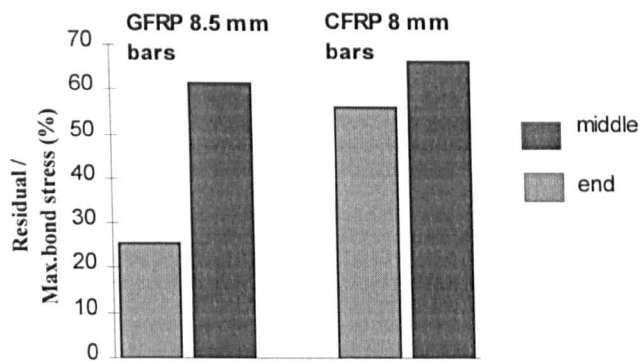


Figure 4.10: Ratio of residual to maximum bond stress for round FRP bars

However, the position of the embedment length in the concrete cube did not seem to influence the maximum bond stress developed or the initial bond stiffness of the bar in the case of G and CFRP round bars. This can be explained by the fact that the unloaded end slip values recorded up to the maximum pullout load were less than 1 mm in all the specimens and the wedging effect could not be significantly activated in such a short distance.

On the contrary, in some cases of square bars a small difference in the maximum recorded bond values was observed for the two positions of embedment length as it will be explained in more detail in section 4.1.3.5.

### 4.1.3 Factors that influence the bond behaviour of FRP bars

A number of important factors that influence the bond behaviour of FRP bars are examined in this study (Achillides et al, 1997b). A proper evaluation of the level of influence of these factors on the bond development will be helpful to the formulation of equations for adequate anchorage lengths for FRP reinforcement.

#### 4.1.3.1 Type of bar fibres

In this experimental series four kinds of FRP bars were tested in order to examine their bond characteristics to concrete: Glass, Carbon, Aramid and Hybrid. In figures 4.11 and 4.12, the maximum average bond stress ( $\tau^*$ ) developed for GFRP and CFRP bars is presented versus the embedment length (L). The examined specimens

were 8 and 8.5 mm diameter round bars of rough surface. By using linear regression, the best-fit line passing through all data points was obtained. However it is important to note here, that the use of linear regression does not suggest that there is a clear linear relationship between  $\tau^*$  and L. The author uses linear regression only for comparison purposes, over a small range of embedment lengths (2 to 10 times the diameter), since it presents clearly the trend in  $\tau^*$  values as L changes.

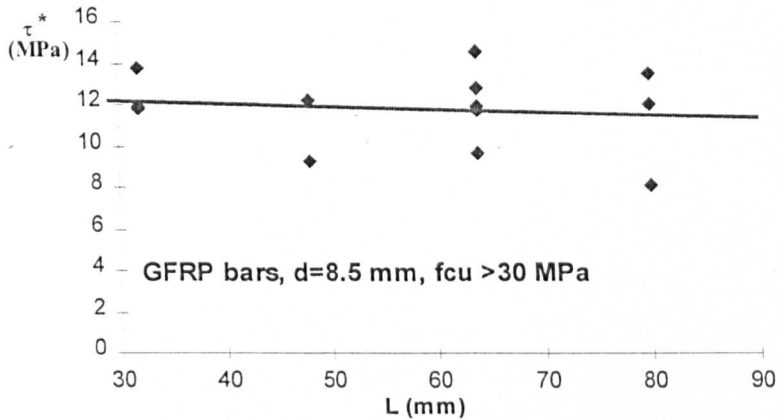


Figure 4.11: Bond stress versus embedment length for GFRP round bars

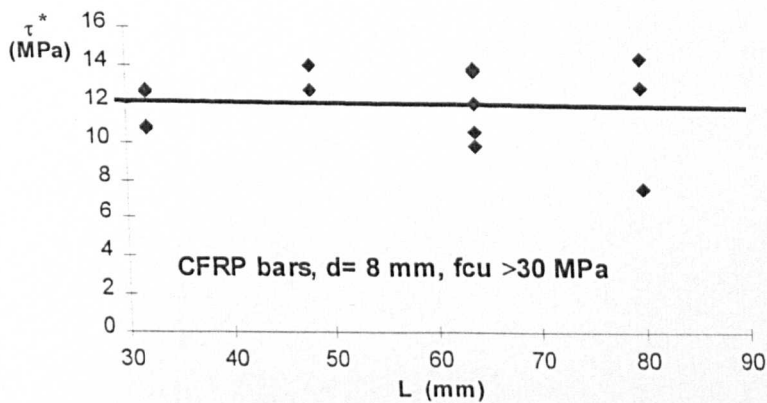


Figure 4.12: Bond stress versus embedment length for CFRP round bars

From the above figures it can be suggested that both Carbon and Glass FRP bars exhibited similar bond behaviour. Their maximum average bond stress at the embedment length of 8 diameters ( $L = 64$  mm) was 11.9 and 12.0 MPa, respectively. On the other hand deformed steel bars, having the same diameter and embedment length, developed  $\tau^*$  equal to 16.5 MPa (for concrete strength 39 MPa). By comparing the

above values, it can be deduced that GFRP and CFRP bars developed about 72% of steel's bond strength which is quite remarkable considering the different nature of their surface. However, it has to be noted that the above percentage is not representative for the whole range of values of concrete strength since the influence of the concrete strength on the bond strength of FRP and steel bars is not the same, as it will be explained in section 4.1.3.3. For example, for lower concrete strength (around 30 MPa) the above bond strength value of steel bars will decrease whereas FRP bars bond value will remain practically the same; consequently, the percentage will increase.

Aramid and Hybrid FRP bars developed around 85% and 90% of the Glass and Carbon FRP bond strength respectively which is also quite satisfactory (see figure 4.13).

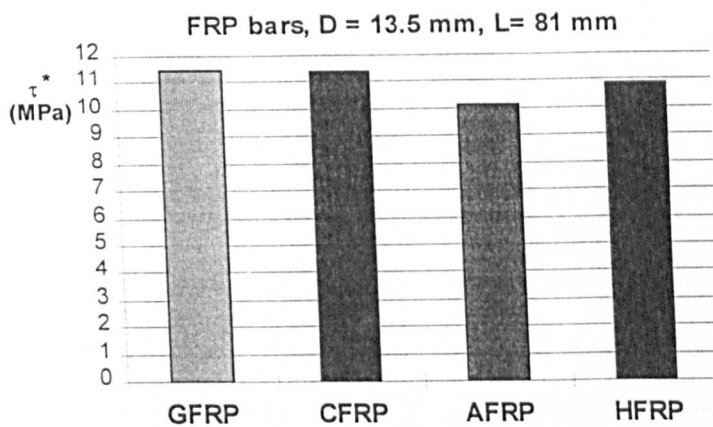


Figure 4.13: Corresponding bond strength values for FRP bars

The above experimental results appear to be in agreement with results published by other researchers, such as Malvar (1995), Larralde and Silva-Rodriguez (1994), Chaallal and Benmokrane (1993) and Nanni et al (1995), despite the fact that different types of FRP rods are used. It is also worth noting that the bond strength of epoxy-coated bars, which are mainly used as anti-corrosive reinforcement varies from 67-95% of that of deformed steel bars (Chaallal and Benmokrane, 1993) which is comparable to the bond strength of FRP bars.

The initial stiffness of the bond-slip curve also depends on the type of FRP bar used and more specifically on the elastic modulus of the bar. GFRP bars are expected to develop greater slip values than CFRP bars, under similar pullout loads, since their Young's Modulus is less than half of CFRP bars. Figure 4.14 shows the influence of

elastic modulus of the bar on the loading branch of the bond-slip curve for low and high strength concrete.

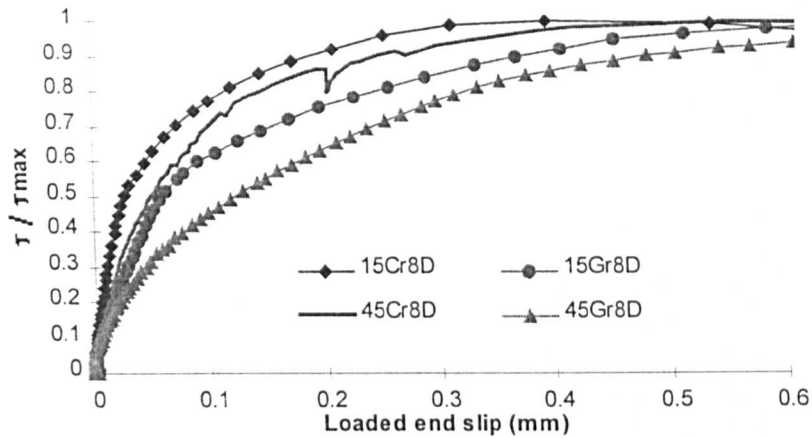


Figure 4.14: Influence of type of bar fibres on the bond-slip curve of FRP bars

From the above set of curves, it is also obvious that the expected loaded end slip of GFRP bars at the ultimate pullout load would be greater than that of CFRP bars, which underlines the importance of the elastic modulus to the formulation of appropriate design anchorage formulas for FRP bars.

#### 4.1.3.2 Embedment length

The value of the embedment length appears to influence the maximum average developed bond stress value ( $\tau^*$ ). As the embedment length increases,  $\tau^*$  decreases as shown in figure 4.15.

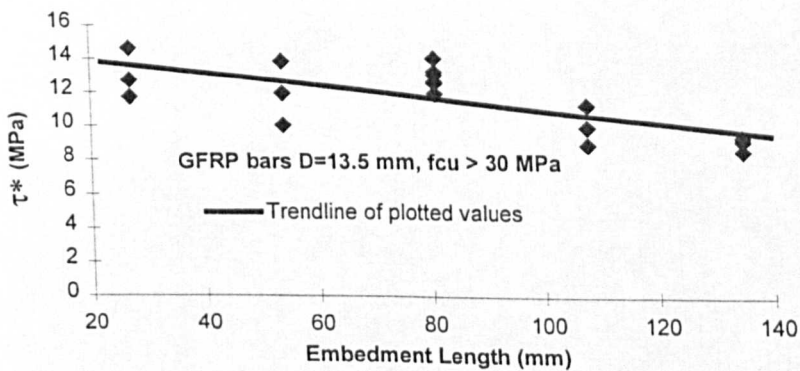


Figure 4.15: Influence of embedment length on  $\tau^*$

The same effect is reported also, for steel bars and is said to be a result of the non-linear distribution of bond stress on the bar as explained in the following. By considering the proposed distribution of bond stresses on a reinforcing bar during pullout (see section 5.1.2.3), the peak bond stress appears to move gradually towards the free end of the bar while the bond stress value at the loaded end decreases considerably. This immigration of peak bond stress is more evident in larger embedment lengths (for example,  $L=10D$ ) and reduces significantly the value of  $\tau^*$  on the bar. However, in even larger embedment lengths, the value of  $\tau^*$  becomes practically constant, since the influence of the peak bond stress to the overall bond strength of the bar becomes unimportant (see figure 5.10).

The embedment length has also significant influence on the applied pullout load and the initial stiffness of FRP bars. Figures 4.16 and 4.17 show this effect on GFRP and CFRP bars.

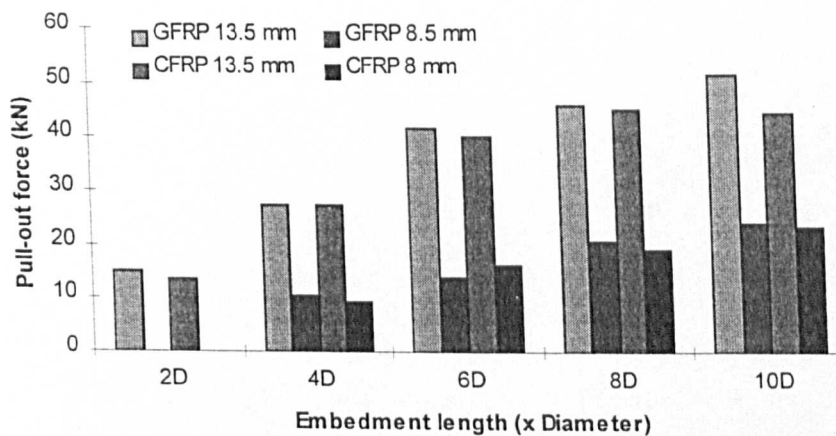


Figure 4.16: Maximum Pullout load versus Embedment length

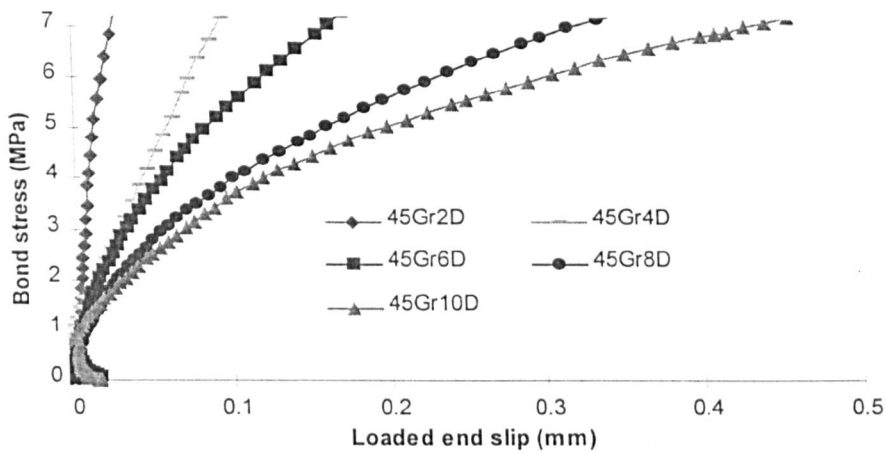


Figure 4.17: Change in the initial bond stiffness of GFRP bars with embedment length

Figure 4.16 shows that the rate of increase of the maximum applied pullout load is greater for small than for larger embedment lengths. This is again assumed to be due to non-linear distribution of bond stresses on the bar, which has a greater influence on, smaller than on larger embedments, as it was mentioned previously.

Figure 4.17 shows the initial stage of the bond - loaded end slip curves of 13.5 mm diameter GFRP bars. The embedment length varies for each bar in multiples of bar diameter. It is obvious from the figure that as the embedment length increases the initial stiffness of the curves decreases. This observation is significant for the bond modelling procedure (presented in a following section of this study) where the author will examine in more detail the rate of change of stiffness of the bond-slip curve.

#### 4.1.3.3 Concrete strength

Results from this study showed that the strength of the surrounding concrete is directly related to the actual mode of bond failure of the bar during pullout. For concretes with compressive strength greater than 30 MPa, the bond failure interface happens in the surface of a FRP bar (see section 4.1.2). Consequently, the bond strength of FRP bars does not depend on the value of concrete strength, as far as the concrete strength is greater than 30 MPa. However, for lower concrete strengths (around 15 MPa) the bond failure mode changes. In this case the failure interface takes place in the concrete matrix and the bond behaviour of the bar is directly related to the concrete

strength. Figure 4.18 shows the change in the value of  $\tau^*$  of FRP bars for different concrete strengths for an embedment length of 6d.

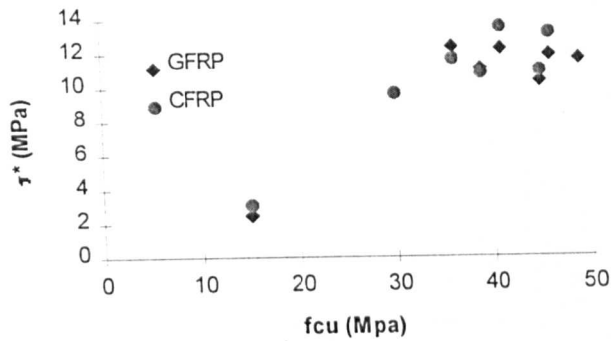


Figure 4.18: Influence of concrete strength on  $\tau^*$  for FRP bars

Figure 4.19 also shows more specifically the effect of concrete strength on 13.5 mm CFRP bars for increasing embedment lengths. The large difference in concrete values does not seem to influence the rate of decrease of bond strength as the embedment length increases.

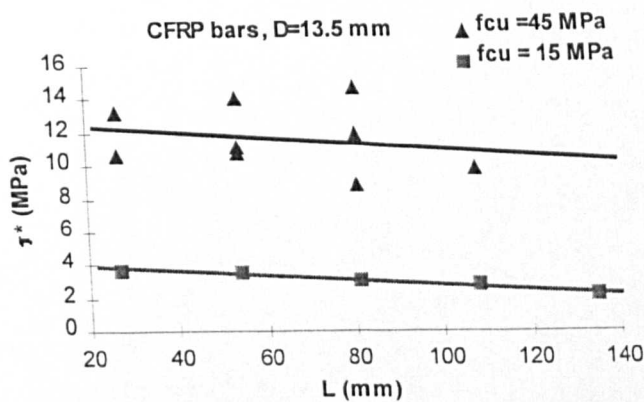


Figure 4.19: Influence of concrete strength on the CFRP bars for various embedment lengths

#### 4.1.3.4 Bar diameter

The bar diameter appears to play an important role in the bond behaviour of FRP bars to concrete. Larger diameter bars developed less average bond strength than smaller diameter bars. In figure 4.20, the maximum average bond strength values of G and

CFRP bars used in this experimental series are presented, showing the influence of diameter on the developed bond strength.

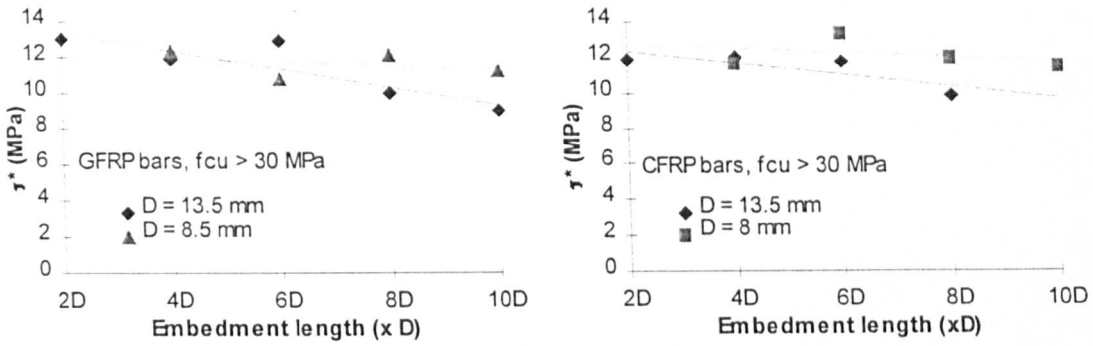


Figure 4.20: Influence of bar diameter on the value of maximum average bond strength

Bond development in FRP bars is thought to be affected by the diameter due to their low shear stiffness in the axial direction. The value of the shear stiffness of FRP bars depends mainly on the shear stiffness of the bar resin and the shear strength capacity at the resin-fibre interface. When an FRP bar is pulled in tension through the surface, there can be a differential movement between the core and the surface fibres, which results in a non-uniform distribution of normal stresses through the cross section of the bar. An indicative distribution of these stresses is shown in figure 4.21.

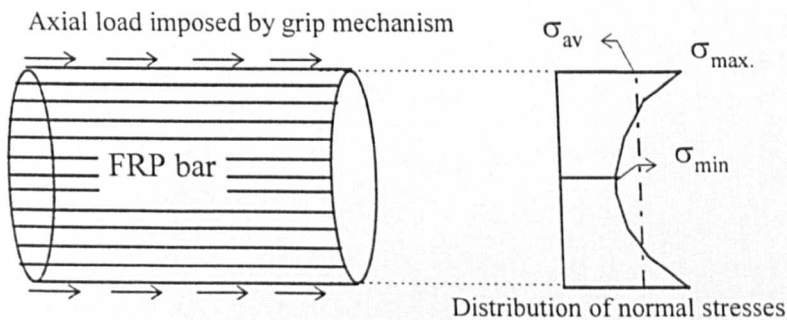


Figure 4.21: Indicative distribution of normal stresses on a FRP bar cross-section subjected to axial load

The actual developed bond strength between the bar and the concrete is directly related to the value of the normal stress that occurs close to the surface of the bar ( $\sigma_{max}$ ). On the other hand, the calculated bond strength that the user anticipates as the “real” bond strength, is proportional to the value of the average normal stress over the whole

cross section of the bar ( $\sigma_{av}$ ). As the diameter of the bar increases, the difference between  $\sigma_{max}$  and  $\sigma_{av}$  is also expected to increase, especially when the axial shear stiffness of the bar is relatively low as in the case of FRP bars, and the “real” bond strength of the bar decreases. This effect, known in the literature as the “shear lag effect”, appears to be more significant for higher normal bar stresses which usually happen at greater embedment lengths.

For steel bars, this effect is not important since the shear strength of steel is significantly higher. Nevertheless some codes, for example ACI Building Code (1989), include the value of the cross section area of the reinforcing bar in the calculations of the anchorage length. EC2 (1989) considers the diameter effect only for diameters greater than 32 mm whereas BS8110 (1985) does not have any special provisions for this effect.

#### 4.1.3.5 Cross sectional shape of the bar

The influence of the shape of the cross section of the bar on the bond development is another important parameter that was investigated in this series of experiments. Two types of cross sections were compared: square (8x8 mm) and round (8 or 8.5 mm diameter). By examining bars with the same embedment lengths at the end of the bar, the square bars appeared to develop superior bond strength values than round bars as shown in figure 4.22:

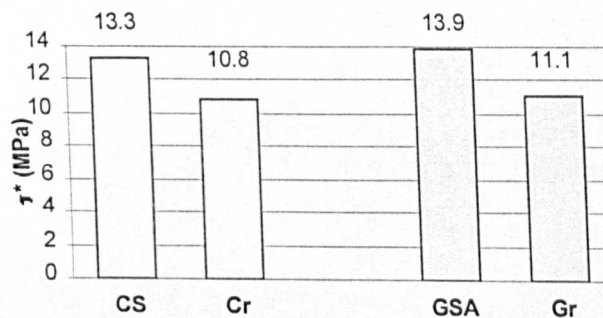


Figure 4.22: Comparisons between round and square cross section FRP bars

In the above figure, the average  $\tau^*$  values from the experimental results (see tables C.1.5, C.1.6 in appendix C.1) are presented for GFRP and CFRP bars, for the

same embedment length ( $L = 64$  mm). The bond values of round bars (Gr, Cr) appear to be around 80% of the bond strength of square bars (GSA, CS).

As it was briefly mentioned in section 4.1.2.1, the embedment length arrangement appeared to influence the value of  $\tau^*$  in the case of square bars. By considering the experimental results of specimens having the same embedment length at the end and the middle of the cube specimen (see table C.1.6 in appendix C.1), it can be suggested that the bond strength of "end" specimens can be increased around 10 to 25% when their embedment length is transferred to the middle of the cube. The author believes that the wedging effect (see section 4.1.2.1) is more important in the case of square bars because of their "edgy" cross section shape. It is assumed that the concentration of shear stresses at the edges of the square section might be the reason for the enlargement of this effect. A closer examination of square bar specimens after pullout supports the above assumption since the bar edges appeared to be more deteriorated than the rest of the bar surface.

#### 4.1.3.6 Surface deformations

Various kinds of FRP bars with different surface deformations were tested in order to investigate their bond performance to concrete. The experimental results showed that the presence of deformations on the surface of FRP bars play a significant role in their bond behaviour since smooth bars appeared to develop only 10-20% of the bond stress of the deformed bars. Similarly to steel bars, the bond strength of FRP bars is assumed to depend mainly on the mechanical interlock of the surface deformations and the concrete matrix, rather than on the chemical adhesion of the two materials.

In order to investigate the influence of the height of deformations on the bond strength of FRP bars, GFRP bars having different bar diameters were tested during this experimental series. In table C.1.4 in appendix C.1, the experimental results are presented, for two types of 10.5 mm GFRP round bars (G30, G24) having smaller surface deformations (0.3 and 0.24 mm respectively) than the standard 8.5 mm deformed bars used in this series (deformation height between 0.5 to 1 mm). The average bond values developed from these bars are presented in figure 4.23 compared with results from the standard deformed bar.

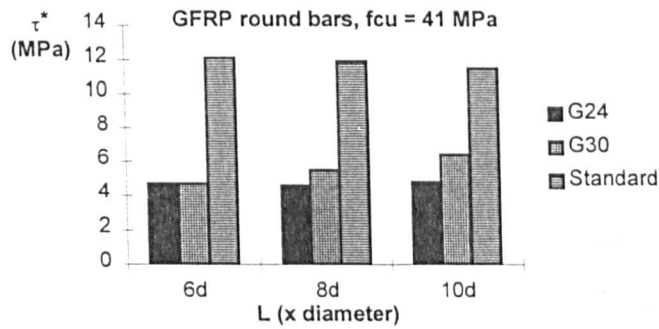


Figure 4.23: Bars with different type of surface deformations

It is clear from the above figure that G30 and G24 FRP bars have not developed adequate bond strength compared to the standard deformed GFRP bar. It can be assumed that FRP bars must necessarily have a minimum height of deformations to develop satisfactory bond behaviour to concrete. The optimum value of this height was not possible to be verified in this research project since only limited types of FRP bars were available for testing. However, the above results seem to verify the observations of Malvar (1994,1995), who suggests that surface deformations of about 5.4% of the bar diameter are sufficient to provide adequate bond behaviour to concrete.

## 4.2 BEAM TESTS

In this section the relevant experimental results from the four phases of beam testing will be presented and discussed. The total volume of the experimental results for beams tested in phases 1-3 are presented in reports by Duranovic et al (1995,1996). In this study special consideration will be given to experimental results obtained from the fourth phase of beam testing.

### 4.2.1 Phases 1 to 3

#### 4.2.1.1 General

A summary of the experimental results of 24 beam tests is presented in tables E.1.1 and E.1.2 of appendix E.1. The mode of failure of each beam is presented in column 4 of the table where it can be seen that only 3 of these beams failed due to bond failure (these beams will be examined in more detail in section 4.2.1.3). Column 5 indicates the maximum longitudinal strain developed in the main reinforcing bars during testing whereas column 6 shows the maximum peak bond stress recorded at the very end of the beam, close to the support region. This bond value was calculated from the values of the successive strain gauges located at the end of the main reinforcing bar (see figure A.5 of appendix A) according to equation (3.3) given in section 3.2.7. Finally, column 7 presents the maximum average bond stress value recorded over the anchorage length of the reinforcing bars. The anchorage length is the distance from the point load to the end of the beam, which is approximately 867 mm for all beams except in beam GB12 where the anchorage length was reduced to 612 mm due to a different load arrangement.

The instrumental longitudinal strain measurements and the respective calculated bond stress values are shown for each beam in appendix E.2, together with the plots of strains and bond stress profiles over the bar length. The strain values are presented in steps of 10 kN load, up to the failure load. Many strain values are not initially equal to zero since the values presented here are for the final load cycle of the beam. It has to be

noted that the beams were initially subjected to a low-level cycle similar to the procedure reported for phase 4 beams (see section 3.2.6).

In the tables of strain values, a number of measurements are not reported due to failure of particular strain gauges before or even during the experiment. This can be attributed to various reasons such as:

- disconnection of the wire from the terminals of the strain gauge, during casting
- damage of the strain gauge during casting
- high longitudinal strains on the bar which damage the strain gauge readings
- breakage of the bar close to the strain gauge region

The bond stress values shown in appendix E.2 illustrate the average bond values developed between successive strain gauges. They were calculated for the chosen force levels by using equation 3.3. Inaccuracies in strain gauge measurements are responsible for negative values of bond stresses that occur mainly at low loads, close to the end of the bar. In contrast, negative values of bond stresses found occasionally at the midpoint of the distance between strain gauges c69 and c51 may be due to the location of concrete cracks relative to the strain gauge location in that area. This issue will be addressed in more detail in section 4.2.2.5.

#### **4.2.1.2 Bond stress profiles on main reinforcing bars**

An important result obtained from all the beam tests in this series, is the development and distribution of bond stresses on the reinforcing bars during the test. A typical graph of this distribution at different load levels is presented for beam GB16, in figure 4.24. The profiles for all beams are given in appendix E.2.

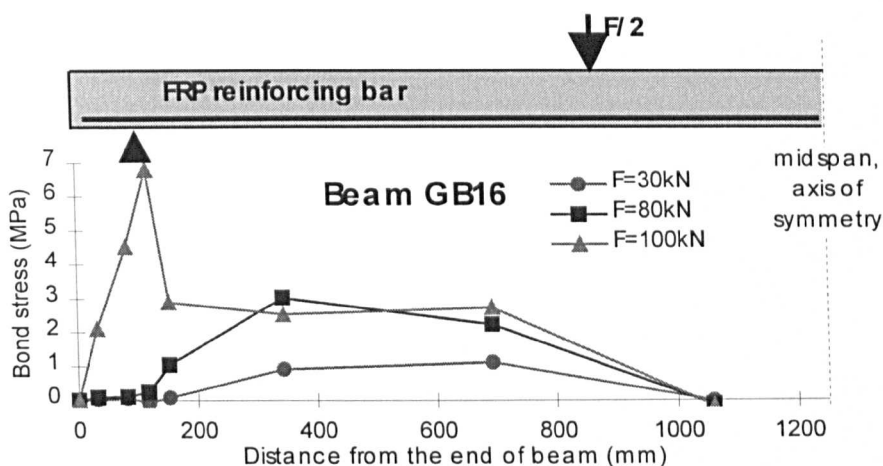


Figure 4.24: Typical bond stress profiles along the bar

The peak bond stress on the bar initially develops under the point load of the beam. This peak gradually propagates towards the end of the beam as the load increases, ahead of flexural cracking. At the region close to the beam's support, the recorded value of the peak bond stress becomes even higher since the flexural crack distribution at this area is very limited. In addition, it is assumed that the support action provides additional external confinement to the bar that enhances the bond strength capacity of the bar at this region. As it will be discussed at a later stage of this study, the confinement action of the support resists the initiation of bond splitting cracks and allows the bar to develop higher bond strength.

However, it is worth noting here that the peak bond values at the region between 200 and 800 mm can not be accurately monitored with the arrangement of strain gauges used in this experimental study. The strain gauges are widely spaced at that region (see appendix A.5) and consequently the respective bond stresses are calculated over a large length and represent an average rather than a peak bond stress value. The author believes that closer spaced strain gauges over the whole anchorage length could monitor the value of the peak bond stress more accurately. More on bond development on FRP reinforcement in beam elements and on the effect of flexural cracking on bond distribution are presented in section 6.3.6 of this study.

It is also significant to observe that the area under the curves in figure 4.24 is directly proportional to the average bond stress developed on the reinforcing bar, for each load step. This gives an indication of the importance of the peak bond stress to the overall bond strength of the anchorage length and explains why smaller anchorage

lengths develop higher average bond strength. For example, by considering the curve  $F=100\text{kN}$  in figure 4.25, the shaded area is proportional to the additional bond strength developed due to the peak bond value of the curve.

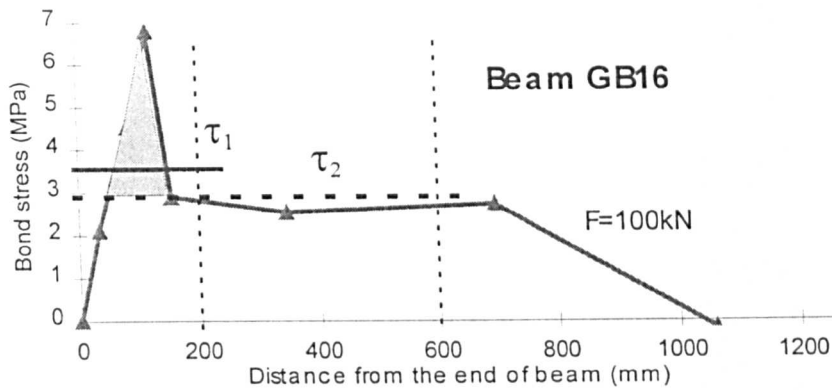


Figure 4.25: Importance of the peak bond value on the size of anchorage length

It is obvious that small anchorage lengths (e.g. 200 mm) develop higher average bond strength ( $\tau_1$ ) than larger lengths (e.g. 600 mm, average bond strength  $\tau_2$ ) since the shaded area is much more dominant in the first case.

#### 4.2.1.3 Bond failures in phases 1 to 3

In phases 1 to 3, only three beams failed in bond (CB20, CGB22 and AB28). In all these beams, the reinforcing bars failed in a pull-through mode of bond failure without any clear signs of splitting cracks along their length.

This mode of failure was expected only in beam CGB22 since confinement was applied by stressed steel straps over the whole length of the beam. The reinforcing bar failed in a pull-through mode by crushing the surrounding concrete in front of the deformations of the bar. The maximum average bond value measured was only around 2.1 MPa, since the concrete used had low compressive strength ( $\cong 18$  MPa). This bond value was very similar to the bond value obtained by testing the same type of hybrid FRP bar in the pull-out testing arrangement reported in section 4.1 (see table C.1.3 in appendix C.1). The bond strength value developed was also compared to the bond value suggested by codes of practise for steel deformed bars. Both Eurocode 2 (1989) and BS8110 (1985) suggest a bond value of 3 MPa (without including the safety factors in

each case) for steel bars embedded in concrete of compressive cube strength equal to 18 MPa, which results that Hybrid FRP bars develop around 70% of steel's bond strength.

However, the author acknowledges the fact that the bond values suggested by the codes are based on the splitting behaviour of steel bars, which is proportional to the strength of the concrete. Since the mode of bond failure observed in these tests was not splitting, the results obtained here can not be directly compared with the values suggested by the codes of practise. Nevertheless the author believes that referring to the values implied by the codes of practice, would give an indication for the range of bond values developed in the tests.

CFRP bars in CB20 beam failed also in a pull-through mode of bond failure despite the fact that the ratios of bar diameter to bottom and side concrete covers were less than 2. When similar size covers were used in phase 4 beams, splitting mode of bond failure was mainly observed, as it will be mentioned in section 4.2.2. However, in the case of CB20, part of the anchorage length of the reinforcing bars was lying above the support of the beam, which is believed to influence the bond development and enhance the bond capacity of the CFRP bars. The confining action of the support on the concrete surrounding the reinforcing bar prevented the initiation of the splitting mode of bond failure and the bar managed to develop higher bond stress values compared to the bond values developed in phase 4 beams. CFRP bars in CB20 beam developed around 4.3 MPa average bond strength which is similar to the bond stress values suggested for steel deformed bars by EC2 and BS8110 (4.5 MPa and 4.1 MPa respectively). However, the author believes that the bond value measured in this particular test should not be taken as a reference value for the bond capacity of CFRP bars under beam conditions, because of the reason explained above.

Finally in beam AB28, AFRP bars failed in a similar manner to the bars in the above two beams by developing an average bond value around 3.7 MPa. No signs of splitting cracks were observed in this beam which is also attributed to the confining action of the support at the end of the bar.

## 4.2.2 Phase 4

The instrumental measurements, collected from all the strain gauges used in phase 4 beams, are presented in a graphical form in appendix E.3. In these graphs, the recorded strain values are plotted against the load imposed on each beam.

The summarised experimental results of the beam testing program are presented in table E.1.3 of appendix E.1. Column 5 of the table shows the mode of bond failure of the single bar anchorage which is designed to fail in bond (I), and the final failure mode of the beam (II). All the beams with additional single bar anchorages were designed so that the single anchorage would fail in bond before the ultimate flexure capacity of the beam was achieved. After slippage of the additional bar, the two other main reinforcing bars sustained the external load. The beams failed only when one of the bars or even both of them, broke. The failure was sudden, accompanied by large deformations. In the case of splices, the beams failed with simultaneous bond failure in both splices so, only one stage of failure is reported.

Column 6 shows the maximum longitudinal strain developed in the main reinforcing bars at the ultimate load stage. In the case of splices, column 6 illustrates the maximum strain value developed at the loaded end of spliced bars. Finally, column 7 presents two values of average bond stress: the average bond stress value recorded when the single anchorage bar starts slipping ( $\tau_s$ ) and the maximum average bond stress developed in the anchorage ( $\tau^*$ ). In splices, the bars started slipping simultaneously with the failure of the beam, so only  $\tau^*$  is presented.

In the rest of this section the most significant experimental results relating to the bond behaviour of FRP reinforcing bars in each beam will be presented.

### 4.2.2.1 Beams GB29 and GB30

Beams GB29 and GB30 are examined together since they have very similar reinforcement and instrumentation configurations (see appendix B.1). Both are reinforced with three 13.5 mm GFRP round bars having the same cover to diameter ratio equal to 1.85. They only differ in the length of the single bar anchorage which is 250 mm for GB29 and 300 mm for GB30.

### Mode of bond failure - Crack patterns

In both beams, the single anchorage bar failed in a splitting mode of bond failure. The crack developed at the bottom face of the beam below the single anchorage, as shown in figures 4.26 and 4.27. The crack initially developed at the very end of the bar and as the load increased, the crack extended along the whole length of the anchorage.

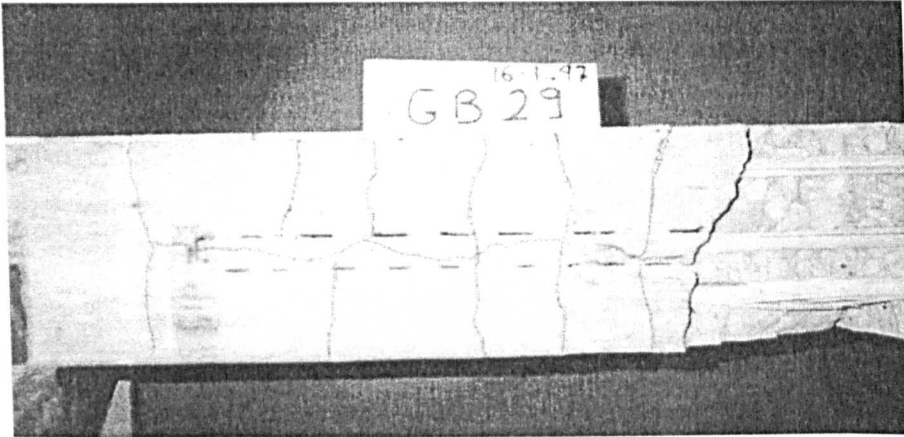


Figure 4.26: Splitting crack pattern in beam GB29

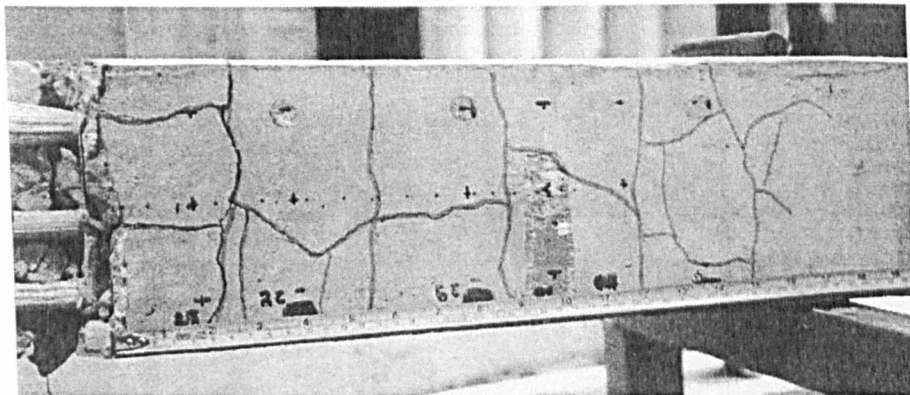
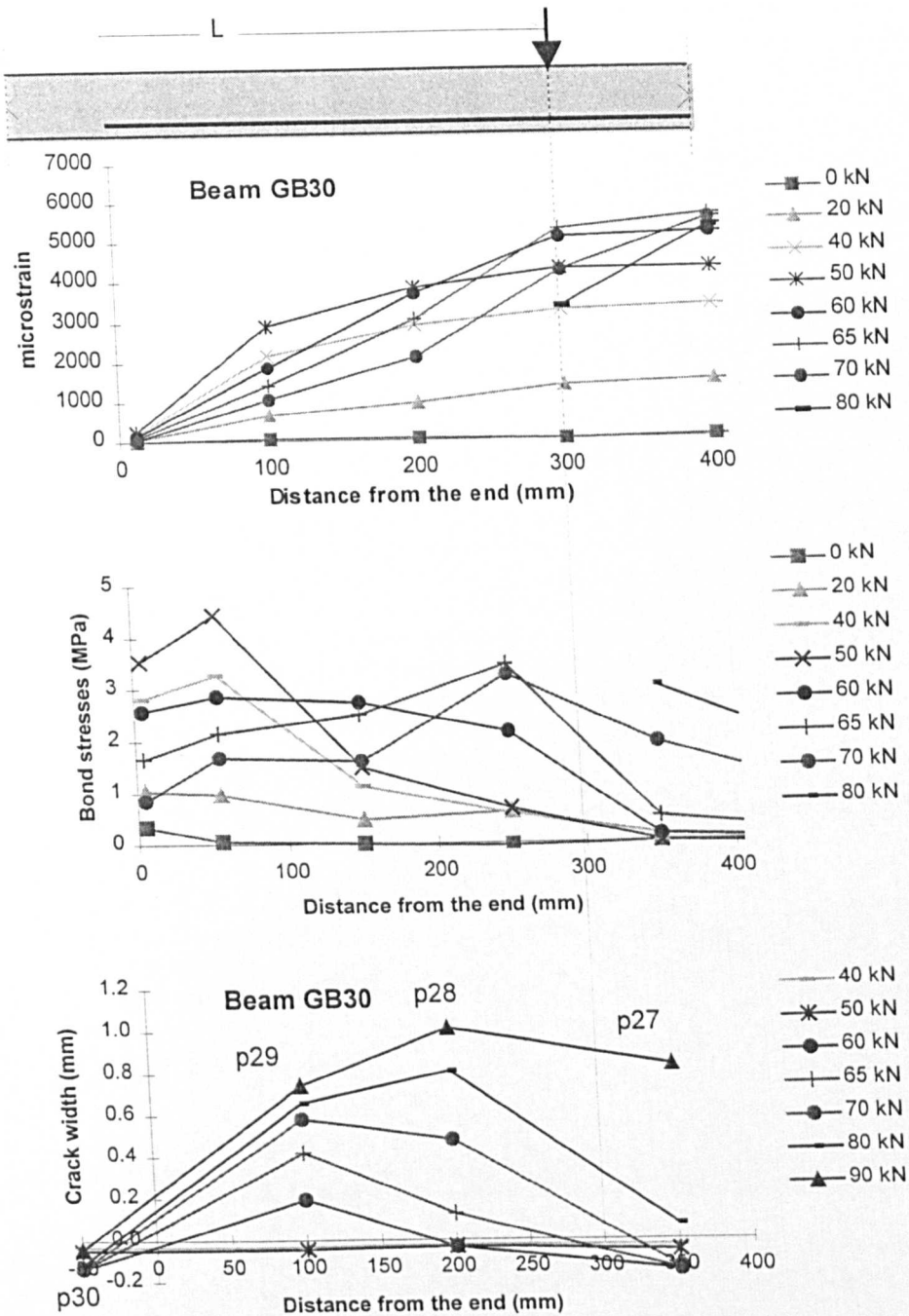


Figure 4.27: Splitting crack pattern in beam GB30

### Strain and bond stress distribution over the anchorage length

A characteristic distribution of normal strains over the single anchorage bar of beam GB30 is shown in figure 4.28, for successive load steps. Similar distribution was also obtained from the strain gauges in beam GB29. The slope of each curve is proportional to the bond stress developed on the bar. The bond stress profiles are shown

along the anchorage length in figure 4.28. It is clear that for low load levels the peak bond stress develops at the end of the bar, up to the load level when the bar starts slipping (around 50 kN) and the first splitting crack initiates under the bar.



Figures 4.28: Strains, bond stresses and crack widths along the anchorage length

When the first splitting crack appears, the peak bond stress migrates from the end of the bar towards the middle of the beam as load increases (see figure 4.28). The reason for this movement can be attributed to the propagation of the splitting cracks

along the reinforcing bar. In order to verify this, specially arranged LVDTs were positioned at the bottom face of the GB30 beam along the length of the middle bar to monitor the widths of the splitting crack during the test (see section 3.2.4.2). The crack widths along the bar are plotted in figure 4.28. It can be easily observed from the above three figures that before the initiation of the splitting crack (load level 50 kN), the maximum bond value is developed at the very end of the bar. With the appearance of the splitting crack at the end of the bar, the peak bond value moves towards the middle of the beam ahead of the crack development.

Two additional remarks emerging from the observation of figure 4.28 have to be made. Firstly, the non-zero values of strains and bond stresses at zero load level can be explained from the fact that these values were recorded at the final load cycle of the beam. The second remark is associated with the movement of peak bond stress value along the anchorage length. In beams tested in phases 1-3, the peak bond value was reported to migrate from the loaded end towards the free end of the anchorage, as the load increased (see section 4.2.1.2). Here, it is not possible to observe this movement since the peak bond value always lies at the end of the bar. This is due to the location of the anchorage length with respect to the flexurally cracked zone of the beam. In this case, the whole anchorage length lies in the cracked region of the beam, where the development of flexural cracks influence the propagation of bond strength along the length of the bar. This influence will be explained and discussed in more detail in chapter 6 of this study. However, for larger anchorage lengths, for example in beam CB37, where the anchorage length extends nearly over the whole shear span of the beam, this immigration of the peak bond stress can be observed more easily, as shown in figure 4.57.

#### Average bond strength values developed

In this section, two values of average bond stress developed by the single bar anchorage will be examined. The first is the average bond value when the single anchorage started slipping ( $\tau_{sl}$ ) and the second is the maximum average bond value ( $\tau^*$ ) recorded during the test.

The problem with measuring  $\tau_{sl}$  is the estimation of the load level at which the bar started slipping. Since no direct access to the end of the bar was possible, the estimation had to be made by examining the strain measurements from the strain gauges

attached on the bar. For this reason, the author used the measurements of the strain gauge attached at the very end of the bar (strain gauge c63 for GB29 and GB30, see appendix B.1). The load level when c63 recorded the maximum local strain value was assumed to be the load just before the bar started slipping.

The value of  $\tau^*$  was much easier to be measured since the maximum strain value of the strain gauge attached at the loaded end of the bar (c69 in the case of GB29 and GB30 beams) was used in the calculation of  $\tau^*$  over the whole embedment length.

The single bar anchorage in beam GB29 started slipping around a load level of 35 kN by developing  $\tau_{sl}$  equal to 2.0 MPa, whereas a value for  $\tau^*$  equal to 3.2 MPa was recorded at the load of 65 kN. For GB30, the bond values where:  $\tau_{sl} = 2.2$  MPa at 50 kN and  $\tau^* = 2.67$  MPa at 66 kN. Figure 4.29 shows the development of  $\tau^*$  during the test for beams GB29 and GB30.

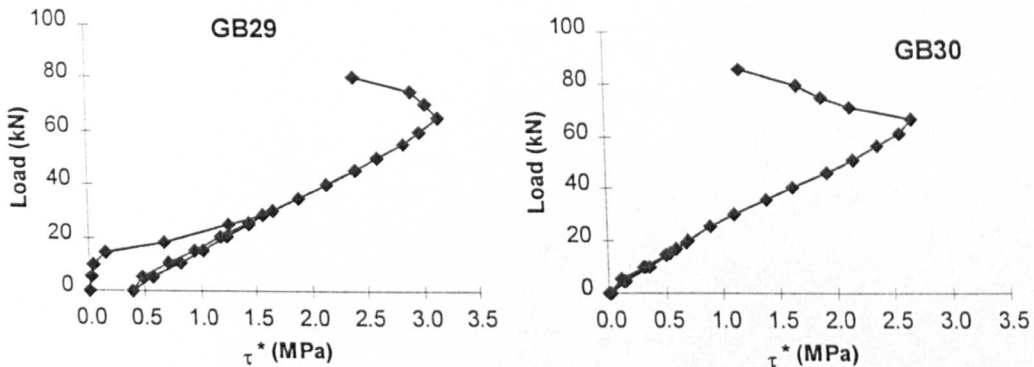


Figure 4.29: Maximum average bond stress Vs load in beams GB29 and GB30

#### Strains on transverse reinforcement

The strains recorded on selected transverse links in beams GB29 and GB30 are presented in figure 4.30. The strain gauges were attached on the vertical legs of the links as shown in appendix B.1, where the location of these gauges is shown with respect to the reinforcement arrangement. Strain gauges were used to monitor any contribution of the links to the bond resistance of the reinforcing bar during testing. However, since splitting cracks developed at the bottom side of the beams, the author did not expect any noticeable contribution from the links lying in the anchorage zone, to the bond strength of the bar. Nevertheless, figure 4.30 shows that in both beams, the links reacted to the formation of the splitting cracks. Strain gauges c75 and c77 were lying in the anchorage

length zone (as seen in appendix B.1) whereas c79 was outside that. The initiation of the splitting crack was monitored by strain gauge c75 in both cases, just after loads 40 kN and 50 kN for GB29 and GB30 respectively, when a rapid increase in the strain value of the vertical leg of the link is noticed.

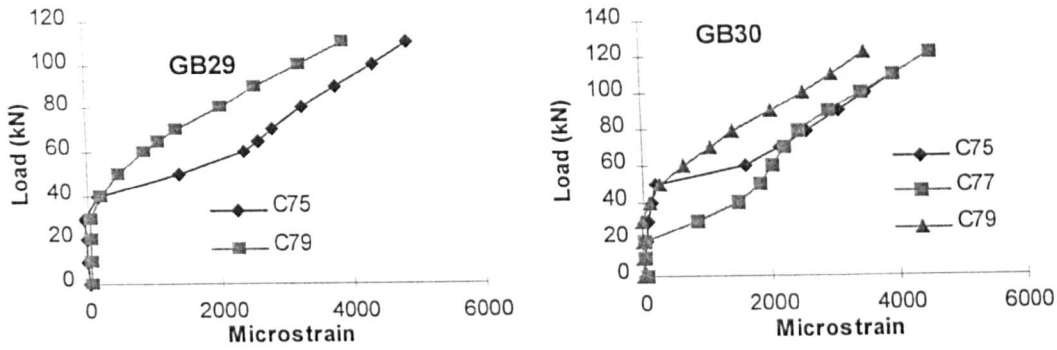


Figure 4.30: Strains in the vertical legs of the links in beams GB29, GB30

It is also quite important to calculate this increase in the link's strain when the bar is about to reach its maximum bond capacity. This happens around the load level of 65kN for both beams. From the graphs above, it can be deduced that an additional strain of 1400 and 1200 micro is recorded in the link (c75) of beam GB29 and GB30 respectively, which corresponds to 66 and 56 MPa additional stress in the vertical leg of the link.

#### 4.2.2.2 Beam GB31

Beam GB31 was reinforced with four 13.5 mm spliced GFRP bars having bottom and side cover to diameter ratios 1.85 and 1.5 respectively. The spliced length was 300 mm in order to facilitate comparisons with the single bar anchorage in beam GB30.

##### Mode of bond failure - Crack patterns

The spliced bars failed in a splitting mode of bond failure, as it was expected. The cracks developed at the bottom and the side face of the beam at the spliced region as shown in figures 4.31 and 4.32. The crack pattern was similar to the face and side split pattern shown in figure 2.13.

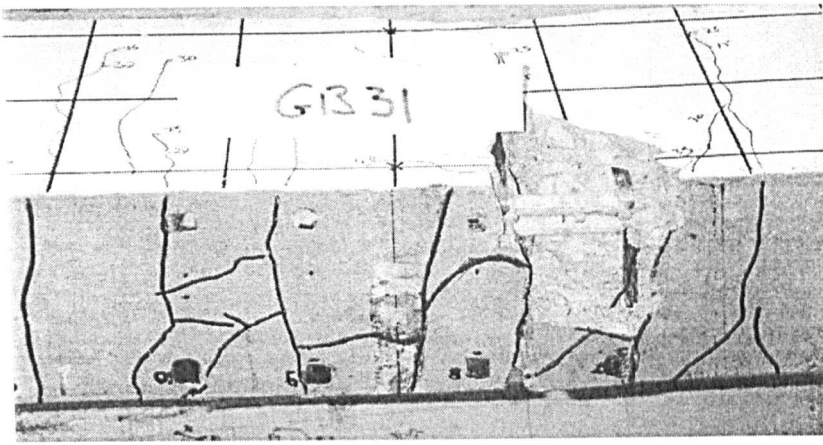


Figure 4.31: Bottom crack pattern of beam GB31

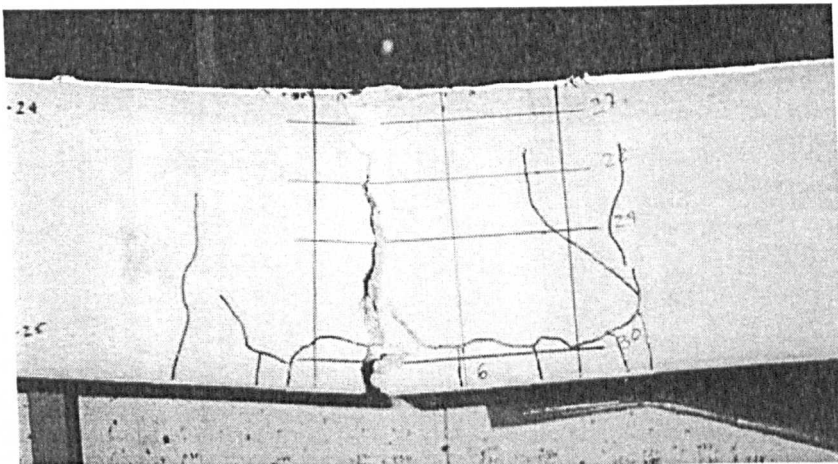


Figure 4.32: Side crack pattern of beam GB31

Cracks initially developed at the bottom of the beam, at the end of the spliced length, but they did not extend immediately along the whole length. On the contrary, horizontal cracks at the side of the beam appeared just before the maximum recorded load and extended along the spliced region only at failure.

In order to monitor the initiation and development of cracks at the bottom side of the beam during the test, specially arranged LVDTs were positioned along the spliced length (see section 3.2.4.2). In figure 4.33, the crack widths are plotted along the spliced length. It can be seen that although the crack initiated at the end of the spliced length at a load level of 25 kN, it did not spread over the entire length before the ultimate failure load.



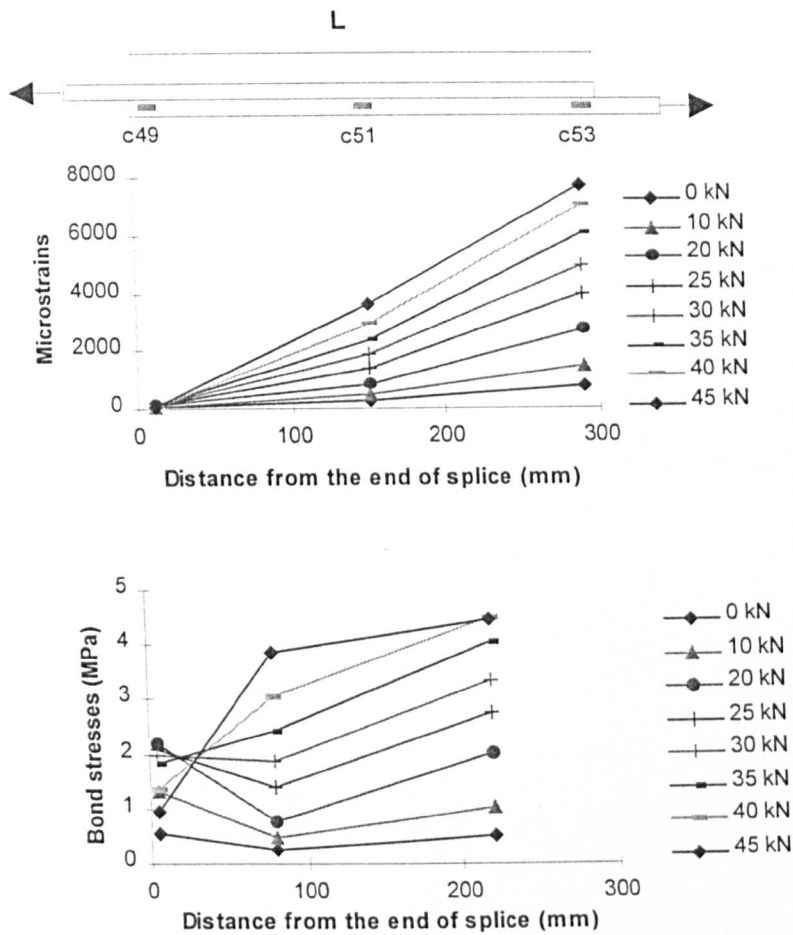


Figure 4.34: Strain and bond stress distribution over a spliced reinforcing bar in GB31

#### Average bond strength values developed

The maximum average bond strength ( $\tau^*$ ) developed in the case of spliced bars in beam GB31 was much greater than in the single bar anchorage in beam GB30. In order to determine  $\tau^*$ , the strain values of the gauges attached at the loaded end of each pair of spliced bars were considered. Hence, in the case of GB31, the average value of the maximum strain measurements of strain gauges c53 and c43 were considered (from the other pair of bars, strain gauge c69 was damaged and no readings were available). The value of  $\tau^*$  calculated over the spliced length was 3.8 MPa at ultimate load level, which was much higher than the value of 2.7 MPa developed in the single anchorage in beam GB30. The maximum average bond strength ( $\tau^*$ ) developed in one of the spliced bars during the test, is shown in figure 4.35.

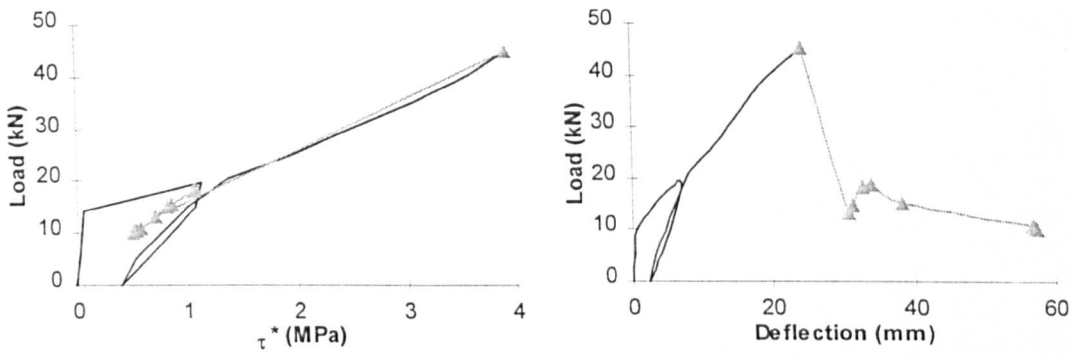


Figure 4.35: Maximum average bond strength developed in one spliced bar and the midspan deflection of beam GB31 vs. Load

It is quite interesting to note in figure 4.35 that even after the maximum recorded load, the spliced bars resisted the ultimate beam collapse. The triangular points in the graph of  $\tau^*$  vs. load represent the bond values recorded after the maximum load which allowed the beam to resist post-ultimate external load. These residual bond stresses are believed to be related to the confining action of the shear links as it will be explained in the following section.

#### Strains in transverse reinforcement

The strains recorded in selected transverse links in beam GB31 are presented in figure 4.36. The strain gauges were attached on the vertical legs of the links in the spliced region, as shown in appendix B.2. Strain gauges were used to monitor any contribution of the links to the bond resistance of the spliced bar during testing.

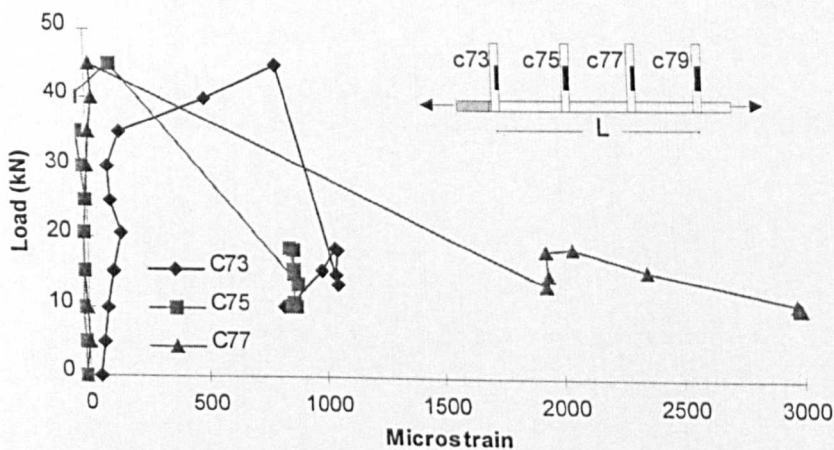


Figure 4.36: Strains recorded in the legs of the links in the spliced region

From figure 4.36, it can be deduced that only the link with the strain gauge c73 contributed to the bond resistance of spliced bars before the beam reaches its maximum load capacity. Its contribution appeared to be very small since the stress recorded in the link was only 38 MPa. However, immediately after the maximum load and the primary failure of the beam, all the links in the spliced region were stressed. This added to the bond resistance of spliced bars that managed to develop average bond values in the region of 0.5 to 1 MPa, as shown in figure 4.35.

#### 4.2.2.3 Beam CB32

Beam CB32 is reinforced with three 8 mm CFRP bars as shown in appendix B.2. The bottom cover to diameter ratio for the single bar anchorage is 3.1 and the anchorage length is 38 times the bar diameter (300 mm) which are both significantly higher than the ones examined in the previously reported beams.

##### Mode of bond failure - Crack patterns

The single anchorage bar failed in a splitting mode of bond failure. The crack developed clearly at the bottom face of the beam below the single anchorage, as shown in figure 4.37. The crack initially developed at the very end of the bar and as the load increased, the crack extended along the whole length of the anchorage.

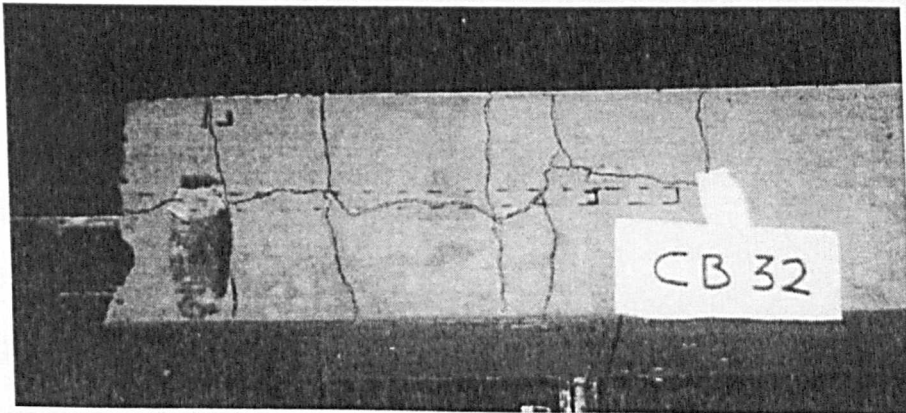


Figure 4.37: Bottom face of beam CB32

## Strain and bond stress distribution over the anchorage length

The strain and bond stress profiles over the single bar anchorage are presented in figure 4.38. For low load levels, the peak bond stress develops close to the free end of the anchorage length. It is noticeable the large values of local bond stress ( $>14$  MPa) developed at the end of the bar before the bar starts slipping. However, when the splitting crack initiates at the end of the anchorage (around load level 45 kN), the peak bond stress moves towards the centre of the beam.

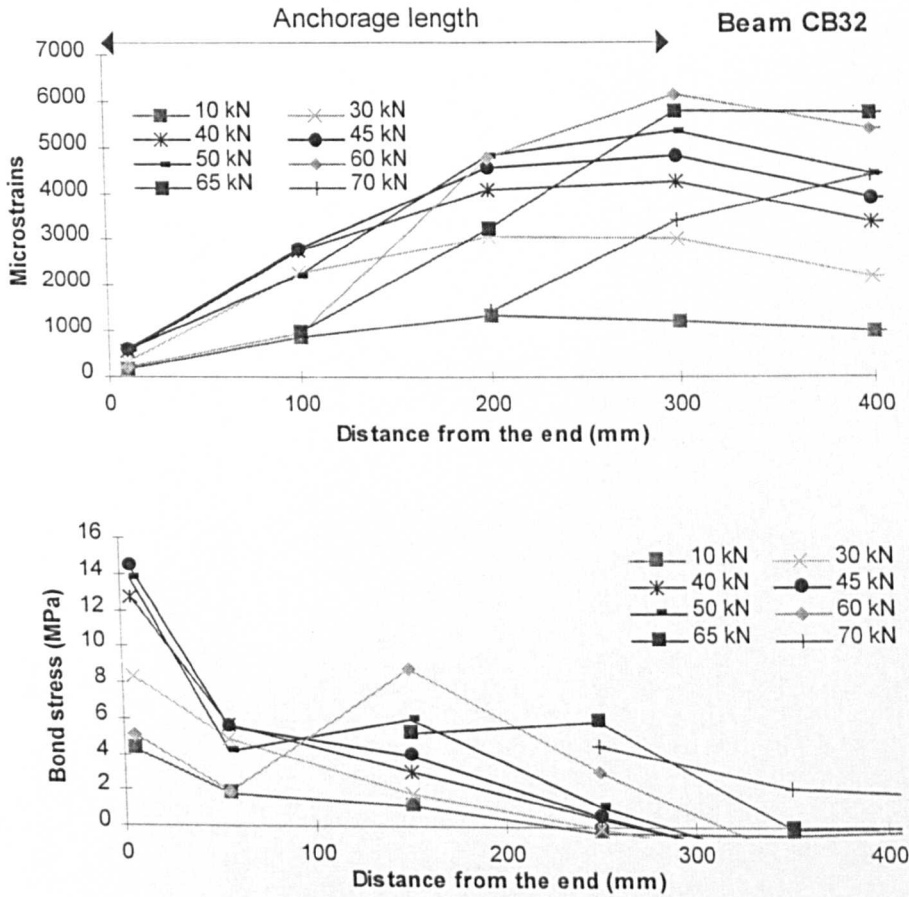


Figure 4.38: Strains and bond stresses profiles over the anchorage length in CB32

### Average bond strength values developed

CFRP single bar anchorage developed significantly higher average bond strength values comparable to the bond values developed in GFRP beams. This is assumed to be due to the larger cover to diameter ratio used in this beam but also due to the better bond behaviour of CFRP bars to concrete (see also section 4.2.2.3). The CFRP single

anchorage bar developed:  $\tau_{sl} = 3.9$  MPa at 48 kN load level and  $\tau^* = 4.6$  MPa at load level of 60 kN. The development of  $\tau^*$  during testing is presented in figure 4.39.

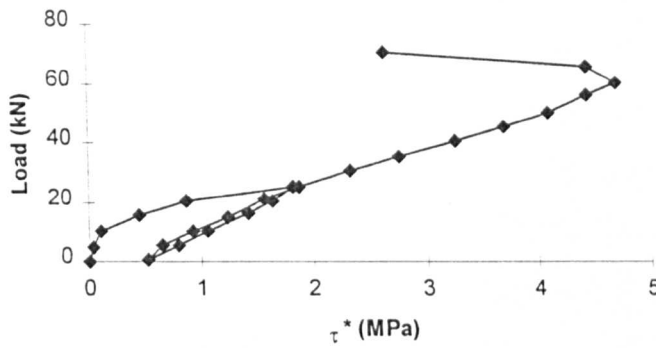


Figure 4.39: Maximum average bond strength of single bar anchorage during testing

### Strains on transverse reinforcement

The strains recorded on the vertical legs of selected links in beam CB32 are presented in figure 4.40. The exact location of these links is shown in appendix B.2.

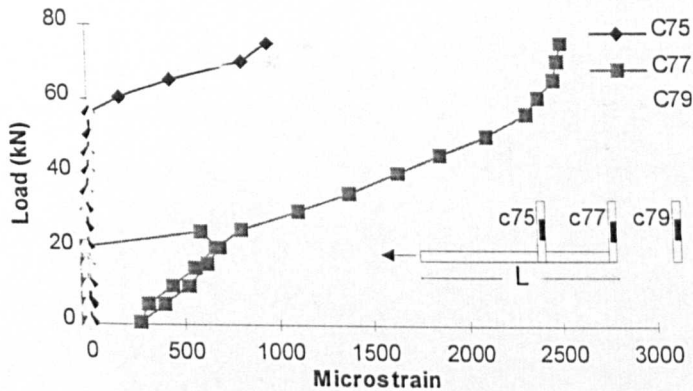


Figure 4.40: Strains in selected links of beam CB32

It is clear from the figure that none of the links appears to react to the formation of the splitting crack at the 48 kN load level, contrary to what was reported for beams GB29 and GB30. This can be explained by the fact that the splitting crack was formed at the bottom side of the beam whereas the strain gauge was attached on the vertical leg of the link. For the above reason, the contribution of the links to the bond capacity of CFRP bar can not be estimated from these measurements.

#### 4.2.2.4 Beams CB33 and GB36

Beams CB33 and GB36 are examined together since they have very similar reinforcement and instrumentation configurations (see appendices B.3 and B.4). They both have a 300 mm spliced length and similar cover to diameter ratios (side cover/diameter  $\cong 2.5$  and bottom cover/diameter  $\cong 3$ ). They are reinforced with 8 mm CFRP bars and 8.5 mm GFRP bars respectively. The main objective of preparing those beams was to compare the bond behaviour of CFRP and GFRP spliced bars under similar experimental conditions. However, the concrete strength of the beams differed significantly (although it was ordered to be the same) which has to be considered in the comparisons of the results. The concrete compressive strength in CB33 beam was 35 MPa whereas in GB36 was around 45 MPa.

##### Mode of bond failure - Crack patterns

In both beams, the spliced bars failed in a splitting mode of failure. In beam CB33, a horizontal splitting crack was developed passing through the axis of the spliced bars as seen in figure 4.41. No signs of cracks at the bottom face of the beam, below the bars, were found.

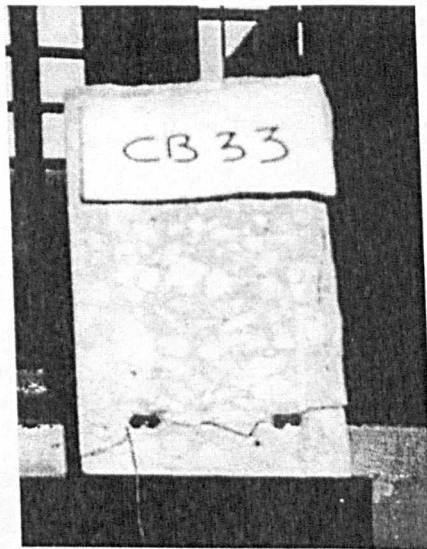


Figure 4.41: Crack pattern in Beam CB33

On the contrary, the spliced bars in beam GB36 failed in a face and side split pattern (see figure 2.13). Cracks developed at the splice region both at the side and bottom face of the beam, as seen in figure 4.42. However, these cracks were initiated only at the last loading cycle of the beam and spread immediately over the whole splice length, at failure load.

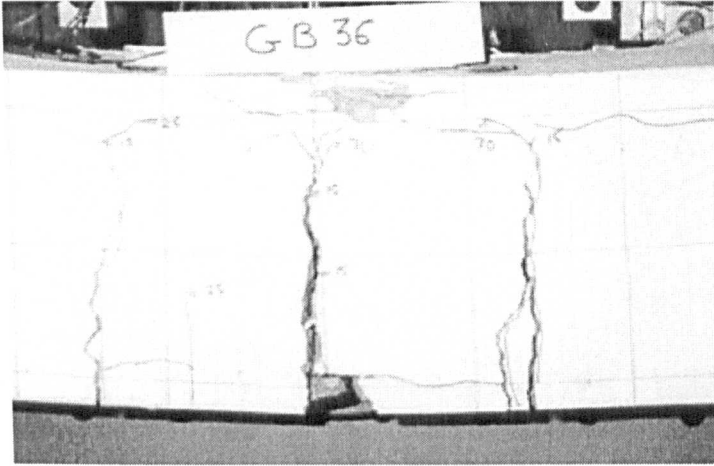


Figure 4.42: Crack pattern in beam GB36

#### Strain and bond stress distribution over the anchorage length

The characteristic distribution of normal strains over a spliced bar in beam CB33, is shown in figure 4.43 at selected load levels. Similar distribution was obtained from a spliced bar in beam GB36, as seen in figure 4.44. The calculated bond stress profiles are shown along the spliced length in the same figures. Unlike the profiles of bond stresses reported in a previous section for beam GB31, the peak bond stress in beams CB33 and GB36 develops close to the loaded end of spliced bars. As the load increases, the peak bond stress seems to migrate towards the free end of spliced bars which is completely opposite to what was reported for beam GB31. This difference is believed to be related to the larger size of splice length in beams CB33 and GB36 compared to beam GB31 (as multiples of bar diameter) and to the location of the strain gauges with respect to the flexural cracks, as will be explained in more detail in section 6.3.6.1.

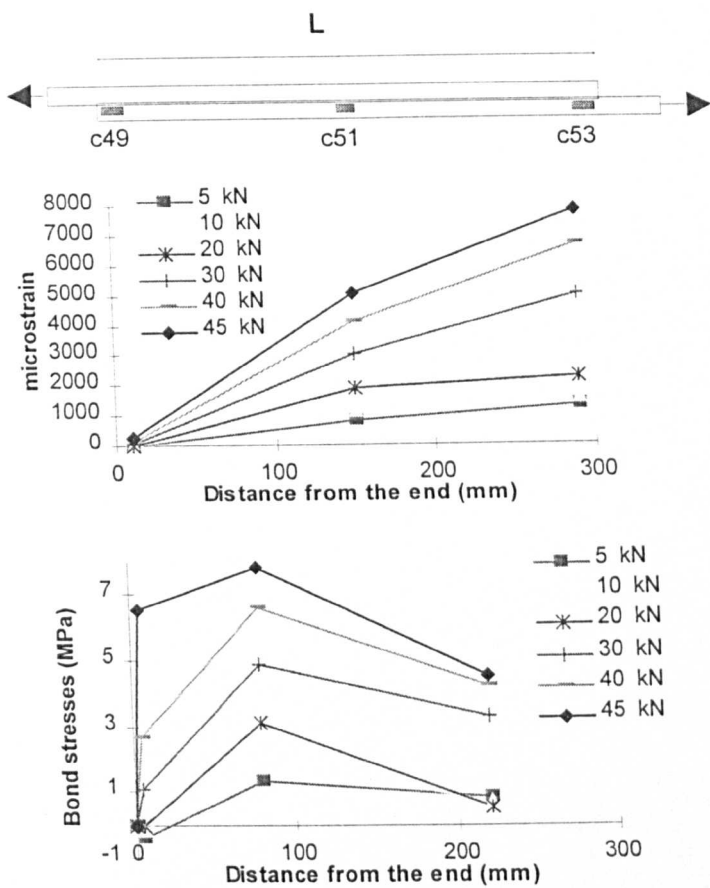


Figure 4.43: Strains and bond stresses profiles over a typical spliced bar in CB33

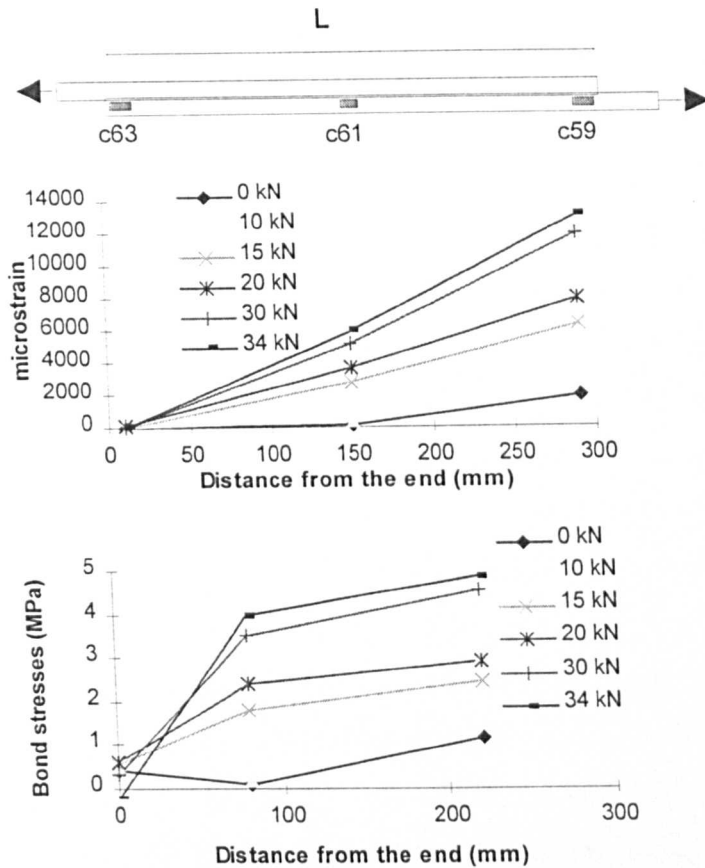


Figure 4.44: Strains and bond stresses profiles over a typical spliced bar in GB36

Average bond strength values developed

The maximum average bond strength ( $\tau^*$ ) developed in the case of spliced bars in beam CB33 was much higher than the value of  $\tau^*$  developed in beam GB36 despite the difference in concrete strength. In order to determine  $\tau^*$ , the strain values of gauges attached at the loaded end of each pair of spliced bars were considered, in a similar manner as described for beam GB31. The value of  $\tau^*$  calculated for CFRP bars over the spliced length was 5.7 MPa at ultimate load level, which was much higher than the value of 4.1 MPa developed in the spliced GFRP bars, in beam GB36. This is a very important outcome since GFRP bars appear to develop significantly less bond strength than CFRP bars in spliced conditions. In the discussion chapter, an attempt will be made to explain this difference which is believed to be related to the different deformability of FRP bars in the axial direction. The development of

maximum average bond strength ( $\tau^*$ ) versus the load over a typical bar in beams CB33 and GB36, is shown in figure 4.45.

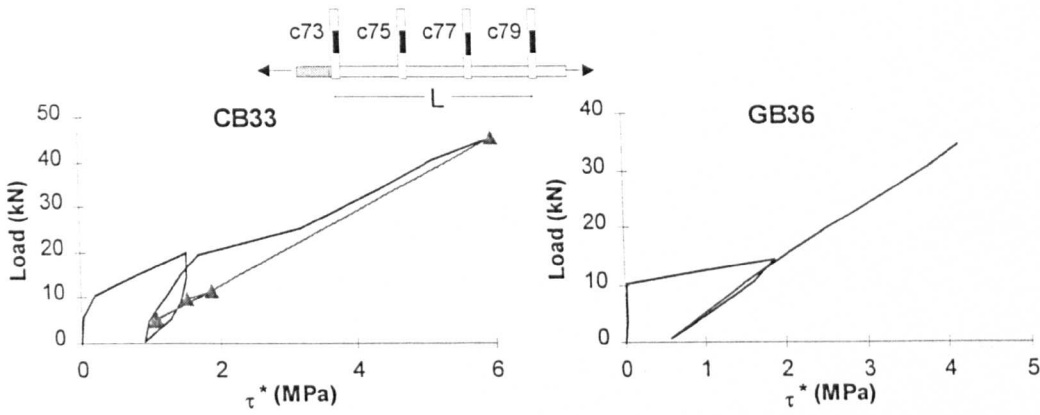


Figure 4.45: Maximum average bond stress vs. Load in beams CB33 and GB36

The spliced bars also showed a significant post-ultimate resistance in both beams. In figure 4.45, this behaviour is shown only for beam CB33 (triangular points) where the bond developed was around 1 - 2 MPa. In beam GB36 the particular strain gauge failed just after the maximum load, so no strain measurements were available. However, in figure 4.46 the plot of the midspan deflection of the beam versus the imposed load shows clearly the post-ultimate behaviour of the beams.

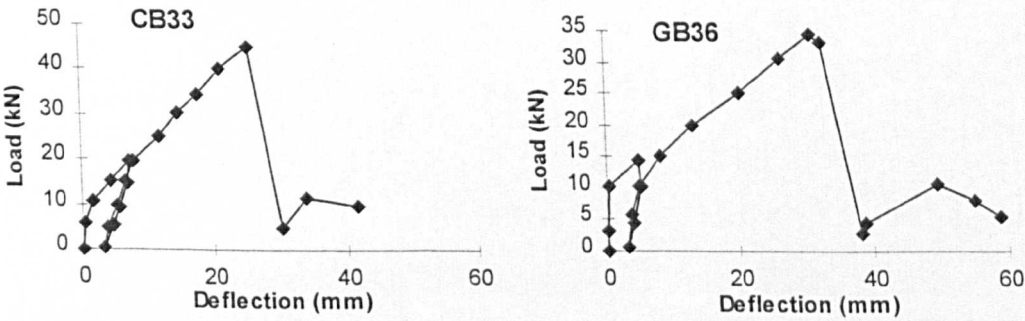


Figure 4.46: Midspan deflection versus the load in beams CB33 and GB36

Strains on transverse reinforcement

The strains recorded on the vertical legs of the links located in the spliced region are presented in figure 4.47. Strain gauges were used to monitor any contribution of the links to the bond resistance of spliced bar during testing.

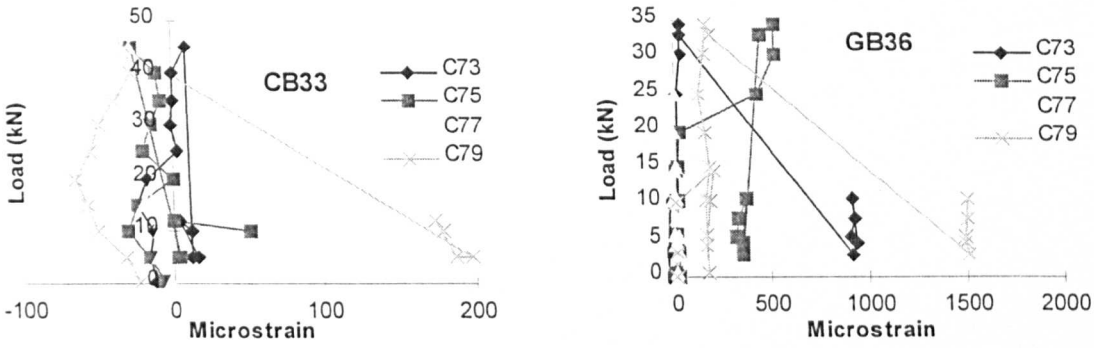


Figure 4.47: Strain values in the vertical legs of links in the spliced region

It is obvious from the figure that the links in beam CB33 did not resist the splitting failure of the spliced bars. Only link c79 appears to react after the maximum load capacity of the beam, but the stress developed in its vertical leg was insignificant (<10 MPa). On the contrary, two of the links in beam GB36 (c75 and c79) appear to contribute slightly to the bond resistance of the bars before the beam reached its maximum load capacity. After the primary failure of the beam, all the links, except link c77, resisted the ultimate failure of the beam and contributed to the bond resistance of the spliced bars.

#### 4.2.2.5 Beam GB35

The single bar anchorage in beam GB35 was an 8.5 mm GFRP bar with a 300 mm anchorage length. The bar was placed at the edge of the cross section of the beam (see appendix B.4) in order to compare its bond behaviour with that of single anchorage bars positioned in the middle of the cross section (e.g. anchorage bar in beam GB34). The bottom and side cover to diameter ratios for the single anchorage were 3 and 2.4, respectively. Strain gauges were attached in both vertical and horizontal legs of the links in the anchorage zone in order to monitor their contribution to the bond resistance of the single bar anchorage.

### Mode of bond failure - Crack patterns

The single bar anchorage failed in a splitting mode of failure. The splitting crack developed at the side face of the beam along the single anchorage, as seen in figure 4.48. The crack initially developed at the region of the anchorage length but, as the load increased, it extended along the whole length of the bar.

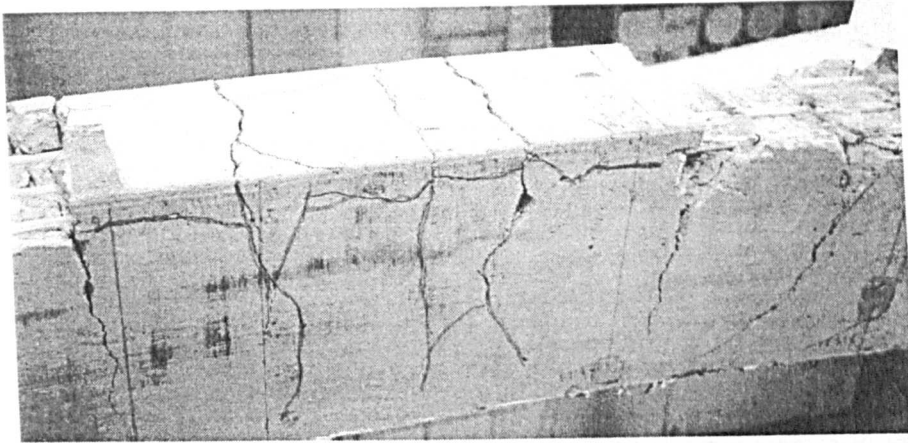


Figure 4.48: Crack pattern of beam GB35

### Strain and bond stress distribution over the anchorage bar

The strain and bond stress profiles over the single bar anchorage are presented in figure 4.49. For low load levels, the peak bond stress develops close to the free end of the anchorage length. When the bar starts slipping (around load 44 kN), the peak bond stress migrates towards the midspan of the beam. The massive fluctuations in the bond stress values along the anchorage bar, shown in figure 4.49, are believed to be related to the development of flexural cracks in the beam. Hence, the relative position of the strain gauges to the flexural cracks influences significantly the recorded strain values as will be discussed in the following sections (beams GB34 and CB37).

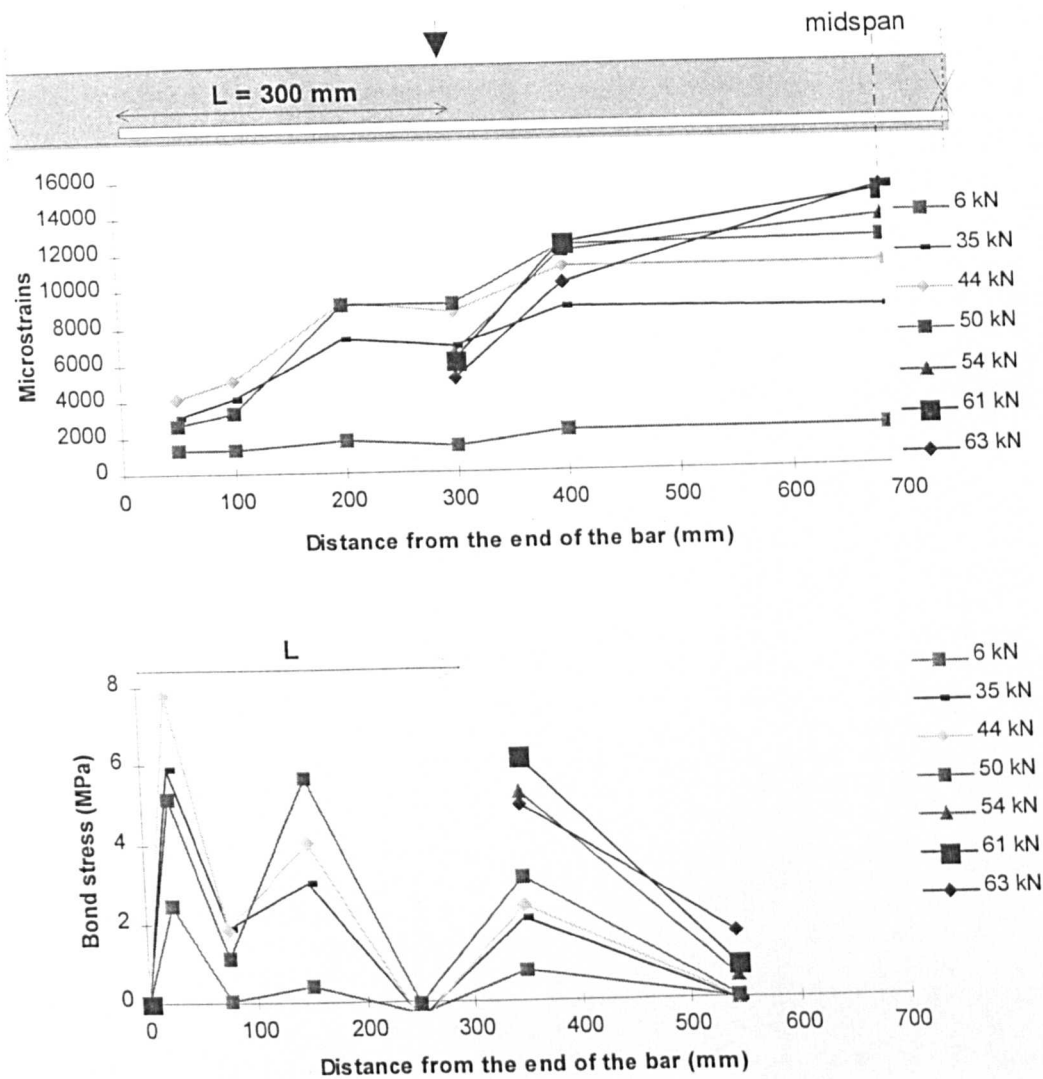


Figure 4.49: Strains and bond stress distribution over the single anchorage bar

#### Average bond strength values developed

The exact load level when the bar started slipping was not possible to be monitored in this test, since no strain gauge was attached at the very end of the anchorage bar. However, by considering the measurements of the last strain gauge on the anchorage bar (c49), it can be assumed that the bar started slipping before the 44 kN load level. At that load, the bar developed  $\tau_{sl} = 2.8$  MPa.

The maximum average bond strength ( $\tau^*$ ) developed was also difficult to be estimated since the strain gauge attached at the loaded end of the anchorage (c55) did not record reliable measurements. For this reason, it was decided to calculate  $\tau^*$  by using the measurements of strain gauge c57 which was attached 400 mm away from

the free end of the anchorage. The value of  $\tau^*$  calculated, was 3 MPa at 50 kN load level.

Strain on the transverse reinforcement

The strains recorded on the links located close to the anchorage length are presented in figure 4.50. It can be seen that the strain gauges c69, c73 and c75 have recorded the development of splitting crack at loads 45 to 50 kN. The contribution of the links to the bond resistance of the anchorage bar can be also estimated from the figure. For example, the vertical leg of link No.2 applied a confining pressure of 45 MPa to the anchorage, at the load level when  $\tau^*$  was developed (load 50 kN).

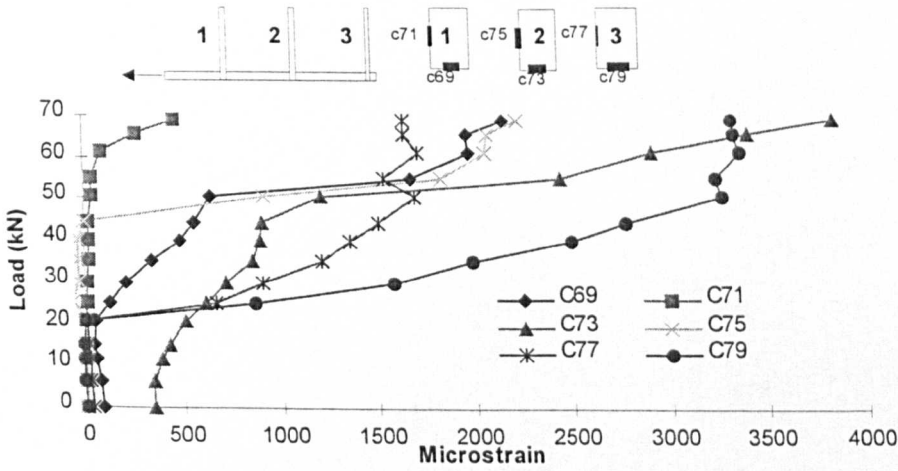


Figure 4.50: Strain values recorded in links of beam GB35

**4.2.2.6 Beam GB34**

Beam GB34 was reinforced with two main 8.5 mm GFRP reinforcing bars and an additional single anchorage GFRP bar of the same diameter having an anchorage length equal to 370 mm (see appendix B.3). The single anchorage was positioned in the middle of the cross section and the bottom cover to diameter ratio was around 3. A special arrangement of strain gauges was adopted on the single anchorage to examine the distribution of bond stresses between consecutive cracks during loading (see section 3.2.4.1).

### Mode of bond failure - Crack patterns

The single bar anchorage failed in a splitting mode of failure. The splitting crack developed at the bottom face of the beam along the single anchorage, as seen in figure 4.51. The crack initially developed under the free end of the bar but as the load increased, it extended along the whole anchorage length.

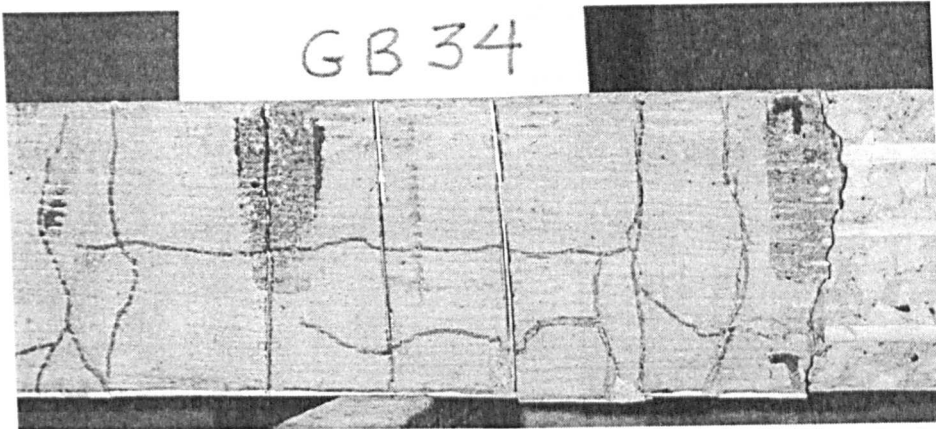


Figure 4.51: Splitting crack developed under the single bar anchorage in beam GB34

However, apart from the expected bond failure of the single anchorage bar, one of the main reinforcing bars failed in bond at the maximum load capacity of the beam. Due to human error during the casting of the beam, the end parts of the main reinforcing bars were not covered by concrete (figure 4.52). This resulted to a reduced anchorage length for the main reinforcing bars (reduction of anchorage length  $\cong$  100 mm). As a consequence, one of the two main bars failed in a splitting mode of bond failure by developing the splitting crack at the bottom face of the beam, as shown in figure 4.52.

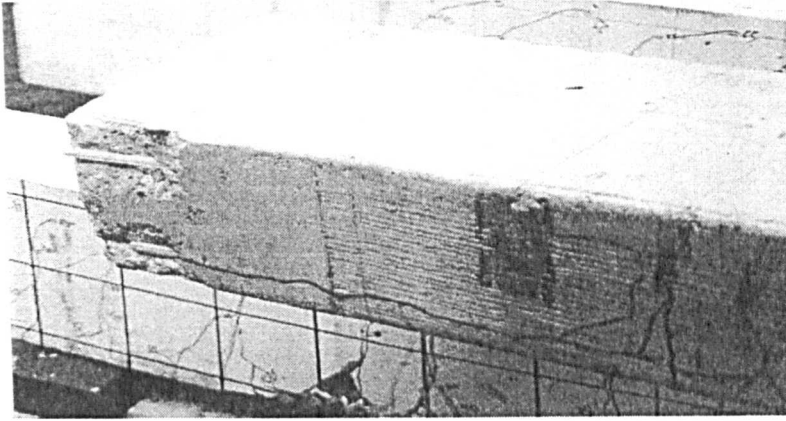


Figure 4.52: Splitting bond failure of one of the main reinforcing bars in beam GB34

#### Strain and bond stress distribution between cracks

Figure 4.53 shows the strain and bond stress distribution on the single anchorage bar between successive cracks of beam GB34. It is quite interesting to observe that the location of strain gauges relative to the flexural cracks influences the recorded strain measurements. A strain gauge located close to a crack indicates, in general, a higher value than a strain gauge positioned in the middle of the distance between successive cracks. This difference is more obvious at higher load levels. As a result, the respective bond stress distribution between consecutive cracks includes both positive and negative values, as shown in figure 4.53.

The high values of bond adjacent to flexural cracks imply that local bond failure is likely, or even necessary, due to the large demand imposed by the large difference in cross-sectional properties.

The average bond strength developed between the cracks is proportional to the area enclosed by the curve. It is clear that this area includes both positive and negative regions with an overall average being positive.

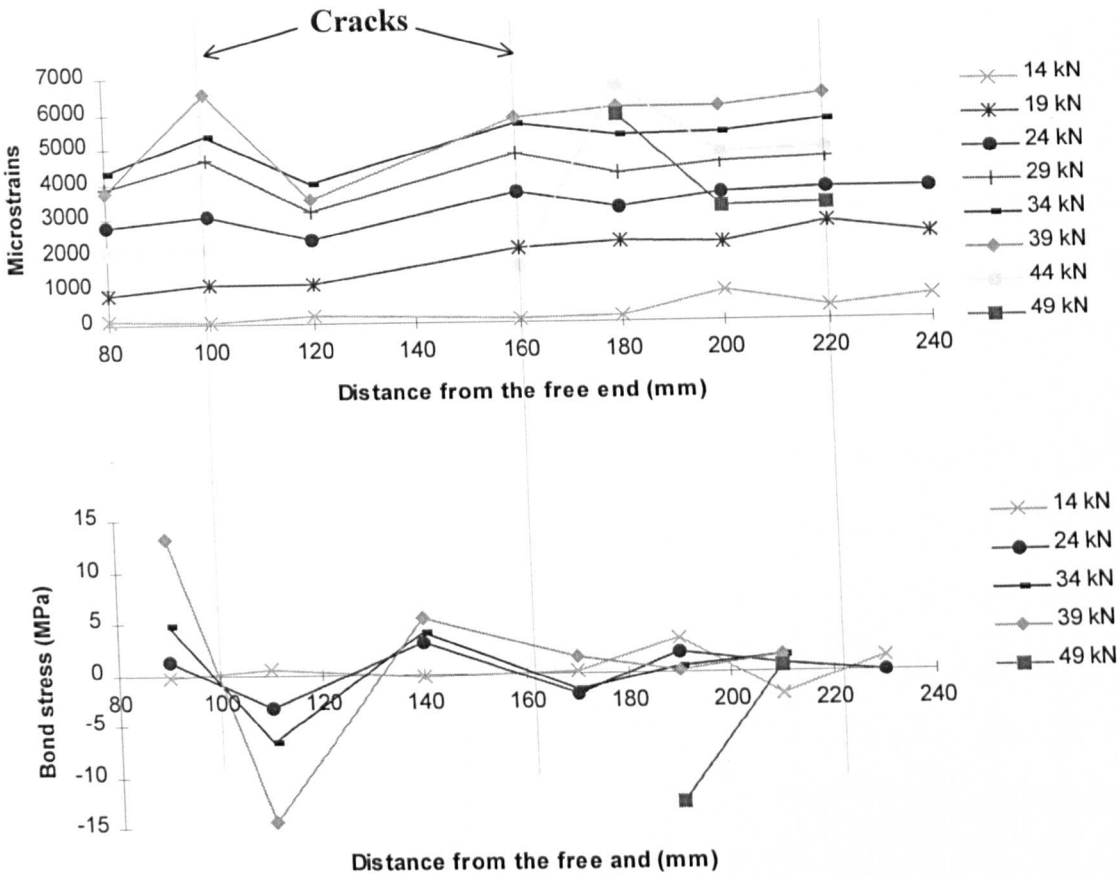


Figure 4.53: Strain and bond stress distribution between successive cracks

#### Average bond strength values developed

The single bar anchorage is assumed to start slipping at around the 38 kN load level, by considering the measurements of strain gauge c47. At this level, the  $\tau_{sl}$  was calculated to be around 2.6 MPa (this value includes the correction factor of 1.08 reported in section 3.2.7). The maximum average bond stress value ( $\tau^*$ ) was calculated from the readings of strain gauge c67 and it was found to be 3.2 MPa at 50kN load level. This value of  $\tau^*$  can be compared with the respective value taken from beam GB35 presented previously (having the anchorage bar at the corner of the cross section). By comparing the two values, it can be concluded that there is no significant difference in the values of  $\tau^*$  although the cover to diameter ratio is different in each case. This can be attributed to the additional confining pressure applied to the bar by the vertical legs of the shear links in the case of beam GB35.

The second bond splitting failure occurred in one of the main reinforcing bars of beam GB34. The value of  $\tau^*$  recorded was not possible to be measured accurately since the strain gauges (c45, c73) attached at the loaded end of the main bars, have failed before the bond failure of the bar. However, by considering the similar loading behaviour of beams GB35 and GB34, after the bond failure of single anchorage bars in each case, it is believed that the main bars in beam GB34 were very close to their failure point just before the ultimate failure of the beam. So, their maximum strains are expected to be about 21500 microstrain, similar to the maximum strain values reported in the main bars of beam GB35. For this strain value,  $\tau^*$  is calculated to be around 2.7 MPa.

### Strain on transverse reinforcement

The strains recorded on the vertical legs of selected links of beam GB34 are presented in figure 4.54. These links were positioned at the end of the anchorage length as shown in appendix B.3. Figure 4.54 shows that the links c77 and c79 reacted to the formation of the splitting crack at a load of 40 kN by a rapid increase in the recorded strain values between loads 40 and 45 kN.

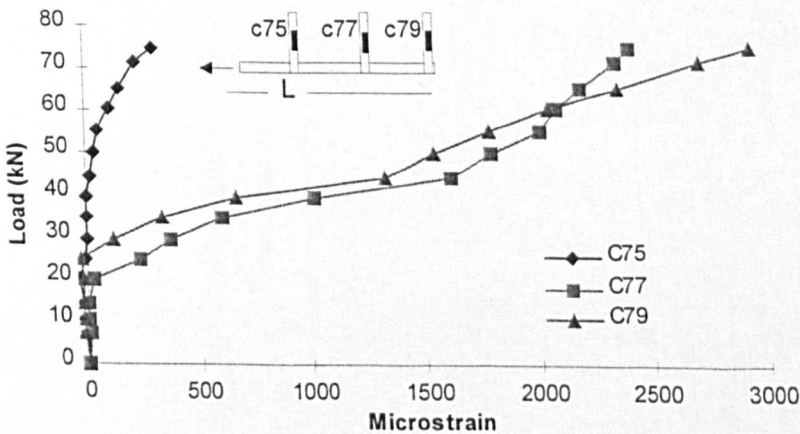


Figure 4.54: Strain values in shear links of beam GB34

#### 4.2.2.7 Beam CB37

Beam CB37 was reinforced with three 8 mm CFRP bars, one of which was a single anchorage bar having a 580 mm anchorage length. The bottom cover to diameter ratio of the single anchorage was around 3.1. A special arrangement of strain gauges was also adopted on the bar, in order to examine the distribution of bond stresses between consecutive cracks (see section 3.2.4.1).

##### Mode of bond failure - Crack patterns

The single bar anchorage failed in a splitting mode of failure. As expected, the splitting crack developed at the bottom face of the beam along the single anchorage, as seen in figure 4.55. The crack initially developed under the free end of the bar but as the load increased, it extended along the whole anchorage length, similar to the failure of single anchorages observed in previously examined beams.

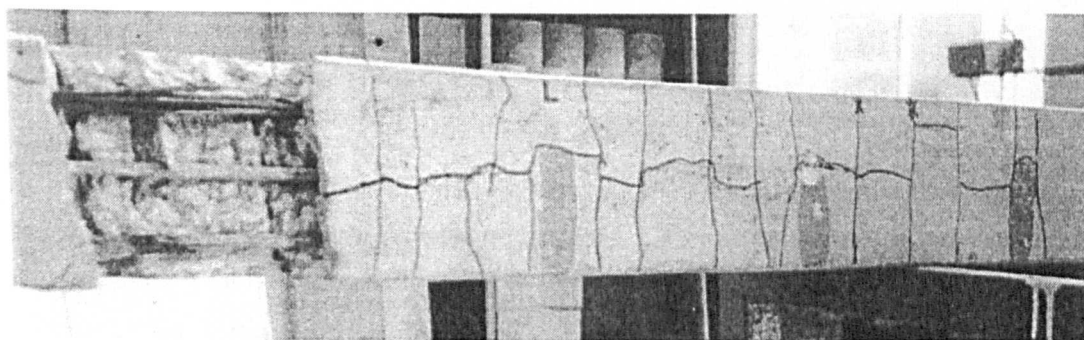


Figure 4.55: Bond failure crack pattern in beam CB37

##### Strain and bond stress distribution between cracks

The strain and bond stress distribution on the single anchorage bar between successive cracks of beam CB37 is shown in figure 4.56. Similar to beam GB34, the location of strain gauges relative to the flexural cracks appears to influence the recorded strain measurements. Strain gauges close to cracks develop higher values than gauges located in the midspan of cracks. As a result, the respective bond stress

distribution between consecutive cracks includes both positive and negative values, as shown in figure 4.56.

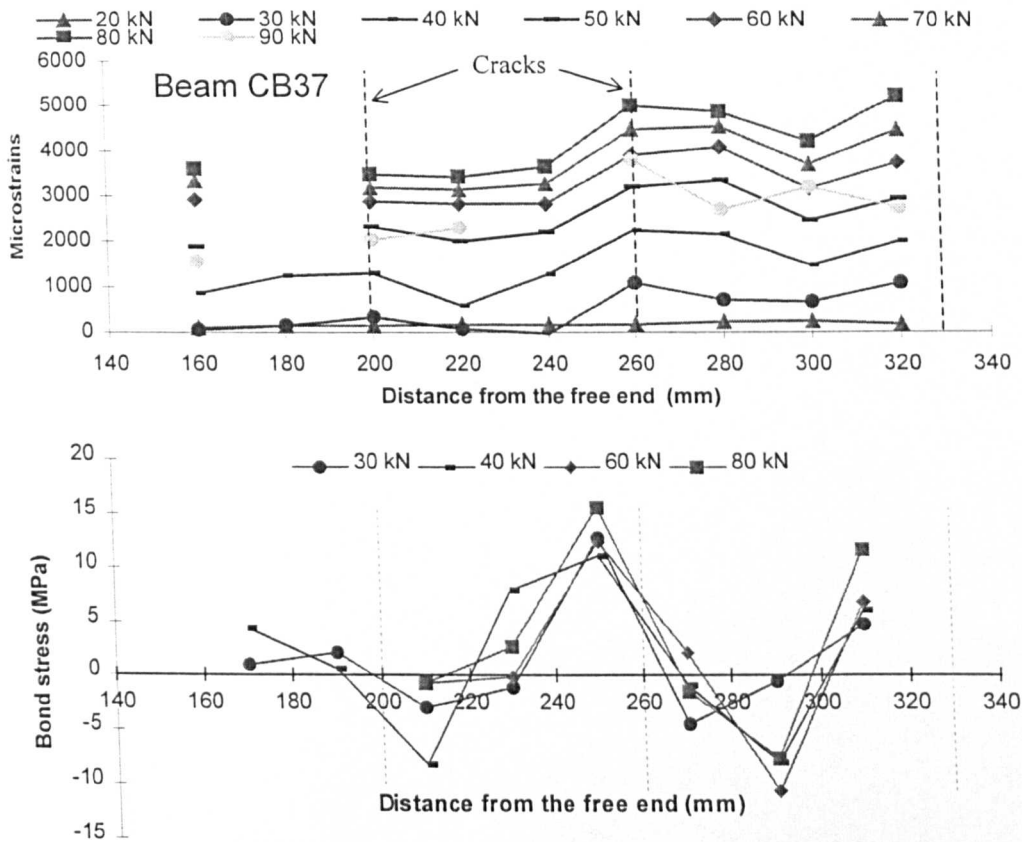


Figure 4.56: Strain and bond stress distribution between successive cracks

### Strain and bond stress over the anchorage length

Another interesting outcome from the experimental data of beam CB37, is the strain and bond stress distribution over the whole anchorage length. For this purpose, only the measurements of strain gauges c47, c49, c65 and c67 were considered since there was no interest in monitoring at this stage the local fluctuations of bond stress values due to flexural cracking. The strain and bond stress profiles over the anchorage length are plotted for selected load steps in figure 4.57.

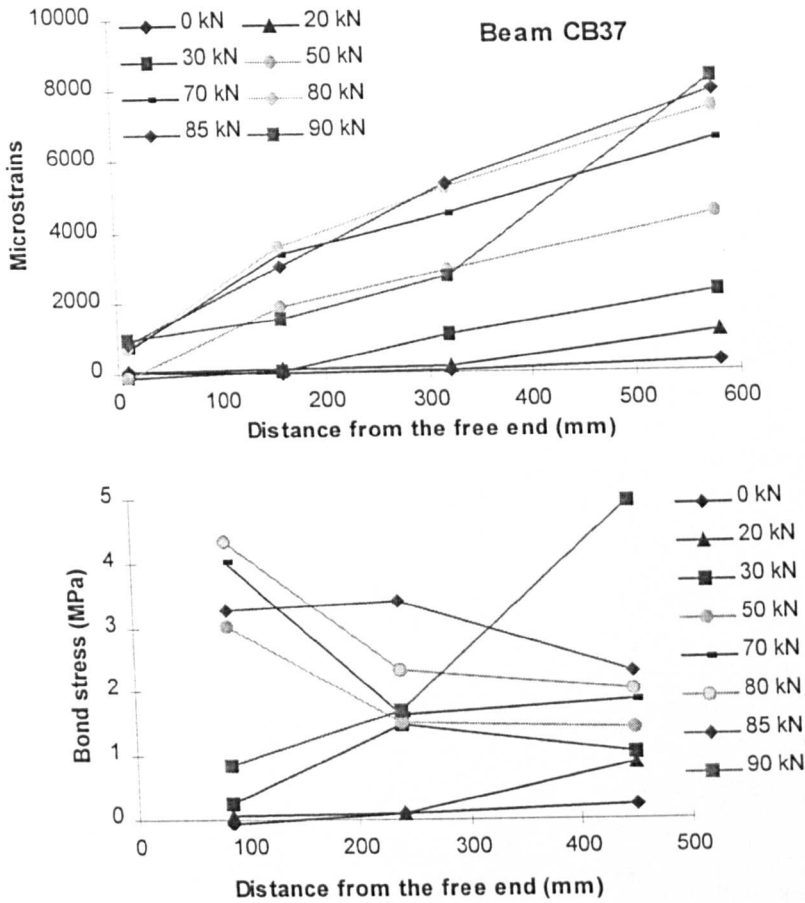


Figure 4.57: Strain and bond stress profiles over the anchorage length

At the beginning of the test, the peak bond stress develops close to the loaded end of the anchorage. As the load increases, the peak migrates towards the free end of the bar. The peak bond value located close to the end of the bar, increases with the load until the bar starts slipping and the concrete cover cracks. The peak value then follows the extension of the splitting crack and propagates towards the centre of the beam, up to the ultimate failure of the anchorage.

#### Average bond strength values developed

In this case it was difficult to assess when actually the bar started slipping, because the readings from the last strain gauge on the bar (c47) were increasing until the failure of the anchorage. However, from examination of the values of the rest of strain gauges attached on the bar, it can be assumed that the bar started slipping between the 60 kN and 80 kN load levels. In the worst case (load equal to 60 kN), the

calculated  $\tau_{sl}$  for the single bar anchorage was 2.4 MPa (the correcting factor 1.055 is included, see section 3.2.7). The maximum average bond stress ( $\tau^*$ ) developed was 3.7 MPa (including the factor 1.055), at the load level of 87 kN.

### Strain on transverse reinforcement

Since the splitting crack was expected at the bottom face of the beam below the single anchorage bar, strain gauges were attached to the horizontal bottom leg of selected shear links, as shown in appendix B.5. Only two of the links (c75 and c77) were located in the anchorage length region, whereas link c79 was positioned after the anchorage length. The strains recorded in these links are presented in figure 4.58.

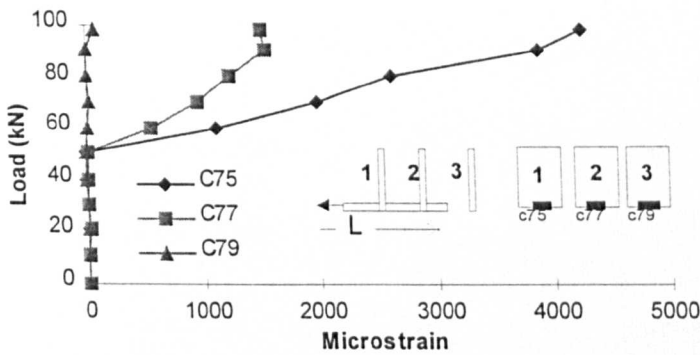


Figure 4.58: Strains in selected links in beam

It is obvious that both the strain gauges c75 and c77 recorded the initiation of the splitting crack just before the load level of 60 kN. Both the links also, appeared to contribute to the bond splitting resistance of the concrete cover when  $\tau^*$  was developed at 90 kN load level.

Further discussion of the experimental results will be made in chapter 6 after the analytical study has been presented.

# **CHAPTER 5**

## **ANALYTICAL STUDY**

In this chapter, the results of the analytical study are presented. Two Finite Element packages (ANSYS and ABAQUS) are used in modeling the bond behaviour of FRP reinforcing bars in cubes and beams. The main purpose of this work is to develop additional understanding of how FRP bars cooperate with concrete in each case in order to sustain the pullout load. Analytical predictions are compared with experimental results and conclusions are made.

### **5.1 PULLOUT CUBE TEST MODEL**

The cube test modeling procedure has two main objectives. The first objective is to help with the understanding of how the bond stress is developed at the FRP-concrete interface during pullout. This was not possible to be deduced from the experimental results since no strain gauges were attached on the embedment length of the bar in order not to disturb the bond development zone. The analytical results are intended to give an "inside view" of the FRP-concrete bond interaction during pullout.

The second objective of the model is to help develop a procedure for predicting the bond behaviour of larger embedment lengths subjected to a pullout force, by using the experimental data from specimens with smaller embedment. This objective is considered to have practical usefulness since it is aimed in reducing the need of testing large numbers of specimens in order to establish the relationship of how the average bond strength is influenced by an increase in the anchorage length (Achillides et al, 1997c). It is accepted that the size of the embedment length influences the developed average bond strength on the bar (see section 4.1.3.2 and also CEB Bulletin 151, 1982). So, in order to use large anchorage lengths in practical applications the need of

calculating the respective bond stress is apparent. The suggested model aims to contribute towards this direction.

The FE package ANSYS 5.0a (1992) was used for modeling the bond behaviour of FRP bars in pullout cube tests. This package was preferred since it provides reliable elastic-analysis results and a user-friendly visual interface. The analysis was conducted by using perfectly-elastic materials (concrete and FRP), since concrete cracking was assumed to be of minor importance under the specific pullout experimental conditions (see pullout test arrangement in section 3.1.4). In addition, the elastic concrete model was favored since it provided a more stable solution, than the solution provided by a non-linear concrete model, which was needed for the investigation of the post-maximum bond behaviour of FRP bars.

The results of the analytical study were compared to the experimental results gathered from the pullout tests. The reader has to acknowledge at this stage that the great variation in the values of the experimental results limits the accuracy of the comparisons between the experimental and analytical results. The following analytical study concentrates mainly on the behaviour of GFRP 13.5 mm bars, since the experimental values gathered for this type of bars are assumed to be adequate for the purposes of the analytical study. However, the described procedure can be easily followed for investigating the bond behaviour of other types of reinforcing bars as far as sufficient amount of experimental pullout test data are available.

## **5.1.1 Description of the model**

### **5.1.1.1 Geometry - elements**

The FRP-concrete cube specimens were modeled by using 2-dimensional elements. The concrete was modeled by 4-noded plane square elements (PLANE42 type) of 150 mm thickness, whereas 2-noded square bar elements (BEAM3 type) of area  $143.13 \text{ mm}^2$  were used to model the FRP bar. Bar and concrete were linked together with non-linear spring elements (COMBIN39 type) at a spacing of 27 mm (27 mm = 2 times the bar diameter). The use of this particular spacing will be explained in section 5.1.1.2, together with the characteristic load-slip curve of the springs.

In order to model the different sizes of embedment length used in the experiments, 4 identical cube models were developed differing only in the number of

connecting springs. Every spring was assumed to represent the bond contribution of a 27 mm bar length to the overall bond behaviour of the embedment length. An example of modeling the 45G10D (GFRP 13.5 mm bar having embedment length =  $10 \times D = 135$  mm  $\Rightarrow$  use of 5 springs) and the 45G6D specimen (GFRP 13.5 mm bar having embedment length =  $6 \times D = 81$  mm  $\Rightarrow$  use of 3 springs) is presented in figure 5.1. The springs connect the bar point A with the concrete point B, both having the same coordinates with respect the origin O, although in figure 5.1 they are shown to be remote from each other.

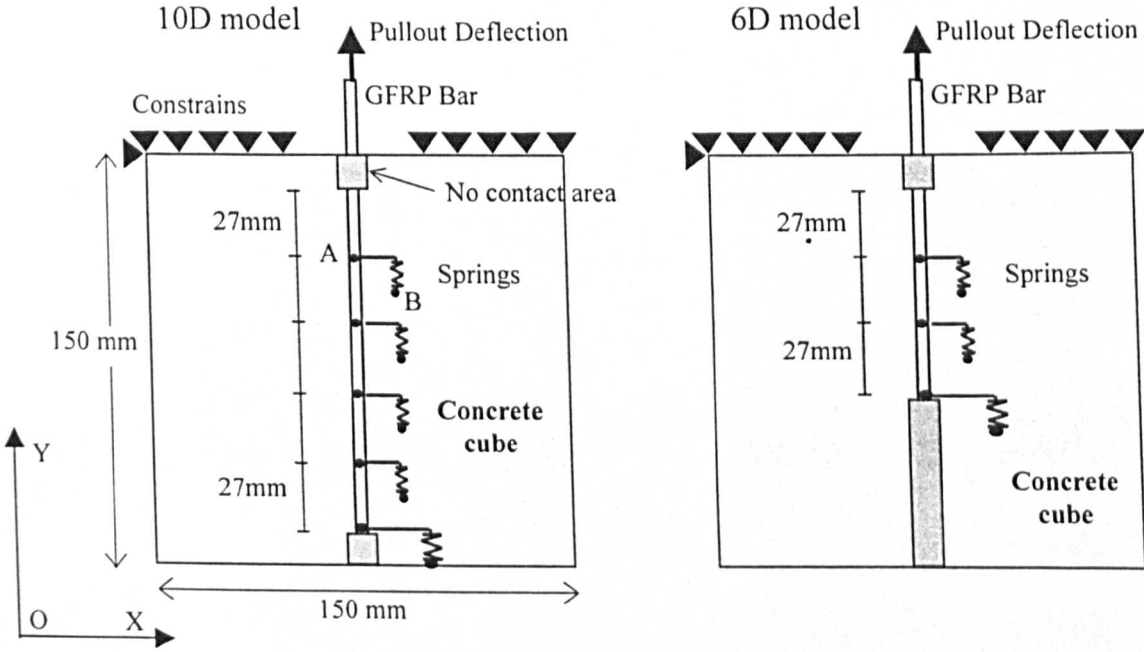


Figure 5.1: Model of 45G10D and 45G6D specimens

The material characteristics of the elements used in the model are shown in table 5.1. The load-slip curve of the spring elements was deduced from the experimental results, as it is explained in the following section.

|                       | Concrete elements<br>(PLANE42) | Bar elements<br>(BEAM3) |
|-----------------------|--------------------------------|-------------------------|
| Young's Modulus (GPa) | 30                             | 45                      |

Table 5.1: Element characteristics

The model was constrained at the top face of the cube in the Y-direction, similar to the experimental set up (see pullout test arrangement in section 3.1.4). However, in

order to avoid a differential movement of the model along the X-axis during pullout, the X-direction was also constrained at the left top corner of the model.

The pullout load was applied on the bar in small increments along the Y-direction. This load was applied in deflection control, so that the study of the post-maximum bond behaviour of the bar would be possible.

### 5.1.1.2 Spring characteristics

The main role of the spring elements in this model was to simulate the bond interaction between the bar and the surrounding concrete during pullout. The required input data that define the behaviour of the springs are the spring extension values and the corresponding force levels applied on the spring. In the case of this model, the spring extension was identified by the bond slip of the bar and the corresponding force was a function of the bond strength of the bar. In order to define the input load-bond slip curve, selected experimental data from the pullout cube tests were used.

Figure 5.2 shows the experimental load-unloaded end slip curves for five specimens having GFRP 13.5 mm embedded bars. The only difference among these tests was the size of the embedment length. It can be seen from the graph that as the embedment length increases, the maximum pullout load also increases by a certain amount. Only the 45G6D specimen is an exception to this rule since it sustains higher pullout load than 45G8D although it has a smaller embedment length. This is attributed to the variability of the experimental values, and for this reason the results of 45G6D are not considered further with this modeling procedure.

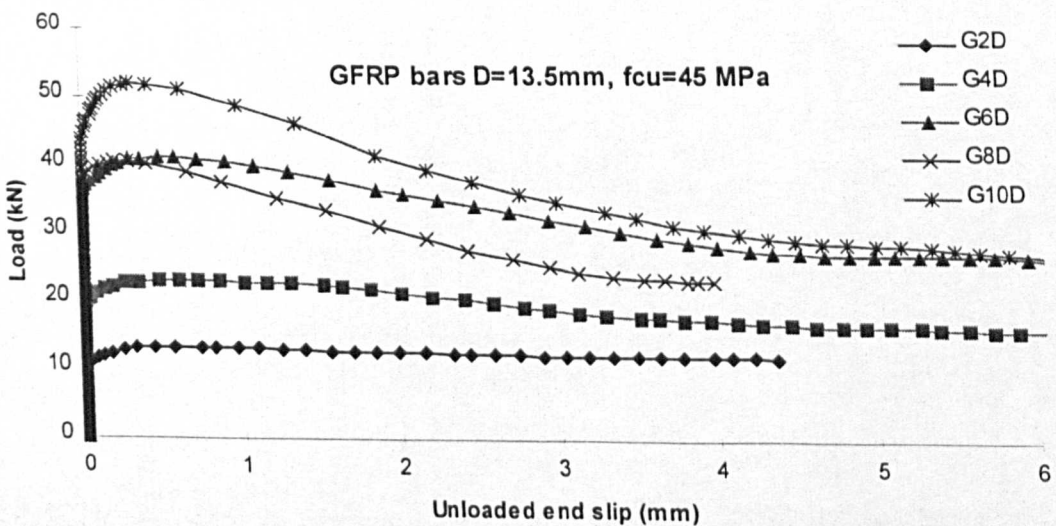


Figure 5.2: Experimental Load - Unloaded end slip curves of GFRP 13.5 mm bars

In order to explain the rationale of the springs' characteristics, the load versus unloaded end slip curves of the specimens 45G4D and 45G2D are considered in more detail. The 4D embedment length is assumed to be identical to two 2D lengths as shown in figure 5.3.

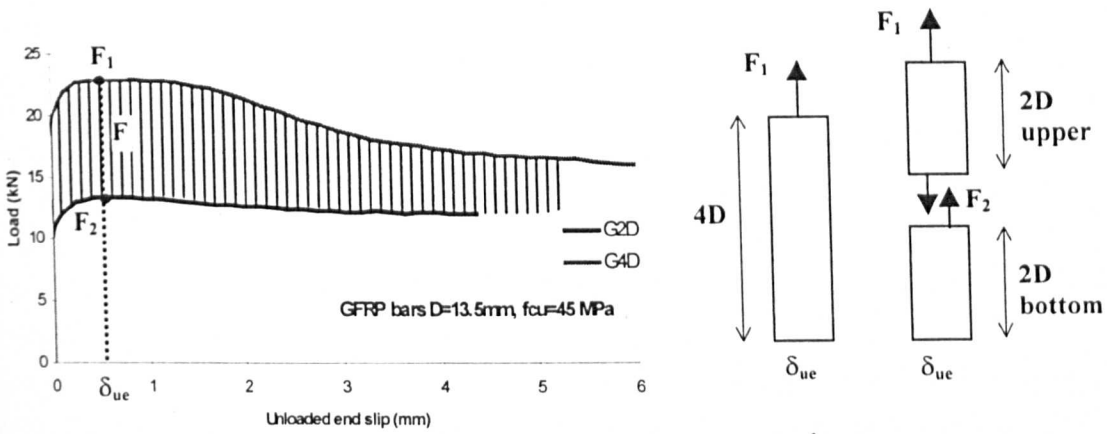


Figure 5.3: Contribution of the upper 2D bar length to the bond behaviour of the bar

The unloaded end slip,  $\delta_{ue}$ , is a function of the load  $F_1$ , which corresponds to the 4D embedment length, but is also a function of the internal load  $F_2$  which corresponds to the bottom 2D embedment length. Since the load values  $F_1$  and  $F_2$  correspond to the *same*  $\delta_{ue}$ , the difference between  $F_1$  and  $F_2$  will give a load value  $F$  that represents the contribution of the upper 2D length at that certain slip. The contribution of the upper 2D embedment to the Load-unloaded end slip curve of the whole 4D embedment, is the shaded area between the 4D and 2D curves. The resultant curve of  $F$  versus  $\delta_{ue}$  is shown in figure 5.5 (curve G4D-G2D).

Similar procedure is also followed for the specimens with embedment lengths 10D and 8D, as shown in figure 5.4. The load values  $F_1$  and  $F_2$  correspond to the same  $\delta_{ue}$  and the difference between  $F_1$  and  $F_2$  will give a load value  $F$  that represents the contribution of the 2D length at that certain slip.

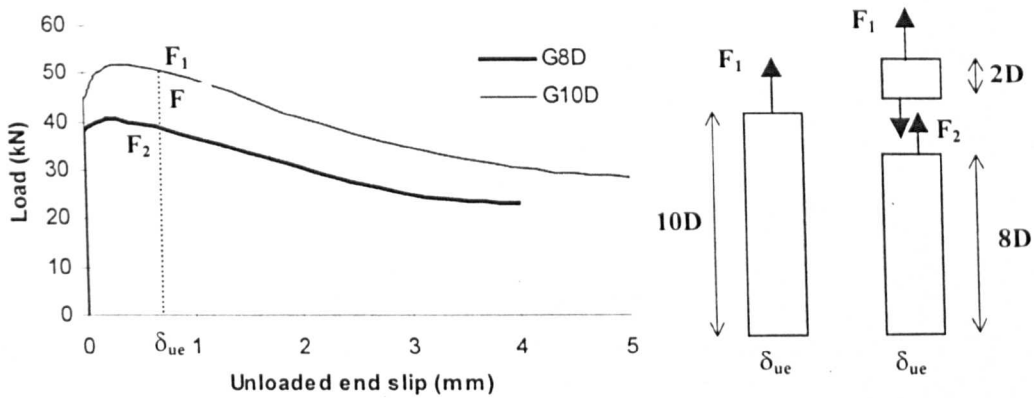


Figure 5.4: Contribution of the 2D bar length to the overall embedment length bond strength

The resultant load-unloaded end slip curve (G10D-G8D) is also shown in figure 5.5 together with the G4D-G2D curve. It is obvious that the differences between the values of these curves are quite small, so it is assumed that the contribution of the additional 2D embedment to the bond behaviour of the whole embedment length in each case is fairly standard. These characteristics, expressed by the  $F-\delta_{ue}$  (G4D-G2D) curve, are used in the modeling procedure of the cube tests.

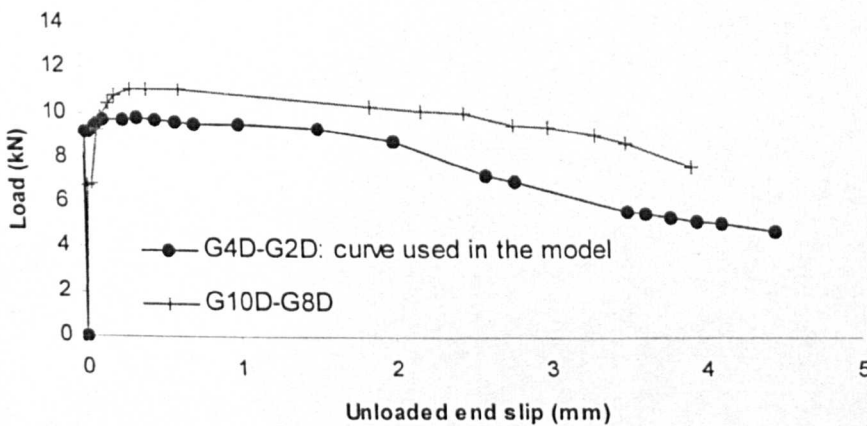


Figure 5.5: Load vs. unloaded end slip for the "basic" embedment length

The above  $F-\delta_{ue}$  curve was introduced in all the springs of the model except the very last one, where the  $F-\delta_{ue}$  curve of the specimen 45G2D was used (see figure 5.2).

## 5.1.2 Results

### 5.1.2.1 Load-slip curve

All 4 models failed in a pull-through mode of bond failure. In order to examine the validity of the modeling procedure, the analytical results were compared with the corresponding experimental ones. In figure 5.6, the load-slip curves at the loaded (LE) and unloaded end (UE) of the models are presented together with the respective experimental curves.

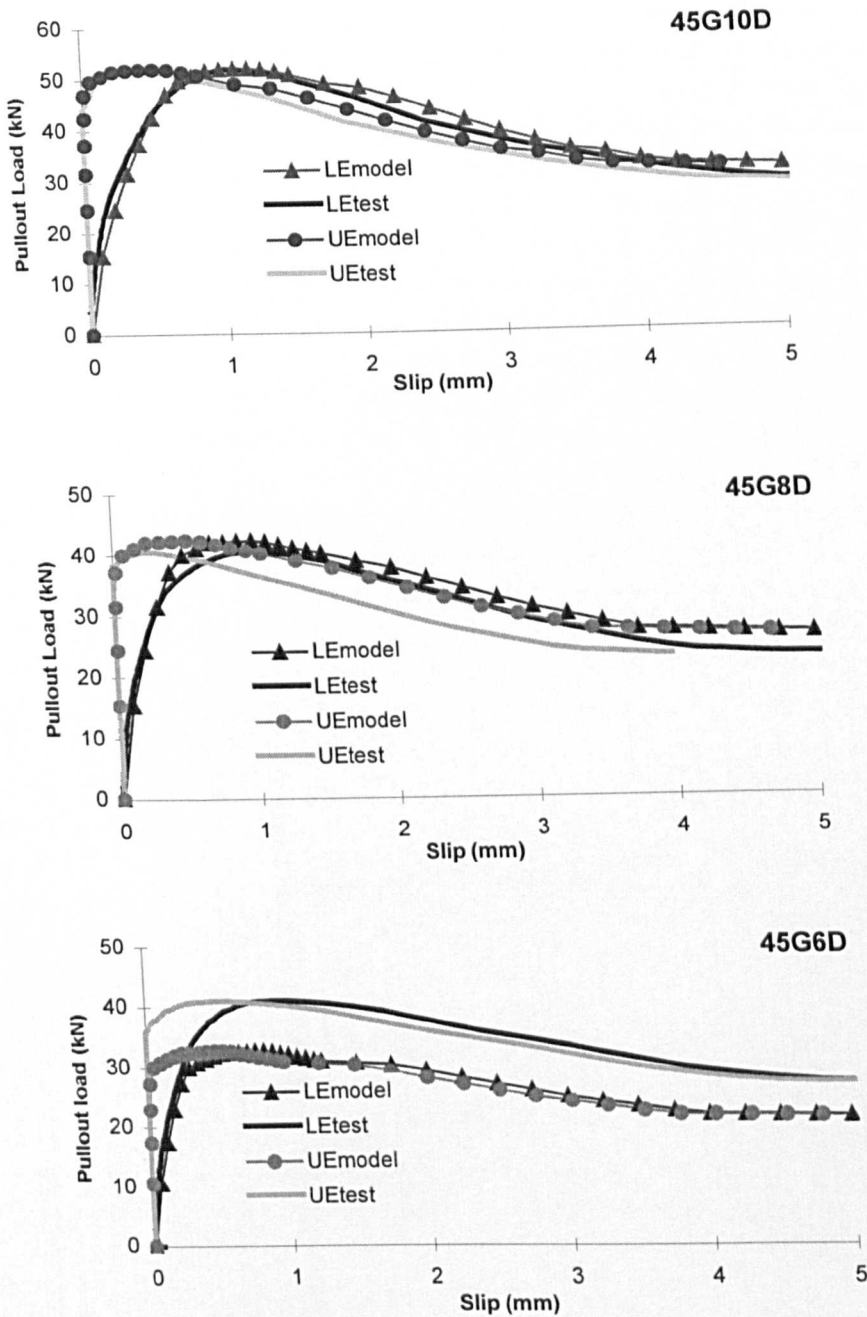


Figure 5.6: Load - slip curves of model and experimental tests

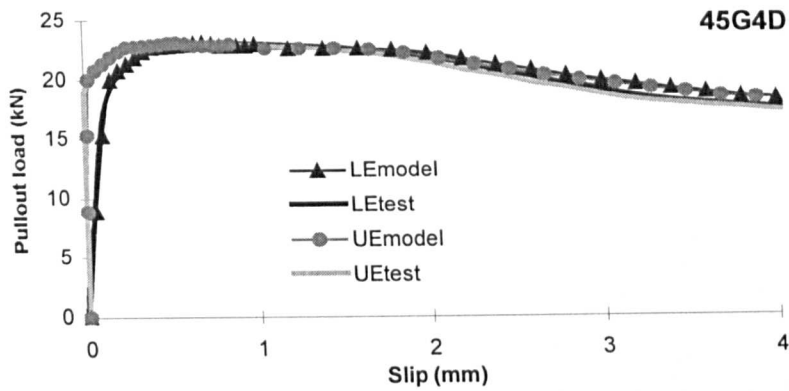


Figure 5.6 (continued): Load - slip curves of model and experimental tests

It is obvious from the above figure that in all cases the analytical results follow closely the experimental results both at the loaded and unloaded end, which proves that the modeling procedure is quite valid. Only in the case of 45G6D specimen, the values of the model defer significantly from the values of the test. However even in this case, the initial stiffness of the loaded end is modeled accurately.

#### 5.1.2.2 Distribution of normal and bond stresses over the embedment length

One of the main objectives of this analytical study is to give an "inside view" of the FRP-concrete bond interaction during pullout. Although the experimental data provide significant evidence of what is happening outside the embedment length (e.g. slip and load measurements), there are no data available that show how actually the bond is developed along the embedment length of the bar. This is an area where the analytical study can contribute towards a better understanding of the bond behaviour of FRP bars in concrete.

Figure 5.7 shows the normal and the bond stress distributions along the embedment length, for the 45G10D model. At low load levels the peak bond stress is developed at the loaded end of the bar. As the pullout load increases, the bond stress seems to be constant along the whole embedment length. Close to the maximum pullout load (52 kN), the peak bond stress migrates towards the unloaded end of the cube, having a slightly higher value than the local bond value at the loaded end of the cube. After the maximum load, the bond stress values decrease over the whole embedment length until a certain load value (31kN) where the bond behaviour of the bar is controlled by the frictional characteristics of the bar-concrete interface.

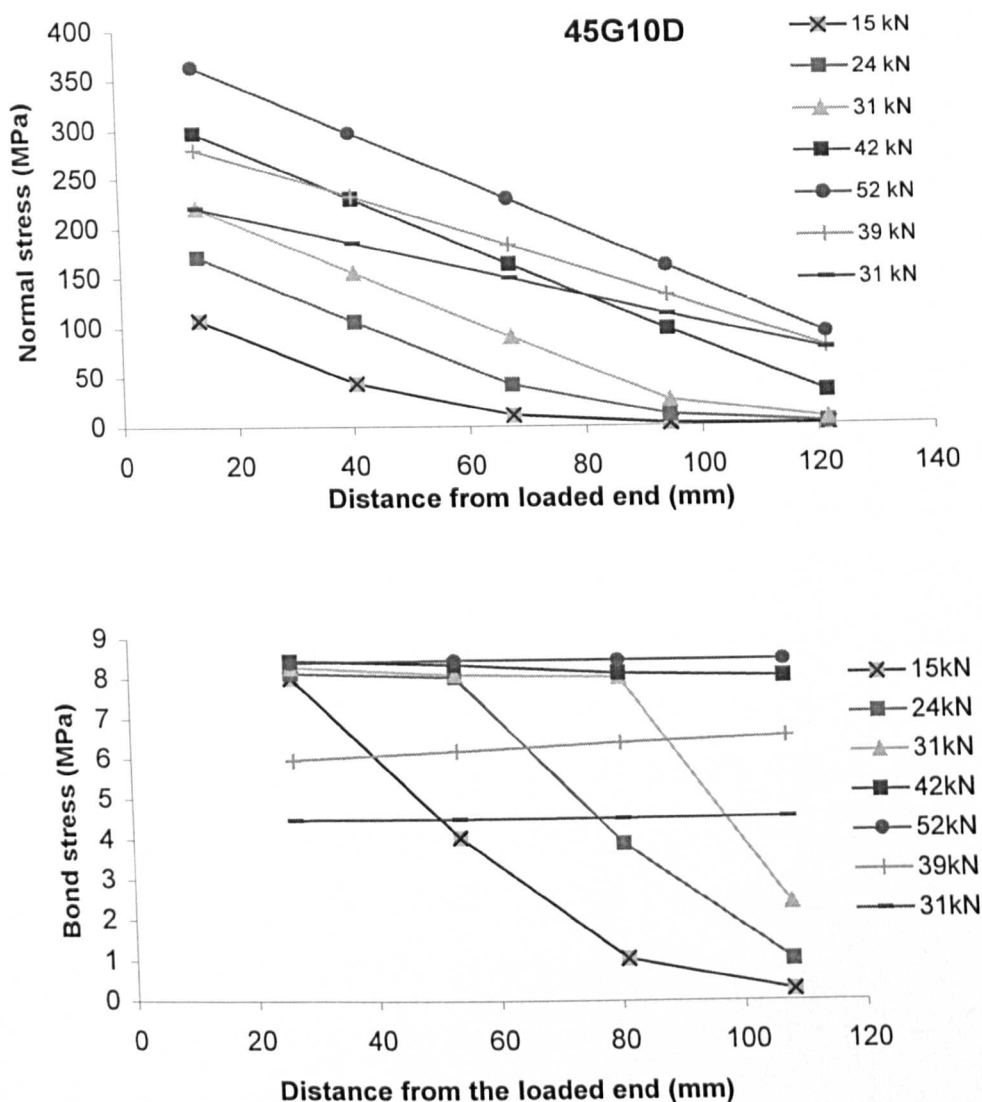


Figure 5.7: Normal bar stress and bond stress distribution along the embedment length of 45G10D model

### 5.1.2.3 Prediction of the bond behaviour of larger embedment lengths

After predicting the bond behaviour for small embedment lengths ( $L \leq 10D$ ), the modeling effort focused on relatively larger embedments. In this case, no experimental data were available for comparison purposes hence, the presented results are solely from the analytical study.

Three larger embedments were examined having lengths equal to 297 mm (22D), 594 mm (44D) and 864 mm (64D). The bar-concrete connecting springs were placed at 27 mm intervals and the concrete cubes had larger dimensions than before.

The geometry of one of these cubes for the embedment length of 22D, is shown in figure 5.8.

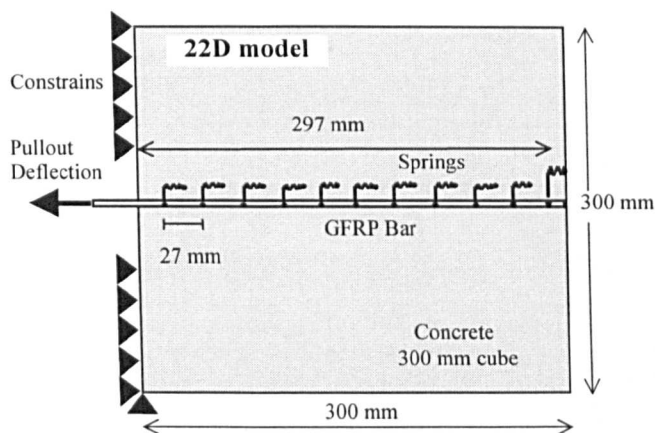


Figure 5.8: Model specimen of an embedment length equal to 22D (297 mm)

The characteristic curve of the connecting springs in the above three models was somewhat different from the one used in the previous models. The two curves differed in the post-maximum bond behaviour of the bar, as shown in figure 5.9. The curve used in the previous models (curve 1) was obtained from tests that had the embedment length of the bar in the middle of the cube. The positioning of the embedment length in the middle of the cube resulted to an increase in the residual (frictional) bond value, as it was explained in section 4.1.2.1. This value of frictional resistance was considered to be rather "plasmatic" than real, because of the mode of bond failure of FRP bars. In order to correct the post-maximum behaviour of curve 1, the frictional load resistance of the bar was calculated by multiplying the maximum load by a factor 0.2, according to section 4.1.2.1. The resulting curve (curve 2) shown in figure 5.9, was used in modeling the larger embedments.

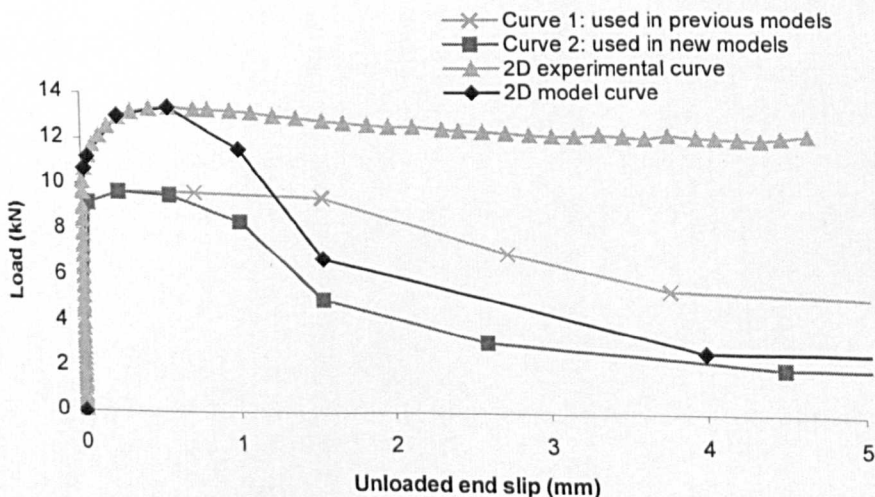


Figure 5.9: Load -slip characteristics of springs used in the new models

The same procedure was also followed for reducing the post-maximum resistance of the last spring that used the load-slip characteristics of the 2D embedment in the previous models (2D experimental curve). The resultant curve (2D model curve) is also shown in figure 5.9.

The analytical results of the above pullout models showed that the bond strength of FRP bars decreases, as the embedment length increases. In figure 5.10, the maximum average bond strength is plotted against the embedment length. It is obvious that the rate of bond decrease is much faster in smaller embedments whereas for larger embedments the bond strength appears to be leveling.

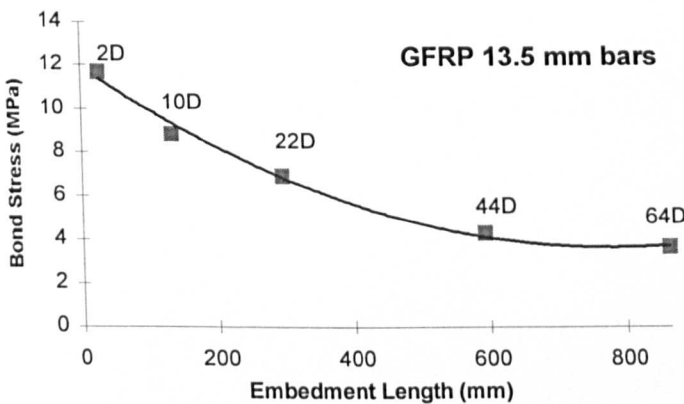


Figure 5.10: Maximum average bond strength versus embedment length for GFRP bars

The distribution of normal and bond stresses along the embedment length as the pullout load increases, is shown in figure 5.11 for the 64D model. The peak bond stress initially develops at the loaded end of the bar and as the load increases, the peak value migrates towards the unloaded end. It can be deduced from the bond stress distribution graph that the contribution of the peak bond stress to the average bond strength of the embedment appears to be more significant in smaller embedments, whereas for larger embedments the frictional bond stress is the critical parameter. This observation supports the findings of figure 5.10 that large embedments appear to have similar values of average bond strength since this value is more influenced by the value of frictional bond stress than the peak bond value. Similar findings, based on the experimental results of beam GB16, were reported in section 4.2.1.2.

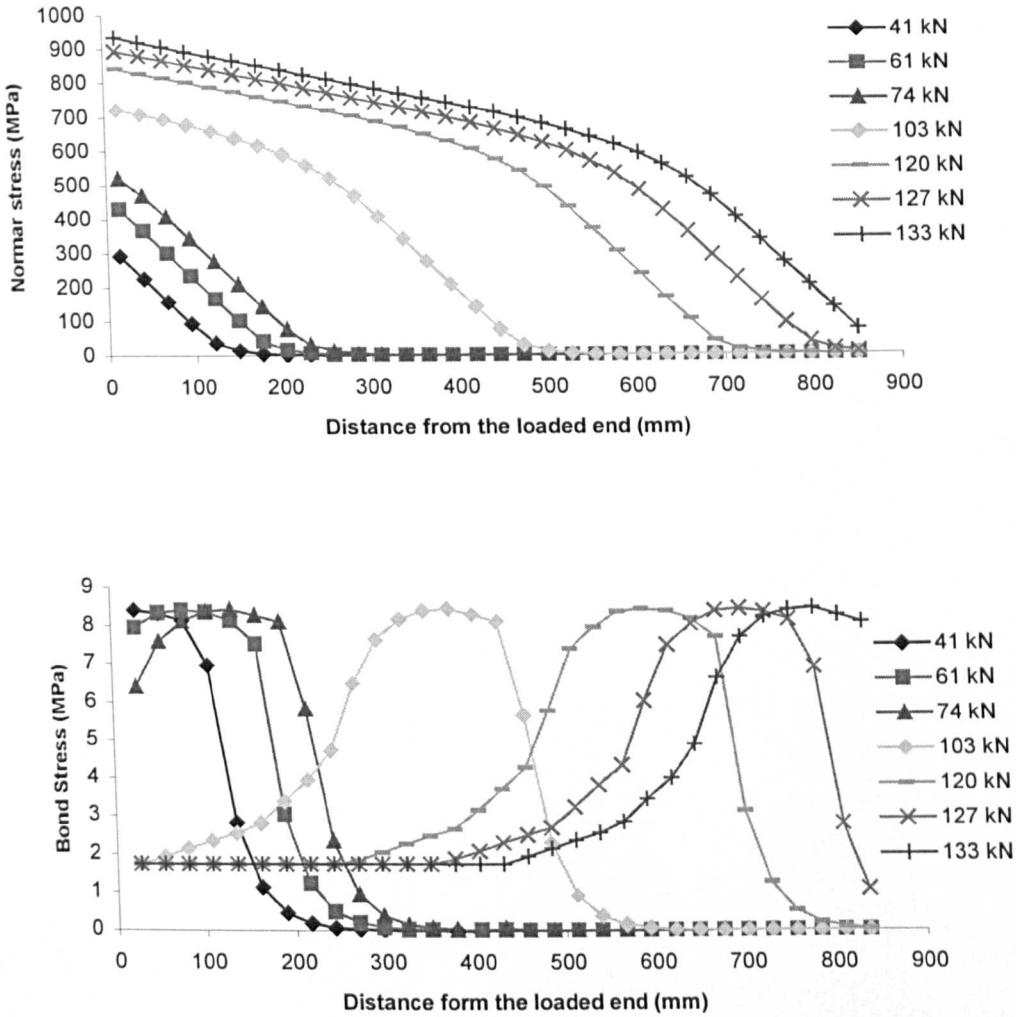


Figure 5.11: Normal bar stress and bond stress distributions along the 64D-embedment length

By considering the regression curve in figure 5.10, it can be suggested that in order to develop the full strength of a 13.5 mm GFRP bar (estimated around 1000 MPa), an embedment length of around 945 mm ( $\cong 70D$ ) is required. The average bond stress value at that length is equal to 3.6 MPa.

It is important to note at this point that no bond splitting is considered in this case, otherwise the required anchorage length would have been much larger, as it is reported in section 6.3.7.2.

## 5.2 BEAM TEST MODEL

Examining the bond behaviour of reinforcement bars in beam elements is one of the main aims in this study. Their bond behaviour appears to differ from the one in cube tests because of the different boundary conditions. Flexural cracks that develop in beam elements due to external loading, influence the bond development along the main reinforcing bars, as reported in the experimental study in chapter 4. In addition, bond failure in beam elements is usually due to concrete splitting which is something quite different from the pull-through mode of failure in cube specimens.

The modelling procedure reported in this analytical study has two objectives. The first objective is to model the behaviour of concrete beams tested for this study and concurrently to examine the bond development on the main reinforcing bars. The second objective is to introduce a method of predicting the bond behaviour of anchorages in beam elements, by using the limited number of experimental data available.

For this modelling effort, the need of a Finite Element package that takes into account the flexural cracking behaviour of concrete in beam elements is apparent. ABAQUS FE package (ABAQUS, 1993) was used for this purpose. ABAQUS was preferred than ANSYS, since it provides the facility of introducing a smeared-crack concrete model in 2-dimensional models. In addition, it is regarded to offer better non-linear solution procedures (RICKS procedure, see ABAQUS manual) for approaching the initiation of cracking in the model.

In the following sections, the modelling procedure is presented and explained for selected beams. The first beam modelled is CB19 beam, reinforced with 13.5 mm CFRP bars and having failed due to concrete crushing (see table E.1.2 in appendix E.1). The next step is to model CB20 beam, which was laterally confined and failed due to bond failure (see table E.1.2 in appendix E) after one of the main reinforcing bars failed in a pull-through mode (without any splitting in the concrete cover). Finally, beams CB32 and CB37 are modelled. These beams had amongst their main reinforcing bars a single

bar anchored in the flexure zone that failed in bond due to concrete cover splitting (see table E.1.3 in appendix E.1).

## 5.2.1 Model of beam CB19

Beam CB19 was reinforced with two 13.5 mm CFRP bars and had a concrete cube compressive strength of around 34 MPa. Further details on the reinforcement arrangement are shown in appendix A.4. The beam failed due to concrete crushing. All the experimental results are shown in table E.1.2 in appendix E.1 and in appendix E.2.

The main purpose of modelling CB19 is to examine whether ABAQUS smeared-crack model can satisfactorily simulate the flexural behaviour of the tested beam. For this reason, the distributions of normal and bond stress on the main reinforcing bars of the model, as well as the overall deflection of the beam versus the externally applied load, are compared with the respective experimental results.

### 5.2.1.1 Description of the model

#### *Geometry*

The geometry of the model is shown in figure 5.12. Since the load arrangement is symmetrical about the vertical axis passing through the midspan of the beam (see test arrangement in figure A.4, appendix A), only one half of the beam was modelled in order to save computational time. The geometrical dimensions of the model, shown in figure 5.12, were chosen to be exactly the same as in the test.

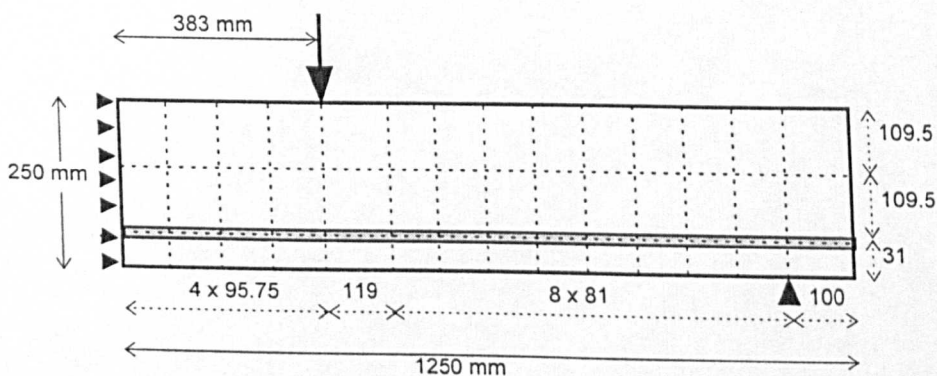


Figure 5.12: Model of CB19 beam

The dotted lines show the mesh used. The rationale of choosing these mesh dimensions is related to the arrangement of springs along the reinforcing bar, as explained in the modelling procedure of beam CB20 in section 5.2.2. However, since beam CB19 did not fail in bond, the main reinforcing bars were assumed to be rigidly connected to the surrounding concrete and no springs were used in this model.

Two main 13.5 mm reinforcing bars were used in the CB19 model having the material characteristics of CFRP bars. GFRP shear links (10 mm x 4 mm cross section) were also used at a 75 mm spacing, according to the experimental model. Both the main bars and the shear links were introduced in the reinforced concrete option of the beam elements.

### *Elements*

The elements used in the modelling of the beam were the 8-noded, plane stress, 2-dimensional elements (CPS8 type, see ABAQUS library\* of elements). In these elements, the reinforced concrete option was introduced.

### *Material characteristics*

The material characteristics of CFRP bars (Young Modulus,  $E_C = 115$  GPa) were introduced in the reinforcing bars of the model whereas, the shear links had the elastic modulus of GFRP bars ( $E_G = 45$  GPa).

The concrete material characteristics are shown in figure 5.13 together with the compressive stress-strain curve of the material.

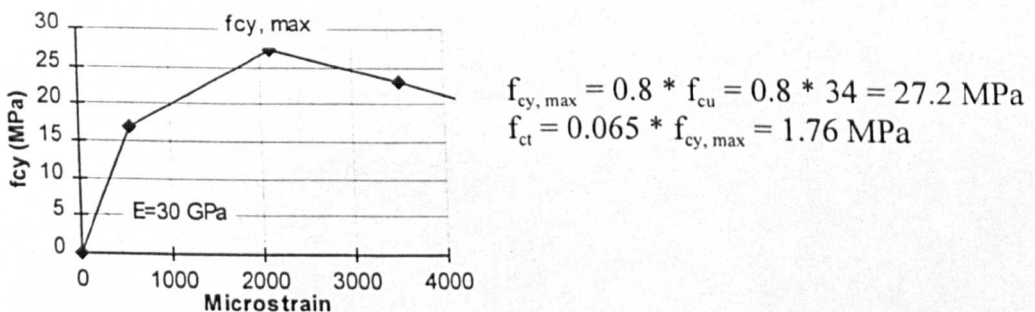


Figure 5.13: Concrete material characteristics

### *Loading procedure*

The load was applied in a deflection control mode by using the RICKS loading procedure (see ABAQUS manual for more details). This procedure was preferred since

it provided a more stable solution during concrete cracking, in comparison to other loading procedures that were not able to converge into a solution.

### 5.2.1.2 Results - comparisons

The model beam failed due to concrete crushing by reaching a maximum load of 116 kN. The load-midspan deflection curve of the model is presented in figure 5.14 together with the experimental one. It can be seen that the model simulates the experimental beam quite accurately up to the load of 60 kN. After that load, although the stiffness of the beam reduces, the analytical model does not predict well this reduction. It is assumed that the propagation of discrete flexural cracks in the experimental beam is partly responsible for this reduction in beam stiffness. The smeared-crack approach that the model beam uses in the solution can not facilitate this reduction. An additional reason for this reduction in beam stiffness might be the increase in the span of the beam due to the horizontal movement of the beam support estimated at 10 to 20 mm. The analytical model does not consider this movement either.

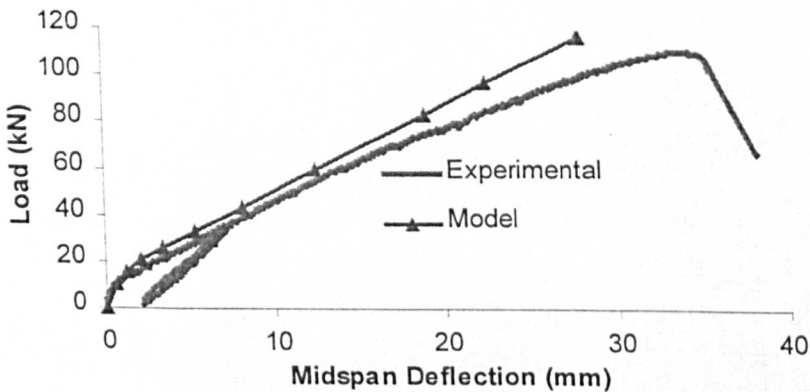


Figure 5.14: Total load versus midspan deflection for experimental and model beam

The predicted distribution of normal bar stresses and bond stresses along the main reinforcing bar are also compared with the experimental results. Figure 5.15 shows this comparison at selected load steps.

It can be seen from the first graph that the model predicts fairly accurately the value of normal bar stress in the constant moment region. In the shear span, however, the values of the normal stress obtained in the experiment are higher than the respective ones in the modelled beam. This difference is assumed to be related to the discrete

flexural cracking occurring in the experiment, whereas the smeared crack approach of the modelled beam results to a smoother distribution of normal stresses along the reinforcing bar.

The same effect is assumed to be also responsible for the differences in the bond stress profiles between the two beams. By examining the two profiles at the same load level (e.g. 60kN), it is clear that the peak bond value of the experimental beam is closer to the end of the beam than the peak bond value of the model.

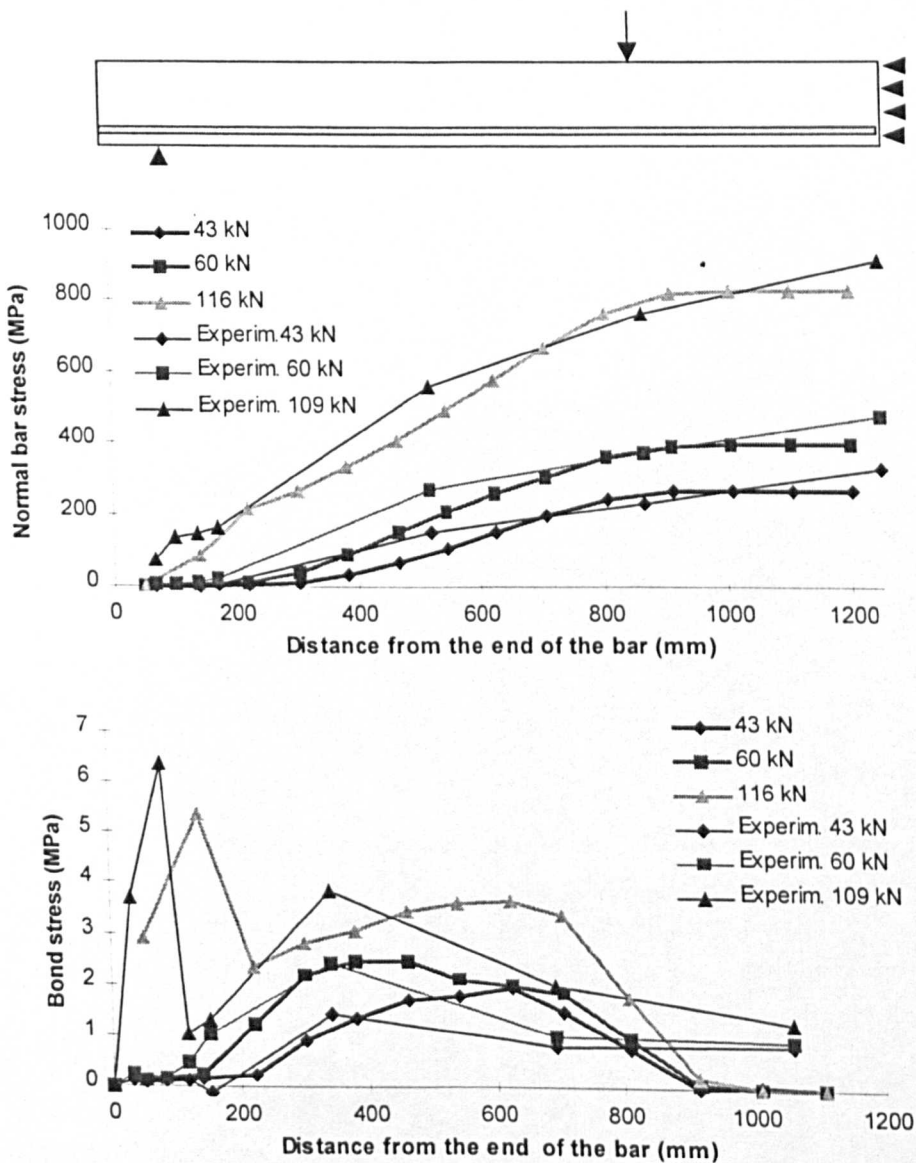


Figure 5.15: Comparison of normal bar stress and Bond stress distribution for experimental and model beams

## 5.2.2 Model of beam CB20

CB20 was one of the few beams in the experimental Phases 1-3 that failed due to bond failure (see table E.1.2 in appendix E.1). One of the two main reinforcing bars of the beam started slipping just before the maximum load, and failed abruptly in a pull-through mode similar to the one reported in the cube tests (section 4.1.2). Since no traces of splitting were observed in the concrete cover of the bar, it was decided to examine the bond behaviour of the reinforcing bar by using a similar method to the one followed in modelling the cube tests in a previous section (see section 5.1). The main purpose of this effort was to try a modelling technique to predict both the behaviour of the beam and the bond behaviour of the reinforcing bar.

### 5.2.2.1 Description of the model

#### *Geometry*

The geometry of the model used was very similar to the model shown in figure 5.12 for beam CB19. The most important difference was that only one bar was introduced as reinforcement in the concrete element CPS8, whereas the second bar was connected externally to the concrete elements by means of connecting springs, as shown in figure 5.19. This second bar was supposed to model the experimental reinforcing bar that failed in bond. Each spring was connecting the bar and concrete at the same coordinates, following a similar procedure to the one described for the cube tests.

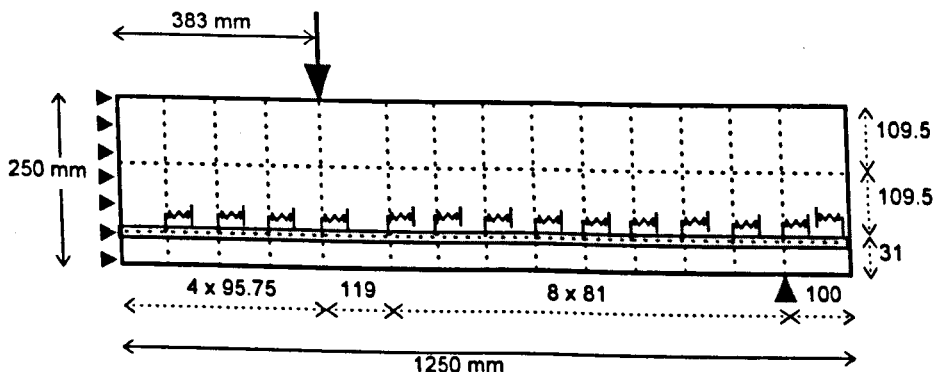


Figure 5.19: Model of beam CB20

Although for the cube tests a “basic” embedment length of  $2D$  (27 mm) was used, in this model a larger embedment ( $81 \text{ mm} = 6D$ ) was chosen. This was clearly

dictated by the capability of ABAQUS to produce a reliable solution, since it was proven that very small mesh dimensions prevented ABAQUS from converging into a solution. This is a well known limitation in concrete FE analysis modelling, which does not allow good results for elements with dimensions less than three times the aggregate dimension.

So in this case, the 81 mm embedment was used as the “basic” embedment length in the shear span of the beam, where the major bond development was expected. However, in order to obtain the exact dimensions required, a different mesh size was used at the two ends of the beam, as shown in figure 5.19.

### *Elements*

The CPS8 type elements with the reinforced concrete option were also used in this model, for the main body of the beam. The “external” CFRP bar was modelled by 2-noded beam elements (type B21) with a circular cross section (radius = 6.75 mm).

The bar and the concrete elements were connected together with JOINTC type springs. The springs were allowed to stretch only in the horizontal direction and their main purpose was to simulate the bond - slip behaviour of the bar. Similar to the pullout cube test modelling (see section 5.1), the spring extension was identified with the bond slip of the bar, whereas the corresponding load was identified with the bond stress value. The Load-slip curve required as input for the springs was decided to be taken from the pullout cube test data since both the reinforcing bar in beam CB20 and the bars in the cube tests failed in the same mode of bond failure (pull-through without splitting).

However, in order to derive the spring characteristics (load-slip curve), some assumptions were needed to be made. In section 5.1.1.2, the load-slip curve of the “basic” embedment length was derived from a procedure that used a series of experimental data from the pullout cube tests of GFRP bars. Unfortunately in this case, no reliable experimental pullout data were available for 13.5 mm CFRP bars to apply this procedure. Nevertheless, by considering the similarity in the maximum pullout bond strength values for GFRP and CFRP at the embedment length of 81 mm (see figure 4.13, section 4.1.3.1), it was decided that the load - slip curve derived from GFRP test could be used for CFRP bars as well. It has to be mentioned at this point that the author acknowledges the fact that although GFRP and CFRP bars develop similar maximum bond strength value at the 81 mm embedment length, they develop it at

different slip values. This difference will be examined in a following section of this study and will be shown to be unimportant to the overall bond behaviour of the bar (see section 5.2.2.3).

The second assumption was associated with the post-maximum bond behaviour of CFRP bars and it was similar to the assumption made in the cube test modelling for the prediction of the bond behaviour of larger embedment lengths (see section 5.1.2.3). In this case, the frictional bond value of CFRP bars was found by multiplying the maximum load value by a factor of 0.55, according to section 4.1.2.1.

By making use of the above two assumptions, the resulting load-slip curve was used in the springs of the CB20 model, as shown in the following figure. The curve was obtained by multiplying the curve used in the cube tests (which referred to a 2D embedment length) by three times in order to get a curve for a 6D embedment (81 mm), and by considering the second assumption regarding the post-maximum bond behaviour of the bar.

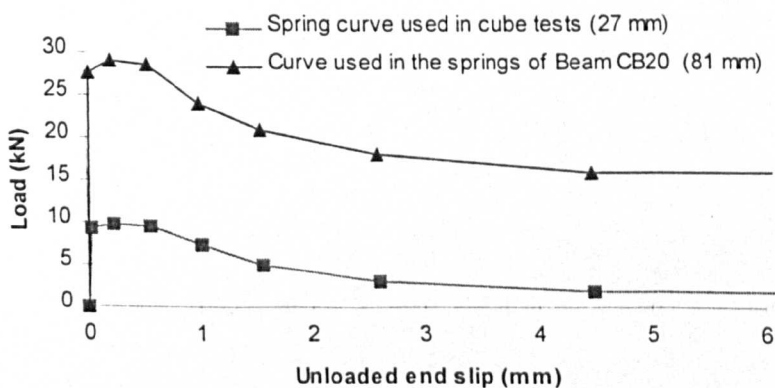


Figure 5.20: Load - Slip curve used for the “basic” embedment length (81 mm) in the CB20 beam model

From figure 5.19, it can be seen that apart from the “basic” embedment length (81 mm) springs, there are other springs which represent the bond contribution of different bar lengths (100, 119, 95.75 mm). Their load -slip curve was found by simply increasing proportionally the load values of the “basic” load - slip curve. This assumption was based on the fact that these embedments, having approximately similar lengths to the “basic” length, will develop similar values of bond strength. In addition, this simplified assumption is justified by the fact that the main bond contribution of the

reinforcing bar was expected to be developed at the region of the first eight 81 mm springs.

### *Material characteristics*

Similar to model beam CB19, the CFRP reinforcing bars had a Young Modulus equal to 115 GPa, whereas the shear links had an elastic modulus of GFRP bars ( $E_G = 45$  GPa).

The concrete compressive strength of the beam could not be measured with conventional methods since the beam was confined with stressed steel straps (see reinforcement arrangement in appendix A.4). For this reason, the concrete confinement model of Eurocode 8 (1988) was used to calculate the concrete strength:

$$\omega_w = \frac{V_s}{V_c} * \frac{f_y}{f_{cy}} \quad (5.1)$$

$$f_{cc}^* = f_{cc} * (1 + 2.5 * \alpha * \omega_w) \quad \text{for } \omega_w \leq 0.1 / \alpha \quad (5.2)$$

$$\varepsilon_{co}^* = \varepsilon_{co} * \left( \frac{f_{cc}^*}{f_{cc}} \right)^2 \quad (5.3)$$

$$\varepsilon_{c,85}^* = \varepsilon_{c,85} + 0.1 * \alpha * \omega_w \quad (5.4)$$

where,

- $\omega_w$  = volumetric mechanical ration of confinement reinforcement
- $V_s$  = Volume of steel =  $[25.4 * 0.8 * (2*250 + 2*150)]$  mm<sup>3</sup>
- $V_c$  = Volume of concrete =  $(250 * 150 * 50)$  mm<sup>3</sup>
- $f_y$  = Yield stress of steel straps (400 MPa)
- $f_{cc}$  = Concrete cylinder compressive strength (27.2 MPa)
- $f_{cc}^*$  = Concrete strain at max. stress at confined model
- $\alpha$  = Effectiveness ratio, max. 1 (estimated = 0.25)
- $\varepsilon_{co}$  = Concrete strain at max. stress at unconfined model (2100 micro)
- $\varepsilon_{co}^*$  = Concrete strain at max. stress at confined model
- $\varepsilon_{c,85}$  = Ultimate concrete strain at unconfined model (3500 micro)
- $\varepsilon_{c,85}^*$  = Ultimate concrete strain at confined model

The concrete stress-strain curve resulted from the EC8 equations is shown in figure 5.21, together with the respective curve of the unconfined concrete model used in CB19. This approach was successfully adopted by Frangou (PhD Thesis 1996) when dealing with similar confined beams.

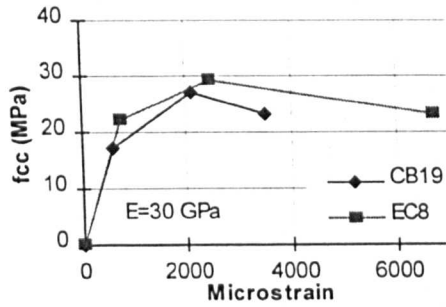


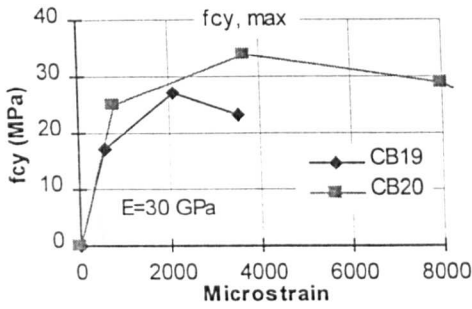
Figure 5.21: Confined concrete model suggested by EC8 (1988)

By applying these concrete values to the model beam CB20 however, the maximum load achieved was only around 80% of the load recorded in the experiment. Therefore, it was decided that the concrete strength had to be increased by a certain amount in order to match the experimental results.

To overcome this difficulty, the identically confined CB18 beam that failed due to concrete crushing was modelled (see appendix A.4), so that the concrete strength could be measured. Since both CB20 and CB18 were cast with the same batch of concrete, the concrete strength was assumed to be the same for both beams.

CB18 was modelled with a similar procedure described for beam CB19 and the analytical results were compared with the respective experimental. The only variable in this modelling effort was the concrete strength of the beam. After a series of modelling solutions, the one that mostly fitted the experimental results was chosen. The concrete characteristics used in this solution were assumed to be similar to the experimental ones for CB18, and consequently for CB20.

The concrete material characteristics used for modelling CB20 are shown in figure 5.22 together with the cylinder compressive stress ( $f_{cy}$ ) - strain curve of the material. For comparison purposes, the concrete characteristics used in CB19 are also shown in this figure.



$$f_{cy, \max} = 34 \text{ MPa}$$

$$f_{ct} = 0.05 * f_{cy, \max} = 1.7 \text{ MPa}$$

Figure 5.22: Concrete compressive stress - strain curve in beam CB20

### Loading Procedure

The load was applied in a deflection control mode, similar to beam CB19, by using the RICKS loading procedure (see ABAQUS manual for more details).

### 5.2.2.2 Results

The modelled beam CB20 failed due to concrete crushing by reaching a maximum load slightly higher than the experimental beam. The load-midspan deflection curve is shown in figure 5.23, together with the respective experimental curve.

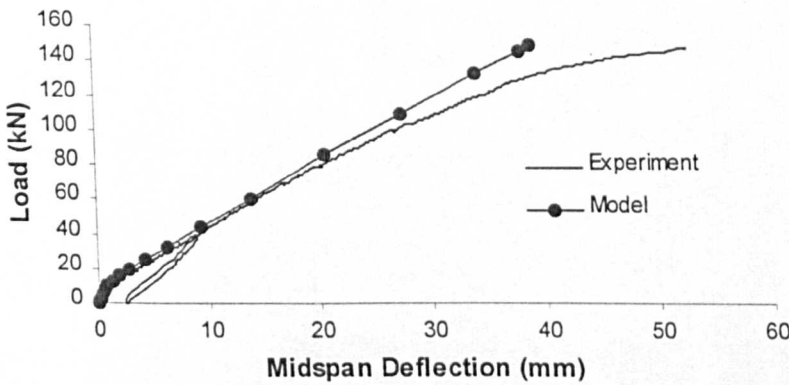


Figure 5.23: Load - Midspan deflection curve for experimental and model CB20 beam

Although at the beginning of loading the model simulates quite accurately the flexural behaviour of the experimental beam, the final mode of failure was completely different. The model failed due to concrete crushing whereas the experimental beam failed due to bond slip of one of the main reinforcing bars. The most obvious reason for this difference is that the springs introduced excessive bond strength to the bar-concrete interface that did not let the bar slip. It appears that the idea of using the springs directly

from pullout tests into beam elements can not produce reliable results despite the fact that the mode of bond failure in both cases is the same. It can be suggested that the flexural cracking and stress conditions round the reinforcing bars might play a significant role in their bond development in beam elements, as it will be discussed in more detail in the next chapter.

In order to find a more reliable load -slip curve for the spring elements that could model more accurately the bond behaviour of the reinforcing bars in CB20 beam, a parametric study was conducted.

### **5.2.2.3 Parametric study on the load - slip values of the characteristic spring curve**

The parametric study was based on the assumption that the load-slip curve (see figure 5.20), introduced in the spring elements to represent the bond behaviour of the reinforcing bar in beam CB20, provided “excessive” bond strength to the bar. It was decided to investigate the effect of either reducing the load values of the curve or increasing the slip values in order to create less “stiff” bond behaviour in the bar.

In the first case, the load values were decreased by a multiplying factor (see figure 5.24) whilst keeping the slip values constant, whereas, in the second case the initial stiffness of the curve was increased whilst keeping the load values constant. The resultant load - slip curves are shown in figure 5.24. Curve C1 is the load - slip curve that was used in the modelling procedure of beam CB20 described in the previous sections.

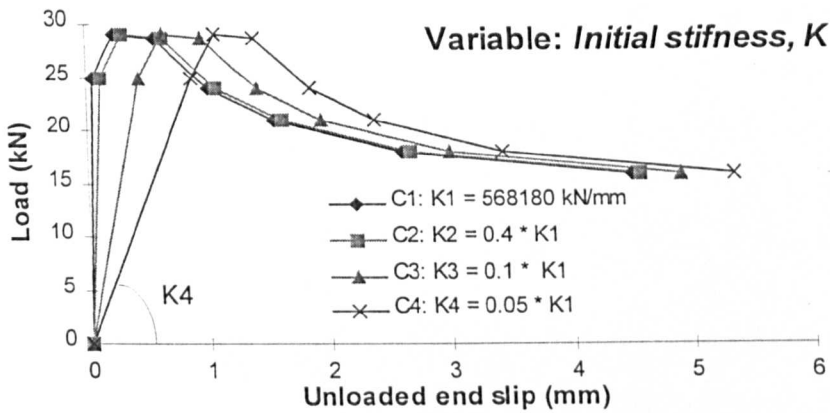
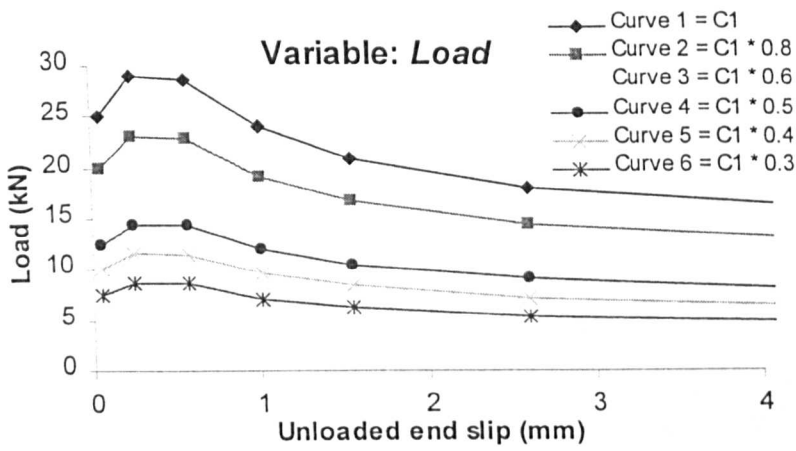


Figure 5.24: Load - Slip curves in parametric study

Each of the above curves was introduced in the “basic” embedment length (81 mm) springs of the model. For the other springs, the curve was modified accordingly following the procedure described in section 5.2.2.1.

A summary of the results of these parametric studies is shown in tables 5.2 and 5.3.

| Variable: Load    |                   |                   |
|-------------------|-------------------|-------------------|
|                   | Mode of failure   | Failure load (kN) |
| <b>Experiment</b> | <b>Bond Slip</b>  | <b>146</b>        |
| C1                | Concrete crushing | 148               |
| C2 = 0.8 C1       | Concrete crushing | 148               |
| C3 = 0.6 C1       | Concrete crushing | 151               |
| C4 = 0.5 C1       | Bond Slip         | 137               |
| C5 = 0.4 C1       | Bond Slip         | 135               |
| C6 = 0.3 C1       | Bond Slip         | 110               |

Table 5.2: First parametric study with variable the load value

| Variable: Initial stiffness |                                |                   |
|-----------------------------|--------------------------------|-------------------|
| Experiment                  | Mode of failure                | Maximum load (kN) |
|                             | <b>Bond Slip</b>               | <b>146</b>        |
| C1, $K_1$                   | Concrete crushing              | 148               |
| C2, $K_2=0.4 K_1$           | Did not converge into solution | 137               |
| C3, $K_3=0.1 K_1$           | Did not converge into solution | 134               |
| C4, $K_4=0.05 K_1$          | Did not converge into solution | 132               |

Table 5.3: Second parametric study with variable the initial stiffness of load-slip curve

### *First parametric study (load variable)*

The first parametric study showed that the spring force had to be decreased nearly to one half (curve C4) before the model beam CB20 would fail in a similar manner to the experimental one. The load - deflection curve and the distributions of normal bar and bond stress on the main reinforcing bar of model beam C4, were compared with the experimental results of CB20 for selected load levels, as shown in figures 5.25 and 5.26.

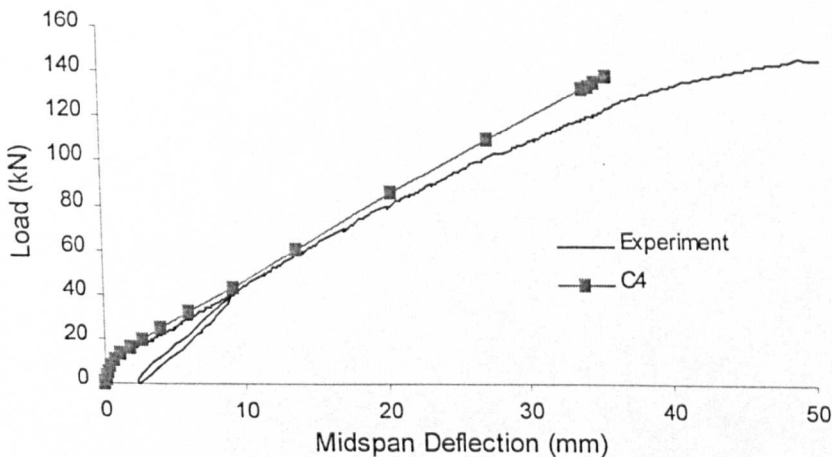


Figure 5.25: Load-midspan deflection curve for the model C4 and the experimental CB20 beam

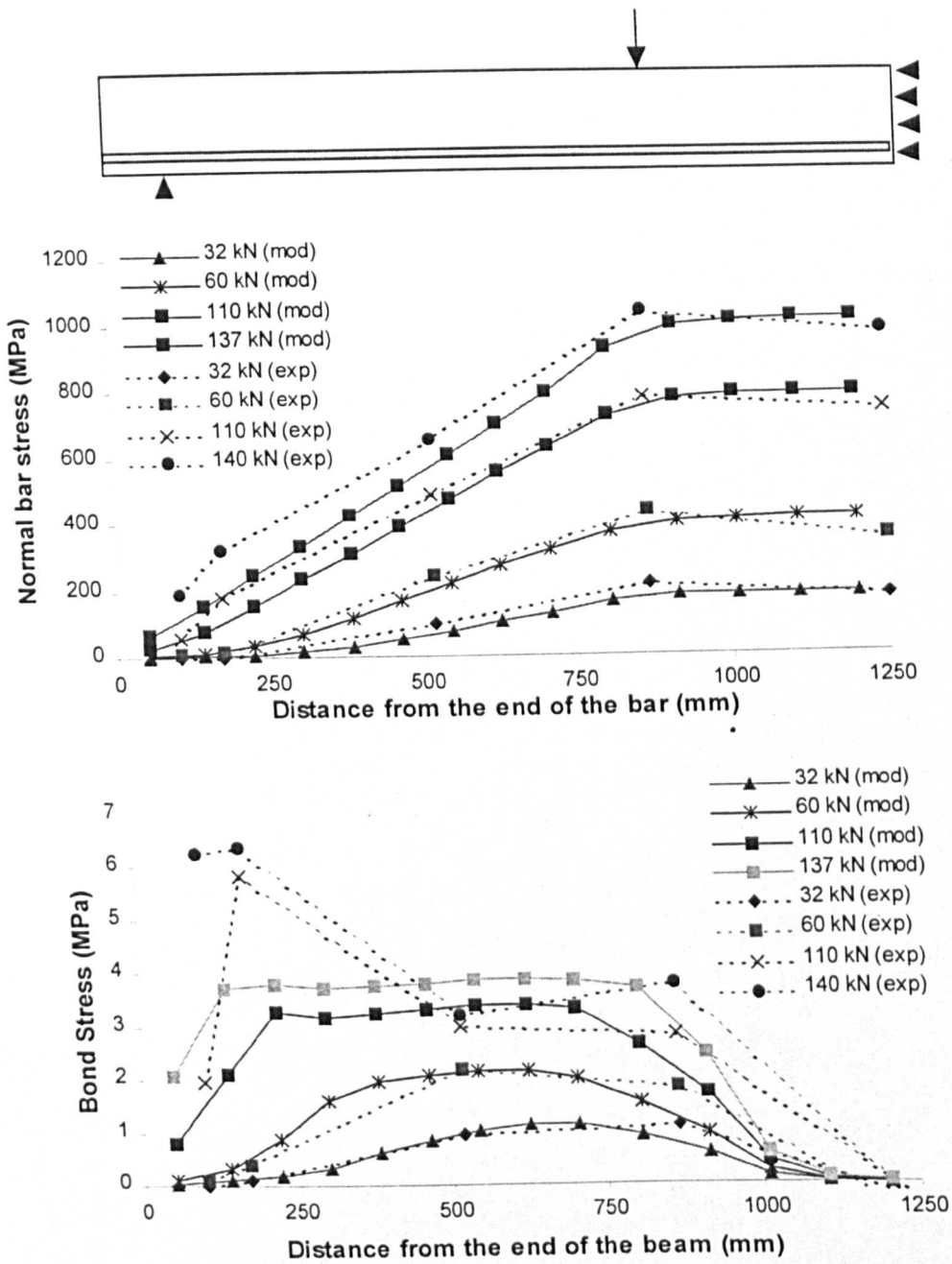


Figure 5.26: Normal bar stress and bond stress distributions over the main reinforcing bar in model C4 and experimental CB20 beam

By considering the load - midspan deflection graph, it can be seen that the model simulates the experimental beam quite accurately, at low load levels. At higher loads, though the stiffness of the experimental beam reduces, the model results remain linear. Similar behaviour was reported previously for model beam CB19 (section 5.2.1.2) and this difference was attributed to the smeared crack approach used for flexural cracking in the FE analysis.

From the first graph of figure 5.26, it can be seen that the model predicts fairly accurately the value of the bar normal stress in the constant moment region, for all load levels. In addition, the values of the normal stress in the shear span are also well predicted, though not as accurately. This difference is again attributed to the discreteness of the flexural cracks in the experimental beam, whereas the smeared crack behaviour of the model beam results to a smoother distribution of normal stresses along the reinforcing bar.

However, an important difference between the model and the experimental results is located in the region close to the beam support. The slope of the normal stress curve is much stiffer in the experiment than in the model in this region, which results to much higher bond values, as can be seen in the bond stress graph. This can be attributed to two factors. The first one is associated to the absence of flexural cracks in the region close to the support, which allows the bar to develop higher bond stresses, as it is explained in more detail in the next chapter (section 6.3.6). The second reason is the confining action of the beam support on the main reinforcing bar, which prevents bond splitting and increases considerably the bond stiffness capacity of the bar locally (see section 6.3.5). However, in the case of the beam model, these high bond values can not be observed, since the development of bond strength in the springs does not depend on the confining action of the support.

### *Second parametric study (initial stiffness variable)*

None of the beams in the second parametric study managed to converge to a solution (see table 5.3). However, by examining the bond stress distribution on the main reinforcing bar and the concrete strain values at the top surface of the model beam, it can be deduced that none of the models was close to failure due to bond slip. In all the cases, the maximum bond stresses developed in the springs were less than 50% of the allowable bond capacity in the springs. For example, the bond stress distribution developed in model C4 is shown in figure 5.27, together with the bond spring capacity.

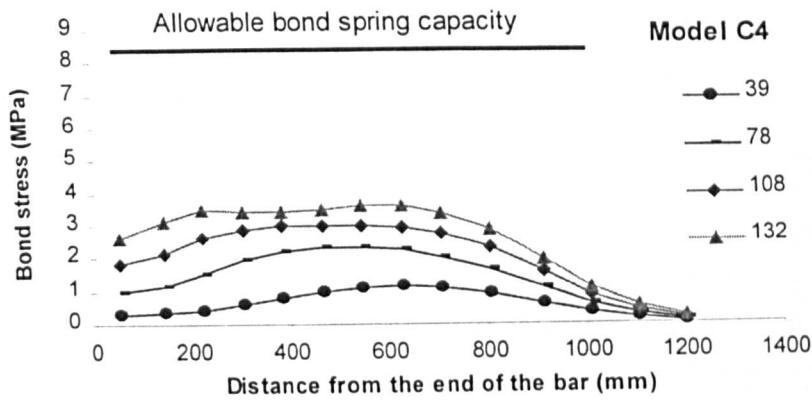


Figure 5.27: Bond stress distribution in model C4

On the contrary, the concrete strains developed at the top surface of model beams, shown in table 5.4, were very close to the failure value ( $\cong$  strain value in model C1), which suggests that a concrete compressive failure was more likely to happen first in all cases.

| Model              | Max. Load (kN) | Max. Concrete compressive strain ( $\times 10^{-6}$ ) | Max. normal bar stress (MPa) |
|--------------------|----------------|---|------------------------------|
| C1, $K_1$          | 148            | 3950  | 1096                         |
| C2, $K_2=0.4 K_1$  | 137            | 3629  | 1008                         |
| C3, $K_3=0.1 K_1$  | 134            | 3551  | 978                          |
| C4, $K_4=0.05 K_1$ | 132            | 3325  | 946                          |

Table 5.4: Comparison of results of second parametric study

The main reason for non-convergence was considered to be the instability that was introduced by the much larger deformability of the bar connected to the more flexible springs compared to the fully bonded bar. In order to overcome this instability, both reinforcing bars were connected with springs to the concrete and each solution procedure was repeated. Unfortunately, the instability introduced to the model with this modelling effort appeared to make matters worse, since none of the models managed to reach higher loads than those shown in table 5.4, nor converged into a reliable solution.

The second parametric study generally showed that a decrease in the initial stiffness of spring characteristics resulted to an increase in the deformability of the bar, which reflected to a slight increase in the overall deformability of the beam (see figure 5.28). This however did not seem to influence significantly the ultimate bond strength of

the bar, as shown in figure 5.29, where the bond distribution of model beams C1 and C4 is presented.

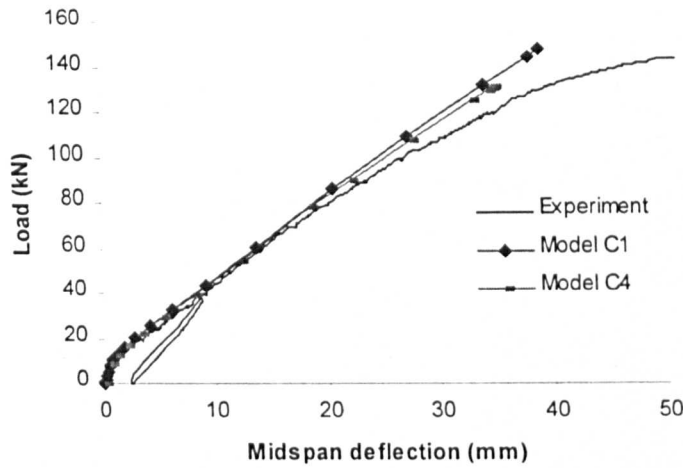


Figure 5.28: Load-midspan deflection of models C1, C4 and beam CB20

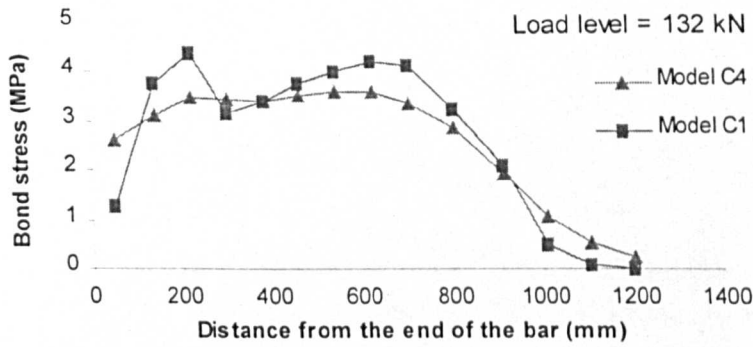


Figure 5.29: Bond distributions in model beams C1 and C4

Based on the results of the two parametric studies, it can be concluded that reducing the load values of the spring curve is far more effective in reducing the bond strength of the anchorage bar. In addition, the first parametric study proved that the bond values developed in anchorage bars in beam elements are significantly lower than the respective bond values in pullout tests. The main reason for this difference is the presence of flexural cracks in beam elements which reduces the bond strength of the bar, as will be explained in more detail in section 6.3.6.

### 5.2.3 Model of beams CB32 and CB37

Beams CB32 and CB37 had similar reinforcement arrangement differing only the length of the single bar anchorage, which was 300 mm for CB32 and 580 mm for CB37 (see appendices B.2 and B.5). In both cases the anchorage bar failed by splitting the concrete cover at the bottom face of the beam (see sections 4.2.2.3 and 4.2.2.6).

In order to model the behaviour of these beams and more specifically, the bond behaviour of the anchorage bars, the influence of the concrete splitting on the bond development had to be considered. For this reason, this modelling effort focused on introducing a working method of evaluating the bond splitting behaviour of the anchorage bars in beam elements.

#### 5.2.3.1 Description of the models

##### *Geometry*

The geometry of CB32 and CB37 model beams was similar to the one used previously in beams CB19 and CB20. Both models were reinforced with two 8 mm CFRP bars embedded in concrete. The additional anchorage bar that was supposed to fail in bond was connected externally to the concrete elements by using springs, as shown in figure 5.30. As in the experiments, GFRP shear links (10 mm x 4 mm cross section) were also modelled at a spacing of 75 mm.

Different mesh dimensions were introduced in each model beam in order to facilitate the exact length of the anchorage bar (figure 5.30). The selection of the mesh sizes was arbitrary since the modelling procedure used is believed to be insensitive to the spring size, and consequently the mesh size. As will be mentioned in section 5.2.3.3, the analysis repeated by using different mesh sizes in order to examine the validity of this modelling procedure and the mesh sensitivity of the results.

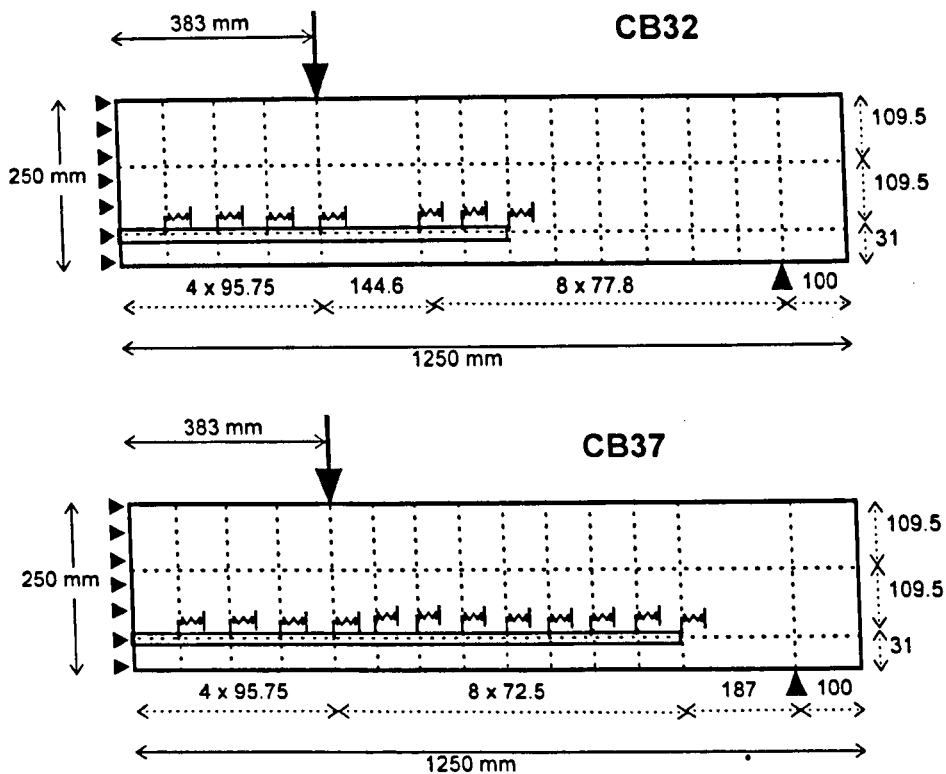


Figure 5.30: Models of CB32 and CB37 beams

### *Elements*

The CPS8 type elements with the reinforced concrete option were used for the embedded bars. The additional anchorage CFRP bar was modelled by 2-noded beam elements (type B21) with circular cross section (diameter = 8 mm).

The anchorage bar and the concrete elements were connected together with JOINTC type springs, similar to previous models.

Although the procedure of determining the load-slip characteristics of the connecting springs was based on the previously described modelling knowledge (see pull-out test and beam CB20 modelling), some new ideas were introduced in order to facilitate the splitting behaviour of the anchorage bar.

It is known from the literature (see section 2.1.2) that bond splitting occurs when there is no adequate concrete cover to the bar, at a lower bond value than the maximum bond strength of the bar. Figure 5.31 shows a typical distribution of bond stress versus the unloaded end slip of the bar together with an indicative bond splitting behaviour.

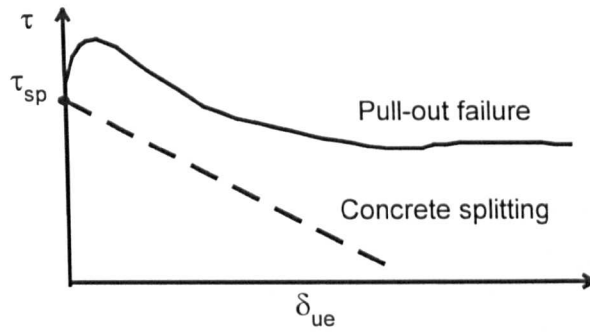


Figure 5.31: Indicative bond - unloaded slip curves for pullout and splitting bond failures

It is obvious that to model the bond splitting behaviour of the anchorage bar, the bond splitting strength ( $\tau_{sp}$ ) has to be quantified. For this reason, the bond values gathered from the experimental data of CB32 and CB37 beams were used.

Figure 5.32, shows the average bond values developed on the anchorage bar of each beam, at the time when the first splitting crack occurred. These values were calculated by using the strain gauge measurements at that load level, divided by the distance of the gauge from the end of the bar.

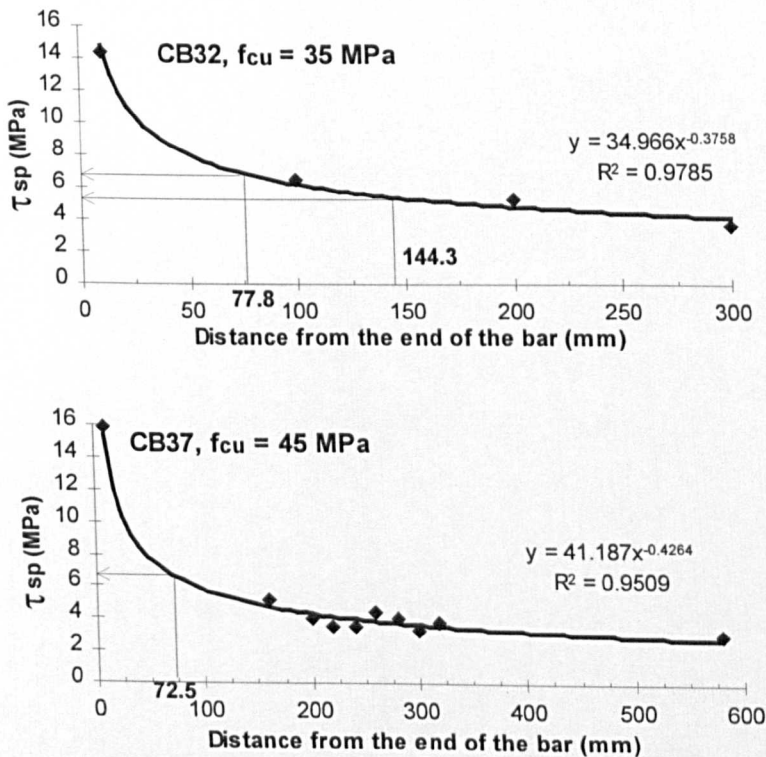


Figure 5.32: Average bond value developed at the time of splitting

Non-linear regression was used to determine the tendency of these values, as indicated by the best-fit lines. It has to be mentioned out that due to gaps in the sequence of data the regression curve might not be very accurate. However, in the absence of any more experimental data from these or any other similar beams, it can be assumed that these distributions are valid for modelling purposes.

Based on the dimensions of the mesh (shown in figure 5.30), the appropriate  $\tau_{sp}$  value was chosen for each type of spring from figure 5.32. This bond value was translated into a load value, by using the basic equation 3.2, and was introduced in the spring characteristics. The corresponding value of the unloaded end slip was assumed to be very small, since the experimental results showed that for CFRP bars the ratio of the recorded bond stress when the unloaded end started to slip to the maximum bond strength was more than 80% (see figure 4.3 in section 4.1.1). In addition in the parametric study presented previously in section 5.2.2.3, it was proven that small changes in the slip values in the springs do not seem to play an important role on the overall bond strength of the bar.

The resulting load - slip characteristic curves introduced in the anchorage length springs in each case are shown in figure 5.33, together with the curves used for the rest of the springs in the models.

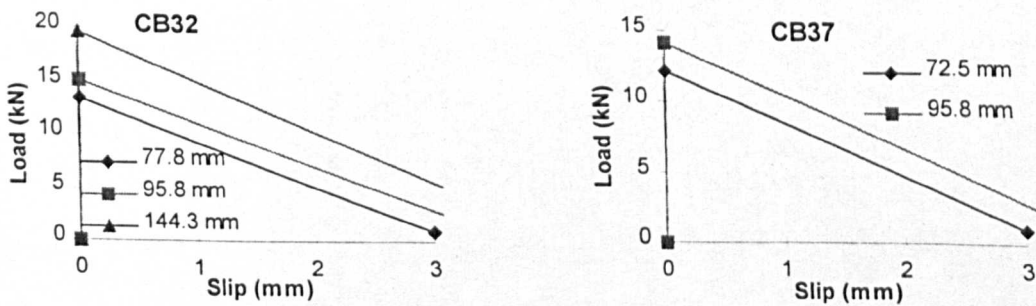
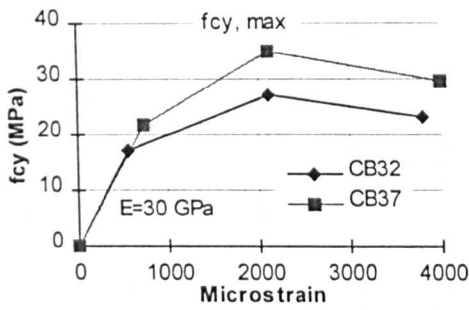


Figure 5.33: Characteristic load - slip curves introduced in the springs, in each model

### *Material characteristics*

Both models were reinforced with CFRP bars having Young Modulus equal to 115 GPa whereas, the shear links had the elastic modulus of GFRP bars ( $E_G = 45$  GPa).

The concrete material characteristics used in the models are shown in figure 5.34, together with the cylinder compressive stress ( $f_{cy}$ ) - strain curve of the material.



**CB32:**

$$f_{cy, \max} = 0.8 * f_{cu} = 0.8 * 35 = 28 \text{ MPa}$$

$$f_{ct} = 0.065 * f_{cy, \max} = 1.82 \text{ MPa}$$

**CB37:**

$$f_{cy, \max} = 0.8 * f_{cu} = 0.8 * 45 = 36 \text{ MPa}$$

$$f_{ct} = 0.065 * f_{cy, \max} = 2.34 \text{ MPa}$$

Figure 5.34: Concrete material characteristics

### *Loading Procedure*

The load was applied in a deflection control mode by using the RICKS loading procedure (see ABAQUS manual for more details).

### 5.2.3.2 Results

Both model beams failed due to bond failure. The experimental results showed good agreement with the respective experimental, as shown in table 5.5.

|               | Splitting Load<br>(kN) | Normal bar stress at<br>loaded end (MPa) | Beam deflection<br>(mm) |
|---------------|------------------------|--|-------------------------|
| Experim. CB32 | 45.5                   | 553                                      | 18                      |
| Experim. CB37 | 80.6                   | 861                                      | 30.2                    |
| Model CB32    | 43.9                   | 512                                      | 15                      |
| Model CB37    | 84.2                   | 926                                      | 27.7                    |

Table 5.5: Comparison of model and experimental results

The small differences between model and experimental values can be attributed to inaccuracies in the determination of the experimental splitting strength.

The load - midspan deflection curves together with the distribution of normal and bond stresses along the anchorage bar for both models are presented and compared with the respective experimental results, in figures 5.35 and 5.36.

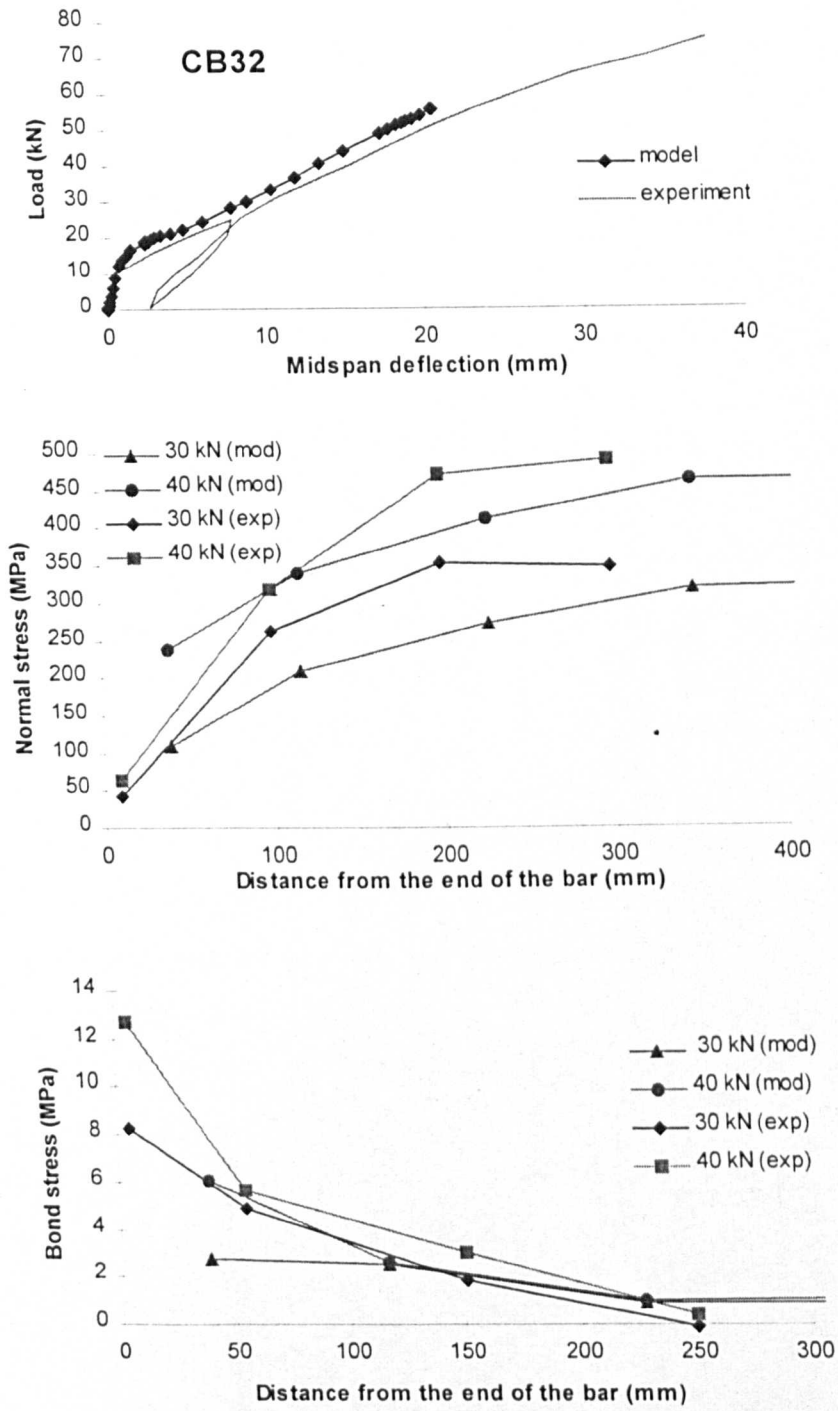


Figure 5.35: Load - deflection curve and normal and bond stress distributions for CB32

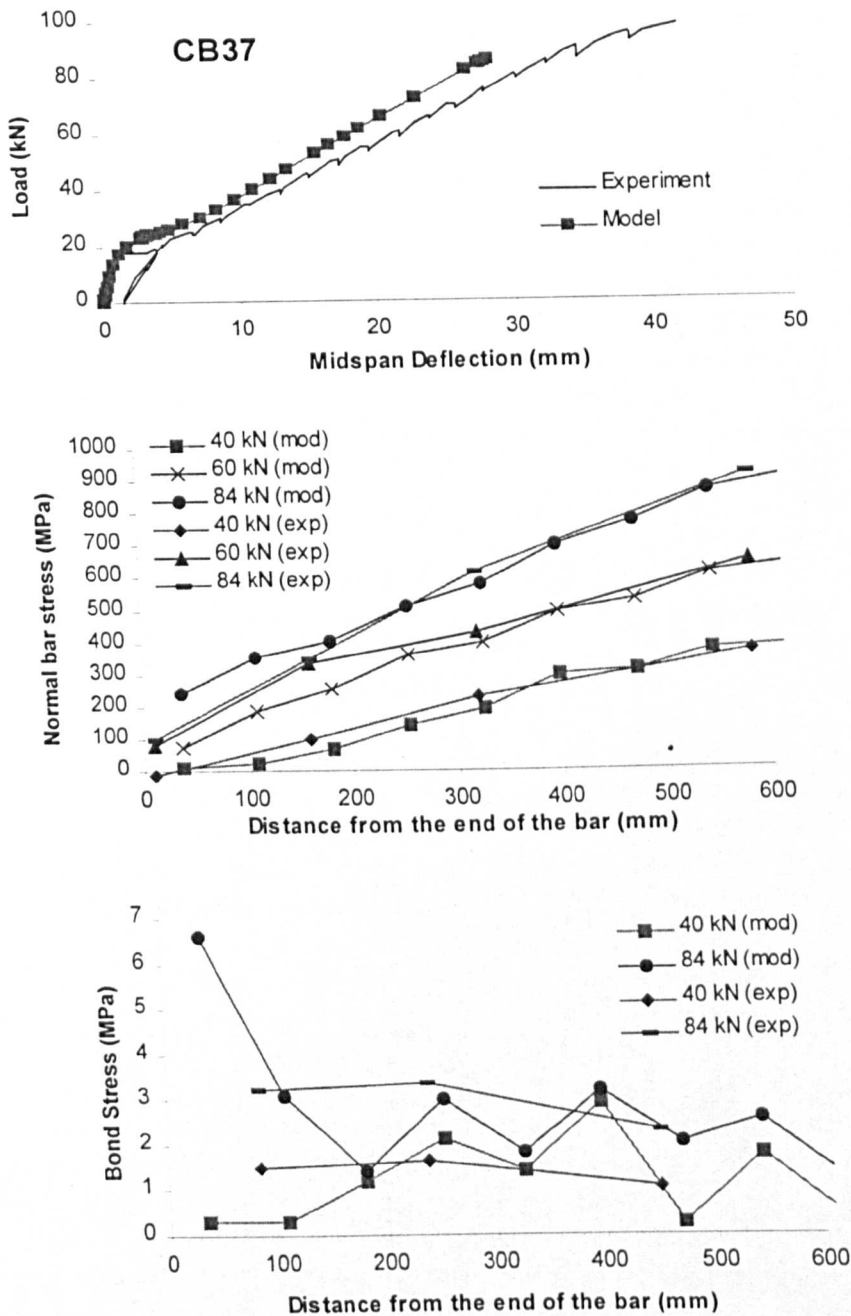


Figure 5.36: Load - deflection curve and normal and bond stress distributions for CB37

By examining the load-deflection curves of both beams, it can be said that they generally follow quite accurately the experimental ones, especially at low load levels. The difference at the ultimate load capacity can be attributed to the incapability of the model beams to sustain additional load after the slippage of the anchorage bar (convergence problems were created), whereas the experimental beams continued to sustain load with the remaining two main reinforcing bars.

The normal bar stress distribution graph of CB32 beam showed that the model predicted fairly accurately the stress value in the constant moment region. However, in

the shear span the experimental stress values appeared to be higher. Nevertheless, it has to be taken into account that the small number of springs used to model the anchorage in this model (only 3 springs) can not facilitate more detailed comparisons. Detailed comparisons should not be made for the distribution of bond stresses, although in this case the model curves (see for example curve Mod. 40kN) predicted quite well the respective experimental ones. Only the large bond value at the very end of the experimental curve could not be predicted by the model because of the relatively large spacing of the springs.

By considering the normal and bond stress distribution in model CB37 beam, similar comments to the above can be made. However in this case, the larger anchorage length and the presence of more springs makes the comparison more accurate. The normal bar stresses both in the constant moment region and in the shear span were predicted quite accurately (see curves at 40 kN), although at higher load levels, close to the bar end, the experimental stress values appeared to be somewhat higher than the analytically predicted ones. This again can be attributed to the smeared crack approach of the FE package as opposed to the discrete cracking that develops in experimental conditions.

Another interesting observation from the graphs of beam CB37 is that the distribution of normal bar stresses is not as “smooth” as it was in the previously reported models, which results to a non-smooth bond distribution along the bar. This is assumed to be related to the small mesh size used in the model that created dependence on the concrete flexural cracking. This, however, does not seem to influence the average bond behaviour of the bar, as it can be seen in the comparisons of the model results with the respective experimental. In addition, the results from modelling the same CB37 beam by using a larger mesh size confirmed this statement (see next section).

### **5.2.3.3 Modelling of CB37 beam by using different mesh size**

In order to validate that the modelling procedure described above does not depend on the spring size used (spring size denotes the size of embedment length whose bond behaviour the spring simulates), beam CB37 was modelled again by using a different mesh size, as shown in figure 5.37.

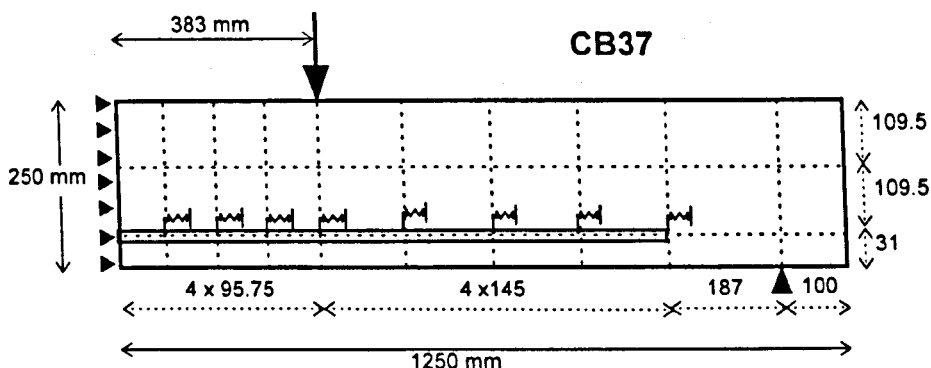


Figure 5.37: New model for beam CB37

All the element and material characteristics were kept the same, except the load - slip curve of the connecting springs that represented the new spring size. The bond stress value of a spring length equal to 145 mm was taken from the graph in figure 5.32, using a similar procedure to the one described in that section (section 5.2.3.1). This value was equal to 4.93 MPa, which corresponds to a load value of 14.2 kN. This load value was used to define the characteristics of the springs and a new solution was obtained.

The model failed due to bond failure at a slightly higher load than the previous one (89 kN instead of 84 kN). This is attributed mainly to inaccuracies in the shape of the regression curve (see figure 5.32), as it was discussed in section 5.2.3.1. The distribution of normal and bond stresses on the anchorage bar of the new model was compared with the respective ones in the previous model. Figure 5.38 shows this comparison which suggests that, as expected, the anchorage bar in both models developed similar bond behaviour.

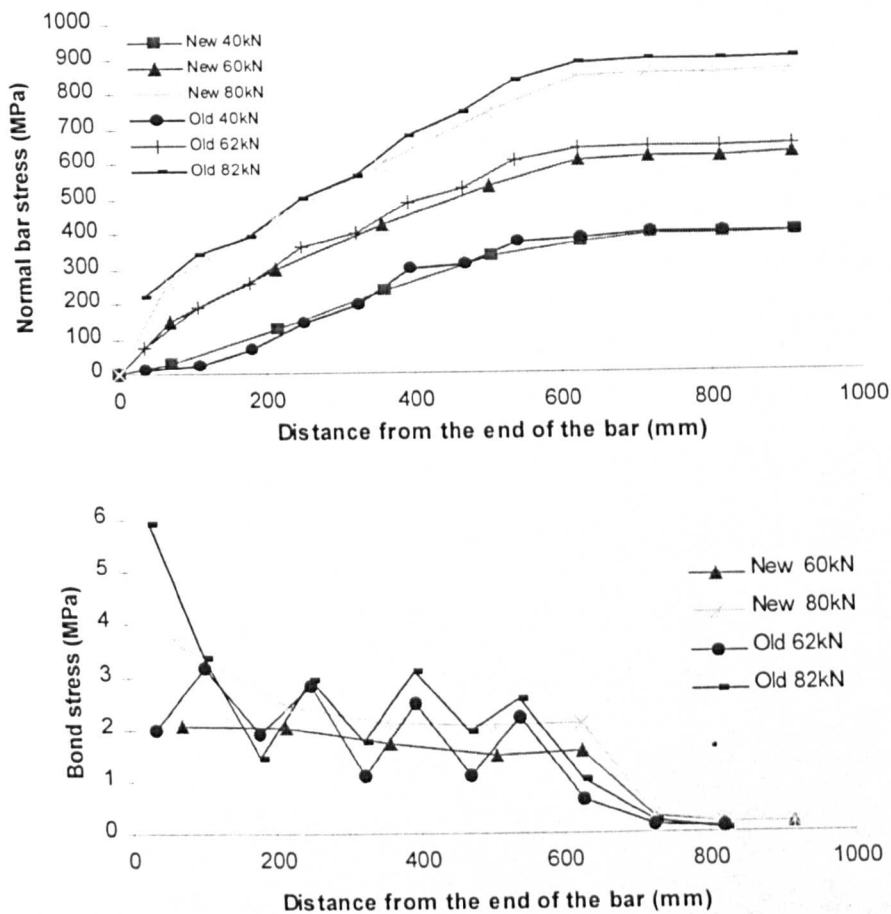


Figure 5.38: Comparison of the stress behaviour of the anchorage bar in beam CB37, by using two different spring sizes

### 5.2.4 Discussion

The analytical approaches examined show promise, since important behavioural aspects of reinforced concrete beams are well predicted. However, it is believed that to achieve further refinements, better constitutive models will have to be developed for modelling concrete in tension and shear. In particular, it is very important when dealing with bond on the micro level to use a discrete crack approach since the effect of cracks was demonstrated in the experimental work to influence the bond demand in a very dramatic manner.

Flexural cracks appear to influence the development of bond on the bar. The negative and positive bond values developed between successive cracks (see sections 4.2.2.7 and 6.3.6.1) reduce the average bond resistance at that region. As a result, the average bond developed in the cracked zone of the beam is significantly lower than the

bond in the uncracked zone. Model CB20 showed that although a reduction in spring values could model the bond strength of the bar in the cracked zone, the much higher bond values developed towards the end of the bar (in uncracked zone) were not possible to be modelled with the same spring characteristics. One approach of modelling this behaviour is to use different types of spring characteristics at the cracked and uncracked zone of the beam. This approach, however, although it might give satisfactory results, deals with bond macroscopically and does not consider the actual bond action on the bar. As a result, the various parameters that influence bond (see section 2.1.3) can not be incorporated in this approach since the spring values will always depend on specific experimental conditions.

An alternative approach to the problem might be to consider the concrete-bar system between successive cracks and examine in more detail the bond development at that region. In this case, the bar would still be connected with springs to concrete, but the springs would have to consider the variation in bond stress at the two crack edges. The results of this system have to be incorporated into an overall beam model, which uses a discrete crack approach to flexure. It is expected that this approach might be able to predict the peak bond values developed on the bar during loading, and give generally more reliable bond behaviour.

As a further step, the bond splitting failure might be able to be incorporated in the above modelling approach. In the method described in section 5.2.3 for modelling the bond splitting behaviour of beams CB32 and CB37, bond development was also examined macroscopically by taking the spring characteristics from experimental beams. Consequently, a dependence of the spring values on certain experimental conditions was apparent.

In order to eliminate this dependence, a more refined modelling approach would have to be introduced. It is known that bond action is accompanied with radial stresses in the surrounding concrete, which might split the concrete cover (see section 2.1.2). Splitting, however, takes place in a plane vertical to the bar axis. So, the model would have to consider a relationship linking bond and radial stresses, so that a certain increase in bond would be accompanied with an increase of the radial stress in the transverse direction. When this stress reaches the splitting strength of the concrete, a splitting crack would have to be developed and the bond strength of the bar would have to decrease.

The above described approach would have to be introduced in the bar-concrete system between successive cracks, so that a more integrated solution could be developed.

In conclusion, it can be suggested that the modelling procedure described for beam elements in section 5.2 enhanced the understanding of how actually bond develops between bar and concrete and highlighted modelling problems that will lead to the development of new approaches to bond splitting. One of these approaches was briefly described above and is expected to form a starting point for future research.

# CHAPTER 6

## GENERAL DISCUSSION

In this chapter, the experimental and analytical results of this study are further compared and discussed. The discussion is focused on both the pull-through and splitting modes of bond failure of FRP bars in concrete. Based on the conclusions of this discussion, relevant design recommendations are presented.

### 6.1 FRP BAR-CONCRETE INTERACTION

The FRP bar-concrete interaction is best described by using the bond versus loaded-end slip curve of a short embedment length subjected to pullout similar to the one used for steel. A typical bond vs. loaded-end slip curve is shown in figure 6.1:

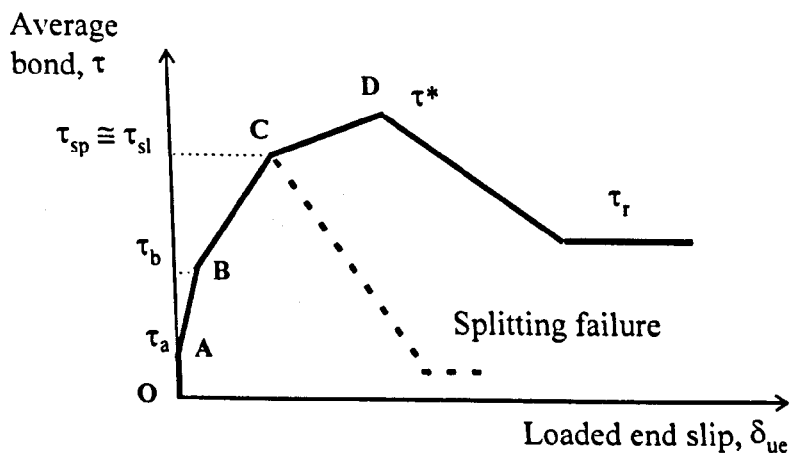


Figure 6.1: Bond - loaded end slip curve of an FRP short embedment

**Section OA:** At the beginning of loading, the main mechanism that resists the external load is the chemical adhesion between the two materials. No measurable slip is observed at this stage. The experimental results of this study showed that the value of adhesive bond,  $\tau_a$ , lies between 0.1 and 1.3 MPa irrespectively of the type of FRP bar and concrete used (see section 4.1.1).

**Section AB:** As the load increases, adhesion breaks and the bond mechanism changes. The slip at the loaded end of the bar gradually increases and the deformations of the bar develop bearing stresses due to their reaction against the surrounding concrete. It is believed that transverse concrete microcracks start to originate at the tips of the bar deformations that allow the bar to slip more. However, since the surface deformations of FRP bars are much “softer” than the deformations of steel bars, it is believed that the initiation of transverse microcracks is relatively delayed. Evidence in literature (Tepfers, 1997) supports this view and suggests that the bond behaviour of FRP bars at this stage is probably better than steel deformed bars.

**Section BC:** At this stage, the bearing forces from the bar deformations to the surrounding concrete increase considerably, as the slip of the bar increases. The resulting direction of these forces is assumed to subtend at an angle  $\alpha$  to the horizontal (see figure 6.2). The value of angle  $\alpha$  is shown later to depend on the value of the elastic modulus of the bar. As explained in more detail in section 6.3.2, the elastic modulus of the bar influences the deformability of the bar inside the concrete and, in parallel, affects the crack geometry and, hence, the concrete shear strength at the location of the crack. Both factors influence the value of angle  $\alpha$  and consequently the bond splitting tendency of the bars.

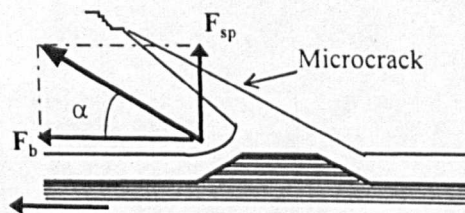


Figure 6.2: Schematic representation of bearing forces induced in the concrete

The radial forces ( $F_{sp}$ ) are balanced against rings of tensile stresses developed in the surrounding concrete (according to figure 2.3 by Tepfers, 1979). If no adequate

confinement is provided to the bar by the concrete cover, and the value of the tensile hoop stress exceeds the tensile strength of concrete, splitting cracks develop along the length of the reinforcing bar. When the splitting crack breaks through the whole concrete cover, the bond fails in a sudden mode without warning of ductile deformation.

The experimental results of this study showed that bond splitting initiates when the unloaded end of the bar starts slipping (see figure 6.1,  $\tau_{sp} \cong \tau_{sl}$ ). The bond splitting value,  $\tau_{sp}$ , can not be easily quantified with respect to the maximum bond strength,  $\tau^*$ , since it depends on many factors such as the size of the embedment length, the experimental stress conditions around the bar (tensile stresses, compressive stresses, confinement etc.) and the concrete cover. In some test cases, the splitting bond stresses over very short embedments (10 mm) were very high (see experimental results of beams CB32, CB37 in figure 5.32 in section 5.2.3.1) and were assumed to be very close to the maximum bond strength of the bar for the same embedment.

*Section CD:* If the splitting resistance of the surrounding concrete is adequate, for example in the case of cube tests, then the bond value can be increased up to the maximum bond strength,  $\tau^*$ . At this stage, both the loaded and unloaded ends of the bar are slipping and the stiffness of the bond is significantly decreased. Depending on the value of concrete strength relatively to the shear strength of the surface bar deformations, two modes of bond failure can be identified for EUROCRETE FRP bars.

- For concrete strengths greater than 35 MPa

The bond failure occurs by shearing off part of the surface deformations of the bar. Consequently, the bond strength of FRP bars in this case is not controlled by the concrete strength, but appears to be governed mainly by the interlaminar shear strength just below the resin rich surface layer (see also section 4.1.2, for more details). So, unlike steel bars, any increase in concrete strength beyond the above limit will not be accompanied by a significant increase in the bond strength of the FRP bar (see figure 4.18 in section 4.1.3.3).

- For lower concrete strengths

For concrete strengths around 15 MPa, FRP bars fail in a mode of failure similar to deformed steel bars. The concrete is crushed in front of the bar deformations and the

bond strength is controlled mainly by the shear strength of the concrete (see also section 4.1.2).

For intermediate values of concrete strength (15 to 35 MPa), there are no available experimental data to show the exact mode of failure of FRP bars, although a combined mode of resin and concrete failure is likely to be developed in this case.

*Section DE:* After the maximum bond stress, the bearing mechanism between bar deformations and concrete corbels breaks and the bond stress decreases considerably. The residual bond strength depends mainly on the frictional resistance,  $\tau_r$ , at the failure interface. The roughness of this interface determines the friction coefficient and consequently the magnitude of  $\tau_r$ .

## **6.2 PULL-THROUGH BOND FAILURE OF FRP BARS**

In this section, the bond failure mechanism of the EUROCRETE bars is examined in more detail. The suitability of the most commonly used pullout cube tests for measuring the bond strength of FRP bars is discussed and some recommendations are proposed. Since the experimental conditions appear to influence the bond behaviour of embedments in concrete, results gathered from different types of test arrangements are compared to examine this influence.

### **6.2.1 Suitability of cube tests for measuring the bond strength of FRP bars**

As it was described in the previous section, the bond failure mechanism of FRP bars can differ significantly from the failure mechanism of steel deformed bars. For this reason, measuring the bond strength of an FRP bar with the conventional pullout tests described in section 2.1.4 must be treated with care. It is important to understand that these test arrangements were primarily designed to compare the bond strength of steel embedments that were expected to fail by crushing the concrete in front of the ribs. With

FRP bars, for most practical concrete strengths, bond failure can take place, at least partly, within the bar's surface.

Figure 2.5 in section 2.1.4 shows the two main types of tests used for evaluating the bond strength of steel bars. Their main difference is the location of the embedment length inside the concrete cube. Various views are expressed in the literature as to which test is better to be used for deformed steel bars. Nevertheless, all the authors recognise that only minor differences exist among the results of those tests. No significant change is expected for the values of  $\tau^*$ ,  $\tau_{sl}$  or  $\tau_r$ .

With FRP bars, however, things appear to be different. Their different mode of failure introduces a dependence of the recorded bond strength to the experimental arrangement used. Since bond failure could take place within the bar's surface, Rehm's experimental arrangement can not be used for measuring the bond of the bar because the undamaged part of the bar that follows the embedded part, enters in the embedment length zone and adds additional resistance to the pullout load (see figure 4.8 in section 4.1.2.1). This results to an increase in the recorded bond values, which do not reflect the real bond characteristics of the bar.

So, in the case of FRP bars an experimental arrangement with the embedded part of the bar lying at the very end of the cube, similar to RILEM test, will be safer to be used for more reliable pullout bond results.

In addition, the use of pullout tests for comparing the bond behaviour of different material bars is also questionable. Experimental results showed that although CFRP and GFRP develop similar bond strengths in pullout cube conditions (see section 4.1.3.1), their bond strength splitting values in beam elements differ significantly. GFRP bars appear to develop less than 75% of the bond strength of similar diameter CFRP bars under identical experimental conditions.

The important conclusion here is that it would be dangerous to assume that two types of bars develop similar bond strengths, based on results from pullout tests, and use this assumption for design purposes in practical applications. Pullout test results appear to be misleading and should not be used for comparing the bond strength of different types of bars.

A third point regarding the suitability of pullout tests in quantifying the bond strength of FRP bars is related to the influence of the experimental conditions on the bond strength value. It is known from tests on steel bars that the experimental conditions in pullout cube tests produce bond values in excess of those used in design (Cairns, 1995). For this reason, the bond strength results gathered from three types of tests, where the FRP bar failed in a pull-through mode of bond failure, are presented in the following sub-section and the influence of the experimental conditions discussed.

### 6.2.2 Influence of experimental conditions on bond strength

In order to study the influence of the experimental conditions on the bond strength of FRP embeddings, three types of tests were examined according to figure 6.3.

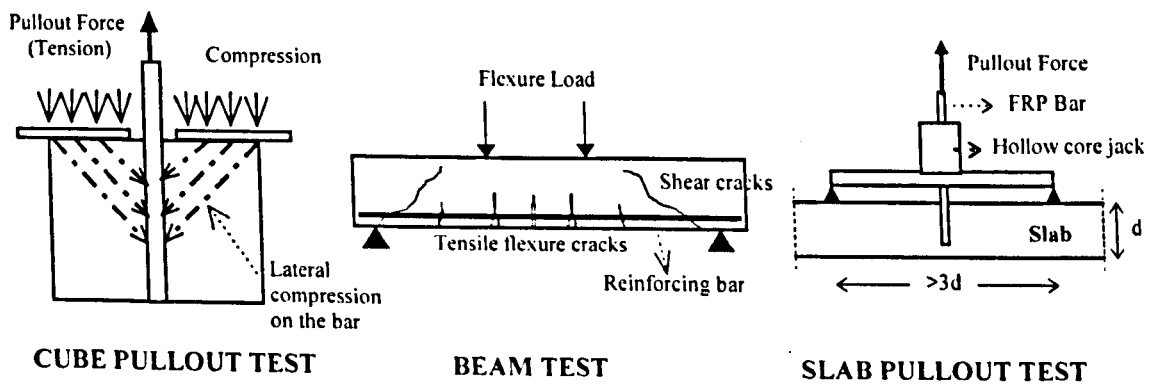


Figure 6.3: Three types of tests where pull-through mode of bond failure occurred

In all the above tests, the reinforcing bar was pulled-through without any indications of splitting. The experimental arrangement and results from the cube and beam tests are presented in detail in chapters 3 and 4, so, here, more emphasis is given on the additional series of slab pullout tests that was conducted by the author as part of another study (Achillides et al, 1996).

In this series, six 13.5 mm GFRP bars were embedded vertically in a 200 mm depth concrete slab, as shown in figure 6.3. The concrete cube compressive strength of the slab was found to be 41 MPa on the day of testing. The GFRP embeddings were

pulled-out by means of a special test rig and a hollow core hydraulic jack. The test rig supports were at a considerable distance from the embedment ( $> 300$  mm) in order not to interfere with the bond development on the bar.

All embedments failed in a pull-through mode of failure by peeling off part of the bar deformations. The experimental results for selected embedment lengths are shown in table 6.1, together with the results of the cube pullout tests at respective embedments.

| Embedment<br>(mm) | Slab tests        |                | Cube tests        |                |
|-------------------|-------------------|----------------|-------------------|----------------|
|                   | Pullout load (kN) | $\tau^*$ (MPa) | Pullout load (kN) | $\tau^*$ (MPa) |
| 80                | 28.2              | 8.3            | 39.8              | 11.6           |
| 120               | 31.6              | 6.2            | 51.9              | 10.2           |
| 200               | 58.4              | 6.9            |                   |                |

Table 6.1: Comparison of experimental results of cube and slab pullout tests

It is obvious from the results above, that the slab pullout tests developed less bond strength than the respective cube tests, and this can be clearly attributed to the different boundary conditions in each experiment.

In cube tests, the bar is subjected to axial pullout load but the adjacent concrete is subjected to normal and lateral compressive stresses from the reaction of the plate on the concrete surface. These stresses act like confinement on the perimeter of the bar and can increase its bond capacity (figure 6.3). On the contrary, in slab pullout tests the surrounding concrete is subjected mainly to mild tension due to the bending action and no normal or lateral compressive forces are developed in the region due to the support action.

In the case of beam elements, although there are no experimental pull-through results for the embedment lengths shown in table 6.1, it is expected that the bond strength of the reinforcing bar will be less than the bond developed in the other cases. There are two reasons for that. Firstly, in beam elements the concrete surrounding the bar is subjected to large longitudinal tensile stresses and, secondly, flexural cracks are expected to influence the development of bond on the bar and affect its overall bond

strength. More details on the effect of flexural cracks on bond development are given in section 6.3.6.

In conclusion, it can be suggested that the bond strength values of FRP bars (for similar type of bond failure) are very dependent on the experimental conditions. The results from the conventional pullout tests, although they give an indication of the maximum bond strength possible to be achieved, they can not be used to predict the bond strength of bars in more practical conditions, such as beams, columns and slabs. On the contrary, the beam type tests similar to those conducted in this study (see section 4.2) reinforced either with single anchorages or spliced bars, can give a reliable indication of the actual bond behaviour of FRP bars. The problem, however, with this type of tests is that they are much more complicated in preparation and thus more capital and resource intensive than the traditional pullout tests. Nevertheless, when suitable instrumentation is applied on the reinforcing bars of these tests, the amount of the experimental effort required will be reduced, according to the working method suggested in section 6.3.7.2 of this study.

## **6.3 SPLITTING BOND FAILURE OF FRP BARS**

### **6.3.1 Experimental evidence**

The splitting mode of bond failure of single anchorage or spliced FRP bars has been examined in phase 4 of the experimental study. The results of this phase are presented in section 4.2.2 and in table E.1.3 in appendix E.1.

The experimental results showed that the CFRP bars develop generally higher bond splitting strengths than GFRP bars under identical experimental conditions (Achillides et al, 1998). This behaviour was quite unexpected since the pullout cube test results, shown in section 4.1.3.1 of this study, suggested that both types of bars develop similar bond strength values.

By considering, for example, the results of beams CB33 and GB36 which were reinforced with the same diameter CFRP and GFRP spliced bars respectively, it can be

seen that CFRP bars develop  $\tau^* = 5.7$  MPa whereas GFRP bars only 4.1 MPa. In addition, the difference in concrete tensile strength between the two needs also to be considered in this comparison. If it is assumed that the concrete tensile strength is proportional to the square root of the concrete cube strength (Tepfers, 1973 - CEB Bulletin 151, 1982 - ACI,1995), then the bond value of the CFRP bars has to be multiplied by a factor equal to  $\sqrt{45}/\sqrt{35}$ . This results to a further increase of the difference among the two values and suggests that GFRP bars develop only 63% of the bond splitting strength of CFRP bars.

Similar conclusions can be drawn by comparing the bond splitting values of beams CB32 and GB34 or even beams GB34 and CB37. In these beams, the comparison is not so straightforward since the single bar anchorages do not have the same length. Nevertheless in both cases, GFRP bars appear to develop considerably lower bond splitting strengths than CFRP bars. It is estimated that GFRP bars developed only around 60 -75% of the bond splitting strength of CFRP bars.

Since from the pullout tests the two types of bars appear to develop the bond stress in a similar fashion, the difference in the bond splitting strength should be attributed to a higher splitting tendency of the GFRP bars. Since the bars are otherwise identical, this tendency should be due to the difference in the Young's modulus between the two materials. In the following section, the importance of the elastic modulus on the bond splitting behaviour of FRP bars is examined in more detail. In addition the effect of the concrete shear stress along the cracks is also considered.

### **6.3.2 Analytical approach to the bond splitting failure**

In order to examine the effect of Young's modulus on the bond splitting strength of a reinforcing bar, the following simplified FE model was analysed by using ANSYS 5.0a. A reinforcing bar was attached on a square concrete block that was constrained at its top side along the vertical and horizontal direction, as shown in figure 6.4. Both bar and concrete were given elastic properties. Element types PLANE42 were used for the concrete (75 mm thickness) and LINK1 for the bar (d=13.5 mm).

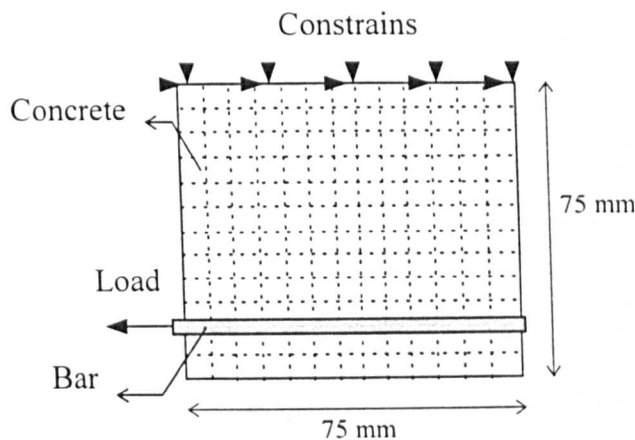


Figure 6.4: FE model for the investigation of the effect of Young's modulus on the bond splitting strength of FRP bars

This model is assumed to simulate the behaviour of an end bar-concrete "system" between successive flexural cracks. This kind of "system" can be found in concrete beam elements reinforced with a single bar anchorage, or it can even be identified with the bar-concrete system between successive microcracks, as shown in figure 2.2. The bar was loaded axially in the horizontal direction and the distribution of stresses normal to the bar axis developed along the bottom side of the bar was monitored. These stresses can be regarded to be the splitting stresses induced by the bar on the bottom concrete cover.

Two solutions were performed by using the above model. In the first one, the bar had the Young's modulus of GFRP bars (45 GPa), whereas in the second solution the bar had the modulus of CFRP bars (115 GPa). The applied load had the same value in both cases (15 kN).

The distribution of stresses normal to the bar axis induced in the bottom concrete cover had the same shape in both models, as shown in figure 6.5. The peak stress however, had a different value for each material. As expected, the peak bond stress value that controls the bond splitting strength of the bar was greater in the GFRP bar. This suggests that GFRP bars can cause higher splitting stresses than CFRP bars under identical pullout load. The ratio between the peak stress of GFRP bar to the peak stress of CFRP bar was calculated to be around 1.16 which means that GFRP bars appear to develop only around 85% of the bond splitting strength of CFRP bars.

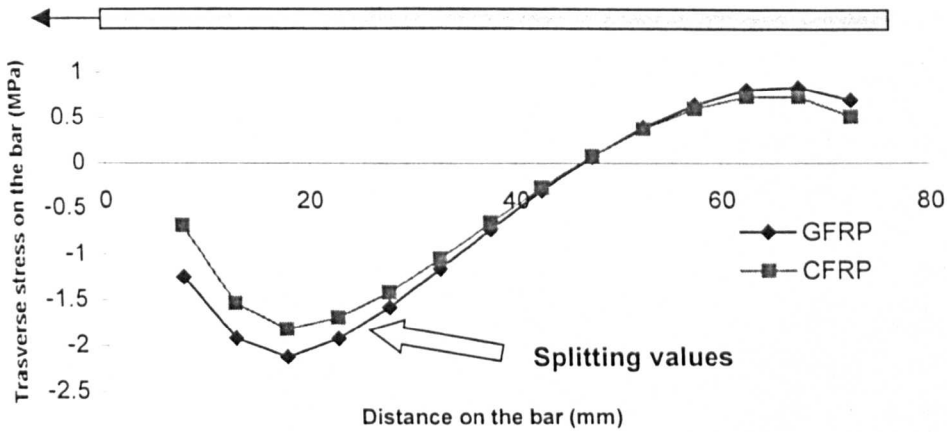


Figure 6.5: Splitting stress distribution along the bar

It is useful to comment at this point that the peak splitting stress develops at the front end of the model whilst in the experiments splitting was observed to develop from the other end. In reality, the bar “slips” relatively to the surrounding concrete due to the pullout load action, which results to the migration of the peak bond stress towards the end of the bar. This example, however, was designed to demonstrate the value of the peak splitting load rather than its location on the bar.

A similar model was used to evaluate the effect of the concrete shear stress along the ends of the block on the bond splitting tendency of reinforcing bars. Shear stresses were added to the two sides of the model, as shown in figure 6.6. These stresses simulate the shear resistance of concrete across cracks that depends mainly on the geometry of the cracks and the deformation characteristics of the concrete block between the cracks. Before the formulation of the cracks, full shear concrete resistance is assumed, whereas as the crack develops, the shear resistance decreases.

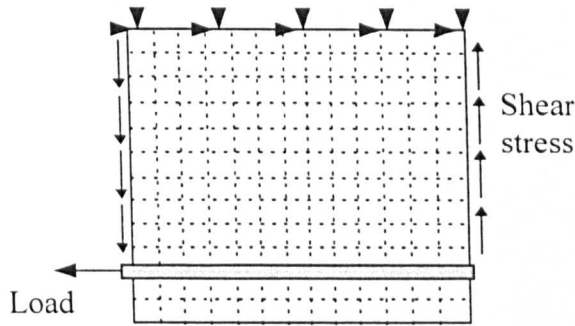


Figure 6.6: FE model for the investigation of the effect of concrete shear stress on bond splitting

Three solutions were performed at different values of shear stress by using the same type of bar (GFRP). The values of the splitting stresses along the bar are shown in the following figure.

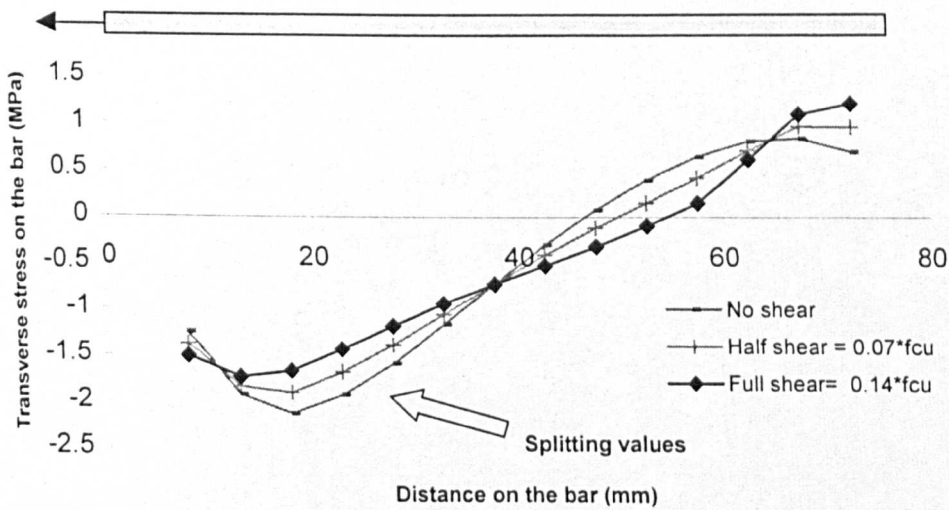


Figure 6.7: Splitting stress distribution along the bar

It can be seen from the above figure that as the concrete shear stress decreases, the peak splitting stress increases, resulting to a higher splitting tendency. This is a very important observation that is also related to the deformability of the reinforcing bar. The concrete shear strength at the crack location depends mainly on the geometric characteristics of the crack (width and length). The crack geometry, however, depends

on the elongation of the bar and this is proportional to the elastic modulus of the bar. So, for example, GFRP bars having a lower elastic modulus than CFRP bars are expected to create wider cracks and, consequently, the concrete shear stress transfer between the cracks will be less. As a result, the splitting tendency of the GFRP bars will be even higher than for CFRP bars.

From the results of the above two modelling studies, it can be concluded that the value of the Young's modulus of reinforcing bars plays an important role in their bond splitting strength. It influences the deformability of the bars inside the concrete and in parallel, it affects the crack geometry and consequently the concrete shear stress at the location of the crack. Both factors influence the splitting tendency of the bars. By considering the effect of both factors GFRP bars are expected to develop less than 80% of the bond splitting strength of CFRP bars which is similar to what was reported in the experimental chapter of this study.

The importance of the shear stress as a likely influencing factor on the bond splitting tendency of reinforcing bars was also reported in the literature by Cairns and Jones (1995, 1996). In their studies, shown in section 2.1.5, they included an additional force,  $F_v$ , to the "classic" equilibrium of forces suggested by Tepfers (1973), which represented the shear stress in the concrete on the inclined bearing surface of the rib, as shown in figure 6.8.

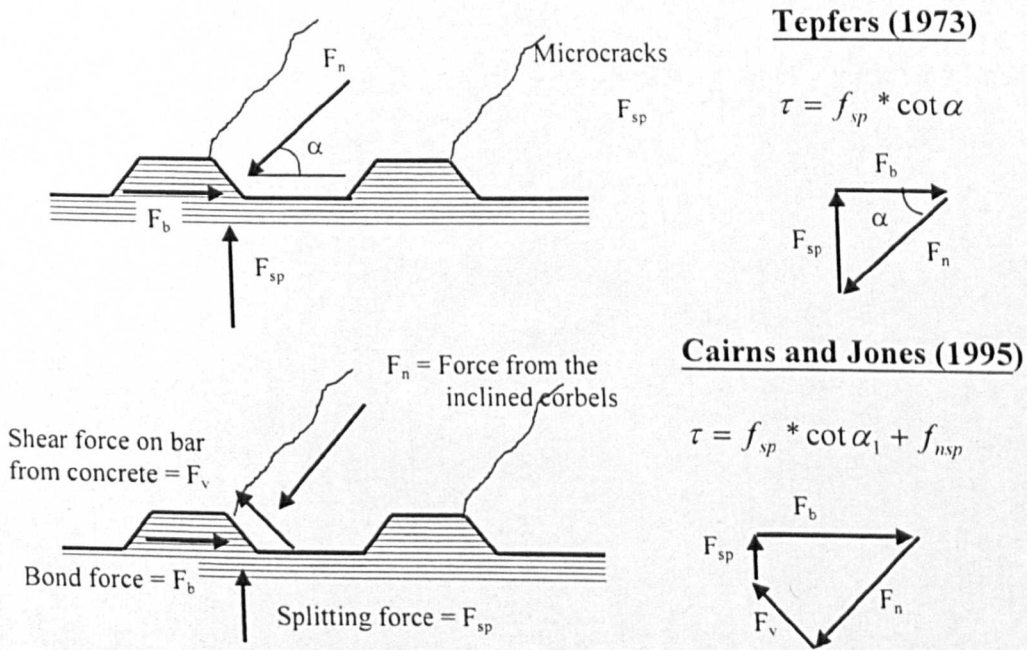


Figure 6.8: Approaches to the bond splitting behaviour of steel bars

The shear stresses due to this shear force require complimentary shear stresses to be developed at the microcrack interface, which are similar to the ones being examined in this study. However, Cairns and Jones implied that this shear force entail only the effect of concrete friction between bar and concrete which is something different to what is suggested in this study.

Tepfers (1973) did not mention in his studies anything about the influence of this concrete shear stress at the microcracks, even though the angle  $\alpha$  of the resultant force,  $F_n$ , and the bar axis, is likely to accommodate this influence (angle  $\alpha = 45^\circ$  for steel deformed bars).

Based on the experience gained in this study and the suggestions of Cairns and Jones (1996), the author resulted to a model that entails the parameters which influence the development of bond and splitting stresses around the bar (figure 6.9). In this model, the equilibrium of stresses in the concrete corbel is considered.

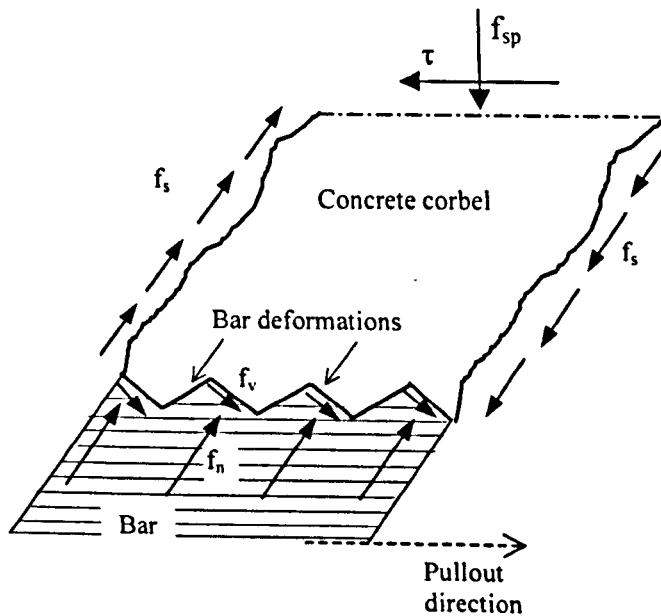


Figure 6.9: Parameters that influence the development of bond and splitting stresses

In this model bond and splitting stresses depend on:

- $f_n$  : the stresses that are induced in the surrounding concrete by the bar deformations, which also entail the effect of the deformability of the bar in the axial and transverse direction
- $f_v$  : the frictional force between bar and concrete induced on the inclined bar surface

- $f_s$  : the concrete shear stresses at the location of the cracks

The bond and splitting stresses act at the edge of the corbel and their distribution along the edge is no longer constant due to the moment introduced by the concrete shear stresses,  $f_s$ . Typical distribution of the splitting stresses,  $f_{sp}$ , was shown in figures 6.5 and 6.7.

The above model suggests that the relationship between  $\tau$  and  $f_{sp}$  can not be expressed in a simple form, as Tepfers (1973) and Cairns and Jones (1995) suggested in their models. The actual values of  $\tau$  and  $f_{sp}$  can be calculated only by solving the corbel stress system at a certain stress stage, since the whole stress system changes during the pullout action. It is also important to note that in the above model any change in the bond strength of the bar, due to a change in  $f_s$  or  $f_v$ , is not necessarily accompanied with a change in the direct splitting component,  $f_{sp}$ .

In the following, the “classic” bond splitting model, introduced by Tepfers (1973), is used in order to estimate the angle  $\alpha$  for the G and CFRP bars, by using the experimental results of this study. It is expected that the value of angle  $\alpha$  will be different for the two materials, which will further confirm the importance of the Young’s modulus on the bond splitting behaviour of these bars.

### 6.3.3 Estimation of angle $\alpha$ for GFRP and CFRP bars

The procedure of calculating the exact value of angle  $\alpha$  is generally quite difficult and unreliable. In the case of deformed steel bars various values were suggested (Tepfers, 1973 - Cairns and Jones, 1995 - Eligehausen, 1979 - Tepfers and Olsson, 1992 - Orangum et al, 1972) lying in the range of 26 and 72 degrees.

In order to be able to evaluate a value of angle  $\alpha$  for the FRP bars, the author relied on the bond splitting results of the phase 4 beam tests. In these tests, all the single anchorage bars had a strain gauge attached at their very end, as shown in appendix B. The readings of these gauges provided the normal strain on the bar at the time of splitting and, consequently, the local bond stress was evaluated, by using equation 3.3. Splitting was assumed to initiate at the load level just after the strain at the end of the

bar reached its maximum value. This assumption was also confirmed by observations during the testing procedure, by monitoring the load level at the initiation of splitting.

The local bond splitting values were introduced in Tepfers (1973) partly-cracked elastic and uncracked plastic bond splitting models (see equations 2.3 and 2.4) and the value of angle  $\alpha$  was calculated for each bar. Both models were used, since indications in literature suggested that the “real” bond splitting strength falls between Tepfers plastic and partly cracked elastic models (Den Uijl and Bigai, 1996).

The influence of the transverse reinforcement (vertical and horizontal legs of shear links) was also considered. For this reason, the readings of the strain gauges attached on the legs of shear links, at the time when splitting initiated, were used. The readings of all strain gauges in beam tests can be found in detail in appendix E.3. When no strain gauges were attached to the leg that was crossing the splitting crack, the concrete tensile strain ( $\cong 100$  micro) was assumed in the links. The author acknowledges that this simplified assumption does not represent the exact experimental conditions in every beam tested. Since all the single anchorage bars lie in the shear span of the beams, certain load is anticipated in the vertical legs of the shear links of the anchorage region, and consequently in the horizontal legs too.

The results of this study are presented in tables 6.2 and 6.3. The equations used for the calculation of angle  $\alpha$  were the following:

$$\text{Partly cracked elastic: } \tau * \tan \alpha * d = \frac{c + d / 2}{1.664} * f_{ct} + \frac{A * \varepsilon_f * E_G}{s} \quad (6.1)$$

$$\text{Uncracked plastic: } \tau * \tan \alpha * d = 2 * c * f_{ct} + \frac{A * \varepsilon_f * E_G}{s} \quad (6.2)$$

where,

$\tau$  = the experimental bond splitting stress at the end of the bar (MPa)

A = the area of the leg of the GFRP shear link crossing the crack

$\varepsilon_f$  = the strain in the leg of the GFRP shear link

and the rest symbols according to general notations

It can be seen from the tables that the results, despite their variation, are relatively consistent. As expected, the value of angle  $\alpha$  was much greater in GFRP bars than in CFRP bars at the time of splitting which can explain the higher splitting tendency of GFRP bars. Based on these results, it can be suggested that the value of angle  $\alpha$  for GFRP bars lies between 47° to 69° degrees, whereas for CFRP bars lies between 29° and 54° degrees. The author acknowledges at this point that much more experimental work is needed to establish more reliable values for angle  $\alpha$ , although the above results can give a reasonable indication of the difference between the two materials.

Table 6.2: Study using the Partly-Cracked Elastic model of Tepfers, 1973

| Beam | Experimental data                   |                              |                            |  |                 |   |  | Results      |                      |   |
|------|-------------------------------------|------------------------------|----------------------------|--|-----------------|---|--|--------------|----------------------|---|
|      | Bar location -<br>splitting pattern | Concrete<br>cover,<br>c (mm) | Bar<br>diameter,<br>d (mm) | Concrete<br>tensile<br>strength<br>(MPa) | $\tau$<br>(MPa) | Microstrains in<br>shear links<br>crossing the<br>crack | Link<br>contribution<br>to splitting<br>(N/mm) | tan $\alpha$ | angle $\alpha^\circ$ | average $\alpha$ ,<br>standard<br>deviation                       |
| GB29 |                                     | 25                           | 13.5                       | 2.8                                      | 5.50            | 100   | 2.4  | 0.752        | 36.9                 | }<br>}  |
| GB30 |                                     | 25                           | 13.5                       | 2.8                                      | 3.53            | 100   | 2.4  | 1.17         | 49.5                 | }<br>}<br>} $\alpha = 47.6^\circ$<br>} $\sigma_{n-1} = 9.6^\circ$ |
| GB34 |                                     | 25                           | 8.5                        | 3.2                                      | 7.07            | 100   | 2.4  | 0.975        | 44.3                 | }<br>}  |
| GB35 |                                     | 20                           | 8.5                        | 3.2                                      | 7.80            |   | 66.7   | 1.709        | 59.7                 | }<br>}  |
| CB32 |                                     | 25                           | 8                          | 2.8                                      | 14.32           | 100   | 2.4  | 0.446        | 24.1                 | }<br>} $\alpha = 29.0^\circ$<br>} $\sigma_{n-1} = 6.8^\circ$      |
| CB37 |                                     | 25                           | 8                          | 3.2                                      | 15.80           |   | 29.0   | 0.670        | 33.8                 | }<br>}  |

Table 6.3: Study using the Uncracked Plastic model of Tepfers, 1973

| Beam | Experimental data                |                        |                      |                                 |              |  |                                       |              |                      |  | Results |  |  |
|------|----------------------------------|------------------------|----------------------|---------------------------------|--------------|--|---------------------------------------|--------------|----------------------|--|---------|--|--|
|      | Bar location - splitting pattern | Concrete cover, c (mm) | Bar diameter, d (mm) | Concrete tensile strength (MPa) | $\tau$ (MPa) | Microstrains in shear links crossing the crack | Link contribution to splitting (N/mm) | tan $\alpha$ | angle $\alpha^\circ$ | average $\alpha$ , standard deviation  |         |  |  |
| GB29 |                                  | 25                     | 13.5                 | 2.8                             | 5.50         | 100  | 2.4                                   | 1.918        | 62.5                 | }<br>}                                 |         |  |  |
| GB30 |                                  | 25                     | 13.5                 | 2.8                             | 3.53         | 100  | 2.4                                   | 2.988        | 71.5                 | }<br>}<br>} $\alpha = 68.7^\circ$      |         |  |  |
| GB34 |                                  | 25                     | 8.5                  | 3.2                             | 7.07         | 100  | 2.4                                   | 2.702        | 69.7                 | }<br>}<br>} $\sigma_{n-1} = 4.2^\circ$ |         |  |  |
| GB35 |                                  | 20                     | 8.5                  | 3.2                             | 7.80         |  | 66.7                                  | 2.936        | 71.2                 | }<br>}                                 |         |  |  |
| CB32 |                                  | 25                     | 8                    | 2.8                             | 14.32        | 100  | 2.4                                   | 1.243        | 51.2                 | }<br>} $\alpha = 53.7^\circ$           |         |  |  |
| CB37 |                                  | 25                     | 8                    | 3.2                             | 15.80        |  | 29.0                                  | 1.495        | 56.2                 | }<br>} $\sigma_{n-1} = 3.5^\circ$<br>} |         |  |  |

### 6.3.4 Radial stresses induced by splices in the surrounding concrete

When splices are axially loaded, they impose radial pressure to the surrounding concrete that can lead to splitting (CEB Bulletin 151, 1982). The most known distributions of radial stresses around spliced steel bars were introduced by Tefpers (1973), Reynolds (1982) and Cairns and Jones (1995) and are shown in figure 6.10 (see also section 2.1.6.2 for more details). The first two distributions (Tefpers1, 2) were deducted analytically, whereas the other two were based mostly on experimental results.

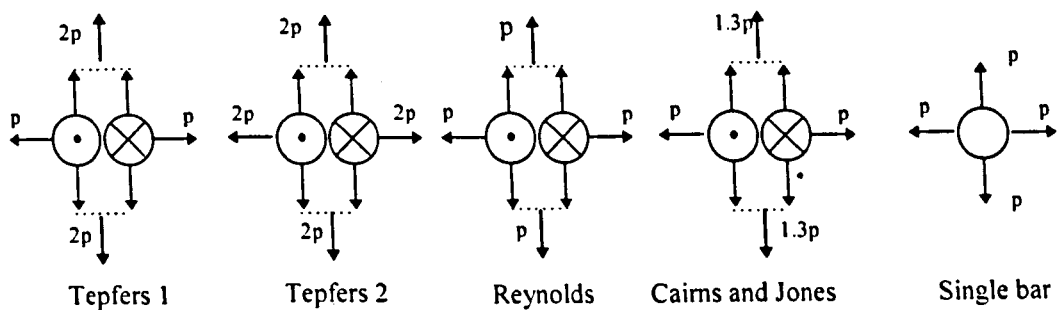


Figure 6.10: Distribution of stresses around splices

In the experimental part of this study, three beams (GB31, CB33 and GB36) were reinforced with FRP bars having their spliced length in the constant moment region, as shown in appendix B. The summary of their results are shown in table E.1.3 in appendix E.1.

In order to assess the distribution of splitting stresses around the spliced bars, their results were compared with respective results from single anchorages. In the following study, the bond stresses developed are assumed to be directly proportional to the radial stresses induced in the surrounding concrete, similar to the relationship suggested by Tefpers (see figure 6.8).

Firstly, the spliced bars in beam GB31 were compared with the single anchorage bar in beam GB30, since both beams were reinforced with 13.5 mm diameter bars, having the same anchorage length (300 mm) and similar concrete strength. The contribution of transverse reinforcement in either case was assumed to be insignificant, based on the experimental results reported in chapter 4. In figure 6.11, the arrangement of reinforcement and the failure crack pattern are shown for both beams.

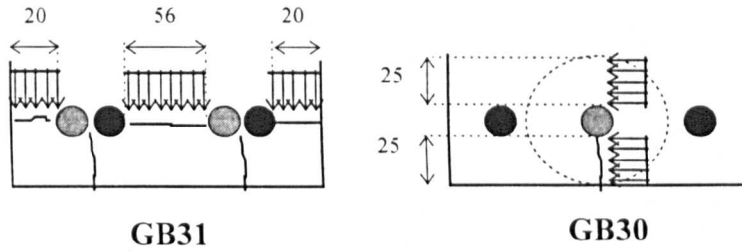


Figure 6.11: Reinforcement arrangement and crack pattern in beams GB31 and GB30

The spliced bars developed bond strength at failure equal to 3.8 MPa, whereas the single anchorage in beam GB30 developed 2.7 MPa. By comparing the size of the concrete failure line, resisting splitting in each case (marked with the stress blocks), it can be suggested that in spliced bars the failure line is approximately double than in the single bar anchorage ( $106 \text{ mm} \cong 2 \times 50 \text{ mm}$ ). If Tepfers radial stress distribution vertical to the plane passing through the axes of the bars was considered to be valid, the bond strength developed in each spliced bar should have had half the value of bond strength developed in the single anchorage. On the contrary, the bond strength developed in spliced bars has a much greater value than the bond strength of the single bar. This appears to suggest that the pair of spliced bars split much less (only 70%), than a single anchorage bar. However, the author regards this conclusion relatively unreliable especially if it is compared with the conclusions drawn from the following two comparisons. It is believed that a more realistic conclusion is that the pair of spliced bars splits equally with a single anchorage bar.

The second comparison is between beams CB33 and CB32. Both beams are reinforced with 8 mm CFRP bars having the same anchorage length (300 mm) and similar concrete strengths. Figure 6.12 shows the arrangement of reinforcement in the beam cross-section and the crack pattern in this case.

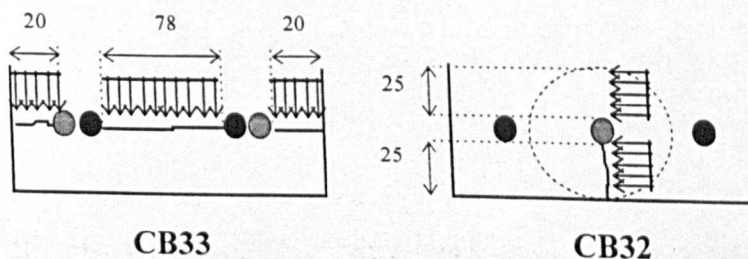


Figure 6.12: Reinforcement arrangement and crack pattern in beams CB33 and CB32

The spliced bars in beam CB33 developed bond strength equal to 5.7 MPa whereas the single bar anchorage in beam CB32 developed only 4.6 MPa. The concrete failure line resisting splitting in CB33 was 118 mm, which was greater than the double value of the concrete line in CB32 (50 mm). In order to compare the two cases, the bond strength value of beam CB33 has to correspond to a concrete failure line equal to approximately 100 mm ( $= 2 \times 50$  mm). For this reason, the bond strength developed in splices (5.7 MPa) is multiplied by the ratio  $100/118$ , resulting to a bond value of 4.8 MPa. It can be suggested that this bond value is very similar to the bond splitting value of the single anchorage in beam GB32, which implies that the pair of spliced bars splits equally with a single anchorage bar.

The third comparison is conducted between beams GB36 and GB34. Both beams are reinforced with 8.5 mm GFRP bars and have similar concrete strengths. The anchorage length in beam GB34 was equal to 370 mm, whereas the spliced length in beam GB36 was equal to 300 mm. Figure 6.13 shows the arrangement of reinforcement in the beam cross-section and the crack pattern developed in each case.

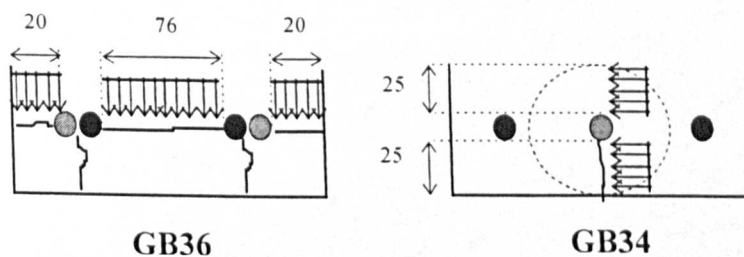


Figure 6.13: Reinforcement arrangement and crack pattern in beams GB36 and GB34

After following a similar procedure to the one described in the previous examples for establishing similar concrete failure lines in both cases, the spliced bars in beam GB36 appear to develop bond splitting strength equal to 3.5 MPa, whereas the single bar anchorage in beam GB34 developed 3.2 MPa. In addition, if the difference in the anchorage length is considered, the bond value of the single anchorage is expected to be somewhat higher, closer to the value reported for the spliced bars.

The above results confirm the distribution of radial stresses proposed by Reynolds (1982) and other researches, such as Orangun, Jirsa and Breen (1977), who

supported that spliced bars and single anchorages develop similar bond splitting stresses.

### **6.3.5 Additional factors that influence the bond splitting behaviour of FRP bars**

#### *Transverse reinforcement*

The experimental results of spliced bars showed that the shear links lying in the spliced region did not contribute significantly in resisting the bond splitting mode of failure. More specifically, no strain was detected in the shear links in beam CB33 before the beam reached its maximum capacity (see figure 4.47). In the case of the other two beams (GB31 and GB36), the links reacted just before the maximum load level, but their contribution to the splitting bond failure was very small, since the stresses developed in the vertical legs of the links were less than 35 MPa (figures 4.36, 4.47). On the contrary, after the development of splitting cracks and the failure of the splice, the links helped the spliced bars to sustain some load and created a “pseudo-ductile” behaviour to the beam (see figures 4.35 and 4.46).

The above observations suggest that the links lying in a constant moment region do not influence the initiation of splitting cracks due to the low strain at which tension cracks form in the concrete. Similar observations were reported in the CEB Bulletin 151 (1982) for the splitting behaviour of steel deformed bars. However, it is believed that if the links were lying in the shear span resisting the shear load of the beam, their contribution would have been more beneficial, as it happened in the case of the single anchorage bar in beam GB35. In this case, the anchorage bar was lying in the shear span of the beam and the vertical leg of the link contributed to the splitting resistance of the surrounding to the bar concrete (see figure 4.50). As a result, the local bond splitting stress of the bar at the location of the link was higher than the respective stresses in GFRP anchorage bars in other beams (see values of  $\tau$  in table 6.2).

It can be concluded that shear links (transverse reinforcement) can possibly enhance the splitting resistance of the surrounding to the bar concrete, only when they are already stressed (for example, located in the shear zone of the beam). Otherwise, the initiation of splitting cracks does not seem to be influenced by the presence of shear

links. However, after the initiation of splitting cracks, the transverse reinforcement restrains the crack opening and contributes to the splitting bond strength of the reinforcing bar.

### *Concrete cover*

In steel reinforced concrete structures the role of the concrete cover has to perform the following functions (Handbook to BS 8110, 1985):

- provide adequate bond between steel and concrete for load transference
- protect the steel from corrosion
- protect the steel from fire

The two factors relating to the external environmental conditions are usually more critical than the bond factor, and dictate the size of the concrete cover.

The situation with FRP bars, however, appears to be quite different. It was demonstrated in the experimental and analytical study presented in the previous sections, that GFRP bars induce splitting at a lower bond stress than CFRP bars. If the assumption that the lower Young's modulus materials will induce higher splitting stresses is accepted, then it is expected that both materials will split more than steel deformed bars. In addition, steel bars are usually bent on site to provide the necessary anchorage resistance, whereas bends are not recommended for FRP bars. The development of splitting cracks in the case of bent bars is delayed and even if a splitting crack initiates, it is not crucial for the structural integrity of the structure, since the bend provides adequate anchorage.

By considering the above, the role of cover providing adequate bond between bar and concrete appears to be much more critical in the case of FRP reinforcement and may be the controlling factor governing the design of concrete cover in certain types of structures.

The size of the concrete cover will also depend on the utilisation of the tensile strength of FRP bars in the concrete structures. There is no point in providing adequate cover to sustain the full utilisation of an FRP bar when this is not going to happen in practice due to serviceability constraints.

### *The role of the beam support (active pressure)*

The role of the beam support to the bond splitting strength of FRP bars is discussed based on the experimental results of beams CB20 and CB37. CB20 was reinforced with 13.5 mm CFRP bars having an anchorage length of 867 mm and bottom/side concrete cover around 1.5/1.9d, whereas CB37 had an 8 mm CFRP single anchorage bar of 580 mm length and a bottom concrete cover around 3d. Under a similar mode of bond failure, the bar in CB37 beam would be expected to develop higher bond strength than the bar in CB20. This, however, did not happen in practice, since the bar in CB20 not only developed higher bond strength (4.2 MPa instead of 3.7 MPa of bar in CB37) but also failed in a pull-through than a splitting mode of bond failure. The main difference between the two cases was that the bar in CB20 extended over the support which seems to have contributed significantly to the bond strength of the bar.

The support action in this case prevented the splitting of the concrete cover and forced the bar to fail in a pull-through bond failure at a higher load. As shown in figure 6.14, the vertical pressure from the support prevented horizontal splitting whereas the frictional stress between concrete and support prevented the vertical splitting.

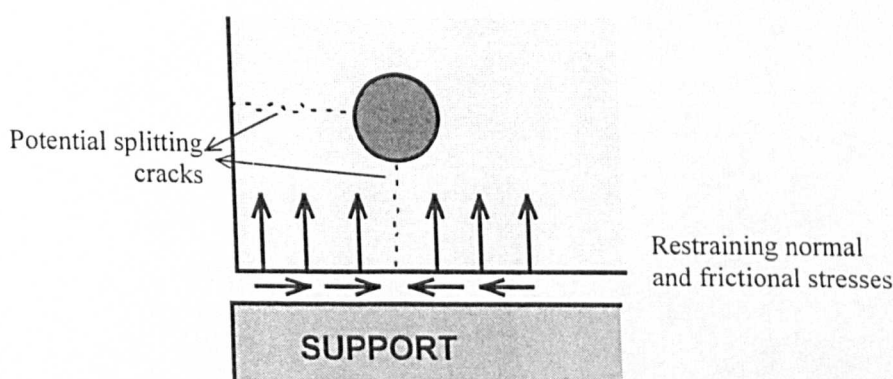


Figure 6.14: Influence of support to the initiation of potential cracks

However, the experimental results do not provide enough evidence as to whether the pull-through bond strength at the bar-concrete interface was also increased from the support action. Evidence in the literature (Malvar, 1994 and 1995 and Tepfers, 1997) suggests that the transverse pressure is less efficient for anchoring FRP bars than

for steel bars, before any splitting cracks are initiated in the concrete. This may be attributed to the lower modulus of elasticity in the transverse direction of FRP bars, which means that the transverse pressure will be dissipated near the bar surface.

### **6.3.6 Influence of flexural cracking on the distribution of bond stresses over the anchorage bar in beam elements**

#### **6.3.6.1 Distribution of normal and bond stresses between successive cracks**

The distributions of normal and bond stresses between successive cracks were examined experimentally in beams CB37 and GB34 and are shown in figures 4.56 and 4.53 respectively.

In order to understand the shape of these distributions the following simplified model is considered:

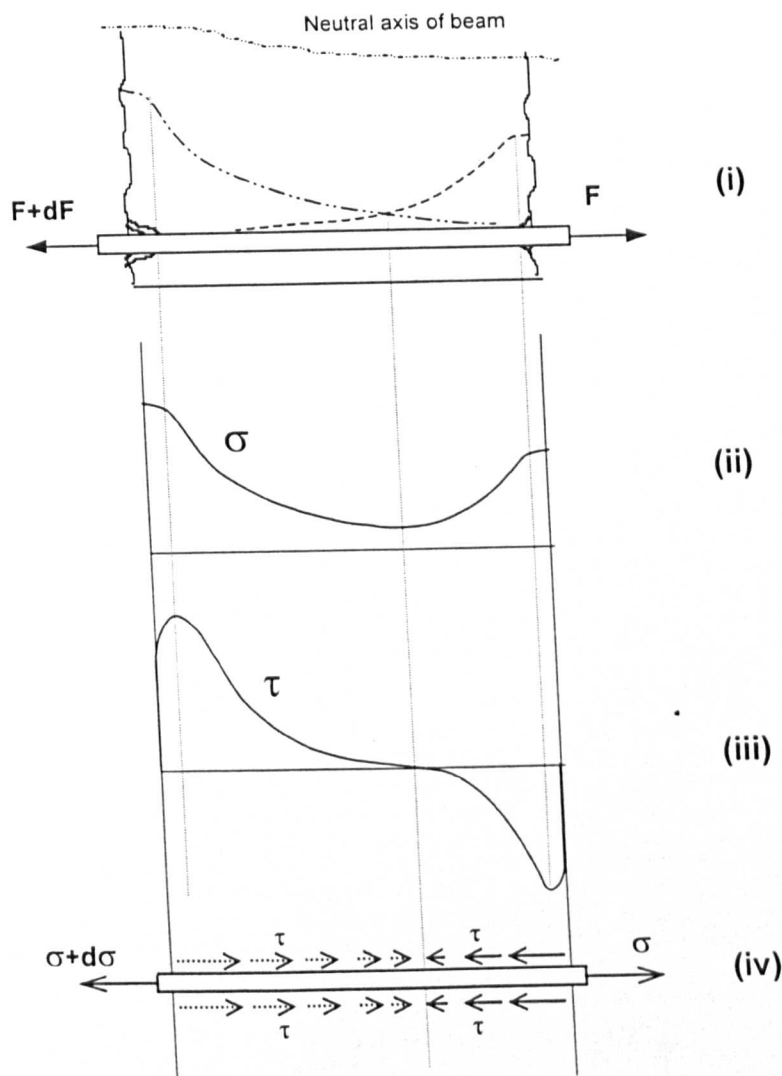


Figure 6.15: Typical strain and bond stress distributions between successive flexural cracks

In this model, the part of the bar-concrete system between two relatively close flexural cracks is examined. The two ends of the bar are subjected to pullout forces. The force closer to the middle of the beam has a higher value ( $F+dF$ ) than the other. Both forces create stress distributions inside the concrete, similar to the one reported in the analytical study for pullout specimens (see section 5.1.2.2). Due to the large stress demand adjacent to the cracks imposed by the large difference in the cross-sectional properties, a cone type cracking is also probable to be developed locally at the very end of the bars, as shown in the above figure.

The resultant normal stress distribution on the reinforcing bar between the cracks is shown in graph (ii) of the same figure. It has the same shape and value as the stress

distributions created by the pullout forces at each side of the bar. The bond stress distribution can then be deduced, since bond is proportional to the rate of change of normal stress on the bar. Graph (iii) in figure 6.15 shows an indicative bond stress distribution between successive cracks.

It can be seen that the bond stress distribution entails both positive and negative values. This is justified by the fact that bond stress has opposite signs at the two ends of the bar in order to resist the pullout forces (graph iv). The average bond stress developed between the two cracks is proportional to the area enclosed by the bond curve and the axis, which is substantially lower than the peak values. This results to relatively low average bond strength, comparable to the average bond strength that can be developed in a direct pullout cube test. The difference in normal stresses at the two ends ( $d\sigma$ ) and the distance between the two cracks determine the value of the average bond strength between cracks.

The above theoretical approach confirms the normal and bond stress distributions obtained in the experimental beams GB34 and CB37. Figure 6.16 shows typical distributions from beam CB37.

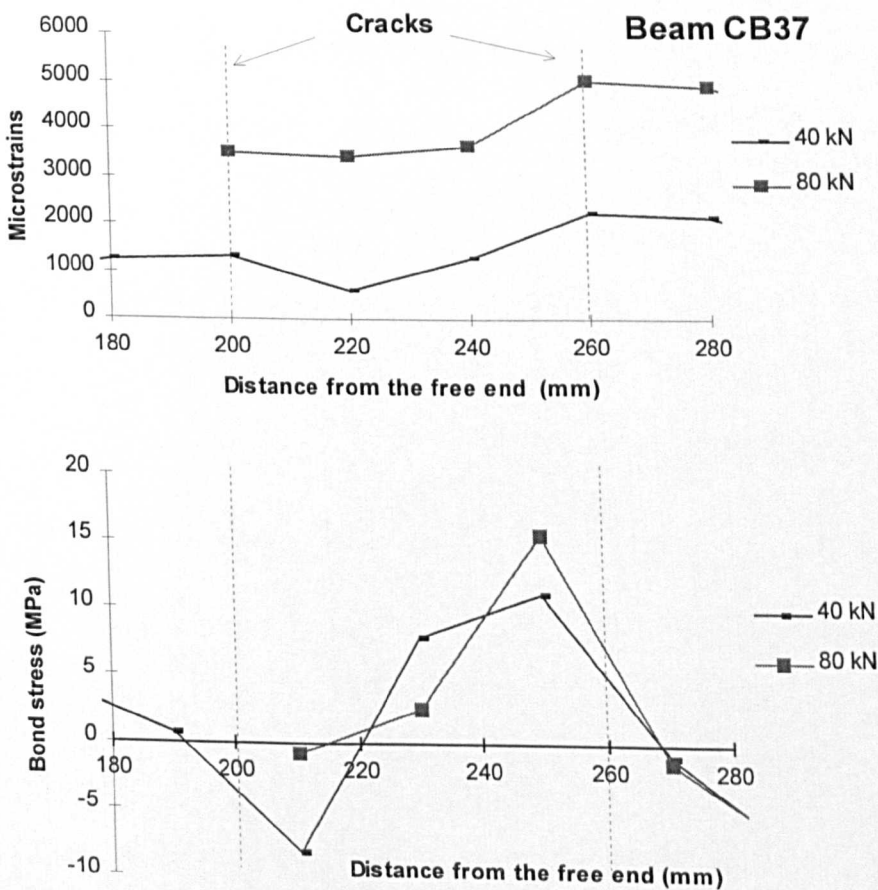


Figure 6.16: Experimental distributions between successive cracks in beam CB37

### 6.3.6.2 Influence of flexural cracking on the bond development over the anchorage length

The distribution of bond stress along a single anchorage bar is influenced by the development of flexural cracks in the beam elements. In order to present this effect, the distribution of bond stresses in beams CB20, CB37 and GB29 are considered.

Beam CB20 failed due to a pull-through mode of bond failure and the distribution of bond stresses along the anchorage length is shown in figure 6.17:

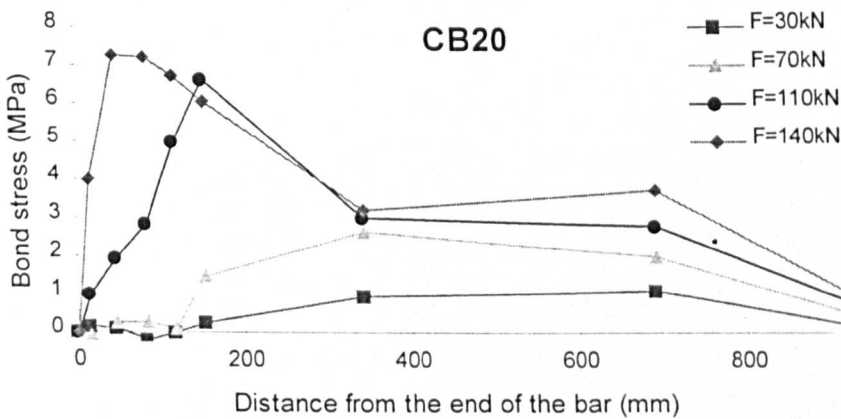


Figure 6.17: Bond distribution over the anchorage length in beam CB20

In this distribution, the peak bond stress migrates from the loaded end towards the unloaded end of the bar. The maximum bond value develops at the end of the bar whereas the peak values in the cracked zone of the beam (a range between 250 mm up to the midspan) are significantly lower.

The difference between the peak values can be attributed to the flexural cracking of the beam. If the beam did not crack and behave in a completely elastic manner, the peak bond value would have been expected to retain the same value as it migrated towards the end of the bar, similar to the distribution of bond stresses shown in figure 5.11 in section 5.1.2.3 of the analytical study.

As it was explained in the previous section, the average bond stress developed between successive cracks is relatively low. As a result the peak bond demand moves towards the uncracked parts of the beam in order to develop the required resistance to the pullout load. At higher load levels ( $F=110$  kN), the only uncracked parts are located

close to the end of the beam where the peak bond stress manages to develop higher values.

A similar bond stress distribution was obtained also in beam CB37 (see figure 6.18). Although beam CB37 failed in bond splitting, its bond distribution shows an agreement with the bond distribution in beam CB20, up to the failure load (load level 80 kN).

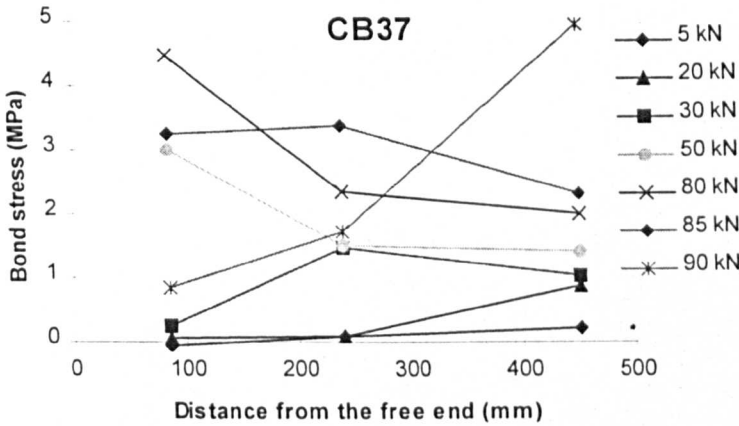


Figure 6.18: Bond stress distribution in beam CB37

The peak bond stress also migrates towards the end of the bar as the load increases, and the maximum peak bond value develops only at the very end of the bar, similar to what was reported for beam CB20. However, when the peak bond stress reaches the bond splitting resistance of the concrete cover the first crack initiates at the end of the bar and the peak bond value decreases immediately. With a further increase of the load, the end part of the bar has already split and the peak bond migrates back towards the midspan of the beam (load levels 85, 90 kN).

- *Anchorage of bars lying entirely in the cracked zone*

Most of the phase 4 beams had the single anchorage bar lying entirely in the cracked beam zone. A typical graph of the bond distribution in one of those beams is shown in figure 6.19.

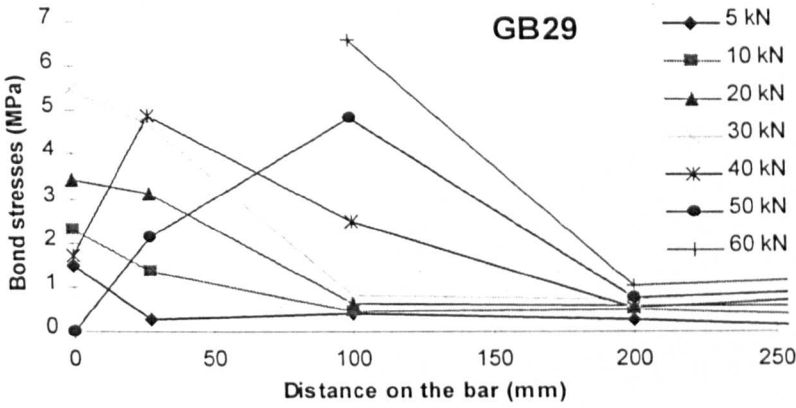


Figure 6.19: Bond stress distribution in beam CB29

In this case, the peak bond stress developed at the very end of the bar from the beginning of loading. This was attributed to the flexural cracking behaviour of the beam, as shown in figure 6.20. Since the average bond strength developed between the cracks is relatively low, the bond resistance has to be activated over the whole anchorage length even at low load levels.

This results to the concentration of the bond demand at the very end of the bar, as it can be seen in figure 6.19. When the peak bond value reaches the bond splitting strength of the concrete cover, a splitting crack initiates and the peak bond stress at the end of the bar drops immediately. The peak value then migrates towards the loaded end ahead of the splitting crack (see also section 4.2.2.1).

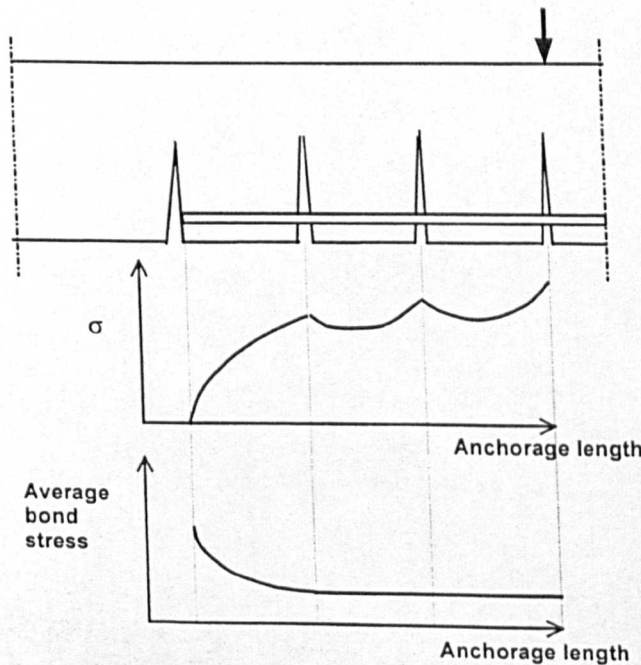


Figure 6.20: Normal stress distribution over the anchorage length

### 6.3.7 Discussion towards design recommendations and future work

In this section, some thoughts are presented regarding the design of anchorage lengths for FRP reinforcing bars in concrete structures. Since the amount of the experimental and analytical work conducted in this study is relatively limited, no final design recommendations can be concluded. The author, however, will try to address some important issues regarding the design of anchorages and suggest a method of working based on the experimental results of this study, where future results can be added towards the formulation of a design code of practice.

#### 6.3.7.1 Parameters to be considered in the formulation of an anchorage length formula for FRP bars

By considering the experimental results of this study, two are the main types of bond failure that were observed; the pull-through and the splitting mode. Among the two, the splitting mode of bond failure appears to be more dangerous, since it happens at lower load levels. Hence, the formulation of any design recommendations is safer to be based on the bond splitting strength of FRP bars, rather than their pull-through bond strength. Nevertheless in certain circumstances, for example, when the bar passes above a support or when a large concrete cover is provided to the bar, the design bond strength of the anchorage can be increased since bond splitting can be prevented.

The bond splitting strength of FRP bars is affected by a series of parameters, the influence of which is necessary to be investigated before the formulation of any design codes. Some of these parameters were examined in this study, although more experimental work is needed to establish more integrated relationships between them and the bond splitting behaviour of FRP bars. The most important of these parameters are briefly presented underneath:

- *Elastic modulus of bar*

The Young's modulus of the bar appears to play an important role to the bond splitting strength of the bar. Bars with lower elastic modulus (e.g. GFRP bars) tend to develop higher splitting stress than higher modulus bars (e.g. CFRP bars). The incorporation of the effect of Young's modulus in the anchorage length formulas is recommended. This approach was adopted by the draft Guidelines for Structural Design

of FRP Reinforced Concrete Building Structures of the Japanese Ministry of Construction (1995) based on the work of Fukuyama et al (1994). They suggested that the bond splitting strength of anchorages should be a function of a factor  $K_{co}$  that incorporates the effect of Young's modulus (see section 2.3.3). By examining the bond strength values recommended in these guidelines for GFRP and CFRP bars ( $E_G = 45$  MPa and  $E_C = 115$  MPa), it is obvious that GFRP bars develop only around 75% of the bond strength of CFRP bars, similar to the findings of the research reported in this study.

### *Concrete strength / cover*

Concrete strength is known to affect the bond splitting strength of reinforcing bars regardless of the type of bar used, since it controls the concrete cover resistance to splitting. The role of the concrete strength has been extensively examined in steel anchorages and this expertise has to be also incorporated in the anchorage formulas for FRP bars. For example, it is accepted that the concrete tensile strength (which controls the concrete cover resistance and thus the bond splitting strength of bars) is proportional to the square root of the concrete cube strength (Tepfers, 1973 - CEB Bulletin 151, 1982 - ACI Code, 1995) and codes of practice base their design recommendations on this assumption. This expertise is irrespective of the type of bar used, so a similar approach can be adopted for FRP bars, as shown in the next section.

As far as the role of the concrete cover is concerned, it was discussed in section 6.3.5 that the concrete cover has a crucial structural importance in the case of FRP bars. FRP bars require adequate concrete cover since they could split more readily than steel bars and unfortunately, at the moment they can not be bent on site to provide the necessary anchorage resistance. Therefore, special consideration has to be given in codes of practice to define the appropriate concrete cover that will secure the structural integrity of the concrete member. In this experimental study, two concrete cover ratios were examined (1.9 and 3 times the bar diameter) which resulted into significant differences in bond splitting strengths, as shown in the previous chapters.

- *Transverse reinforcement*

The influence of transverse reinforcement, although it was not examined as a variable in this study, is believed to have an important role in restraining the opening of splitting cracks and enhancing the bond splitting strength of anchorages. All the

reported codes of practice for steel and FRP bars (see chapter 2) incorporate in their anchorage formulas the beneficiary effect of transverse reinforcement. However, special consideration has to be given when different material shear links are used as transverse reinforcement, since their contribution is expected to be influenced by the value of their elastic modulus (JSCE Code, 1997).

- *Utilisation of the tensile strength of FRP bars*

Another important issue that must be considered in the formulation of anchorage length formulas, is the utilisation of the tensile strength of FRP bars in concrete members. Although FRP bars can develop up to four times the tensile strength of steel bars, their low elastic modulus is possible to limit their full utilisation in most concrete structures. In addition, it has been reported (Clarke et al, 1997) that durability factors are also very likely to limit the full utilisation of FRP bars. For example, Clarke et al (1997) suggest that a safety factor of 3.6 has to be imposed on the tensile strength of GFRP bars to counteract the long-term effect of “stress corrosion”. Hence, it is important for the anchorage length formula to consider the “practical” rather than the nominal tensile strength of an FRP bar.

- *Diameter of bar*

The effect of the diameter on the bond strength of an FRP bar has been examined in this study only in the case of pullout cube tests, and it was found that the size of the bar diameter affects significantly the bond strength of the bar (see section 4.1.3.4). It is, hence, expected to influence the value of the bond splitting strength as well. The ACI Code (1989) incorporates the influence of bar diameter in the anchorage length formula in the case of steel bars, so a similar approach might be reasonable to be adopted also in the case of FRP bars where the effect is believed to be more significant.

- *Bar surface deformations*

Last but not least is the effect of the surface bar deformations on the bond splitting strength. Different types of bar deformation are expected to develop different splitting behaviour in the surrounding to the bar concrete. A standardised pullout test might be useful to be introduced in this case, to classify the “appropriate” types of bar surface necessary to develop an acceptable, for structural purposes, level of bond strength.

The beam tests used in this study, either reinforced with single anchorage bars or splices, formed an example of "appropriate" test, since they reproduce experimental conditions that they can be found in practical applications. The problem with this type of tests is their complicated form compared to the standard pullout tests, as mentioned in section 6.2.2. The author, however, could not find in the literature more simple type of tests that can give reliable results. For example, Tepfers (1997) suggested that the eccentric type of pullout test (shown in figure 2.27 in section 2.3.2.2), which is much simpler than beam tests, can be considered for investigating the splitting behaviour of bars. However, when Tepfers tested C-BARs with this type of test, C-BARs appear to crack the concrete cover at a higher load than respective steel bars, which suggests that C-BARs have higher splitting resistance than steel. Nevertheless, when the same bars were tested in beam elements, they developed only 70% of the bond splitting strength of steel bars.

#### **6.3.7.2 Suggested method of working towards the formulation of design recommendations**

The experimental results of the beams reinforced with single anchorage bars are used to establish a method of calculating the required anchorage lengths for the types of bars used in this study

In order to calculate the required anchorage length for the 13.5 mm GFRP bars, the experimental results of the single anchorage bars in beams GB29, GB30 are considered. The maximum average bond stress values,  $\tau^*$ , developed on the anchorage bar of each beam are calculated by using the maximum strain gauge measurements divided by the distance of the gauge from the end of the bar, similar to the procedure reported in section 5.2.3.1. Figure 6.21 shows these bond values versus the distance from the end of the bar (anchorage length,  $L$ ), for both beams.

In addition to them, the results of spliced bars in beam GB31 and the beams tested by SINTEF (1996) are also considered, since it is assumed that spliced bars develop similar bond stresses to single bar anchorages (see section 6.3.4). SINTEF experiments can be used in this example, since the same kind of EUROCRETE bars was tested under very similar experimental conditions to the tests described in this study.

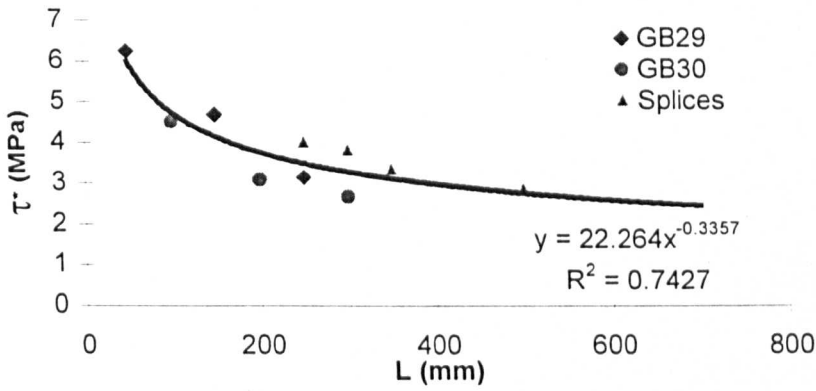


Figure 6.21: Maximum bond splitting strength of 13.5 mm GFRP bar anchorages

A non-linear regression analysis was conducted to establish a trend among the bond values, although the author acknowledges that the reliability of this curve is limited by the small amount of data used. It is also important to note that this curve expresses a relationship between bond-anchorage length values under certain experimental conditions; i.e. concrete cover/bar diameter ratio=1.85,  $f_{cu} = 35$  MPa,  $2 \times 40 \text{ mm}^2$  GFRP shear links spaced at 75 mm c/c in the anchorage region, and 13.5 mm GFRP EUROCRETE bars. When one of these factors changes, the shape of the curve may change.

Based on this curve, an extrapolation of values is conducted to find the required anchorage length to develop the full tensile strength of the GFRP bar, which is estimated to be 800 MPa. By using equation the basic equation of calculating the anchorage length of a bar (eq. 6.3) and the equation of the regression curve shown in figure 6.21, the value of the required anchorage length is calculated to be around 1370 mm (100D). At this anchorage value, the bond splitting strength of the bar is around 1.97 MPa.

$$L = \frac{d}{4} * \frac{\sigma_t}{\tau^*} \quad (6.3)$$

The above method is also used for the rest of the beams of this study. The bond splitting values of the 8.5 mm GFRP single anchorage bars in beams GB34 and GB35 are plotted against the anchorage length, as shown in figure 6.22.

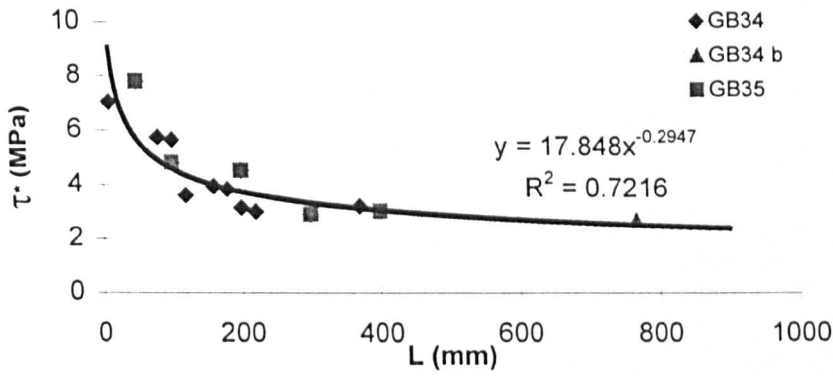


Figure 6.22: Maximum bond splitting strength of 8.5 mm GFRP anchorages

In this case, the experimental conditions are: concrete cover/bar diameter ratio = 2.5-3.0,  $f_{cu} = 45$  MPa,  $2 \times 40$  mm<sup>2</sup> GFRP shear links spaced at 75 mm c/c in the anchorage region, and 8.5 mm GFRP EUROCRETE bars.

It is interesting to note that the regression curve in the above graph considered only the experimental results of GB34 and GB35. An extrapolation of this curve towards larger anchorage lengths appears to predict the bond value of GB34b which corresponds to the "unexpected" failure of one of the main reinforcing bars in beam GB34 (see section 4.2.2.6).

Based on the regression curve, the required anchorage length to develop the full strength of the 8.5 mm GFRP bar (estimated around 1000 MPa) is calculated. The value of this anchorage is around 875 mm ( $\cong 100D$ ) which corresponds to a bond splitting strength of 2.4 MPa.

The same procedure was followed also in the case of CB32 and CB37 beams. These beams were reinforced with 8 mm CFRP bars and their concrete cover/bar diameter ratio was around 3. Although the concrete compressive strength was different in those beams (see section 3.2.3.4) the bond-anchorage length values were plotted in the same graph, as shown in figure 6.23.

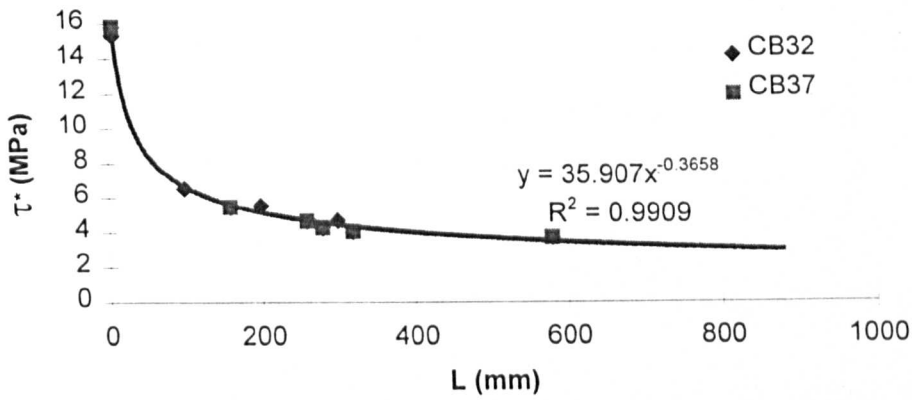


Figure 6.23: Maximum bond splitting strength of 8 mm CFRP anchorages

The required anchorage length to yield the full strength of the 8 mm CFRP bar (estimated around 1350 MPa) is calculated. The value of this anchorage is around 1125mm ( $\cong 140D$ ) which corresponds to a bond splitting strength of 2.45 MPa. In order to compare the bond strength of CFRP bars with the corresponding strength of GFRP bars, the required anchorage length to yield a tensile stress of 1000 MPa is also calculated. This length was found to be 566 mm ( $\cong 71D$ ) which suggests that GFRP bars develop only 70% of the bond strength of CFRP bars.

In all the above examples, the calculated anchorage lengths do not include any safety factors that will accommodate any variation in the bond strength values. In addition, the anchorage lengths were calculated to yield the full strength of FRP bars in each case, although this is unlikely to be required in practical conditions. As it was mentioned in the previous section, durability and serviceability parameters are expected to limit the full strength utilisation of FRP bars and, consequently, the required anchorage lengths will be smaller.

Another important point is that the above approach does not consider any beneficiary effects due to the support action, which is usually present in practical applications. When the anchorage length lies above a support, the mode of bond failure changes from splitting to pull-through and the respective bond strength is significantly higher. In this case, the design code should allow the engineers to use reduced anchorage lengths. The beneficiary effect of the support was demonstrated in the beams of phases 1-3 in this study (see appendix E.1.1). For example in beams GB14 and GB16, 13.5 mm GFRP bars developed their full tensile strength without bond failure by

having an anchorage length equal to 867 mm (64D), which is significantly smaller than the anchorage length calculated in the above examples for 13.5 mm GFRP bars ( $L=1370$  mm). In the case when bond splitting is prevented, the analytical approach presented in section 5.1.2.3 might be useful for predicting the required anchorage length for developing the full strength of an FRP bar. By considering the graph in figure 5.10, it can be suggested that an anchorage length of around 675 mm (50D) might be sufficient to develop the full tensile strength of 13.5 mm GFRP bars (800 MPa).

In general, the main advantage of the method described in this section is that by using a limited amount of experimental data, predictions can be made on the bond strength of reinforcing bars at much larger anchorage lengths. The disadvantage, however, is that each regression curve depends on specific experimental parameters. A better understanding of the effect of those parameters on the bond splitting strength of FRP bars, will help the reduction of the experimental effort required to calculate the necessary bond-anchorage length curves and apply this method. For example, if it is assumed that the effect of concrete strength on bond splitting is proportional to the square root of the concrete cube strength similar to what is reported for steel bars, then for example, based on the curve shown in figure 6.21 for 13.5 mm GFRP bars, a family of curves can be produced for different concrete strengths by simply multiplying the curve values with the appropriate ratio (see figure 6.24).

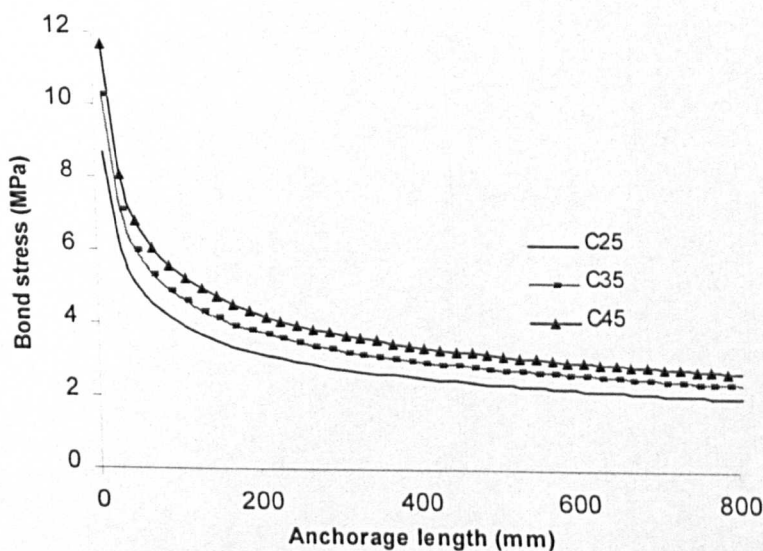


Figure 6.24: Maximum bond splitting strength of 13.5 mm GFRP anchorages for different values of concrete strength

A similar approach can also be applied to account for the effect of other parameters that affect bond splitting such as concrete cover and transverse reinforcement. It can be concluded that future work needs to be focused on the evaluation of the effect of those parameters on the bond splitting strength.

### **6.3.7.3 Splices**

The experimental data of the beams reinforced with spliced bars in this study suggest that spliced bars develop similar bond splitting strengths to single anchorages. Again, the author acknowledges that the amount of data examined is very limited, although it appears to be very consistent. Based on the above results, there is no need for an increase of the design anchorage length in splices.

# CHAPTER 7

## CLOSURE

### 7.1 GENERAL CONCLUSIONS

A summary of the general conclusions of this study is presented hereafter. Specific conclusions that were discussed during the presentation of the work in the previous chapters are not included here for the sake of compactness.

- The main aim of this study was to investigate the bond behaviour of the EUROCRETE FRP bars in concrete elements. Two major experimental series were conducted for this reason. In the first series, more than 100 specimens were tested in direct pullout whereas in the second, the bond development of FRP reinforcing bars was examined in nine beams tested in four point bending. Results from other 28 beams, tested for the EUROCRETE project, were also analysed to help the understanding of the bond behaviour of FRP reinforcing bars.
- All the specimens in the experimental series of pullout tests failed in a pull-through mode of failure since the concrete cube provided adequate confinement to the bars to enable them to reach their maximum bond strength. The mode of bond failure of FRP bars in certain cases differs substantially from the respective mode of bond failure of steel deformed bars. For concrete strengths greater than 30 MPa, the failure occurs partly on the surface of the bar, and not just in the concrete as in the case of steel bars, by peeling away part of the surface layer of the bar. Consequently, the bond strength of FRP bars is not controlled as much by the concrete strength but appears to be influenced by the interlaminar shear strength just below the resin rich surface layer of the bar. For concrete strengths less than 15 MPa, the concrete is crushed in

front of the bar deformations and the bond strength is controlled mainly by the shear strength of concrete. For intermediate values of concrete strength a combined mode of resin and concrete failure is expected to develop.

- The series of pullout cube tests highlighted some of the factors that influence the bond strength of FRP bars. The influence of these factors is summarised in the following:

*Type of bar fibres:* No significant difference was found between the bond strengths developed by GFRP and CFRP bars.

*Embedment length:* An increase in the embedment length is accompanied by a decrease in bond strength.

*Concrete strength:* The concrete strength influences the bond strength only when the bond failure takes place in the concrete matrix.

*Bar diameter:* Smaller diameter bars develop a higher bond strength than larger diameter bars. This difference is believed to be more significant in FRP than in steel bars, due to their low axial shear stiffness.

*Cross sectional shape of bar:* Square bars develop higher bond strength than round bars. The “wedging effect” due to the edgy cross section shape seems to be responsible for this difference.

*Surface deformations:* A minimum height of deformations is necessary to develop satisfactory bond behaviour to concrete.

- In the experimental series of beam tests, single anchorage bars and splices failed due to bond splitting. Unexpectedly, GFRP bars developed only around 65 - 75% of the bond splitting strength of CFRP bars under similar experimental conditions. This is attributed to the lower Young's modulus of GFRP bars which is believed to play an important role to the bond splitting behaviour of reinforcing bars.
- An analytical model was formed to examine the importance of the elastic modulus in bond splitting. The results showed that the elastic modulus influences the deformability of the bars inside the concrete and in parallel, it affects the crack geometry and consequently the concrete shear strength at the location of the crack. Both factors influence the splitting tendency of reinforcing bars.

- By comparing the experimental results of spliced FRP bars to single anchorages, it was found that spliced bars develop similar bond strength values to single anchorage bars. The distribution of radial stresses induced to the surrounding concrete by a pair of spliced bars is, therefore, assumed to be similar to the stress distribution induced by a single bar. Consequently, there is no immediate need for increasing the design anchoring length in the case of splices.
- The contribution of the transverse reinforcement to the bond splitting strength of FRP reinforcing bars was also examined. Shear links enhanced the splitting resistance of the surrounding to the bar concrete, only when they were already stressed (for example, located in the shear zone of the beam). Otherwise, the initiation of splitting cracks did not seem to be influenced by the presence of shear links. However, after the initiation of splitting cracks, the transverse reinforcement restrained the crack opening and contributed to the residual splitting bond strength of the reinforcing bar.
- Concrete cover has a significant role in the bond splitting strength of FRP bars. Although in steel reinforcement the concrete cover is more needed for the protection of reinforcement from the external environment, in FRP bars its structural role to resist bond splitting is far more crucial, since FRP bars tend to split more than steel bars.
- Transverse pressure to the potential splitting plane (for example, support action) can delay or even prevent the initiation of splitting crack and thus, enhance the bond strength of the reinforcing bar.
- The flexural cracking in beam elements influences the bond development over the anchorage length. Between successive flexural cracks, bond develops both positive and negative values resulting to a relatively low average bond stress. The peak bond stress develops its maximum value always at the very end of the bar. After the initiation of the first splitting crack, the peak bond stress migrates towards the centre of the bar, ahead of the development of the splitting crack.
- The suitability of the traditional pullout cube tests for measuring the bond strength of FRP bars is questioned. Although these tests can give an indication of the maximum achievable bond strength for a reinforcing bar, their results can not be used for

comparing the bond strength of bars in practical conditions where splitting is expected to be the mode of bond failure.

- The bond strength values of FRP bars were proved to be dependent on the experimental conditions. A study was conducted to compare the bond strengths developed in three different types of tests (cube, beam and slab tests), and it was found that the stress conditions in the surrounding to the bar concrete influence the value of the bond strength of the bar.
- A FE analytical study was conducted to investigate the bond behaviour of FRP bars in concrete. Pullout cube tests and selected beam tests were modelled by using ANSYS50a and ABAQUS FE packages.
- In the case of pullout tests, a modeling procedure was introduced where non-linear springs were used to model the bond behaviour at the bar-concrete interface. The basic spring characteristic load-slip curve was taken from the results of the experimental study. The analytical results showed a very good correlation with the respective experimental and helped develop a further understanding of the bar-concrete interaction during pullout. As a step further, the above modeling procedure was used for evaluating the bond behaviour of larger embedment lengths when no bond splitting was expected.
- In the case of beam tests, four beams were modelled; beam CB19 that did not fail in bond, beam CB20 that failed in a pull-through mode of bond failure and beams CB32 and CB37 that failed due to bond splitting. In all models, the smeared-crack concrete option of ABAQUS package was introduced. Springs were also used in all model beams (except in CB19) to simulate the bond behaviour at the bar-concrete interface. The characteristics of springs were taken from the pullout cube tests and they were modified accordingly to encounter the experimental conditions and the mode of bond failure in each specific case.
- The smeared-crack approach used by the FE package was proved to be inadequate to simulate accurately the discrete flexural cracking in the experimental beams and resulted to differences in the bond development between experimental and model beams. However, the overall modeling results were compared with the respective experimental and showed, generally, a good agreement. The FE model was found to

be sensitive to small mesh sizes ( $< 70$  mm) since it did not manage to converge into ultimate solutions in this case. A parametric study was also conducted, as part of the modeling procedure, on the load-slip values of the characteristic spring curve used in the models. It was found that changes in the value of the maximum load were more important on the bond strength of the bar than changes in the slip values. Finally, the modeling procedure was further validated since the results were proved not to depend on the spring size used in the models.

In summary, the current thesis has contributed towards the understanding of the bond behaviour of FRP bars in concrete elements by identifying the various parameters that influence bond development and failure, by understanding the influence of those parameters and by introducing new methods of evaluating the effect of those parameters towards the formulation of design codes of practice for the evaluation of required anchorage lengths for FRP bars.

## **7.2 SUGGESTIONS FOR FUTURE WORK**

A number of interesting questions still remain unanswered, new topics of research have been opened for investigation and several propositions require validation. The subject of bond of FRP bars in concrete is very wide, may be even wider than bond of steel bars, and this study has contributed only a tiny amount of knowledge hoping that further investigation will continue towards the better understanding of the subject. It is believed that further development is required in the following:

- More experimental work is required in understanding and quantifying the effect of the various parameters that influence the bond splitting strength of FRP bars. Beam type tests are more suitable for this purpose, since they reflect more accurately practical conditions.
- The distribution of radial stresses induced by spliced bars in the surrounding concrete and the corresponding bond strength of spliced bars with respect to single anchorages, requires more experimental and analytical investigation.

- There is a pressing need for the establishment of a standardised test for measuring the bond splitting strength of various types of FRP bars, since the growing number of types of FRP bars reaching the market is making difficult the formulation of universal anchorage length guidelines.
- The effect of shear on the bond behaviour of reinforcing bars is believed to be an important issue that requires further investigation.
- Further development on the analytical modeling of the bond interaction is required, in order to consider the effect of concrete cover, transverse reinforcement and pressure, and shear transfer in concrete microcracks.

# REFERENCES

ABAQUS version 5.3, Hibbit, Kalsson and Sorensen Inc., 1993

Achillides Z. and Pilakoutas K., "Bond strength of FRP bars in concrete", 12<sup>th</sup> Greek Conference for Concrete, 29-31 Oct. 96, Limassol, Cyprus (in Greek)

Achillides Z., Pilakoutas K. and Waldron P., "Anchorage Systems - Bond improvement", EUROCRETE Report No CCC/96, Centre for Cement and Concrete, The University of Sheffield, Oct. 1996b

Achillides Z. and Pilakoutas K., "Bond behaviour of FRP reinforcing bars in concrete structures", 5<sup>th</sup> International Conference for Composite Materials and Structures, 5-7 Jul. 1997, Xanthi, Greece

Achillides Z., Pilakoutas K. and Waldron P., "Bond behaviour of FRP bars to concrete", 3<sup>rd</sup> International Symposium on Non-Metallic (FRP) Reinforcement for Concrete Structures, 14-16 Oct. 1997b, Sapporo, Japan, pp 341-348

Achillides Z., Pilakoutas K. and Waldron P., "Modeling of FRP rebar bond behaviour", 3<sup>rd</sup> International Symposium on Non-Metallic (FRP) Reinforcement for Concrete Structures, 14-16 Oct. 97, Sapporo, Japan, pp 423-430

Achillides Z., Pilakoutas K. and Waldron P., "Bond of FRP anchorages and splices in concrete beams", 8<sup>th</sup> European Conference of Composite Materials, Vol. 2, June 1998, Naples, Italy, pp 277-284

ACI 318-89 Building Code and Commentary, "Building code requirements for reinforced concrete", Chapter 12 - Development and splices of reinforcement, American Concrete Institute, 1989

ACI 318-95 Building Code and Commentary, "Building code requirements for structural concrete", Chapter 12 - Development and splices of reinforcement, American Concrete Institute, 1995

ACI Committee 440, "State-of-the-Art Report on Fiber Reinforced Plastic Reinforcement for Concrete Structures", ACI 440R-96, Detroit, Michigan, Feb. 1996

ANSYS version 5.0a, Swanson Analysis Systems Inc., 1992

Al-Dulaijen S., Nanni A., Al-Zaharani M., Bakis S. and Boothby T., "Bond evaluation of environmentally conditioned GFRP/concrete systems", Advanced Composite Materials in Bridges and Structures: 2<sup>nd</sup> International Conference, Ed. El-Badry M., Montreal, Quebec, Canada, Aug. 1996, pp 845-852

Al-Zaharani M., Nanni A., Al-Dulaijen S. and Bakis S., "Bond of FRP to concrete in reinforcing rods with axisymmetric deformations", Advanced Composite Materials in Bridges and Structures: 2<sup>nd</sup> International Conference, Ed. El-Badry M., Montreal, Quebec, Canada, Aug. 1996, pp 853-860

Atshiko M. (Editor), State-of the Art Report on Continuous Fiber Reinforcing Materials, 2<sup>nd</sup> Research Committee on CFRM, Japan Society of Civil Engineers, Concrete Engineering Series 3, Tokyo, October, 1993

Bakis G. E., "FRP Reinforcement: Materials and Manufacturing", Fiber-Reinforced-Plastic (FRP) reinforcement for concrete structures: Properties and applications, Ed. Nanni A., Elsevier, 1993, pp 13-58

Benmokrane B., Tighiouart B., Chaallal O., "Investigation on bond performance of FRP rebars", ACI Convention, San Francisco, Session on Bond of FRP Rebars, 20-25 March 1994

Benmokrane B., Tighiouart B., Chaallal O., "Bond strength and load distribution of composite GFRP reinforcing bars in concrete", ACI Materials Journal, Vol. 93, No. 3, May-June 1996, pp. 246-253

Benmokrane B., Tighiouart B. and Theriault M., "Bond strength of FRP rebar splices", Proceedings of the 3<sup>rd</sup> International Symposium on Non-Metallic (FRP) Reinforcement for Concrete Structures: Non-Metallic (FRP) Reinforcement for Concrete Structures, JCI, Vol. 2, Sapporo, Japan, Oct. 1997, pp 405-412

British Standards 8110, "Structural use of concrete", British Standards Institution, London, 1985

Cairns J. and Abdullah R., "An evaluation of bond pullout tests and their relevance to structural performance", The Structural Engineer, Vol.73, No 11, 6 June 1995, pp 179-185

Cairns J. and Jones K., "The splitting forces generated by bond", Magazine of Concrete Research, Vol. 47, No. 171, June 1995, pp 153-165

Cairns J., Jones K., "An evaluation of the bond-splitting action of ribbed bars", ACI Materials Journal, Jan.-Feb. 1996, pp 10-19

Chaallal O., Benmokrane B., "Pullout and bond of glass-fibre rods embedded in concrete and cement grout", Materials and Structures, Vol 26, 1993, pp 167-175

Clarke J., "The need for durable reinforcement", Alternative materials for the reinforcement and prestressing of concrete, ed. Clark J. L., Blackie Academic and Professional, London 1993, pp 1-33

Clarke J., O'Regan D., Thirugnanendran C., "EUROCRETE PROJECT: Modification of design rules to incorporate Non-Ferrous Reinforcement", Confidential report, January 1996

Clarke J., O'Regan D., Thirugnanendran C., "EUROCRETE PROJECT: Modification of design rules to incorporate Non-Ferrous Reinforcement", Final report, April 1997

Clarke J., Waldron P., "The reinforcement of concrete structures with advanced composites", The Structural Engineer, Vol. 74, No. 17, Sep. 1996

Comite Euro-international du Beton Bulletin 151, State-of-the-Art Report, "Bond action and bond behaviour of reinforcement", April 1982

Comite Euro-international du Beton, International Conference "Bond in Concrete from research to practice", Riga, Latvia, Oct. 1992

Cosenza E., Manfredi G., Realfonzo R., "Analytical modelling of bond between FRP reinforcing bars and concrete", Non-Metallic (FRP) Reinforcement for Concrete Structures, ed. L. Taerwe, Aug 95, pp 164-171

Cosenza E., Manfredi G., Realfonzo R., "Bond characteristics and anchorage length of FRP rebars", *Advanced Composite Materials in Bridges and Structures: 2<sup>nd</sup> International Conference*, Montreal, Quebec, Canada, Aug. 1996, pp 909-918

Cosenza E., Manfredi G. and Realfonzo R., "Behaviour and modelling of Bond of FRP rebars to concrete", *Journal of Composites for Construction*, Vol. 1, No. 2, May 1997, pp. 40-51

De Larrard F., Schaller I., Fuches J., "Effect of bar diameter on the bond strength of passive reinforcement in high-performance concrete", *ACI Materials Journal*, Vol. 90, No. 4, July-Aug. 1993, pp. 333-339

Del Uijl J., "Bond and fatigue properties of Arapree", *Proceedings on the 2<sup>nd</sup> International RILEM Symposium: Non-Metallic (FRP) Reinforcement for Concrete Structures*, Ghent, Aug. 95, ed. Taerwe L., E and FN Spoon, London, 1995, pp 146-153

Den Uijl J., Bigaj A., "A bond model for ribbed bars based on concrete confinement", *HERON*, Vol. 41, No. 3, 1996, pp. 201-226

Duranovic N., Pilakoutas K. and Waldron P., "Experimental program - Structural test on R.C. Beams", *Centre for Cement and Concrete, The University of Sheffield*:

- Test for beams 1-12 of phase I, Report Nos. CCC/95/19A, 20A, 21A, Feb. 1995
- Test for beams 13-24 of phase II, Report Nos. CCC/95/22A Jun.95, CCC/95/33A Oct.95, CCC/96/41A May 96
- Test for beams 25-28 of phase III, Report Nos. CCC/96/42A June 96

Duranovic N., Pilakoutas K. and Waldron P., "General testing arrangement for R.C. beams", Report No. CCC/95/17A, Feb. 1995, *Centre for Cement and Concrete, The University of Sheffield*

Ehsani M. R., "Glass-fiber reinforcing bars", *Alternative materials for the reinforcement and prestressing of concrete*, ed. Clark J. L., Blackie Academic and Professional, London 1993, pp 34-54

Ehsani M.R., Saadatmanesh H., Tao S., "Bond of hooked Glass Fiber Reinforced Plastic (GFRP) reinforcing bars to concrete", *ACI Materials Journal*, V.92, No.4, July-August 1995, pp 391-400

Eshani M.R., Saadatmanesh H., Tao S., "Design Recommendations For Bond of GFRP Rebars to Concrete", *Journal of Structural Engineering*, March 1996, pp. 247-254

Eshani M.R., Saadatmanesh H., Tao S., "Bond behaviour and design recommendations for Fiberglass reinforcing bars", *1<sup>st</sup> International Conference on Composites in Infrastructure*, Ed. Saadatmanesh, Eshani, Tuscon, Arizona, USA, Jan. 1996,

Eligehausen R., Bertero V. V., Popov E. P., "Local bond stress-slip relationships of deformed bars under generalised excitations: tests and analytical model", *Technical Report UCB/EERC-83*, Earthquake Engineering Research Center, University of California, Berkeley, 1983

Eurocode No. 2, "Design of concrete structures", 5.2 Steel for Reinforced Concrete, December 1989

Eurocode No. 8, "Structures in seismic regions - Design", Report EUR 12266 EN, Industrial Processes, Building and Civil Engineering, Commission of the European Communities, May 1988

Hattori A., Inoue S., Miyagawa T. and Fujii M., "A study on bond creep behaviour of FRP rebars embedded in concrete", Proceedings on the 2<sup>nd</sup> International RILEM Symposium: Non-Metallic (FRP) Reinforcement for Concrete Structures, Ghent, Aug. 95, ed. Taerwe L., E and FN Spon, London, 1995, pp 172-179

Hattori A., Kawasaki K., Miyakawa T. and Fujii M., "Bond behaviours of carbon fiber strand and aramid fiber deformed bar", Proceedings of the 3<sup>rd</sup> International Symposium on Non-Metallic (FRP) Reinforcement for Concrete Structures: Non-Metallic (FRP) Reinforcement for Concrete Structures, JCI, Vol. 2, Sapporo, Japan, Oct. 1997, pp 349-356

Head P.R., "Advanced composites in civil engineering - a critical overview at this high interest, low use stage of development", Advanced Composite materials in bridges and structures, 2<sup>nd</sup> Inter. Conf., Montreal, Quebec, Canada, Aug. 1996, pp 3-16

Faoro M., "The influence of stiffness and bond of FRP bars and tendons on the structural behaviour of reinforced concrete members", Advanced Composite Materials in Bridges and Structures: 2<sup>nd</sup> International Conference, Ed. El-Badry M., Montreal, Quebec, Canada, Aug. 1996, pp. 885-892

Fasa S., CangaRao H., "Bending and bond behaviour of beams reinforced with plastic rebars", Transportation Research Record 1290, 1990, pp.185-193

Faza S., Wagner O., Deusser S. and McClaskey C., "A new generation of fiber reinforced polymer rebars for concrete reinforcement", Proceedings of the 3<sup>rd</sup> International Symposium on Non-Metallic (FRP) Reinforcement for Concrete Structures: Non-Metallic (FRP) Reinforcement for Concrete Structures, JCI, Vol. 2, Sapporo, Japan, Oct. 1997, pp 99-106

Ferguson P. M., Breen J. E., "Lapped splices for high strength reinforcing bars", Journal of the ACI, 1965, pp 1063-1072

Frangou M., "Strengthening of concrete by lateral confinement", PhD Thesis, Dept. of Civil and Structural Eng., The University of Sheffield, 1996

FRP Reinforced Concrete Research Croup, "Guidelines for Structural Design of FRP Reinforced Concrete Building Structures" (Draft), Building Research Institute, Japanese Ministry of Construction, July 1995

Fukuyama H., Sonobe Y., Fujisawa M., Kanakubo T., Yonemaru K., "Bond Splitting Strength of Concrete Members Reinforced with FRP Bars", Session on Bond of FRP Rebars, ACI Convention, San Francisco, 20-25 March 1994

GangaRao H., Faza S., "Glass FRP reinforcing bars for concrete", Fiber-Reinforced-Plastic (FRP) reinforcement for concrete structures: Properties and applications", Ed. Nanni A., Elsevier, 1993, pp 167-188

Gambarova P., Rosati P., Sharif O., "Bond and splitting in concrete", International Conference Bond in Concrete from Research to Practice, Riga, Latvia, Vol. 1, October 1992, pp 48-57

Gentry T. and Hudak C., "Thermal compatibility of plastic composite reinforcement and concrete", Advanced Composite Materials in Bridge Structures: 2<sup>nd</sup> International Conference, Montreal, Quebec, Canada, Aug. 1996, pp 149-158

Giuriani E., Plizzari G., Schumm C., "Role of stirrups and residual tensile strength of cracked concrete on bond", Journal of Structural Engineering, Vol. 117, No. 1, January 1991, pp 1-18

Goto Y., "Cracks formed in concrete around deformed tension bars", Journal of the American Concrete Institute, Vol. 68, 1971, pp 244-251

Japan Concrete Institute, Proceedings of the 3<sup>rd</sup> International Symposium on Non-Metallic (FRP) Reinforcement for Concrete Structures, "Non-Metallic (FRP) Reinforcement for Concrete Structures", Sapporo, Japan, Oct. 1997

Japanese Society of Civil Engineers, "Recommendation for design and construction of concrete structures using Continuous Fiber Reinforcing Materials", ed. Machida A., Research Committee on Continuous Fiber Reinforcing Materials, JSCE, Oct 1997

Jerret C., Ahmad S., "Bond tests of Carbon Fiber Reinforced Plastic (CFRP) rods", Non-Metallic (FRP) Reinforcement for Concrete Structures, ed. L. Taerwe, Aug 95, pp. 180-191

Kimura H., Jirsa J., "Effects of bar deformation and concrete strength on bond of reinforcing steel to concrete", International Conference Bond in Concrete from Research to Practice, Riga, Latvia, Vol. 1, October 1992, pp 100-109

Larralde J. Silva-Rodriguez R., "Bond and slip of FRP repairs in concrete", Journal of Materials in Civil Engineering, Vol 5, No 1, Feb 93, pp 30-39

Malvar L. J., "Bond of reinforcement under controlled confinement", ACI Materials Journal, Vol. 89, No. 6, Nov-Dec 1992, pp. 593-601

Malvar J., "Bond stress-slip characteristics of FRP rebars", Session on Bond of FRP Rebars, ACI Convention, San Francisco, 20-25 March 1994

Malvar J. L., "Tensile and Bond Properties of GFRP Reinforcing Bars", ACI Materials Journal, V. 92, No. 3, May-June 1995, pp 276-285

Nagamoto K., Kaku T., "Bond behaviour of deformed bars under lateral compressive and tensile stress", International Conference Bond in Concrete from Research to Practice, Riga, Latvia, Vol. 1, October 1992, pp 69-78

Nanni A., Al-Zaharani M., Al-Dulaijen S., Bakis S. and Boothby T., "Bond of FRP reinforcement to concrete - Experimental results", Non-Metallic (FRP) Reinforcement for Concrete Structures, ed. L. Taerwe, Aug 95, pp 137-145

Orangun C., Jirsa J., Breen J., "A reevaluation of test data on development length and splices", Journal of the ACI, Title no. 74-11, March 1977, pp 114-122

Pilakoutas K, Achillides Z and Waldron P, "Non-ferrous reinforcement (FRP) for the repair of concrete structures", Fifth International Conference on Deterioration and Repair of Reinforced Concrete in the Arabian Gulf, Bahrain, 27-29 October, 1997a

Pilakoutas K, Achillides Z and Waldron P, "Non-ferrous reinforcement in concrete structures", Mouchel Centenary Conference, Cambridge, August, 1997b

Pleiman L., "Strength, modulus of elasticity, and bond of deformed FRP rods", *Advanced Composite Materials in Civil Engineering Structures*, Proceedings of the speciality conference, ASCE, Las Vegas, Feb. 1991

Plizzari G., Deldossi M., Massimo S., "Experimental study on anchored bars in R.C. elements with transverse reinforcement", *Materials and Structures*, Vol. 29, November 1996, pp. 534-542

Rehm G, "The fundamentals of bond between steel reinforcement and concrete", *Deutscher Ausschuss für Stahlbeton*, Heft 138, p. 59, 1961 - in German (referenced in CEB Bulletin 151, 1982)

Reynolds G. C., Beeby A. W., "Bond strength of deformed bars", *Bond In Concrete*, Edited P. Bartos, Applied Science Publishers, London, 1982

Reynolds G. C., "Bond strength of deformed bars in tension", *Cement and Concrete Association*, Technical Report 548, May, 1982

RILEM/CEB/FIP Recommendation RC. 5, "Test of the bond strength of reinforcement of concrete: Test by bending", 1978

RILEM/CEB/FIP Recommendation RC6, "Bond test for reinforcing steel 2. Pullout test", 1978

Rosati G. P., Schumm C.E., "Modelling of local bar-to-concrete bond in R.C. beams", *International Conference Bond in Concrete from Research to Practice*, Riga, Latvia, Vol. 3, October 1992, pp 12.34-12.43

Rossetti V., Galeota D., Giammateo M., "Local bond stress-slip relationships of glass fibre reinforced plastic bars embedded in concrete", *Materials and Structures*, Vol.28, 1995, pp. 340-344

Rostacy F.S, "FRP: The European Perspective", *Fiber Composites in Infrastructure*, 1<sup>st</sup> Inter. Conf. in Infrastructure, ed. Saadatmanesh and Eshani, Arizona, USA, Jan. 1996, pp 12-20

Seible F. and Karbhari V., "Advanced Composites for Civil Engineering Applications in the United States", 1<sup>st</sup> Inter. Conference in Infrastructure, ed. Saadatmanesh and Eshani, Arizona, USA, Jan. 1996, pp 21-37

Sheard P., Clarke J., Dill M., Hammersley G. and Richardson D., "EUROCRETE - Taking account of durability for design of FRP reinforced concrete structures", *Proceedings of the 3<sup>rd</sup> International Symposium on Non-Metallic (FRP) Reinforcement for Concrete Structures: Non-Metallic (FRP) Reinforcement for Concrete Structures*, JCI, Vol. 2, Sapporo, Japan, Oct. 1997, pp 75-82

Shield C., French C. and Retika A., "Thermal and mechanical fatigue effects on GFRP rebar - concrete bond", *Proceedings of the 3<sup>rd</sup> International Symposium on Non-Metallic (FRP) Reinforcement for Concrete Structures: Non-Metallic (FRP) Reinforcement for Concrete Structures*, JCI, Vol. 2, Sapporo, Japan, Oct. 1997, pp 381-388

SINTEF-EUROCRETE, "Non-ferrous reinforcement for concrete structures, Small beam test-Bond splice length", Restricted report STF22 F96828, 12-8-96

Sonobe Y., "An Overview of R&D in Japan", Fiber-Reinforced-Plastic (FRP) reinforcement for concrete structures: Properties and applications", Ed. Nanni A., Elsevier, 1993, pp 115-128

Soretz S., "Comparizon of beam tests and pull-out tests", Materials and Constructions, Vol. 5, No. 28, 1972, pp. 261-264

Takagi N., Kojima T., Iwamoto K. and Inoue S., "A study on bond of continuous fiber rods embedded in beam specimen", Proceedings of the 3<sup>rd</sup> International Symposium on Non-Metallic (FRP) Reinforcement for Concrete Structures: Non-Metallic (FRP) Reinforcement for Concrete Structures, JCI, Vol. 2, Sapporo, Japan, Oct. 1997, pp 365-372

Tassios Th., "Properties of bond between concrete and steel under load cycles idealising seismic actions", CEB Bulletin 131, Rome, Italy, 1979

Tassios Th., Tsoukantas Y., Yiannopoulos I., Trezos P., "Reinforced Concrete", National Technical University of Athens, Athens 1993 (in Greek)

Tepfers R., "A theory of bond applied to overlapped tensile reinforcement splices for deformed bars", Publication 73:2, Division of Concrete Structures, Chalmers University of Technology, Goteborg, Sweden, 1973

Tepfers R., "Cracking of concrete cover along anchored deformed reinforcing bars", Magazine of Concrete Research, Vol. 31, No. 106, Mar. 1979, pp 3-12

Tepfers R. and Olsson P., "Ring test for evaluation of bond properties of reinforcing bars", International Conference "Bond in Concrete from research to practice", Riga, Latvia, Vol. 1, Oct. 1992, pp 89-99

Tepfers R., "Bond of FRP reinforcement in concrete: A state-of-the-art in preparation", Chalmers University of Technology, Pupl. 91:1, Work No 15, April, 1997

Tepfers R. and Karlsson M., "Pull-out and tensile reinforcement splice tests using FRP C-Bars", Proceedings of the 3<sup>rd</sup> International Symposium on Non-Metallic (FRP) Reinforcement for Concrete Structures: Non-Metallic (FRP) Reinforcement for Concrete Structures, JCI, Vol. 2, Sapporo, Japan, Oct. 1997, pp 357-364

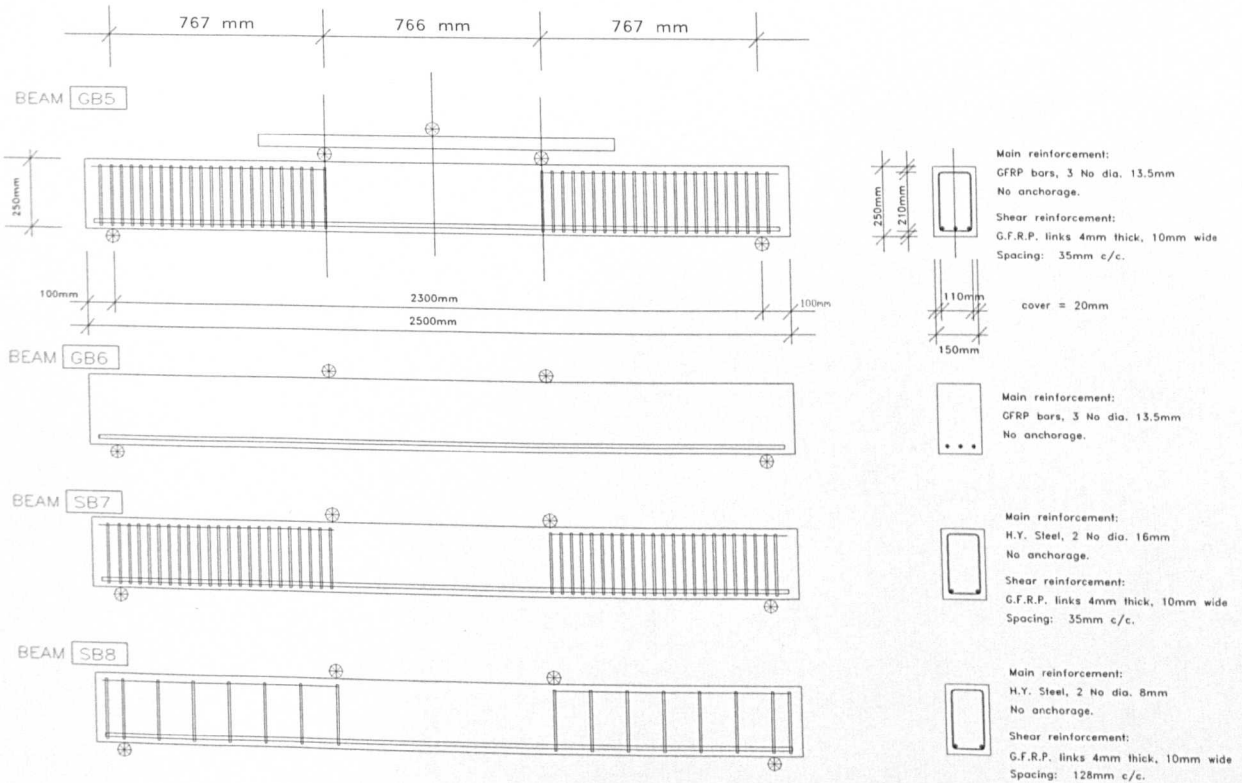
Uppuluri V., Bakis S., Al-Dulaijen S., Nanni A. and Boothby T., "Analysis of the bond mechanism in FRP reinforcement rods: the effect of rod design and properties", Advanced Composite Materials in Bridge Structures: 2<sup>nd</sup> International Conference, Montreal, Quebec, Canada, Aug. 1996, pp 893-900

Van der Veen C., "Theoretical and experimental determination of crack width in reinforced concrete at very low temperatures", HERON, Vol. 35, No. 2, 1990

# APPENDIX A

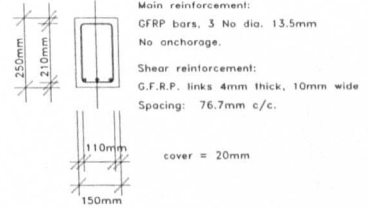
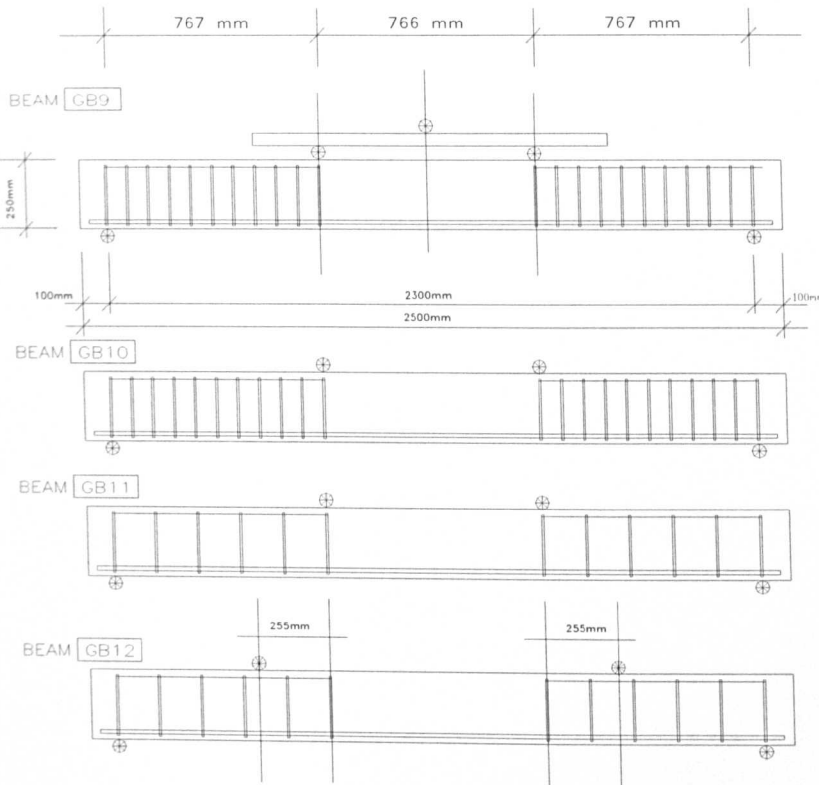
## Reinforcement arrangement and instrumentation of Beams in Phases 1-3

### A.1 Reinforcement arrangement in beams GB5 to GB8



d:\fibra\acaddwg\gb5-8

## A.2 Reinforcement arrangement in beams GB9 to GB16



Main reinforcement:  
GFRP bars, 3 No dia. 13.5mm  
No anchorage.  
Shear reinforcement:  
G.F.R.P. links 4mm thick, 10mm wide  
Spacing: 76.7mm c/c.

cover = 20mm



Main reinforcement:  
GFRP bars, 3 No dia. 13.5mm  
No anchorage.  
Spacing: 76.7mm c/c.  
Shear reinforcement:  
G.F.R.P. links 4mm thick, 10mm wide  
Spacing: 76.7mm c/c.

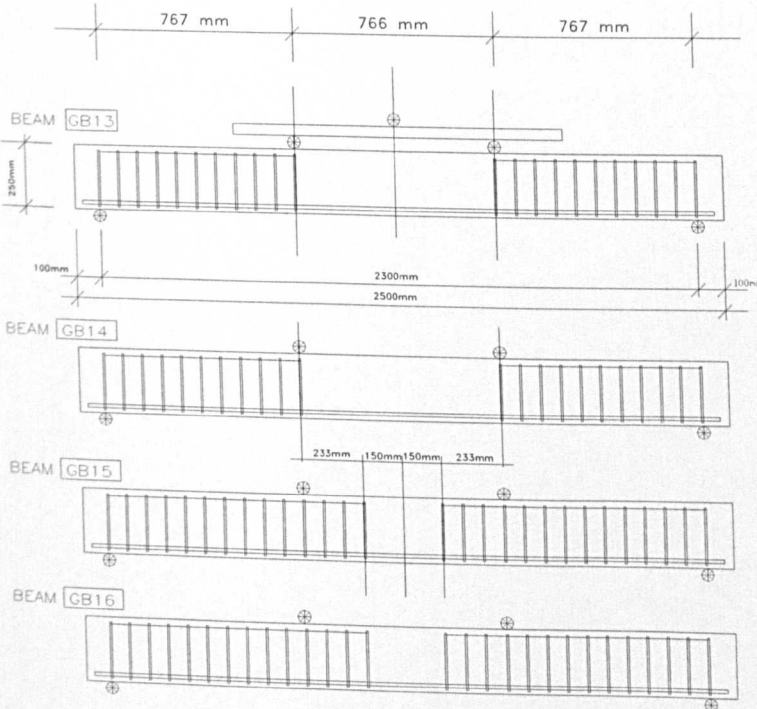


Main reinforcement:  
GFRP bars, 3 No dia. 13.5mm  
No anchorage.  
Shear reinforcement:  
G.F.R.P. links 4mm thick, 10mm wide  
Spacing: 153mm c/c.



Main reinforcement:  
GFRP bars, 3 No dia. 13.5mm  
No anchorage.  
Shear reinforcement:  
G.F.R.P. links 4mm thick, 10mm wide  
Spacing: 153mm c/c.

d:\fibre\acaddwg\gb9-12



Main reinforcement:  
GFRP bars, 2 No dia. 13.5mm  
No anchorage.  
Shear reinforcement:  
G.F.R.P. Links: 4mm thick; 10mm wide  
Spacing: 76.7mm c/c.

cover = 20mm



Main reinforcement:  
GFRP bars, 2 No dia. 13.5mm  
Shear reinforcement:  
G.F.R.P. Links: 4mm thick; 10mm wide @ 76.7mm  
Concrete confinement:  
Straps 25.4mm wide x 0.8mm thick @ 50mm c/c  
(area of no shear and to 750 mm from the midspan)  
Straps 25.4mm wide x 0.8mm thick @ 100mm c/c  
(for the rest of the beam)



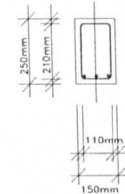
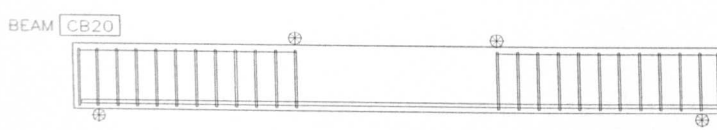
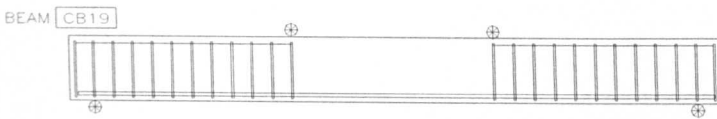
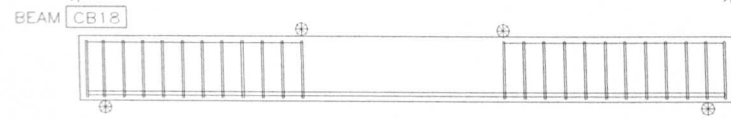
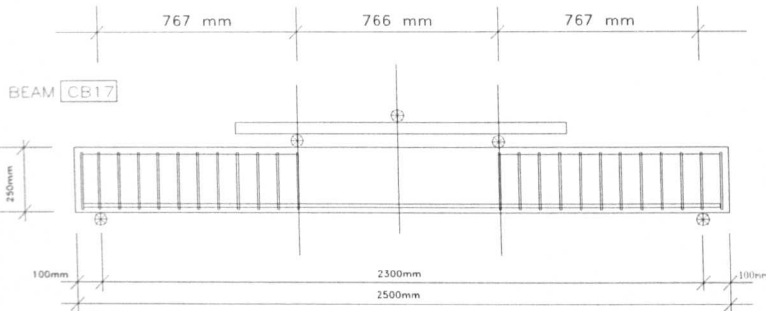
Main reinforcement:  
GFRP bars, 2 No dia. 13.5mm  
Shear reinforcement:  
G.F.R.P. Links: 4mm thick; 10mm wide  
Spacing: 76.7mm c/c.  
Concrete confinement:  
Straps 25.4mm wide x 0.8mm thick @ 200mm c/c



Main reinforcement:  
GFRP bars, 2 No dia. 13.5mm  
Shear reinforcement:  
G.F.R.P. Links: 4mm thick; 10mm wide  
Spacing: 76.7mm c/c.  
Concrete confinement:  
Straps 12mm wide x 0.5mm thick @ 62mm c/c

C:\FIBRE\ACADDWGS\B13-16

### A.3 Reinforcement arrangement in beams CB17 to CGB22



**Main reinforcement:**  
CFRP bars, 3 No dia. 13.5mm  
No anchorage.  
**Shear reinforcement:**  
G.F.R.P. links 4mm thick, 10mm wide  
Spacing: 76.7mm c/c.

cover = 20mm



**Main reinforcement:**  
CFRP bars, 3 No dia. 13.5mm  
No anchorage.  
Spacing: 76.7mm c/c.  
**Shear reinforcement:**  
G.F.R.P. links 4mm thick, 10mm wide  
Spacing: 76.7mm c/c.

**Concrete confinement:**  
Straps 25.4mm wide x 0.8mm thick @ 50mm c/c



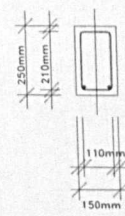
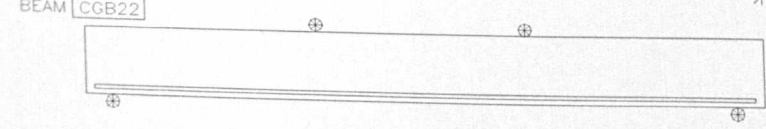
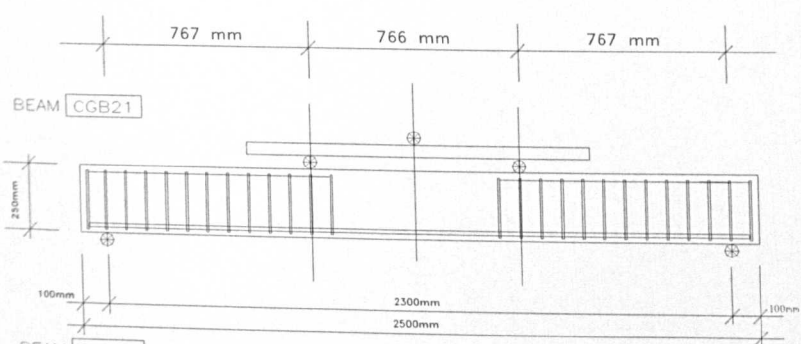
**Main reinforcement:**  
CFRP bars, 2 No dia. 13.5mm  
No anchorage.  
Spacing: 76.7mm c/c.  
**Shear reinforcement:**  
G.F.R.P. links 4mm thick, 10mm wide  
Spacing: 76.7mm c/c.



**Main reinforcement:**  
CFRP bars, 2 No dia. 13.5mm  
No anchorage.  
Spacing: 76.7mm c/c.  
**Shear reinforcement:**  
G.F.R.P. links 4mm thick, 10mm wide  
Spacing: 76.7mm c/c.

**Concrete confinement:**  
Straps 25.4mm wide x 0.8mm thick @ 50mm c/c

c:\fibres\acadwps\cb17-20



**Main reinforcement:**  
C&GFRP bars, 2 No dia. 13.5mm  
No anchorage.  
**Shear reinforcement:**  
G.F.R.P. links 4mm thick, 10mm wide  
Spacing: 76.7mm c/c.

cover = 20mm

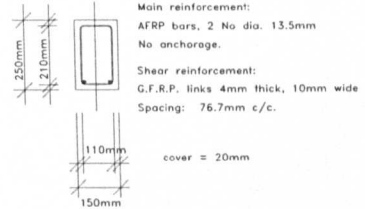
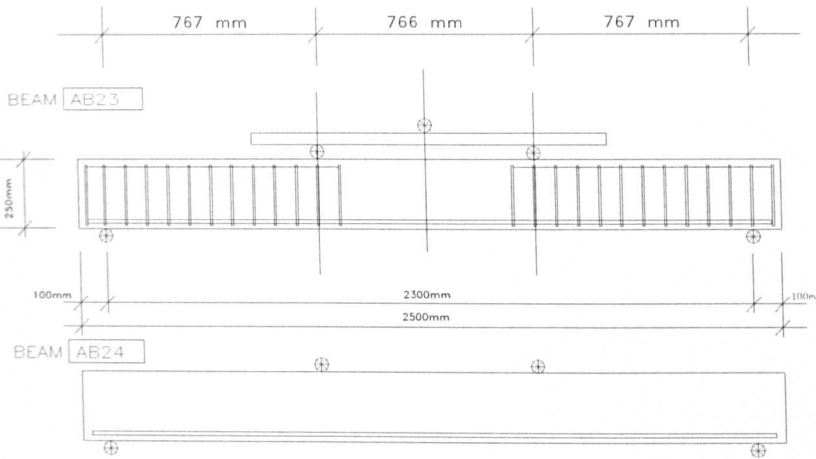


**Main reinforcement:**  
C&GFRP bars, 3 No dia. 13.5mm  
No anchorage.  
**Shear reinforcement:**  
None

**Concrete confinement:**  
Between the loading points: Straps 25.4 mm wide x 0.8 mm thick @ 30 mm c/c  
From the loading to the support point: straps 25.4 mm wide x 0.8 mm thick @ 75 mm c/c

c:\fibres\acadwps\cgb21-22

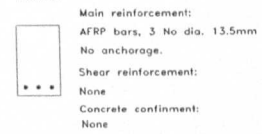
## A.4 Reinforcement arrangement in beams AB23 to AB28



Main reinforcement:  
AFRP bars, 2 No dia. 13.5mm  
No anchorage.

Shear reinforcement:  
G.F.R.P. links 4mm thick, 10mm wide  
Spacing: 76.7mm c/c.

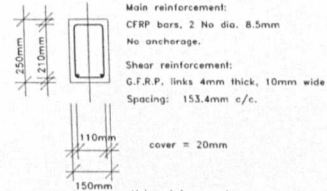
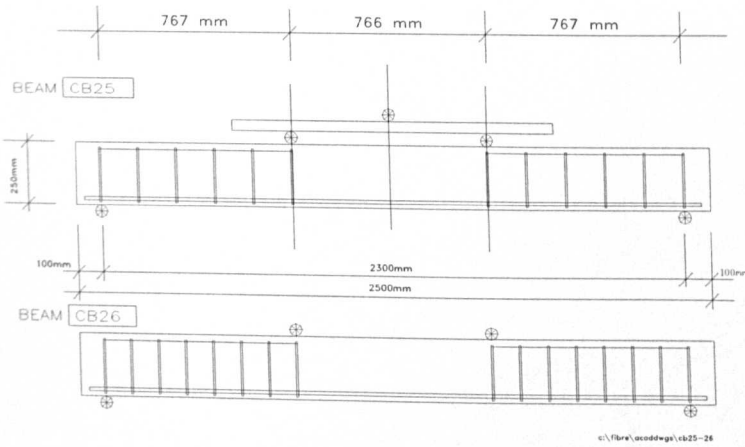
cover = 20mm



Main reinforcement:  
AFRP bars, 2 No dia. 13.5mm  
No anchorage.

Shear reinforcement:  
None  
Concrete confinement:  
None

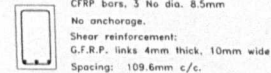
c:\fibres\ocodddwg\ab23-24



Main reinforcement:  
CFRP bars, 2 No dia. 8.5mm  
No anchorage.

Shear reinforcement:  
G.F.R.P. links 4mm thick, 10mm wide  
Spacing: 153.4mm c/c.

cover = 20mm

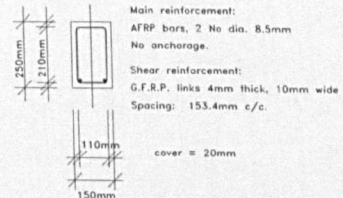
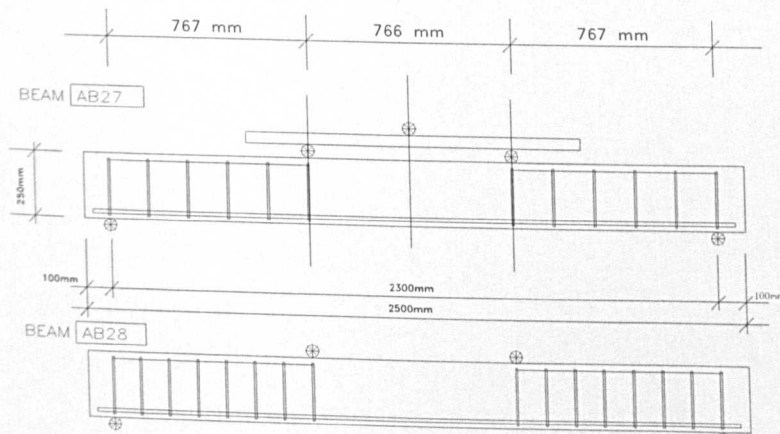


Main reinforcement:  
CFRP bars, 3 No dia. 8.5mm  
No anchorage.

Shear reinforcement:  
G.F.R.P. links 4mm thick, 10mm wide  
Spacing: 109.6mm c/c.

Confinement:  
Straps 25.4 mm wide x 0.8 mm thick @ 30 mm c/c

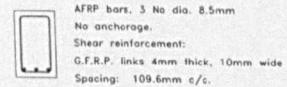
c:\fibres\ocodddwg\cb25-26



Main reinforcement:  
AFRP bars, 2 No dia. 8.5mm  
No anchorage.

Shear reinforcement:  
G.F.R.P. links 4mm thick, 10mm wide  
Spacing: 153.4mm c/c.

cover = 20mm



Main reinforcement:  
AFRP bars, 3 No dia. 8.5mm  
No anchorage.

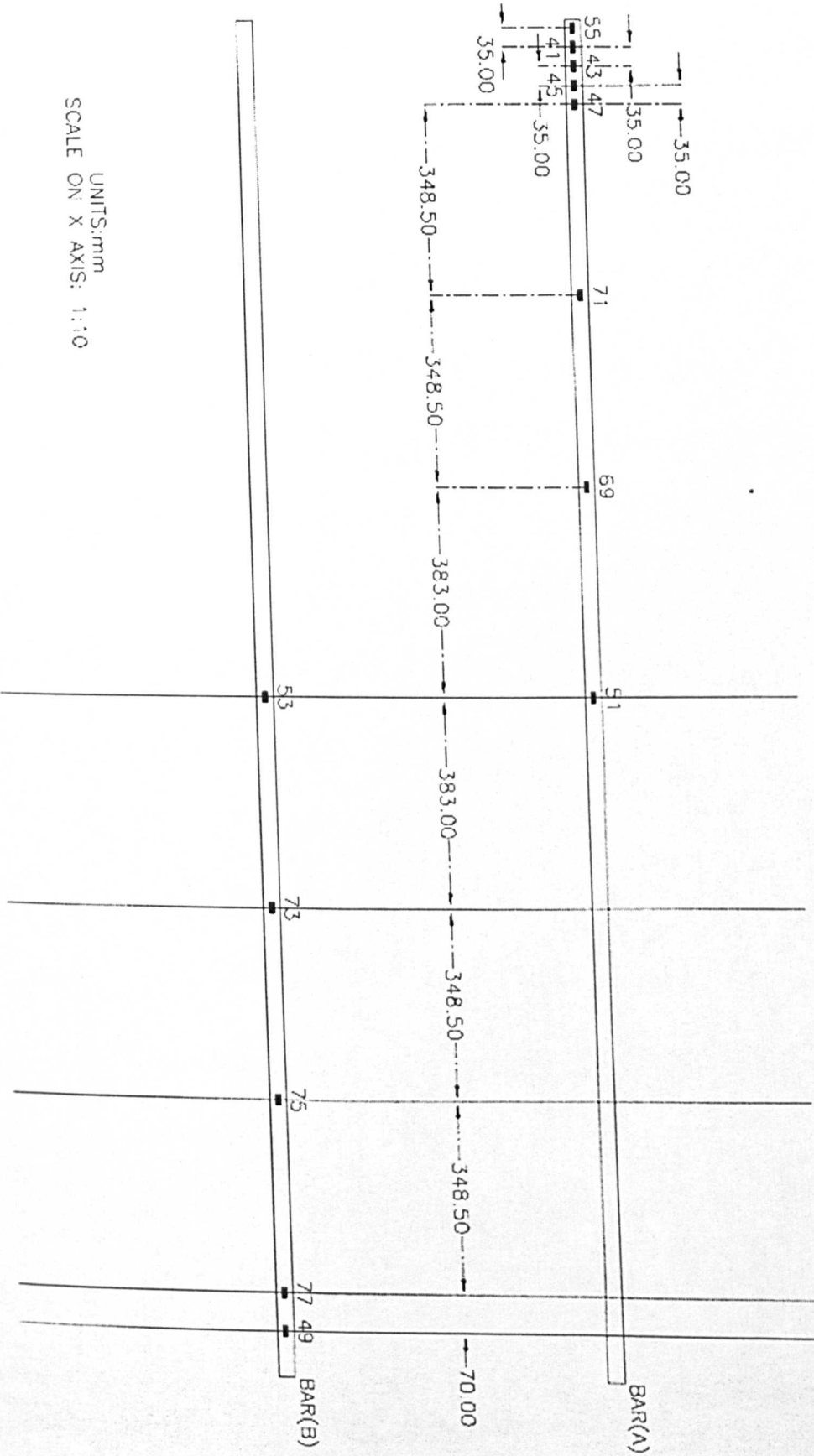
Shear reinforcement:  
G.F.R.P. links 4mm thick, 10mm wide  
Spacing: 109.6mm c/c.

Confinement:  
Straps 25.4 mm x 0.8 mm thick @ 30 mm c/c

**A.5 Arrangement of strain gauges in beams of phases 1-3**

**STRAIN GAUGES ARRANGEMENT**

GAUGES 41-45:  
5mm long  
THE REST:  
10mm long

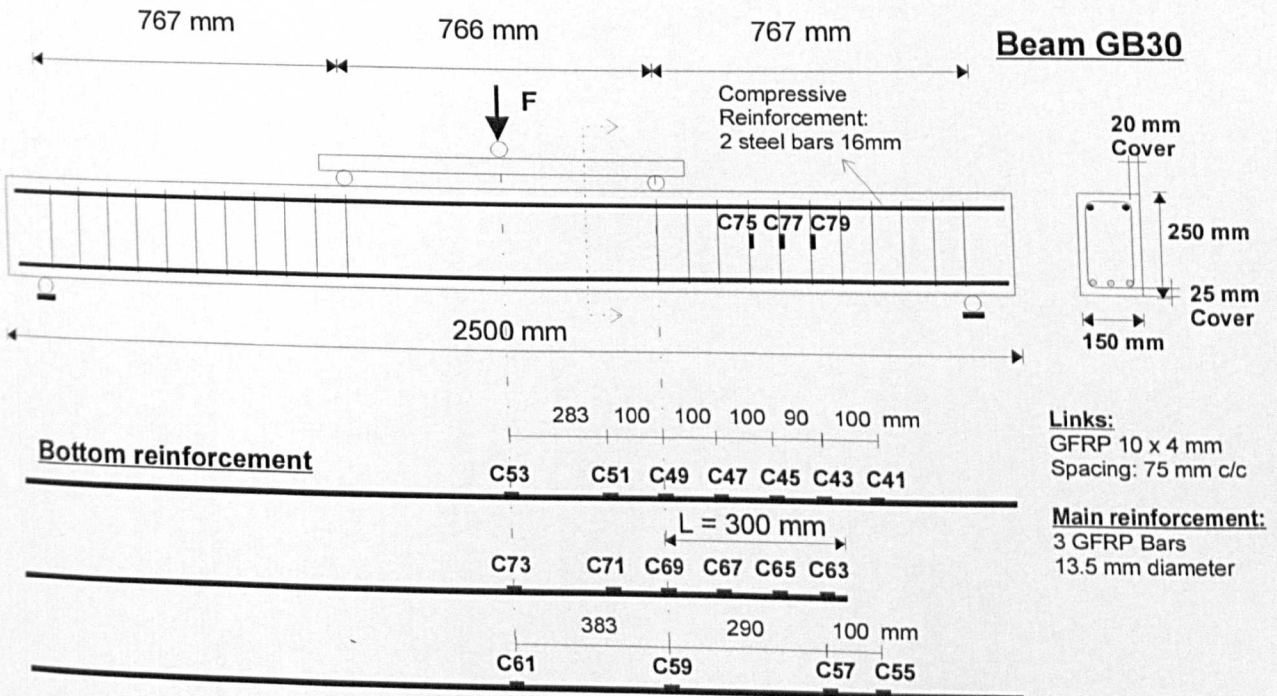
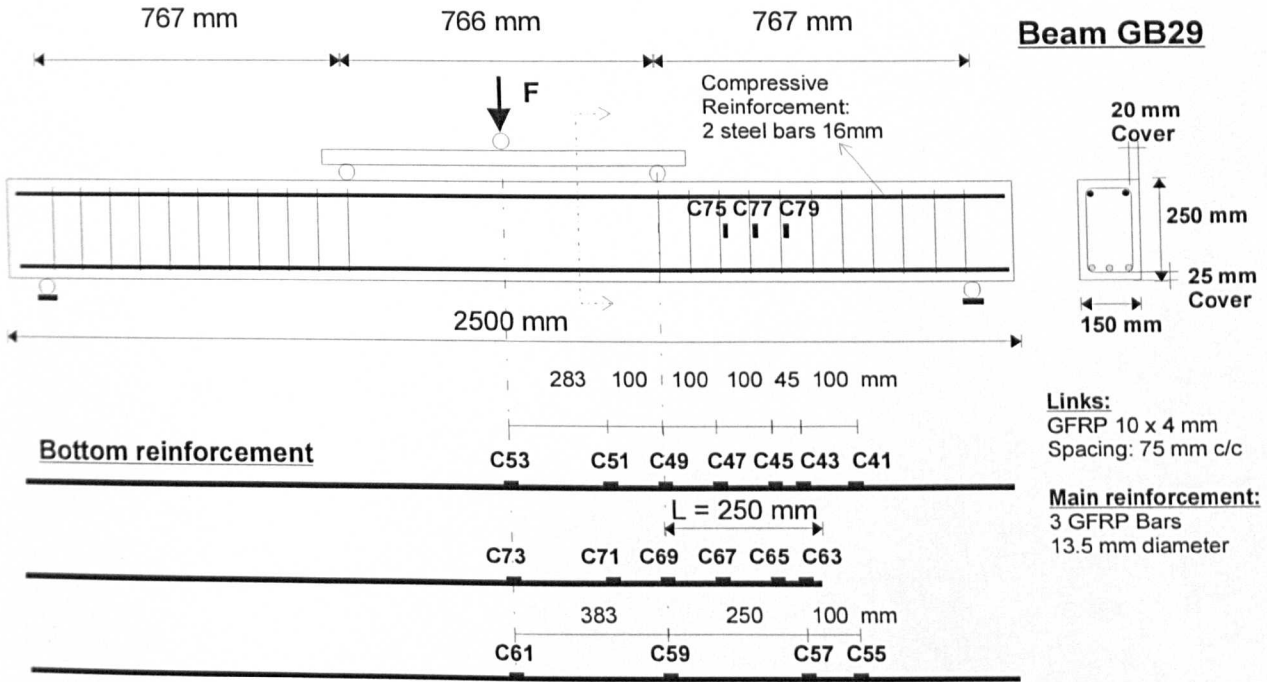


UNITS: mm  
SCALE ON X AXIS: 1:10

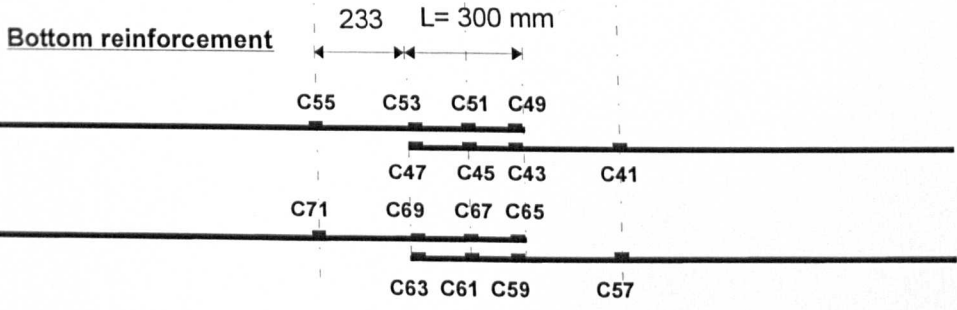
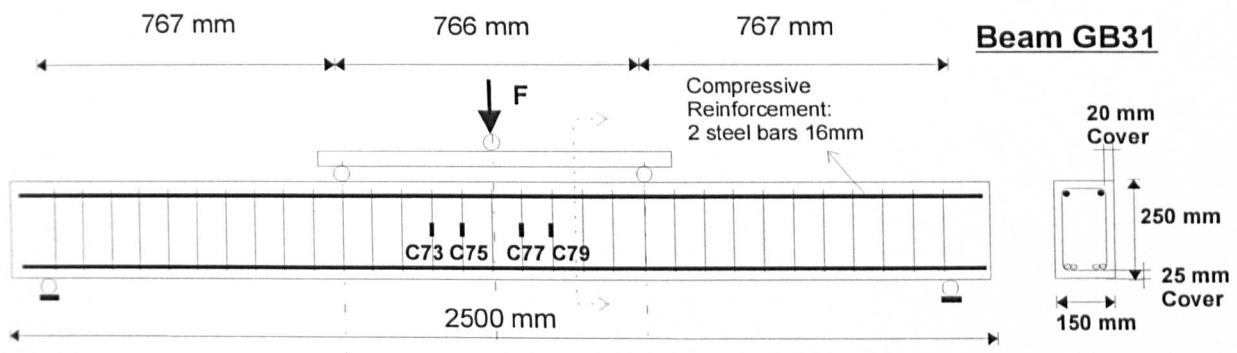
# APPENDIX B

## Reinforcement arrangement and instrumentation in Phase 4 beams

### B.1 Reinforcement and strain gauge arrangement in beams GB29 and GB30

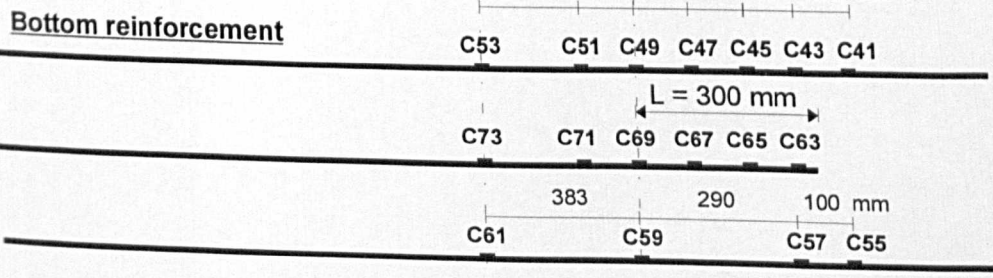
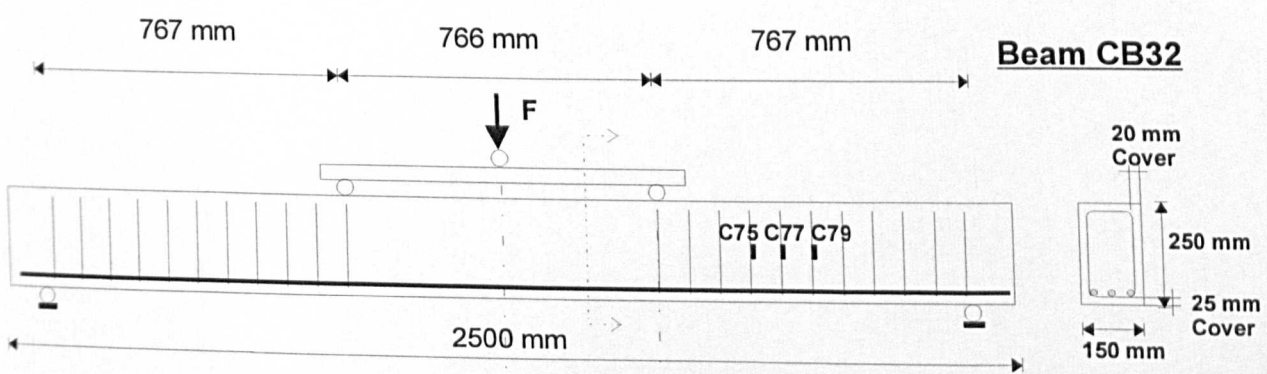


**B.2 Reinforcement and strain gauge arrangement in beams GB31 and CB32**



**Links:**  
GFRP 10 x 4 mm  
Spacing: 75 mm c/c

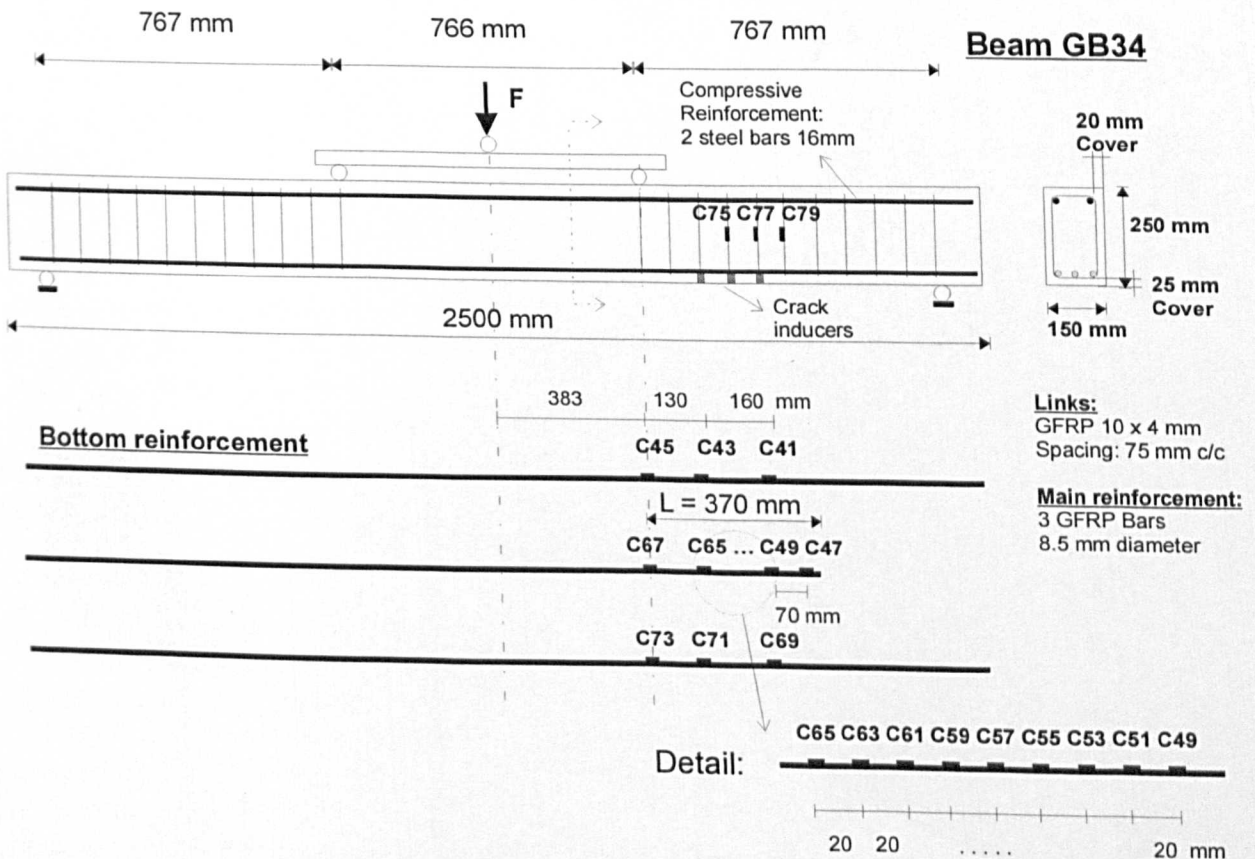
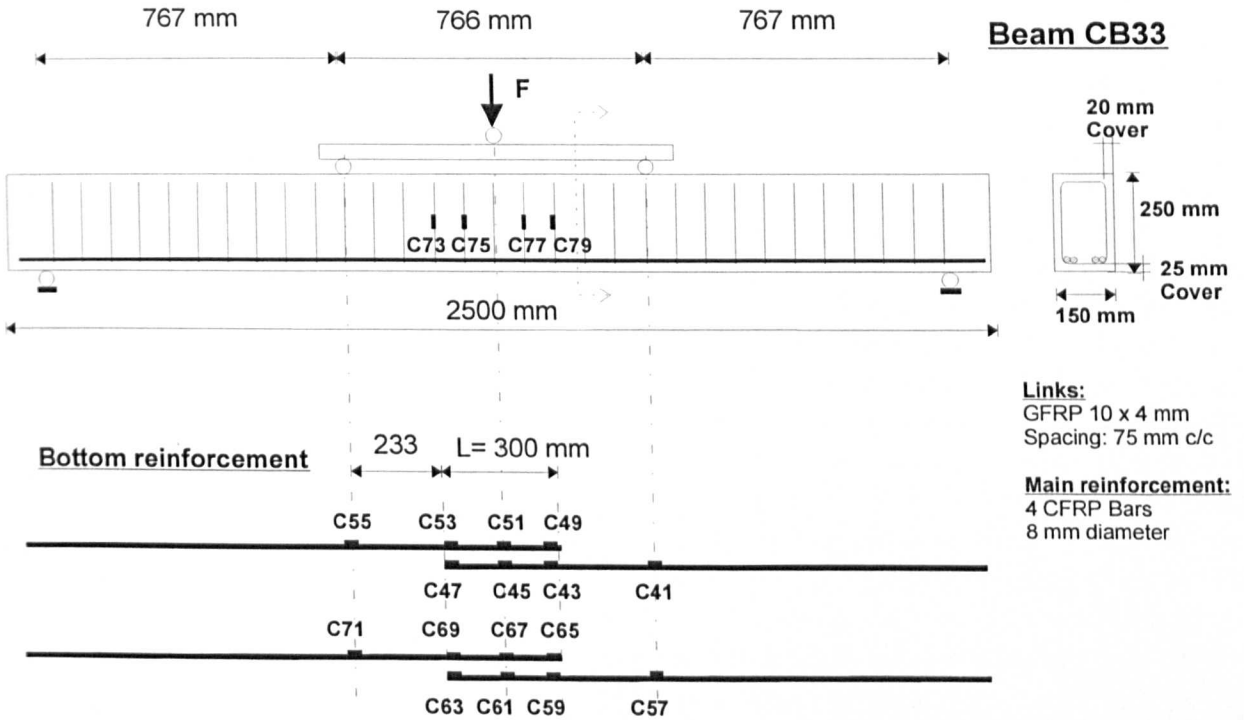
**Main reinforcement:**  
4 GFRP Bars  
13.5 mm diameter



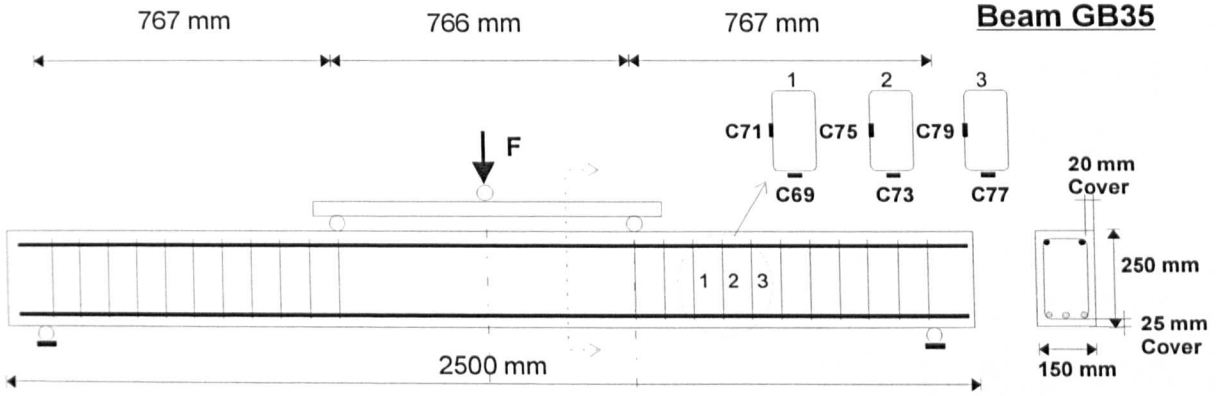
**Links:**  
GFRP 10 x 4 mm  
Spacing: 75 mm c/c

**Main reinforcement:**  
3 CFRP Bars  
8 mm diameter

### B.3 Reinforcement and strain gauge arrangement in beams CB33 and GB34



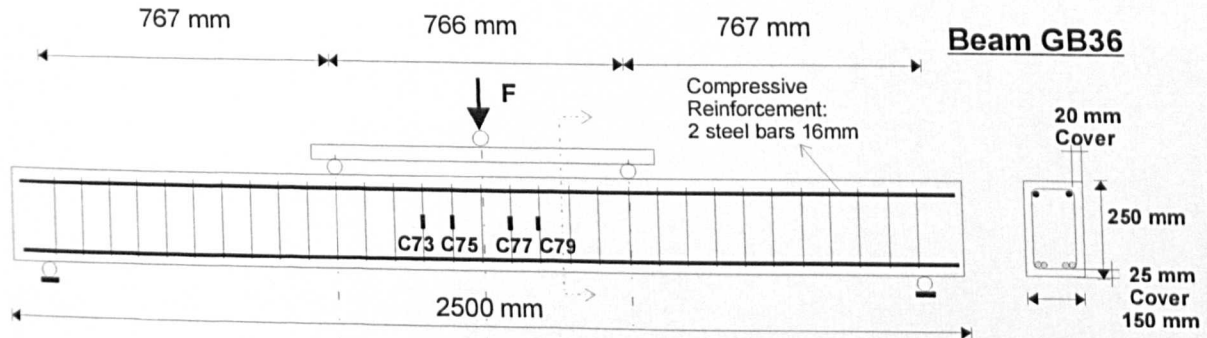
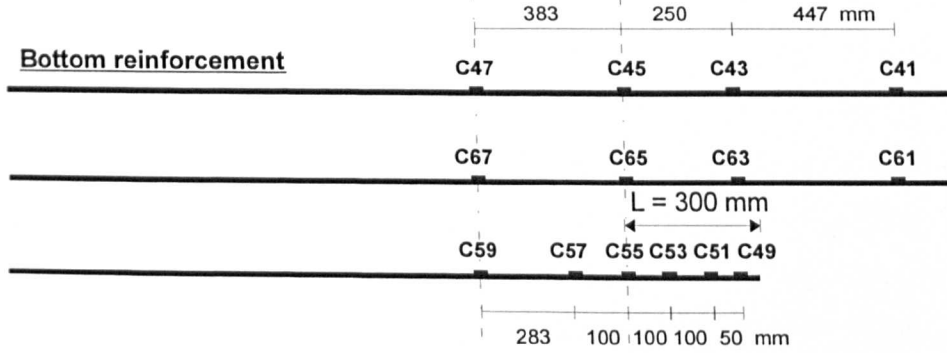
## B.4 Reinforcement and strain gauge arrangement in beams GB35 and GB36



**Links:**  
 GFRP 10 x 4 mm  
 Spacing: 75 mm c/c

**Main reinforcement:**  
 3 GFRP Bars  
 8.5 mm diameter

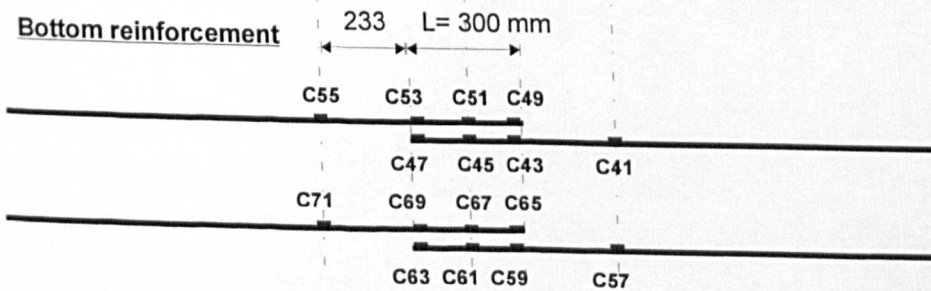
### Bottom reinforcement



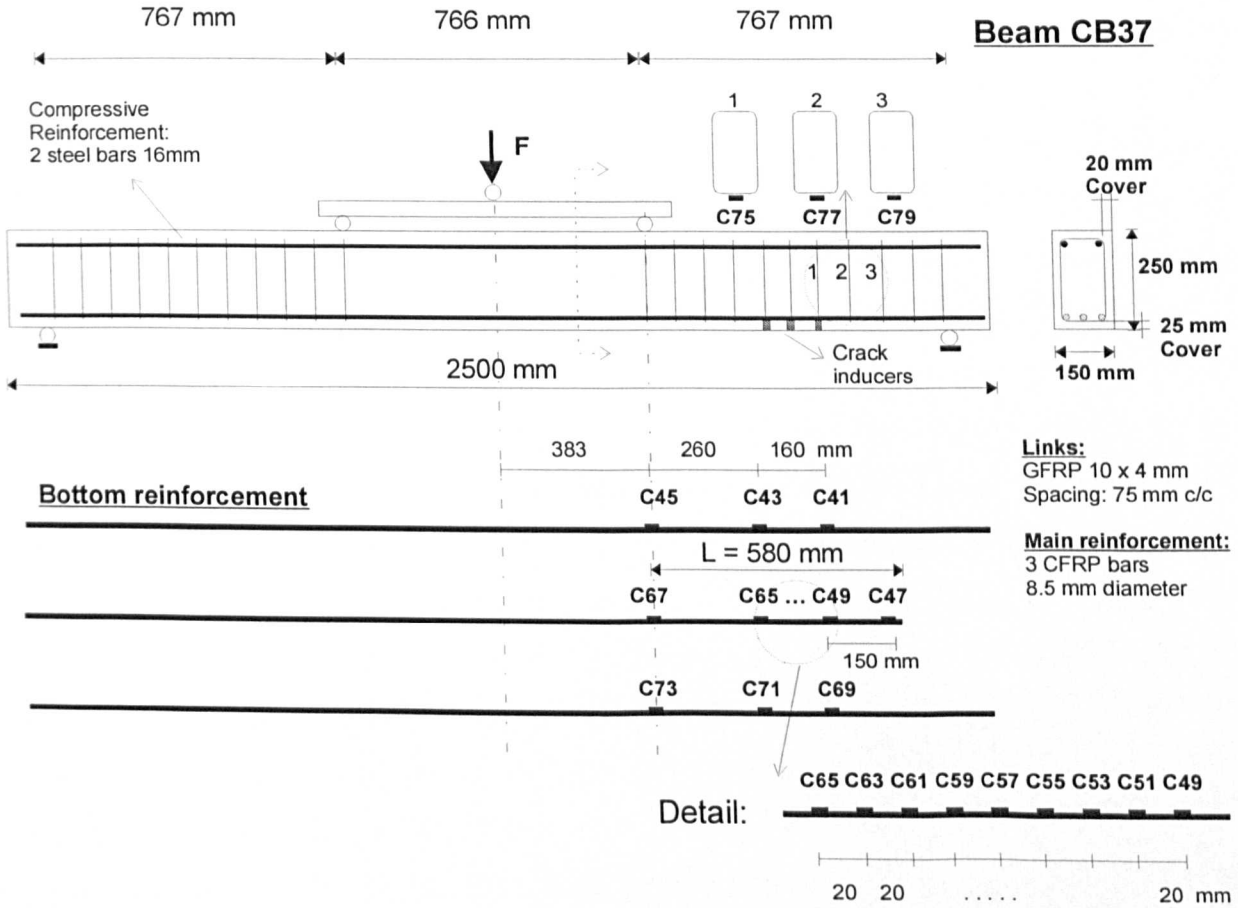
**Links:**  
 GFRP 10 x 4 mm  
 Spacing: 75 mm c/c

**Main reinforcement:**  
 4 GFRP Bars  
 8.5 mm diameter

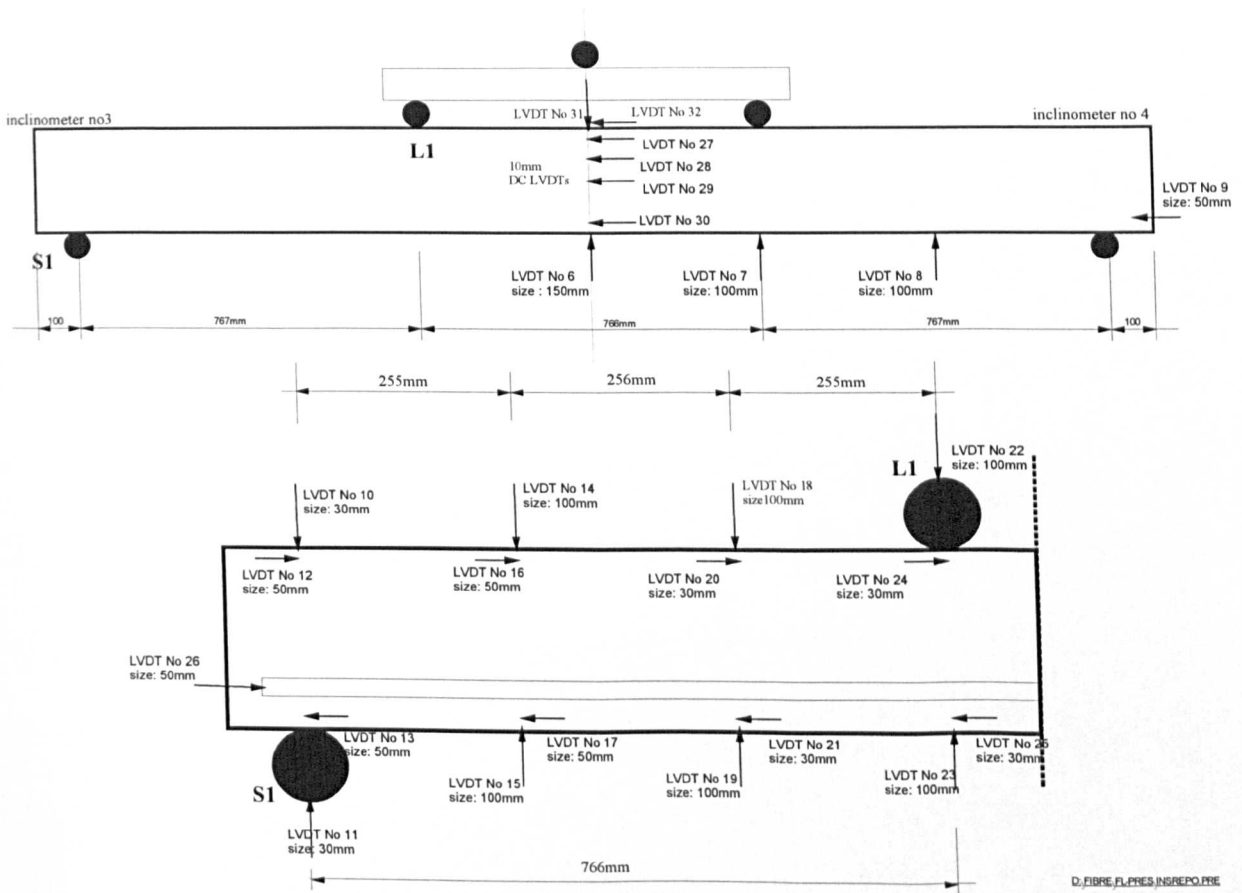
### Bottom reinforcement



# B.5 Reinforcement and strain gauge arrangement in beams CB37



## B.6 Arrangement of LVDTs used in beam testing



# APPENDIX C

## Pullout test results

### C.1 Summary of the pullout test results

Table C.1.1

|           | D<br>(mm) | L<br>(mm) | F <sub>max</sub><br>(kN) | σ <sub>max</sub><br>(MPa) | δ <sub>1</sub><br>(mm) | δ <sub>2</sub><br>(mm) | τ*<br>(MPa) | f <sub>cu</sub><br>(MPa) | Failure<br>mode |
|-----------|-----------|-----------|--------------------------|---------------------------|------------------------|------------------------|-------------|--------------------------|-----------------|
| 37Gr2DI   | 13.5      | 27        | 14.5                     | 101                       | ~                      | ~                      | 12.7        | 37                       | PO              |
| 37Gr2DII  | 13.5      | 27        | 16.7                     | 116                       | ~                      | ~                      | 14.6        | 37                       | PO              |
| 37Gr4DI   | 13.5      | 54        | 31.7                     | 221                       | ~                      | ~                      | 13.8        | 37                       | PO              |
| 37Gr4DII  | 13.5      | 54        | 27.3                     | 190                       | ~                      | ~                      | 11.9        | 37                       | PO              |
| 49Gr6DI   | 13.5      | 81        | 43.0                     | 300                       | ~                      | ~                      | 12.5        | 49                       | PO              |
| 49Gr6DII  | 13.5      | 81        | 44.7                     | 312                       | ~                      | ~                      | 13.0        | 49                       | PO              |
| 46Gr6DI   | 13.5      | 81        | 43.1                     | 301                       | ~                      | ~                      | 12.6        | 46                       | PO              |
| 46Gr6DII  | 13.5      | 81        | 45.3                     | 316                       | ~                      | ~                      | 13.2        | 46                       | PO              |
| 46Gr6DIII | 13.5      | 81        | 26.9#                    | 188                       | ~                      | ~                      | 7.8         | 46                       | PO              |
| 46Gr6DIV  | 13.5      | 81        | 48.2                     | 337                       | ~                      | ~                      | 14.0        | 46                       | PO              |
| 49Gr8DI   | 13.5      | 108       | 51.2                     | 357                       | ~                      | ~                      | 11.2        | 49                       | PO              |
| 49Gr8DII  | 13.5      | 108       | 45.3                     | 316                       | ~                      | ~                      | 9.9         | 49                       | PO              |
| 46Gr10DI  | 13.5      | 135       | 48.4                     | 338                       | ~                      | ~                      | 8.5         | 46                       | PO              |
| 46Gr10DII | 13.5      | 135       | 53.5                     | 373                       | ~                      | ~                      | 9.3         | 46                       | PO              |
| 30Cr2DI   | 13.5      | 30        | 13.5                     | 94                        | ~                      | ~                      | 10.6        | 30                       | PO              |
| 30Cr3DI   | 13.5      | 45        | 21.2                     | 148                       | ~                      | ~                      | 11.1        | 30                       | PO              |
| 30Cr4.5DI | 13.5      | 60        | 27.5                     | 192                       | ~                      | ~                      | 10.8        | 30                       | PO              |
| 30Cr5.5DI | 13.5      | 75        | 23.4#                    | 163                       | ~                      | ~                      | 7.4         | 30                       | PO              |
| 46Cr6DI   | 13.5      | 81        | 40.4                     | 282                       | ~                      | ~                      | 11.8        | 46                       | PO              |
| 46Cr6DII  | 13.5      | 81        | 50.1                     | 350                       | ~                      | ~                      | 14.6        | 46                       | PO              |

#### Notation:

D = Diameter of bar / dimensions of bar's cross section  
L = Embedment Length  
F<sub>max</sub> = Maximum pull-out load  
σ<sub>max</sub> = Maximum normal stress  
δ<sub>1</sub> = Loaded end slip at F<sub>max</sub>

δ<sub>2</sub> = Unloaded end slip at F<sub>max</sub>  
τ\* = Maximum average bond stress  
PO = Pull-out mode of failure  
# = Not reliable result

**Table C.1.2**

|         | D<br>(mm) | L<br>(mm) | $F_{max}$<br>(kN) | $\sigma_{max}$<br>(MPa) | $\delta_1$<br>(mm) | $\delta_2$<br>(mm) | $\tau^*$<br>(MPa) | $f_{cu}$<br>(MPa) | Failure<br>mode |
|---------|-----------|-----------|-------------------|-------------------------|--------------------|--------------------|-------------------|-------------------|-----------------|
| 45Gr2D  | 13.5      | 27        | 13.4              | 93                      | 0.58               | 0.57               | 11.7              | 45                | PO              |
| 45Gr4D  | 13.5      | 54        | 23.0              | 160                     | 0.66               | 0.47               | 10.0              | 45                | PO              |
| 45Gr6D  | 13.5      | 81        | 41.0              | 286                     | 0.91               | 0.48               | 11.9              | 45                | PO              |
| 45Gr8D  | 13.5      | 108       | 40.5              | 283                     | 0.96               | 0.21               | 8.9               | 45                | PO              |
| 45Gr10D | 13.5      | 135       | 51.9              | 362                     | 1.03               | 0.32               | 9.1               | 45                | PO              |
| 45Cr2D  | 13.5      | 27        | 15.1              | 105                     | 0.43               | ~                  | 13.2              | 45                | PO              |
| 45Cr4D  | 13.5      | 54        | 32.1              | 223                     | 0.44               | 0.34               | 14.0              | 45                | PO              |
| 45Cr6D  | 13.5      | 81        | 30.1              | 210                     | 0.44               | 0.25               | 8.8               | 45                | PO              |
| 45Cr8D  | 13.5      | 108       | 44.8              | 313                     | 0.55               | 0.32               | 9.8               | 45                | PO              |
| 45Cr10D | 13.5      | 135       | 44.2              | 308                     | 0.53               | 0.19               | 7.7               | 45                | PO              |
| 45Ar6D  | 13.5      | 81        | 34.8              | 242                     | 0.42               | 0.33               | 10.1              | 45                | PO              |
| 45Hr6D  | 13.5      | 81        | 37.3              | 260                     | 0.72               | 0.23               | 10.9              | 45                | PO              |
| 45Gr10d | 8.5       | 81        | 16.5              | 328                     | 0.66               | 0.40               | 8.1               | 45                | PO              |
| 45Cr10d | 8         | 81        | 15.3              | 303                     | 0.49               | 0.25               | 7.5               | 45                | PO              |
| 45Cc    | 21        | 81        | 46.1              | 172                     | ~                  | ~                  | 8.6               | 45                | PO              |
| 45Gsm   | 16        | 81        | 4.9               | 24                      | 0.65               | ~                  | 1.2               | 45                | PO              |
| 45Hsm   | 8         | 81        | 2.6               | 51                      | 0.19               | 0.02               | 1.3               | 45                | PO              |
| 45Gs    | 8x8       | 81        | 24.5              | 339                     | 0.99               | 0.41               | 8.9               | 45                | PO              |
| 45Cs    | 8x8       | 81        | 25.0              | 346                     | 0.57               | 0.32               | 9.0               | 45                | PO              |
| 45As    | 8x8       | 81        | 14.8              | 204                     | ~                  | ~                  | 5.4               | 45                | PO              |

**Notation:**

- D = Diameter of bar / dimensions of bar's cross section  
L = Embedment length  
 $F_{max}$  = Maximum pull-out load  
 $\sigma_{max}$  = Maximum normal stress  
 $\delta_1$  = Loaded end slip at  $F_{max}$   
 $\delta_2$  = Unloaded end slip at  $F_{max}$   
 $\tau^*$  = Maximum average bond stress  
PO = Pull-out mode of failure  
Cc = CFRP bar with ring cross section  
( $r_{out}=21\text{mm}$ ,  $r_{in}=10\text{mm}$ )  
Gsm = GFRP smooth surface bar  
Hsm = Hybrid smooth bar

**Table C.1.3**

|         | D<br>(mm) | L<br>(mm) | $F_{max}$<br>(kN) | $\sigma_{max}$<br>(MPa) | $\delta_1$<br>(mm) | $\delta_2$<br>(mm) | $\tau^*$<br>(MPa) | $f_{cu}$<br>(MPa) | Failure<br>mode |
|---------|-----------|-----------|-------------------|-------------------------|--------------------|--------------------|-------------------|-------------------|-----------------|
| 15Gr2D  | 13.5      | 27        | 3.2               | 22                      | 0.79               | 0.65               | 2.8               | 15                | PO              |
| 15Gr4D  | 13.5      | 54        | 7.1               | 50                      | 0.44               | 0.42               | 3.1               | 15                | PO              |
| 15Gr6D  | 13.5      | 81        | 6.7               | 46                      | 0.80               | 0.70               | 1.9               | 15                | PO              |
| 15Gr8D  | 13.5      | 108       | 11.5              | 80                      | 0.67               | 0.47               | 2.5               | 15                | PO              |
| 15Gr10D | 13.5      | 135       | 14.8              | 103                     | 0.81               | 0.42               | 2.6               | 15                | PO              |
| 15Cr2D  | 13.5      | 27        | 4.2               | 29                      | 0.44               | 0.43               | 3.7               | 15                | PO              |
| 15Cr4D  | 13.5      | 54        | 8.0               | 56                      | 0.48               | ~                  | 3.5               | 15                | PO              |
| 15Cr6D  | 13.5      | 81        | 10.8              | 75                      | 0.30               | 0.16               | 3.1               | 15                | PO              |
| 15Cr8D  | 13.5      | 108       | 13.0              | 91                      | 0.40               | 0.29               | 2.8               | 15                | PO              |
| 15Cr10D | 13.5      | 135       | 12.7              | 88                      | 0.49               | 0.41               | 2.2               | 15                | PO              |
| 15Ar6D  | 13.5      | 81        | 4.2               | 29                      | 1.17               | 1.11               | 1.2               | 15                | PO              |
| 15Hr6D  | 13.5      | 81        | 7.6               | 52                      | 0.65               | 0.53               | 2.2               | 15                | PO              |
| 15Gr10d | 8.5       | 81        | 4.8               | 95                      | 0.70               | 0.51               | 2.3               | 15                | PO              |
| 15Cr10d | 8.0       | 81        | 4.4               | 87                      | 0.43               | 0.28               | 2.2               | 15                | PO              |
| 15Ar10d | 8.0       | 81        | 4.9               | 97                      | 0.37               | 0.23               | 2.4               | 15                | PO              |
| 15Cc    | 21.0      | 81        | 15.6              | 58                      | 0.74               | 0.62               | 2.9               | 15                | PO              |
| 15Gsm   | 16.0      | 81        | 0.3               | 2                       | 0.37               | 0.36               | 0.1               | 15                | PO              |
| 15Hsm   | 8.0       | 81        | 1.4               | 28                      | 0.09               | ~                  | 0.7               | 15                | PO              |
| 15Gs    | 8x8       | 81        | 8.7               | 120                     | 0.42               | 0.14               | 3.1               | 15                | PO              |
| 15Cs    | 8x8       | 81        | 5.6               | 76                      | 0.48               | ~                  | 2.0               | 15                | PO              |
| 15As    | 8x8       | 81        | 7.4               | 102                     | 0.24               | 0.00               | 2.7               | 15                | PO              |

**Notation:**

- D = Diameter of bar / dimensions of bar's cross section  
L = Embedment length  
 $F_{max}$  = Maximum pull-out load  
 $\sigma_{max}$  = Maximum normal stress  
 $\delta_1$  = Loaded end slip at  $F_{max}$   
 $\delta_2$  = Unloaded end slip at  $F_{max}$   
 $\tau^*$  = Maximum average bond stress  
PO = Pull-out mode of failure  
Cc = CFRP bar with ring cross section  
( $r_{out}=21\text{mm}$ ,  $r_{in}=10\text{mm}$ )  
Gsm = GFRP smooth surface bar  
Hsm = Hybrid smooth surface bar

**Table C.1.4**

|             | D<br>(mm) | L<br>(mm) | F <sub>max</sub><br>(kN) | σ <sub>max</sub><br>(MPa) | δ <sub>1</sub><br>(mm) | δ <sub>2</sub><br>(mm) | τ*<br>(MPa) | f <sub>cu</sub><br>(MPa) | Failure<br>mode |
|-------------|-----------|-----------|--------------------------|---------------------------|------------------------|------------------------|-------------|--------------------------|-----------------|
| 41Gr6dI     | 8.5       | 48        | 15.6                     | 274                       | 1.27                   | 1.16                   | 12.2        | 41                       | PO              |
| 41Gr6dII    | 8.5       | 48        | 11.9                     | 208                       | 1.01                   | 0.80                   | 9.3         | 41                       | PO              |
| 41Gr8dI     | 8.5       | 64        | 21.9                     | 386                       | 1.07                   | 0.75                   | 12.8        | 41                       | PO              |
| 41Gr8dII    | 8.5       | 64        | 24.8                     | 436                       | 1.07                   | 0.71                   | 14.5        | 41                       | PO              |
| 41Gr10dI    | 8.5       | 80        | 25.6                     | 451                       | 1.31                   | 0.65                   | 12.0        | 41                       | PO              |
| 41Gr10dII   | 8.5       | 80        | 28.8                     | 508                       | -                      | -                      | 13.5        | 41                       | PO              |
| 41Cr6dI     | 8         | 48        | 16.9                     | 336                       | 0.43                   | 0.37                   | 14.0        | 41                       | PO              |
| 41Cr6dII    | 8         | 48        | 15.4                     | 305                       | 0.46                   | 0.31                   | 12.7        | 41                       | PO              |
| 41Cr8dI     | 8         | 64        | 22.1                     | 439                       | 0.59                   | 0.37                   | 13.7        | 41                       | PO              |
| 41Cr8dII    | 8         | 64        | 22.2                     | 440                       | 0.51                   | 0.02                   | 13.8        | 41                       | PO              |
| 41Cr10dI    | 8         | 80        | 25.7                     | 510                       | 0.73                   | 0.41                   | 12.8        | 41                       | PO              |
| 41Cr10dII   | 8         | 80        | 28.7                     | 571                       | 0.53                   | 0.34                   | 14.3        | 41                       | PO              |
| 41G24/6dI   | 10.5      | 60        | 10.4                     | 120                       | 0.24                   | 0.96                   | 5.3         | 41                       | PO              |
| 41G24/6dII  | 10.5      | 60        | 8.0                      | 92                        | 0.23                   | 0.02                   | 4.0         | 41                       | PO              |
| 41G24/8dI   | 10.5      | 80        | 11.0                     | 127                       | 0.39                   | 0.04                   | 4.2         | 41                       | PO              |
| 41G24/8dII  | 10.5      | 80        | 13.3                     | 153                       | 0.51                   | 0.16                   | 5.0         | 41                       | PO              |
| 41G24/10dI  | 10.5      | 100       | 12.4                     | 143                       | 0.37                   | 0.08                   | 3.8         | 41                       | PO              |
| 41G24/10dII | 10.5      | 100       | 18.7                     | 216                       | 0.55                   | 0.13                   | 5.7         | 41                       | PO              |
| 41G30/6dI   | 10.5      | 60        | 9.2                      | 106                       | 0.27                   | 0.04                   | 4.7         | 41                       | PO              |
| 41G30/6dII  | 10.5      | 60        | 9.1                      | 105                       | 0.26                   | 0.06                   | 4.6         | 41                       | PO              |
| 41G30/8dI   | 10.5      | 80        | 18.3                     | 211                       | 0.60                   | 0.18                   | 6.9         | 41                       | PO              |
| 41G30/8dII  | 10.5      | 80        | 10.6                     | 122                       | 0.37                   | 0.10                   | 4.0         | 41                       | PO              |
| 41G30/10dI  | 10.5      | 100       | 20.2                     | 233                       | 0.51                   | 0.05                   | 6.1         | 41                       | PO              |
| 41G30/10dII | 10.5      | 100       | 22.0                     | 254                       | -                      | -                      | 6.7         | 41                       | PO              |

**Notation:**

- D = Diameter of bar
- L = Embedment length
- F<sub>max</sub> = Maximum pull-out load
- σ<sub>max</sub> = Maximum normal stress
- δ<sub>1</sub> = Loaded end slip at F<sub>max</sub>
- δ<sub>2</sub> = Unloaded end slip at F<sub>max</sub>
- τ\* = Maximum average bond stress
- PO = Pull-out mode of failure
- G24/= GFRP round bar with different type of surface deformations (24 rovings)

G36/= GFRP round bar with different type of surface deformations (36 rovings)

**Table C.1.5**

|           | D<br>(mm) | L<br>(mm) | F <sub>max</sub><br>(kN) | σ <sub>max</sub><br>(MPa) | δ <sub>1</sub><br>(mm) | δ <sub>2</sub><br>(mm) | τ*<br>(MPa) | f <sub>cu</sub><br>(MPa) | Failure<br>mode |
|-----------|-----------|-----------|--------------------------|---------------------------|------------------------|------------------------|-------------|--------------------------|-----------------|
| 39GSAI    | 8x8       | 64        | 32.1                     | 501                       | 0.88                   | 0.67                   | 15.7        | 39                       | SPO             |
| 39GSAIL   | 8x8       | 64        | 32.5                     | 508                       | 0.70                   | 0.19                   | 15.9        | 39                       | SPO             |
| 39GSAIII  | 8x8       | 64        | 31.9                     | 498                       | 0.87                   | 0.16                   | 15.6        | 39                       | SPO             |
| 39Gr8dI   | 8.5       | 64        | 20.1                     | 354                       | 0.92                   | 0.63                   | 11.7        | 39                       | PO              |
| 39Gr8dII  | 8.5       | 64        | 20.3                     | 358                       | 0.95                   | 0.65                   | 11.9        | 39                       | PO              |
| 39Gr8dIII | 8.5       | 64        | 16.6                     | 292                       | 0.63                   | 0.34                   | 9.7         | 39                       | PO              |
| 39Cr8dI   | 8         | 64        | 19.4                     | 386                       | 0.57                   | 0.45                   | 12.0        | 39                       | PO              |
| 39Cr8dII  | 8         | 64        | 15.7                     | 312                       | 0.64                   | 0.07                   | 9.8         | 39                       | PO              |
| 39Cr8dIII | 8         | 64        | 16.9                     | 336                       | 0.57                   | 0.50                   | 10.5        | 39                       | PO              |
| 39GSDI    | 8x8       | 64        | 25.5                     | 398                       | 0.96                   | 0.37                   | 12.5        | 39                       | PO              |
| 39GSDII   | 8x8       | 64        | 31.5                     | 492                       | 1.00                   | 0.42                   | 15.4        | 39                       | SPO             |
| 39GSDIII  | 8x8       | 64        | 22.5                     | 351                       | 0.95                   | 0.44                   | 11.0        | 39                       | PO              |
| 39CSI     | 8x8       | 64        | 31.4                     | 491                       | 0.45                   | 0.20                   | 15.3        | 39                       | SPO             |
| 39CSII    | 8x8       | 64        | 30.3                     | 473                       | 0.50                   | 0.00                   | 14.8        | 39                       | SPO             |
| 39CSIII   | 8x8       | 64        | 27.8                     | 434                       | 0.40                   | 0.00                   | 13.6        | 39                       | SPO             |
| 39Gsl     | 8x8       | 64        | 26.6                     | 415                       | 0.84                   | 0.64                   | 13.0        | 39                       | PO              |
| 39GsII    | 8x8       | 64        | 26.0                     | 406                       | 0.94                   | 0.70                   | 12.7        | 39                       | PO              |
| 39Csl     | 8x8       | 64        | 24.6                     | 384                       | 0.57                   |                        | 12.0        | 39                       | PO              |
| 39CsII    | 8x8       | 64        | 21.9                     | 342                       | 0.60                   | 0.39                   | 10.7        | 39                       | PO              |
| 39GSTI    | 10x10     | 81        | 7.5                      | 75                        | 6.80                   | 6.20                   | 2.4         | 39                       | PO              |
| 39GSTII   | 10x10     | 81        | 11.0                     | 110                       | 6.65                   | 5.10                   | 3.4         | 39                       | PO              |
| 39Ar8dI   | 8         | 64        | 18.0                     | 358                       | 0.55                   | 0.24                   | 11.2        | 39                       | PO              |
| 39Ar8dII  | 8         | 64        | 15.4                     | 306                       | 0.49                   | 0.22                   | 9.6         | 39                       | PO              |

**Notation:**

D = Diameter of bar/ Dimensions of bar  
L = Embedment length  
F<sub>max</sub> = Maximum pull-out load  
σ<sub>max</sub> = Maximum normal stress  
δ<sub>1</sub> = Loaded end slip at F<sub>max</sub>  
δ<sub>2</sub> = Unloaded end slip at F<sub>max</sub>  
τ\* = Maximum average bond stress  
PO = Pull-out mode of failure  
SPO = Sudden pull-out failure  
GSA = GFRP square Atlas 580 (different kind bar surface deformations and resin)

GSD = GFRP square Daron (different kind of resin)  
CS = CFRP square Zoltek / Atlas580 (different kind bar surface deformations and resin)  
GST = GFRP square smooth bar with twisted shape

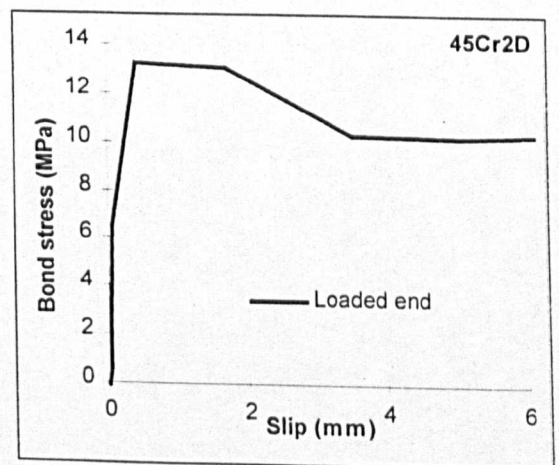
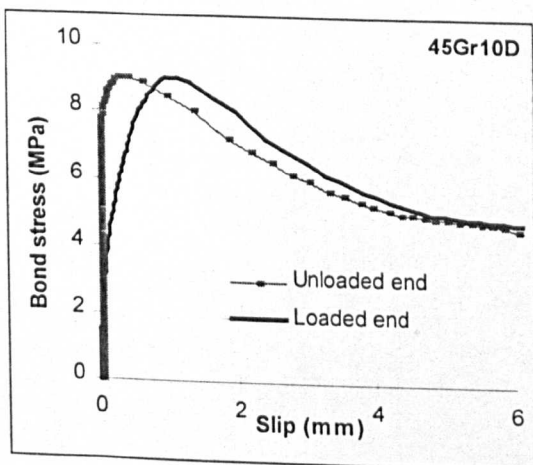
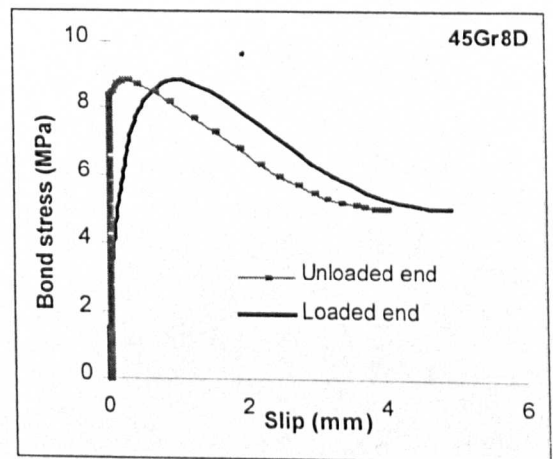
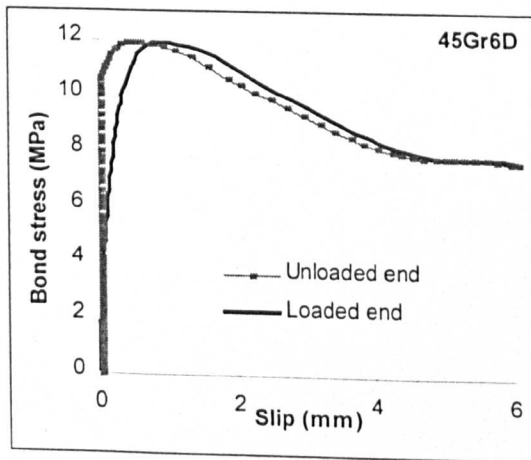
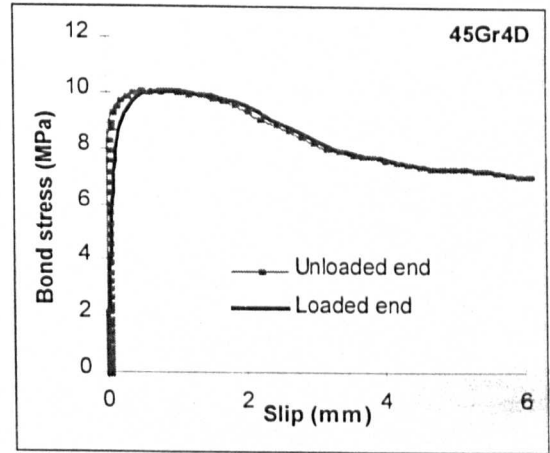
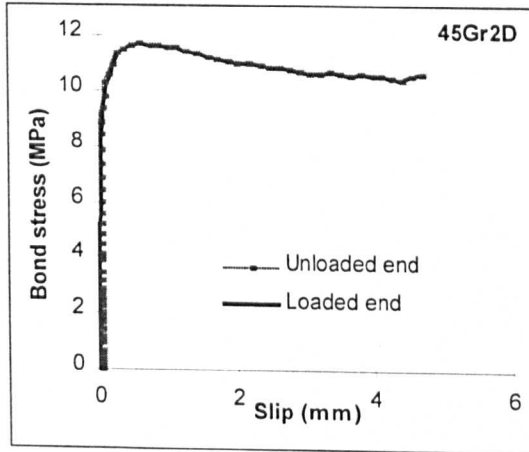
**Table C.1.6**

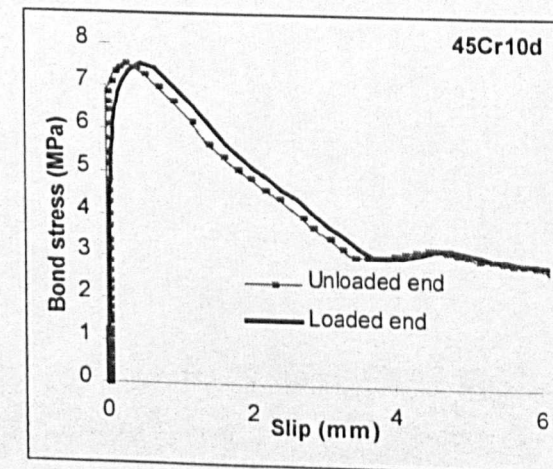
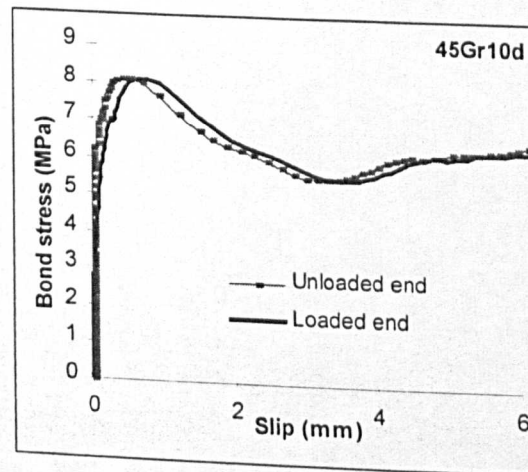
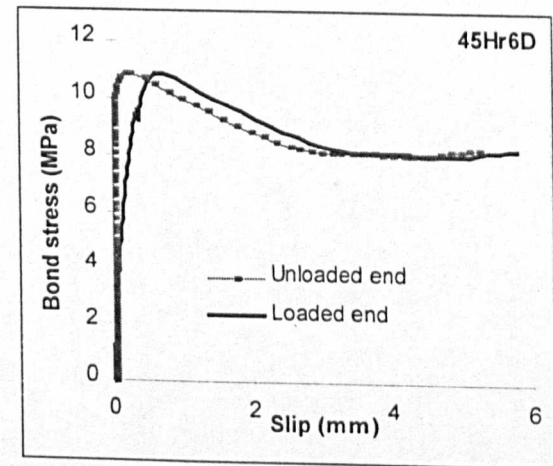
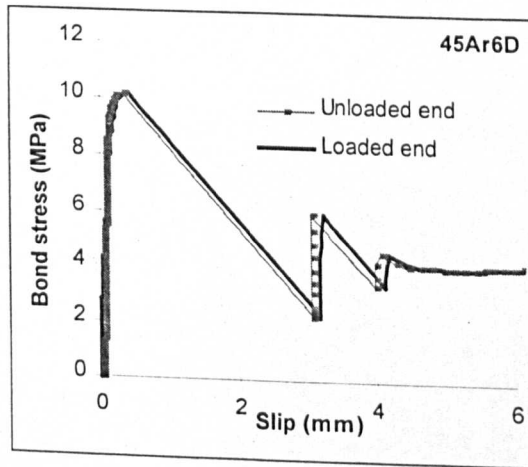
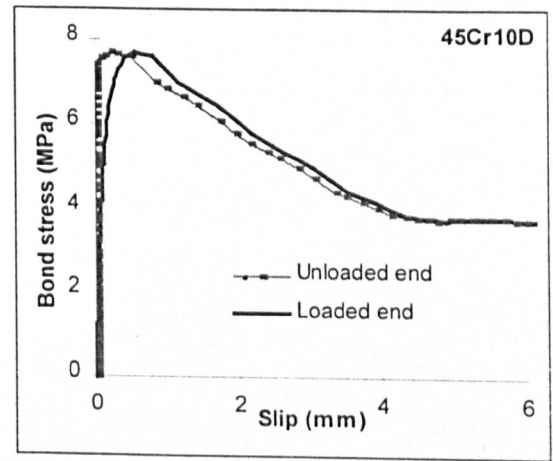
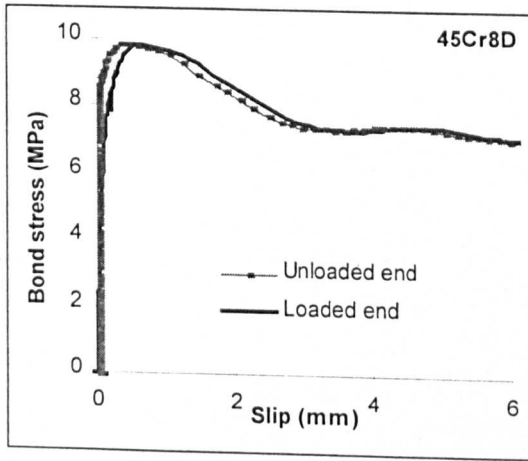
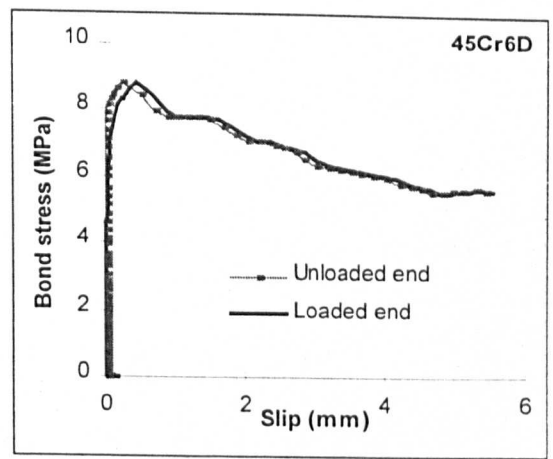
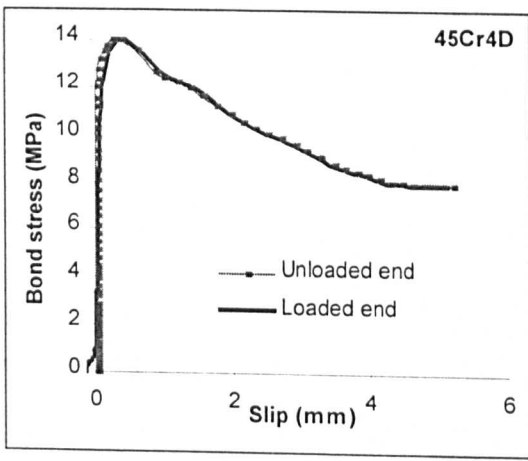
|           | D<br>(mm) | L<br>(mm) | F <sub>max</sub><br>(kN) | σ <sub>max</sub><br>(MPa) | δ <sub>1</sub><br>(mm) | δ <sub>2</sub><br>(mm) | τ*<br>(MPa) | f <sub>cu</sub><br>(MPa) | Failure<br>mode |
|-----------|-----------|-----------|--------------------------|---------------------------|------------------------|------------------------|-------------|--------------------------|-----------------|
| 36GSAI    | 8x8       | 64end     | 29.2                     | 456                       | 0.92                   | 0.07#                  | 14.3        | 36                       | SPO             |
| 36GSAILI  | 8x8       | 64end     | 27.3                     | 426                       | 0.73                   | 0.35                   | 13.4        | 36                       | SPO             |
| 36GSAIII  | 8x8       | 32end     | 13.5                     | 211                       | 0.18#                  | 0.28                   | 13.3        | 36                       | PO              |
| 36GSAIV   | 8x8       | 32end     | 17.4                     | 272                       | 0.54                   | 0.37                   | 17.2        | 36                       | SPO             |
| 36Gr4dI   | 8.5       | 32end     | 10.1                     | 178                       | 0.80                   | 0.75                   | 11.8        | 36                       | PO              |
| 36Gr4dII  | 8.5       | 32end     | 11.8                     | 208                       | 0.51                   | 0.40                   | 13.8        | 36                       | PO              |
| 36Gr4dIII | 8.5       | 32mid     | 10.2                     | 180                       | 0.50                   | 0.31                   | 11.9        | 36                       | PO              |
| 36Gr4dIV  | 8.5       | 32mid     | 10.1                     | 178                       | 0.96                   | 0.94                   | 11.8        | 36                       | PO              |
| 36Cr4dI   | 8         | 32end     | 8.7                      | 173                       | 0.57#                  | 0.62#                  | 10.8        | 36                       | PO              |
| 36Cr4dII  | 8         | 32end     | 10.1                     | 201                       | 0.72                   | 0.54                   | 12.6        | 36                       | PO              |
| 36Cr4dIII | 8         | 32mid     | 10.2                     | 203                       | 0.44                   | 0.37                   | 12.7        | 36                       | PO              |
| 36Cr4dIV  | 8         | 32mid     | 8.6                      | 171                       | 0.33                   | 0.33                   | 10.7        | 36                       | PO              |
| 36CSI     | 8x8       | 64end     | 27.2                     | 425                       | 0.50                   | 0.36                   | 13.3        | 36                       | SPO             |
| 36CSII    | 8x8       | 64end     | 27.2                     | 425                       | 0.27                   | -                      | 13.3        | 36                       | SPO             |
| 36GSI     | 8x8       | 64end     | 18.8                     | 293                       | 1.13                   | 0.49                   | 9.3         | 36                       | PO              |
| 36GSII    | 8x8       | 64end     | 22.1                     | 345                       | 0.83                   | 0.76                   | 10.9        | 36                       | PO              |
| 36CSI     | 8x8       | 32end     | 10.5                     | 164                       | 0.43                   | 0.39                   | 10.4        | 36                       | PO              |
| 36CSII    | 8x8       | 32end     | 14.0                     | 218                       | 0.60                   | 0.38                   | 13.9        | 36                       | PO              |
| 36StI     | 8         | 64end     | 26.7                     | 531                       | 0.88                   | 0.87                   | 16.6        | 36                       | PO              |
| 36StII    | 8         | 64end     | 26.5                     | 527                       | 0.29#                  | 0.78                   | 16.5        | 36                       | PO              |

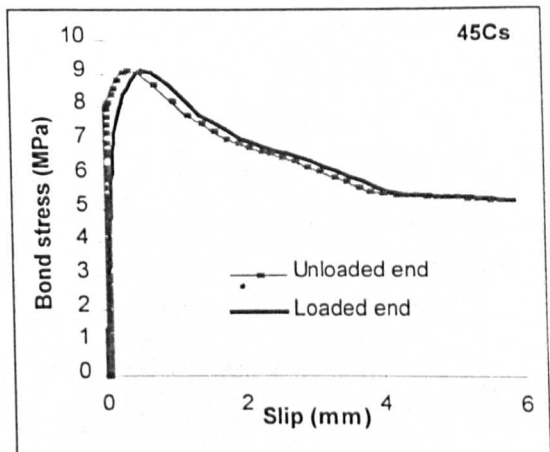
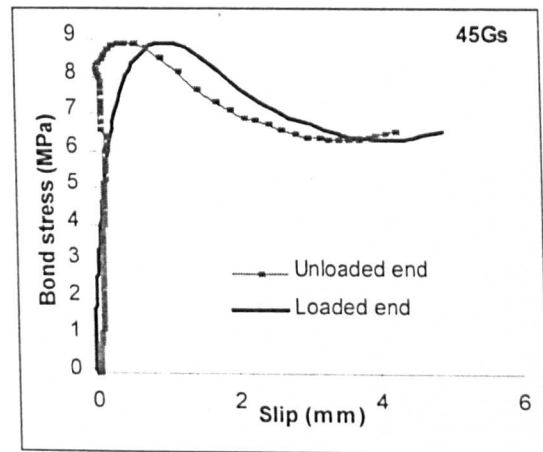
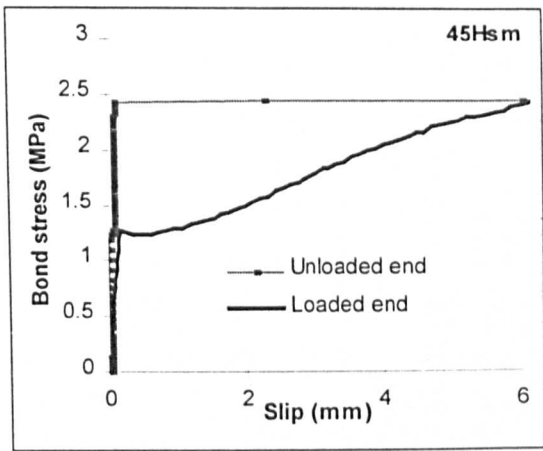
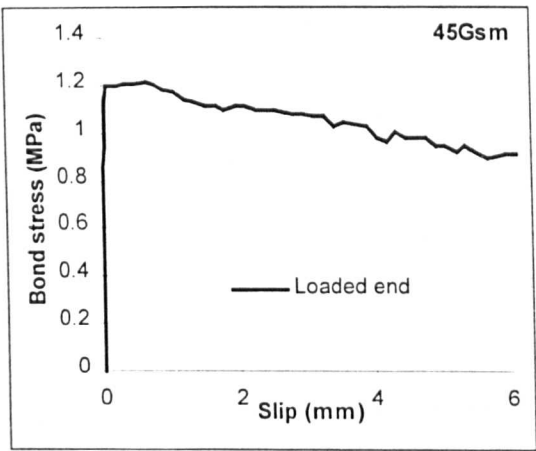
**Notation:**

- D = Diameter of bar/ Dimensions of bar
- L = Embedment length
- F<sub>max</sub> = Maximum pull-out load
- σ<sub>max</sub> = Maximum normal stress
- δ<sub>1</sub> = Loaded end slip at F<sub>max</sub>
- δ<sub>2</sub> = Unloaded end slip at F<sub>max</sub>
- τ\* = Maximum average bond stress
- PO = Pull-out mode of failure
- SPO = Sudden pull-out failure
- GSA = GFRP square Atlas 580 (different kind bar surface deformations and resin)
- CS = CFRP square Zoltek/Atlas 580 (different kind bar surface deformations and resin)
- St = High strength steel deformed bar
- # = Not reliable result

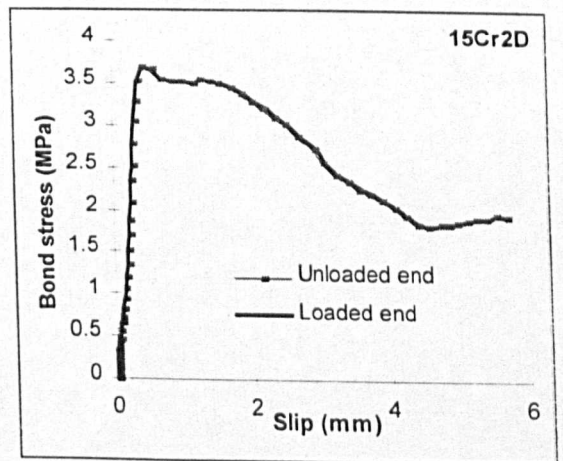
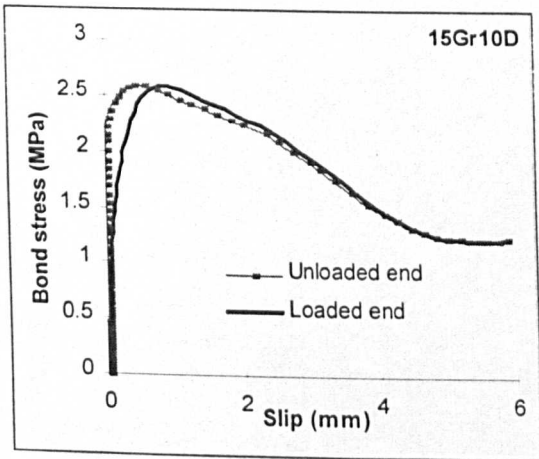
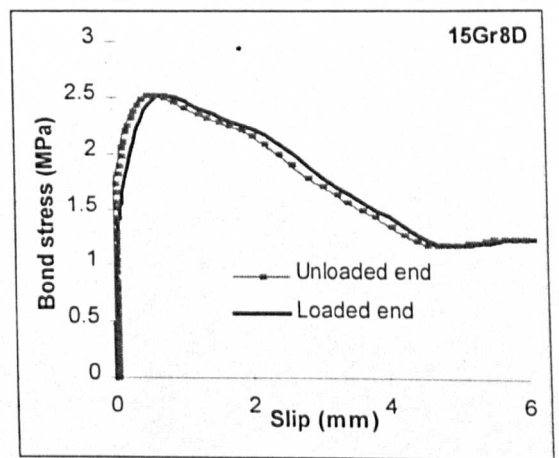
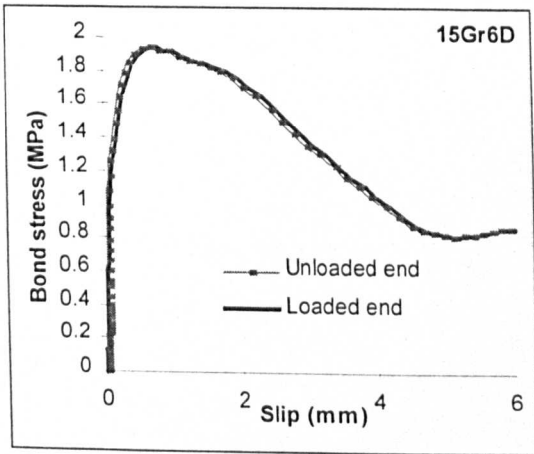
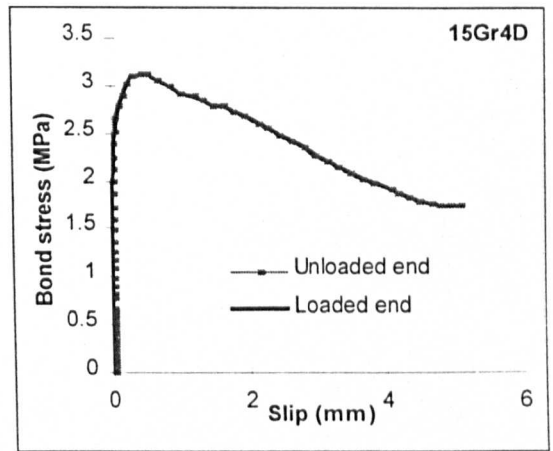
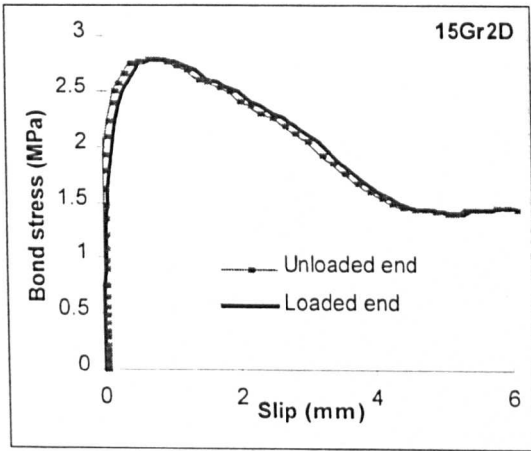
## C.2 Bond-Slip curves for pullout tests presented in Table C.1.2

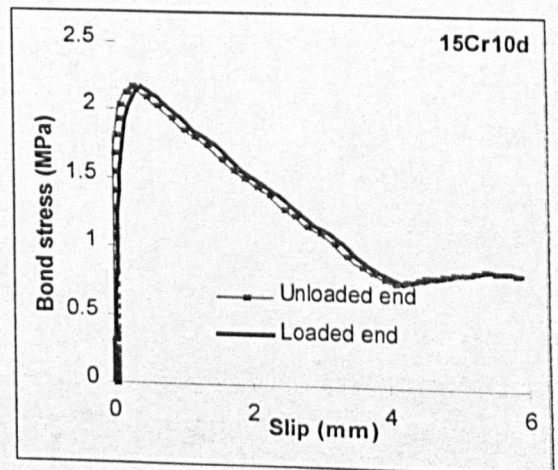
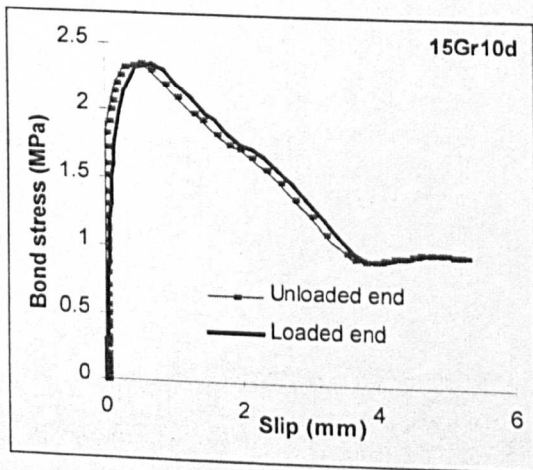
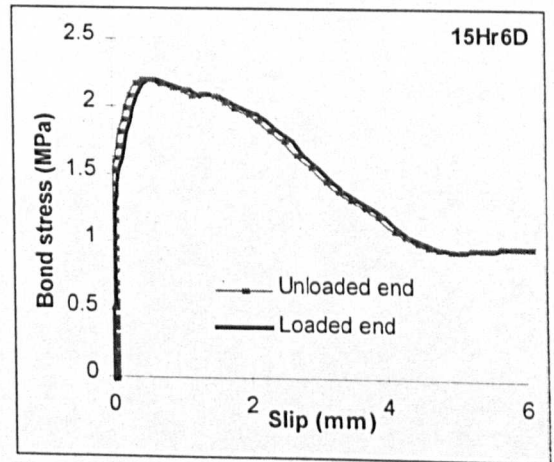
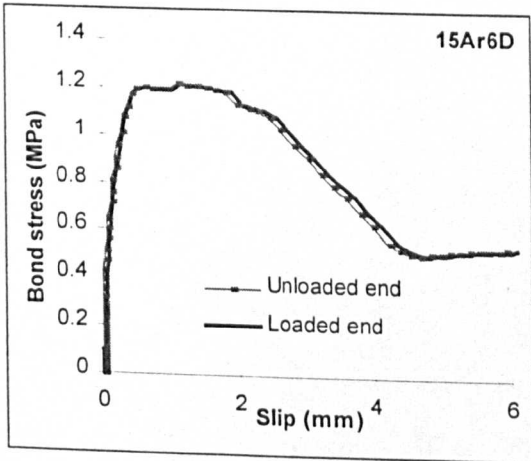
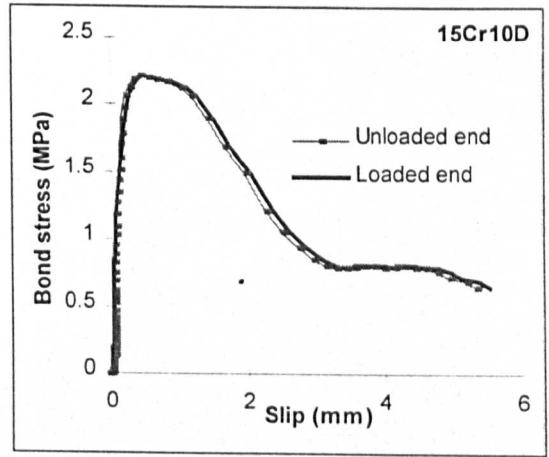
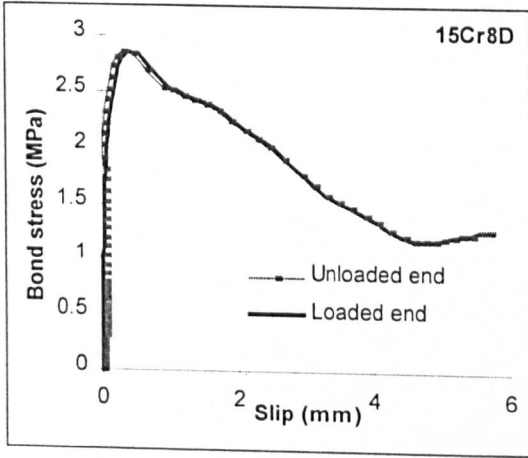
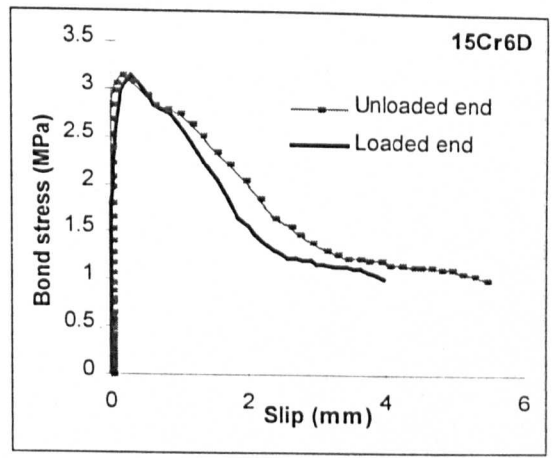
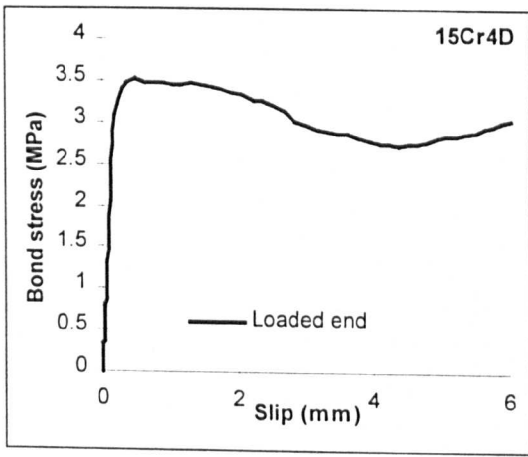


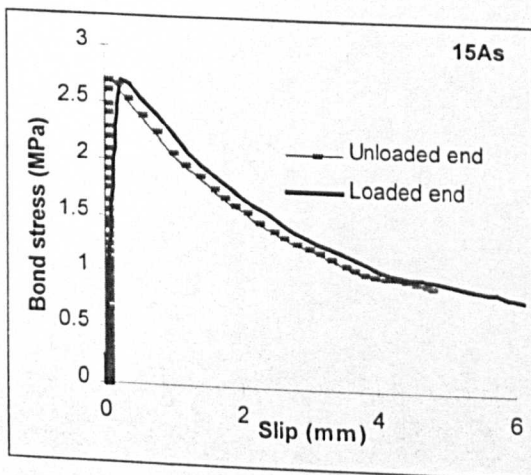
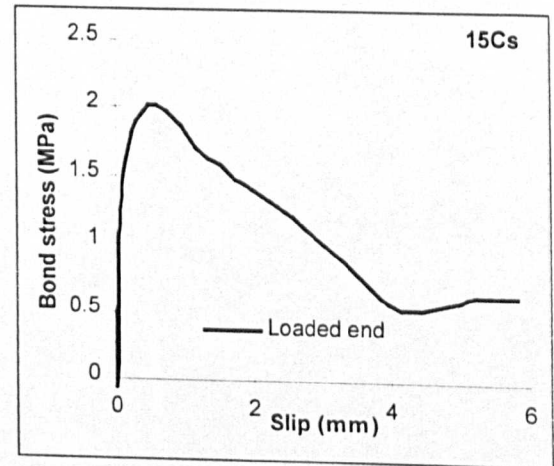
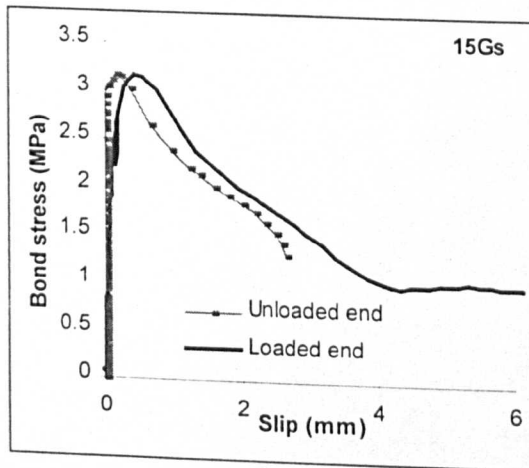
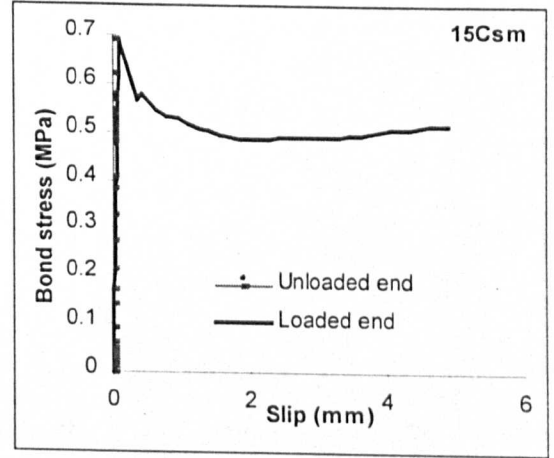
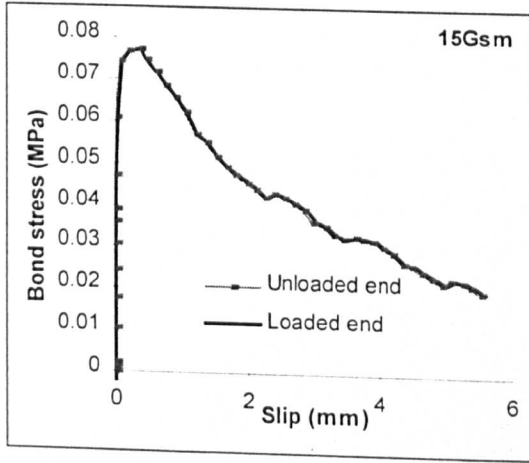
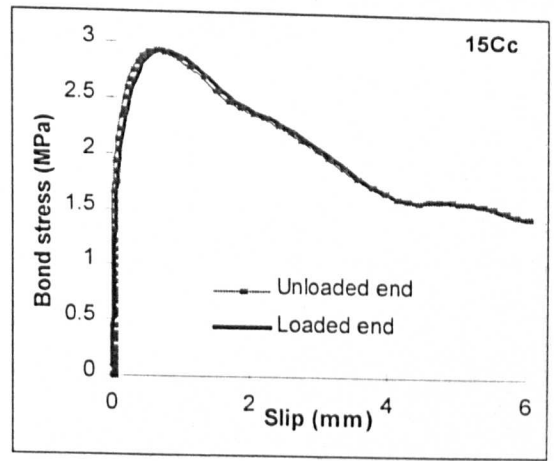
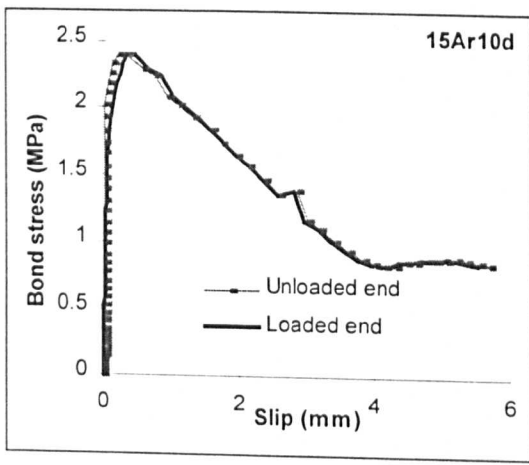




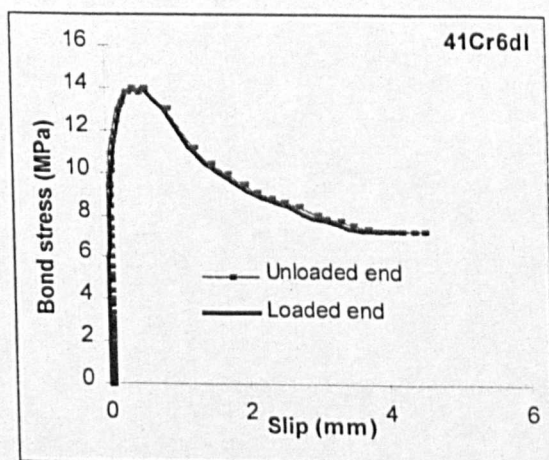
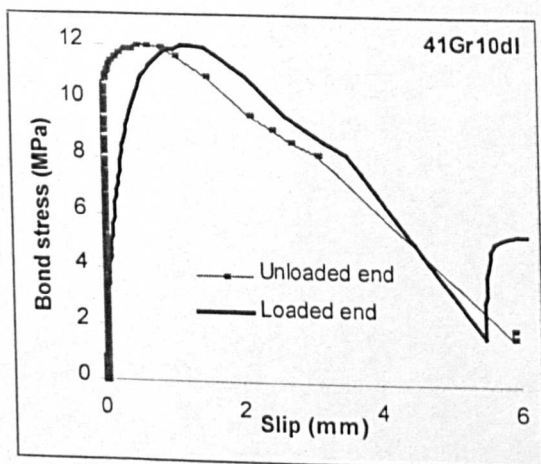
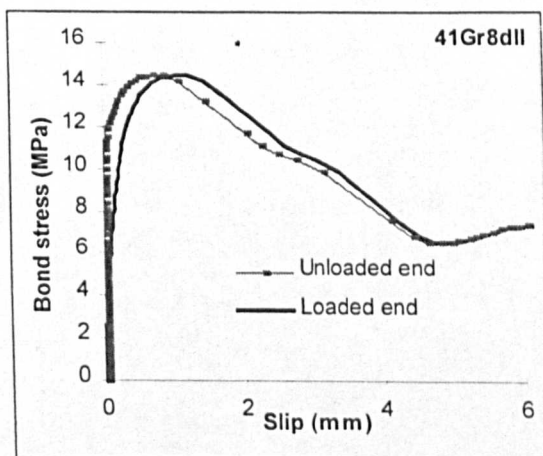
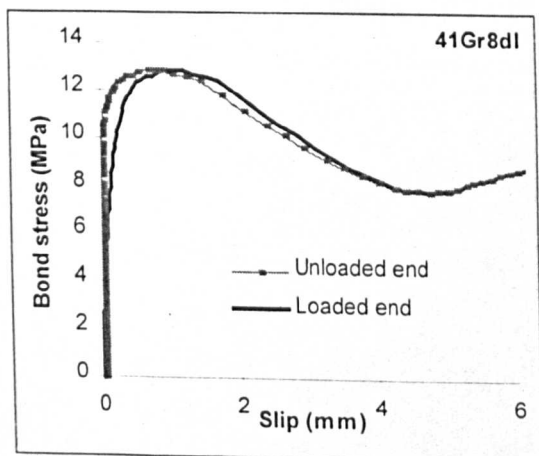
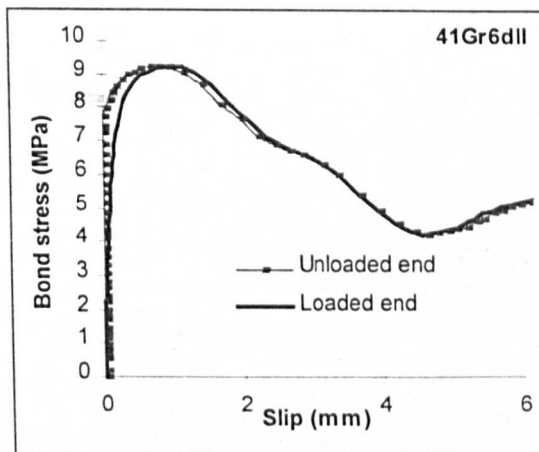
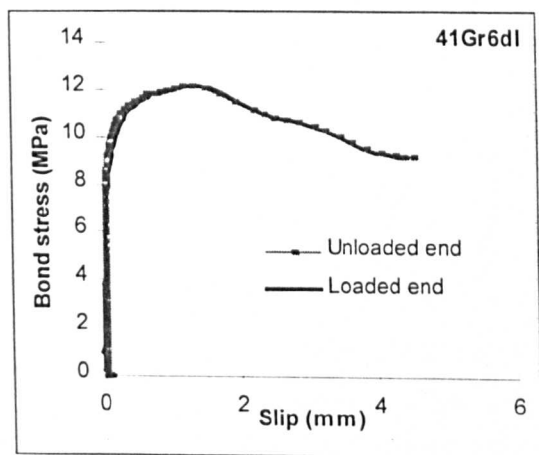
## C.2 Bond-Slip curves for pullout tests presented in Table C.1.3

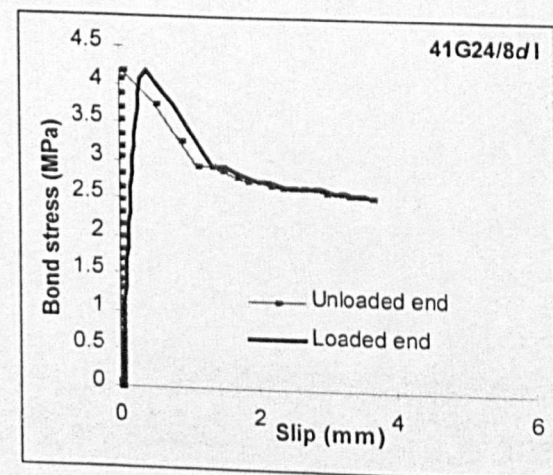
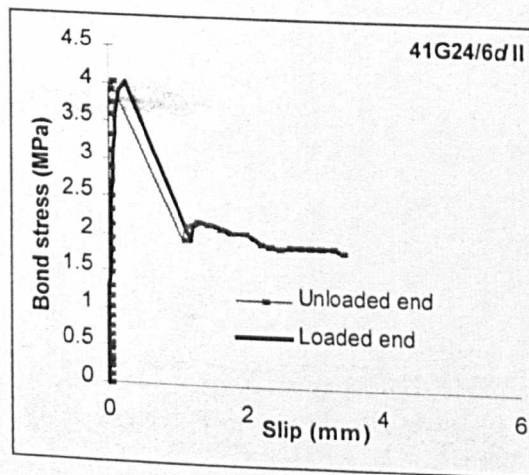
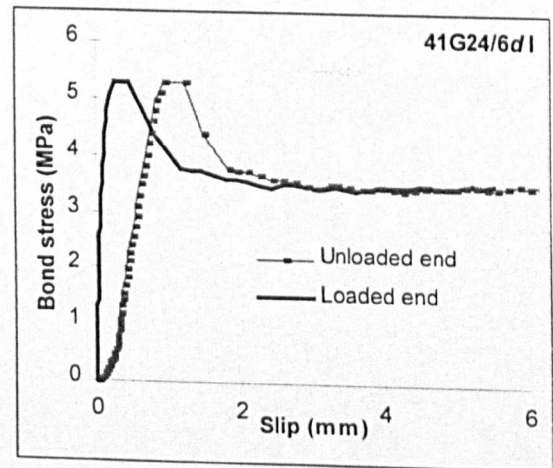
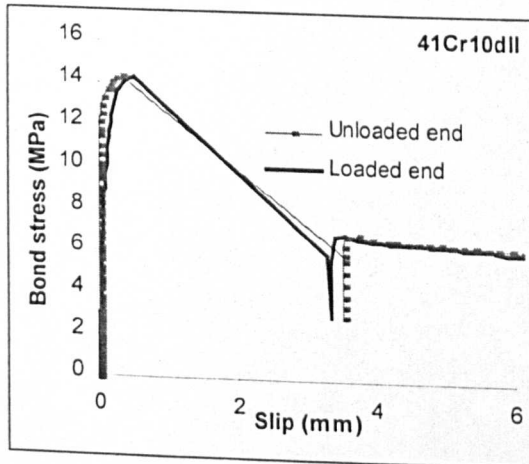
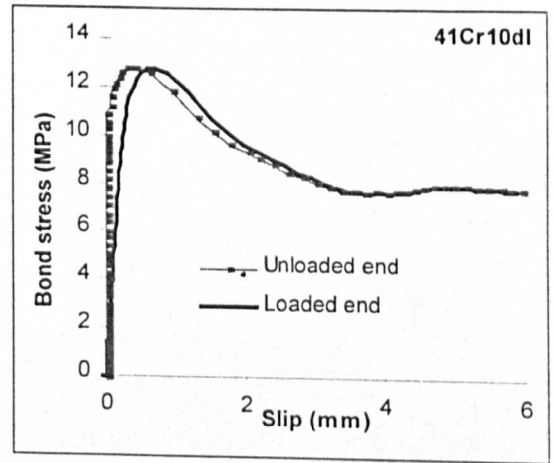
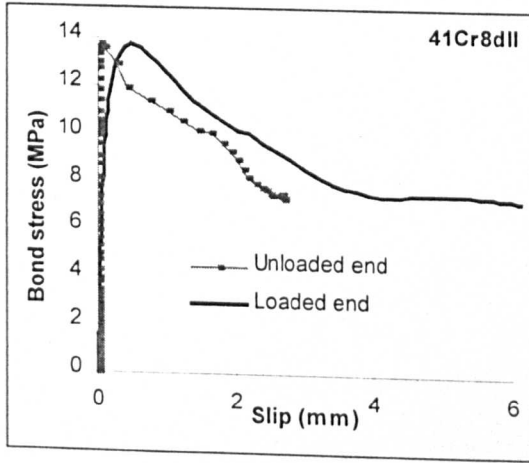
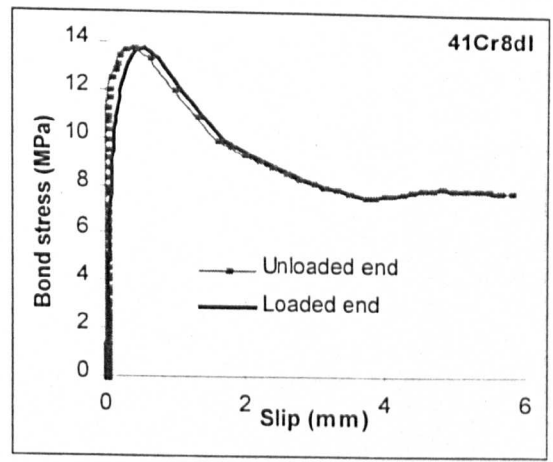
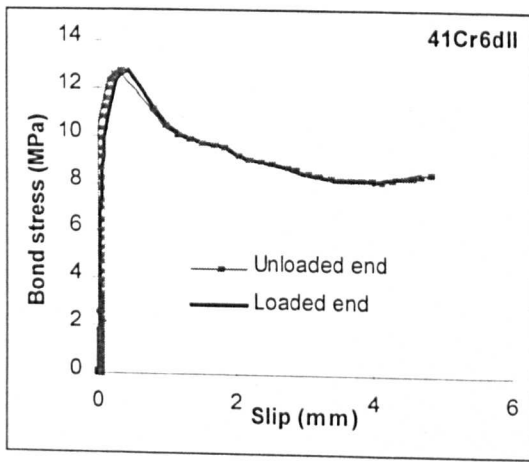


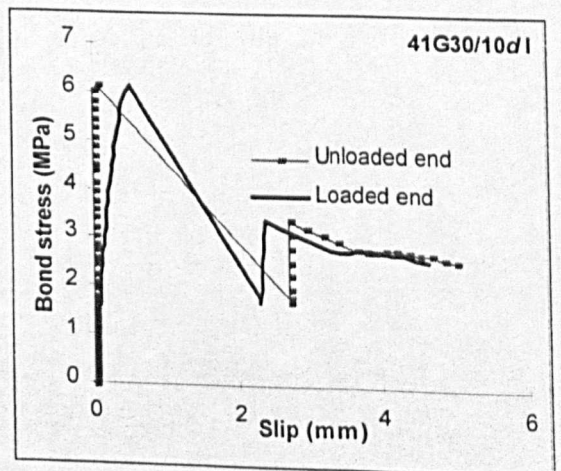
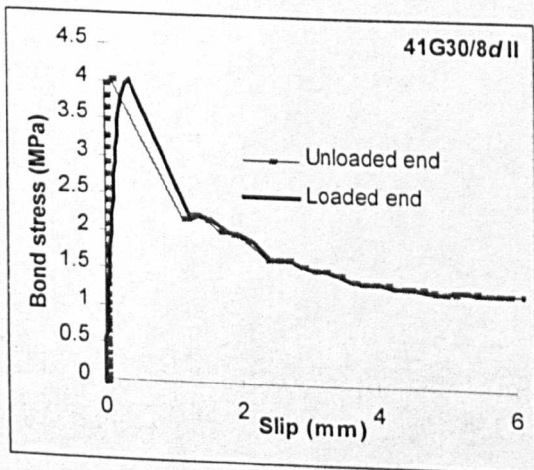
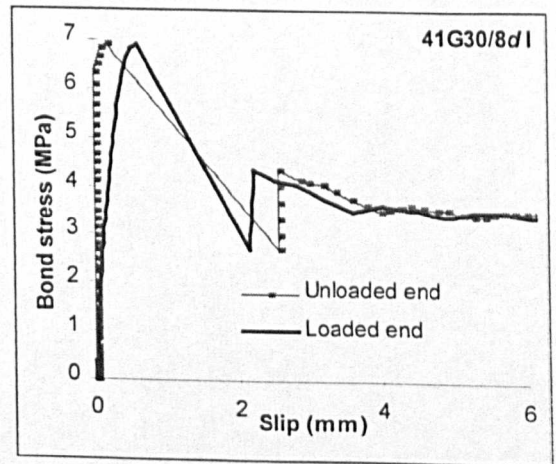
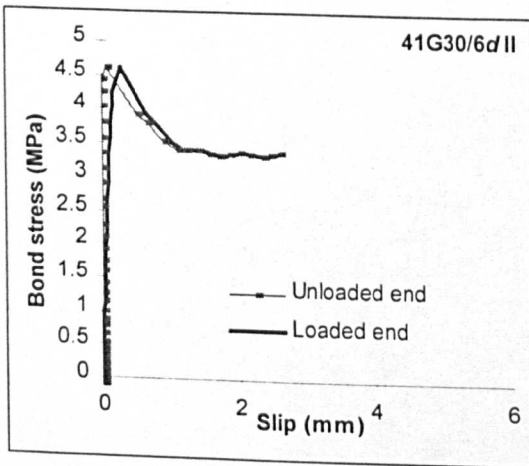
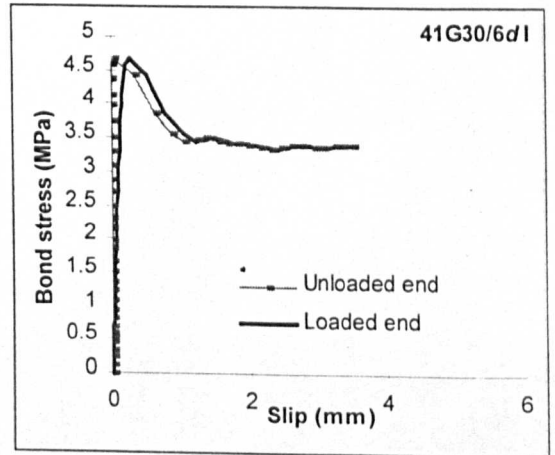
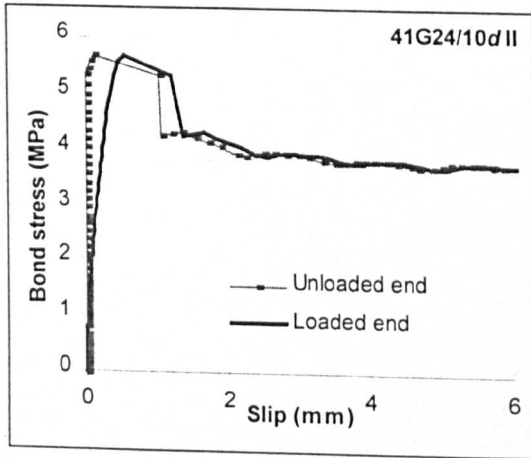
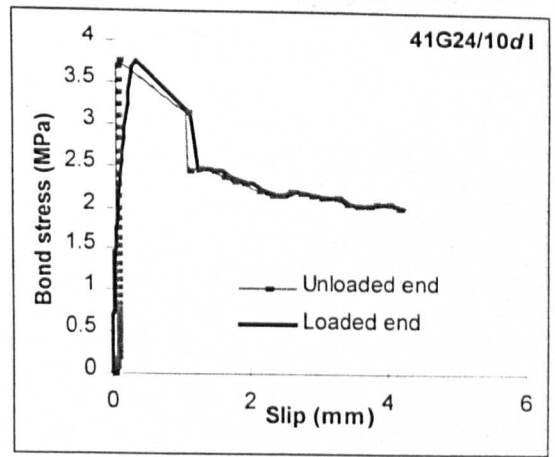
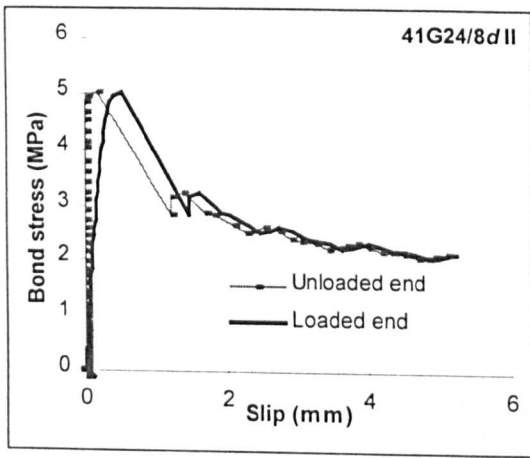




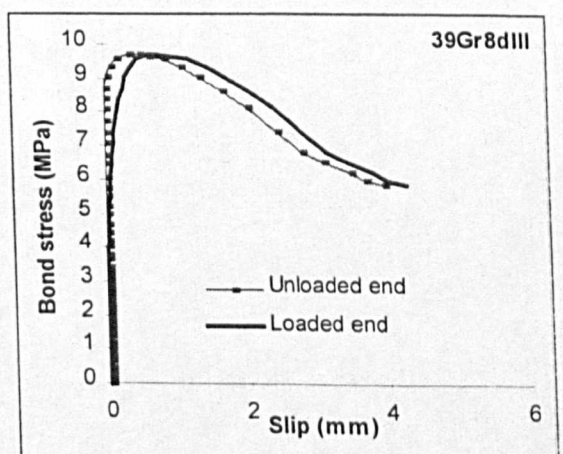
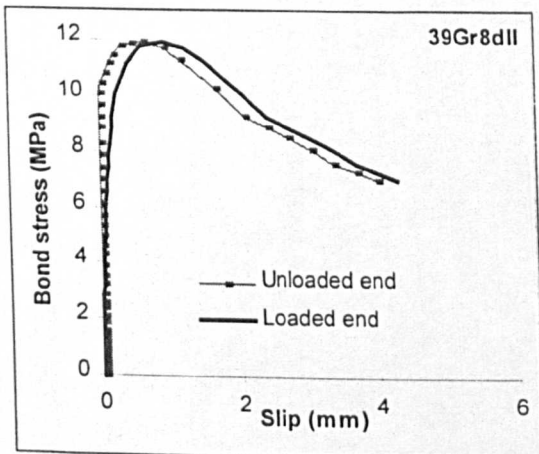
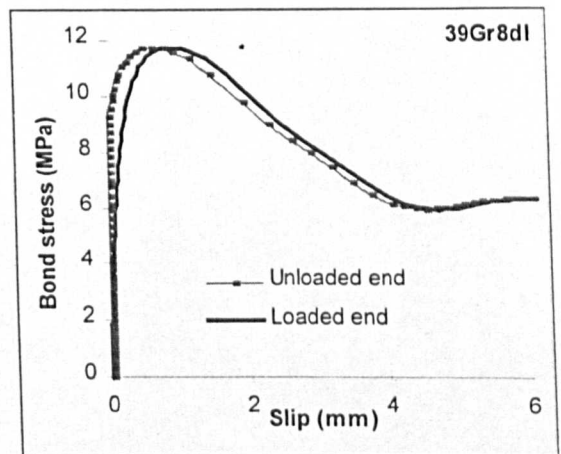
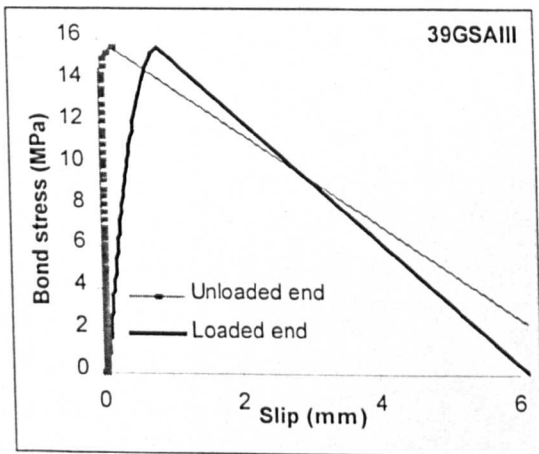
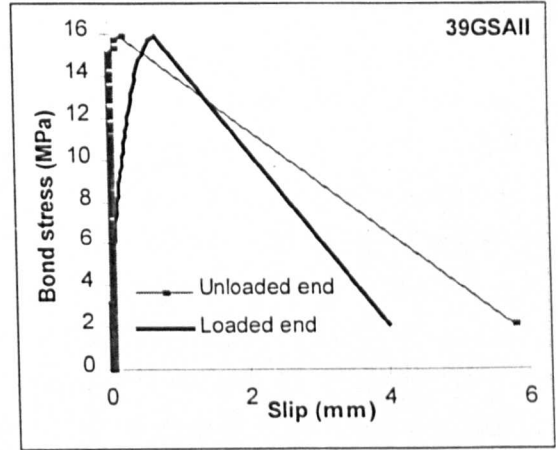
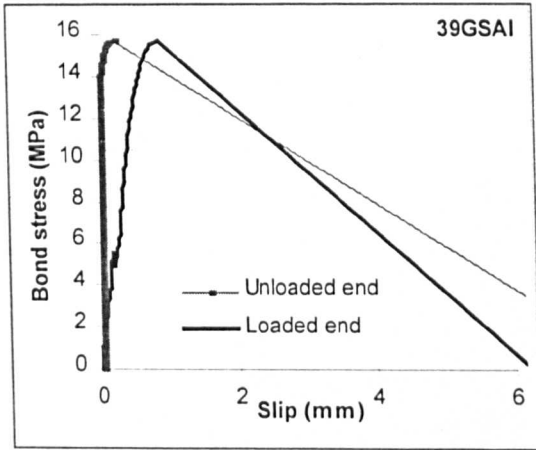
## C.2 Bond-Slip curves for pullout tests presented in Table C.1.4

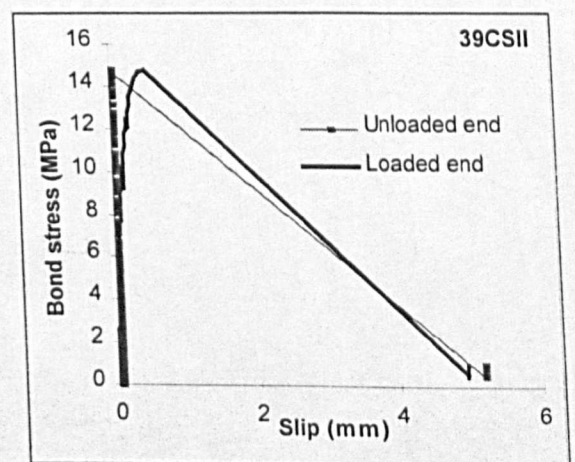
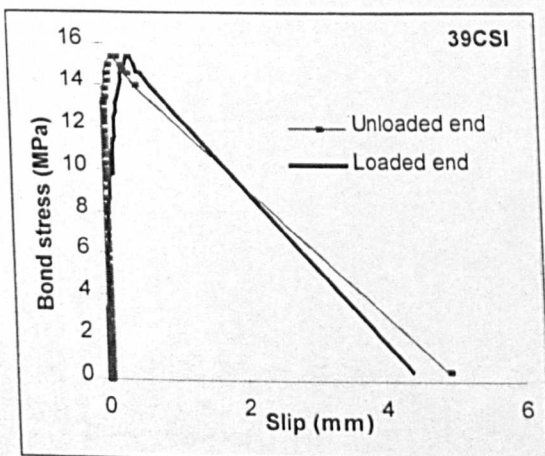
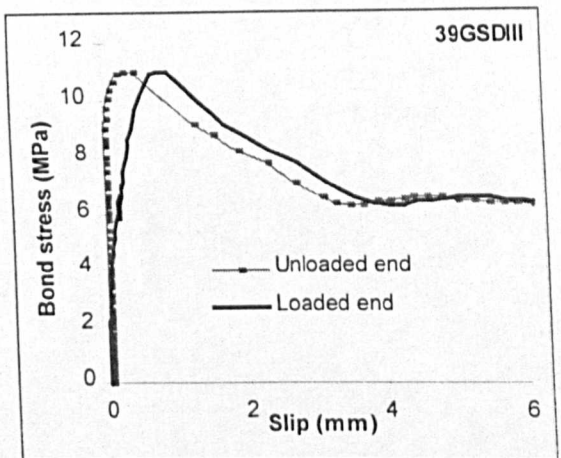
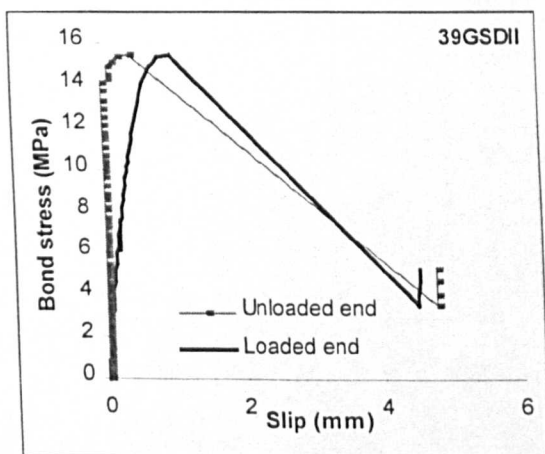
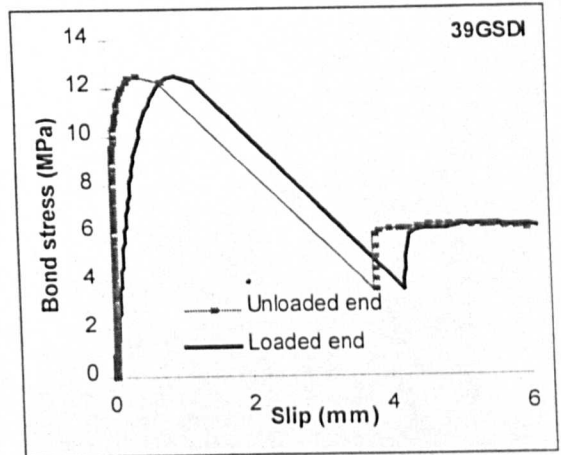
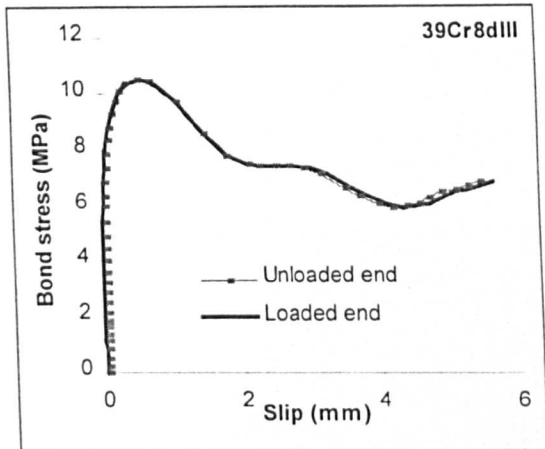
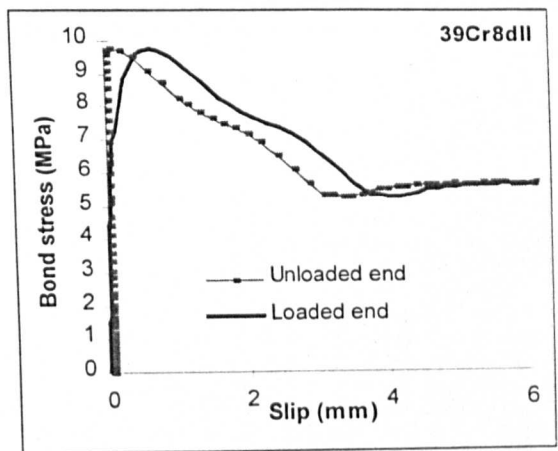
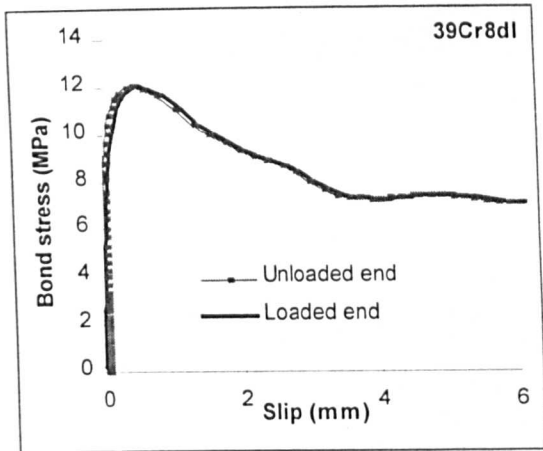


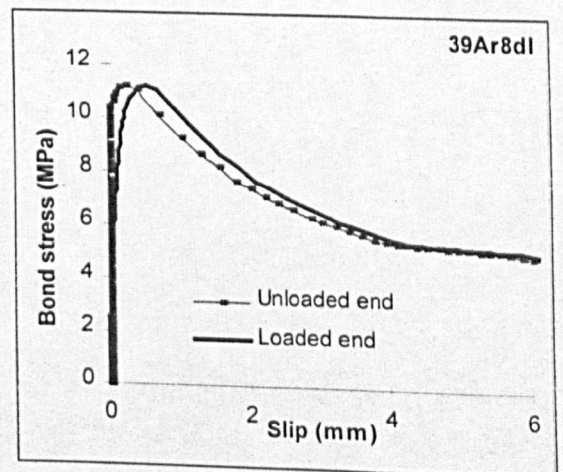
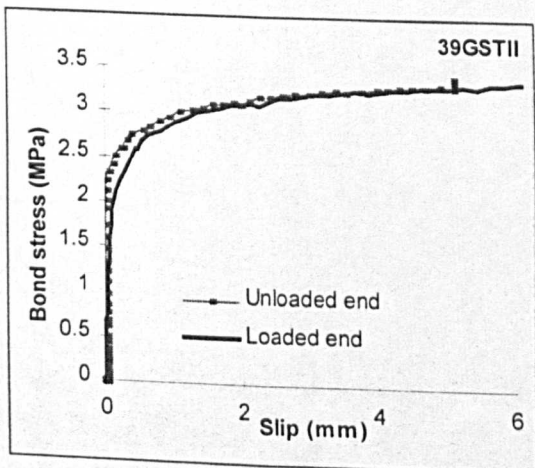
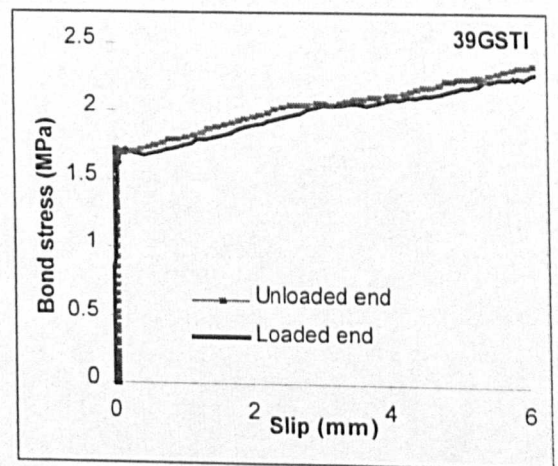
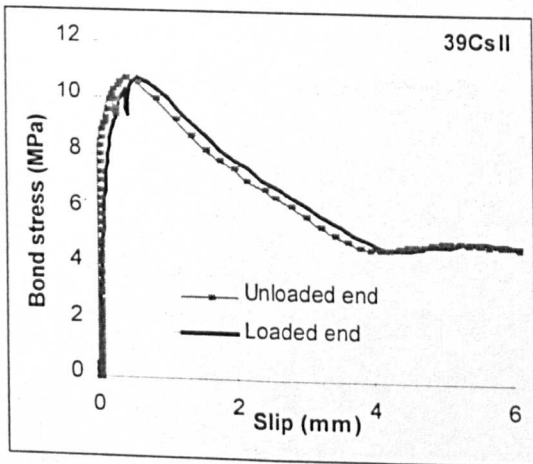
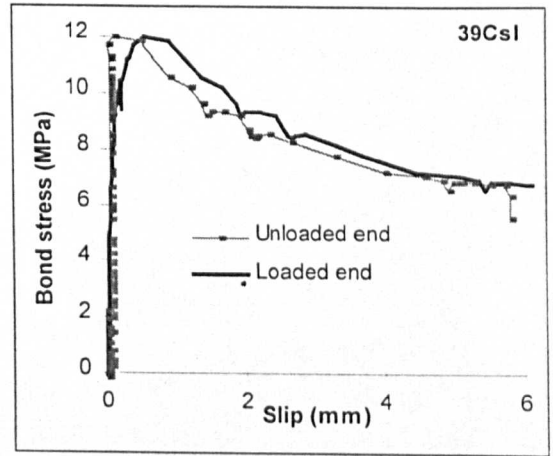
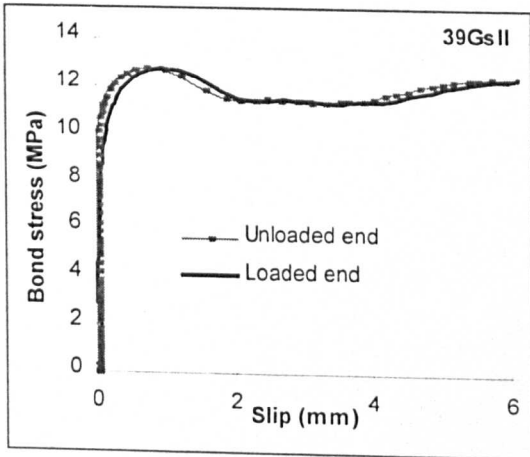
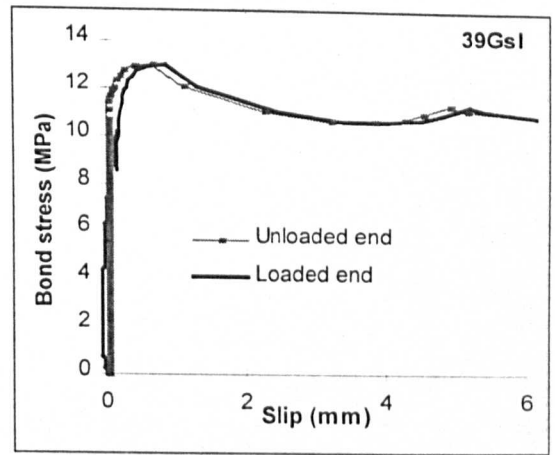
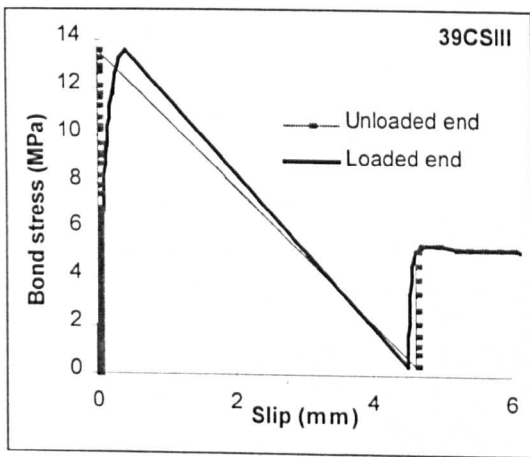


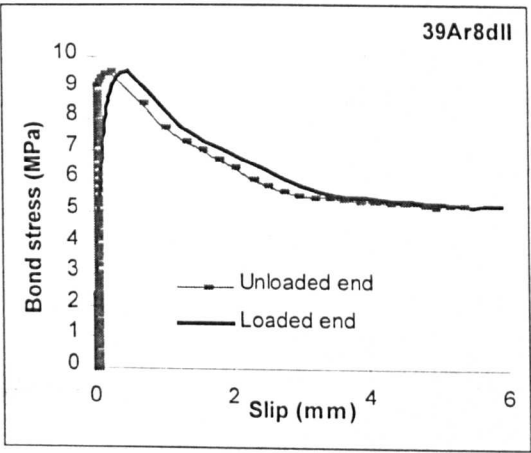


## C.2 Bond-Slip curves for pullout tests presented in Table C.1.5

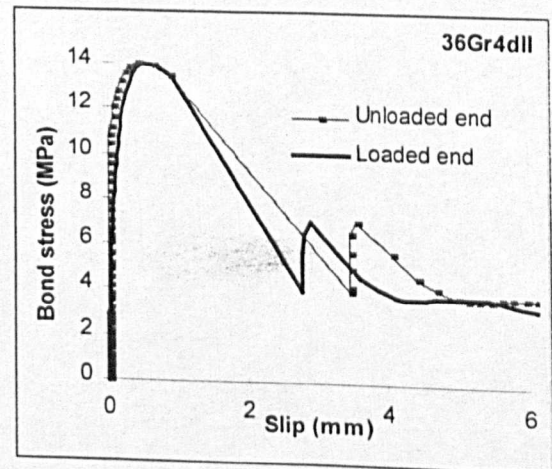
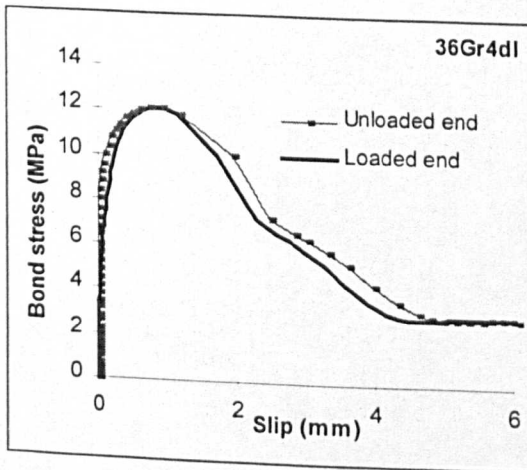
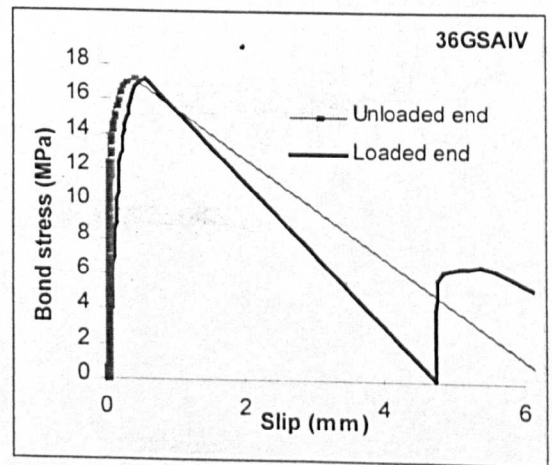
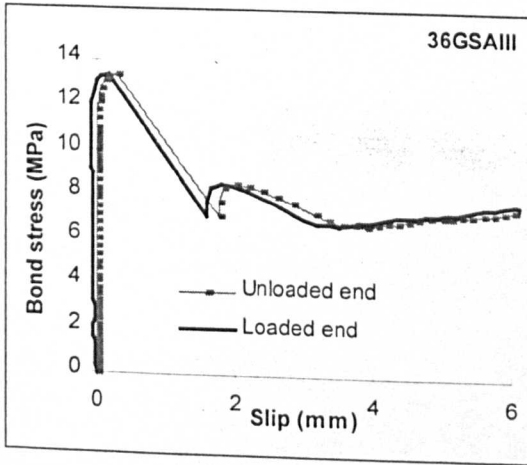
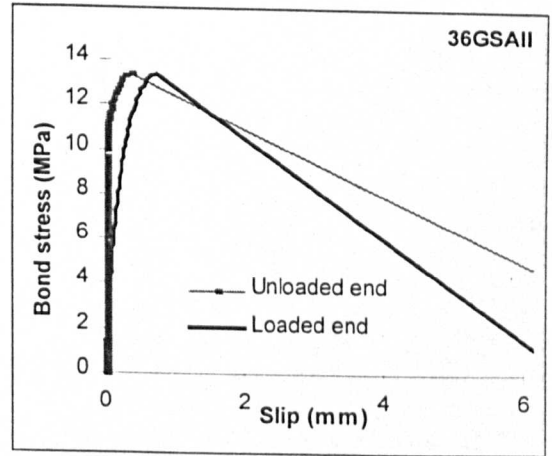
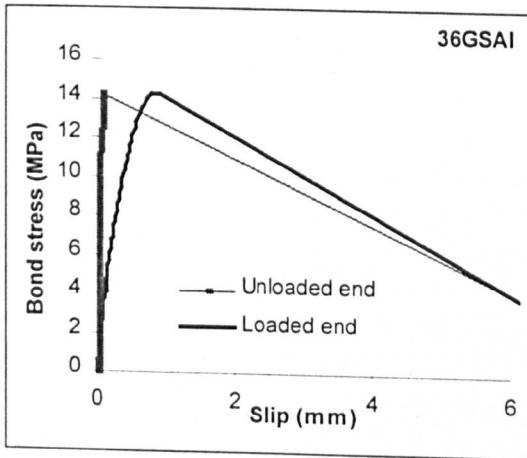


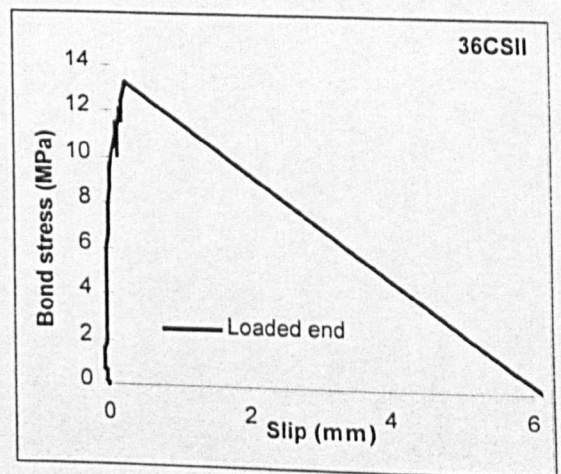
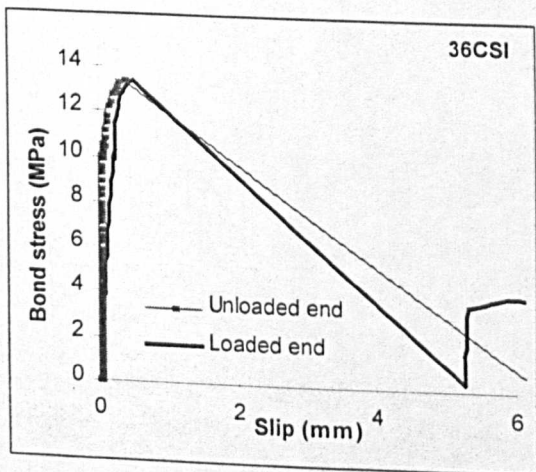
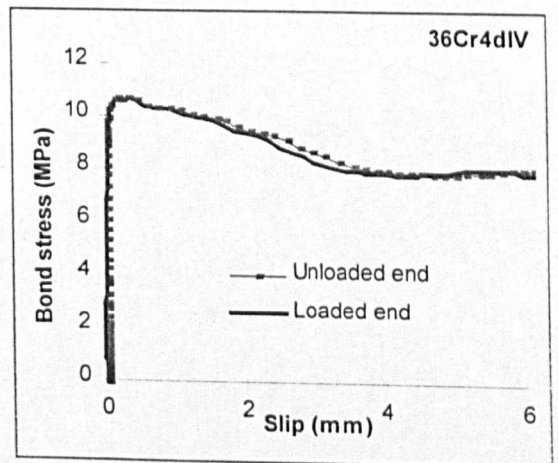
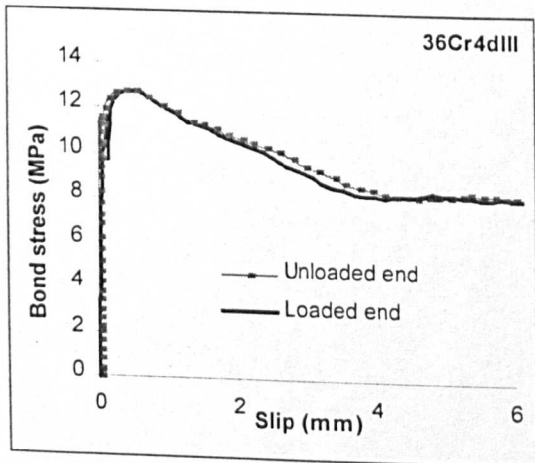
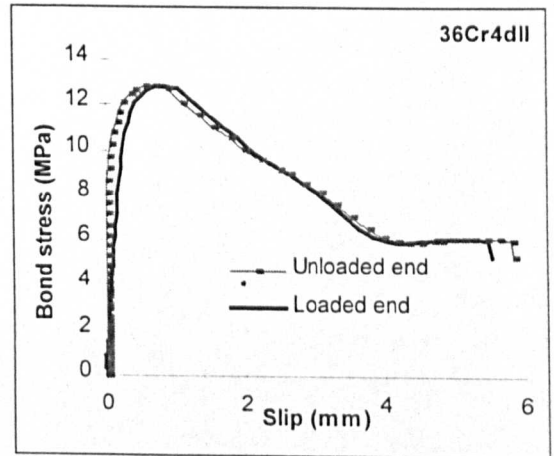
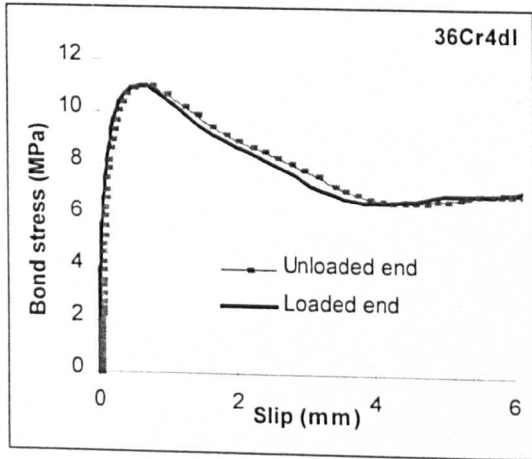
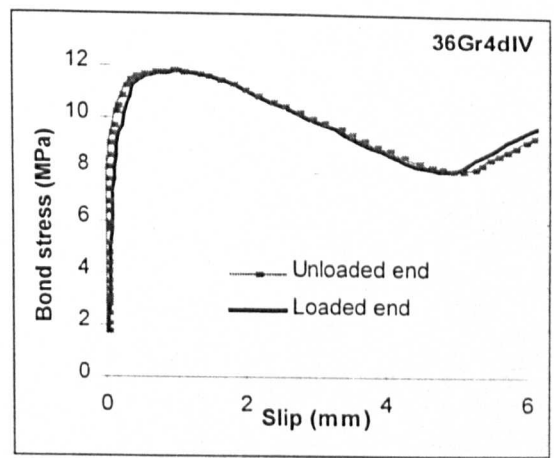
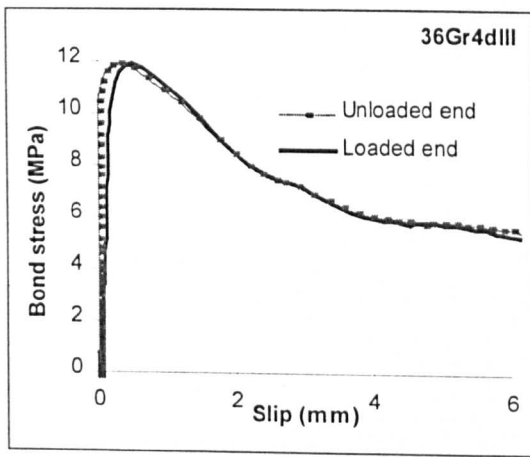


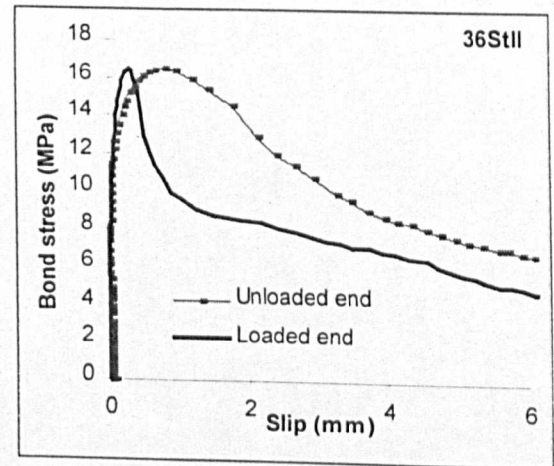
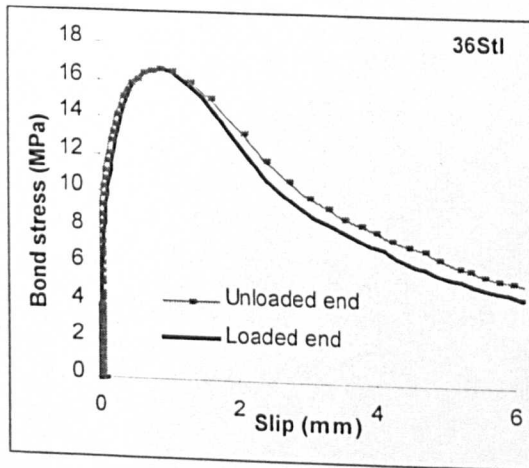
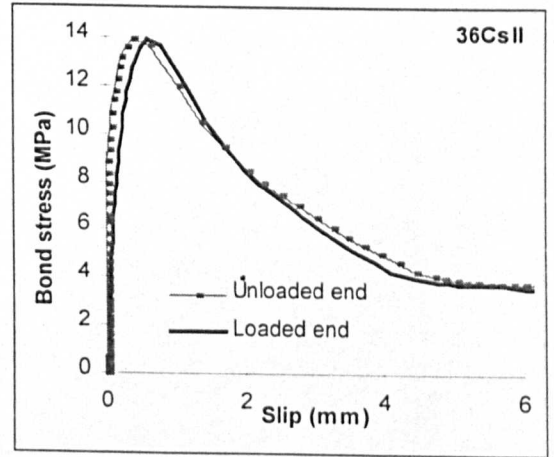
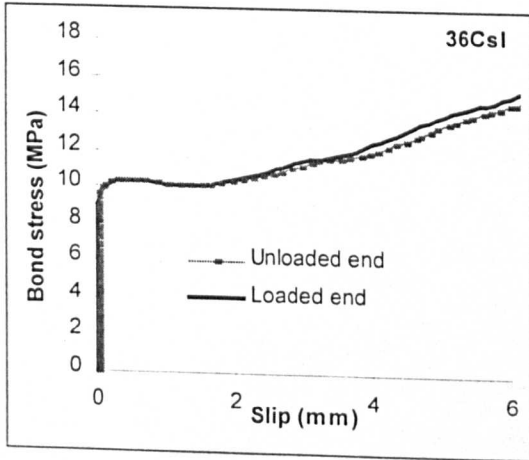
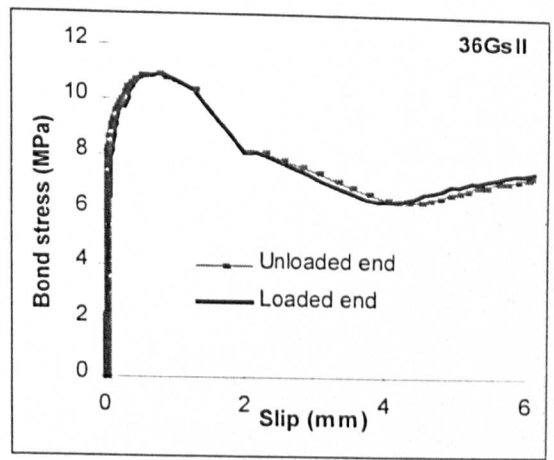
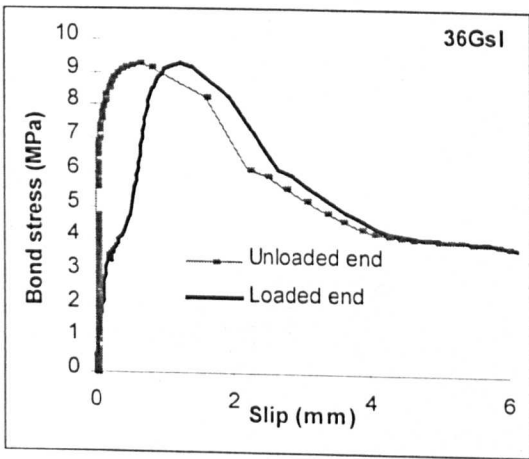




## C.2 Bond-Slip curves for pullout tests presented in Table C.1.6







## APPENDIX D

### Microscope images of FRP bond failures

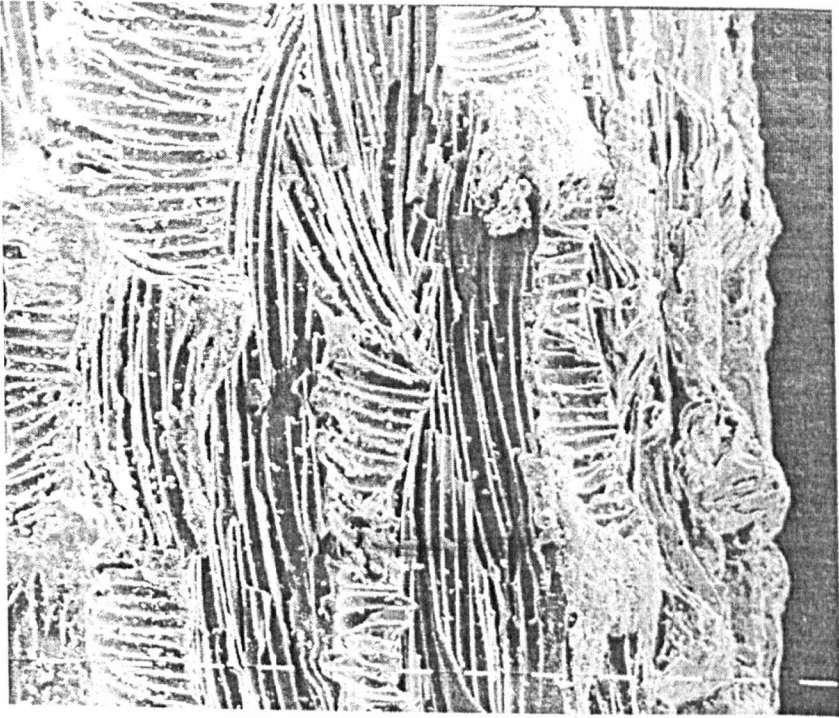


Figure D.1: CFRP bar before testing

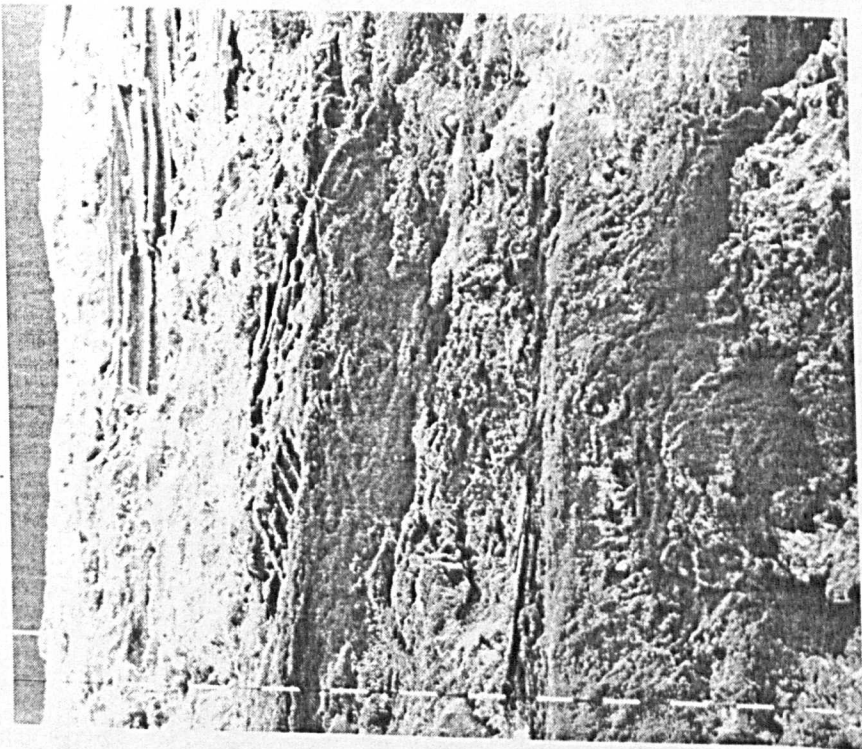


Figure D.2: CFRP bar after testing

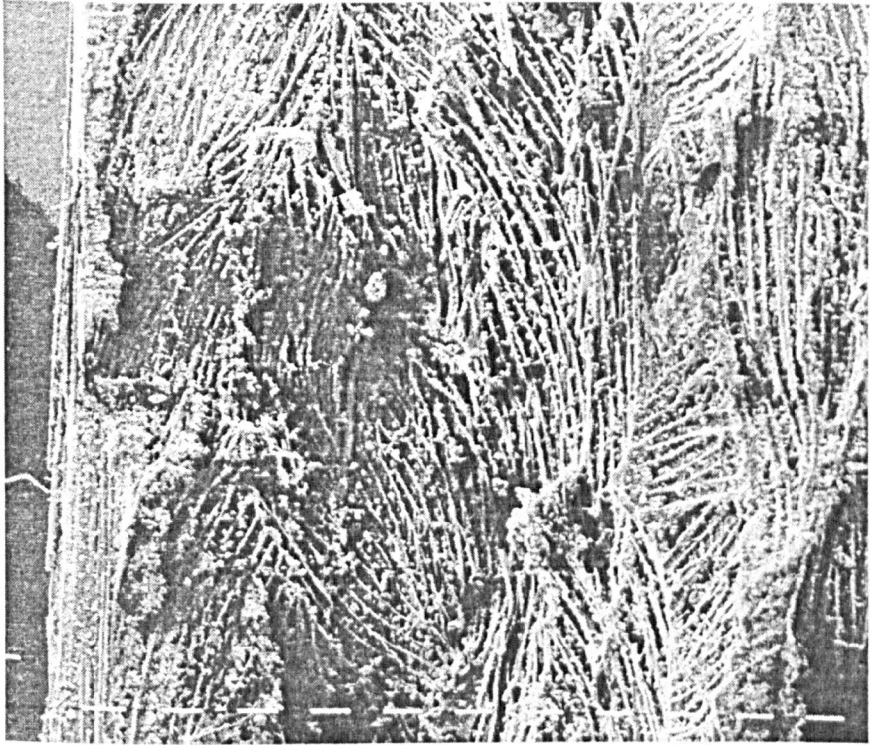


Figure D.3: GFRP bar before testing



Figure D.4: GFRP bar after testing



Figure D.5: Concrete side bond failure interface for CFRP bar

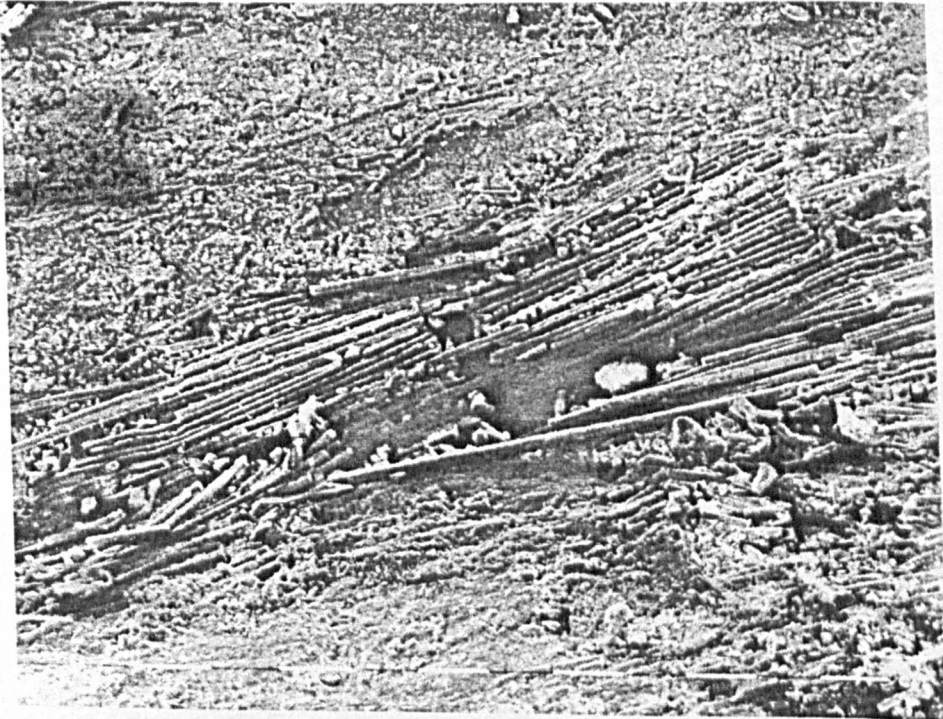


Figure D.6: Concrete side bond failure interface for GFRP bar

# APPENDIX E

## Beam test results

### E.1 Summary of beam test results

Table E.1.1

| Beam | Main - Shear reinforcement - confinement   | Load capacity of beam (kN) | Type of failure                     | Max. recorded normal bar strain | Max. peak bond stress (MPa) | Max. average bond stress (MPa) | Concrete strength (MPa) |
|------|--|----------------------------|-------------------------------------|---------------------------------|-----------------------------|--------------------------------|-------------------------|
| GB5  | 3 GFRP bars d=13.5mm<br>GFRP links, 35mm c/c   | 105.1                      | Concrete, compressive               | 0.0101                          | 3.4                         | 1.8                            | 31.2                    |
| GB6  | 3 GFRP bars d=13.5mm<br>No links   | 43.9                       | Shear                               | 0.0040                          | 1.1                         | 0.7                            | 32.9                    |
| SB7  | 2 Steel bars d=16mm<br>GFRP links, 35mm c/c  | 126.5                      | Concrete, compressive               | 0.0063                          | 7.8                         | 2.3                            | 32.9                    |
| SB8  | 2 Steel bars d=8mm<br>GFRP links, 128mm c/c  | 34.9                       | Flexural, Steel yield               | >0.0030                         | 5.9                         | 1.6                            | 32.9                    |
| GB9  | 3 GFRP bars d=13.5mm<br>GFRP links, 76.5mm c/c                                       | 103.6                      | Concrete, compressive               | 0.0104                          | 4.4                         | 1.8                            | 39.8                    |
| GB10 | 3 GFRP bars d=13.5mm<br>GFRP links, 76.5mm c/c                                       | 103.0                      | Concrete, compressive               | 0.0099                          | 3.7                         | 1.7                            | 39.8                    |
| GB11 | 3 GFRP bars d=13.5mm<br>GFRP links, 153mm c/c  | 97.9                       | Shear                               | 0.0093                          | 5.5                         | 1.6                            | 39.8                    |
| GB12 | 3 GFRP bars d=13.5mm<br>GFRP links, 153mm c/c<br>(Reduced anchorage length = 612 mm) | 133.1                      | Shear                               | 0.0086                          | 6.4                         | 2.1                            | 39.8                    |
| GB13 | 2 GFRP bars d=13.5mm<br>GFRP links, 76.7mm c/c                                       | 90.6                       | Concrete, compressive               | 0.0139                          | 5.5                         | 2.4                            | 43.4                    |
| GB14 | 2 GFRP bars d=13.5mm<br>GFRP links, 76.7mm c/c<br>Concrete confinement               | 106.5                      | Bar failure                         | 0.0166                          | 6.3                         | 2.9                            | 43.4                    |
| GB15 | 2 GFRP bars d=13.5mm<br>GFRP links, 76.7mm c/c<br>Concrete confinement               | 94.6                       | Concrete, compressive + Bar failure | 0.0158                          | 3.2                         | 2.8                            | 43.4                    |
| GB16 | 2 GFRP bars d=13.5mm<br>GFRP links, 76.7mm c/c<br>Concrete confinement               | 103.4                      | Bar failure                         | 0.0158                          | 6.8                         | 2.8                            | 43.4                    |

**Table E.1.2**

| Beam  | Main - Shear reinforcement - confinement                               | Load capacity of beam (kN) | Type of failure        | Max. recorded normal bar strain | Max. peak bond stress (MPa) | Max. average bond stress (MPa) | Concrete strength (MPa) |
|-------|--|----------------------------|------------------------|---------------------------------|-----------------------------|--------------------------------|-------------------------|
| CB17  | 3 CFRP bars d=13.5mm<br>GFRP links, 76.7mm c/c                         | 127.6                      | Concrete, compressive  | 0.0049                          | 5.9                         | 2.2                            | 34.0                    |
| CB18  | 3 CFRP bars d=13.5mm<br>GFRP links, 76.7mm c/c<br>Concrete confinement | 163.5                      | Concrete, compressive  | 0.0085                          | 8.5                         | 3.8                            | 34.0                    |
| CB19  | 2 CFRP bars d=13.5mm<br>GFRP links, 76.7mm c/c                         | 109.6                      | Concrete, compressive  | 0.0079                          | 7.2                         | 3.5                            | 34.0                    |
| CB20  | 2 CFRP bars d=13.5mm<br>GFRP links, 76.7mm c/c<br>Concrete confinement | 146.2                      | Bond failure           | 0.0094                          | 8.2                         | 4.2                            | 34.0                    |
| CGB21 | 2 HFRP bars d=13.5mm<br>GFRP links, 76.7mm c/c                         | 58.0                       | Concrete, compressive  | 0.0078                          | 5.1                         | 1.5                            | 18.1                    |
| CGB22 | 3 HFRP bars d=13.5mm<br>No links<br>Concrete confinement               | 98.7                       | Bond failure           | 0.0106                          | 4.8                         | 2.1                            | 18.1                    |
| AB23  | 2 AFRP bars d=13.5mm<br>GFRP links, 76.7mm c/c                         | 64.1                       | Concrete, compressive  | 0.0074                          | 3.9                         | 1.9                            | 18.1                    |
| AB24  | 3 AFRP bars d=13.5mm<br>No links                                       | 36.6                       | Concrete shear failure | 0.0027                          | 1.3                         | 0.7                            | 18.1                    |
| CB25  | 2 CFRP bars d=8.5mm<br>GFRP links, 76.7mm c/c                          | 86.3                       | Bar failure            | 0.0118                          | 10.1                        | 3.7                            | 47.8                    |
| CB26  | 3 CFRP bars d=8.5mm<br>GFRP links, 76.7mm c/c                          | 122.6                      | Bar failure            | 0.0114                          | 7.0                         | 3.2                            | 47.8                    |
| AB27  | 2 AFRP bars d=8.5mm<br>GFRP links, 76.7mm c/c                          | 70.6                       | Concrete, compressive  | 0.0175                          | 4.4                         | 2.9                            | 47.8                    |
| AB28  | 3 AFRP bars d=8.5mm<br>GFRP links, 76.7mm c/c                          | 84.6                       | Bond failure           | 0.0224                          | 8.4                         | 3.7                            | 47.8                    |

**Table E.1.3**

| Beam | Reinforcement arrangement / L (mm, times bar diameter) | Main / Shear reinforcement                  | Max. Load (kN) | Type of failure   | $\sigma_{\max}$ | Bond stress values (MPa)                                       | Concrete strength (MPa) |
|------|--|---|----------------|---|-----------------|--|-------------------------|
| GB29 | Single bar anchorage / L=250 (19D)                     | 3 GFRP bars (13.5mm) / GFRP links 75 mm c/c | 110            | (I) Bond splitting crack under the middle bar<br>(II) Bar failure                             | 0.0170          | $\tau_{sl}=2.0$<br>$\tau^*=3.2$                                | 35                      |
| GB30 | Single bar anchorage / L=300 (22D)                     | 3 GFRP bars (13.5mm) / GFRP links 75 mm c/c | 122            | (I) Bond splitting crack under the middle bar<br>(II) Bar failure                             | 0.0180          | $\tau_{sl}=2.2$<br>$\tau^*=2.7$                                | 35                      |
| GB31 | Spliced bars / L=300 (22D)                             | 4 GFRP bars (13.5mm) / GFRP links 75 mm c/c | 45             | Face and side bond splitting failure  | 0.0070          | $\tau^*=3.8$   | 35                      |
| CB32 | Single bar anchorage / L=300 (38D)                     | 3 CFRP bars (8 mm) / GFRP links 75 mm c/c   | 75             | (I) Bond splitting crack under the middle bar<br>(II) Bar failure                             | 0.0092          | $\tau_{sl}=3.9$<br>$\tau^*=4.6$                                | 35                      |
| CB33 | Spliced bars / L=300 (38D)                             | 4 CFRP bars (8 mm) / GFRP links 75 mm c/c   | 45             | Side bond splitting failure   | 0.0078          | $\tau^*=5.7$   | 35                      |
| GB34 | Single bar anchorage / L=370 (44D)                     | 3 GFRP bars (8.5mm) / GFRP links 75 mm c/c  | 75             | (I) Bond splitting crack under the middle bar<br>(II) Bond splitting crack under the edge bar | 0.0215          | (I)<br>$\tau_{sl}=2.6$<br>$\tau^*=3.2$<br>(II)<br>$\tau^*=2.7$ | 45                      |
| GB35 | Single bar anchorage / L=300 (35D)                     | 3 GFRP bars (8.5mm) / GFRP links 75 mm c/c  | 69             | (I) Bond splitting crack at the side face of beam<br>(II) Bar failure                         | 0.0215          | $\tau_{sl}=2.8$<br>$\tau^*=3.0$                                | 45                      |
| GB36 | Spliced bars / L=300 (35D)                             | 4 GFRP bars (8.5mm) / GFRP links 75 mm c/c  | 34             | Face and side bond splitting failure  | 0.0130          | $\tau^*=4.1$   | 45                      |
| CB37 | Single bar anchorage / L=580 (72D)                     | 3 CFRP bars (8 mm) / GFRP links 75 mm c/c   | 99             | (I) Bond splitting crack under the middle bar<br>(II) Bar failure                             | 0.0117          | $\tau_{sl}=2.4$<br>$\tau^*=3.7$                                | 45                      |

**Notations:**

$\tau_{sl}$  : estimated average bond value developed when the anchorage started slipping

$\tau^*$  : maximum average bond value developed in the anchorage length

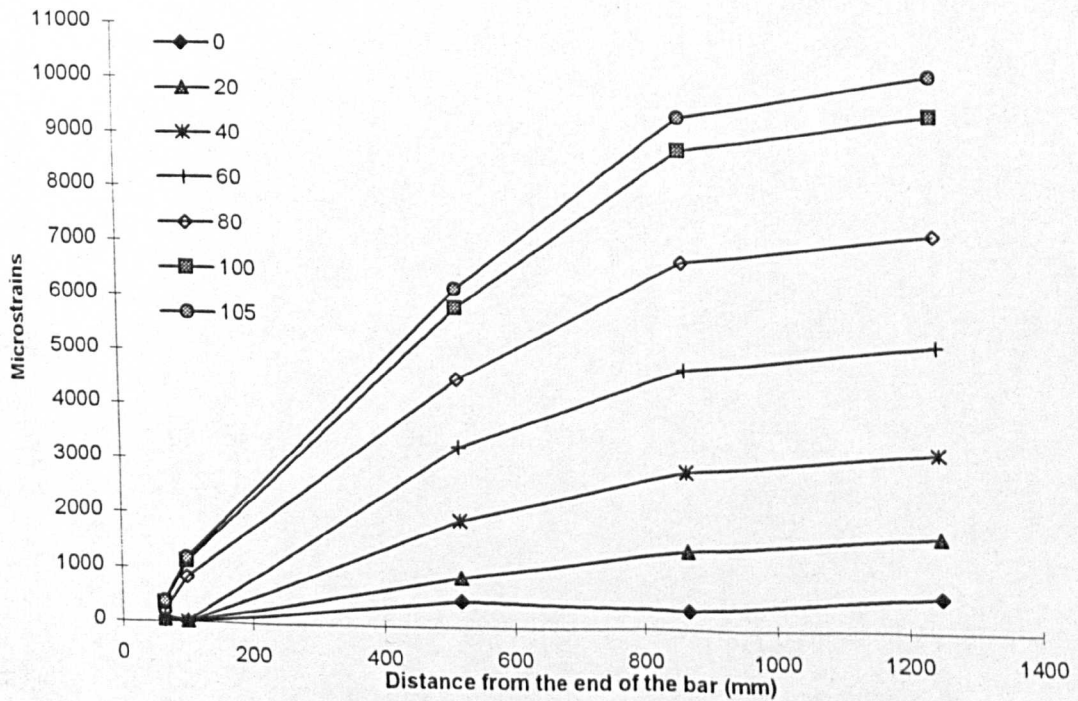
$\sigma_{\max}$  : maximum recorded normal bar strain at the loaded end of the anchorage bar

## E.2 Test results of Phase 1-3 beams

### BEAM GB 5

#### Normal strains on the main reinforcing bar

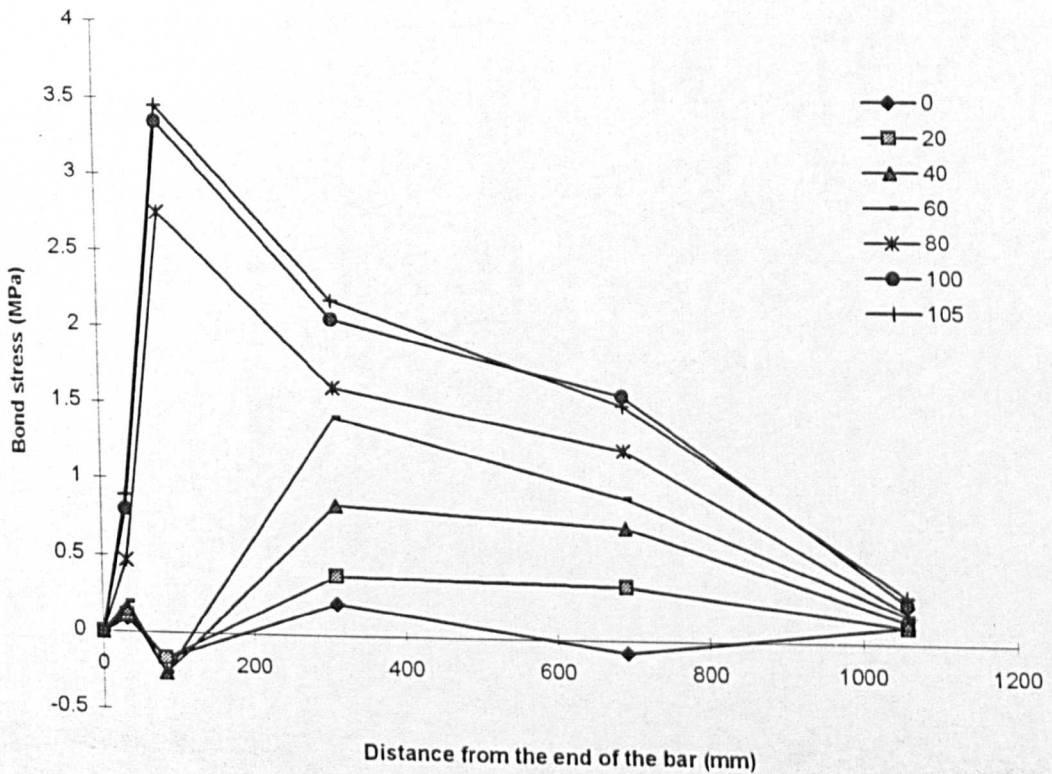
| Load (kN) | Microstrains ( <i>Distance from the end of the bar, mm</i> ) |      |      |      |       |
|-----------|--|------|------|------|-------|
|           | 65   | 100  | 519  | 867  | 1250  |
| 0         | 39   | 2    | 485  | 347  | 627   |
| 10        | 49   | 8    | 629  | 765  | 1020  |
| 20        | 47   | 10   | 906  | 1423 | 1692  |
| 30        | 53   | 3    | 1185 | 1953 | 2264  |
| 40        | 64   | 4    | 1943 | 2856 | 3211  |
| 50        | 72   | 7    | 2621 | 3800 | 4199  |
| 60        | 83   | 24   | 3275 | 4727 | 5179  |
| 70        | 82   | 62   | 3883 | 5680 | 6144  |
| 80        | 201  | 834  | 4533 | 6689 | 7198  |
| 90        | 263  | 981  | 5109 | 7652 | 8207  |
| 100       | 343  | 1114 | 5849 | 8739 | 9381  |
| 105       | 382  | 1177 | 6195 | 9336 | 10101 |



## BEAM GB 5 (cont.)

### Bond stress on the main reinforcing bar

| Load (kN) | Average bond stress, MPa ( <i>Distance from the end of the bar, mm</i> ) |      |       |      |       |        |
|-----------|--|------|-------|------|-------|--------|
|           | 0  | 33   | 83    | 310  | 692   | 1058.5 |
| 0         | 0  | 0.09 | -0.16 | 0.21 | -0.07 | 0.11   |
| 10        | 0  | 0.11 | -0.18 | 0.27 | 0.12  | 0.10   |
| 20        | 0  | 0.11 | -0.16 | 0.39 | 0.35  | 0.11   |
| 30        | 0  | 0.12 | -0.22 | 0.52 | 0.46  | 0.12   |
| 40        | 0  | 0.15 | -0.26 | 0.85 | 0.73  | 0.14   |
| 50        | 0  | 0.17 | -0.28 | 1.14 | 0.81  | 0.16   |
| 60        | 0  | 0.19 | -0.26 | 1.42 | 0.92  | 0.18   |
| 70        | 0  | 0.19 | -0.09 | 1.67 | 1.05  | 0.18   |
| 80        | 0  | 0.47 | 2.75  | 1.61 | 1.22  | 0.20   |
| 90        | 0  | 0.61 | 3.12  | 1.80 | 1.36  | 0.22   |
| 100       | 0  | 0.80 | 3.35  | 2.06 | 1.58  | 0.25   |
| 105       | 0  | 0.89 | 3.45  | 2.19 | 1.52  | 0.30   |

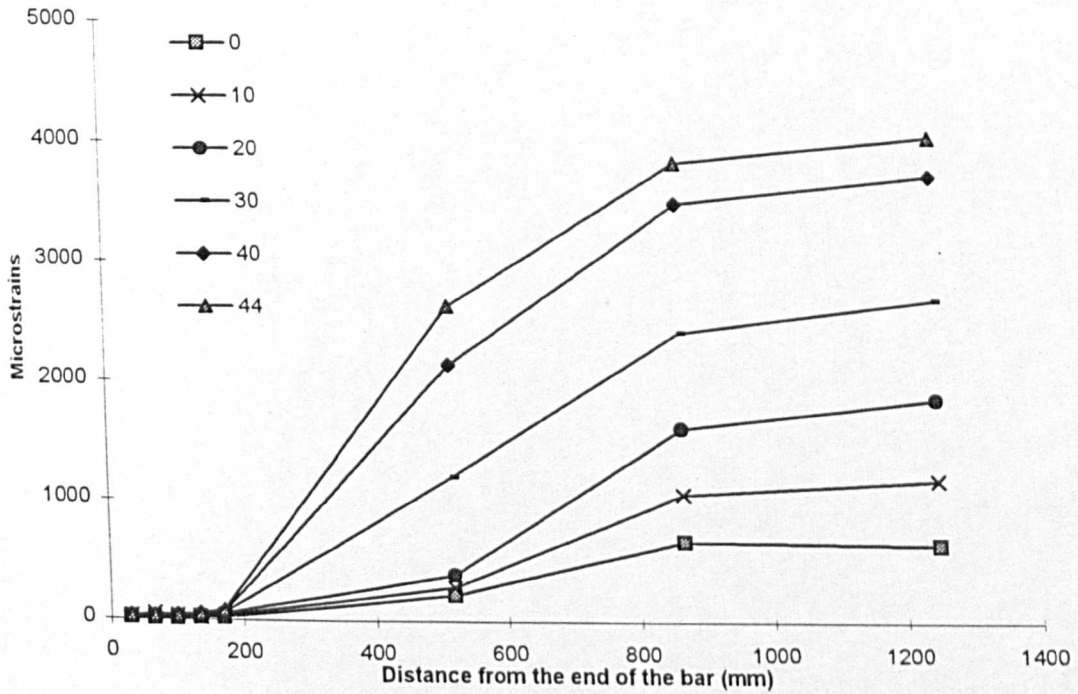


## E.2 Test results of Phase 1-3 beams

### BEAM GB 6

#### Normal strains on the main reinforcing bar

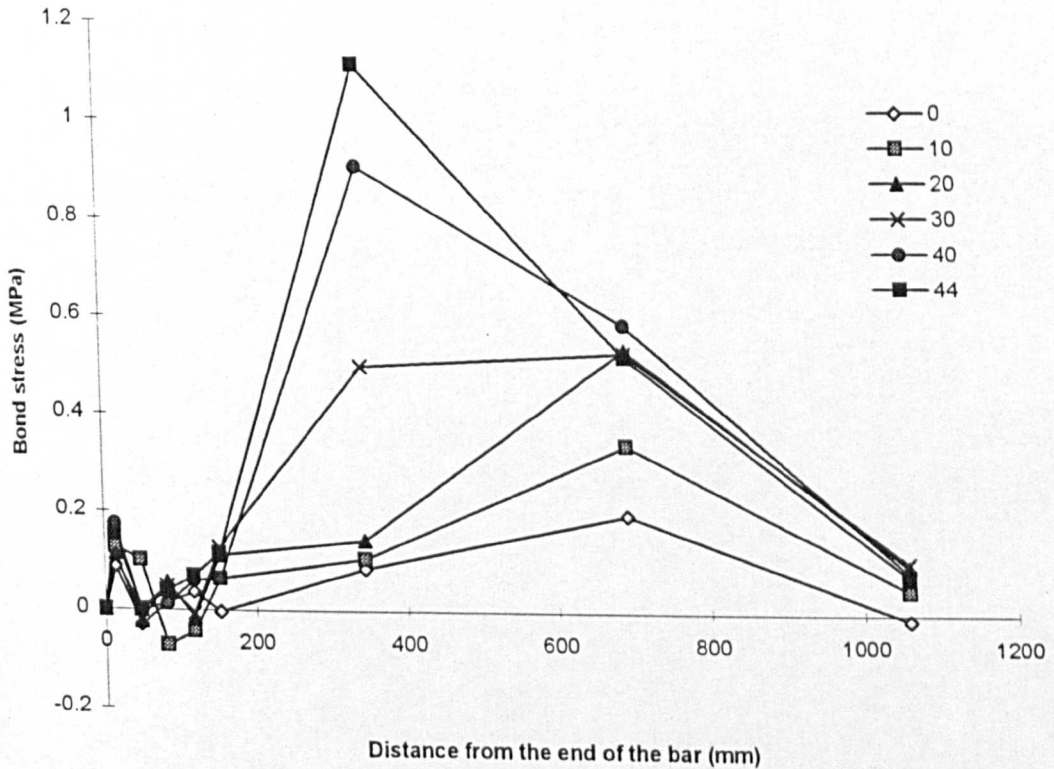
| Load (kN) | Microstrains ( <i>Distance from the end of the bar, mm</i> ) |    |     |     |     |      |      |      |
|-----------|--|----|-----|-----|-----|------|------|------|
|           | 30   | 65 | 100 | 135 | 170 | 519  | 867  | 1250 |
| 0         | 17   | 10 | 13  | 22  | 21  | 217  | 670  | 643  |
| 10        | 25   | 48 | 32  | 22  | 37  | 281  | 1060 | 1180 |
| 20        | 22   | 17 | 29  | 26  | 52  | 380  | 1603 | 1849 |
| 30        | 20   | 20 | 31  | 30  | 59  | 1202 | 2410 | 2673 |
| 40        | 34   | 34 | 37  | 51  | 65  | 2141 | 3482 | 3696 |
| 44        | 30   | 30 | 39  | 55  | 82  | 2631 | 3821 | 4015 |



## BEAM GB 6 (cont.)

### Bond stress on the main reinforcing bar

| Load (kN) | Average bond stress, MPa ( <i>Distance from the end of the bar, mm</i> ) |       |        |        |        |        |       |       |        |
|-----------|--|-------|--------|--------|--------|--------|-------|-------|--------|
|           | 0  | 15    | 48     | 83     | 118    | 153    | 345   | 693   | 1059   |
| 0         | 0  | 0.087 | -0.031 | 0.014  | 0.036  | -0.003 | 0.085 | 0.198 | -0.011 |
| 10        | 0  | 0.128 | 0.100  | -0.071 | -0.043 | 0.063  | 0.106 | 0.340 | 0.048  |
| 20        | 0  | 0.113 | -0.025 | 0.056  | -0.015 | 0.112  | 0.143 | 0.533 | 0.098  |
| 30        | 0  | 0.103 | 0.000  | 0.048  | -0.007 | 0.127  | 0.498 | 0.527 | 0.104  |
| 40        | 0  | 0.173 | 0.000  | 0.012  | 0.060  | 0.063  | 0.904 | 0.584 | 0.085  |
| 44        | 0  | 0.154 | 0.000  | 0.039  | 0.069  | 0.116  | 1.111 | 0.519 | 0.077  |

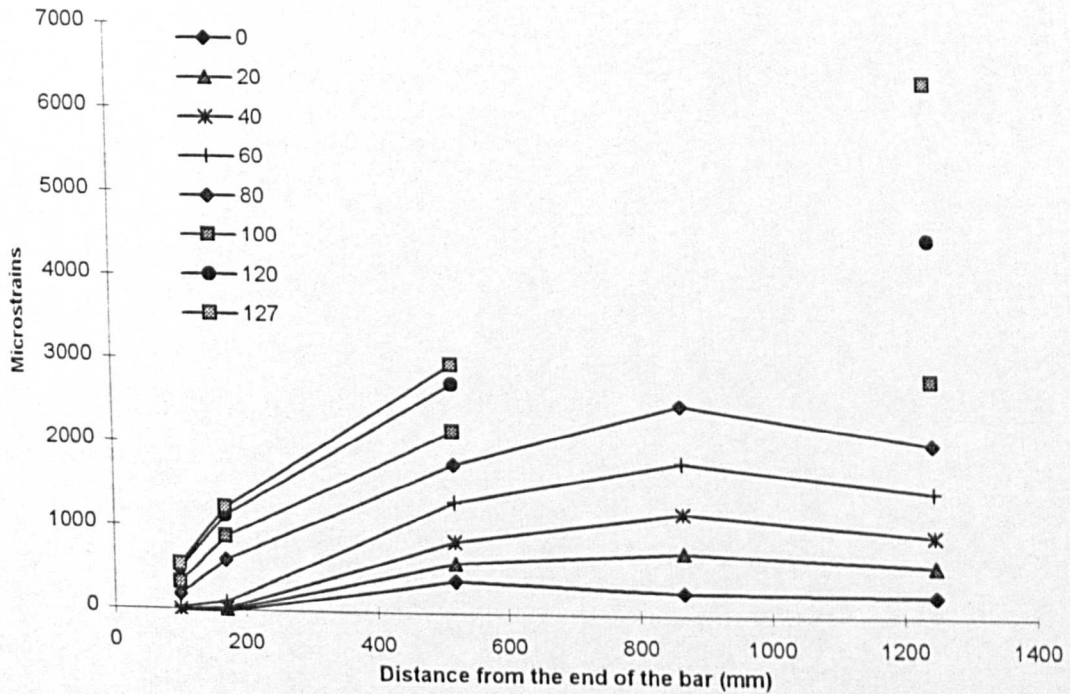


## E.2 Test results of Phase 1-3 beams

### BEAM SB7

#### Normal strains on the main reinforcing bar

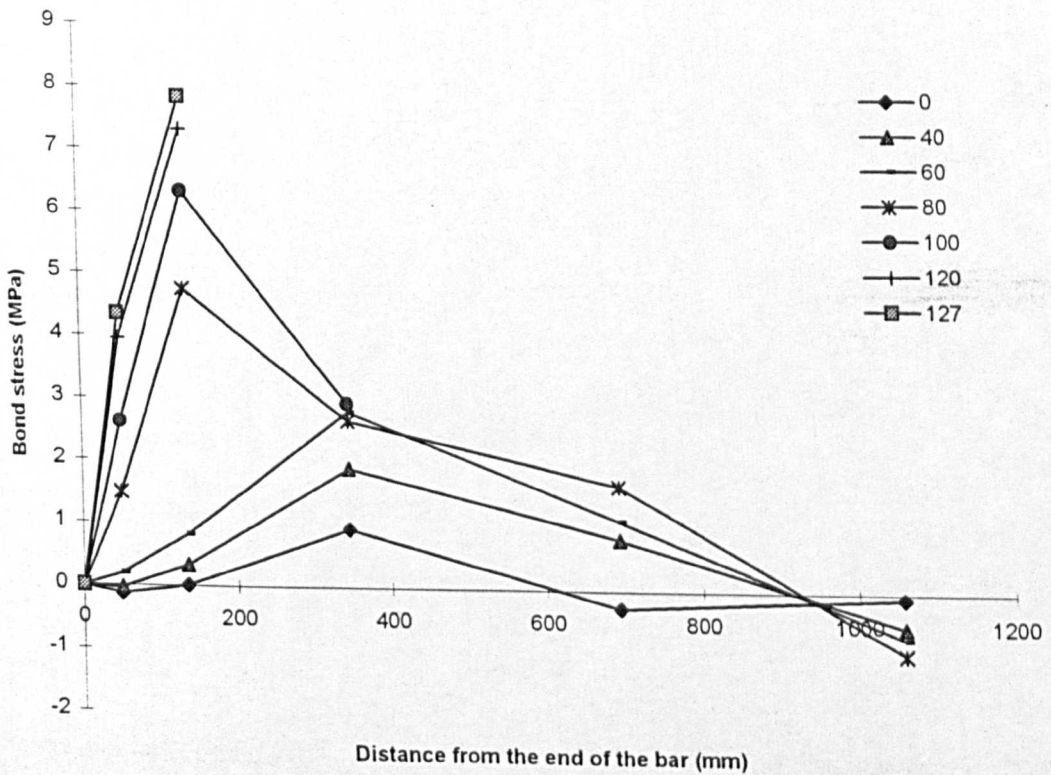
| Load (kN) | Microstrains ( <i>Distance from the end of the bar, mm</i> ) |      |      |      |      |
|-----------|--|------|------|------|------|
|           | 100  | 170  | 519  | 867  | 1250 |
| 0         | -16  | -15  | 388  | 270  | 236  |
| 10        | -18  | -4   | 471  | 485  | 402  |
| 20        | -8   | 3    | 595  | 737  | 593  |
| 30        | 1  | 12   | 713  | 961  | 765  |
| 40        | -3   | 25   | 850  | 1203 | 950  |
| 50        | 5  | 65   | 1085 | 1523 | 1222 |
| 60        | 25   | 96   | 1319 | 1800 | 1462 |
| 70        | 65   | 324  | 1550 | 2114 | 1738 |
| 80        | 186  | 601  | 1761 | 2486 | 2033 |
| 90        | 243  | 749  | 1950 | 2968 | 2394 |
| 100       | 327  | 880  | 2158 |      | 2792 |
| 110       | 402  | 1011 | 2439 |      | 3429 |
| 120       | 493  | 1133 | 2725 |      | 4457 |
| 127       | 542  | 1226 | 2957 |      | 6316 |



## BEAM SB7 (cont.)

### Bond stress on the main reinforcing bar

| Load (kN) | Average bond stress, MPa ( <i>Distance from the end of the bar, mm</i> ) |       |      |      |       |       |
|-----------|--|-------|------|------|-------|-------|
|           | 0  | 50    | 135  | 345  | 693   | 1059  |
| 0         | 0  | -0.13 | 0.01 | 0.93 | -0.27 | -0.07 |
| 10        | 0  | -0.15 | 0.16 | 1.09 | 0.03  | -0.17 |
| 20        | 0  | -0.07 | 0.13 | 1.36 | 0.33  | -0.30 |
| 30        | 0  | 0.01  | 0.12 | 1.61 | 0.57  | -0.41 |
| 40        | 0  | -0.03 | 0.33 | 1.89 | 0.81  | -0.53 |
| 50        | 0  | 0.04  | 0.69 | 2.34 | 1.01  | -0.63 |
| 60        | 0  | 0.20  | 0.82 | 2.81 | 1.10  | -0.70 |
| 70        | 0  | 0.52  | 2.96 | 2.81 | 1.30  | -0.79 |
| 80        | 0  | 1.49  | 4.74 | 2.66 | 1.66  | -0.95 |
| 90        | 0  | 1.94  | 5.79 | 2.76 |       |       |
| 100       | 0  | 2.62  | 6.31 | 2.94 |       |       |
| 110       | 0  | 3.22  | 6.96 |      |       |       |
| 120       | 0  | 3.95  | 7.31 |      |       |       |
| 127       | 0  | 4.34  | 7.82 |      |       |       |

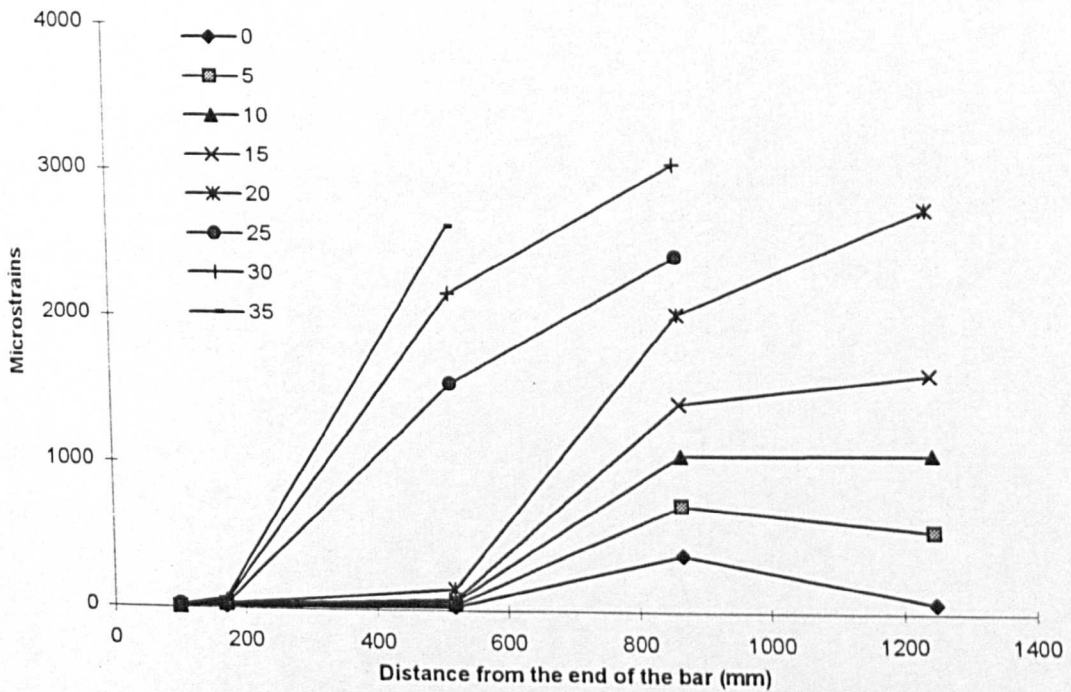


## E.2 Test results of Phase 1-3 beams

### BEAM SB8

#### Normal strains on the main reinforcing bar

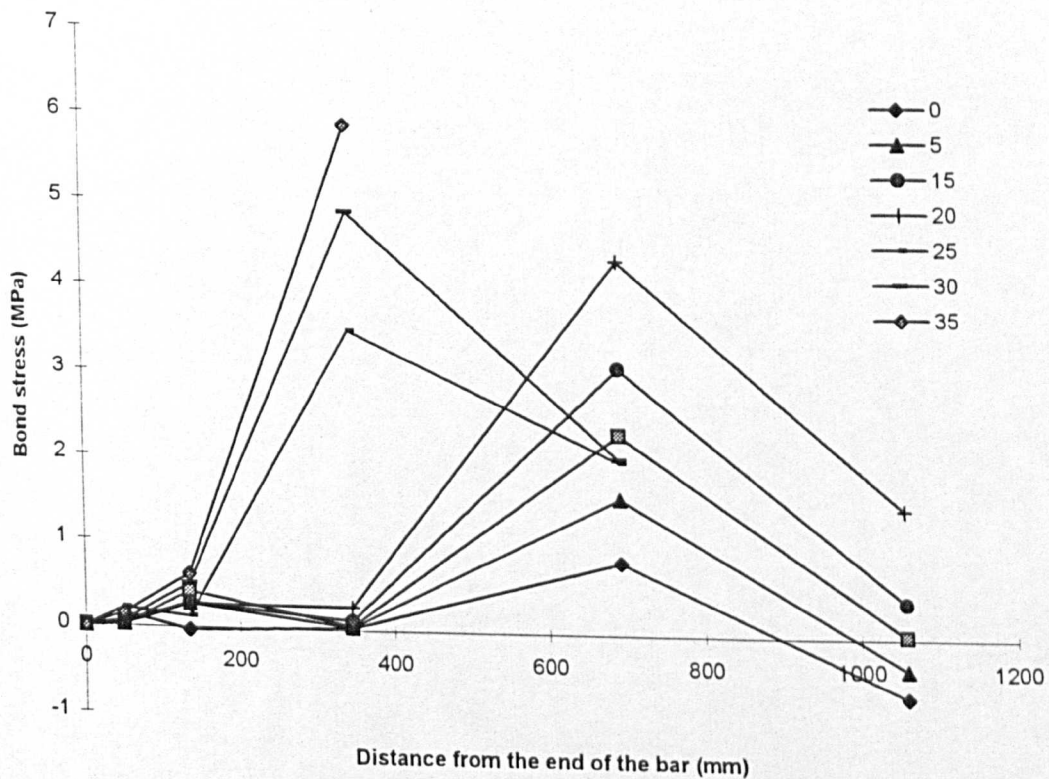
| Load (kN) | Microstrains ( <i>Distance from the end of the bar, mm</i> ) |     |      |      |      |
|-----------|--|-----|------|------|------|
|           | 100  | 170 | 519  | 867  | 1250 |
| 0         | 18   | 15  | 26   | 386  | 66   |
| 5         | 3  | 26  | 40   | 723  | 553  |
| 10        | 2  | 37  | 60   | 1066 | 1079 |
| 15        | 5  | 29  | 77   | 1423 | 1621 |
| 20        | 8  | 31  | 146  | 2033 | 2743 |
| 25        | 26   | 37  | 1554 | 2426 |      |
| 30        | 8  | 52  | 2169 | 3053 |      |
| 35        | 18   | 72  | 2629 |      |      |



## BEAM SB8 (cont.)

### Bond stress on the main reinforcing bar

| Load (kN) | Average bond stress, MPa ( <i>Distance from the end of the bar, mm</i> ) |      |       |      |      |       |
|-----------|--|------|-------|------|------|-------|
|           | 0  | 50   | 135   | 345  | 693  | 1059  |
| 0         | 0  | 0.14 | -0.03 | 0.02 | 0.83 | -0.67 |
| 5         | 0  | 0.02 | 0.27  | 0.03 | 1.57 | -0.36 |
| 10        | 0  | 0.01 | 0.41  | 0.05 | 2.31 | 0.03  |
| 15        | 0  | 0.04 | 0.28  | 0.11 | 3.09 | 0.41  |
| 20        | 0  | 0.06 | 0.26  | 0.26 | 4.33 | 1.48  |
| 25        | 0  | 0.21 | 0.12  | 3.48 | 2.00 |       |
| 30        | 0  | 0.06 | 0.50  | 4.86 | 2.03 |       |
| 35        | 0  | 0.14 | 0.62  | 5.87 |      |       |

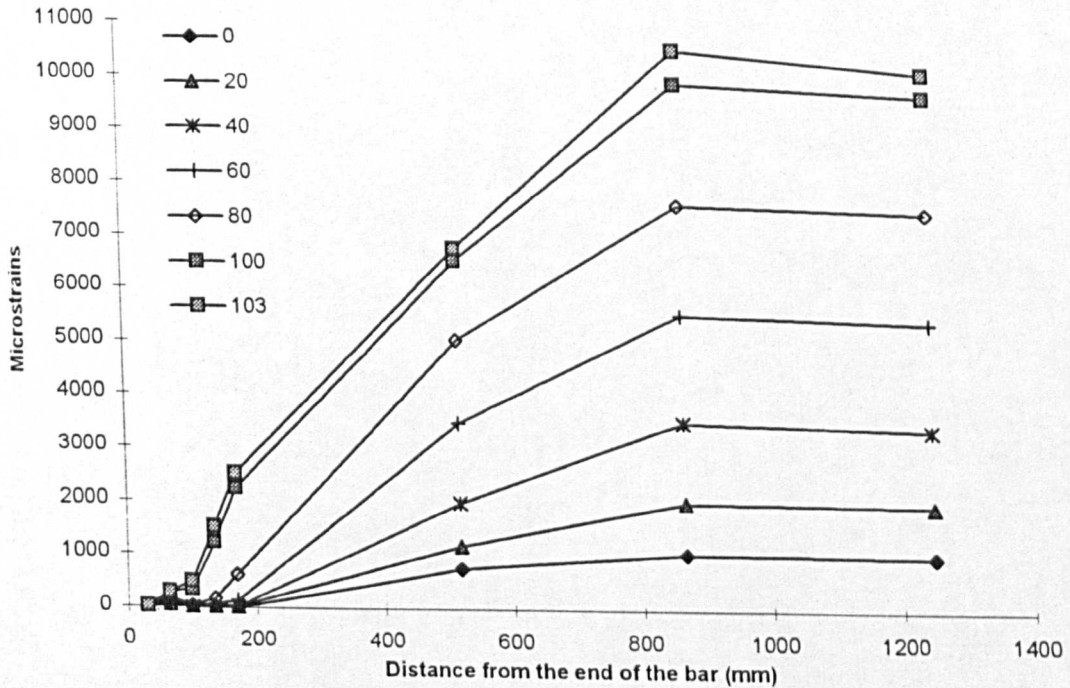


## E.2 Test results of Phase 1-3 beams

### BEAM GB9

#### Normal strains on the main reinforcing bar

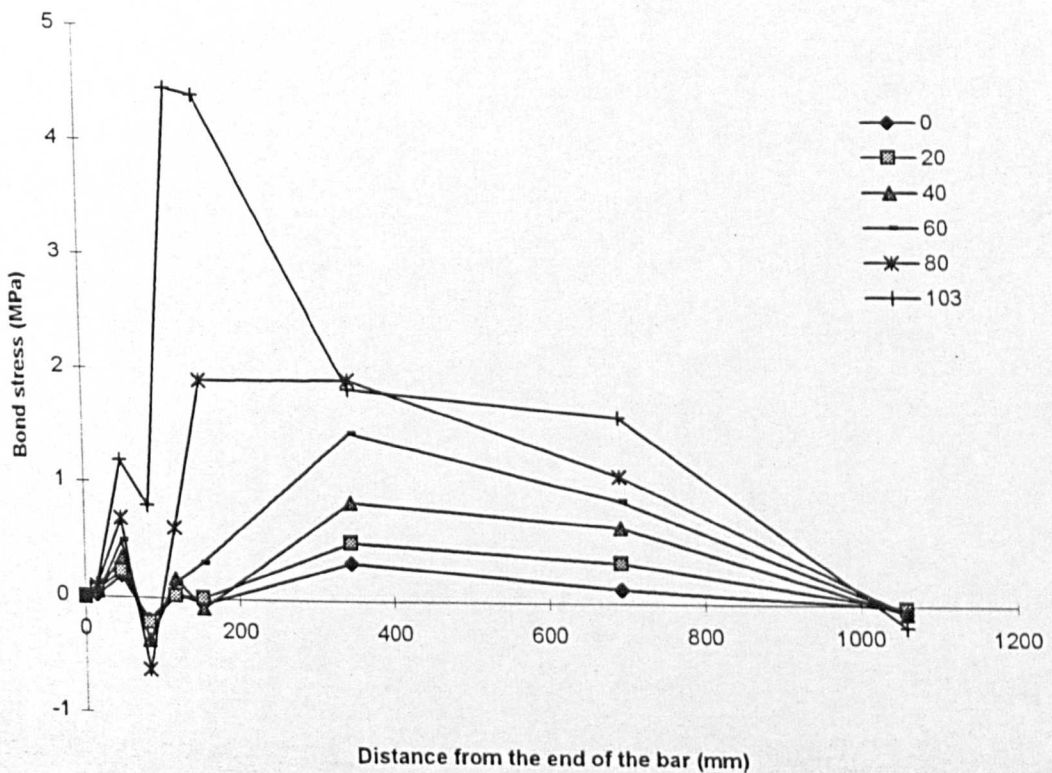
| Load (kN) | Microstrains ( <i>Distance from the end of the bar, mm</i> ) |     |     |      |      |      |       |      |
|-----------|--|-----|-----|------|------|------|-------|------|
|           | 30   | 65  | 100 | 135  | 170  | 519  | 867   | 1250 |
| 0         | 4  | 47  | 3   | 13   | 2    | 752  | 1036  | 995  |
| 10        | 4  | 64  | -12 | 36   | 7    | 842  | 1291  | 1248 |
| 20        | 12   | 65  | 16  | 22   | 23   | 1178 | 1980  | 1930 |
| 30        | 18   | 95  | 2   | 47   | 28   | 1545 | 2751  | 2660 |
| 40        | 10   | 89  | 5   | 44   | 24   | 1978 | 3476  | 3324 |
| 50        | 16   | 110 | 20  | 31   | 64   | 2777 | 4485  | 4337 |
| 60        | 3  | 117 | 29  | 60   | 131  | 3464 | 5488  | 5328 |
| 70        | 6  | 138 | 28  | 97   | 289  | 4216 | 6486  | 6337 |
| 80        | 19   | 178 | 35  | 175  | 612  | 5018 | 7539  | 7387 |
| 90        | 32   | 231 | 81  | 414  | 1260 | 5831 | 8626  | 8482 |
| 100       | 19   | 292 | 337 | 1224 | 2238 | 6515 | 9798  | 9545 |
| 103       | 22   | 296 | 481 | 1507 | 2520 | 6735 | 10429 | 9975 |



## BEAM GB9 (cont.)

### Bond stress on the main reinforcing bar

| Load (kN) | Average bond stress, MPa ( <i>Distance from the end of the bar, mm</i> ) |      |      |       |      |       |      |      |       |
|-----------|--|------|------|-------|------|-------|------|------|-------|
|           | 0  | 15   | 48   | 83    | 118  | 153   | 345  | 693  | 1059  |
| 0         | 0  | 0.02 | 0.19 | -0.19 | 0.04 | -0.05 | 0.33 | 0.12 | -0.02 |
| 10        | 0  | 0.02 | 0.26 | -0.33 | 0.21 | -0.13 | 0.36 | 0.20 | -0.02 |
| 20        | 0  | 0.06 | 0.23 | -0.21 | 0.02 | 0.01  | 0.50 | 0.35 | -0.02 |
| 30        | 0  | 0.09 | 0.33 | -0.40 | 0.19 | -0.08 | 0.66 | 0.53 | -0.04 |
| 40        | 0  | 0.05 | 0.34 | -0.36 | 0.17 | -0.09 | 0.85 | 0.65 | -0.06 |
| 50        | 0  | 0.08 | 0.41 | -0.39 | 0.05 | 0.14  | 1.18 | 0.74 | -0.06 |
| 60        | 0  | 0.02 | 0.49 | -0.38 | 0.13 | 0.31  | 1.45 | 0.88 | -0.06 |
| 70        | 0  | 0.03 | 0.57 | -0.48 | 0.30 | 0.83  | 1.71 | 0.99 | -0.06 |
| 80        | 0  | 0.10 | 0.69 | -0.62 | 0.61 | 1.89  | 1.92 | 1.10 | -0.06 |
| 90        | 0  | 0.16 | 0.86 | -0.65 | 1.45 | 3.67  | 1.99 | 1.22 | -0.06 |
| 100       | 0  | 0.10 | 1.18 | 0.20  | 3.85 | 4.40  | 1.86 | 1.43 | -0.10 |
| 103       | 0  | 0.11 | 1.19 | 0.80  | 4.45 | 4.39  | 1.84 | 1.61 | -0.18 |

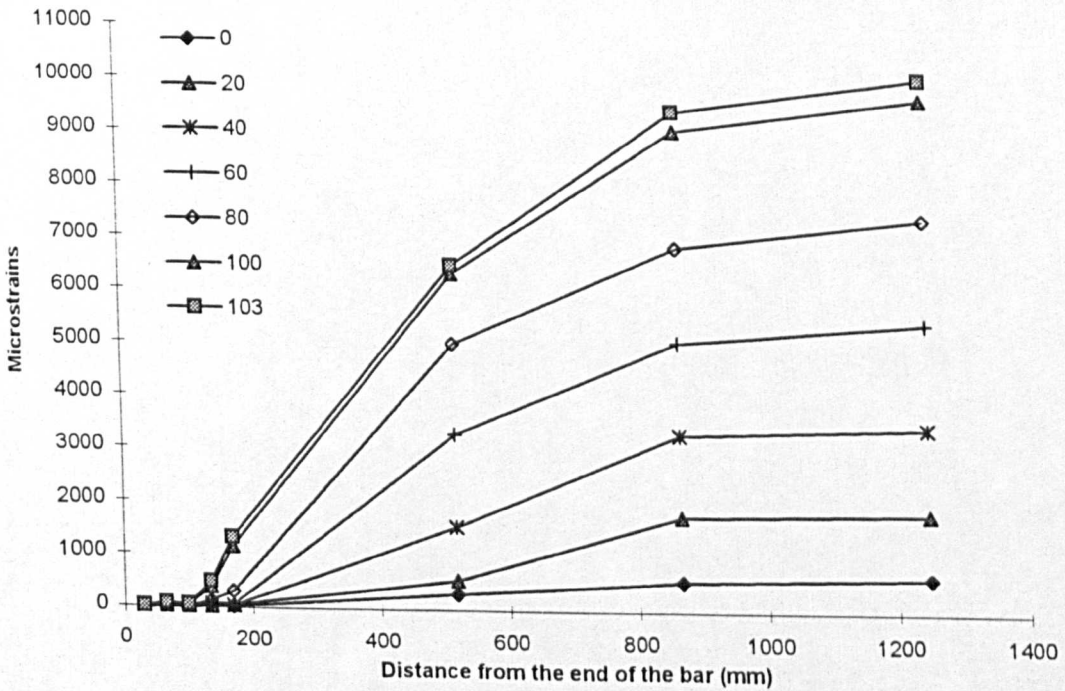


## E.2 Test results of Phase 1-3 beams

### BEAM GB10

Normal strains on the main reinforcing bar

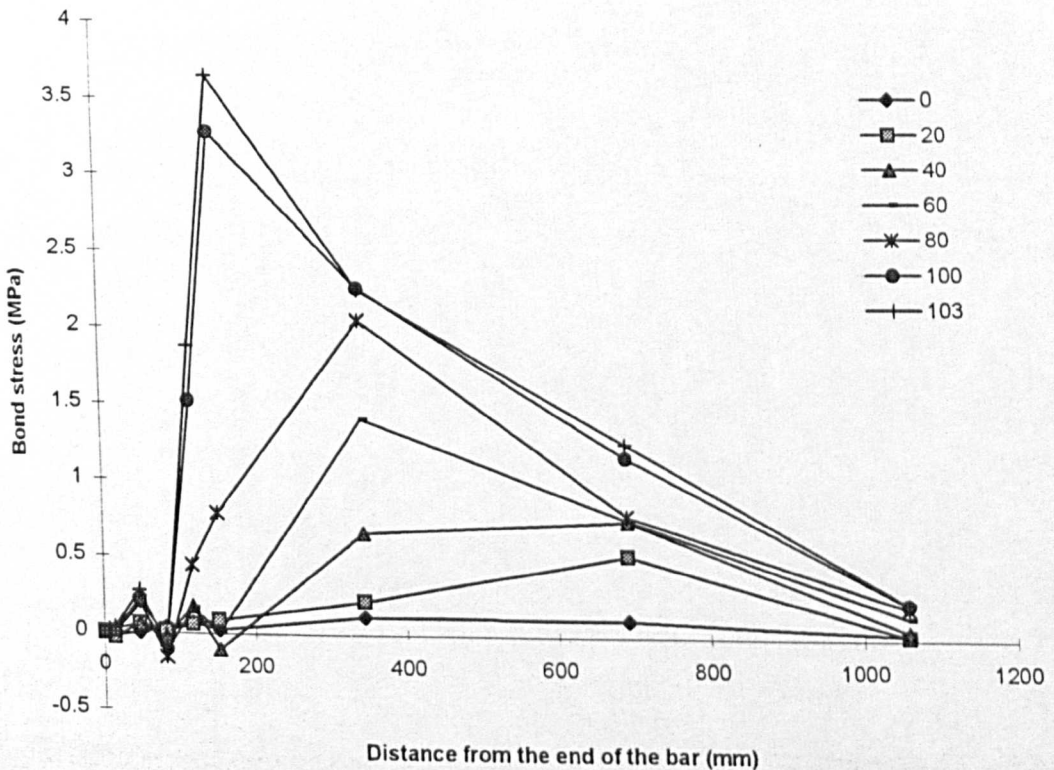
| Load (kN) | Microstrains ( <i>Distance from the end of the bar, mm</i> ) |    |     |     |      |      |      |      |
|-----------|--|----|-----|-----|------|------|------|------|
|           | 30   | 65 | 100 | 135 | 170  | 519  | 867  | 1250 |
| 0         | -4   | -4 | 5   | 22  | 28   | 303  | 562  | 638  |
| 10        | 0  | 4  | -3  | 42  | 19   | 398  | 1043 | 1112 |
| 20        | -6   | 8  | 12  | 26  | 46   | 556  | 1768 | 1832 |
| 30        | -8   | 19 | 13  | 32  | 47   | 727  | 2411 | 2444 |
| 40        | 5  | 18 | 15  | 56  | 33   | 1556 | 3286 | 3422 |
| 50        | 8  | 18 | 17  | 63  | 38   | 2305 | 4084 | 4299 |
| 60        | 0  | 43 | 18  | 56  | 59   | 3290 | 5033 | 5389 |
| 70        | 4  | 47 | 19  | 83  | 119  | 4169 | 5852 | 6301 |
| 80        | 4  | 50 | 15  | 118 | 300  | 5007 | 6809 | 7328 |
| 90        | -4   | 62 | 28  | 181 | 658  | 5671 | 7899 | 8457 |
| 100       | 2  | 53 | 43  | 393 | 1148 | 6326 | 8997 | 9571 |
| 103       | 7  | 70 | 50  | 483 | 1323 | 6486 | 9362 | 9942 |



## BEAM GB10 (cont.)

### Bond stress on the main reinforcing bar

| Load (kN) | Average bond stress, MPa ( <i>Distance from the end of the bar, mm</i> ) |       |      |       |      |       |      |      |      |
|-----------|--|-------|------|-------|------|-------|------|------|------|
|           | 0  | 15    | 48   | 83    | 118  | 153   | 345  | 693  | 1059 |
| 0         | 0  | -0.02 | 0.00 | 0.04  | 0.07 | 0.03  | 0.12 | 0.11 | 0.03 |
| 10        | 0  | 0.00  | 0.02 | -0.03 | 0.19 | -0.10 | 0.17 | 0.28 | 0.03 |
| 20        | 0  | -0.03 | 0.06 | 0.02  | 0.06 | 0.09  | 0.22 | 0.53 | 0.03 |
| 30        | 0  | -0.04 | 0.12 | -0.02 | 0.08 | 0.06  | 0.30 | 0.73 | 0.01 |
| 40        | 0  | 0.02  | 0.06 | -0.02 | 0.18 | -0.10 | 0.66 | 0.75 | 0.05 |
| 50        | 0  | 0.04  | 0.04 | -0.01 | 0.20 | -0.11 | 0.99 | 0.78 | 0.08 |
| 60        | 0  | 0.00  | 0.19 | -0.11 | 0.17 | 0.01  | 1.41 | 0.76 | 0.14 |
| 70        | 0  | 0.02  | 0.18 | -0.12 | 0.28 | 0.16  | 1.77 | 0.73 | 0.18 |
| 80        | 0  | 0.02  | 0.20 | -0.15 | 0.45 | 0.79  | 2.05 | 0.79 | 0.21 |
| 90        | 0  | -0.02 | 0.29 | -0.14 | 0.66 | 2.07  | 2.18 | 0.97 | 0.22 |
| 100       | 0  | 0.01  | 0.22 | -0.04 | 1.52 | 3.28  | 2.26 | 1.16 | 0.23 |
| 103       | 0  | 0.03  | 0.27 | -0.09 | 1.88 | 3.65  | 2.25 | 1.25 | 0.23 |

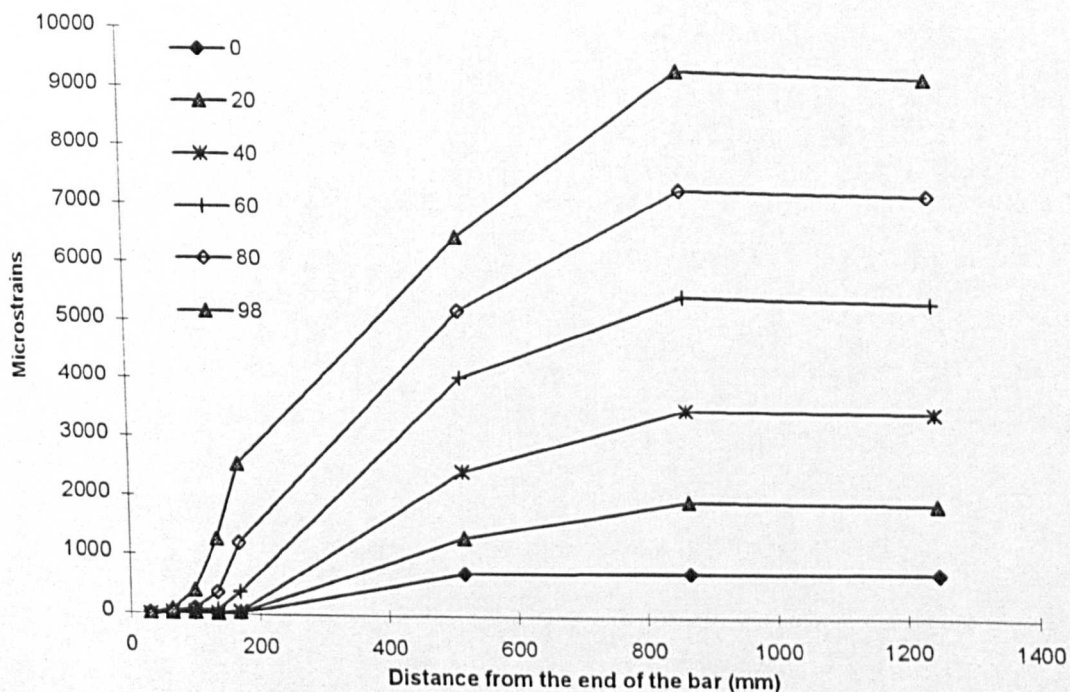


## E.2 Test results of Phase 1-3 beams

### BEAM GB11

#### Normal strains on the main reinforcing bar

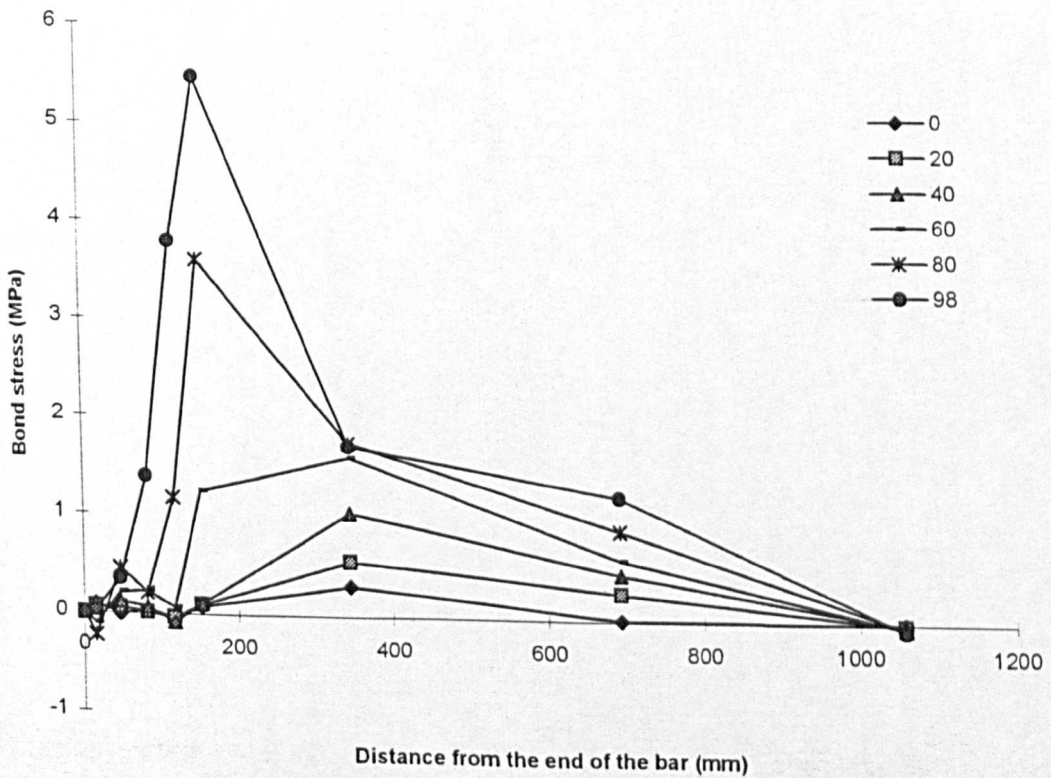
| Load (kN) | Microstrains ( <i>Distance from the end of the bar, mm</i> ) |    |     |      |      |      |      |      |
|-----------|--|----|-----|------|------|------|------|------|
|           | 30   | 65 | 100 | 135  | 170  | 519  | 867  | 1250 |
| 0         | 17   | 15 | 23  | 16   | 33   | 728  | 745  | 734  |
| 10        | 20   | 20 | 30  | 18   | 40   | 911  | 1228 | 1180 |
| 20        | 12   | 25 | 28  | 19   | 41   | 1318 | 1949 | 1891 |
| 30        | 6  | 19 | 51  | 31   | 31   | 1747 | 2669 | 2596 |
| 40        | 5  | 31 | 46  | 28   | 53   | 2444 | 3501 | 3431 |
| 50        | -30  | 46 | 49  | 42   | 57   | 3367 | 4411 | 4337 |
| 60        | -22  | 27 | 79  | 93   | 380  | 4046 | 5433 | 5305 |
| 70        | -40  | 38 | 78  | 190  | 717  | 4620 | 6312 | 6176 |
| 80        | -45  | 60 | 107 | 377  | 1207 | 5200 | 7253 | 7123 |
| 90        | -4   | 85 | 240 | 907  | 2062 | 5929 | 8446 | 8297 |
| 98        | 6  | 86 | 407 | 1279 | 2538 | 6454 | 9278 | 9097 |



## BEAM GB11 (cont.)

### Bond stress on the main reinforcing bar

| Load (kN) | Average bond stress, MPa ( <i>Distance from the end of the bar, mm</i> ) |       |       |      |       |      |      |      |       |
|-----------|--|-------|-------|------|-------|------|------|------|-------|
|           | 0  | 15    | 48    | 83   | 118   | 153  | 345  | 693  | 1059  |
| 0         | 0  | 0.09  | -0.01 | 0.04 | -0.03 | 0.08 | 0.30 | 0.01 | 0.00  |
| 10        | 0  | 0.10  | 0.00  | 0.04 | -0.05 | 0.10 | 0.38 | 0.14 | -0.02 |
| 20        | 0  | 0.06  | 0.06  | 0.01 | -0.04 | 0.09 | 0.56 | 0.28 | -0.02 |
| 30        | 0  | 0.03  | 0.06  | 0.14 | -0.09 | 0.00 | 0.75 | 0.40 | -0.03 |
| 40        | 0  | 0.03  | 0.11  | 0.07 | -0.08 | 0.11 | 1.04 | 0.46 | -0.03 |
| 50        | 0  | -0.15 | 0.33  | 0.01 | -0.03 | 0.07 | 1.44 | 0.45 | -0.03 |
| 60        | 0  | -0.11 | 0.21  | 0.22 | 0.06  | 1.24 | 1.60 | 0.60 | -0.05 |
| 70        | 0  | -0.20 | 0.34  | 0.18 | 0.48  | 2.29 | 1.70 | 0.74 | -0.05 |
| 80        | 0  | -0.23 | 0.45  | 0.21 | 1.17  | 3.60 | 1.74 | 0.89 | -0.05 |
| 90        | 0  | -0.02 | 0.38  | 0.67 | 2.89  | 5.01 | 1.69 | 1.10 | -0.06 |
| 98        | 0  | 0.03  | 0.35  | 1.39 | 3.79  | 5.46 | 1.71 | 1.23 | -0.07 |

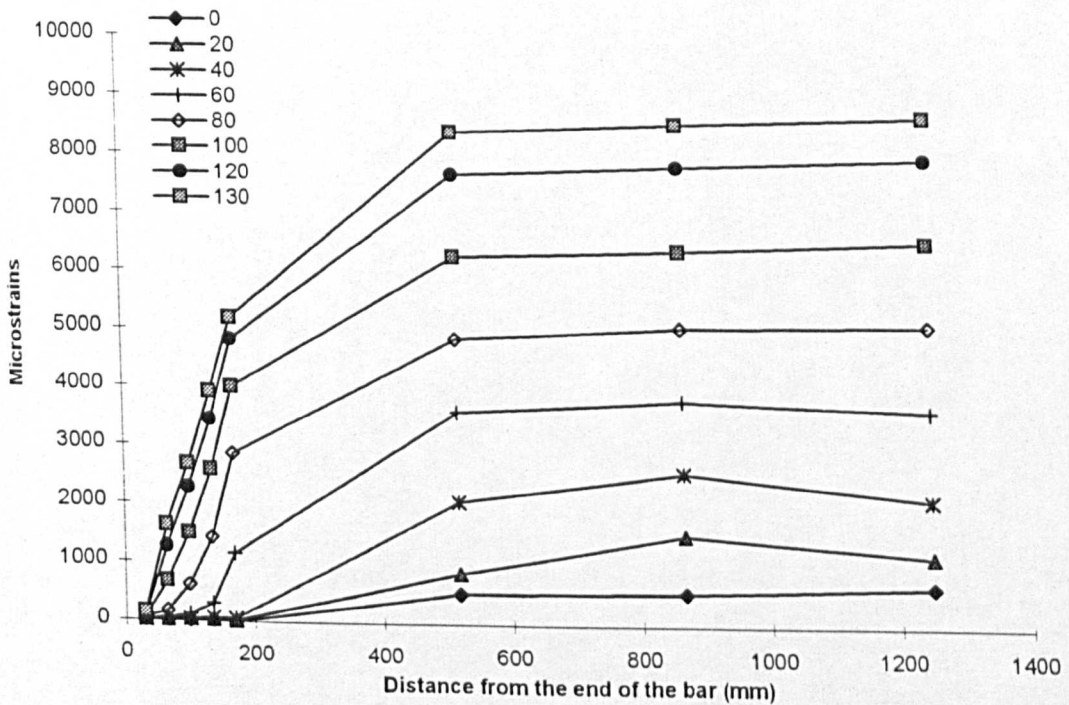


## E.2 Test results of Phase 1-3 beams

### BEAM GB12

Normal strains on the main reinforcing bar

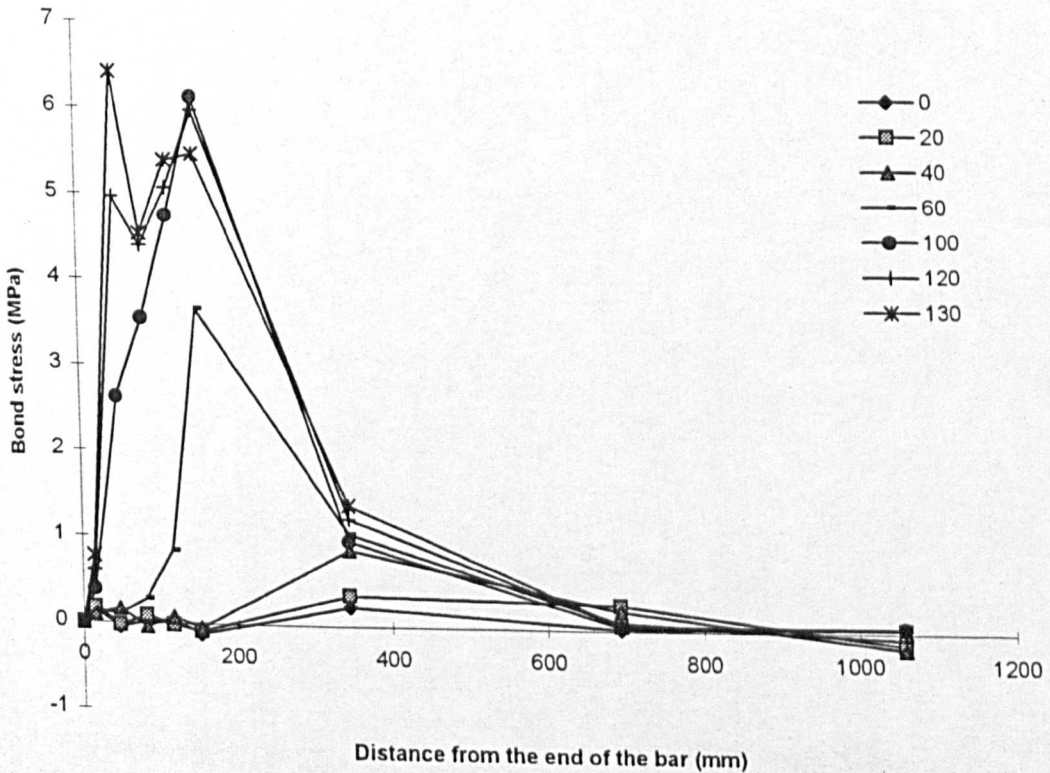
| Load (kN) | Microstrains ( <i>Distance from the end of the bar, mm</i> ) |      |      |      |      |      |      |      |
|-----------|--|------|------|------|------|------|------|------|
|           | 30   | 65   | 100  | 135  | 170  | 519  | 867  | 1250 |
| 0         | 27   | 16   | 21   | 29   | 2    | 517  | 555  | 675  |
| 10        | 29   | 18   | 45   | 32   | 22   | 623  | 1010 | 845  |
| 20        | 35   | 29   | 50   | 45   | 26   | 854  | 1522 | 1173 |
| 30        | 16   | 48   | 42   | 51   | 46   | 1097 | 2034 | 1500 |
| 40        | 18   | 56   | 46   | 62   | 52   | 2069 | 2577 | 2118 |
| 50        | 20   | 55   | 54   | 63   | 73   | 3038 | 3164 | 2870 |
| 60        | 28   | 51   | 116  | 311  | 1152 | 3596 | 3801 | 3626 |
| 70        | 34   | 86   | 217  | 733  | 1943 | 4265 | 4449 | 4382 |
| 80        | 55   | 177  | 626  | 1434 | 2862 | 4850 | 5053 | 5081 |
| 90        | 67   | 377  | 1070 | 2033 | 3495 | 5517 | 5686 | 5772 |
| 100       | 76   | 680  | 1496 | 2590 | 4001 | 6244 | 6347 | 6493 |
| 110       | 95   | 943  | 1853 | 3005 | 4387 | 6913 | 7022 | 7169 |
| 120       | 122  | 1265 | 2277 | 3445 | 4820 | 7648 | 7777 | 7894 |
| 130       | 153  | 1632 | 2676 | 3918 | 5176 | 8375 | 8499 | 8608 |



## BEAM GB12 (cont.)

### Bond stress on the main reinforcing bar

| Load (kN) | Average bond stress, MPa ( <i>Distance from the end of the bar, mm</i> ) |      |       |       |       |       |      |      |       |
|-----------|--|------|-------|-------|-------|-------|------|------|-------|
|           | 0  | 15   | 48    | 83    | 118   | 153   | 345  | 693  | 1059  |
| 0         | 0  | 0.14 | -0.05 | 0.02  | 0.04  | -0.12 | 0.22 | 0.02 | 0.05  |
| 10        | 0  | 0.14 | -0.04 | 0.11  | -0.05 | -0.05 | 0.26 | 0.17 | -0.07 |
| 20        | 0  | 0.17 | -0.02 | 0.09  | -0.02 | -0.08 | 0.36 | 0.29 | -0.14 |
| 30        | 0  | 0.08 | 0.14  | -0.02 | 0.04  | -0.02 | 0.46 | 0.41 | -0.21 |
| 40        | 0  | 0.09 | 0.16  | -0.04 | 0.07  | -0.05 | 0.88 | 0.22 | -0.18 |
| 50        | 0  | 0.10 | 0.15  | 0.00  | 0.04  | 0.04  | 1.29 | 0.05 | -0.12 |
| 60        | 0  | 0.14 | 0.10  | 0.28  | 0.84  | 3.65  | 1.06 | 0.09 | -0.07 |
| 70        | 0  | 0.17 | 0.23  | 0.57  | 2.24  | 5.25  | 1.01 | 0.08 | -0.03 |
| 80        | 0  | 0.28 | 0.53  | 1.95  | 3.50  | 6.20  | 0.87 | 0.09 | 0.01  |
| 90        | 0  | 0.34 | 1.35  | 3.01  | 4.18  | 6.35  | 0.88 | 0.07 | 0.03  |
| 100       | 0  | 0.39 | 2.62  | 3.54  | 4.75  | 6.12  | 0.98 | 0.04 | 0.06  |
| 110       | 0  | 0.48 | 3.68  | 3.95  | 5.00  | 6.00  | 1.10 | 0.05 | 0.06  |
| 120       | 0  | 0.62 | 4.96  | 4.39  | 5.07  | 5.97  | 1.23 | 0.06 | 0.05  |
| 130       | 0  | 0.77 | 6.42  | 4.53  | 5.39  | 5.46  | 1.39 | 0.05 | 0.04  |

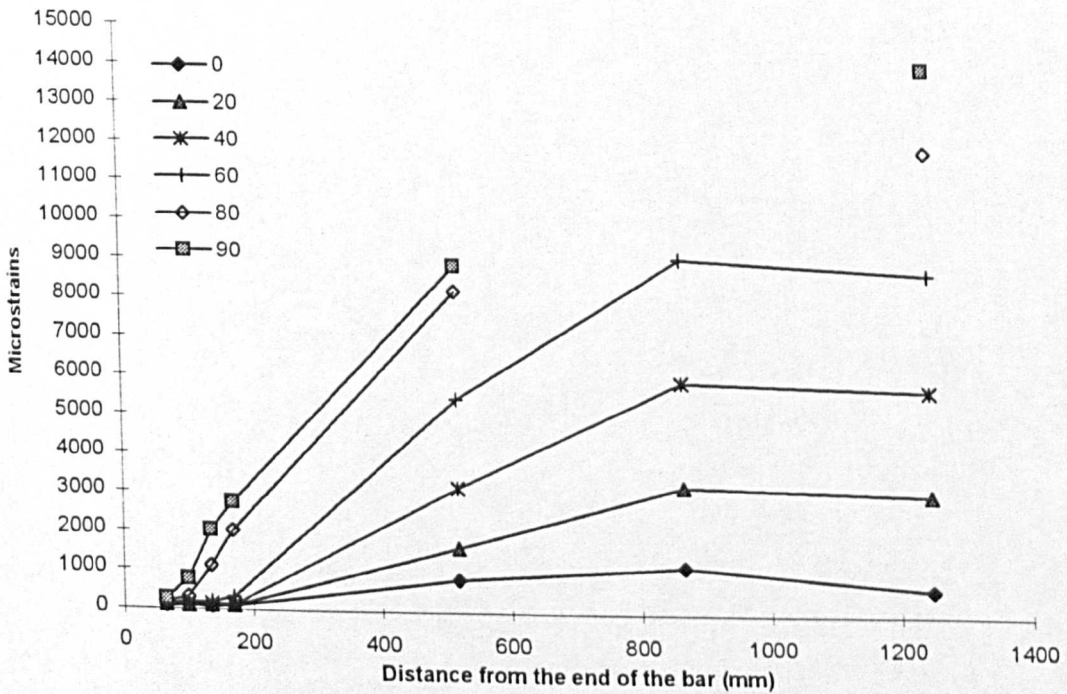


## E.2 Test results of Phase 1-3 beams

### BEAM GB13

#### Normal strains on the main reinforcing bar

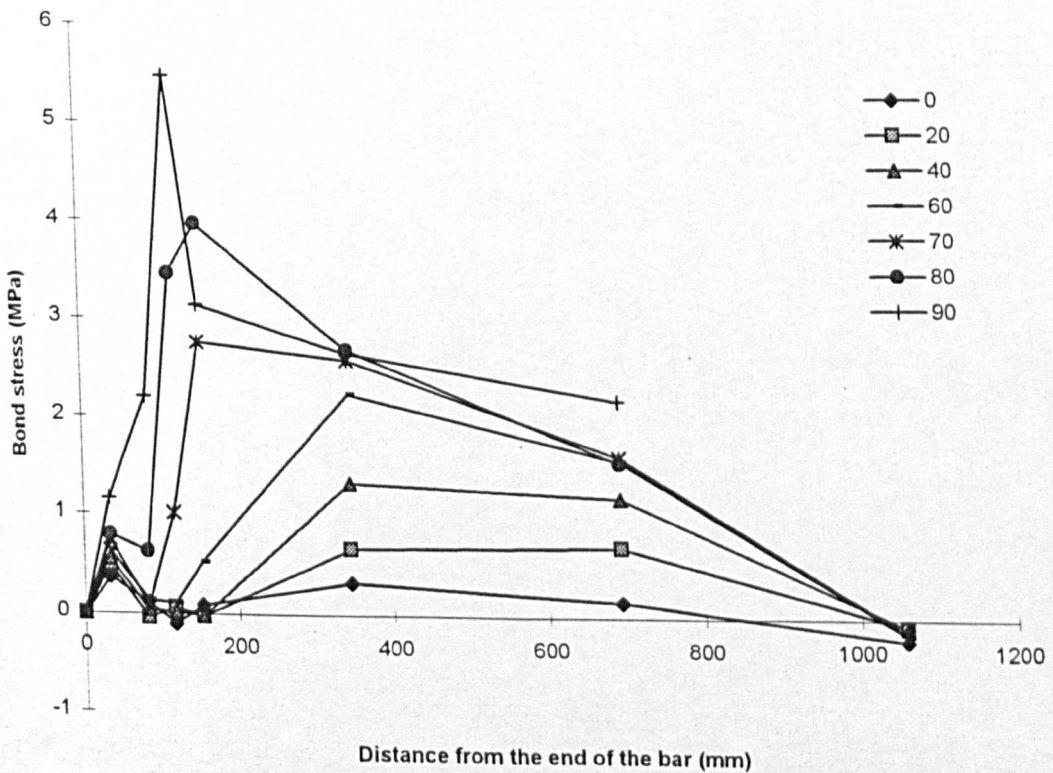
| Load (kN) | Microstrains ( <i>Distance from the end of the bar, mm</i> ) |     |      |      |      |       |       |
|-----------|--|-----|------|------|------|-------|-------|
|           | 65   | 100 | 135  | 170  | 519  | 867   | 1250  |
| 0         | 84   | 110 | 87   | 108  | 849  | 1198  | 667   |
| 10        | 89   | 118 | 95   | 109  | 1151 | 2061  | 1749  |
| 20        | 112  | 103 | 118  | 112  | 1642 | 3250  | 3054  |
| 30        | 123  | 117 | 113  | 129  | 2124 | 4358  | 4260  |
| 40        | 127  | 135 | 141  | 136  | 3189 | 5924  | 5711  |
| 50        | 143  | 171 | 160  | 170  | 4500 | 7718  | 7363  |
| 60        | 146  | 177 | 201  | 322  | 5464 | 9066  | 8661  |
| 70        | 172  | 191 | 424  | 1059 | 7003 | 10704 | 10325 |
| 80        | 182  | 327 | 1124 | 2038 | 8219 |       | 11776 |
| 90        | 267  | 775 | 2035 | 2759 | 8856 |       | 13878 |



## BEAM GB13 (cont.)

### Bond stress on the main reinforcing bar

| Load (kN) | Average bond stress, MPa ( <i>Distance from the end of the bar, mm</i> ) |      |       |       |       |      |      |       |
|-----------|--|------|-------|-------|-------|------|------|-------|
|           | 0  | 33   | 83    | 118   | 153   | 345  | 693  | 1059  |
| 0         | 0  | 0.36 | 0.11  | -0.10 | 0.09  | 0.32 | 0.15 | -0.21 |
| 10        | 0  | 0.38 | 0.13  | -0.10 | 0.06  | 0.45 | 0.40 | -0.12 |
| 20        | 0  | 0.49 | -0.04 | 0.07  | -0.02 | 0.67 | 0.70 | -0.08 |
| 30        | 0  | 0.53 | -0.02 | -0.02 | 0.07  | 0.87 | 0.97 | -0.04 |
| 40        | 0  | 0.55 | 0.04  | 0.03  | -0.02 | 1.33 | 1.19 | -0.08 |
| 50        | 0  | 0.62 | 0.12  | -0.05 | 0.04  | 1.89 | 1.40 | -0.14 |
| 60        | 0  | 0.64 | 0.13  | 0.11  | 0.52  | 2.24 | 1.57 | -0.16 |
| 70        | 0  | 0.75 | 0.08  | 1.01  | 2.76  | 2.59 | 1.61 | -0.15 |
| 80        | 0  | 0.79 | 0.63  | 3.46  | 3.96  | 2.69 | 1.55 |       |
| 90        | 0  | 1.16 | 2.20  | 5.47  | 3.14  | 2.66 | 2.19 |       |

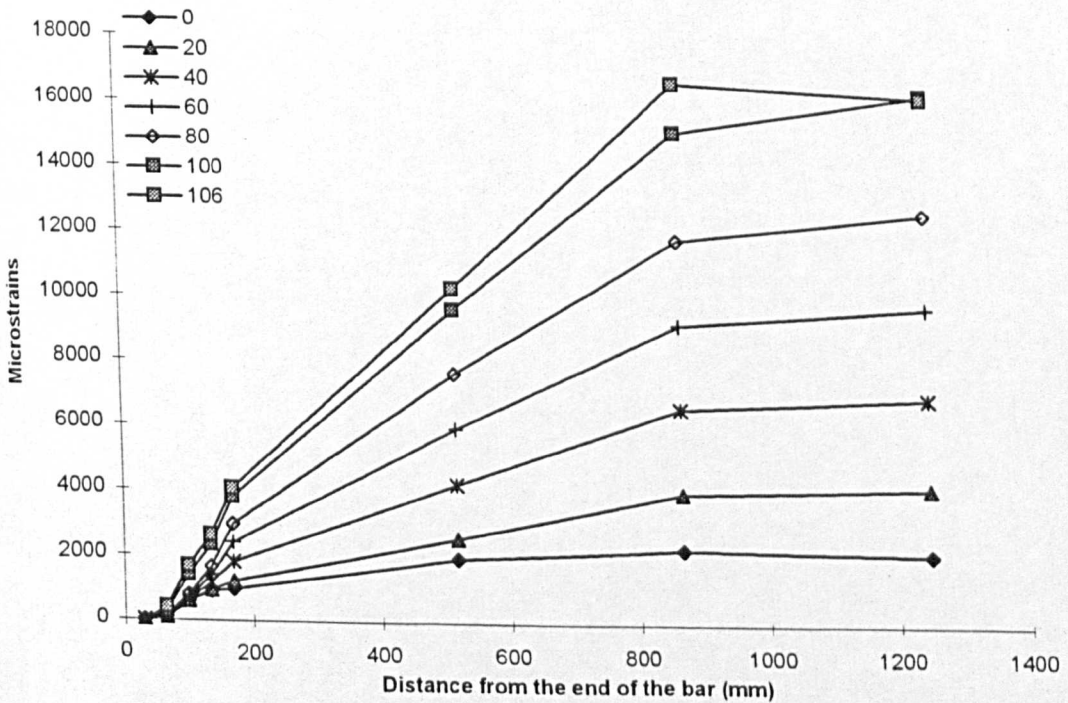


## E.2 Test results of Phase 1-3 beams

### BEAM GB14

Normal strains on the main reinforcing bar

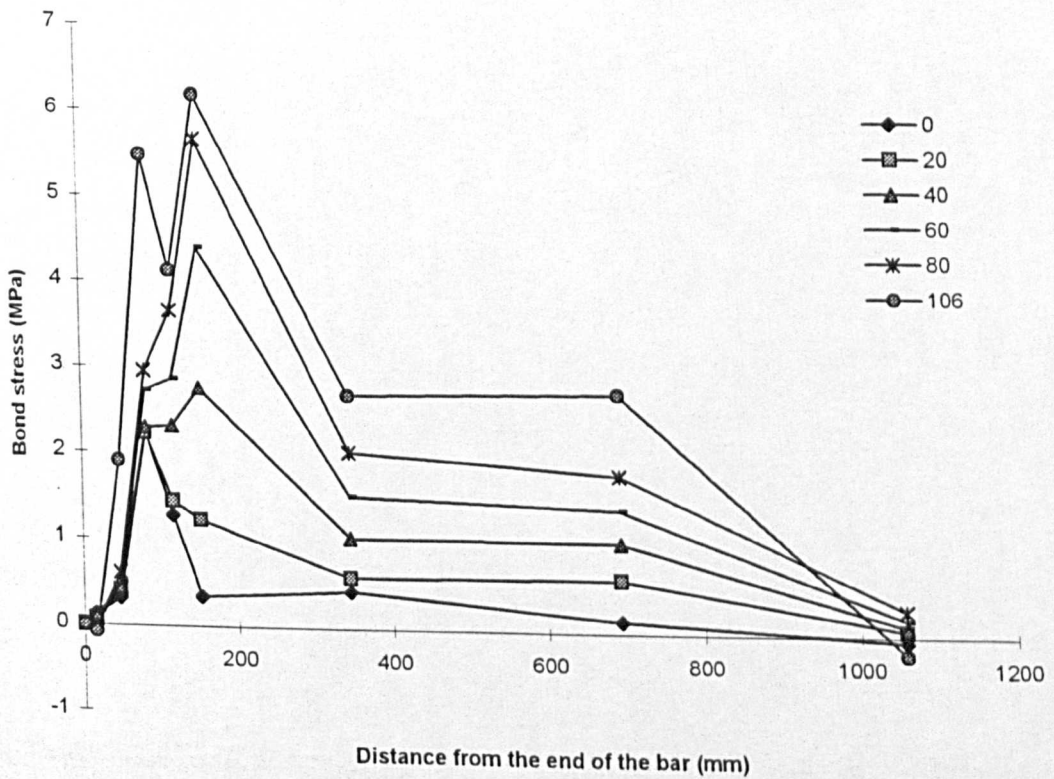
| Load (kN) | Microstrains ( <i>Distance from the end of the bar, mm</i> ) |     |      |      |      |       |       |       |
|-----------|--|-----|------|------|------|-------|-------|-------|
|           | 30   | 65  | 100  | 135  | 170  | 519   | 867   | 1250  |
| 0         | 24   | 96  | 613  | 908  | 987  | 1970  | 2285  | 2148  |
| 10        | 22   | 98  | 616  | 913  | 1029 | 2068  | 2643  | 2652  |
| 20        | 13   | 106 | 618  | 950  | 1233 | 2582  | 3982  | 4138  |
| 30        | 21   | 116 | 623  | 1059 | 1505 | 3343  | 5230  | 5441  |
| 40        | 22   | 122 | 650  | 1184 | 1820 | 4221  | 6583  | 6869  |
| 50        | 10   | 129 | 685  | 1282 | 2105 | 5031  | 7823  | 8200  |
| 60        | -2   | 113 | 740  | 1400 | 2414 | 5919  | 9154  | 9647  |
| 70        | -6   | 124 | 795  | 1509 | 2671 | 6678  | 10336 | 10889 |
| 80        | 1  | 141 | 821  | 1663 | 2968 | 7633  | 11771 | 12519 |
| 90        | -11  | 162 | 1029 | 1925 | 3347 | 8537  | 13201 | 14013 |
| 100       | -26  | 300 | 1433 | 2344 | 3797 | 9603  | 15074 | 16112 |
| 106       | -16  | 422 | 1685 | 2636 | 4060 | 10252 | 16560 | 16045 |



## BEAM GB14 (cont.)

### Bond stress on the main reinforcing bar

| Load (kN) | Average bond stress, MPa ( <i>Distance from the end of the bar, mm</i> ) |       |      |      |      |      |      |      |       |
|-----------|--|-------|------|------|------|------|------|------|-------|
|           | 0  | 15    | 48   | 83   | 118  | 153  | 345  | 693  | 1059  |
| 0         | 0  | 0.12  | 0.31 | 2.24 | 1.28 | 0.34 | 0.43 | 0.14 | -0.05 |
| 10        | 0  | 0.11  | 0.33 | 2.25 | 1.29 | 0.50 | 0.45 | 0.25 | 0.00  |
| 20        | 0  | 0.06  | 0.40 | 2.22 | 1.44 | 1.23 | 0.59 | 0.61 | 0.06  |
| 30        | 0  | 0.11  | 0.41 | 2.20 | 1.89 | 1.94 | 0.80 | 0.82 | 0.08  |
| 40        | 0  | 0.11  | 0.43 | 2.29 | 2.31 | 2.76 | 1.05 | 1.03 | 0.11  |
| 50        | 0  | 0.05  | 0.52 | 2.41 | 2.59 | 3.57 | 1.28 | 1.22 | 0.15  |
| 60        | 0  | -0.01 | 0.50 | 2.72 | 2.86 | 4.40 | 1.53 | 1.41 | 0.20  |
| 70        | 0  | -0.03 | 0.57 | 2.91 | 3.10 | 5.04 | 1.75 | 1.59 | 0.22  |
| 80        | 0  | 0.01  | 0.61 | 2.95 | 3.65 | 5.66 | 2.03 | 1.80 | 0.30  |
| 90        | 0  | -0.06 | 0.75 | 3.76 | 3.89 | 6.17 | 2.26 | 2.03 | 0.32  |
| 100       | 0  | -0.13 | 1.41 | 4.92 | 3.95 | 6.30 | 2.53 | 2.38 | 0.41  |
| 106       | 0  | -0.08 | 1.90 | 5.48 | 4.13 | 6.18 | 2.70 | 2.75 | -0.20 |

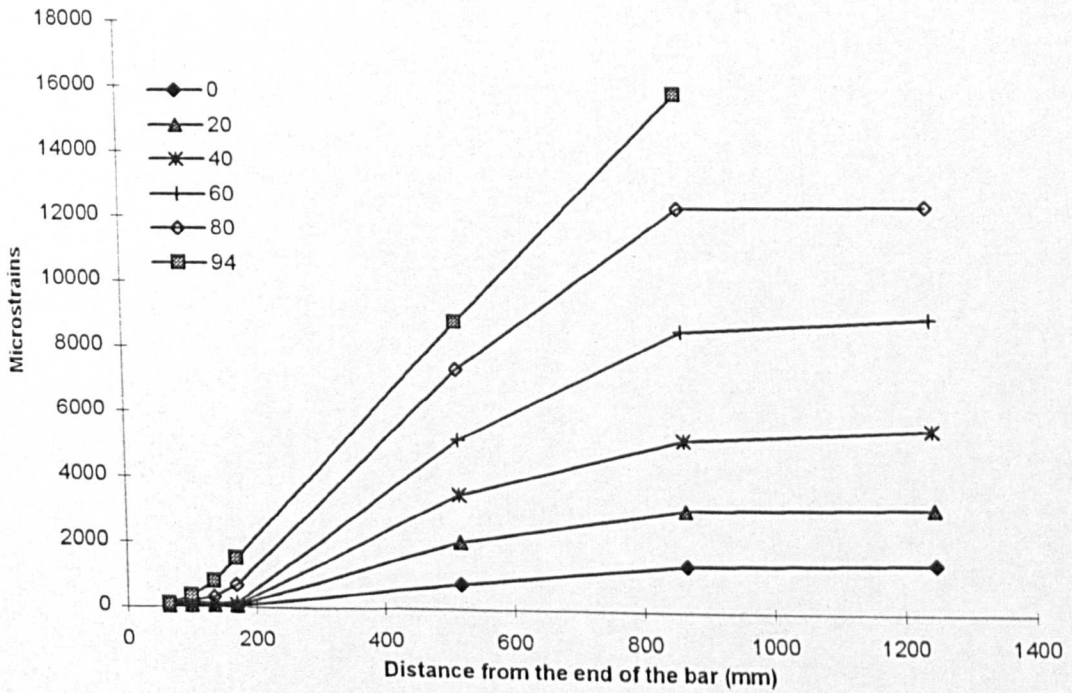


## E.2 Test results of Phase 1-3 beams

### BEAM GB15

**Normal strains on the main reinforcing bar**

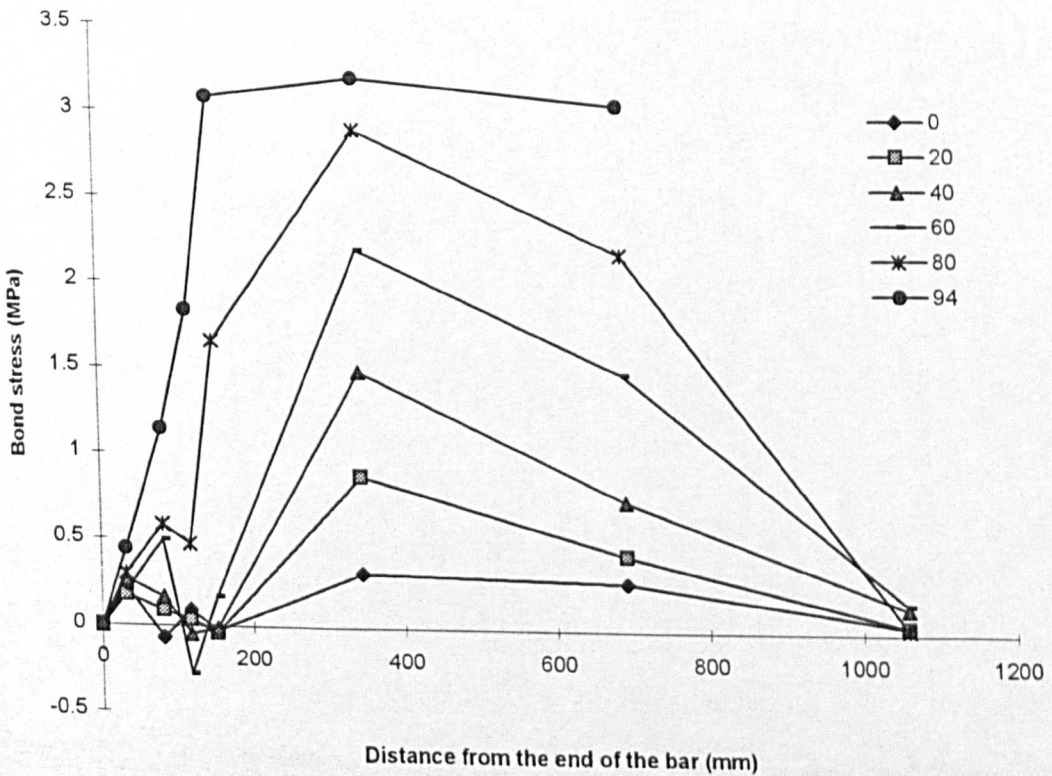
| Load (kN) | Microstrains ( <i>Distance from the end of the bar, mm</i> ) |     |     |      |      |       |       |
|-----------|--|-----|-----|------|------|-------|-------|
|           | 65   | 100 | 135 | 170  | 519  | 867   | 1250  |
| 0         | 51   | 35  | 56  | 49   | 775  | 1408  | 1508  |
| 10        | 29   | 65  | 44  | 63   | 1287 | 1973  | 1981  |
| 20        | 41   | 61  | 69  | 60   | 2069 | 3063  | 3164  |
| 30        | 39   | 75  | 72  | 62   | 2745 | 3940  | 4157  |
| 40        | 62   | 100 | 90  | 87   | 3491 | 5201  | 5568  |
| 50        | 66   | 136 | 86  | 115  | 4278 | 6973  | 7467  |
| 60        | 47   | 161 | 97  | 136  | 5164 | 8559  | 8978  |
| 70        | 69   | 168 | 132 | 306  | 6293 | 10528 | 10773 |
| 80        | 70   | 205 | 314 | 695  | 7337 | 12321 | 12393 |
| 90        | 82   | 305 | 653 | 1248 | 8243 | 14915 |       |
| 94        | 103  | 366 | 789 | 1499 | 8821 | 15792 | •     |



## BEAM GB15 (cont.)

### Bond stress on the main reinforcing bar

| Load (kN) | Average bond stress, MPa ( <i>Distance from the end of the bar, mm</i> ) |      |       |       |       |      |      |      |
|-----------|--|------|-------|-------|-------|------|------|------|
|           | 0  | 33   | 83    | 118   | 153   | 345  | 693  | 1059 |
| 0         | 0  | 0.22 | -0.07 | 0.09  | -0.03 | 0.32 | 0.28 | 0.04 |
| 10        | 0  | 0.12 | 0.16  | -0.09 | 0.08  | 0.53 | 0.30 | 0.00 |
| 20        | 0  | 0.18 | 0.09  | 0.03  | -0.04 | 0.88 | 0.43 | 0.04 |
| 30        | 0  | 0.17 | 0.16  | -0.01 | -0.04 | 1.17 | 0.52 | 0.09 |
| 40        | 0  | 0.27 | 0.17  | -0.05 | -0.01 | 1.48 | 0.74 | 0.15 |
| 50        | 0  | 0.28 | 0.30  | -0.22 | 0.13  | 1.81 | 1.17 | 0.20 |
| 60        | 0  | 0.20 | 0.50  | -0.28 | 0.17  | 2.19 | 1.48 | 0.17 |
| 70        | 0  | 0.30 | 0.43  | -0.16 | 0.75  | 2.61 | 1.85 | 0.10 |
| 80        | 0  | 0.30 | 0.59  | 0.47  | 1.66  | 2.89 | 2.17 | 0.03 |
| 90        | 0  | 0.36 | 0.96  | 1.51  | 2.58  | 3.05 | 2.91 |      |
| 94        | 0  | 0.45 | 1.14  | 1.84  | 3.08  | 3.19 | 3.04 |      |

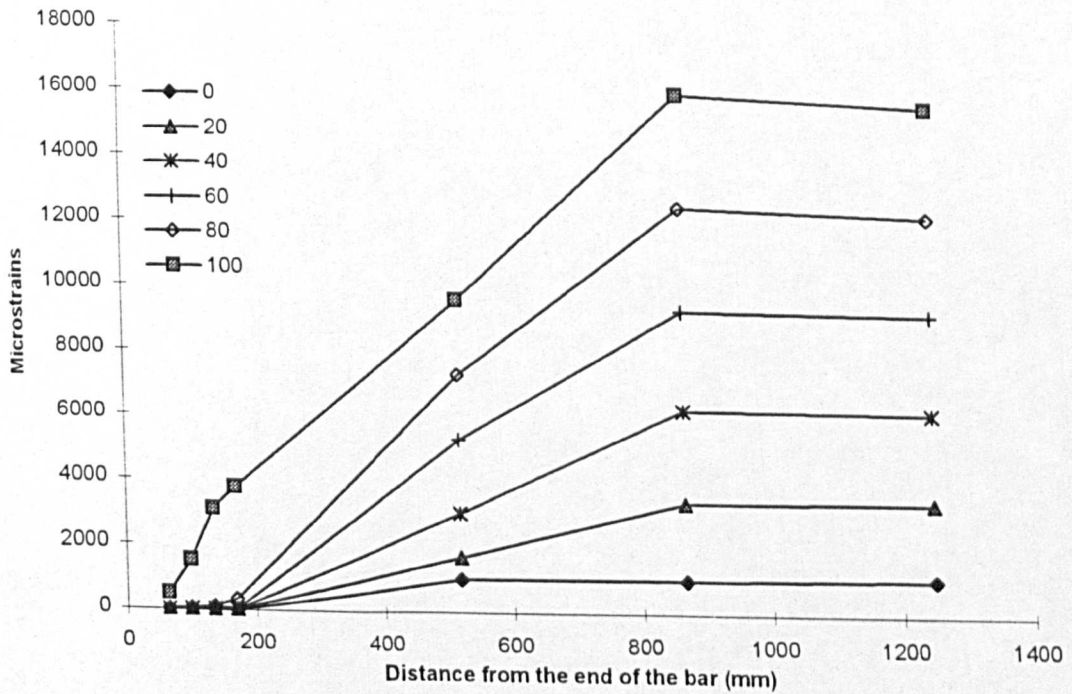


## E.2 Test results of Phase 1-3 beams

### BEAM GB16

#### Normal strains on the main reinforcing bar

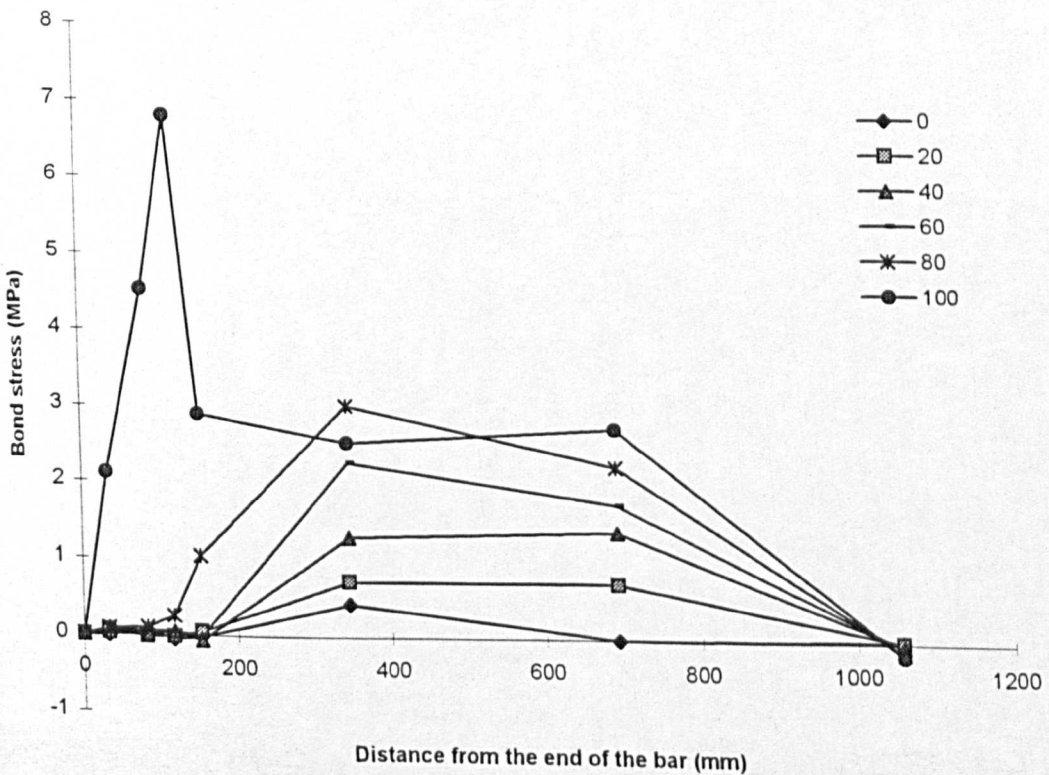
| Load (kN) | Microstrains ( <i>Distance from the end of the bar, mm</i> ) |      |      |      |      |       |       |
|-----------|--|------|------|------|------|-------|-------|
|           | 65   | 100  | 135  | 170  | 519  | 867   | 1250  |
| 0         | -2   | 16   | 5    | 2    | 1002 | 1019  | 1085  |
| 10        | 19   | 1    | 14   | 8    | 1220 | 1991  | 2040  |
| 20        | 15   | 11   | 8    | 20   | 1683 | 3343  | 3378  |
| 30        | 8  | 25   | 11   | 30   | 2147 | 4706  | 4672  |
| 40        | 8  | 14   | 26   | 13   | 3008 | 6196  | 6126  |
| 50        | 24   | 6    | 39   | 26   | 4176 | 7586  | 7517  |
| 60        | 19   | 30   | 43   | 42   | 5266 | 9257  | 9127  |
| 70        | 20   | 38   | 44   | 124  | 6229 | 10765 | 10562 |
| 80        | 20   | 45   | 103  | 344  | 7284 | 12404 | 12093 |
| 90        | 268  | 1064 | 2565 | 3318 | 8330 | 14004 | 13665 |
| 100       | 486  | 1531 | 3098 | 3765 | 9577 | 15841 | 15434 |



## BEAM GB16 (cont.)

### Bond stress on the main reinforcing bar

| Load (kN) | Average bond stress, MPa ( <i>Distance from the end of the bar, mm</i> ) |       |       |       |       |      |      |       |
|-----------|--|-------|-------|-------|-------|------|------|-------|
|           | 0  | 33    | 83    | 118   | 153   | 345  | 693  | 1059  |
| 0         | 0  | -0.01 | 0.08  | -0.05 | -0.01 | 0.44 | 0.01 | 0.03  |
| 10        | 0  | 0.08  | -0.08 | 0.06  | -0.03 | 0.53 | 0.34 | 0.02  |
| 20        | 0  | 0.06  | -0.02 | -0.01 | 0.05  | 0.72 | 0.72 | 0.01  |
| 30        | 0  | 0.04  | 0.07  | -0.06 | 0.08  | 0.92 | 1.12 | -0.01 |
| 40        | 0  | 0.04  | 0.02  | 0.05  | -0.06 | 1.31 | 1.39 | -0.03 |
| 50        | 0  | 0.10  | -0.08 | 0.14  | -0.05 | 1.81 | 1.49 | -0.03 |
| 60        | 0  | 0.08  | 0.05  | 0.06  | -0.01 | 2.28 | 1.74 | -0.05 |
| 70        | 0  | 0.08  | 0.08  | 0.03  | 0.35  | 2.66 | 1.98 | -0.08 |
| 80        | 0  | 0.09  | 0.11  | 0.25  | 1.04  | 3.02 | 2.23 | -0.12 |
| 90        | 0  | 1.16  | 3.45  | 6.51  | 3.27  | 2.18 | 2.47 | -0.13 |
| 100       | 0  | 2.11  | 4.53  | 6.80  | 2.90  | 2.53 | 2.73 | -0.16 |

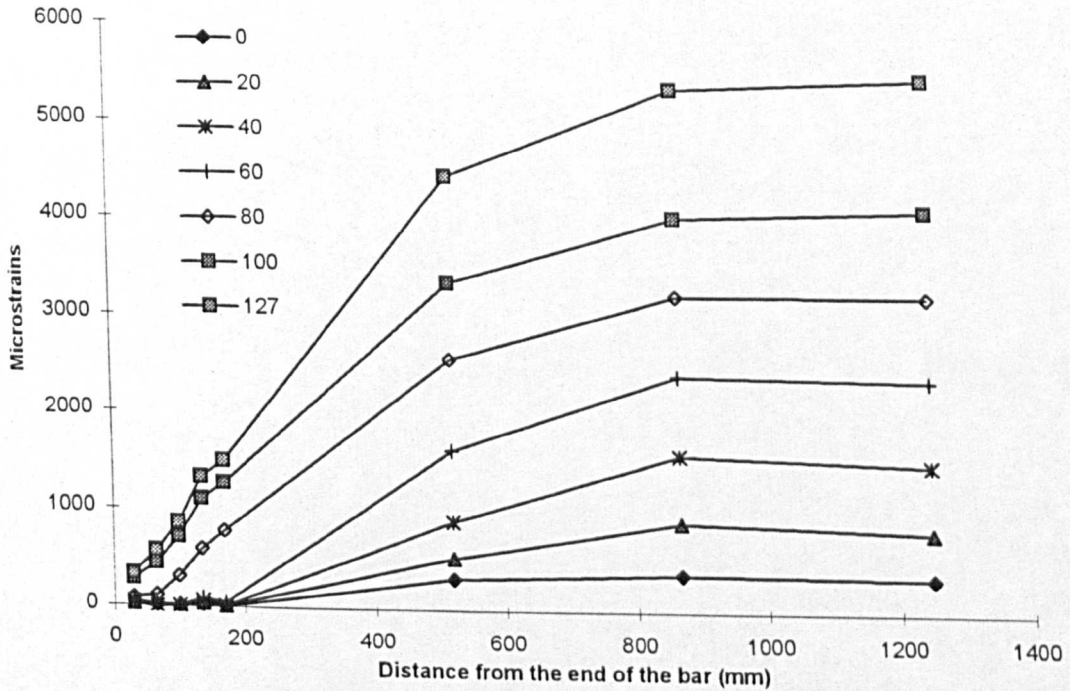


## E.2 Test results of Phase 1-3 beams

### BEAM CB17

**Normal strains on the main reinforcing bar**

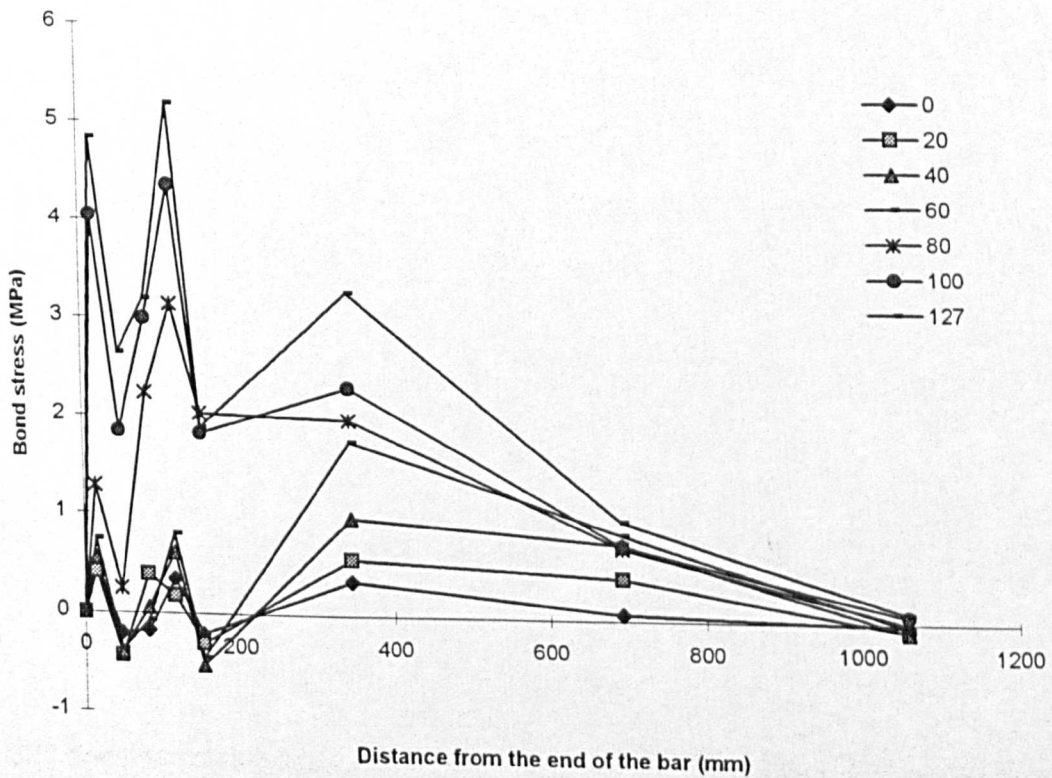
| Load (kN) | Microstrains ( <i>Distance from the end of the bar, mm</i> ) |     |     |      |      |      |      |      |
|-----------|--|-----|-----|------|------|------|------|------|
|           | 30   | 65  | 100 | 135  | 170  | 519  | 867  | 1250 |
| 0         | 31   | 13  | -3  | 29   | 10   | 318  | 376  | 350  |
| 10        | 42   | 13  | -8  | 48   | 9    | 376  | 559  | 507  |
| 20        | 28   | -11 | 24  | 40   | 13   | 525  | 901  | 811  |
| 30        | 42   | 7   | -3  | 60   | 12   | 666  | 1207 | 1113 |
| 40        | 37   | 2   | 7   | 62   | 15   | 896  | 1579 | 1484 |
| 50        | 27   | -8  | 39  | 49   | 45   | 1246 | 1960 | 1892 |
| 60        | 50   | 17  | 11  | 83   | 43   | 1619 | 2387 | 2342 |
| 70        | 38   | 25  | 37  | 82   | 124  | 2013 | 2779 | 2790 |
| 80        | 88   | 110 | 312 | 595  | 778  | 2557 | 3208 | 3198 |
| 90        | 212  | 360 | 693 | 1000 | 1190 | 2975 | 3614 | 3649 |
| 100       | 277  | 443 | 713 | 1105 | 1270 | 3340 | 4010 | 4074 |
| 110       | 304  | 486 | 765 | 1189 | 1351 | 3691 | 4454 | 4515 |
| 120       | 321  | 537 | 814 | 1259 | 1431 | 4071 | 4910 | 4973 |
| 127       | 331  | 569 | 857 | 1325 | 1495 | 4435 | 5320 | 5407 |



## BEAM CB17 (cont.)

### Bond stress on the main reinforcing bar

| Load (kN) | Average bond stress, MPa ( <i>Distance from the end of the bar, mm</i> ) |      |       |       |      |       |      |      |       |
|-----------|--|------|-------|-------|------|-------|------|------|-------|
|           | 0  | 15   | 48    | 83    | 118  | 153   | 345  | 693  | 1059  |
| 0         | 0  | 0.45 | -0.20 | -0.18 | 0.35 | -0.21 | 0.34 | 0.06 | -0.03 |
| 10        | 0  | 0.62 | -0.33 | -0.23 | 0.62 | -0.43 | 0.41 | 0.20 | -0.05 |
| 20        | 0  | 0.41 | -0.44 | 0.39  | 0.18 | -0.30 | 0.57 | 0.42 | -0.09 |
| 30        | 0  | 0.61 | -0.39 | -0.10 | 0.70 | -0.53 | 0.73 | 0.60 | -0.09 |
| 40        | 0  | 0.55 | -0.39 | 0.05  | 0.61 | -0.52 | 0.98 | 0.76 | -0.10 |
| 50        | 0  | 0.39 | -0.39 | 0.53  | 0.11 | -0.05 | 1.34 | 0.79 | -0.07 |
| 60        | 0  | 0.74 | -0.37 | -0.07 | 0.80 | -0.44 | 1.76 | 0.86 | -0.05 |
| 70        | 0  | 0.55 | -0.14 | 0.13  | 0.50 | 0.47  | 2.10 | 0.85 | 0.01  |
| 80        | 0  | 1.28 | 0.25  | 2.24  | 3.14 | 2.03  | 1.98 | 0.73 | -0.01 |
| 90        | 0  | 3.10 | 1.64  | 3.69  | 3.40 | 2.11  | 1.99 | 0.71 | 0.03  |
| 100       | 0  | 4.04 | 1.84  | 2.99  | 4.35 | 1.83  | 2.31 | 0.75 | 0.07  |
| 110       | 0  | 4.44 | 2.02  | 3.10  | 4.70 | 1.80  | 2.61 | 0.85 | 0.06  |
| 120       | 0  | 4.70 | 2.40  | 3.07  | 4.94 | 1.90  | 2.94 | 0.93 | 0.06  |
| 127       | 0  | 4.84 | 2.64  | 3.19  | 5.18 | 1.88  | 3.27 | 0.99 | 0.09  |

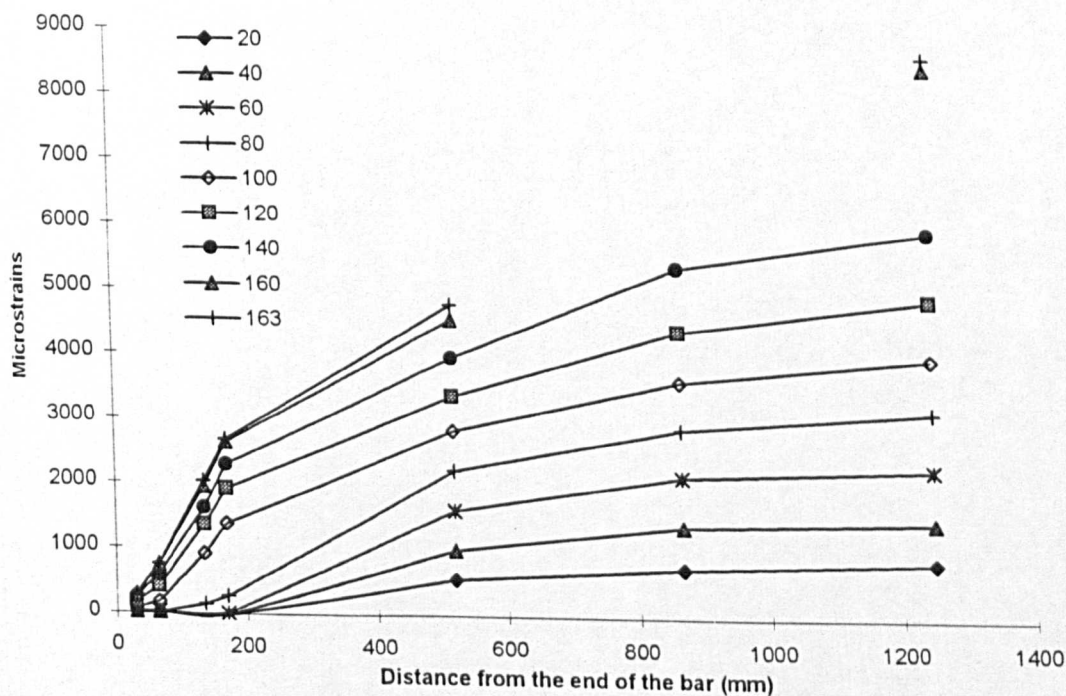


## E.2 Test results of Phase 1-3 beams

### BEAM CB18

#### Normal strains on the main reinforcing bar

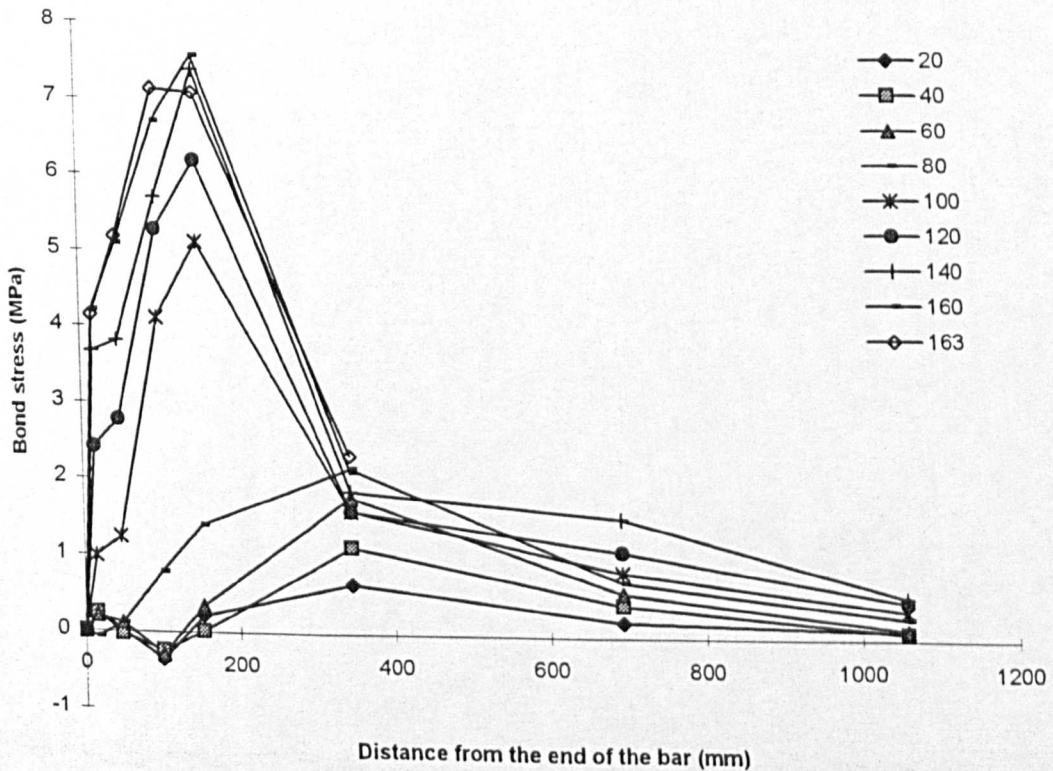
| Load (kN) | Microstrains ( <i>Distance from the end of the bar, mm</i> ) |     |      |      |      |      |      |
|-----------|--|-----|------|------|------|------|------|
|           | 30   | 65  | 135  | 170  | 519  | 867  | 1250 |
| 20        | 17   | 19  | -45  | -25  | 559  | 741  | 850  |
| 30        | 16   | 21  | -44  | -16  | 708  | 1014 | 1130 |
| 40        | 17   | 15  | -27  | -25  | 997  | 1375 | 1460 |
| 50        | -2   | 2   | -3   | -15  | 1312 | 1773 | 1903 |
| 60        | 14   | 25  | -26  | 6    | 1608 | 2128 | 2259 |
| 70        | 17   | 23  | -5   | 20   | 1929 | 2515 | 2708 |
| 80        | -4   | 6   | 148  | 274  | 2207 | 2853 | 3125 |
| 90        | 27   | 83  | 522  | 889  | 2448 | 3229 | 3552 |
| 100       | 68   | 180 | 922  | 1383 | 2822 | 3585 | 3944 |
| 110       | 122  | 302 | 1083 | 1671 | 3074 | 3969 | 4370 |
| 120       | 165  | 416 | 1365 | 1922 | 3359 | 4358 | 4833 |
| 130       | 202  | 489 | 1514 | 2088 | 3686 | 4733 | 5275 |
| 140       | 251  | 595 | 1621 | 2285 | 3952 | 5331 | 5863 |
| 150       | 249  | 635 | 1808 | 2436 | 4252 | 5717 | 6715 |
| 160       | 288  | 746 | 1953 | 2634 | 4533 |      | 8370 |
| 163       | 283  | 750 | 2034 | 2672 | 4760 |      | 8513 |



## BEAM CB18 (cont.)

### Bond stress on the main reinforcing bar

| Load (kN) | Average bond stress, MPa ( <i>Distance from the end of the bar, mm</i> ) |       |       |       |       |      |      |      |
|-----------|--|-------|-------|-------|-------|------|------|------|
|           | 0  | 15    | 48    | 100   | 153   | 345  | 693  | 1059 |
| 20        | 0  | 0.25  | 0.02  | -0.35 | 0.22  | 0.65 | 0.20 | 0.11 |
| 30        | 0  | 0.23  | 0.06  | -0.36 | 0.31  | 0.81 | 0.34 | 0.12 |
| 40        | 0  | 0.25  | -0.02 | -0.23 | 0.02  | 1.14 | 0.42 | 0.09 |
| 50        | 0  | -0.02 | 0.04  | -0.03 | -0.14 | 1.48 | 0.51 | 0.13 |
| 60        | 0  | 0.21  | 0.12  | -0.28 | 0.35  | 1.78 | 0.58 | 0.13 |
| 70        | 0  | 0.24  | 0.07  | -0.15 | 0.27  | 2.13 | 0.65 | 0.20 |
| 80        | 0  | -0.06 | 0.12  | 0.78  | 1.40  | 2.15 | 0.72 | 0.28 |
| 90        | 0  | 0.39  | 0.63  | 2.43  | 4.07  | 1.74 | 0.87 | 0.33 |
| 100       | 0  | 0.99  | 1.24  | 4.11  | 5.10  | 1.60 | 0.85 | 0.36 |
| 110       | 0  | 1.78  | 2.00  | 4.33  | 6.52  | 1.56 | 1.00 | 0.41 |
| 120       | 0  | 2.42  | 2.78  | 5.26  | 6.18  | 1.60 | 1.11 | 0.48 |
| 130       | 0  | 2.95  | 3.18  | 5.69  | 6.36  | 1.78 | 1.17 | 0.55 |
| 140       | 0  | 3.67  | 3.81  | 5.69  | 7.37  | 1.86 | 1.53 | 0.54 |
| 150       | 0  | 3.64  | 4.28  | 6.51  | 6.96  | 2.02 | 1.63 | 1.01 |
| 160       | 0  | 4.21  | 5.08  | 6.69  | 7.55  | 2.11 |      |      |
| 163       | 0  | 4.14  | 5.18  | 7.12  | 7.07  | 2.33 |      |      |

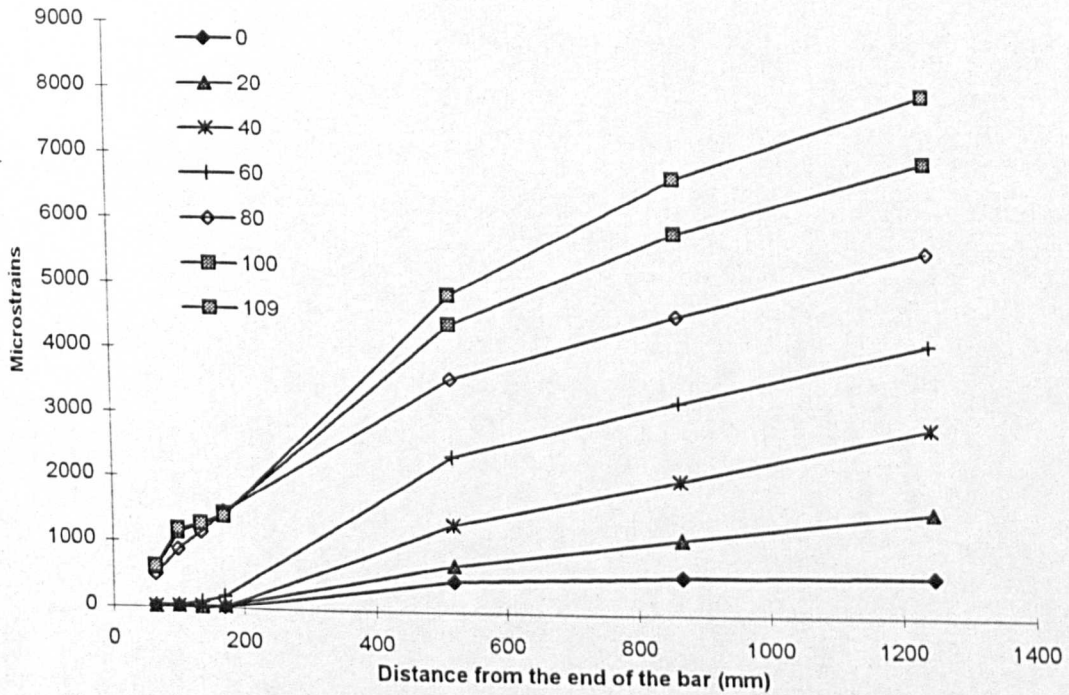


## E.2 Test results of Phase 1-3 beams

### BEAM CB19

#### Normal strains on the main reinforcing bar

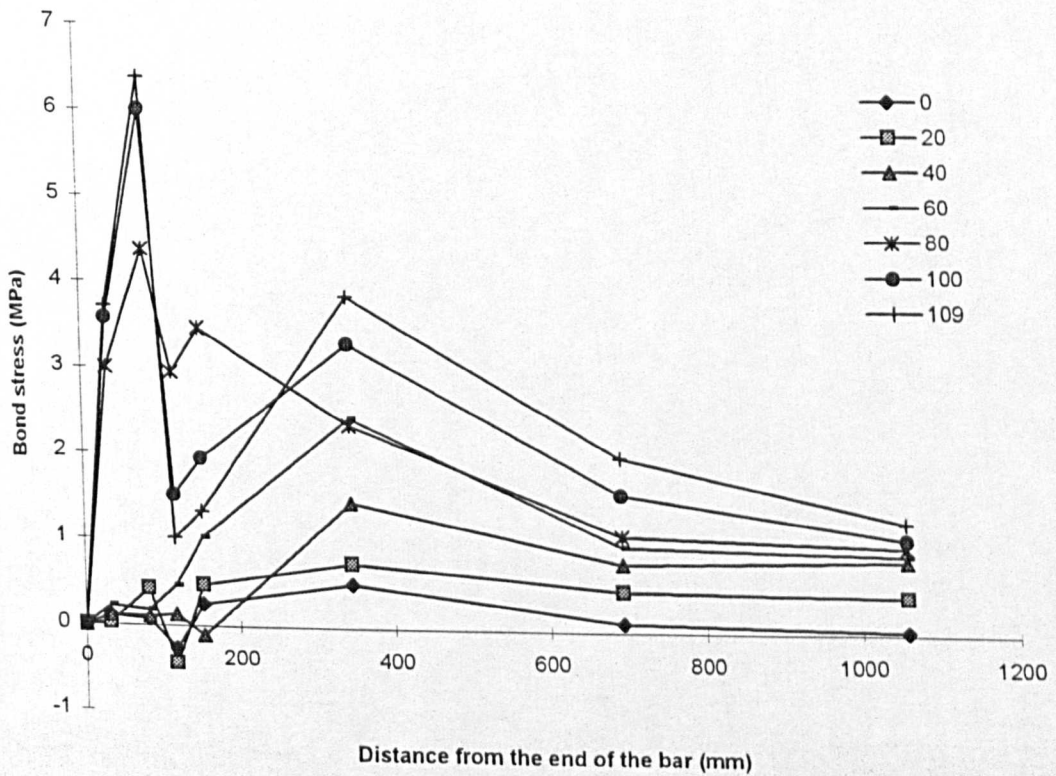
| Load (kN) | Microstrains ( <i>Distance from the end of the bar, mm</i> ) |      |      |      |      |      |      |
|-----------|--|------|------|------|------|------|------|
|           | 65   | 100  | 135  | 170  | 519  | 867  | 1250 |
| 0         | 19   | 25   | 1    | 24   | 479  | 573  | 605  |
| 10        | -11  | 42   | -3   | 31   | 541  | 782  | 987  |
| 20        | 4  | 42   | 3    | 46   | 715  | 1139 | 1559 |
| 30        | 25   | 27   | 25   | 32   | 928  | 1481 | 2185 |
| 40        | 19   | 28   | 40   | 30   | 1324 | 2029 | 2856 |
| 50        | 14   | 44   | 45   | 43   | 1894 | 2686 | 3524 |
| 60        | 38   | 53   | 95   | 187  | 2363 | 3239 | 4127 |
| 70        | 56   | 152  | 279  | 639  | 2954 | 3910 | 4808 |
| 80        | 502  | 896  | 1161 | 1473 | 3579 | 4565 | 5536 |
| 90        | 563  | 1062 | 1221 | 1427 | 3985 | 5199 | 6191 |
| 100       | 598  | 1139 | 1275 | 1450 | 4412 | 5824 | 6888 |
| 109       | 621  | 1197 | 1288 | 1408 | 4859 | 6655 | 7906 |



## BEAM CB19 (cont.)

### Bond stress on the main reinforcing bar

| Load (kN) | Average bond stress, MPa ( <i>Distance from the end of the bar, mm</i> ) |       |      |       |       |      |      |      |  |
|-----------|--|-------|------|-------|-------|------|------|------|--|
|           | 0  | 33    | 83   | 118   | 153   | 345  | 693  | 1059 |  |
| 0         | 0  | 0.11  | 0.07 | -0.26 | 0.25  | 0.51 | 0.11 | 0.03 |  |
| 10        | 0  | -0.07 | 0.58 | -0.49 | 0.38  | 0.57 | 0.27 | 0.21 |  |
| 20        | 0  | 0.02  | 0.42 | -0.44 | 0.48  | 0.75 | 0.47 | 0.43 |  |
| 30        | 0  | 0.15  | 0.02 | -0.02 | 0.08  | 1.00 | 0.62 | 0.71 |  |
| 40        | 0  | 0.11  | 0.11 | 0.13  | -0.11 | 1.44 | 0.78 | 0.84 |  |
| 50        | 0  | 0.09  | 0.33 | 0.01  | -0.02 | 2.06 | 0.88 | 0.85 |  |
| 60        | 0  | 0.23  | 0.17 | 0.46  | 1.02  | 2.42 | 0.98 | 0.90 |  |
| 70        | 0  | 0.34  | 1.07 | 1.41  | 3.99  | 2.58 | 1.07 | 0.91 |  |
| 80        | 0  | 3.00  | 4.37 | 2.94  | 3.46  | 2.34 | 1.10 | 0.98 |  |
| 90        | 0  | 3.36  | 5.54 | 1.76  | 2.28  | 2.85 | 1.35 | 1.01 |  |
| 100       | 0  | 3.57  | 6.00 | 1.51  | 1.94  | 3.30 | 1.57 | 1.08 |  |
| 109       | 0  | 3.71  | 6.38 | 1.02  | 1.33  | 3.84 | 2.00 | 1.27 |  |

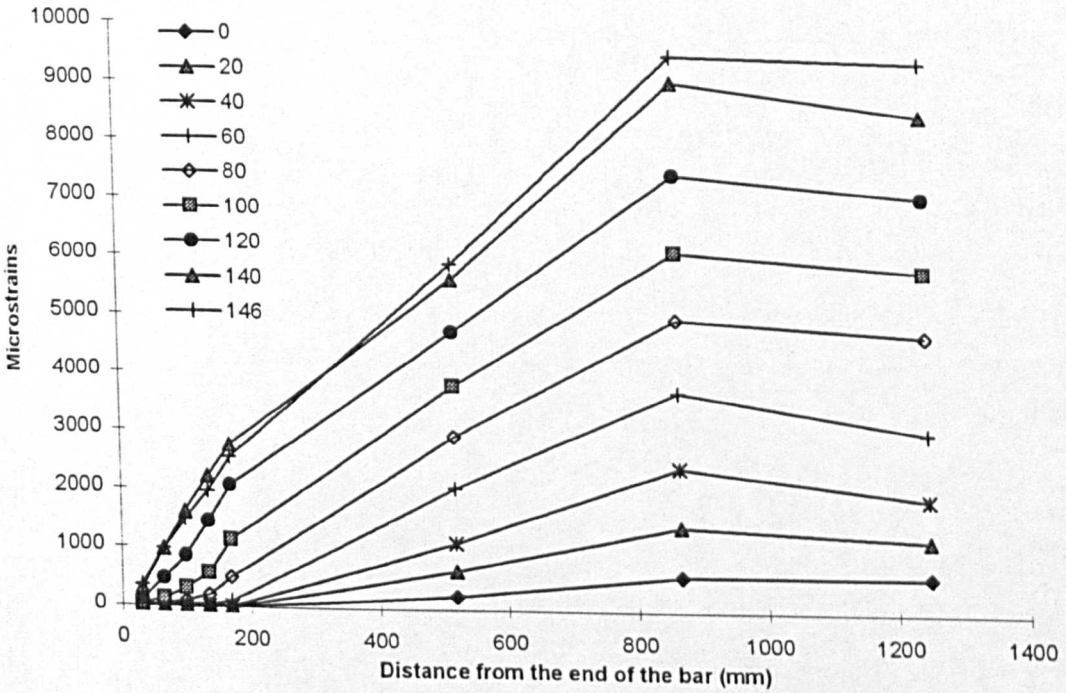


## E.2 Test results of Phase 1-3 beams

### BEAM CB20

#### Normal strains on the main reinforcing bar

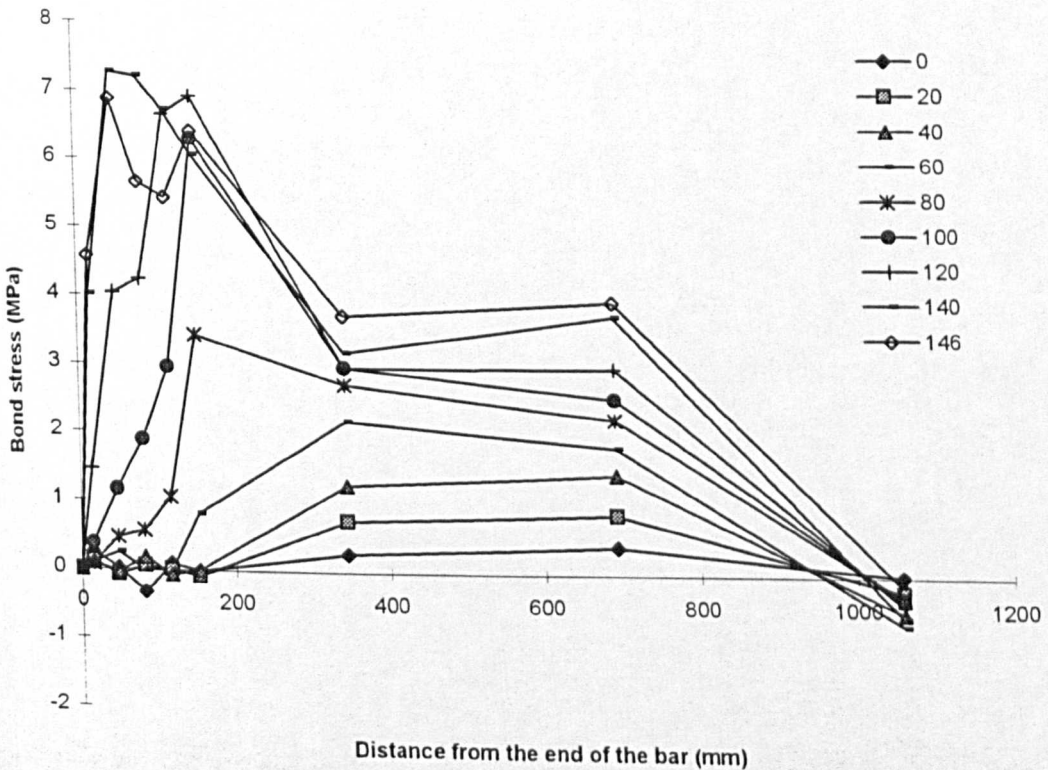
| Load (kN) | Microstrains ( <i>Distance from the end of the bar, mm</i> ) |     |      |      |      |      |      |      |
|-----------|--|-----|------|------|------|------|------|------|
|           | 30   | 65  | 100  | 135  | 170  | 519  | 867  | 1250 |
| 0         | 19   | 20  | -9   | -1   | -2   | 229  | 589  | 606  |
| 10        | 24   | 22  | -6   | 9    | 6    | 390  | 835  | 777  |
| 20        | 9  | 2   | 7    | 8    | -1   | 659  | 1433 | 1226 |
| 30        | 12   | 23  | 2    | 1    | 23   | 879  | 1859 | 1528 |
| 40        | 7  | 3   | 19   | 13   | 13   | 1136 | 2426 | 1911 |
| 50        | 0  | 18  | 23   | 4    | 53   | 1557 | 3065 | 2443 |
| 60        | 8  | 29  | 29   | 29   | 102  | 2068 | 3716 | 3030 |
| 70        | -6   | 20  | 44   | 54   | 188  | 2531 | 4322 | 3975 |
| 80        | 6  | 47  | 99   | 194  | 503  | 2950 | 4967 | 4677 |
| 90        | 38   | 98  | 188  | 420  | 848  | 3345 | 5541 | 5243 |
| 100       | 29   | 134 | 304  | 571  | 1139 | 3814 | 6100 | 5770 |
| 110       | 76   | 252 | 507  | 957  | 1557 | 4253 | 6768 | 6409 |
| 120       | 112  | 476 | 857  | 1457 | 2080 | 4744 | 7429 | 7023 |
| 130       | 176  | 744 | 1307 | 1956 | 2580 | 5203 | 8166 | 7665 |
| 140       | 309  | 964 | 1614 | 2220 | 2766 | 5632 | 8997 | 8417 |
| 146       | 353  | 974 | 1483 | 1973 | 2551 | 5899 | 9447 | 9303 |



## BEAM CB20 (cont.)

### Bond stress on the main reinforcing bar

| Load (kN) | Average bond stress, MPa ( <i>Distance from the end of the bar, mm</i> ) |       |       |       |       |       |      |      |       |
|-----------|--|-------|-------|-------|-------|-------|------|------|-------|
|           | 0  | 15    | 48    | 83    | 118   | 153   | 345  | 693  | 1059  |
| 0         | 0  | 0.24  | 0.01  | -0.32 | 0.09  | -0.02 | 0.26 | 0.40 | 0.02  |
| 10        | 0  | 0.31  | -0.02 | -0.32 | 0.17  | -0.04 | 0.43 | 0.50 | -0.06 |
| 20        | 0  | 0.12  | -0.08 | 0.05  | 0.01  | -0.09 | 0.73 | 0.86 | -0.21 |
| 30        | 0  | 0.15  | 0.13  | -0.23 | -0.01 | 0.24  | 0.95 | 1.09 | -0.34 |
| 40        | 0  | 0.09  | -0.04 | 0.18  | -0.07 | 0.00  | 1.25 | 1.44 | -0.52 |
| 50        | 0  | 0.00  | 0.20  | 0.05  | -0.22 | 0.55  | 1.67 | 1.68 | -0.63 |
| 60        | 0  | 0.10  | 0.24  | 0.00  | 0.00  | 0.81  | 2.19 | 1.84 | -0.69 |
| 70        | 0  | -0.08 | 0.29  | 0.27  | 0.11  | 1.49  | 2.61 | 2.00 | -0.35 |
| 80        | 0  | 0.08  | 0.46  | 0.57  | 1.06  | 3.43  | 2.73 | 2.25 | -0.29 |
| 90        | 0  | 0.49  | 0.67  | 1.00  | 2.56  | 4.75  | 2.78 | 2.45 | -0.30 |
| 100       | 0  | 0.38  | 1.16  | 1.89  | 2.96  | 6.30  | 2.98 | 2.55 | -0.33 |
| 110       | 0  | 0.99  | 1.94  | 2.83  | 4.99  | 6.65  | 3.00 | 2.80 | -0.36 |
| 120       | 0  | 1.45  | 4.04  | 4.23  | 6.65  | 6.91  | 2.97 | 2.99 | -0.41 |
| 130       | 0  | 2.28  | 6.29  | 6.24  | 7.20  | 6.92  | 2.92 | 3.30 | -0.51 |
| 140       | 0  | 4.00  | 7.26  | 7.20  | 6.72  | 6.06  | 3.19 | 3.75 | -0.59 |
| 146       | 0  | 4.57  | 6.88  | 5.65  | 5.43  | 6.40  | 3.73 | 3.95 | -0.15 |

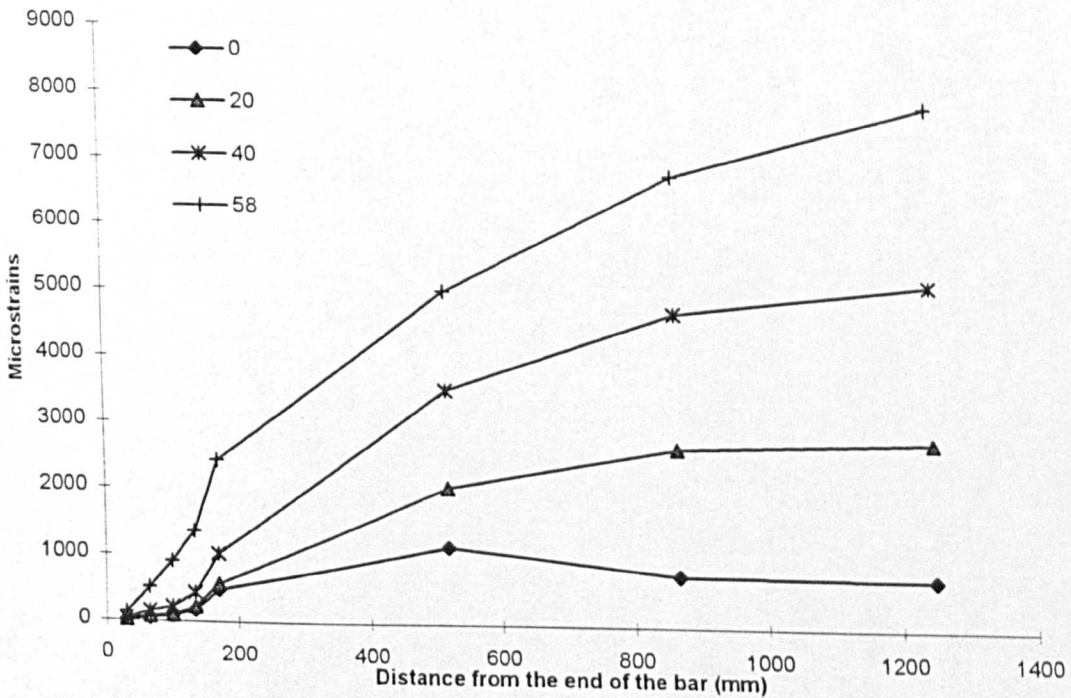


## E.2 Test results of Phase 1-3 beams

### BEAM CGB21

#### Normal strains on the main reinforcing bar

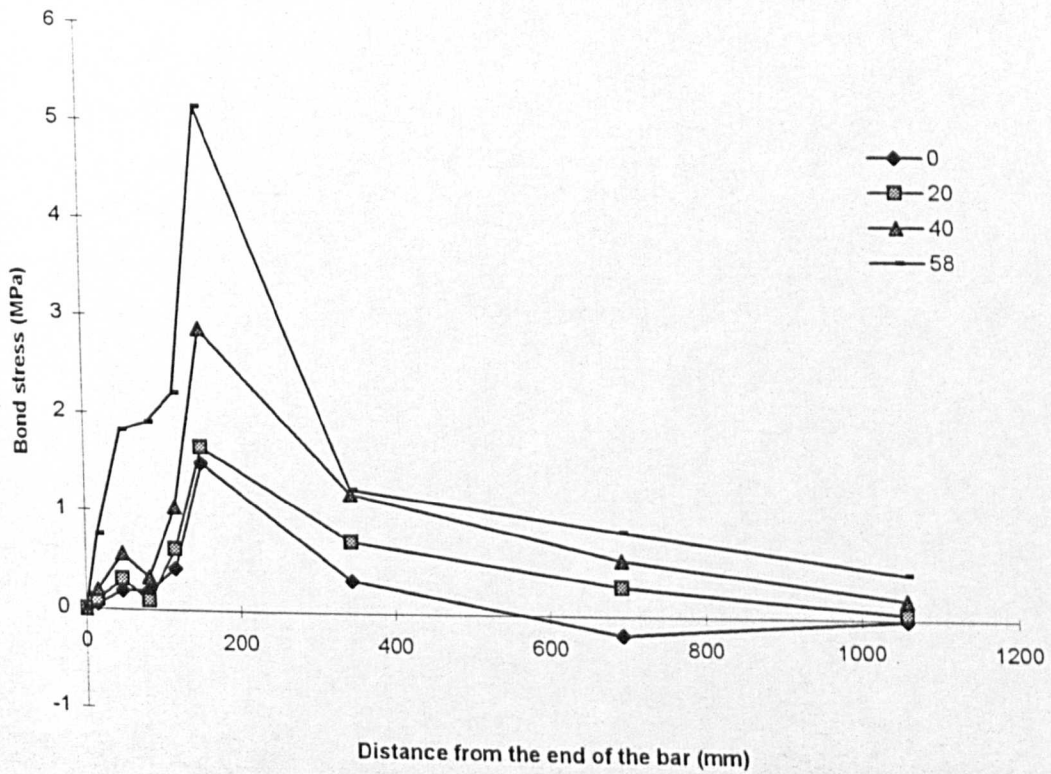
| Load (kN) | Microstrains ( <i>Distance from the end of the bar, mm</i> ) |     |     |      |      |      |      |      |
|-----------|--|-----|-----|------|------|------|------|------|
|           | 30   | 65  | 100 | 135  | 170  | 519  | 867  | 1250 |
| 0         | 9  | 47  | 88  | 175  | 484  | 1157 | 765  | 740  |
| 10        | 20   | 82  | 83  | 194  | 507  | 1442 | 1619 | 1664 |
| 20        | 16   | 80  | 99  | 225  | 569  | 2056 | 2655 | 2771 |
| 30        | 14   | 93  | 126 | 249  | 649  | 2672 | 3644 | 3899 |
| 40        | 34   | 151 | 218 | 434  | 1029 | 3518 | 4681 | 5114 |
| 50        | 60   | 298 | 500 | 857  | 1728 | 4580 | 5818 | 6521 |
| 58        | 135  | 513 | 909 | 1367 | 2431 | 5010 | 6748 | 7772 |



## BEAM CGB21 (cont.)

### Bond stress on the main reinforcing bar

| Load (kN) | Average bond stress, MPa ( <i>Distance from the end of the bar, mm</i> ) |      |      |      |      |      |      |       |       |
|-----------|--|------|------|------|------|------|------|-------|-------|
|           | 0  | 15   | 48   | 83   | 118  | 153  | 345  | 693   | 1059  |
| 0         | 0  | 0.05 | 0.19 | 0.19 | 0.42 | 1.49 | 0.33 | -0.19 | -0.01 |
| 10        | 0  | 0.11 | 0.30 | 0.00 | 0.54 | 1.51 | 0.45 | 0.09  | 0.02  |
| 20        | 0  | 0.09 | 0.31 | 0.09 | 0.61 | 1.66 | 0.72 | 0.29  | 0.05  |
| 30        | 0  | 0.08 | 0.38 | 0.16 | 0.59 | 1.93 | 0.98 | 0.47  | 0.11  |
| 40        | 0  | 0.19 | 0.56 | 0.32 | 1.04 | 2.87 | 1.21 | 0.56  | 0.19  |
| 50        | 0  | 0.34 | 1.15 | 0.97 | 1.72 | 4.20 | 1.38 | 0.60  | 0.31  |
| 58        | 0  | 0.76 | 1.82 | 1.91 | 2.21 | 5.13 | 1.25 | 0.84  | 0.45  |

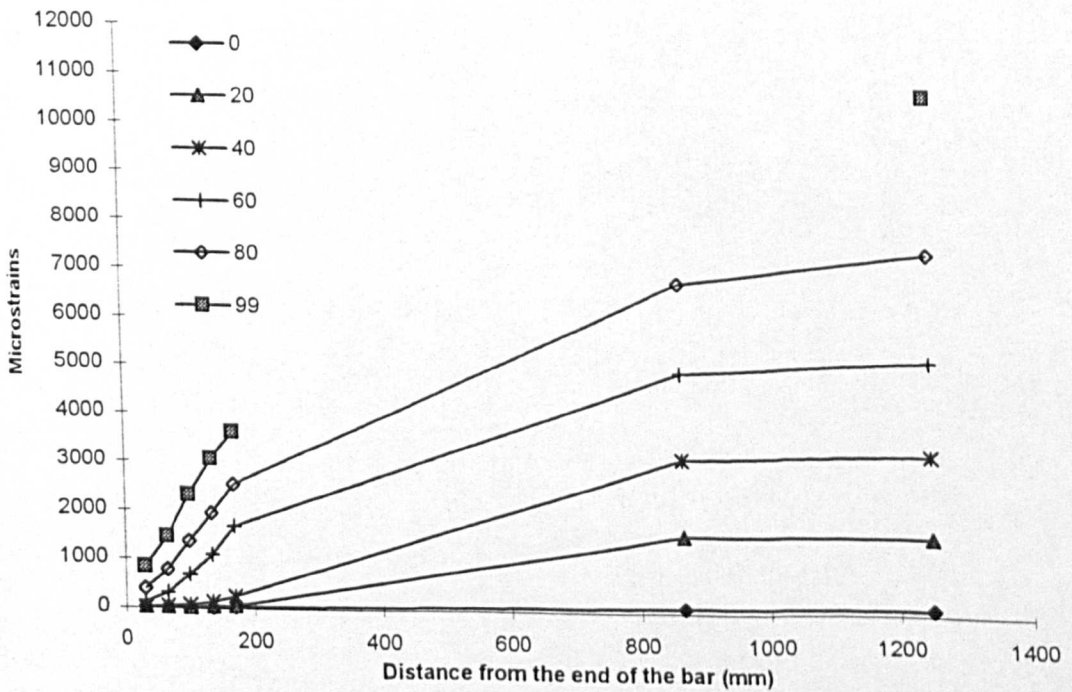


## E.2 Test results of Phase 1-3 beams

### BEAM CGB22

#### Normal strains on the main reinforcing bar

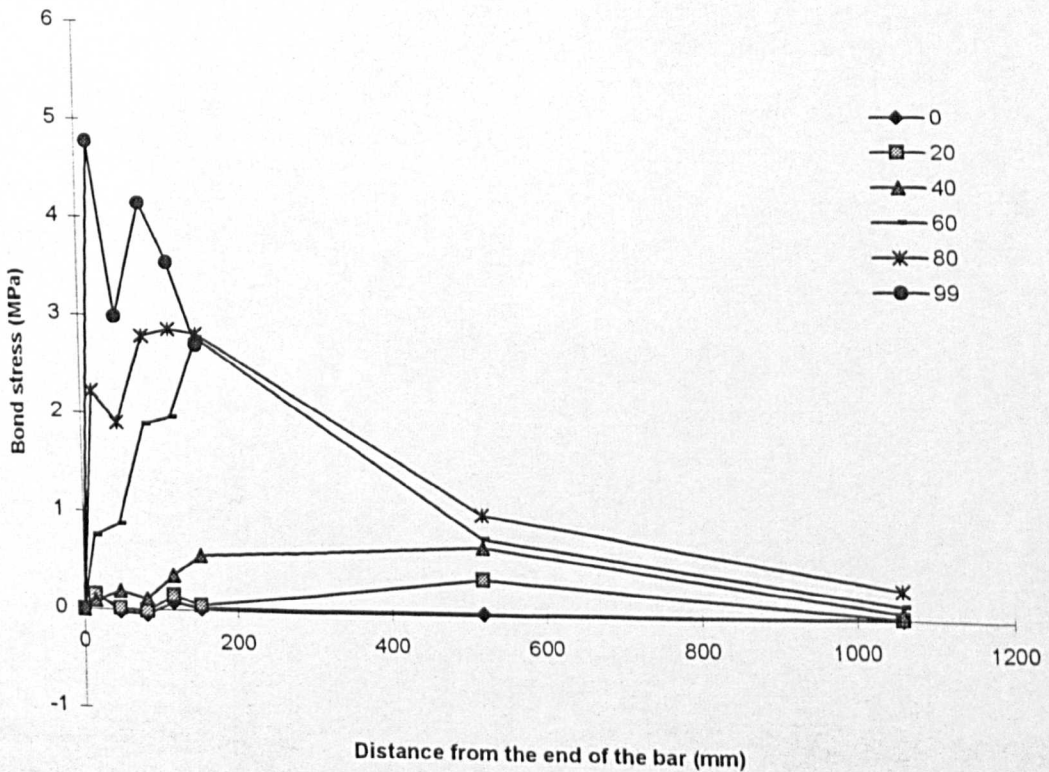
| Load (kN) | Microstrains ( <i>Distance from the end of the bar, mm</i> ) |      |      |      |      |      |       |
|-----------|--|------|------|------|------|------|-------|
|           | 30   | 65   | 100  | 135  | 170  | 867  | 1250  |
| 0         | 29   | 24   | 14   | 30   | 34   | 101  | 113   |
| 10        | 27   | 30   | 14   | 45   | 47   | 780  | 759   |
| 20        | 26   | 28   | 24   | 55   | 65   | 1569 | 1590  |
| 30        | 25   | 31   | 37   | 66   | 82   | 2279 | 2331  |
| 40        | 16   | 54   | 77   | 151  | 267  | 3128 | 3263  |
| 50        | 36   | 104  | 291  | 510  | 917  | 3989 | 4205  |
| 60        | 134  | 315  | 706  | 1112 | 1687 | 4894 | 5195  |
| 70        | 247  | 560  | 1035 | 1545 | 2161 | 5784 | 6227  |
| 80        | 395  | 789  | 1367 | 1960 | 2543 | 6749 | 7418  |
| 90        | 588  | 1108 | 1811 | 2450 | 3072 | 7748 | 9040  |
| 99        | 849  | 1469 | 2328 | 3062 | 3622 |      | 10626 |



## BEAM CGB22 (cont.)

### Bond stress on the main reinforcing bar

| Load (kN) | Average bond stress, MPa ( <i>Distance from the end of the bar, mm</i> ) |      |       |       |      |      |      |       |
|-----------|--|------|-------|-------|------|------|------|-------|
|           | 0  | 15   | 48    | 83    | 118  | 153  | 519  | 1059  |
| 0         | 0  | 0.16 | -0.02 | -0.05 | 0.08 | 0.02 | 0.02 | 0.01  |
| 10        | 0  | 0.15 | 0.01  | -0.08 | 0.15 | 0.01 | 0.18 | -0.01 |
| 20        | 0  | 0.15 | 0.01  | -0.02 | 0.15 | 0.05 | 0.36 | 0.01  |
| 30        | 0  | 0.14 | 0.03  | 0.03  | 0.14 | 0.08 | 0.53 | 0.02  |
| 40        | 0  | 0.09 | 0.18  | 0.11  | 0.35 | 0.56 | 0.69 | 0.06  |
| 50        | 0  | 0.20 | 0.33  | 0.90  | 1.06 | 1.96 | 0.74 | 0.10  |
| 60        | 0  | 0.75 | 0.87  | 1.89  | 1.96 | 2.77 | 0.78 | 0.13  |
| 70        | 0  | 1.39 | 1.51  | 2.29  | 2.46 | 2.97 | 0.88 | 0.20  |
| 80        | 0  | 2.22 | 1.90  | 2.79  | 2.86 | 2.81 | 1.02 | 0.29  |
| 90        | 0  | 3.31 | 2.50  | 3.39  | 3.08 | 3.00 | 1.13 | 0.57  |
| 99        | 0  | 4.78 | 2.99  | 4.14  | 3.54 | 2.70 | .    |       |

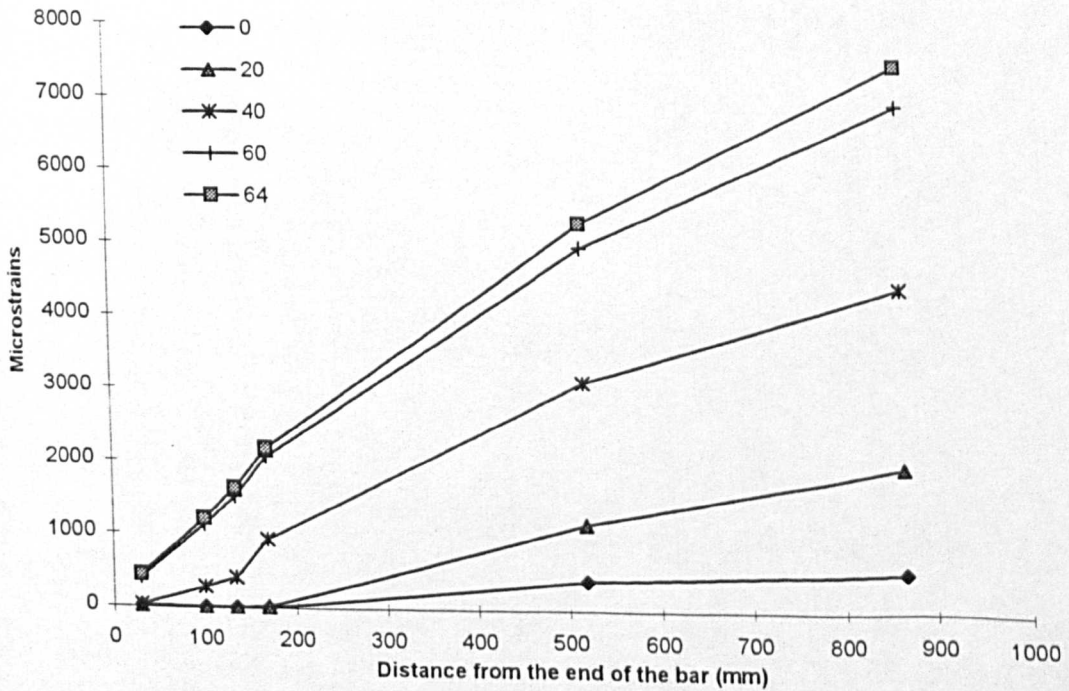


## E.2 Test results of Phase 1-3 beams

### BEAM AB23

#### Normal strains on the main reinforcing bar

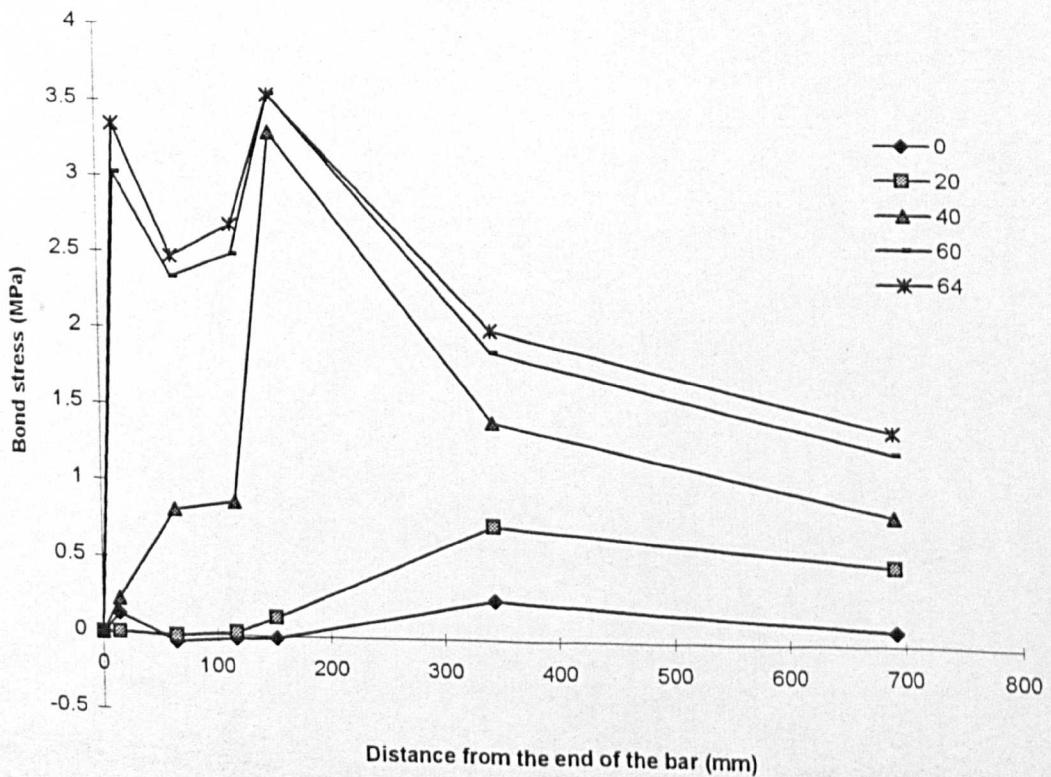
| Load (kN) | Microstrains ( <i>Distance from the end of the bar, mm</i> ) |      |      |      |      |      |
|-----------|--|------|------|------|------|------|
|           | 30   | 100  | 135  | 170  | 519  | 867  |
| 0         | 17   | 3    | 0    | -1   | 401  | 538  |
| 10        | -13  | -14  | 0    | 0    | 746  | 1162 |
| 20        | 1  | -3   | 0    | 19   | 1168 | 1954 |
| 30        | -1   | 22   | 0    | 58   | 2175 | 3282 |
| 40        | 30   | 282  | 417  | 929  | 3118 | 4401 |
| 50        | 226  | 795  | 1096 | 1708 | 4239 | 5736 |
| 60        | 401  | 1125 | 1511 | 2062 | 4956 | 6870 |
| 64        | 443  | 1209 | 1625 | 2174 | 5291 | 7419 |



## BEAM AB23 (cont.)

### Bond stress on the main reinforcing bar

| Load (kN) | Average bond stress, MPa ( <i>Distance from the end of the bar, mm</i> ) |       |       |       |       |      |      |
|-----------|--|-------|-------|-------|-------|------|------|
|           | 0  | 15    | 65    | 118   | 153   | 344  | 693  |
| 0         | 0  | 0.13  | -0.05 | -0.02 | -0.01 | 0.26 | 0.09 |
| 10        | 0  | -0.10 | 0.00  | 0.09  | 0.00  | 0.48 | 0.27 |
| 20        | 0  | 0.01  | -0.01 | 0.02  | 0.12  | 0.75 | 0.51 |
| 30        | 0  | -0.01 | 0.07  | -0.14 | 0.37  | 1.37 | 0.72 |
| 40        | 0  | 0.22  | 0.81  | 0.88  | 3.31  | 1.42 | 0.83 |
| 50        | 0  | 1.71  | 1.84  | 1.95  | 3.95  | 1.64 | 0.97 |
| 60        | 0  | 3.02  | 2.34  | 2.50  | 3.56  | 1.88 | 1.24 |
| 64        | 0  | 3.34  | 2.47  | 2.69  | 3.55  | 2.02 | 1.38 |

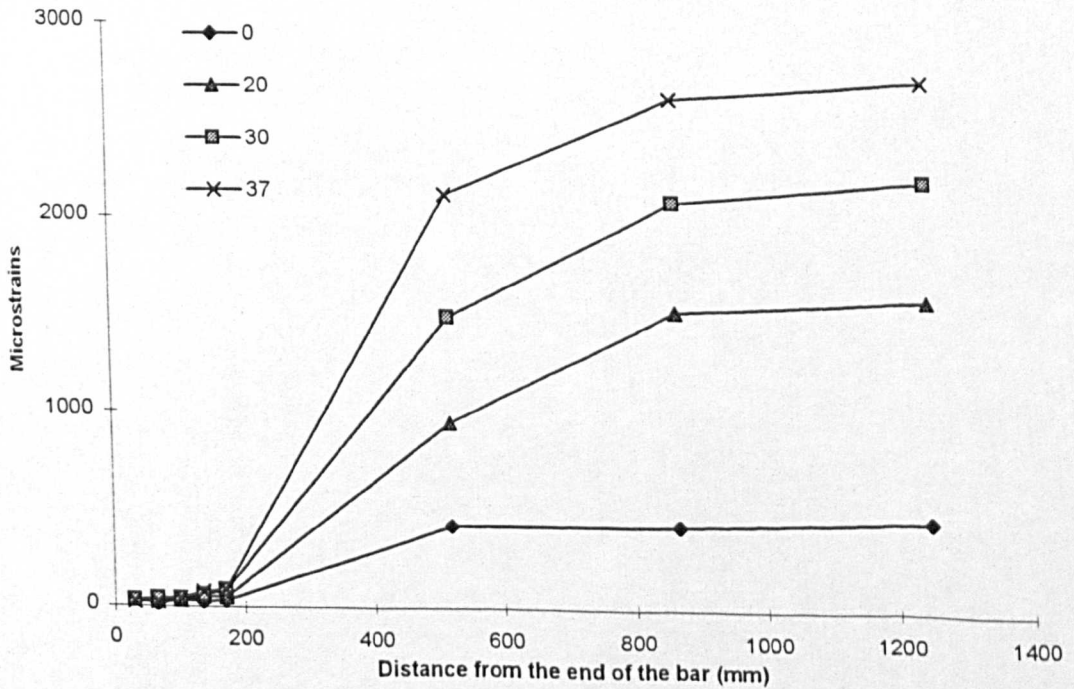


## E.2 Test results of Phase 1-3 beams

### BEAM AB24

#### Normal strains on the main reinforcing bar

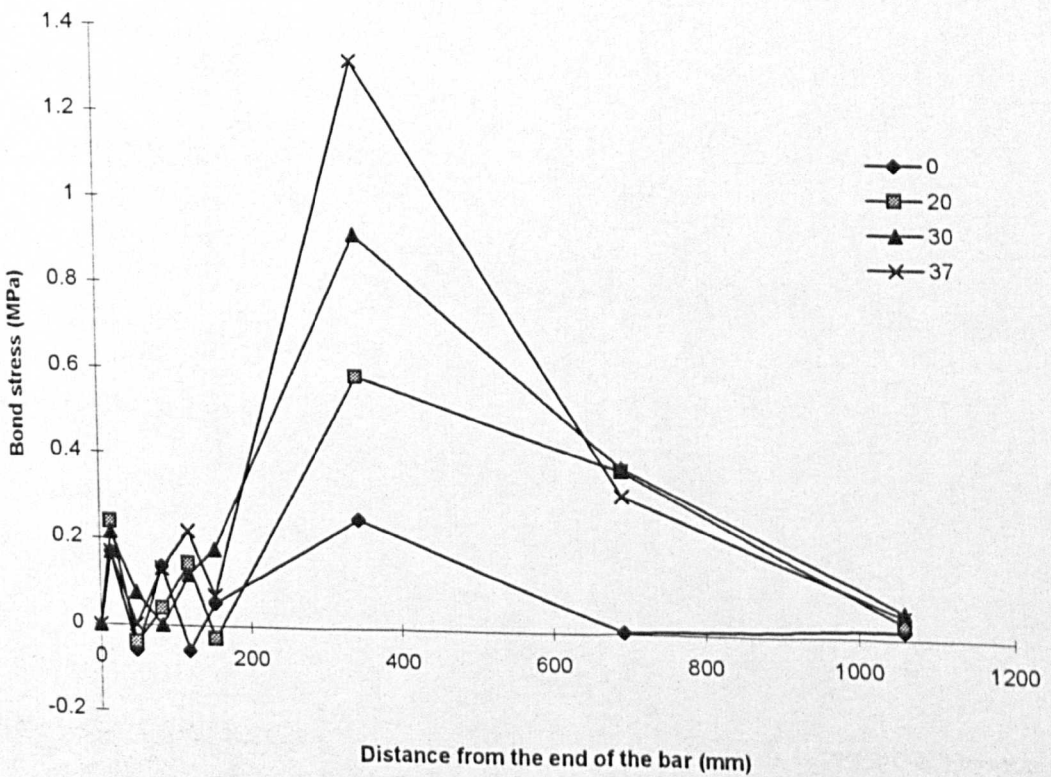
| Load (kN) | Microstrains ( <i>Distance from the end of the bar, mm</i> ) |    |     |     |     |      |      |      |
|-----------|--|----|-----|-----|-----|------|------|------|
|           | 30   | 65 | 100 | 135 | 170 | 519  | 867  | 1250 |
| 0         | 22   | 13 | 35  | 26  | 34  | 423  | 430  | 462  |
| 10        | 24   | 33 | 25  | 31  | 52  | 613  | 859  | 900  |
| 20        | 32   | 25 | 32  | 54  | 49  | 953  | 1533 | 1591 |
| 30        | 29   | 40 | 40  | 59  | 86  | 1499 | 2089 | 2195 |
| 37        | 22   | 22 | 43  | 77  | 88  | 2125 | 2617 | 2702 |



## BEAM AB24 (cont.)

### Bond stress on the main reinforcing bar

| Load (kN) | Average bond stress, MPa ( <i>Distance from the end of the bar, mm</i> ) |        |       |       |       |       |      |      |      |
|-----------|--|--------|-------|-------|-------|-------|------|------|------|
|           | 0  | 15     | 48    | 83    | 118   | 153   | 344  | 693  | 1059 |
| 0         | 0  | 0.1694 | -0.06 | 0.14  | -0.06 | 0.05  | 0.25 | 0.00 | 0.02 |
| 10        | 0  | 0.1788 | 0.06  | -0.05 | 0.04  | 0.14  | 0.36 | 0.16 | 0.02 |
| 20        | 0  | 0.2388 | -0.04 | 0.04  | 0.15  | -0.03 | 0.59 | 0.38 | 0.03 |
| 30        | 0  | 0.2154 | 0.08  | 0.00  | 0.12  | 0.18  | 0.92 | 0.38 | 0.06 |
| 37        | 0  | 0.1687 | 0.00  | 0.13  | 0.22  | 0.07  | 1.32 | 0.32 | 0.05 |

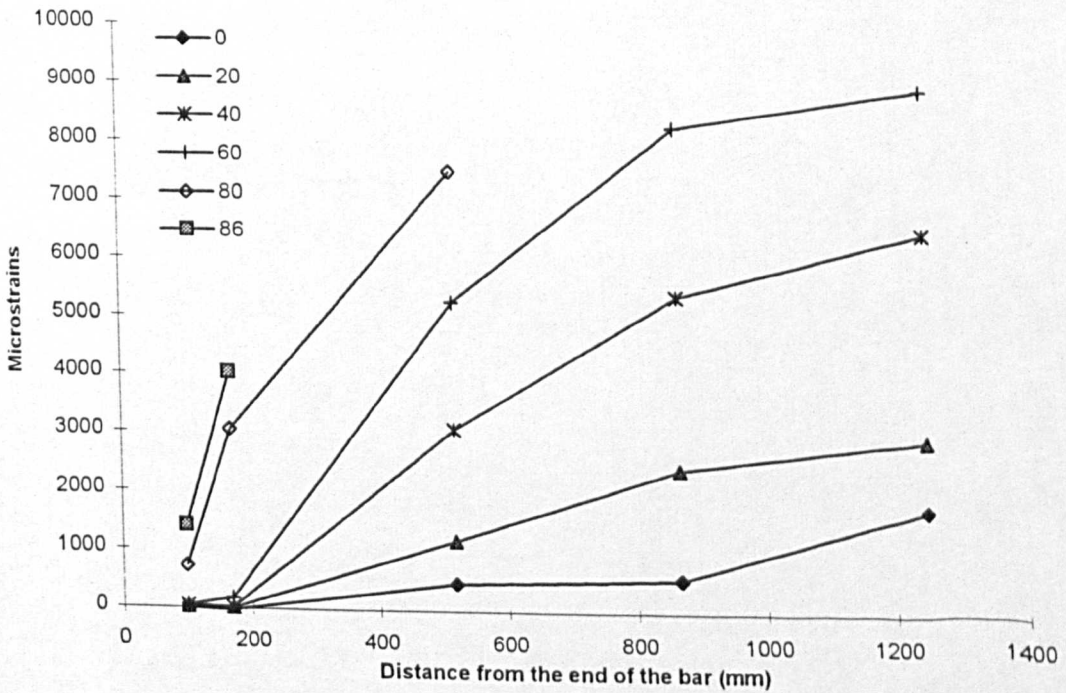


## E.2 Test results of Phase 1-3 beams

### BEAM CB25

#### Normal strains on the main reinforcing bar

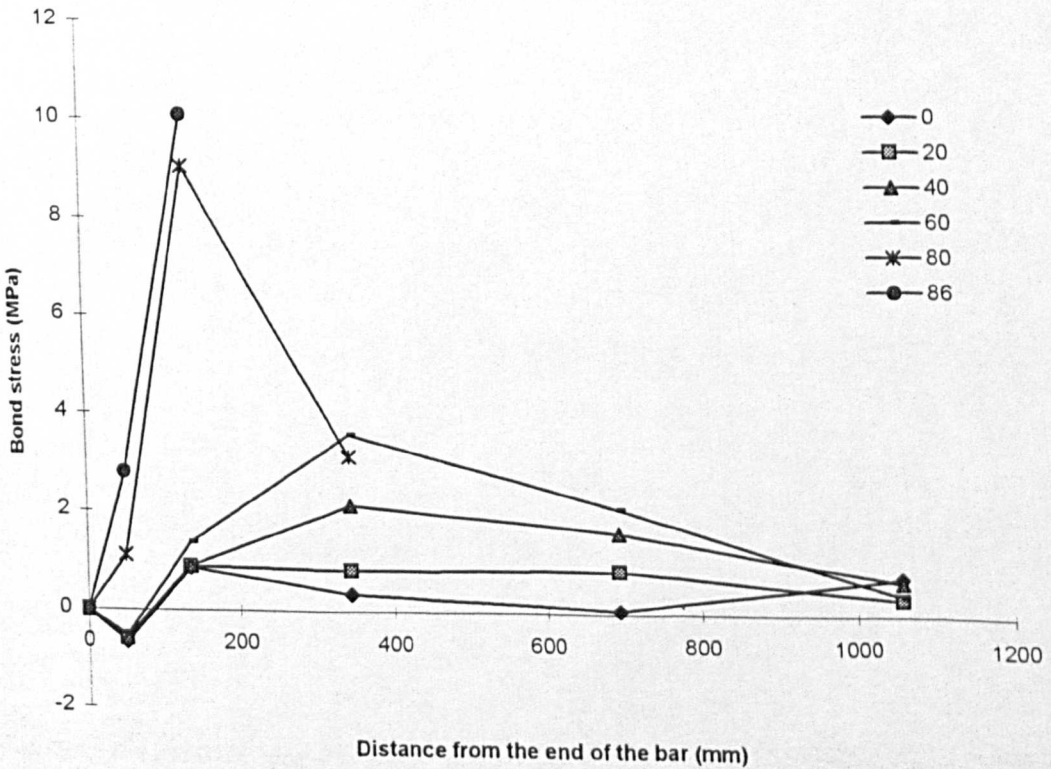
| Load (kN) | Microstrains ( <i>Distance from the end of the bar, mm</i> ) |      |       |      |       |
|-----------|--|------|-------|------|-------|
|           | 100  | 170  | 518.5 | 867  | 1250  |
| 0         | 0  | -24  | 470   | 572  | 1759  |
| 10        | 2  | -15  | 771   | 1348 | 2191  |
| 20        | 28   | 9    | 1195  | 2440 | 2937  |
| 30        | 41   | 4    | 1935  | 3730 | 4719  |
| 40        | 39   | 27   | 3088  | 5417 | 6469  |
| 50        | 16   | 11   | 4206  | 6859 | 7956  |
| 60        | 54   | 176  | 5278  | 8288 | 8908  |
| 70        | 107  | 1233 | 6336  | 9312 | 11844 |
| 80        | 726  | 3043 | 7517  |      |       |
| 86        | 1412   | 4029 |       |      |       |



## BEAM CB25 (cont.)

### Bond stress on the main reinforcing bar

| Load (kN) | Average bond stress, MPa ( <i>Distance from the end of the bar, mm</i> ) |       |       |      |      |      |
|-----------|--|-------|-------|------|------|------|
|           | 0  | 50    | 135   | 344  | 693  | 1059 |
| 0         | 0  | -0.66 | 0.86  | 0.35 | 0.07 | 0.76 |
| 10        | 0  | -0.66 | 0.89  | 0.55 | 0.41 | 0.54 |
| 20        | 0  | -0.59 | 0.88  | 0.83 | 0.87 | 0.32 |
| 30        | 0  | -0.56 | 0.82  | 1.35 | 1.26 | 0.63 |
| 40        | 0  | -0.57 | 0.91  | 2.14 | 1.64 | 0.67 |
| 50        | 0  | -0.62 | 0.93  | 2.94 | 1.86 | 0.70 |
| 60        | 0  | -0.53 | 1.37  | 3.57 | 2.11 | 0.40 |
| 70        | 0  | -0.40 | 4.88  | 3.57 | 2.09 | 1.62 |
| 80        | 0  | 1.11  | 9.04  | 3.13 |      |      |
| 86        | 0  | 2.79  | 10.08 |      |      |      |

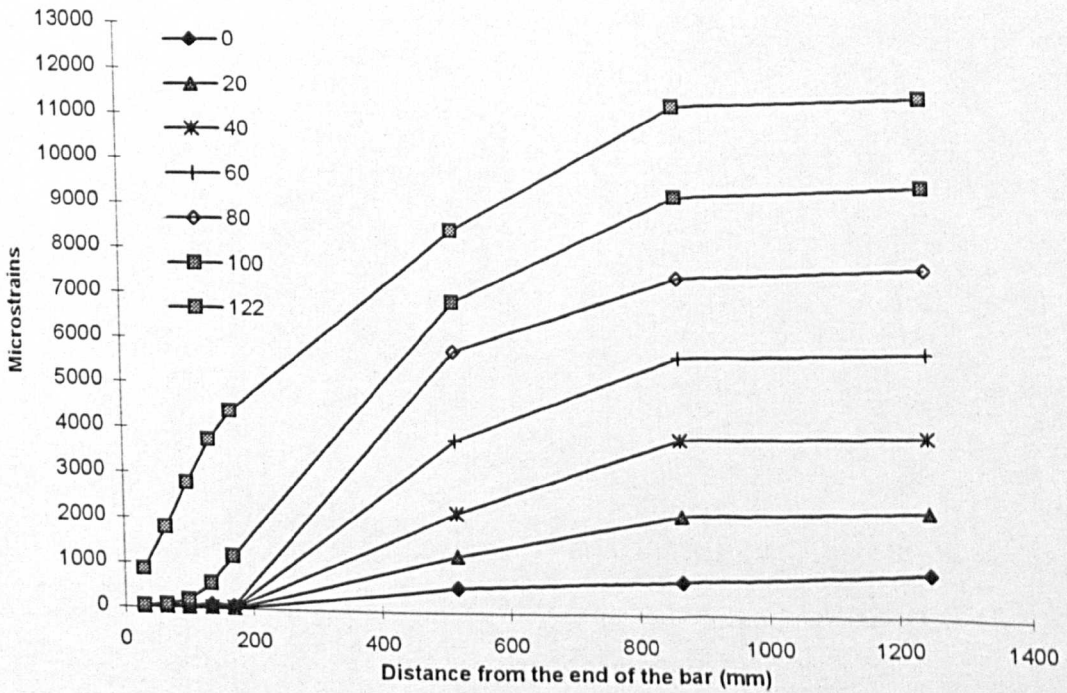


## E.2 Test results of Phase 1-3 beams

### BEAM CB26

#### Normal strains on the main reinforcing bar

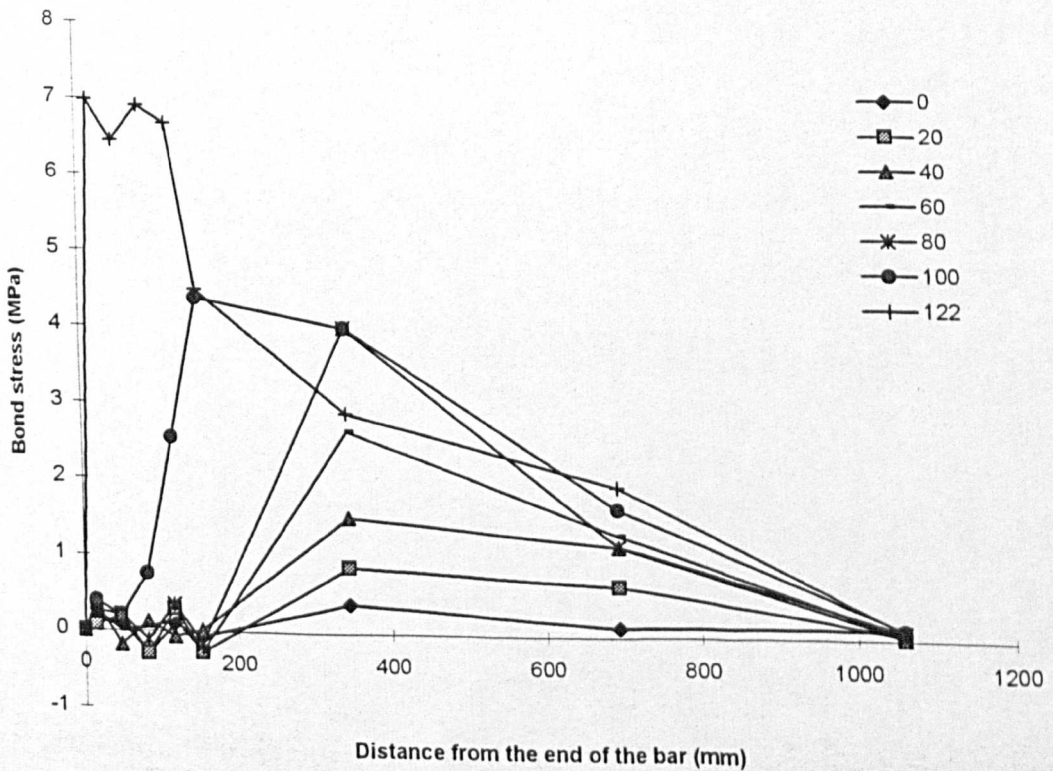
| Load (kN) | Microstrains ( <i>Distance from the end of the bar, mm</i> ) |      |      |      |      |      |       |       |
|-----------|--|------|------|------|------|------|-------|-------|
|           | 30   | 65   | 100  | 135  | 170  | 519  | 867   | 1250  |
| 0         | 18   | 37   | -3   | 11   | 2    | 559  | 742   | 941   |
| 10        | 17   | 26   | 2    | 34   | -9   | 861  | 1379  | 1480  |
| 20        | 10   | 40   | -1   | 41   | 3    | 1250 | 2200  | 2293  |
| 30        | 43   | 17   | 32   | 23   | 22   | 1658 | 3037  | 3089  |
| 40        | 44   | 20   | 38   | 29   | 31   | 2201 | 3886  | 3943  |
| 50        | 20   | 43   | 25   | 68   | 21   | 3024 | 4797  | 4884  |
| 60        | 33   | 35   | 42   | 64   | 28   | 3797 | 5709  | 5800  |
| 70        | 33   | 68   | 45   | 80   | 58   | 4992 | 6608  | 6746  |
| 80        | 32   | 64   | 49   | 100  | 79   | 5783 | 7488  | 7657  |
| 90        | 52   | 49   | 85   | 171  | 439  | 6317 | 8405  | 8585  |
| 100       | 49   | 78   | 187  | 551  | 1177 | 6881 | 9268  | 9471  |
| 110       | 79   | 323  | 860  | 1628 | 2519 | 7507 | 10245 | 10431 |
| 120       | 570  | 1463 | 2346 | 3333 | 4034 | 8229 | 11113 | 11298 |
| 122       | 857  | 1780 | 2769 | 3724 | 4366 | 8475 | 11276 | 11446 |



## BEAM CB26 (cont.)

### Bond stress on the main reinforcing bar

| Load (kN) | Average bond stress, MPa ( <i>Distance from the end of the bar, mm</i> ) |      |       |       |       |       |      |      |      |
|-----------|--|------|-------|-------|-------|-------|------|------|------|
|           | 0  | 15   | 48    | 83    | 118   | 153   | 345  | 693  | 1059 |
| 0         | 0  | 0.15 | 0.13  | -0.28 | 0.10  | -0.06 | 0.39 | 0.13 | 0.13 |
| 10        | 0  | 0.13 | 0.06  | -0.17 | 0.22  | -0.30 | 0.61 | 0.36 | 0.06 |
| 20        | 0  | 0.08 | 0.21  | -0.29 | 0.30  | -0.27 | 0.87 | 0.67 | 0.06 |
| 30        | 0  | 0.35 | -0.18 | 0.11  | -0.06 | -0.01 | 1.15 | 0.97 | 0.03 |
| 40        | 0  | 0.36 | -0.17 | 0.13  | -0.07 | 0.02  | 1.52 | 1.18 | 0.04 |
| 50        | 0  | 0.17 | 0.15  | -0.12 | 0.30  | -0.33 | 2.11 | 1.24 | 0.06 |
| 60        | 0  | 0.27 | 0.01  | 0.05  | 0.16  | -0.25 | 2.64 | 1.34 | 0.06 |
| 70        | 0  | 0.27 | 0.24  | -0.16 | 0.24  | -0.16 | 3.46 | 1.13 | 0.09 |
| 80        | 0  | 0.26 | 0.22  | -0.11 | 0.36  | -0.15 | 4.00 | 1.20 | 0.11 |
| 90        | 0  | 0.43 | -0.03 | 0.25  | 0.60  | 1.87  | 4.12 | 1.46 | 0.11 |
| 100       | 0  | 0.40 | 0.20  | 0.76  | 2.54  | 4.37  | 4.00 | 1.67 | 0.13 |
| 110       | 0  | 0.64 | 1.71  | 3.75  | 5.36  | 6.22  | 3.50 | 1.92 | 0.12 |
| 120       | 0  | 4.64 | 6.24  | 6.17  | 6.89  | 4.89  | 2.94 | 2.02 | 0.12 |
| 122       | 0  | 6.98 | 6.45  | 6.90  | 6.67  | 4.49  | 2.88 | 1.96 | 0.11 |

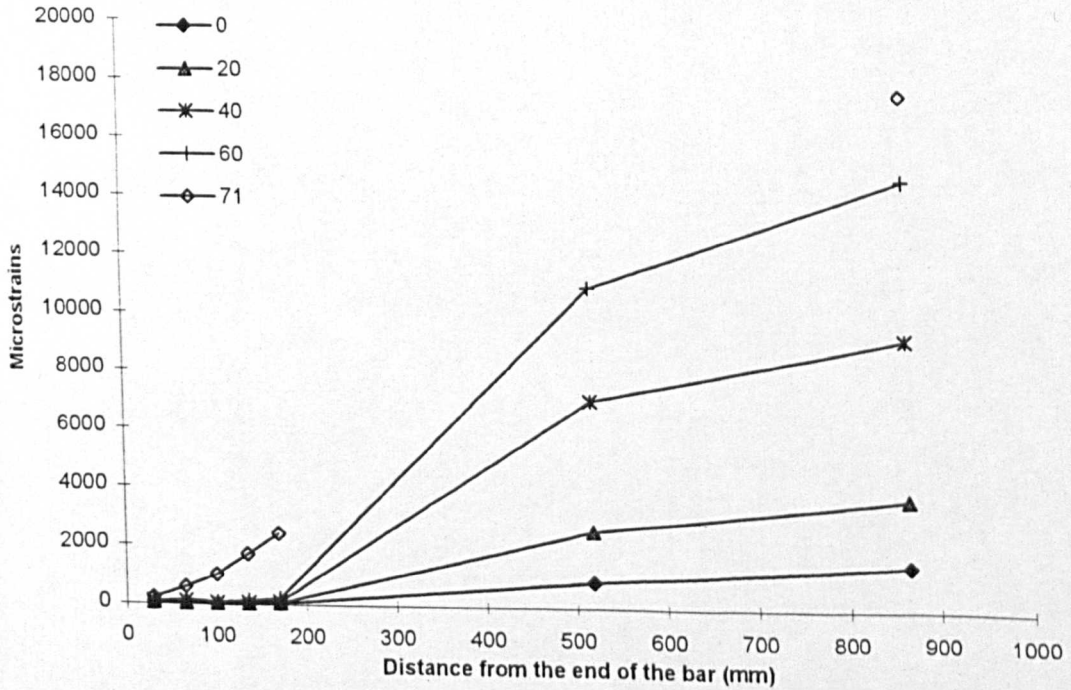


## E.2 Test results of Phase 1-3 beams

### BEAM AB27

#### Normal strains on the main reinforcing bar

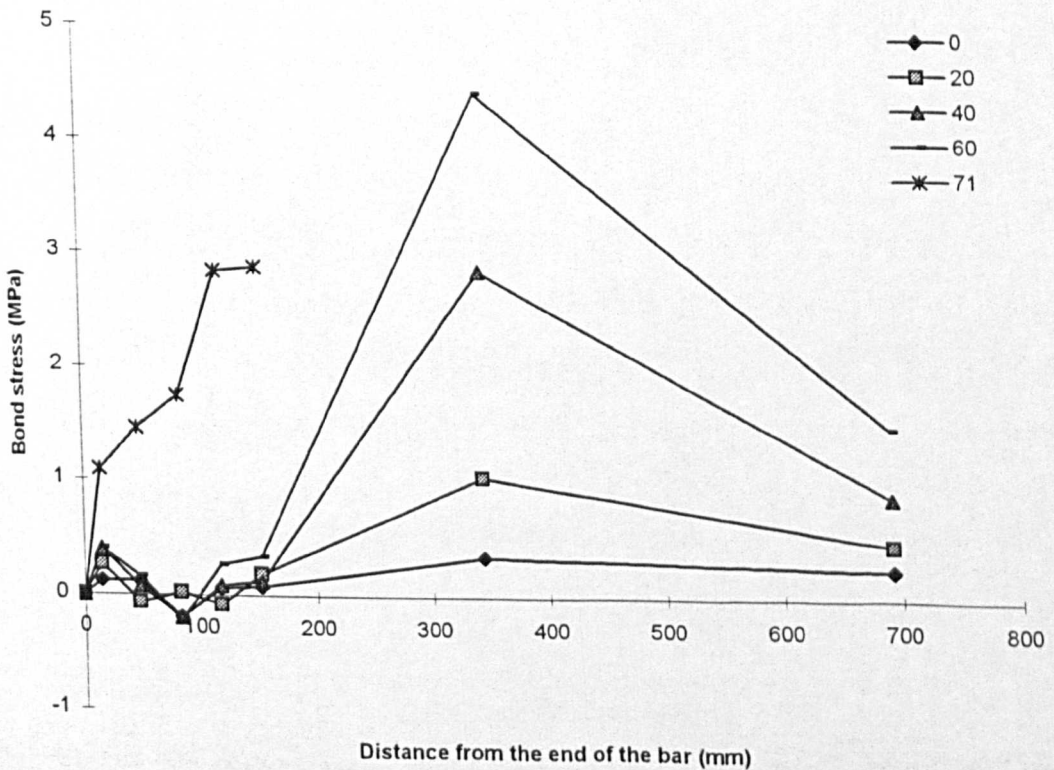
| Load (kN) | Microstrains ( <i>Distance from the end of the bar, mm</i> ) |     |      |      |      |       |       |
|-----------|--|-----|------|------|------|-------|-------|
|           | 30   | 65  | 100  | 135  | 170  | 519   | 867   |
| 0         | 26   | 56  | 9    | 24   | 44   | 897   | 1519  |
| 10        | 57   | 31  | 39   | 20   | 51   | 1577  | 2384  |
| 20        | 56   | 40  | 46   | 26   | 73   | 2615  | 3761  |
| 30        | 81   | 64  | 55   | 70   | 68   | 4478  | 6128  |
| 40        | 83   | 102 | 53   | 74   | 105  | 7079  | 9224  |
| 50        | 110  | 116 | 64   | 88   | 130  | 9282  | 12128 |
| 60        | 84   | 123 | 68   | 133  | 217  | 10981 | 14606 |
| 70        | 139  | 212 | 545  | 1028 | 1523 |       | 17110 |
| 71        | 230  | 588 | 1015 | 1713 | 2419 |       | 17517 |



## BEAM AB27 (cont.)

### Bond stress on the main reinforcing bar

| Load (kN) | Average bond stress, MPa ( <i>Distance from the end of the bar, mm</i> ) |      |       |       |       |       |      |      |
|-----------|--|------|-------|-------|-------|-------|------|------|
|           | 0  | 15   | 48    | 83    | 118   | 153   | 344  | 693  |
| 0         | 0  | 0.12 | 0.12  | -0.19 | 0.06  | 0.08  | 0.35 | 0.25 |
| 10        | 0  | 0.27 | -0.11 | 0.03  | -0.08 | 0.13  | 0.62 | 0.33 |
| 20        | 0  | 0.27 | -0.07 | 0.02  | -0.08 | 0.19  | 1.04 | 0.47 |
| 30        | 0  | 0.38 | -0.07 | -0.04 | 0.06  | -0.01 | 1.80 | 0.67 |
| 40        | 0  | 0.39 | 0.07  | -0.20 | 0.09  | 0.13  | 2.85 | 0.88 |
| 50        | 0  | 0.52 | 0.02  | -0.21 | 0.10  | 0.17  | 3.74 | 1.16 |
| 60        | 0  | 0.40 | 0.16  | -0.22 | 0.26  | 0.34  | 4.40 | 1.48 |
| 70        | 0  | 0.66 | 0.30  | 1.35  | 1.97  | 2.01  |      |      |
| 71        | 0  | 1.09 | 1.45  | 1.74  | 2.84  | 2.87  |      |      |

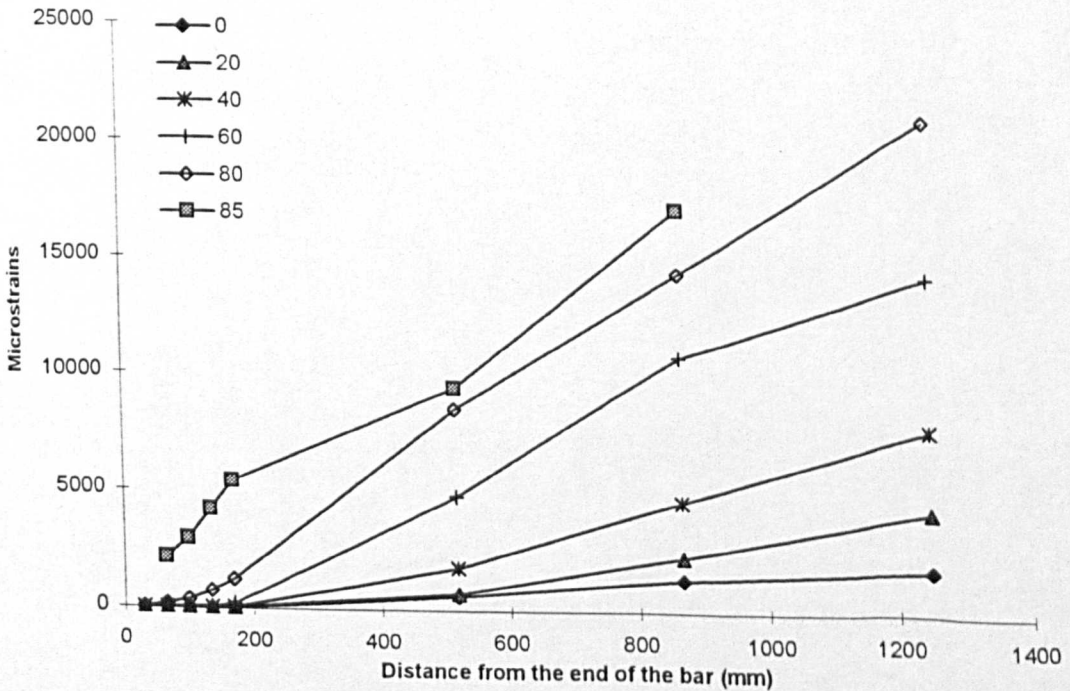


## E.2 Test results of Phase 1-3 beams

### BEAM AB28

#### Normal strains on the main reinforcing bar

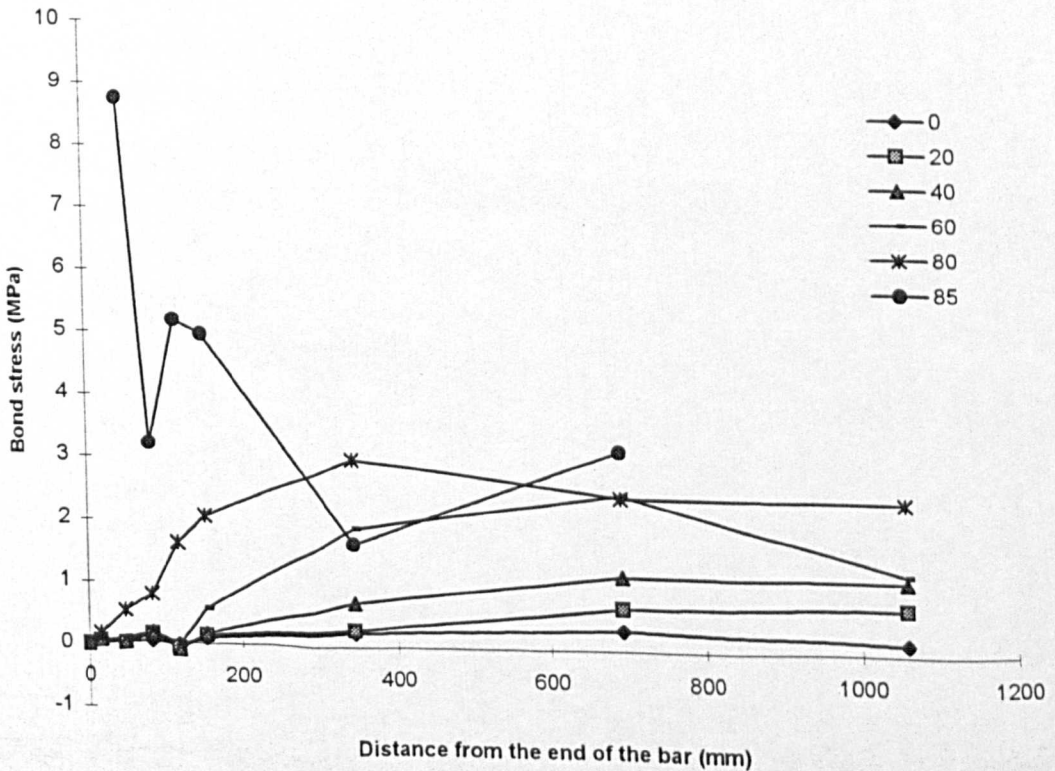
| Load (kN) | Microstrains ( <i>Distance from the end of the bar, mm</i> ) |      |      |      |      |      |       |       |
|-----------|--|------|------|------|------|------|-------|-------|
|           | 30   | 65   | 100  | 135  | 170  | 519  | 867   | 1250  |
| 0         | 13   | 14   | 18   | 9    | 31   | 595  | 1374  | 1841  |
| 10        | 25   | 28   | 12   | 25   | 36   | 610  | 1609  | 2666  |
| 20        | 10   | 8    | 38   | 15   | 48   | 707  | 2345  | 4288  |
| 30        | 19   | 28   | 27   | 20   | 54   | 852  | 3136  | 5899  |
| 40        | 12   | 13   | 51   | 23   | 62   | 1809 | 4674  | 7752  |
| 50        | 33   | 34   | 27   | 61   | 76   | 3163 | 8905  | 10359 |
| 60        | 12   | 25   | 64   | 55   | 194  | 4845 | 10856 | 14247 |
| 70        | 32   | 39   | 60   | 170  | 374  | 6348 | 12716 | 17079 |
| 80        | 37   | 163  | 350  | 743  | 1248 | 8556 | 14449 | 20889 |
| 85        |  | 2151 | 2930 | 4201 | 5421 | 9456 | 17158 |       |



## BEAM AB28 (cont.)

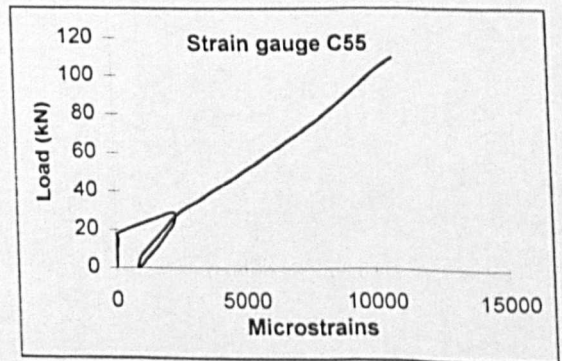
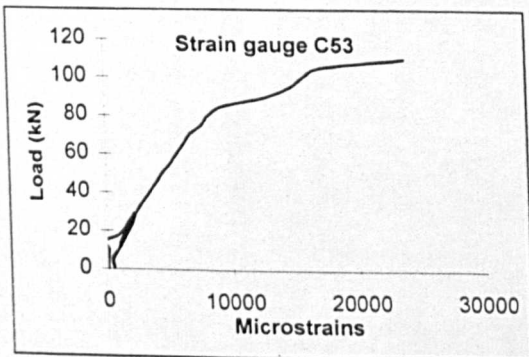
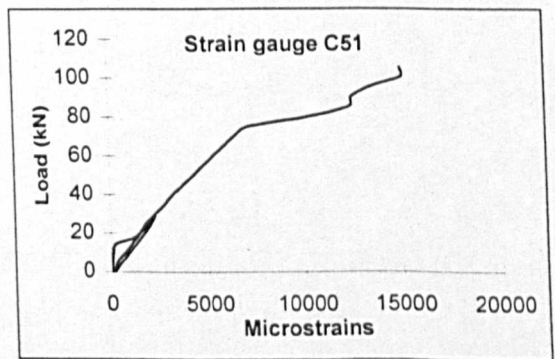
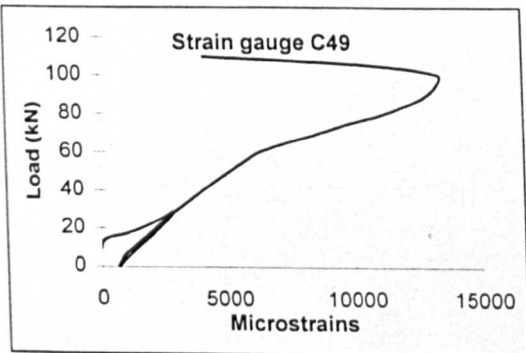
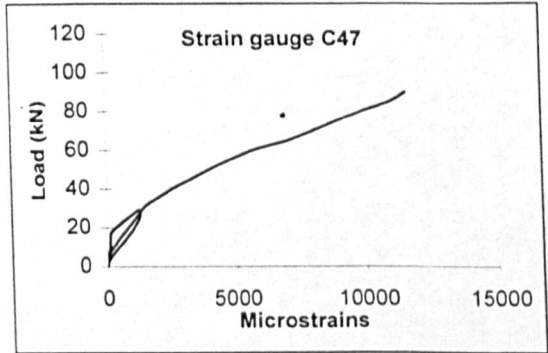
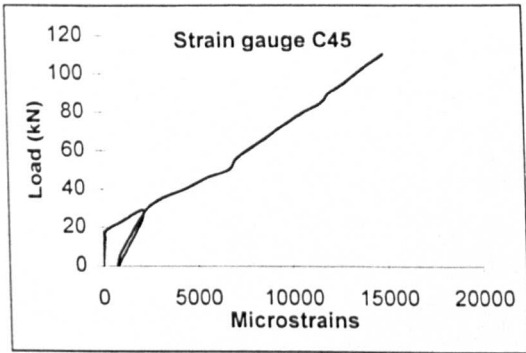
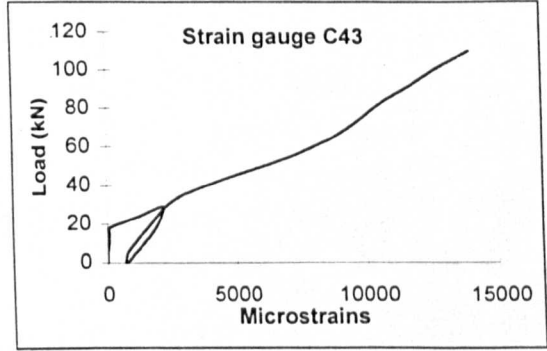
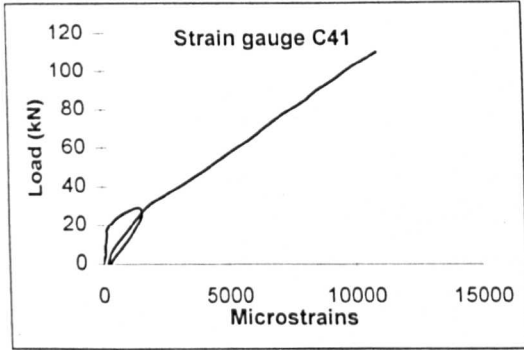
**Bond stress on the main reinforcing bar**

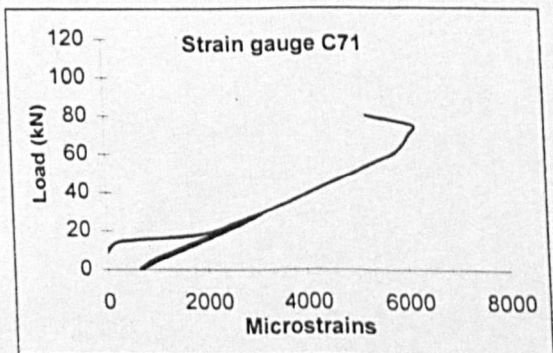
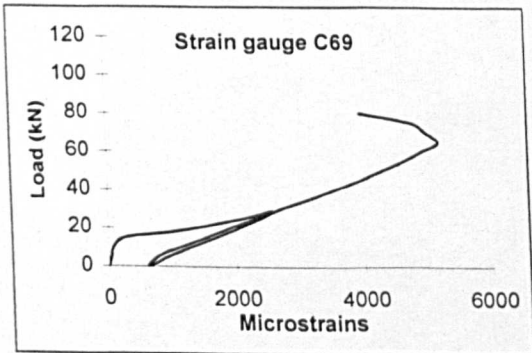
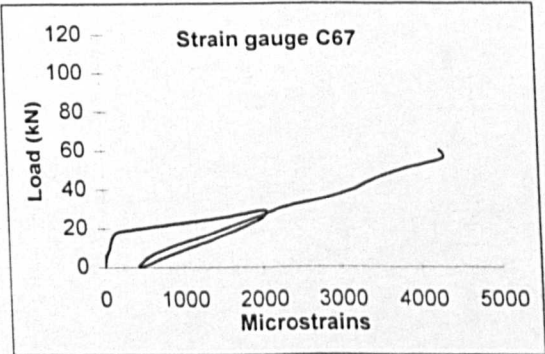
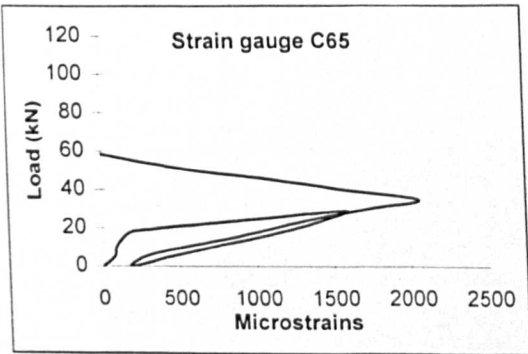
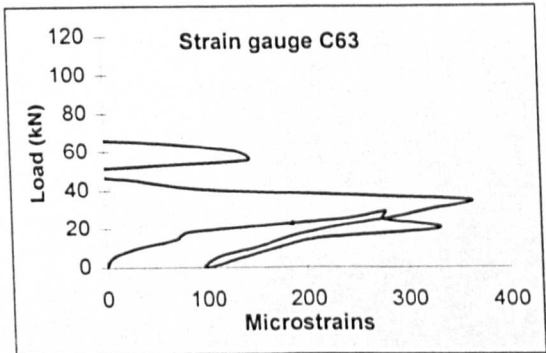
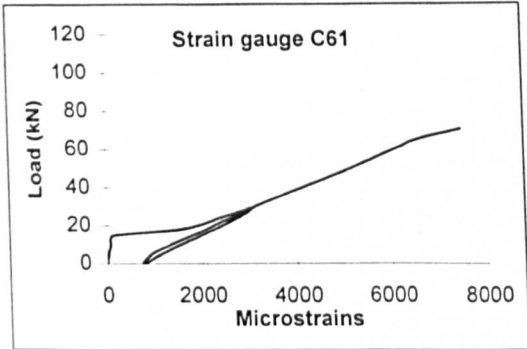
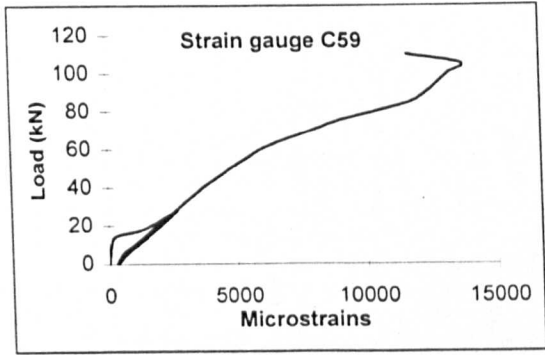
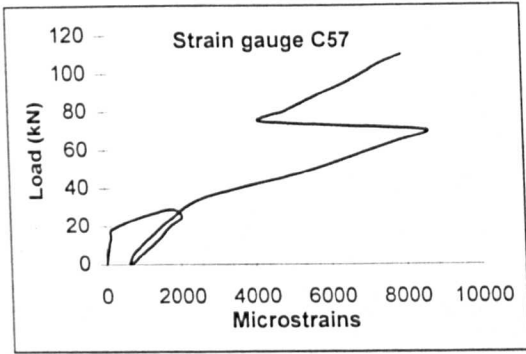
| Load (kN) | Average bond stress, MPa ( <i>Distance from the end of the bar, mm</i> ) |      |       |       |       |      |      |      |      |
|-----------|--|------|-------|-------|-------|------|------|------|------|
|           | 0  | 15   | 48    | 83    | 118   | 153  | 344  | 693  | 1059 |
| 0         | 0  | 0.06 | 0.00  | 0.01  | -0.04 | 0.09 | 0.23 | 0.32 | 0.17 |
| 10        | 0  | 0.12 | 0.01  | -0.07 | 0.05  | 0.04 | 0.23 | 0.41 | 0.39 |
| 20        | 0  | 0.05 | -0.01 | 0.12  | -0.10 | 0.14 | 0.27 | 0.67 | 0.72 |
| 30        | 0  | 0.09 | 0.04  | 0.00  | -0.03 | 0.14 | 0.33 | 0.93 | 1.03 |
| 40        | 0  | 0.06 | 0.00  | 0.16  | -0.11 | 0.16 | 0.71 | 1.17 | 1.14 |
| 50        | 0  | 0.16 | 0.00  | -0.03 | 0.14  | 0.06 | 1.26 | 2.35 | 0.54 |
| 60        | 0  | 0.06 | 0.05  | 0.16  | -0.04 | 0.57 | 1.90 | 2.46 | 1.26 |
| 70        | 0  | 0.15 | 0.03  | 0.09  | 0.45  | 0.83 | 2.44 | 2.60 | 1.62 |
| 80        | 0  | 0.17 | 0.51  | 0.76  | 1.60  | 2.05 | 2.99 | 2.41 | 2.39 |
| 85        | 0  |      | 8.75  | 3.17  | 5.17  | 4.96 | 1.65 | 3.15 |      |

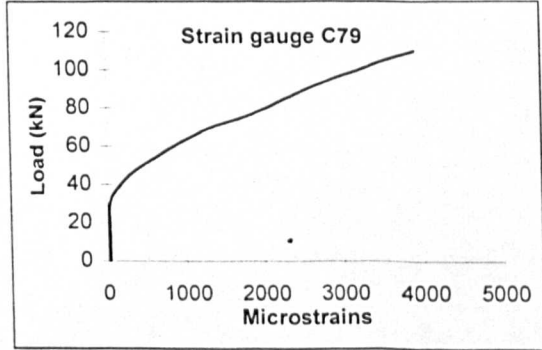
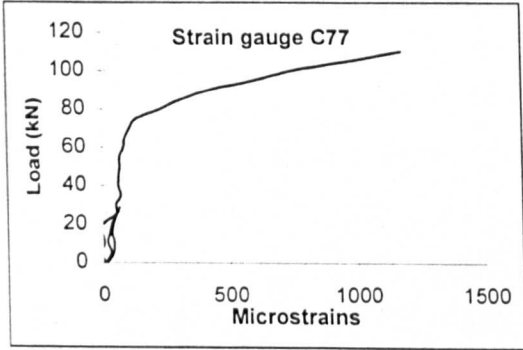
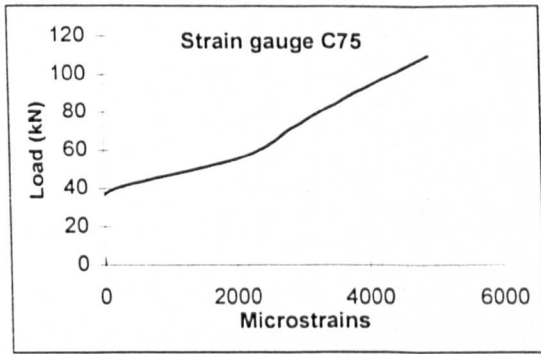
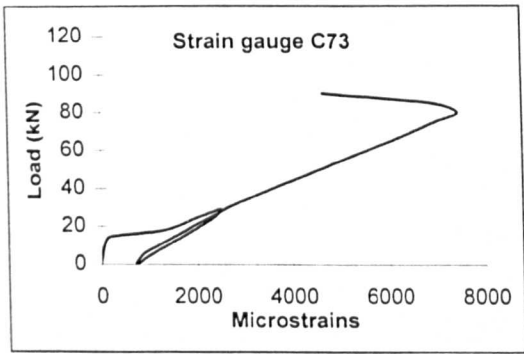


### E.3 Strain gauge readings of phase 4 beams

#### Beam GB29

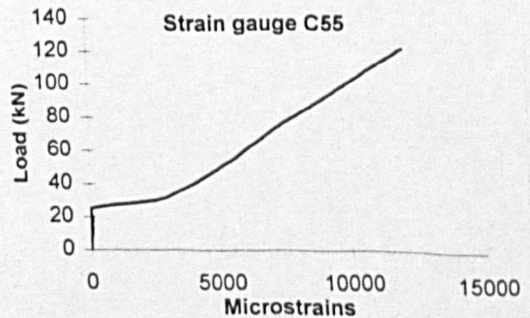
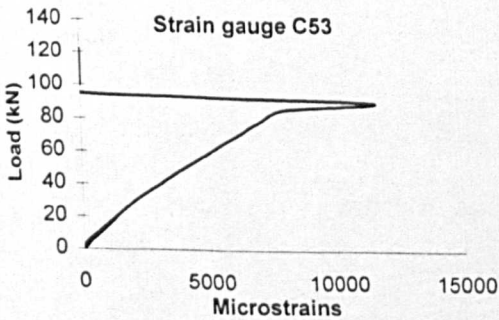
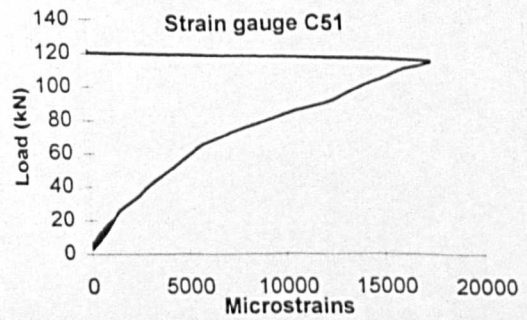
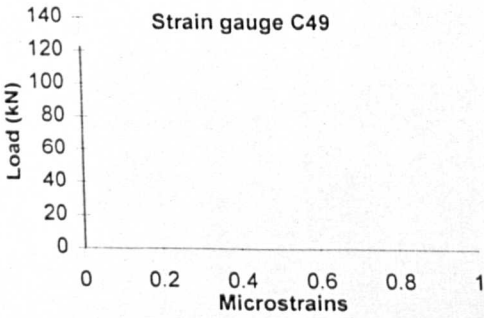
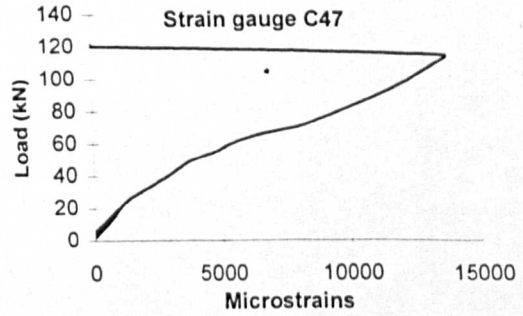
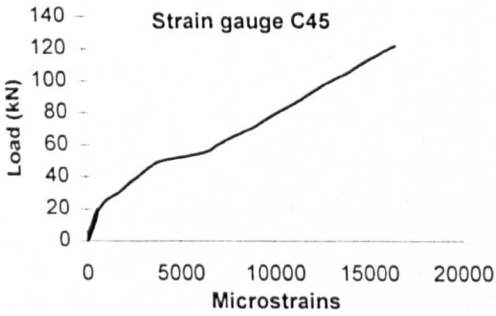
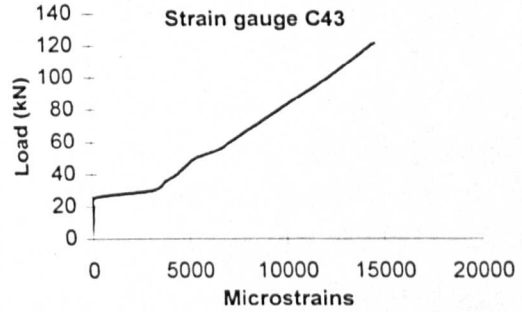
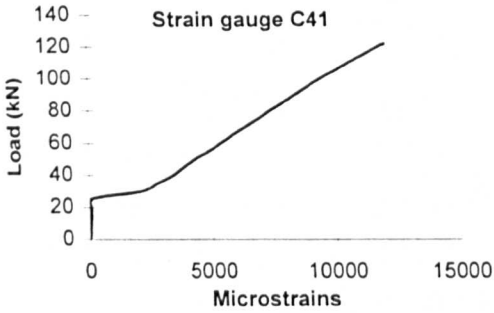


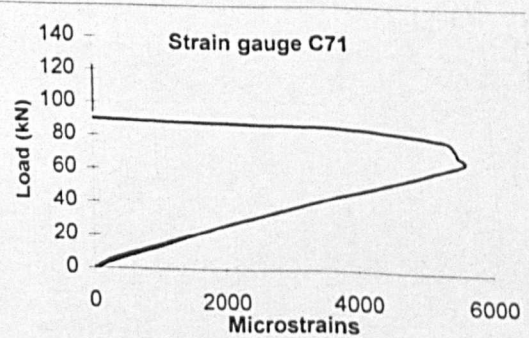
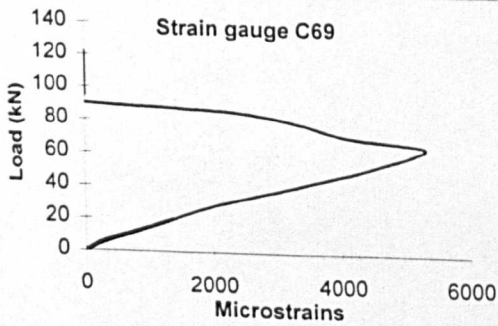
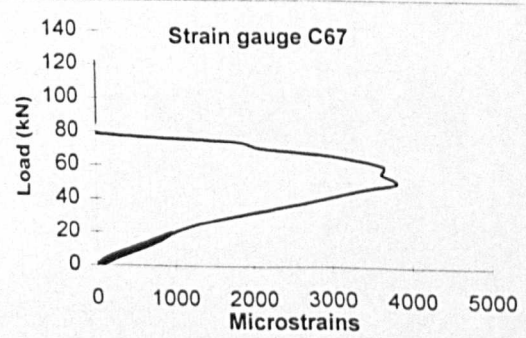
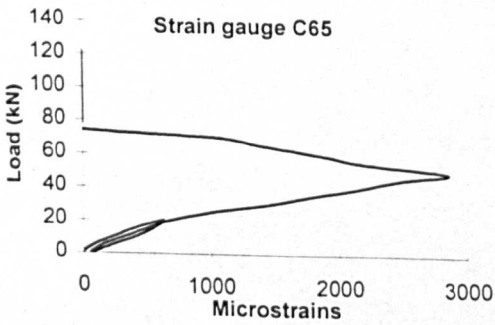
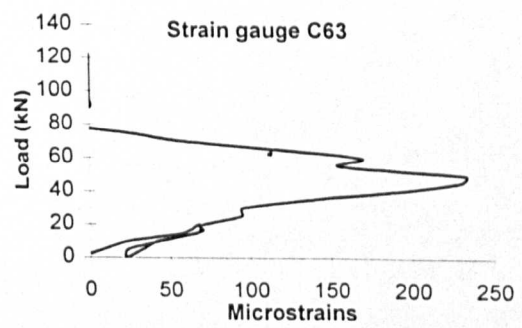
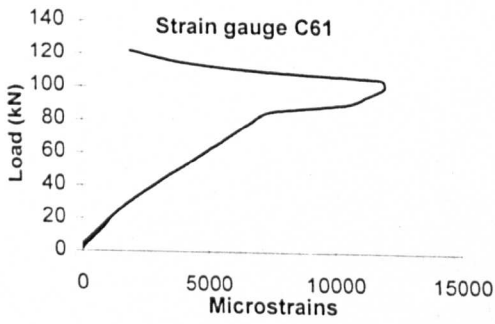
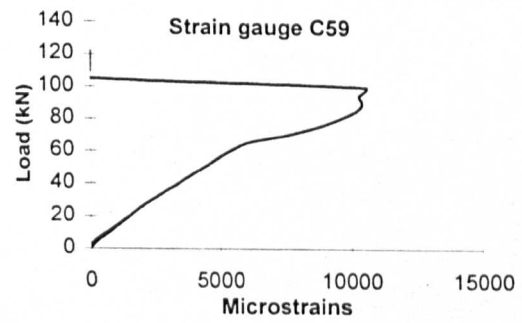
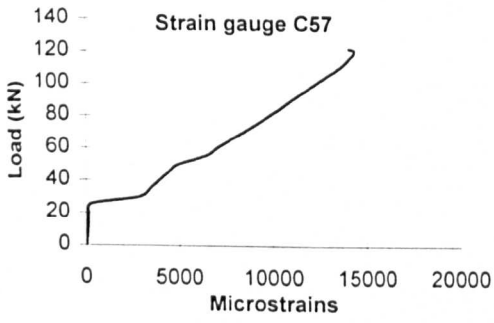


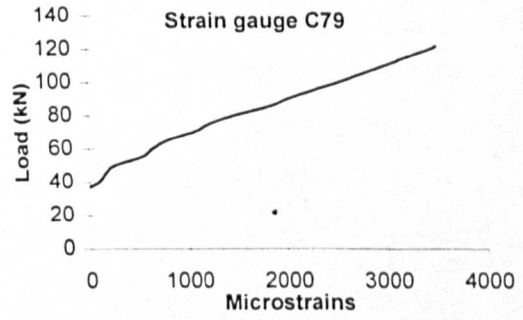
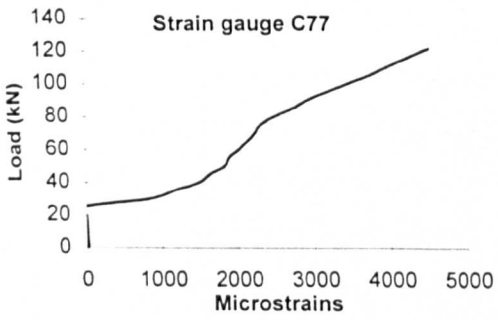
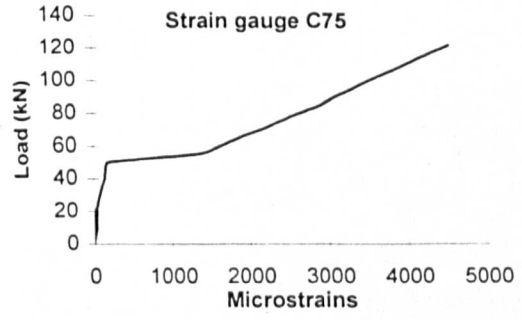
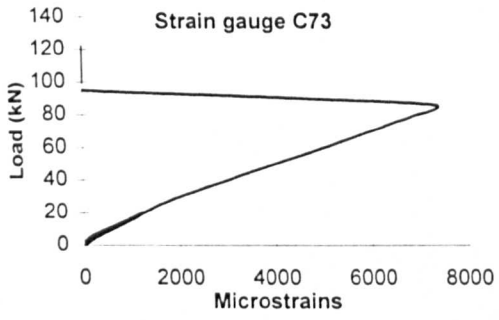


## E.3 Strain gauge readings of phase 4 beams

### Beam GB30

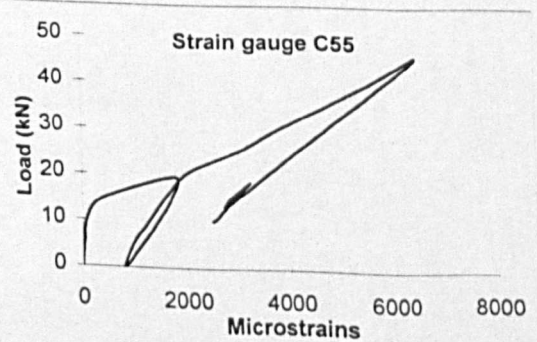
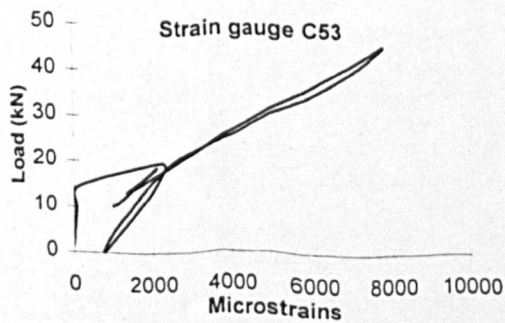
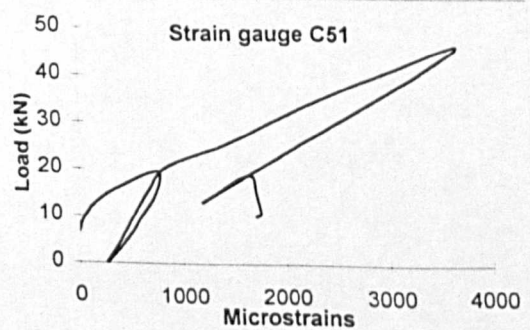
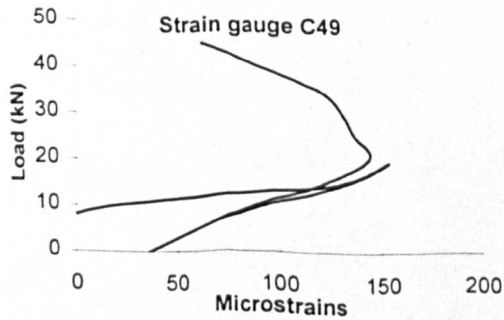
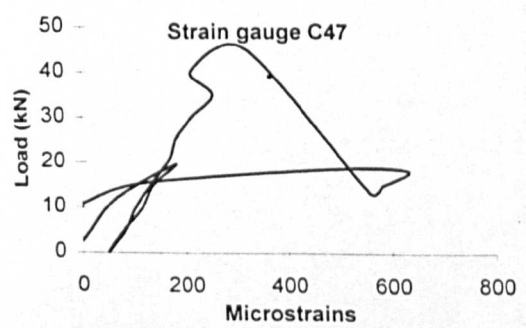
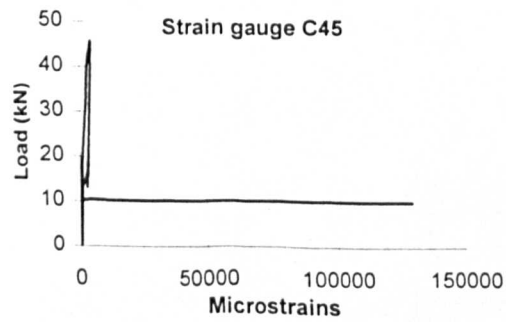
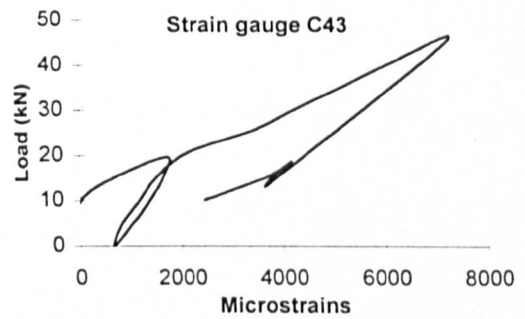
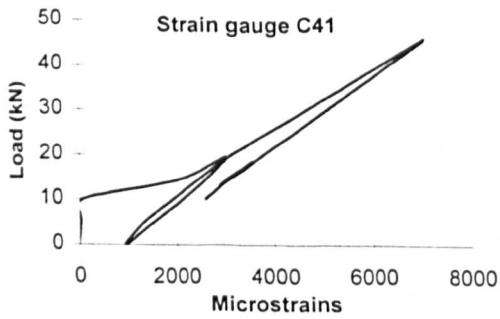


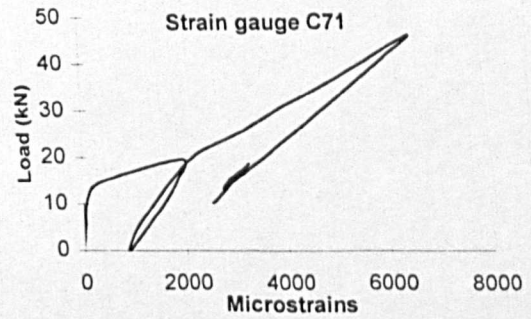
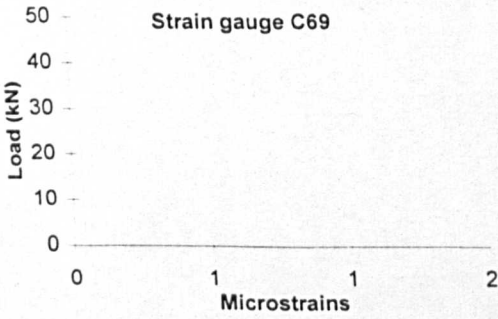
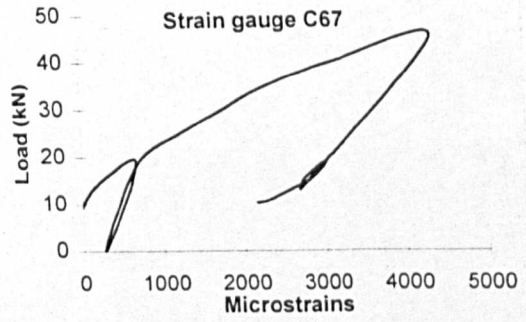
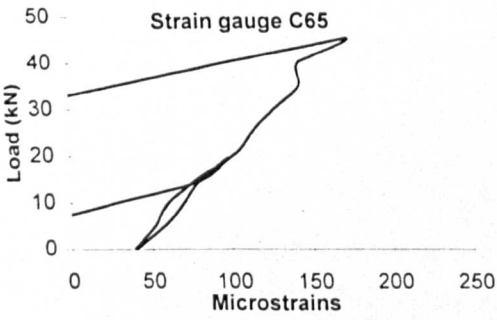
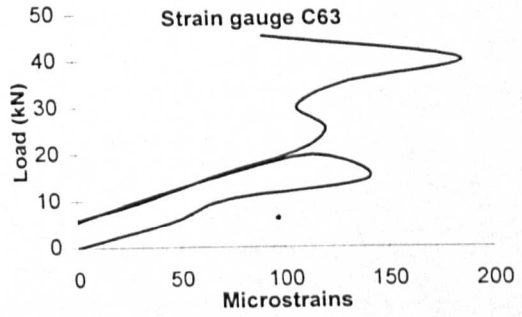
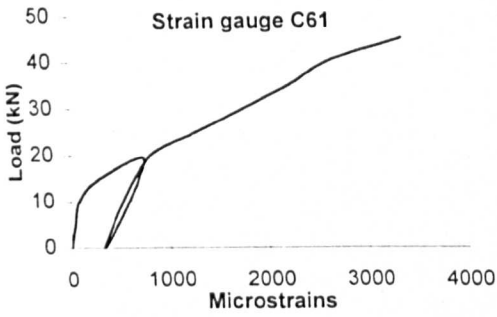
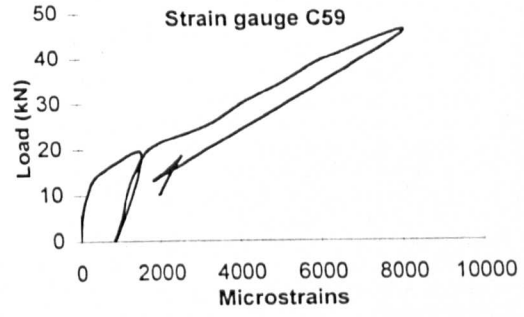
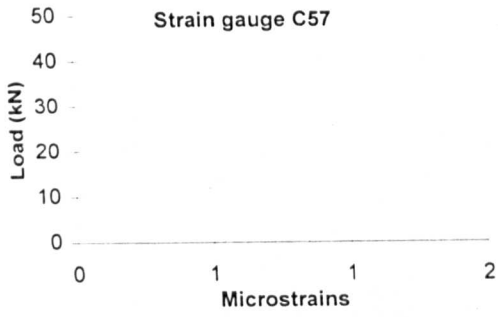


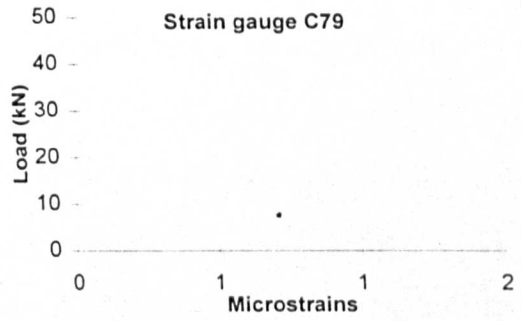
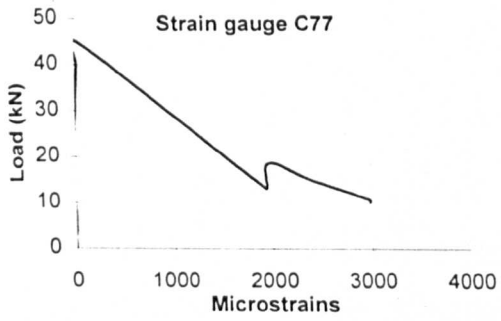
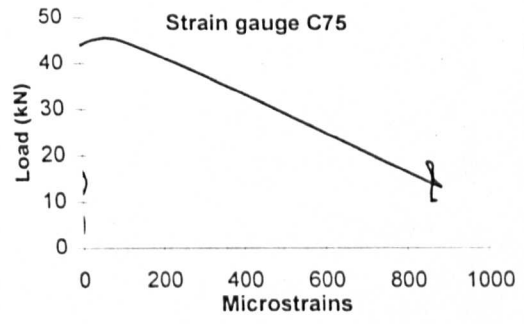
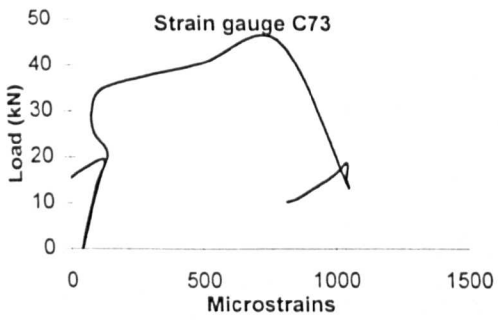


### E.3 Strain gauge readings of phase 4 beams

#### Beam GB31

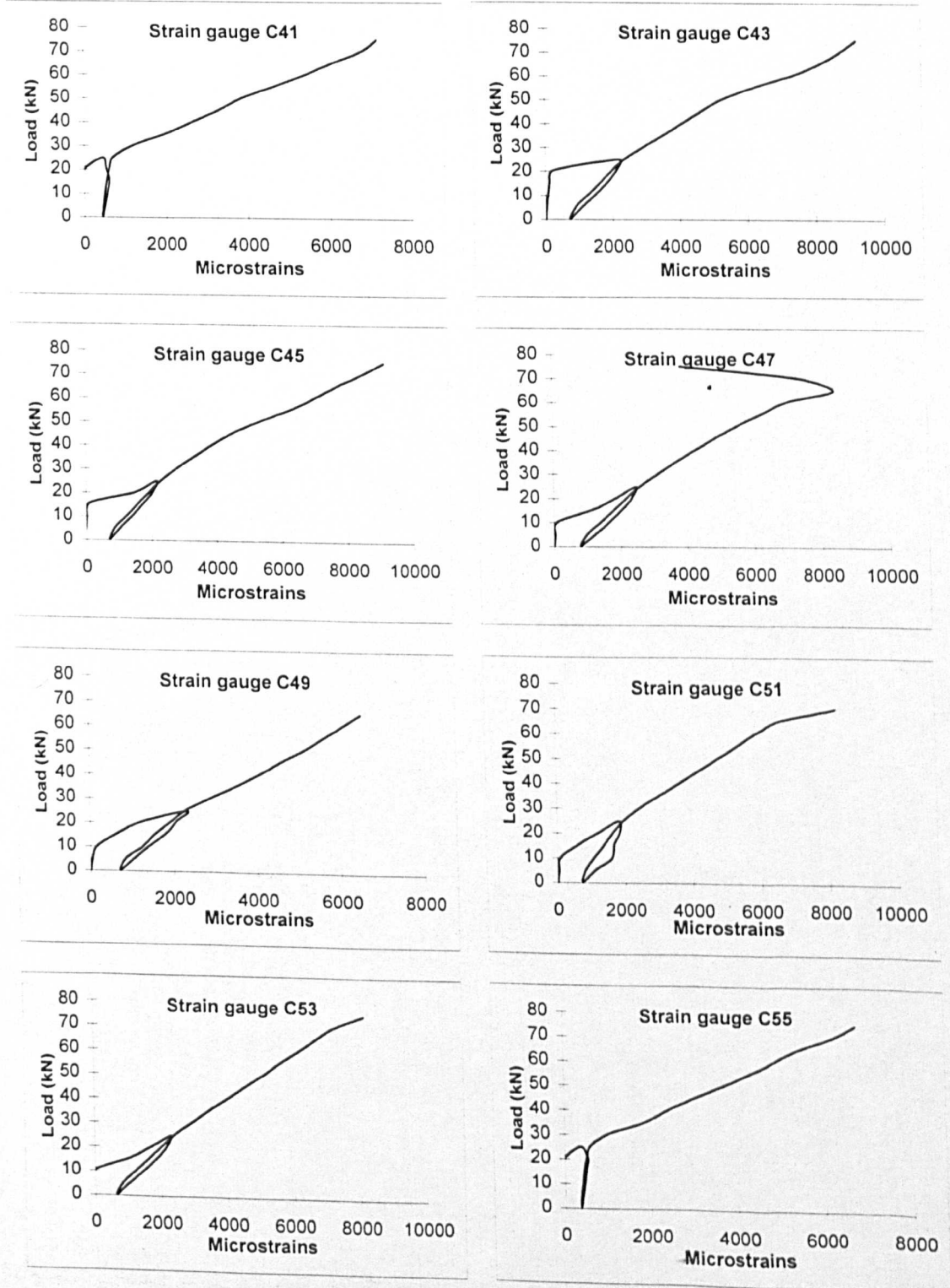


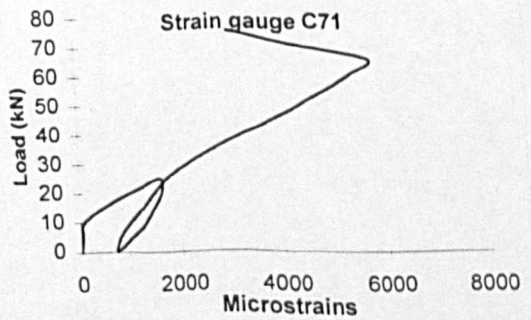
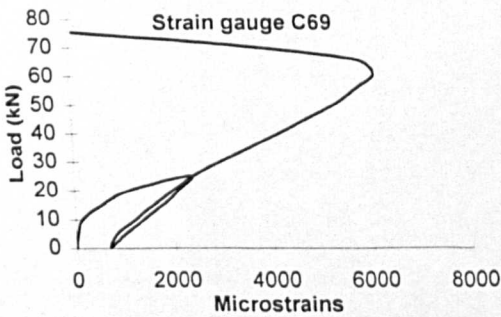
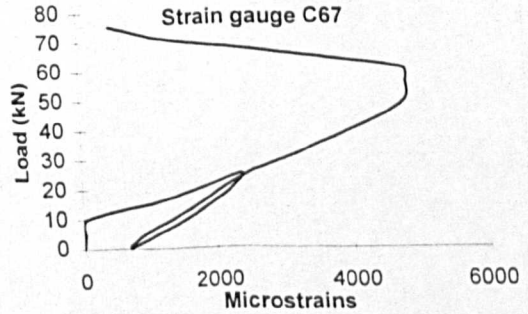
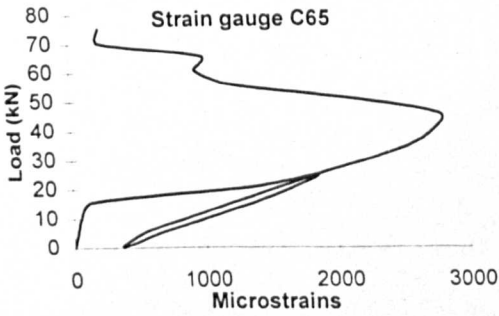
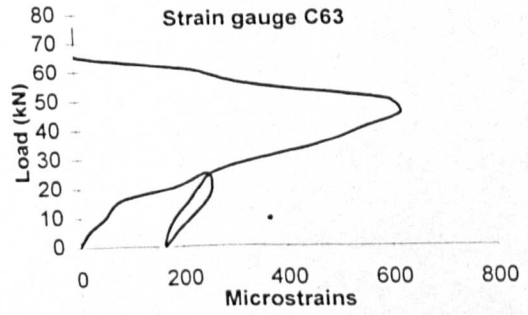
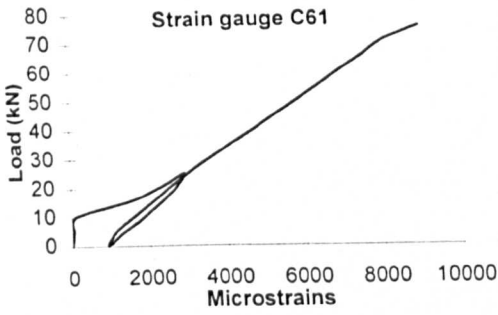
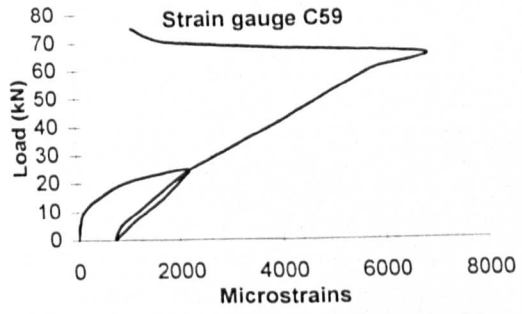
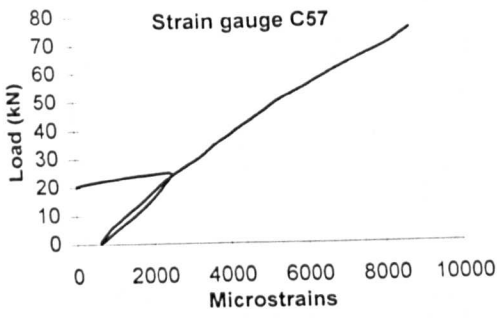


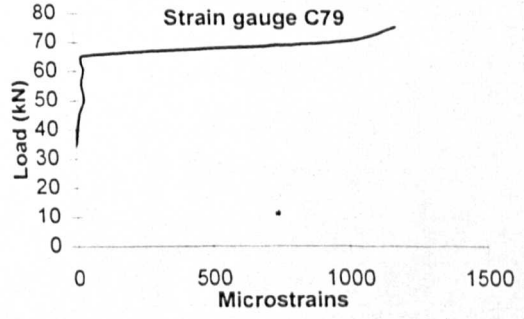
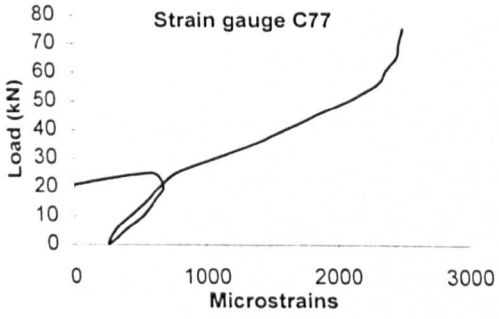
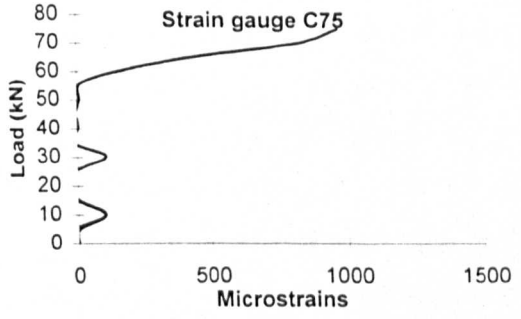
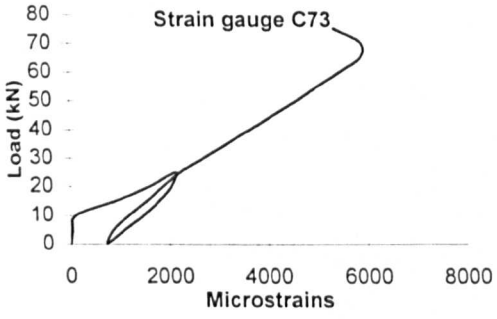


### E.3 Strain gauge readings of phase 4 beams

#### Beam CB32

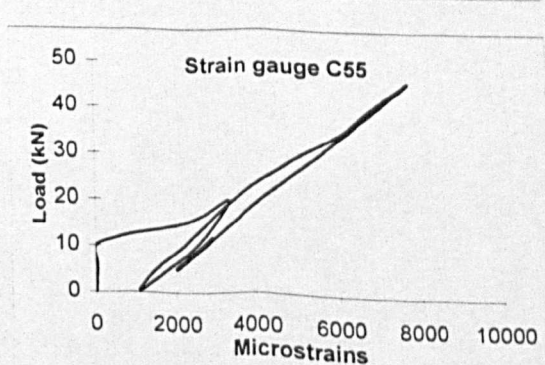
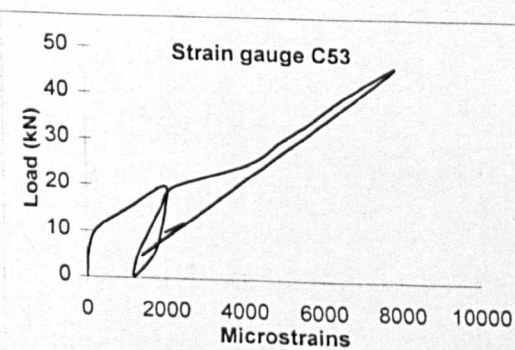
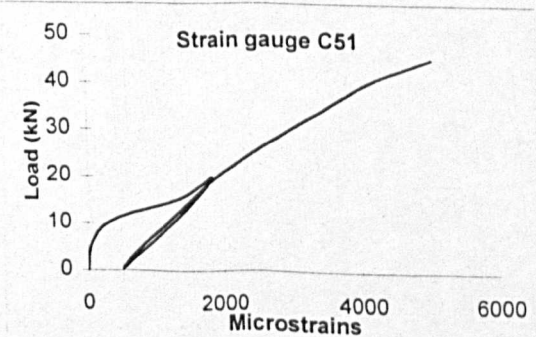
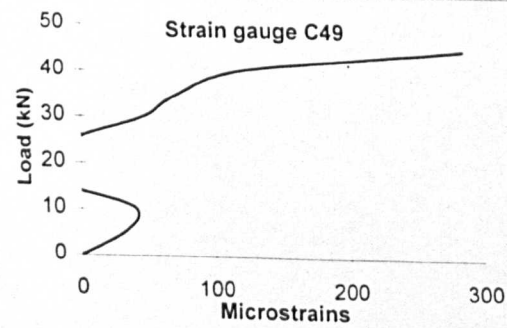
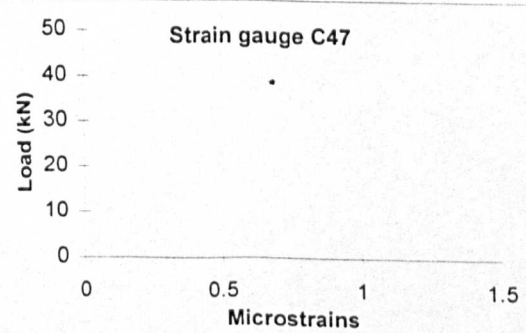
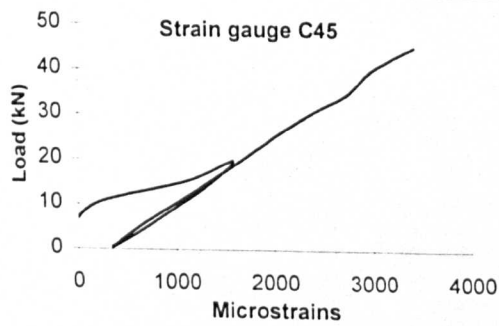
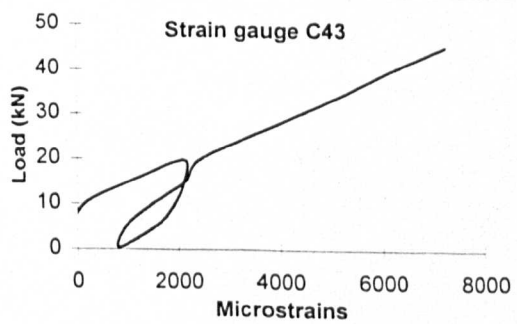
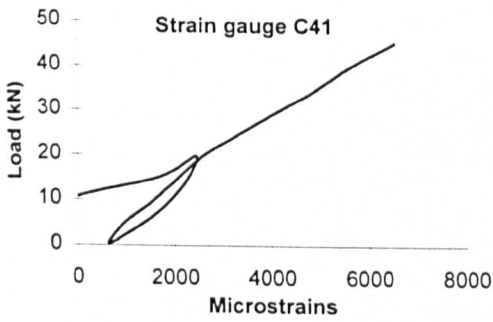


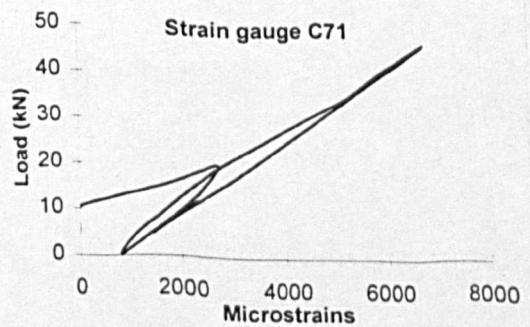
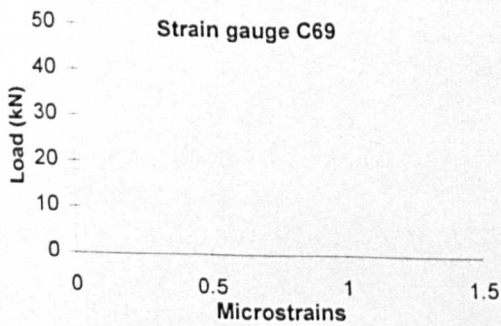
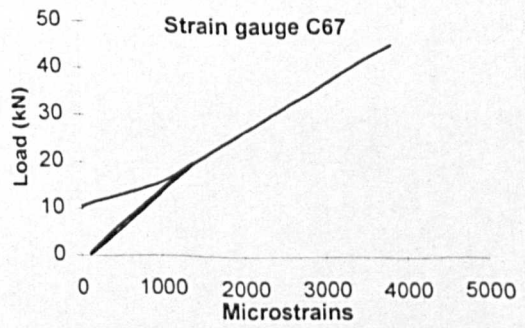
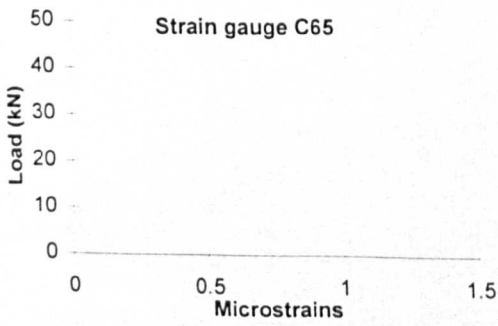
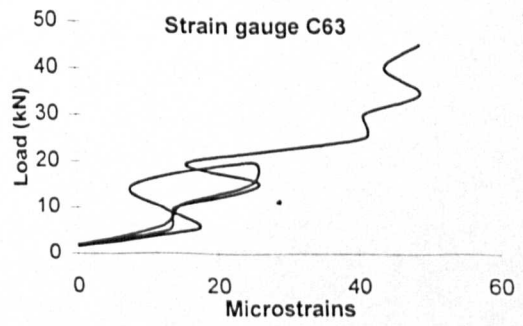
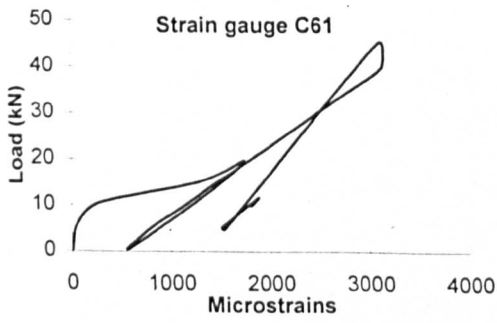
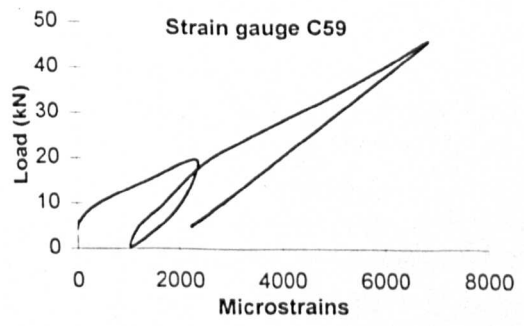
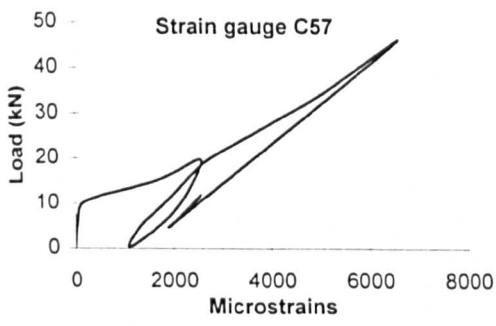


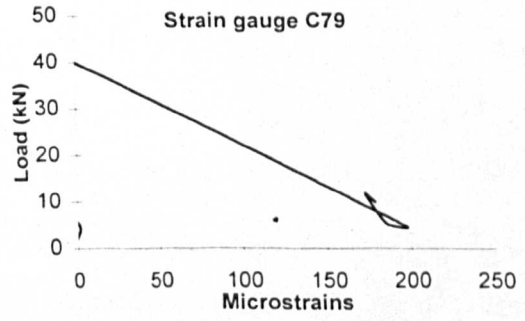
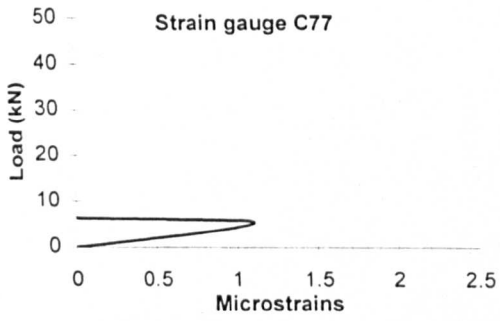
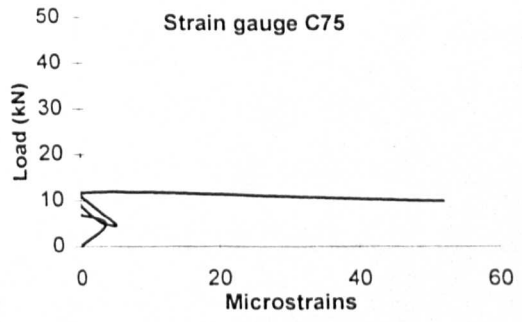
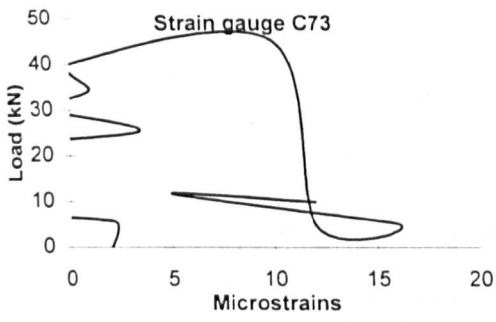


### E.3 Strain gauge readings of phase 4 beams

#### Beam CB33

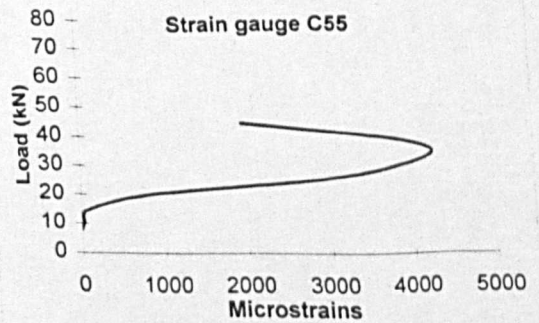
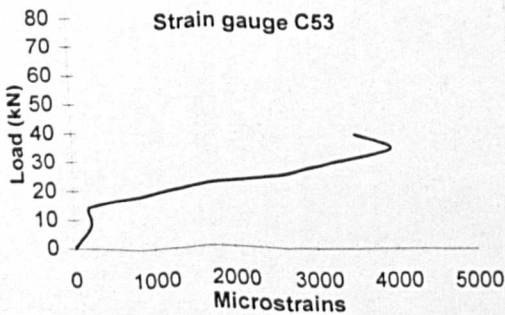
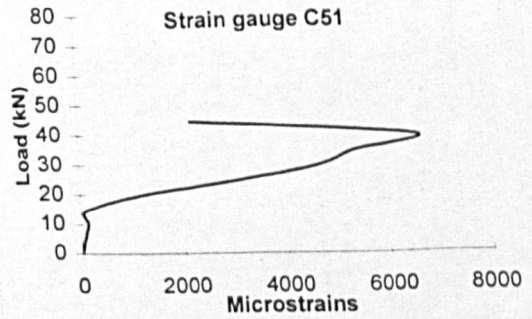
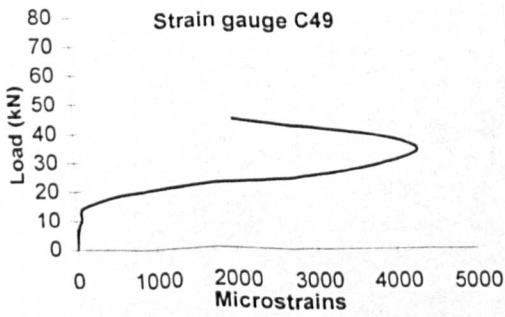
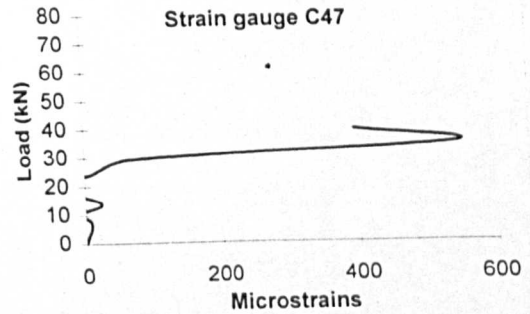
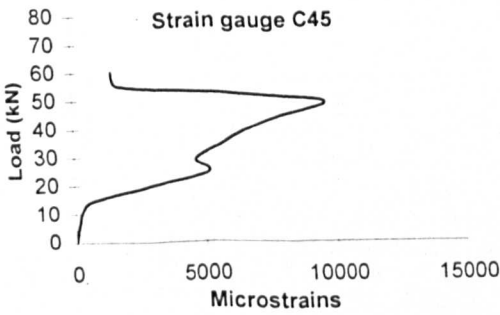
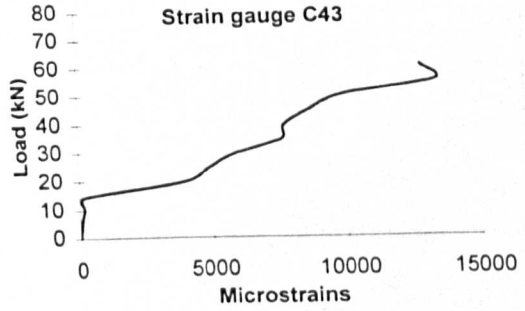
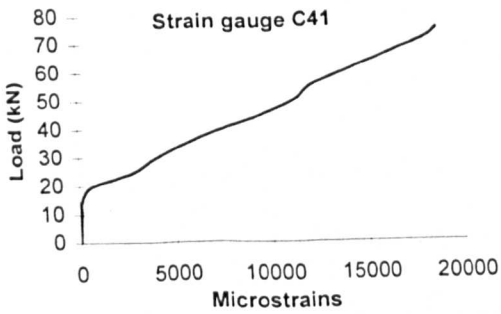


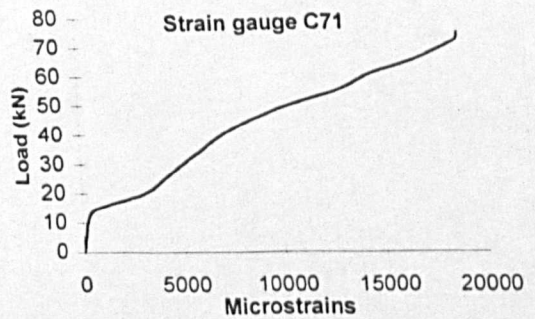
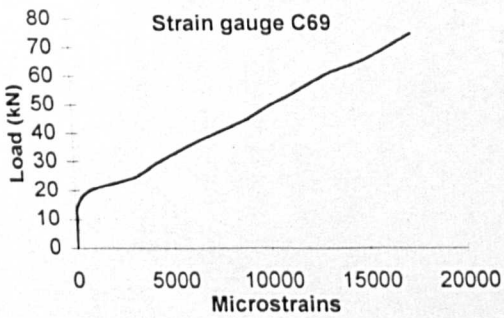
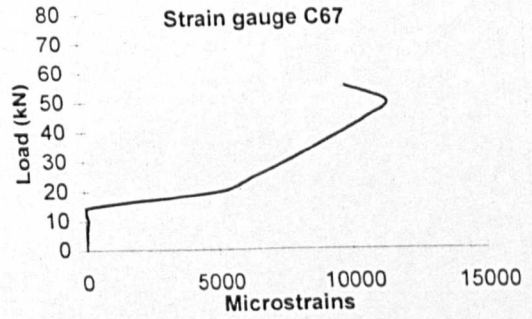
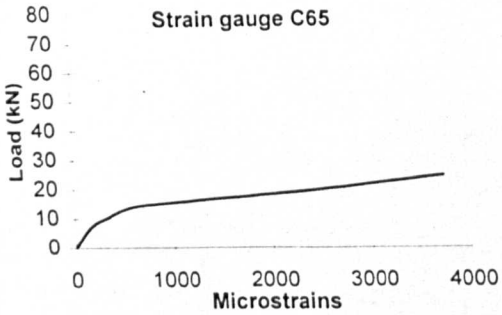
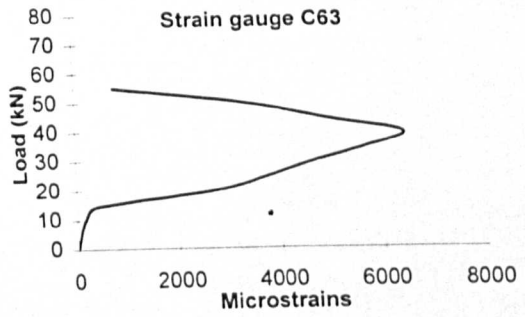
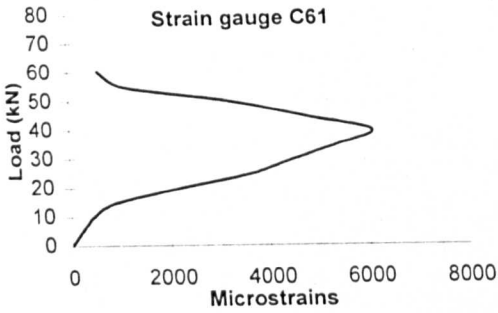
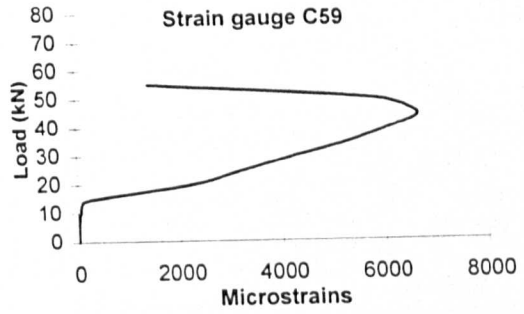
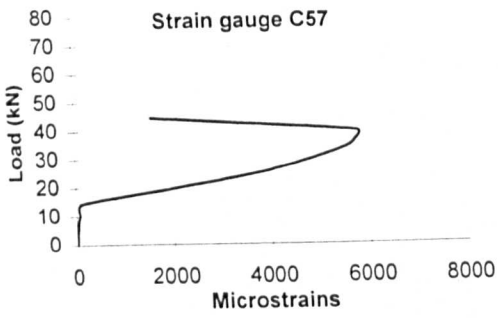


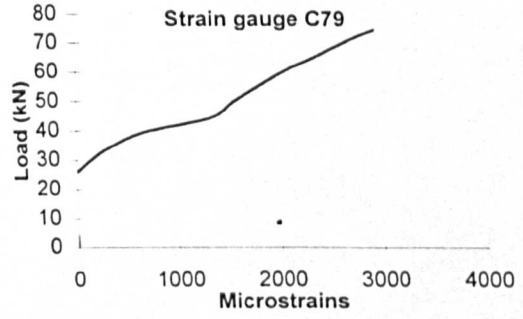
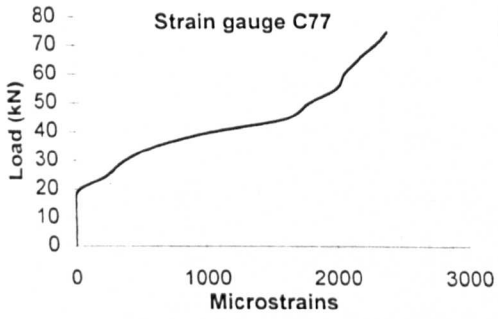
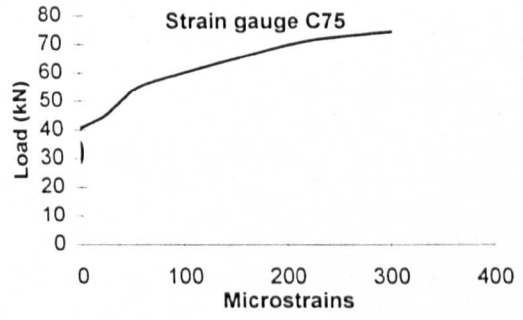
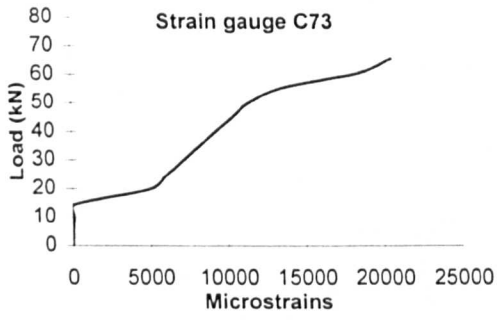


## E.3 Strain gauge readings of phase 4 beams

### Beam GB34

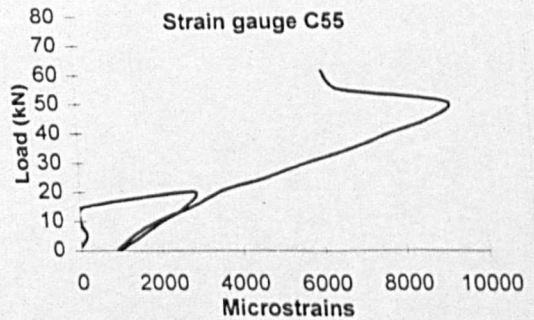
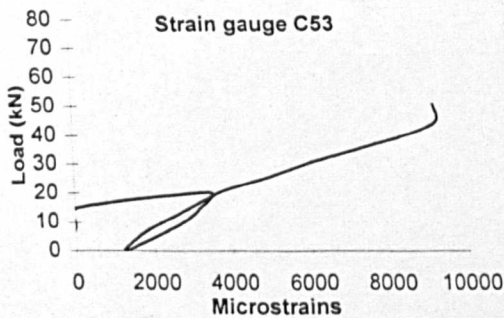
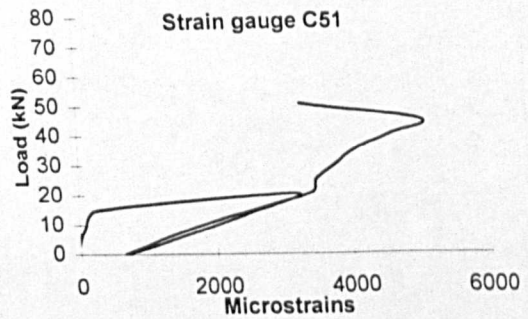
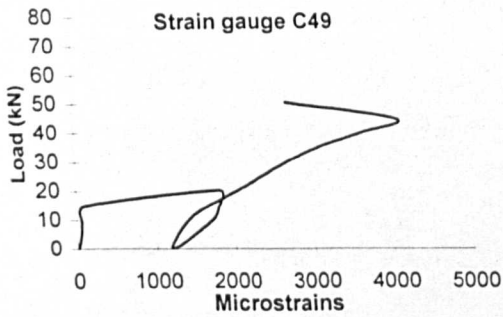
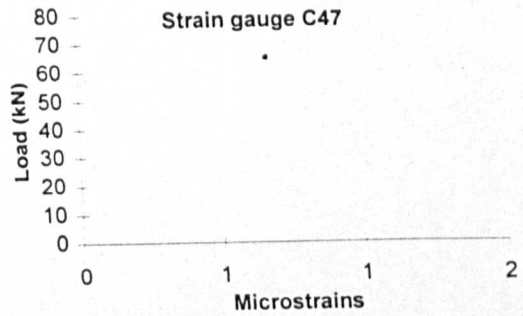
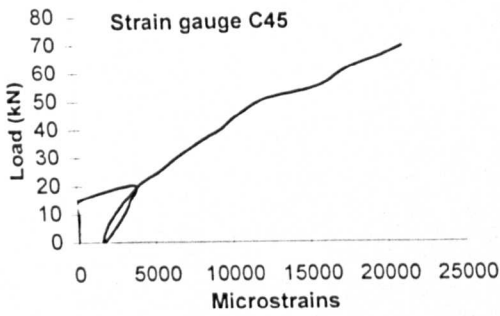
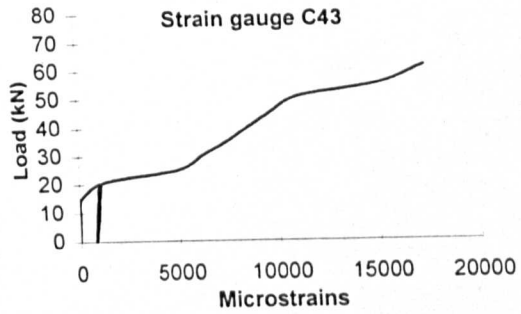
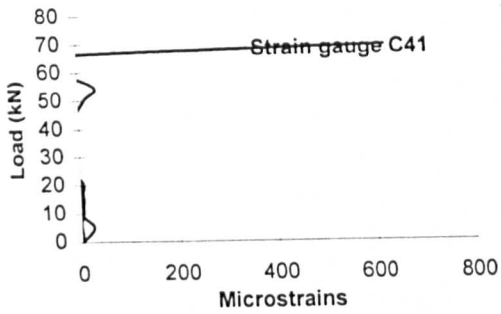


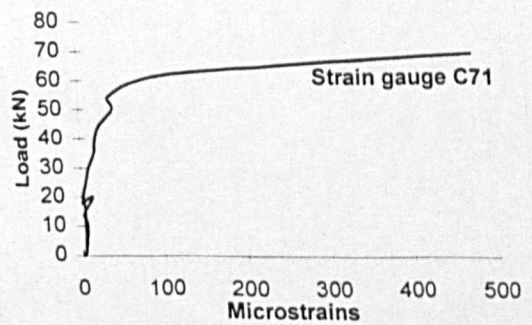
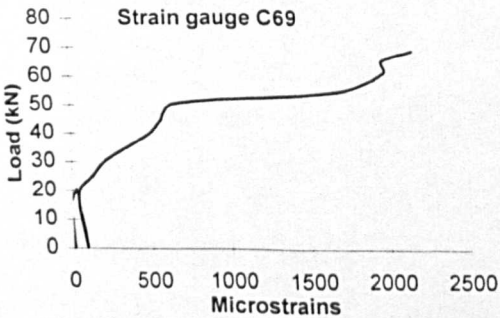
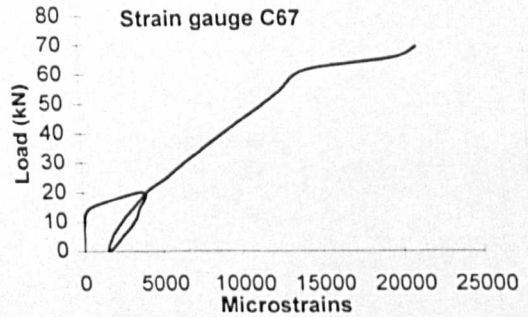
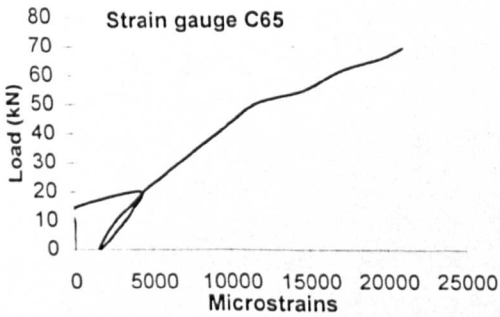
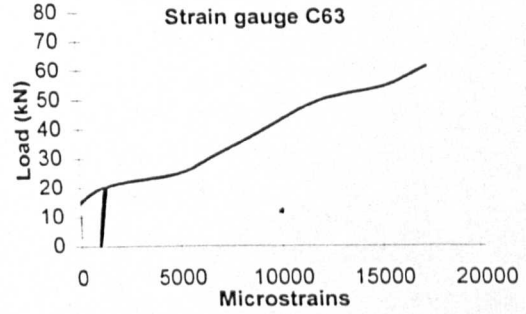
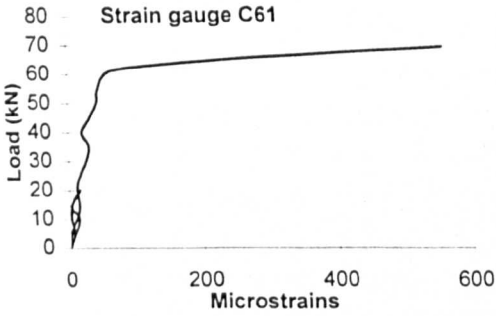
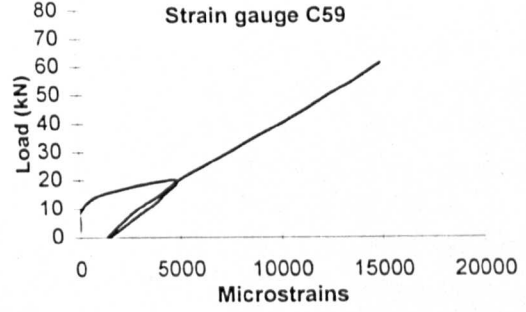
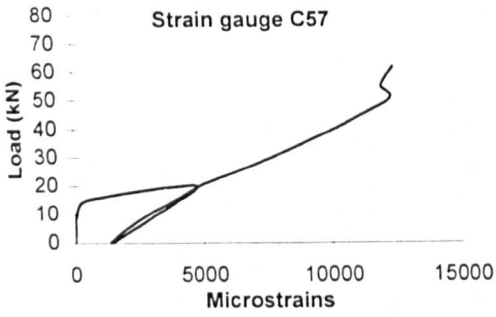


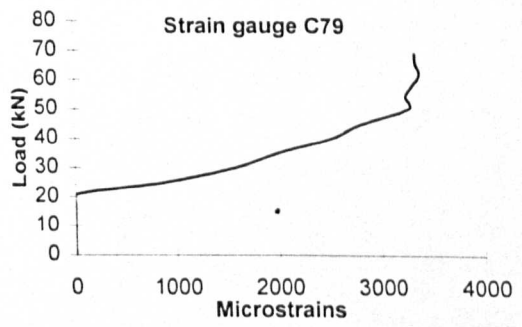
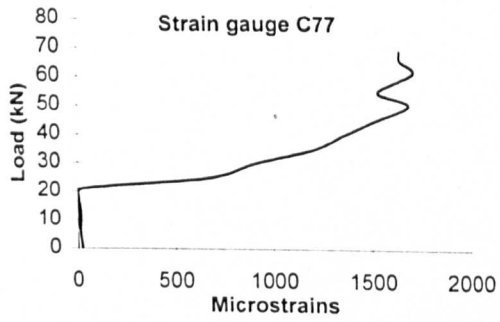
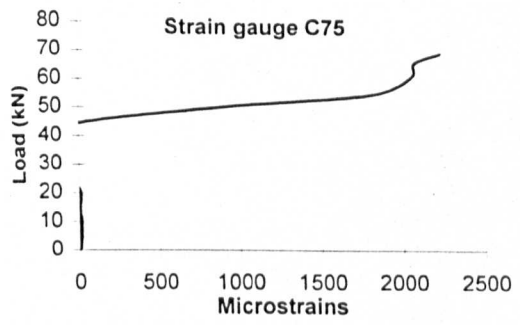
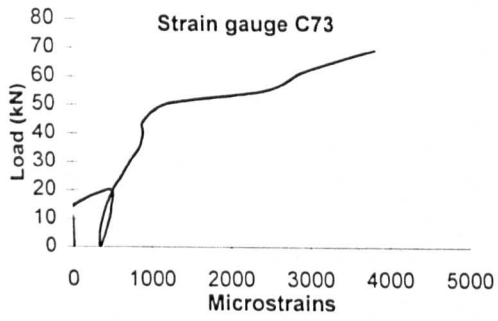


## E.3 Strain gauge readings of phase 4 beams

### Beam GB35

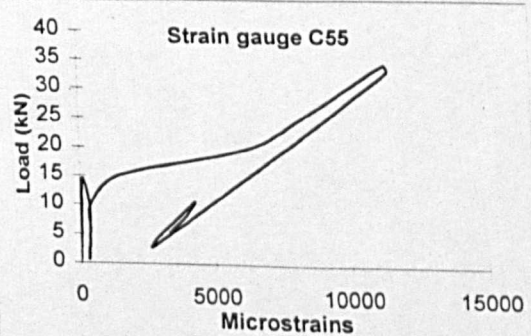
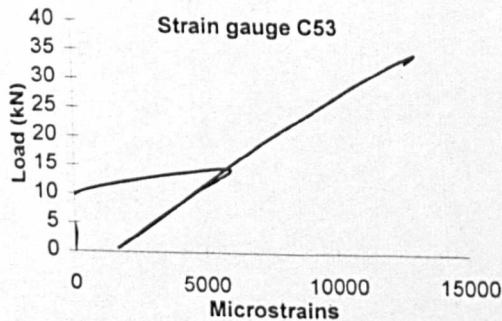
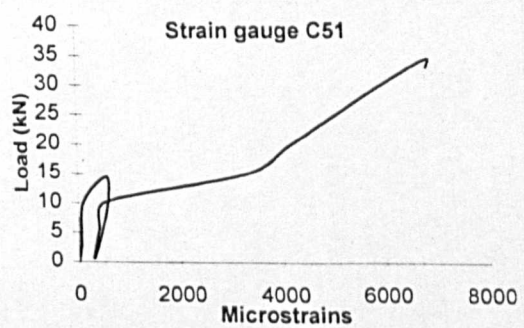
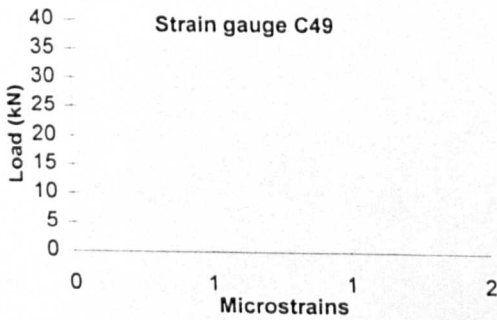
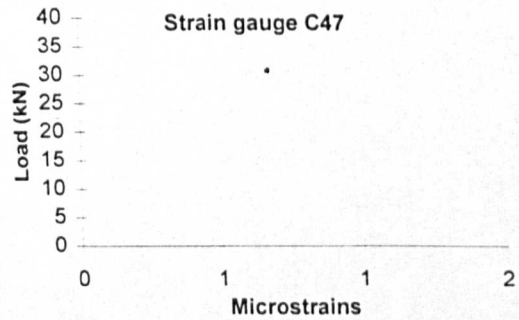
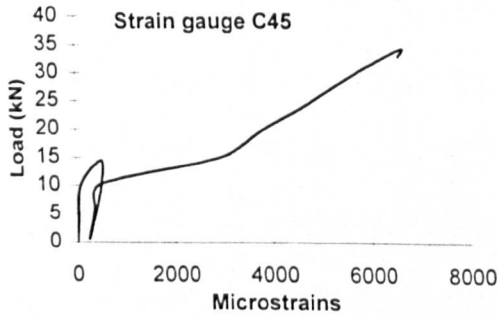
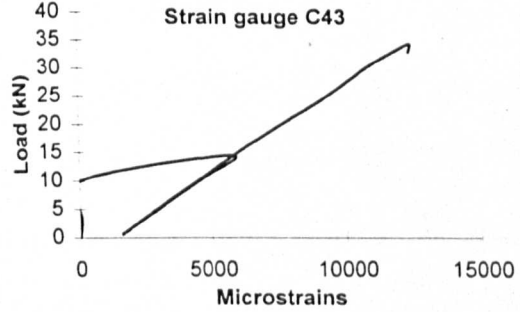
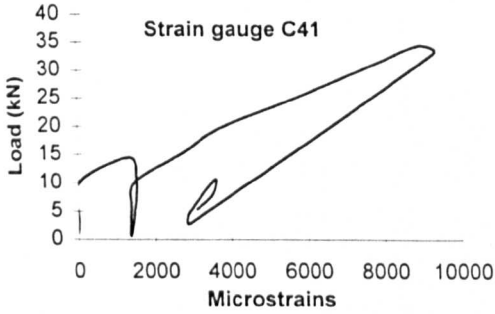


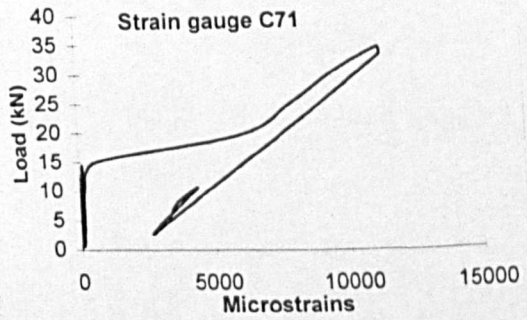
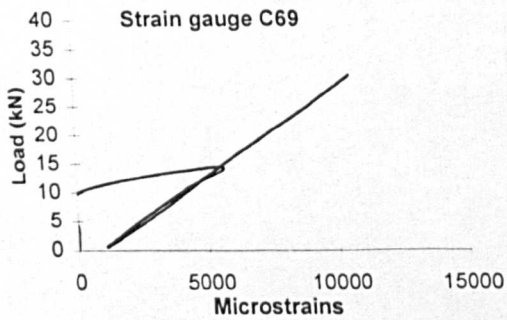
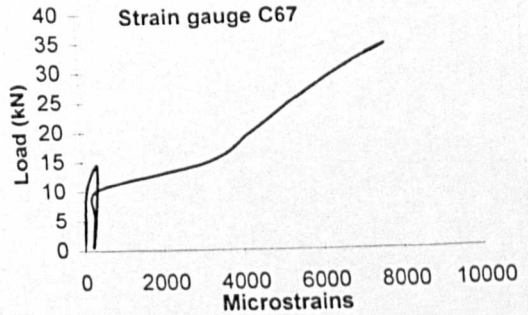
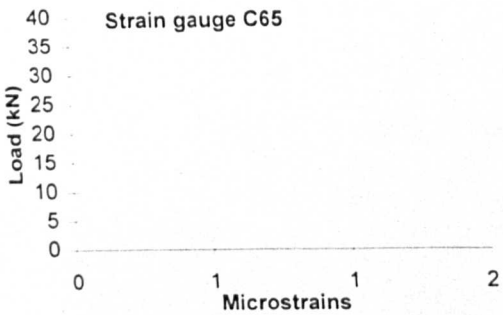
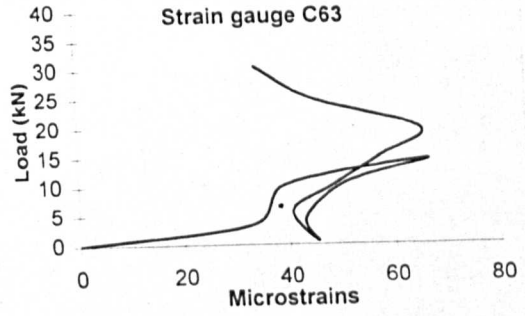
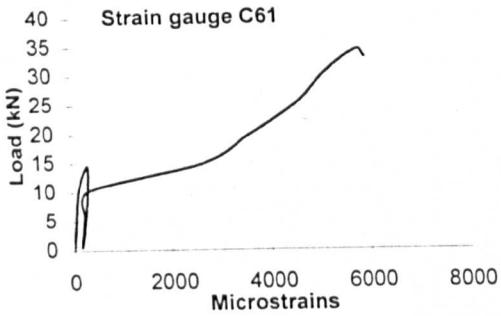
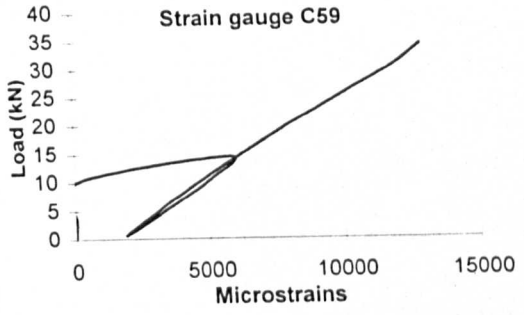
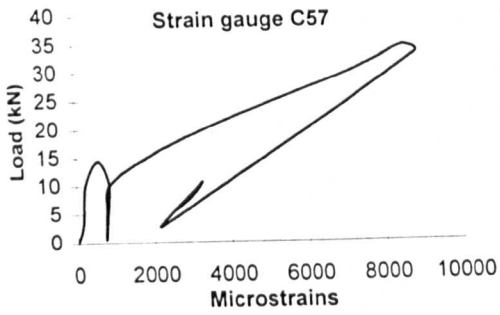


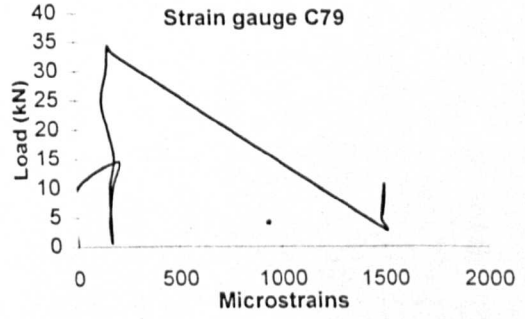
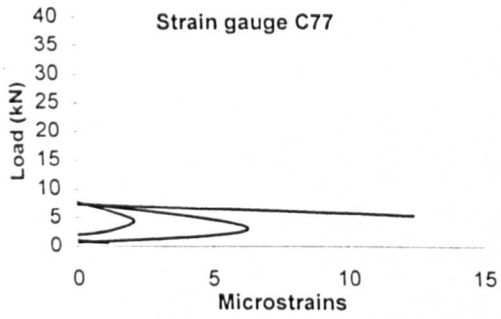
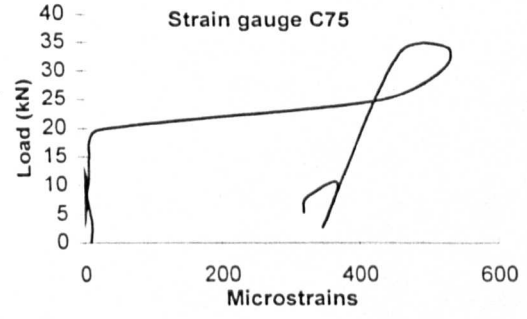
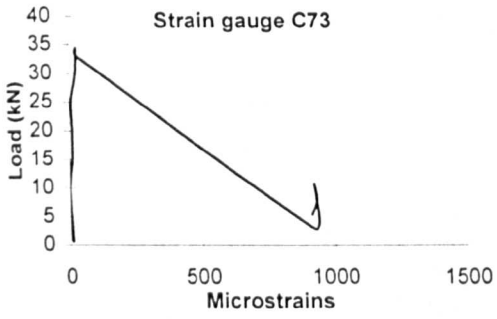


### E.3 Strain gauge readings of phase 4 beams

#### Beam GB36







## E.3 Strain gauge readings of phase 4 beams

### Beam CB37

